

Progress in Inflammation Research 91

Series Editors: Michael J. Parnham · Thorsten J. Maier

Emanuela Ricciotti · Carmela Matrone

Francis Man

Simon J. Cleary *Editors*

Imaging Inflammation

 Springer

Progress in Inflammation Research

Volume 91

Series Editors

Michael J. Parnham, Faculty of Chemistry, Biochemistry and Pharmacy, Goethe University Frankfurt am Main, Frankfurt am Main, Germany

Thorsten J. Maier, Federal Institute for Vaccines and Biomedicines, Paul Ehrlich Institute, Langen, Germany

Emanuela Ricciotti, Perelman School of Medicine, University of Pennsylvania, Philadelphia, PA, USA

Carmela Matrone, Dept. of Neurosciences, University of Naples Federico II, Naples, Italy

This book series addresses all key topical aspects of basic research, therapy and its clinical implications in the field of inflammatory diseases. It provides a unique reference source for academic and industrial biomedical researchers, drug development personnel, immunologists, rheumatologists, cardiologists, allergologists and many other relevant clinical disciplines. Each publication supplies regular scientific updates on newest developments and allow providing access to state-of-the-art techniques and technologies.

The series gathers knowledge from leading authorities on the multiple facets of inflammation research, making it a valuable asset for advanced students in biomedical sciences, early career investigators and for professionals in both basic and translational research and in the clinic. Each volume comprises a carefully selected collection of high-quality review articles on the respective field of expertise. They also introduce new investigators to the most pertinent aspects of inflammatory disease and allow established investigators to understand fundamental ideas, concepts and data on sub-fields that they may not normally follow.


Thus chapters should not comprise extensive data reviews nor provide a means for authors to present new data that would normally be published in peer-reviewed journals. Instead, the chapters should provide a concise overview and guide to the most pertinent and important literature, thus reflecting a conceptual approach rather than a complete review of the particular field of research. Moreover, each chapter should be intelligible for less experienced researchers or even newcomers to the fields of pathology, mechanisms and therapy of inflammatory disease. To this end, authors should consider introducing PhD students or postdocs who are new to the laboratory to the major concepts and the most critical literature in their chosen field of research.

Francis Man • Simon J. Cleary
Editors

Imaging Inflammation

 Springer

Editors

Francis Man 
Institute of Pharmaceutical Science
King's College London
London, UK

Simon J. Cleary
Department of Medicine
University of California, San Francisco
San Francisco, CA, USA

ISSN 1422-7746

ISSN 2296-4525 (electronic)

Progress in Inflammation Research

ISBN 978-3-031-23660-0

ISBN 978-3-031-23661-7 (eBook)

<https://doi.org/10.1007/978-3-031-23661-7>

© The Editor(s) (if applicable) and The Author(s), under exclusive license to Springer Nature Switzerland AG 2023

This work is subject to copyright. All rights are solely and exclusively licensed by the Publisher, whether the whole or part of the material is concerned, specifically the rights of translation, reprinting, reuse of illustrations, recitation, broadcasting, reproduction on microfilms or in any other physical way, and transmission or information storage and retrieval, electronic adaptation, computer software, or by similar or dissimilar methodology now known or hereafter developed.

The use of general descriptive names, registered names, trademarks, service marks, etc. in this publication does not imply, even in the absence of a specific statement, that such names are exempt from the relevant protective laws and regulations and therefore free for general use.

The publisher, the authors, and the editors are safe to assume that the advice and information in this book are believed to be true and accurate at the date of publication. Neither the publisher nor the authors or the editors give a warranty, expressed or implied, with respect to the material contained herein or for any errors or omissions that may have been made. The publisher remains neutral with regard to jurisdictional claims in published maps and institutional affiliations.

This Springer imprint is published by the registered company Springer Nature Switzerland AG
The registered company address is: Gewerbestrasse 11, 6330 Cham, Switzerland

Compliance with Ethical Standards

Funding: *Francis Man has received salary support from the Sackler Institute of Pulmonary Pharmacology at King's College London. Simon Cleary received salary support from an American Society of Transplantation/CSL Behring Fellowship Basic Science Research Grant and a National Blood Foundation Early-Career Scientific Research Grant from the Association for the Advancement of Blood & Biotherapies.*

Conflict of Interest: *Francis Man is an employee and shareholder of GE HealthCare. The views expressed are his own and not necessarily those of GE HealthCare. Simon Cleary has no financial conflicts of interest.*

Ethical Approval: *This chapter does not involve studies with human participants or animals.*

Preface

We are no longer entirely reliant on assessments of redness, swelling and exudate to identify inflammation by sight—many techniques are now available for molecular imaging of inflammatory responses. New imaging techniques are rapidly being adopted for use in immunology research, and these methods rarely completely supersede existing approaches. This leaves those of us interested in imaging inflammatory responses with a complex choice of which imaging method or methods to use for solving the problem at hand.

We compiled this volume to give researchers interested in the biology of inflammation and immunity a broad guide to some of the imaging techniques that are likely most useful for use in answering their research questions. The readers will find in each chapter of *Imaging Inflammation* a brief introduction to the technical aspects of the respective imaging modalities, followed by examples and discussions of their application in inflammation research.

Imaging Inflammation begins with a historical perspective on imaging on immune responses from Doreen Lau, taking us on a journey from the first observations of living cells by Antonie van Leeuwenhoek to non-invasive whole-body imaging of immune cells by positron emission tomography.

The book chapters then follow an approximate scale that starts from the largest field of view, with whole-body molecular imaging modalities, and progressively narrows down to high-resolution techniques which enable spatial visualisation of gene transcription patterns.

Nuclear imaging modalities are addressed by George Keeling and Francis Man, beginning with brief descriptions of the principles of single-photon emission computed tomography (SPECT) and positron emission tomography (PET) and the various structural classes of radiotracers. This chapter provides an overview of the use of nuclear imaging for the detection and monitoring of inflammatory diseases in patients. It then covers molecular processes involved in inflammation that have more recently become imaging targets and are mostly at the preclinical research stage, including amino acid transporters, fibroblast activation protein and markers of specific subsets of immune cells.

Magnetic resonance imaging (MRI) is another imaging modality that allows whole-body imaging as well as more organ-focused imaging. Here, Vanessa Johanssen, Niloufar Zarghami and Nicola Sibson provide their insights on MRI of neuroinflammation, with a focus on use of magnetic iron nanoparticles targeted towards markers of vascular inflammation and immune cell activation.

Matthew Muller, Jonathan Lindner and Matthew Hagen offer the reader their perspective of ultrasound imaging, using for example B-mode, Doppler, and contrast-enhanced ultrasound to explore rheumatoid arthritis, atherosclerosis and myocardial ischaemia. They demonstrate how targeted microbubbles can enable imaging of specific molecular processes non-invasively, using low-cost handheld probes.

Optical imaging is a modality crossing through a range of scales and can be used for whole-body imaging, tissue-level and subcellular imaging. In their chapter, Jen-Chieh Tseng and Jeffrey Peterson describe the use of chemiluminescence and near-infrared fluorescence for whole-body imaging of inflammation. In particular, they explore the use of reactive probes that emit light in response to the production of reactive oxygen species in inflamed tissues, as well as activatable probes that contain peptide sequences uniquely cleaved by inflammatory proteases such as cathepsins. Perhaps less well known but no less fascinating is the possibility of 3D *in vivo* fluorescence imaging, which is also briefly covered.

Photoacoustic imaging is a relatively recent imaging modality that combines an optical input signal with an ultrasonic output, combining advantages of both techniques. In this chapter by Jingqin Chen, Zhihua Xie, Liang Song, Xiaojing Gong and Chengbo Liu, readers can learn about label-free photoacoustic imaging of endogenous molecules, such as haemoglobin, and activatable probes that respond to changes in the inflammatory microenvironment. An interesting feature of photoacoustic imaging is its ability to image at different scales depending on instrument configuration, ranging from photoacoustic microscopy that images at high resolutions (a few microns laterally) but limited depths (a few millimetres) to photoacoustic tomography that can image tissues several centimetres deep but at more modest spatial resolution (a few hundred microns). The optical component also enables multispectral imaging, meaning that probes and endogenous molecules that absorb at different wavelengths can be imaged simultaneously and discriminated. This allows multiple inflammatory processes to be captured concomitantly.

Marco De Donatis, Frédéric Fercoq and Leo Carlin explore the use of intravital microscopy to image inflammation in living tissues, tracking single cells as they migrate between blood vessels and organs. In particular, they highlight how intravital microscopy allows the study of systems that are difficult to model *in vitro* because of their complexity, such as host–parasite interactions and viral infections. This chapter gives an update on the latest intravital microscopy approaches, which allow imaging of multiple markers at the same time with high temporal and spatial resolution. These features allow precise determination of cell migration, plasma extravasation and tissue remodelling in live tissues.

Finally, Kenneth Hu takes the reader to the frontier where imaging meets transcriptomics, describing how the spatial organisation of tissues can be mapped

with the low bias and high dimensionality offered by mRNA sequencing. With spatial transcriptomic techniques such as multiplexed fluorescent *in situ* hybridisation, Slide-seq and ZipSeq, analysis is no longer limited to single-digit numbers of targets per sample and transcriptomes can be related to their locations of expression.

Some emerging approaches for imaging that we think will be of future interest to immunologists are not yet covered in this series. These methods include imaging mass spectrometry, imaging mass cytometry, techniques for immunofluorescence imaging of many proteins in the same sample including histo-cytometry, electron and super-resolution microscopy approaches, lattice light sheet imaging and tissue clearing and expansion approaches for sample preparation.

We would like to stress is that there is no ‘magic bullet’ imaging modality combining the ideal characteristics of a whole-body field-of-view with high spatio-temporal resolution, high sensitivity, unlimited depth of penetration, unbiased imaging of all molecular contents of samples, zero toxicity and low cost. To efficiently advance our fields, it is therefore imperative on us as researchers to choose the techniques we use for our problems wisely and to work on improving methods for continuing progress in inflammation research and beyond.

London, UK
San Francisco, CA, USA

Francis Man
Simon J. Cleary

Acknowledgements

The editors would like to thank Prof. Mike Parnham for the invitation to shape this volume and the authors and reviewers who gave time to produce and refine its contents.

Contents

Imaging Inflammation: A Historical Perspective	1
Doreen Lau	
Nuclear Imaging of Inflammation	23
George Keeling and Francis Man	
Magnetic Resonance Imaging of Neuroinflammation	91
Vanessa A. Johanssen, Niloufar Zarghami, and Nicola R. Sibson	
Ultrasound Imaging in Inflammation Research	119
Matthew Muller, Jonathan R. Lindner, and Matthew W. Hagen	
Whole-Body Chemiluminescence and Fluorescence Imaging of Inflammation	143
Jen-Chieh Tseng and Jeffrey D. Peterson	
Photoacoustic Imaging in Inflammation Research	191
Jingqin Chen, Zhihua Xie, Liang Song, Xiaojing Gong, and Chengbo Liu	
Imaging Inflammation by Intravital Microscopy	223
Marco De Donatis, Frédéric Fercoq, and Leo M. Carlin	
Spatial Transcriptomics in Inflammation: Dissecting the Immune Response in 3D in Complex Tissues	243
Kenneth Hu	

About the Editors

Francis Man was until recently a postdoctoral scholar at King's College London, where he developed novel PET radiotracers for tracking therapeutic cells and investigated methods for imaging lung epithelial permeability. He has a PhD in Chemical Biology from King's College London and a PharmD from the University of Strasbourg. Francis is currently a Senior Scientist at GE Healthcare, in charge of the preclinical development of imaging agents.

Simon J. Cleary is a postdoctoral scholar at UCSF where he studies mechanisms of acute lung injury and develops new approaches for lung imaging under the mentorship of Mark Looney. He has a PhD in Pharmacology and a BSc in Physiology & Pharmacology from King's College London. Simon was recently awarded an early career grant from the National Blood Foundation for his research into transfusion reactions and organ transplant rejection.

Imaging Inflammation: A Historical Perspective



Doreen Lau

Abstract Inflammation is the body's response to invading pathogens, foreign particles, and abnormal cells. It is a complex set of processes orchestrated by numerous cell types and chemical signalling cascades during disease and injury. Imaging offers direct visual evidence of the cellular and molecular processes involved in inflammation. The five cardinal signs of inflammation—*calor* (heat), *dolor* (pain), *rubor* (redness), *tumor* (swelling), *penuria* (loss of function)—can be felt or seen, but identifying the exact mechanisms underlying these responses and their stimuli has required technological developments in biomedical imaging. Imaging has played a huge role in building our understanding of inflammatory processes and how these sequences of events are involved in inflammatory changes in human health and disease. This review is intended to provide a brief, and by no means complete, historical overview of imaging in inflammation and as a prelude to the subsequent chapters by other authors who will discuss the technicalities and application of advanced imaging techniques.

Keywords Imaging inflammation · Germ theory · Humoral and Cell-mediated immunity · Microscopy · CT · SPECT · PET · Ultrasound · Photoacoustic imaging · MRI

If I have seen further, it is by standing upon the shoulders of giants.
Sir Isaac Newton (1675)

D. Lau (✉)

Oxford Centre for Immuno-Oncology, Nuffield Department of Medicine, University of Oxford, Oxfordshire, UK

e-mail: donc0882@ox.ac.uk

1 Microscopy for Imaging Inflammation: The Germ Theory

The history of imaging inflammation began in the seventeenth century when Antonius van Leeuwenhoek (1632–1723) made his first observation of unicellular microorganisms under the microscope (Fig. 1). Known as the “Father of Microbiology,” van Leeuwenhoek was one of the first microscopists to discover the existence of microorganisms [1]. Raised in Delft in what was then known as the Dutch Republic,



Fig. 1 Illustrations from the works of Antonius van Leeuwenhoek, one of the world’s first microscopists to examine the details of unicellular life. (a) Portrait of van Leeuwenhoek holding his simple microscope. From *Antonius van Leeuwenhoek. Mezzotint* by J. Verkolje, 1686. Public Domain Mark. Wellcome Collection. (b) An illustration on the design of van Leeuwenhoek’s single-lens microscopes by Henry Baker. From *Arcana naturae detecta / Ab Antonio van Leeuwenhoek, 1695*. Wellcome Collection. (c) A replica of van Leeuwenhoek’s simple microscope. From *Leeuwenhoek simple microscope (copy)*, Leyden, 1901–1930. Science Museum, London. Wellcome Collection. (d) Drawings from van Leeuwenhoek’s notes, depicting the size, shape, and movement of bacteria in a dental plaque sample observed under the microscope. From *Arcana naturae detecta/Ab Antonio van Leeuwenhoek*. (b, c, d) Reproduced with permission under CC-BY-4.0 licence (<https://creativecommons.org/licenses/by/4.0/>). Credit: Wellcome Collection

van Leeuwenhoek was a cloth merchant running a draper's shop when he developed an interest in lens-making, as he wanted a better tool to examine the thread counts and quality of linen and other fabrics better than the magnifying lenses of his time. Van Leeuwenhoek was a great admirer of Robert Hooke's *Micrographia* (1665) when he began making his own improvements to the microscope. He made more than 500 simple microscopes in his lifetime, using crafting methods that he kept as trade secrets. Each microscope consisted of single convex lens held in a silver or copper frame with very short focal length, a magnification factor of about 275 times, and could resolve objects as small as 1 micrometre [2]. Although van Leeuwenhoek was largely self-taught with no formal scientific training, his skills of careful observation and great patience enabled him to make scientific discoveries of fundamental importance and demonstrate the existence of unicellular life. In 1674, he was the first to see this unimagined world of bacteria and protozoa using his single-lens microscopes. He curiously termed the moving objects as *animalcules*, or tiny animals, and accurately described their structures, size, and behaviour [3]. In letters written to the Royal Society of London between 1681 and 1683, van Leeuwenhoek described and illustrated the different types of bacteria present in dental plaque samples. He compared his own oral and faecal microbiota and recorded the morphological differences between bacteria found in different body sites and between health and disease [4]. These discoveries made under the light microscope provided the first direct observation of bacteria, supporting early claims about the germ theory and the existence of disease-causing microorganisms [1]. The light microscope would remain the workhorse for imaging microorganisms until the 1930s, when transmission electron microscopy (TEM) was invented by Ernst Ruska (1906–1988). TEM uses electrons of very short wavelength instead of visible light as the source of illumination and heavy metal staining techniques to produce high resolution images of microorganisms. It provides superior resolving power that captures detailed subcellular structures of bacteria and magnifies the nanometre sizes and geometrical shapes of viruses compared to the micrometre scale detected by light microscopy. Morphological differences between viruses that caused infectious diseases in those days, e.g., the smallpox and chickenpox viruses, have been demonstrated using electron microscopy [5].

In addition to his contributions to the field of microbiology, van Leeuwenhoek performed one of the earliest intravital microscopy experiments, which confirmed William Harvey's theory on blood circulation (1628). Using a special aquatic microscope he had designed, and small live eels mounted in water through a glass tube, van Leeuwenhoek observed the movement of erythrocytes through the capillaries in the tail fins [6]. He demonstrated the transition of blood from the arterial to the venous system and depicted the size and shape of *red corpuscles*, i.e., erythrocytes. He went on to describe and measure erythrocytes and their nuclei in other fishes, amphibians, and mammals, despite not fully understanding the function of blood transportation and the role of microcirculation in inflammation [7]. Van Leeuwenhoek meticulously dissected his specimens with an open razor into thin sections and carefully enclosed them in small paper packets and into larger envelopes attached with his letters to the Royal Society for peer review. He would make

every effort not to introduce tiny animals from any other sources into his experiments and only used snow water which was the purest water available then to replenish evaporated water containing the microorganisms he was examining as he was acutely aware of contamination issues. To provide a measurement scale for this invisible new world, he developed a practical system of micrometry for describing the size of the unicellular organisms he observed under the microscope: “bacteria in pepper-water (2–3 μ), a human erythrocyte (7.2 μ), a hair from his beard (100 μ), and a grain of coarse sand (870 μ).” By the time of his death in 1723, van Leeuwenhoek had written at least 190 letters to the Royal Society detailing his observations of the *animalcules*, which still hold largely true today.

2 Imaging Leukocyte Function in Humoral and Cell-Mediated Immunity

Microscopes have been integral to inflammation research ever since, with generations of intravital microscopists peering curiously into the invisible world to examine the wonders of nature. Henri Dutrochet (1776–1847), a French botanist and physiologist best known for his work on osmosis and contributions to the cell theory, was the first to report his microscopic observations of leukocytes in 1824 [8]. Dutrochet used a simple microscope for his experiments on plant and animal tissues, instead of a compound microscope as the instrument was practically useless in those days due to chromatic aberration and mechanical instability [9]. He described seeing the movement of *vesicular globules*, i.e., leukocytes, through the transparent mucous membrane of living frogs whereby *masses of them surround both the blood vessels and migrated into tissues during acute inflammation* [9]. In 1839, the German anatomist Rudolf Wagner (1805–1864) provided the first detailed drawing of leukocyte rolling in blood vessels [10]. Described as *lymph-corpuscles*, these leukocytes were seen moving more slowly than other blood cells and in close contact with the vessel wall in the webbed feet of a grass frog.

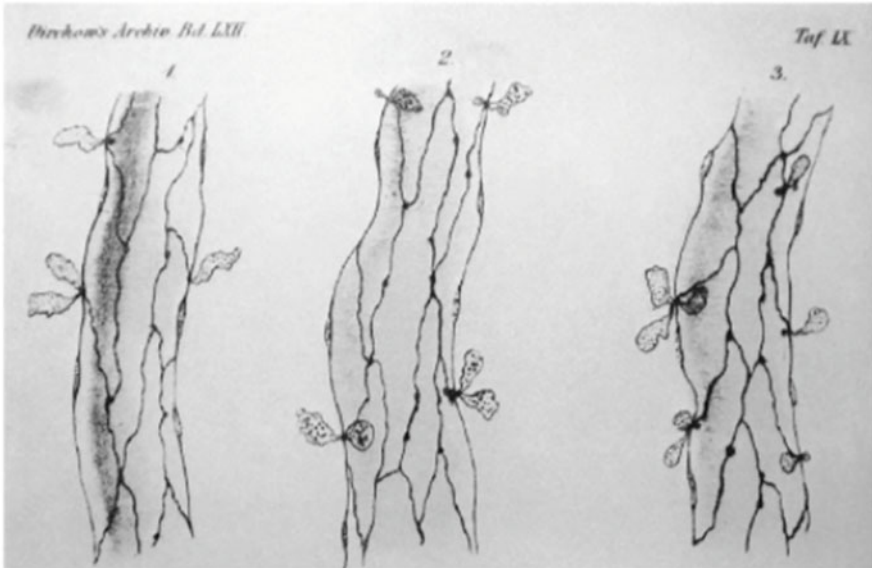
Studies using intravital microscopy techniques were vital in determining the function of leukocytes. During the nineteenth century, research by Julius Cohnheim (1839–1884), Paul Ehrlich (1854–1915), and Élie Metchnikoff (1845–1916) contributed to major discoveries through the use of microscopy in studying inflammation and to the establishment of fundamental concepts in immunology. At the Pathological Institute in Berlin in the 1860s, Julius Cohnheim, a German-Jewish pathologist and skilled microscopist, was conducting extensive research on the causes of inflammation with the “Father of Modern Pathology,” Rudolf Virchow (1821–1902), when he visualised the process of leukocyte transmigration in blood vessels. Cohnheim served briefly as a surgeon with the German Army during the Second Schleswig War against Denmark (1864) treating injured soldiers before returning to Berlin to become the chief assistant to Virchow. He published several papers over the years, most notably *Über Entzündung und Eiterung* (On

Inflammation and Suppuration) in 1867 which described his microscopic observations of vasodilation, leakage of plasma, and migration of leukocytes at the site of tissue injury during acute inflammation. He further proved the origin of pus as debris formed by the emigration of leukocytes, solving a medical mystery that had puzzled doctors for centuries [11]. In his *Vorlesungen über allgemeine Pathologie (Lectures on General Pathology)* in 1889, Cohnheim gave a detailed description of the leukocyte adhesion cascade seen under his microscope through the foot webs and tongues of frogs: “First, in a vein with typical margination of white blood cells, one sees a pointed edge in the outer vessel wall. This moves further away to the outside and if finally connected only through a thin, long stalk. Finally, this stalk is detached, and now a colourless, matte-shining, contractile corpuscle is sitting outside, a white blood cell.” With great foresight, he hypothesised that molecular changes in the vascular endothelium may have allowed the *white blood corpuscles* to cross the capillary walls and migrate into tissues [12, 13]. Similar observations were made by others and depicted in Fig. 2.

In the 1870s, Karl Weigert, a German-Jewish pathologist, began assisting Julius Cohnheim in much of his microscopy work. He developed methods for staining bacteria with aniline dyes in histology and bacterial diagnostics, as bacteria were difficult to visualise with the microscope in those days [15]. Karl Weigert was a great influence on his cousin Paul Ehrlich (Fig. 3). As a young schoolboy (and a man soon to become the future Nobel Prize laureate), Ehrlich had always been fascinated by the process of tissue staining for microscopy and therefore decided to continue the research started by his cousin by spending the eighth semester of his medical school perfecting the use of the red dye dahlia (monophenylrosaniline) for histological staining [16]. In 1878, Ehrlich completed his doctorate under Julius Cohnheim at Leipzig University with a dissertation entitled *Beiträge zur Theorie und Praxis der Histologischen Färbung (Contributions to the Theory and Practice of Histological Staining)*, during which he discovered a new type of cell in blood. Ehrlich named his new discovery the mast cell (derived from the German word for an animal-fattening feed, *mast*) as he thought that the presence of many granules in the cytoplasm (made visible with the help of an alkaline dye) was a sign of good nourishment [17]. He also presented an entire spectrum of cell-staining techniques and chemistry of pigment dyes. Ehrlich continued to perfect his immunohistochemistry techniques at the Charité Hospital in Berlin where he used both alkaline and acidic dyes to create neutral-pH dyes for staining blood samples. These chemical dyes revealed different types of leukocytes that could be identified under the microscope based on the staining of their granules and nuclei. Nongranular lymphocytes, mono- and polynuclear leukocytes, neutrophilic and eosinophilic granulocytes, and mast cells, as well as some bloodborne pathogens, were distinguishable from each other. This laid the foundation for clinical diagnostics in haematology and pathology [16].

Ehrlich’s innovation stemmed from his obsession with structural organic chemistry and selective cell staining with dyes for microscopic examinations. He was passionate about the idea that different chemicals could interact specifically with cells or proteins in pathological states and devised experiments for “in vivo staining” and therapeutic targeting. This led to the development of chemotherapy and the

A



B

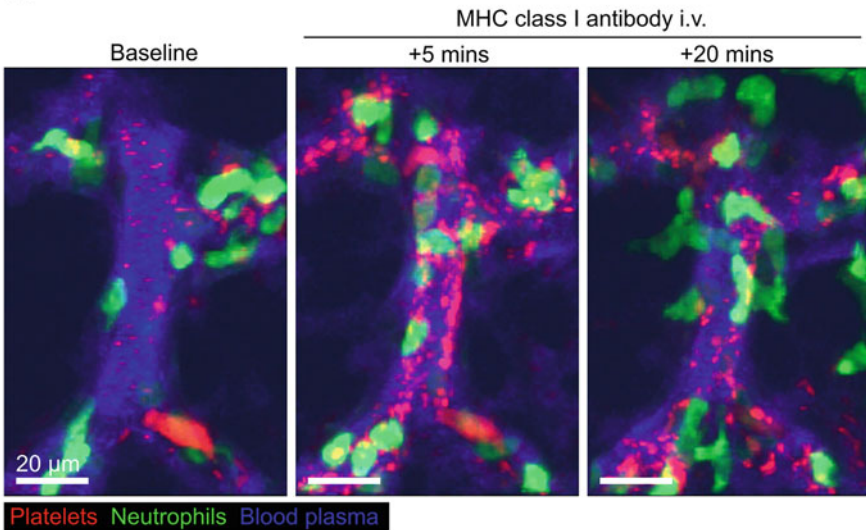


Fig. 2 Leukocytes exiting from the inflamed blood vessels. (a) Historical drawings of leukocyte transmigration at the blood vessels of a frog's tongue, mesentery, and bladder. From Arnold J., in *Archiv für Pathologische Anatomie und Physiologie und für Klinische Medicin*, Virchow R. (ed.) 1875, vol 62, page 487. The drawings are juxtaposed to (b) modern micrographs obtained on intravital microscopy. Reproduced with permission under CC-BY-4.0 licence, © 2020, Cleary et al. [14]

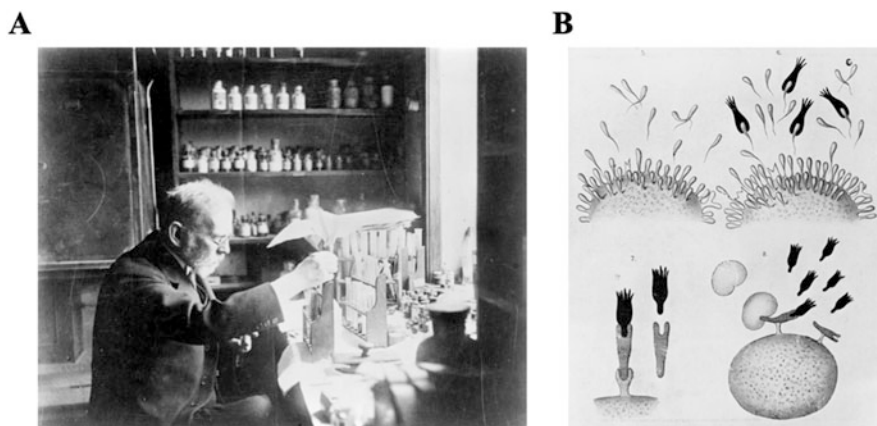


Fig. 3 Paul Ehrlich used chemistry to characterise leukocytes and tissues under the microscope, thereby establishing the “magic bullet” and “side-chain” theories. These influenced the development of molecular imaging techniques years later for theranostic applications. (a) Portrait of Paul Ehrlich performing immunohistochemistry in his laboratory. (b) Diagram on Ehrlich’s side-chain theory illustrating the formation and effector functions of antibodies binding to antigens. Proceedings of the Royal Society of London (1856–1905). (a, b) reproduced with permission under CC-BY-4.0 licence. Credit: Wellcome Collection

establishment of the “magic bullet” theory [18]. In 1896, Ehrlich joined the Institute for Serum Research and Testing as its founding director and began work on antitoxins for diphtheria and their binding to antibodies in the blood. Ever an organic chemist and microscopist at heart, Ehrlich was fascinated by the idea of a specific immune reaction and its cellular and serological basis. He formulated thoughts on the “side-chain” theory and drew an analogy between antibody production and antigen recognition with how the side chains of chemical dyes are related to their colouring properties in cells or tissues visualised under the microscope [19]. By providing a theoretical and chemical basis for immunology, Ehrlich was jointly awarded the Nobel Prize for Physiology or Medicine in 1908 with Élie Metchnikoff, the “Father of Innate Immunity,” who established the theory of cell-mediated immunity [19]. Interestingly, Ehrlich’s early contributions to the “side-chain” theory of antibody-antigen interactions and the “magic bullet” theory of specific targeting in diseases also laid the foundation for research in molecular imaging and therapy (*theranostics*). Chemical agents based on labelled antibodies, peptides, and small molecules to target specific proteins expressed on abnormal cells or biological processes in pathological conditions such as cancer, infection, and inflammatory disorders have become important tools for radionuclide imaging and therapy [20]. With the advent of cryogenic electron microscopy (cryo-EM) in the 1970s, the natural structure of biological specimens can be preserved, embedded in their native environment, and protected from damage by electron beams using rapid cooling techniques [21]. 3D images at near-atomic resolution can now be obtained for studying the subcellular structures of viruses, macromolecules, receptor-ligand

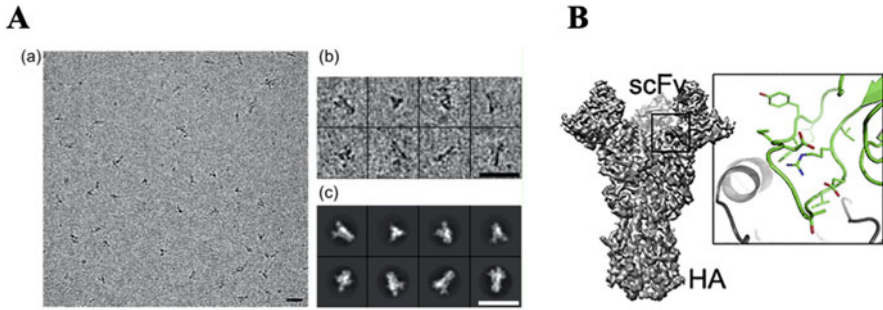


Fig. 4 Structure-based vaccine design using single-particle cryoEM as a tool to image the structure of the antibody-antigen complexes, e.g., influenza virus hemagglutinin (HA):single-chain variable domain fragment (scFv). (a) Cryomicrographs at different stages of image processing. (b) 3D surface rendering of the HA:scFv structure. Reproduced from Liu et al. [24] with permission, © 2017, Elsevier Ltd.

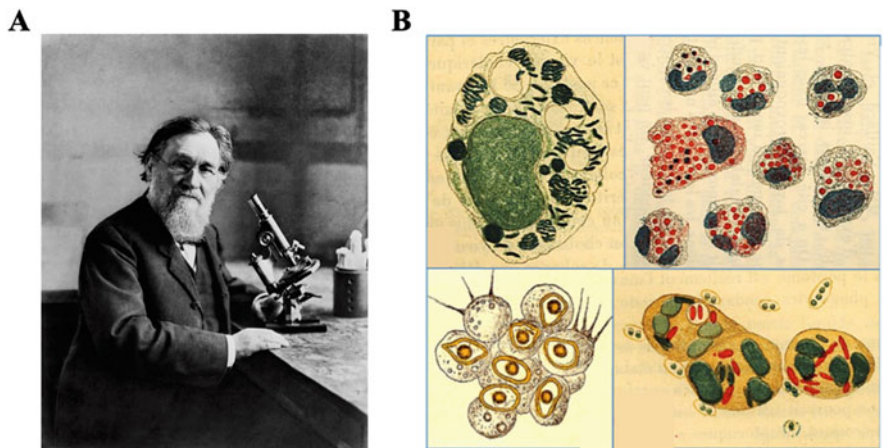


Fig. 5 Élie Metchnikoff was an enthusiastic microscopist and evolutionary embryologist who established the theory of “cell-mediated immunity.” (a) Photograph: portrait of Élie Metchnikoff in his laboratory. Reproduced with permission under CC-BY-4.0 licence. Credit: Wellcome Collection. (b) Intricate drawings of phagocytosis by Metchnikoff (from top left to bottom right): a macrophage filled with *Vibrio cholerae*; leukocytes from a rabbit filled with tetanus spores; macrophages engulfing damaged erythrocytes; peritoneal fluid containing free streptococci and macrophages engulfing *Proteus bacilli*. From Metchnikoff, E. (1901) *L’immunité dans les maladies infectieuses*. Paris, Masson

interactions (e.g., the T cell receptor (TCR)-CD3 complex), as well as antibody-antigen interactions for structure-based drugs and vaccine design as shown in Fig. 4 [22, 23].

Élie Metchnikoff (Fig. 5a) would use microscopy to discover a major reason why leukocytes migrate out of inflamed blood vessels (Fig. 3). In 1882, Metchnikoff was on a working vacation with his family in Messina, Sicily, when he discovered the

process of phagocytosis in a starfish larva at the Mediterranean coast—a “Eureka!” moment while on holiday [25]. He recounted, “One day when the whole family had gone to a circus to see some extraordinary performing apes, I remained alone with my microscope, observing the life in the mobile cells of a transparent starfish larva, when a new thought suddenly flashed across my brain. It struck me that similar cells might serve in the defence of the organism against intruders. Feeling that there was in this something of surpassing interest, I felt so excited that I began striding up and down the room and even went to the seashore to collect my thoughts. . . I said to myself that, if my supposition was true, a splinter introduced into the body of a starfish larva, devoid of blood vessels or a nervous system, should soon be surrounded by mobile cells as is to be observed in a man who runs a splinter into his finger. This was no sooner said than done. . . There was a small garden to our dwelling, in which we had a few days previously organised a ‘Christmas tree’ for the children on a little tangerine tree; I fetched from it a few rose thorns and introduced them at once under the skin of some beautiful starfish larvae as transparent as water. . . I was too excited to sleep that night in the expectation of the results of my experiment, and very early the next morning I ascertained that it had finally succeeded. . . That experiment formed the basis of the phagocyte theory, to the development of which I devoted the next twenty-five years of my life” [25]. Metchnikoff named these mobile cells “phagocytes” from the Greek words *phagein* meaning “to eat” and *kytos* meaning “cell.” In 1883, he published a key paper describing phagocytosis in frogs [26]. He explained how phagocytosis was important not just for host defense but also the elimination of degenerating or dying cells in the same host during metamorphosis from tadpoles to adult frogs: “The traits of the phagocyte have been retained most completely in the mesoderm where a large number of amoeboid cells occur to ingest the body’s own dead or weak as well as foreign particles such as senescent red blood cells.” This was one of the earliest descriptions of the function of our innate immune system in recognising self from nonself [27]. He described the engulfment of foreign particles and the morphological changes in the phagocytes he observed under the microscope (Fig. 5b) [28]: “These cells accumulate at the point of inflammation and devour the particles available to them. I have observed, for example, that star-shaped stromal cells feed on red blood cells, carmine and pigment particles. In cases where such cells ingest small numbers of foreign particles, they maintain their star-like shape with only some minor changes in the finest pseudopodia.”

Metchnikoff combined microscopy and cell staining with neutral red and other dyes to evaluate the acidity of phagosomes, cell viability, and the fate of ingested microorganisms and foreign particles [29]. He took a comparative approach to infection and immunity, embracing natural history with experimentation in a wide range of model organisms from unicellular protozoa to transparent invertebrates, rodents, and even primates and humans [29]. Interpretations of microscopy experiments by Metchnikoff established the concept of cell-mediated immunity, while the microscopy studies of Ehrlich laid the foundation for humoral immunity [30]. Intravital microscopy has continued to expand our understanding of the immune system. It offers the opportunity for direct visualisation and characterisation of cellular

behaviour and the spatiotemporal dynamics of physiological processes within living organisms [31]. These include imaging biological events such as chemokine signalling and cell migration, the leukocyte adhesion cascade, endothelial transmigration, phagocytosis of foreign pathogens and damaged cells by macrophages and neutrophils, antigen presentation, and activation of effector T cells (Fig. 6) [32–34]. The ability to capture the cellular and molecular events of the immune system has improved our understanding on the biological mechanisms involved in health and diseases and equipped us with new knowledge in developing novel immunotherapies [35]. For applications of intravital microscopy to immunological problems and particularly inflammation, we direct the reader to the dedicated chapter *Imaging Inflammation by Intravital Microscopy* by De Donatis et al. in this book. Other advanced imaging techniques based on optical excitation and detection of biological events from a single-cell or subcellular level to whole-body scale are described in the chapters: *Spatial Transcriptomics in Inflammation: Dissecting the Immune Response in 3D in Complex Tissues* by Hu and *Whole-Body Chemiluminescence and Fluorescence Imaging of Inflammation* by Tseng and Peterson.

3 The Dawn of Radiology and Noninvasive Imaging of Inflammation

Metchnikoff and Ehrlich lived in a time when numerous giants of the scientific disciplines made outstanding contributions to medicine and influenced future research in imaging inflammation (Fig. 7). Most notably, the serendipitous discovery of X-rays in December 1895 by the German physicist Wilhelm Conrad Röntgen (1845–1923) marked the dawn of radiology and the emergence of noninvasive whole-body imaging techniques for disease diagnosis [36, 37]. While experimenting with the flow of electric current in a cathode ray tube, Röntgen observed a fluorescent effect on a small cardboard screen painted with barium platinocyanide when the tube was in operation. He reasoned that the fluorescence was caused by invisible rays originating from the cathode ray tube, which penetrated the opaque black paper wrapped around the tube. Further experiments were performed which confirmed that this unknown ray (thereby designated as “X”) could pass through most substances, including the soft tissues of the body, but was absorbed by dense materials such as bones and metallic objects [38]. Six weeks following his discovery, Röntgen took the first medical X-ray of the hand of his wife Anna Bertha. After seeing the ghostly image of the bones in her hand for the first time and her wedding ring “hovering” on one finger, she reportedly exclaimed, “I have seen my death.” For his discovery of X-rays and its potential use in medicine, Wilhelm Conrad Röntgen was awarded the Nobel Prize in Physics in 1901 [38]. Doctors began as early as January 1896 to use X-rays on patients for investigating skeletal abnormalities and subsequently to explore the lungs and other organs [39]. A simple chest X-ray and cross-sectional imaging using computed tomography (CT; pioneered by Sir Godfrey Hounsfield

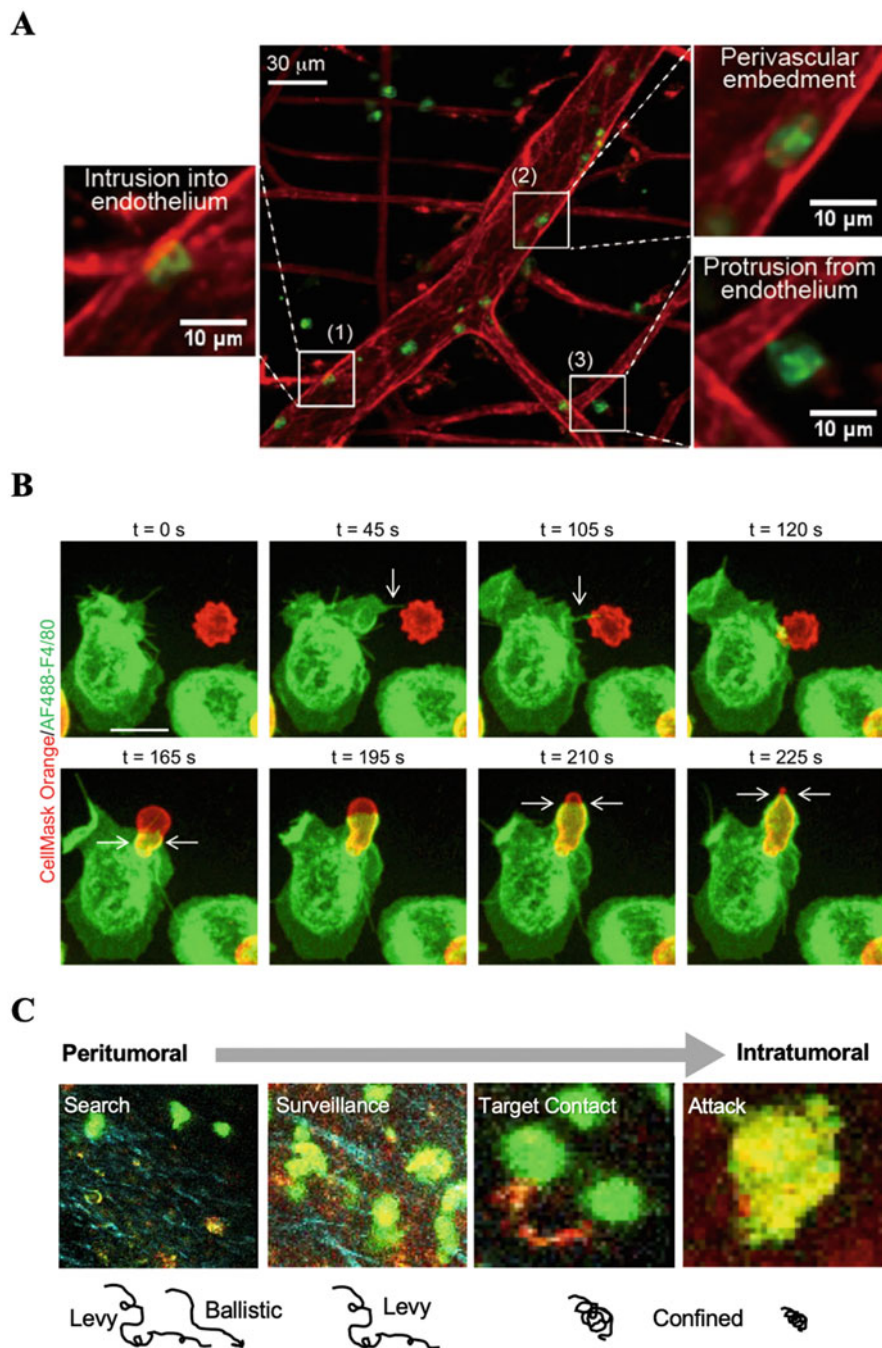


Fig. 6 Key concepts in immunology observed with intravital microscopy. (a) Neutrophil extravasation in tissues is a multistep event involving the adhesion of neutrophils in the blood to the vascular endothelium and eventual transmigration through the vessel wall to reach the site of infection or inflammation. Reproduced from [32] with permission. © 2019, Hyun et al.

(1919–2004) and Allan Cormack (1924–1998)) have become routine tests for diagnosing tissue structural abnormalities in many inflammatory conditions such as pneumonia, bronchitis, and even acute respiratory distress syndrome (ARDS) associated with COVID-19 infection [40, 41].

The discovery of spontaneous radioactivity by the French physicist Henri Becquerel (1852–1908) is another famous example of serendipity in science [43]. In early 1896, after a wave of excitement following Röntgen’s discovery of X-rays, Becquerel was investigating the relationship between the absorption of light and phosphorescence in uranium compounds when he suspected that his luminescent materials might emit some of these mysterious X-rays. He began his own study of the X-rays by simulating Röntgen’s experiments and accidentally discovered the spontaneous emission of radiation from the uranium compounds he kept in a dark drawer with a photographic plate [44]. A period of intense research on radioactivity followed, including the discovery of additional radioactive elements polonium and radium by the French couple Pierre Curie (1859–1906) and Marie Skłodowska Curie (1867–1934) [45]. Marie Curie ingeniously used a piezoelectric quartz electrometer developed by Pierre Curie and his brother Jacques Curie (1855–1941) and attached it to an ionisation chamber to search for elements that emit ionising radiation. This enabled the quantification of radioactivity and discovery of medically useful radioactive elements such as radium. In 1903, Henri Becquerel and Marie and Pierre Curie were jointly awarded the Nobel Prize in Physics for their research on radioactivity. For her discovery and isolation of radium and polonium, Marie Curie was awarded the Nobel Prize in Chemistry in 1911. Many decades later, further developments by others in the field led to the discovery of gamma-emitting and positron-emitting radioisotopes, forming the basis of radionuclide imaging and nuclear medicine [46].

Gallium-67 (^{67}Ga)-labelled citrate has been used for scintigraphy and single-photon emission computed tomography (SPECT) of infections and inflammatory disorders for over 30 years. Gallium functions as an iron analogue *in vivo* by binding to transferrin and extravasates within inflammatory sites due to increased blood flow and vascular permeability. However, gallium-67 has a long physical half-life (78 hours) and exhibits nonspecific uptake in tissues such as the liver, nasopharynx, and lacrimal and salivary glands [47, 48]. This imaging method has now been superseded by techniques such as white blood cell (WBC) scintigraphy or SPECT and fluorine-18 fluorodeoxyglucose (^{18}F)FDG positron emission tomography

Fig. 6 (continued) (CC-BY-4.0 license). **(b)** Snapshots from a time-lapse video showing a mouse macrophage capturing a mouse immunoglobulin G (IgG)-opsonised human erythrocyte via a filopodium. This was followed by the formation of a phagocytic cup and engulfment of the erythrocyte. Images reproduced from Horsthemke et al. [33] with permission. **(c)** Antigen-specific T cells demonstrated distinct behaviours during tumour infiltration. The interactions between T cells and their target cancer cells during antigen presentation and T cell cytotoxic attack on the cancer cells were captured in living mice on intravital microscopy. Images reproduced with permission under CC-BY-4.0 licence, © 2020, Lau et al. [34]

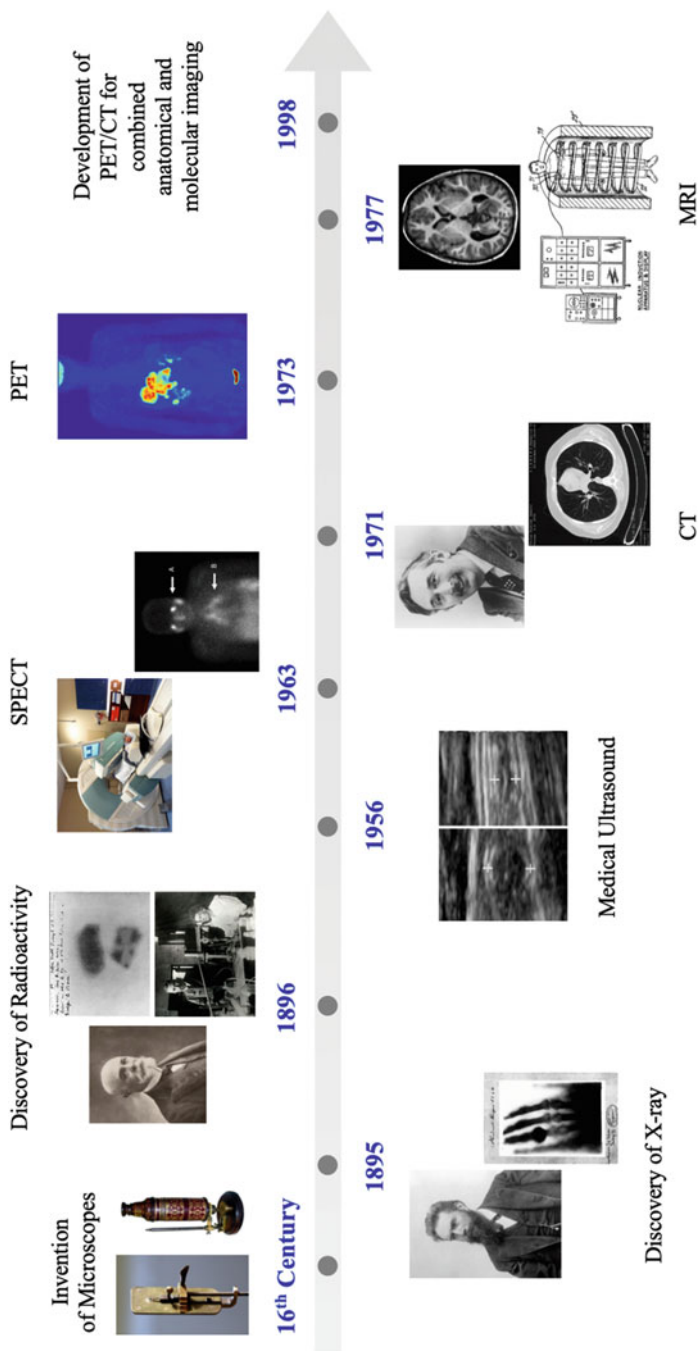


Fig. 7 Historical timeline of the invention of biomedical imaging tools. Illustration by the author (D. Lau) created from Wikimedia public domain images unless otherwise indicated. Top line, left to right: replica of a van Leeuwenhoek microscope, image by Jeroen Rouwkema (CC BY-SA 3.0 license); Hooke microscope, Billings Microscope Collection, National Museum; portrait of Henri Becquerel by Paul Nadar, ca. 1905; photographic plate by H. Becquerel showing effects of exposure to radioactivity; portrait of Pierre Curie and Marie Skłodowska-Curie; SPECT/CT scanner, image by Wikimedia user Ytrottier (CC BY-SA 3.0 license); gallium-67 scan of a patient with sarcoidosis, reproduced from [42] under CC BY-SA 4.0 license, © 2014, Allard et al.; maximum intensity projection of an ^{18}F -FDG-PET/CT scan of a patient with metastatic colorectal cancer, image by Jens Langner. Bottom line, left to right: portrait of Wilhelm Röntgen; X-ray of Anna Röntgen's hand by W. Röntgen; ultrasound image of the appendix, without and with compression, Mikael Högström; portrait of Godfrey Hounsfield ca. 1975; frame from a chest CT scan, image by Wikimedia user Prump16 (CC BY-SA 4.0 license); schematic drawing of a prototypical MRI scanner, 1972, Raymond Damadian, (US government Patent number 3789832)

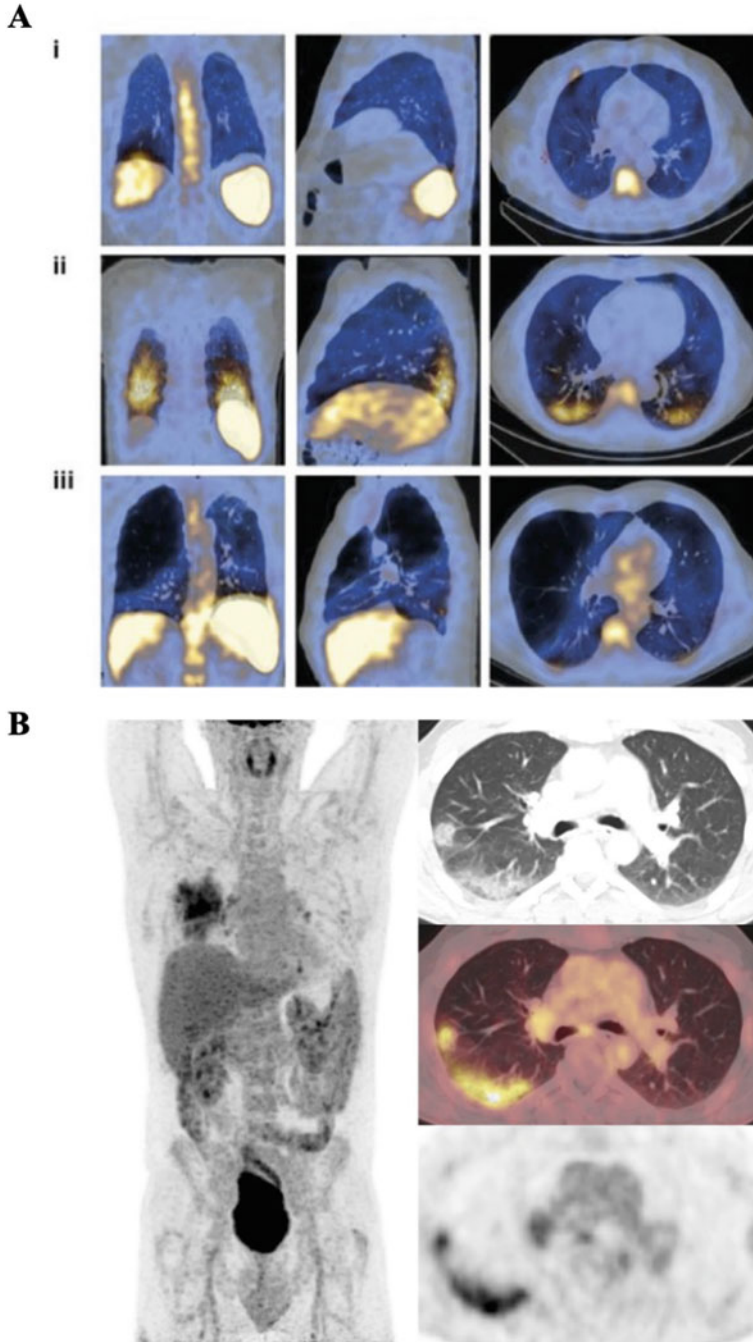


Fig. 8 White blood cell scintigraphy or SPECT/CT and [^{18}F]FDG PET/CT are routine clinical imaging techniques used for imaging different biological processes in infections and inflammatory disorders. (a) SPECT imaging of [$^{99\text{m}}\text{Tc}$]Tc-HMPAO-radiolabelled autologous neutrophils has been used in experimental medicine studies for studying chronic obstructive pulmonary disease

(PET) as shown in Fig. 8 [49, 50]. WBC scintigraphy is a gold standard technique introduced in 1976 for routine clinical use in detecting inflammation and unknown sites of infection, e.g., osteomyelitis and vascular graft infections [49]. The technique involves the ex vivo radiolabelling of autologous leukocytes (primarily neutrophils) using lipophilic, cell-permeable radiopharmaceuticals such as technetium-99m (^{99m}Tc) hexamethylpropyleneamine oxime (HMPAO) and indium-111 (^{111}In) oxine to image the migration kinetics of the radiolabelled cells and infiltration at the inflamed tissues following reinjection [51]. In recent years, SPECT imaging of radiolabelled autologous neutrophils has also been used in experimental medicine studies to investigate changes in neutrophil migratory behaviour, tissues, and systemic biodistribution in lung inflammatory disorders such as ARDS and chronic obstructive pulmonary disease (COPD) [52, 53]. On the other hand, [^{18}F]FDG is a radiolabelled glucose analogue that can be taken up by glucose transporters and remain trapped in cells following phosphorylation by hexokinase. Leukocytes such as neutrophils, monocytes, and macrophages exhibit higher expression of glucose transporters such as GLUT1 and rapidly increase their glucose consumption upon activation [54]. [^{18}F]FDG PET has been used for detecting metabolic inflammatory foci in nonmalignant conditions such as tuberculosis and inflammatory bowel disease [55, 56]. However, the use of [^{18}F]FDG PET for monitoring infection or inflammatory processes in the presence of malignancy can often complicate diagnosis as both cancer cells and leukocytes are metabolically active cell types [50]. Thus, special precautions and clinical triage should be made when interpreting radiological scans in the presence of both diseases [57]. In recent years, novel radiopharmaceuticals targeting the expression of immune-related biomarkers such as CD8, granzyme B, and PD-1 have been developed for immuno-oncology applications [58–60]. These methods enable the detection and characterisation of specific tissue-resident leukocyte subtypes, as well as the detection of markers of leukocyte activation or immunosuppression within inflamed tissues as potential alternative approaches to biopsy. PET and SPECT imaging of inflammation are further detailed by Keeling and Man in the chapter *Nuclear Imaging of Inflammation* of this book.

The discovery of the piezoelectric properties of quartz deformation by Pierre and Jacques Curie also laid the foundation for the development of ultrasound imaging. Ultrasound was first used in 1917 during World War I by the physicist Paul Langevin (1872–1946) for the detection of submarines [61]. The technology was subsequently adapted for medical ultrasound in 1956 by Ian Donald (1910–1987),



Fig. 8 (continued) (COPD). Shown over here are the 45 min thoracic SPECT/CT scans of (i) a saline-challenged healthy volunteer, (ii) a healthy volunteer challenged with lipopolysaccharide, and (iii) a patient with COPD, showing differences in neutrophil migration and tissue infiltration in the inflamed lungs. Images reproduced with permission under CC-BY-4.0 licence, © 2019, Tregay et al. [53]. (b) [^{18}F]FDG PET of a cancer patient with COVID-19, showing incidental findings on follow-up scans of a new hypermetabolic area in the right upper and lower lung. Ground glass opacities in the periphery/subpleural regions of the lungs were concurrently seen on CT. Images reproduced with permission from Czernin et al. [57] under CC-BY-4.0 licence, © 2020, Society of Nuclear Medicine and Molecular Imaging

which uses handheld ultrasonic probes or transducers comprising of piezoelectric crystals and alternating current electrodes to transmit and receive high-frequency sound waves through tissues. The reflected echoes from tissues result in deformation of the piezoelectric components and interconversion of the mechanical energy into electrical pulses. Images reflecting the stiffness and density of the tissues are produced based on the depth and speed of sound waves propagating through tissues [62]. Ultrasound is a relatively low-cost technique suitable for imaging soft tissues and real-time monitoring of blood flow using Doppler imaging. Ultrasound is particularly useful for road-mapping and guiding needle intervention. It is commonly used for image-guided tumour biopsy in cancer diagnosis [63], and there is increasing interest in using ultrasound for image guidance during intratumoral delivery of immunotherapies into deeper and non-palpable tumours [64], as well as focused ultrasound for immunomodulation of the tumour microenvironment [65]. Ultrasound has been used for visualising needle puncture and draining of abscesses or postoperative collections from infected tissues [66]. It enables the identification of adjacent anatomical structures and helps determine the best tract and safest route for intervention [67]. As ultrasound does not involve the use of ionising radiation and the scanner is usually mobile and can be made into portable handheld versions, it is used in settings such as paediatrics, critical care, and emergency medicine for point-of-care bedside imaging of infections in the lungs and pleural cavity, soft tissues, and musculoskeletal regions and the monitoring of interventional procedures [68–70]. The use of ultrasound imaging in inflammation is further detailed in the dedicated chapter of this book *Ultrasound Imaging in Inflammation Research* by Muller et al. A related and more recent technique is photoacoustic imaging, which is based on the detection of ultrasound waves generated by optical excitation of tissues and contrast agents; see the chapter *Photoacoustic Imaging in Inflammation Research* by Chen and Xie et al. in this book.

In the twentieth century, the discovery of nuclear magnetic resonance (NMR) in biomolecules and developments in imaging physics and instrumentation for spatial encoding of NMR signals using magnetic field gradients by the British and American trio Sir Peter Mansfield (1933–2017), Paul Lauterbur (1929–2007), and Raymond Damadian (born 1936) led to the introduction of magnetic resonance imaging (MRI) [71]. MRI is now a clinically available tool in hospitals for disease diagnosis and treatment monitoring. Images with excellent soft tissue contrast and high spatial resolution can be obtained without the use of ionising radiation, together with physiological measurements of biological processes such as blood flow, edema, and cellular changes associated with inflammation. MRI is based on the principle of NMR, in which certain atomic nuclei such as protons (^1H) absorb and re-emit radiofrequency energy when placed in an external magnetic field [72]. Tissue contrast obtained on MRI is based on the spin-lattice relaxation (T_1) and spin-spin relaxation (T_2) times, which are dependent on the chemical structures of the molecules imaged and the local chemical environment within the tissues [73]. Several MRI and MR spectroscopic techniques have been developed over the years for imaging microstructural, functional, and molecular changes in infection and

inflammatory disorders. Some of these methods include imaging microstructural and functional changes in the tumour microenvironment following cancer immunotherapy [74], as well as imaging changes in sodium metabolism as a biomarker for neurodegeneration and neuroinflammation in patients with multiple sclerosis [75, 76]. In addition, molecular MR imaging approaches have been developed at the preclinical level to improve specificity in detecting inflammatory processes. These include using antibody-conjugated nanoparticles, e.g., microparticles of iron oxide (MPIO) targeting vascular cell adhesion molecule-1 (VCAM-1) and intercellular adhesion molecule-1 (ICAM-1) expressed on endothelial cells and activated leukocytes [77, 78]. Cell tracking approaches using superparamagnetic iron oxide (SPIO) nanoparticles and fluorine-19 (^{19}F) perfluorocarbons for labeling leukocytes [79, 80], as well as MRI reporter genes, e.g., ferritin, have been developed for monitoring therapeutic cells and viral vector-mediated gene therapy [81, 82]. The use of MRI for imaging inflammation particularly for neurological applications is further detailed in the chapter *Magnetic Resonance Imaging of Neuroinflammation* by Johansen et al. in this book.

4 Conclusion

In conclusion, advancements in biomedical imaging over the years have contributed to discoveries in immunology, diagnosis, and treatment of infections and inflammatory disorders. Intravital microscopy has progressed considerably and is a powerful tool for examining single live cell behaviour, cell-cell interactions, cellular energetics, and persistence in inflamed tissues for basic immunology studies at the preclinical level. Continuous improvements in medical physics, imaging hardware, and algorithms and the development of functional and molecular imaging agents have contributed to the evolution of noninvasive whole-body imaging methods, e.g., SPECT, PET and MRI, for disease diagnosis and longitudinal monitoring of treatment response in patients. These remarkable contributions of biomedical imaging to progress in inflammation research are engraved in history, with newer developments in imaging inflammation (as described in subsequent chapters by other authors) to be celebrated in the years to come.

Acknowledgments Special thanks to Simon Cleary and Francis Man for their helpful comments on the manuscript.

Compliance with Ethical Standards **Funding:** Doreen Lau is supported by a Worldwide Cancer Research Fund (grant no. 20–0229) and a Cancer Research UK Oxford Centre Development Fund (grant no. CRUKDF-DL; C5255/A18085) at the University of Oxford.

Conflict of Interest: The author has no conflict of interest to declare.

Ethical approval: No studies with human participants or animals were conducted by the author for the preparation of this chapter.

References

1. Gest H. The discovery of microorganisms by Robert Hooke and Antoni van Leeuwenhoek, Fellows of The Royal Society. *Notes Rec R Soc Lond.* 2004;58:187–201. <https://doi.org/10.1098/rsnr.2004.0055>.
2. Zuylen J. The microscopes of Antoni van Leeuwenhoek. *J Microsc.* 1981;121:309–28. <https://doi.org/10.1111/j.1365-2818.1981.tb01227.x>.
3. Lane N. The unseen world: reflections on Leeuwenhoek (1677) ‘Concerning little animals.’. *Philos Trans R Soc B Biol Sci.* 2015;370:20140344. <https://doi.org/10.1098/rstb.2014.0344>.
4. Pariente N. A field is born. *Nature.* 2019;S3-4.
5. Goldsmith CS, Miller SE. Modern uses of electron microscopy for detection of viruses. *Clin Microbiol Rev.* 2009;22:552–63. <https://doi.org/10.1128/CMR.00027-09>.
6. Porter JR. Antony van Leeuwenhoek: tercentenary of his discovery of bacteria. *Bacteriol Rev.* 1976;40:260–9. <https://doi.org/10.1128/br.40.2.260-269.1976>.
7. Ley K. The microcirculation in inflammation. *Microcirculation.* Elsevier. 2008:387–448. <https://doi.org/10.1016/B978-0-12-374530-9.00011-5>.
8. Dutrochet H. *Recherches anatomiques et physiologiques sur la structure intime des animaux et des végétaux, et sur leur motilité.* Paris, France, J. B. Baillière; 1824.
9. Wilson JW. Dutrochet and the cell theory. *Isis.* 1947;37:14–21.
10. Wagner R. *Erläuterungstafeln zur Physiologie und Entwicklungsgeschichte.* Leipzig, Germany: Leopold Voss; 1839.
11. Cohnheim J. Ueber Entzündung und Eiterung. *Arch für Pathol Anat und Physiol und für Klin Med.* 1867;40:1–79. <https://doi.org/10.1007/BF02968135>.
12. Cohnheim J. *Lectures on general pathology: a handbook for practitioners and students.* London: The New Sydenham Society; 1889.
13. Muller WA. Mechanisms of leukocyte transendothelial migration. *Annu Rev Pathol Mech Dis.* 2011;6:323–44. <https://doi.org/10.1146/annurev-pathol-011110-130224>.
14. Cleary SJ, Kwaan N, Tian JJ, Calabrese DR, Mallavia B, Magnen M, et al. Complement activation on endothelium initiates antibody-mediated acute lung injury. *J Clin Invest.* 2020;130:5909–23. <https://doi.org/10.1172/JCI138136>.
15. Wohlrab F, Henoch U. The life and work of Carl Weigert (1845-1904) in Leipzig 1878-1885. *Zentralblatt für Allg Pathol u Pathol Anat.* 1988;134:743–51.
16. Buchwalow I, Boecker W, Tiemann M. The contribution of Paul Ehrlich to histochemistry: a tribute on the occasion of the centenary of his death. *Virchows Arch.* 2015;466:111–6. <https://doi.org/10.1007/s00428-014-1677-4>.
17. Beaven MA. Our perception of the mast cell from Paul Ehrlich to now. *Eur J Immunol.* 2009;39:11–25. <https://doi.org/10.1002/eji.200838899>.
18. Bosch F, Rosich L. The contributions of Paul Ehrlich to pharmacology: a tribute on the occasion of the centenary of his Nobel prize. *Pharmacology.* 2008;82:171–9. <https://doi.org/10.1159/000149583>.
19. Kaufmann SHE. Immunology’s foundation: the 100-year anniversary of the Nobel Prize to Paul Ehrlich and Elie Metchnikoff. *Nat Immunol.* 2008;9:705–12. <https://doi.org/10.1038/ni0708-705>.
20. Wright BD, Lapi SE. Designing the magic bullet? The advancement of Immuno-PET into clinical use. *J Nucl Med.* 2013;54:1171–4. <https://doi.org/10.2967/jnumed.113.126086>.
21. Cressey D, Callaway E. Cryo-electron microscopy wins chemistry Nobel. *Nature.* 2017;550:167. <https://doi.org/10.1038/nature.2017.22738>.
22. Earl LA, Subramaniam S. Cryo-EM of viruses and vaccine design. *Proc Natl Acad Sci.* 2016;113:8903–5. <https://doi.org/10.1073/pnas.1609721113>.
23. Dong D, Zheng L, Lin J, Zhang B, Zhu Y, Li N, et al. Structural basis of assembly of the human T cell receptor–CD3 complex. *Nature.* 2019;573:546–52. <https://doi.org/10.1038/s41586-019-1537-0>.

24. Liu Y, Pan J, Jenni S, Raymond DD, Caradonna T, Do KT, et al. CryoEM Structure of an Influenza Virus Receptor-Binding Site Antibody–Antigen Interface. *J Mol Biol.* 2017;429: 1829–39. <https://doi.org/10.1016/j.jmb.2017.05.011>.
25. Metchnikoff O. *Life of Elie Metchnikoff, 1845–1916.* Cornell University Library; 2009.
26. E M. Untersuchungen über die mesodermalen Phagocyten einiger Wirbeltiere. *Biol Cent.* 1883;3:560–5.
27. Medzhitov R, Janeway CA. Decoding the patterns of self and nonself by the innate immune system. *Science* (80-). 2002;296:298–300. <https://doi.org/10.1126/science.1068883>.
28. Merien F. A journey with Elie Metchnikoff: from innate cell mechanisms in infectious diseases to quantum biology. *Front Public Health.* 2016;4:125. <https://doi.org/10.3389/fpubh.2016.00125>.
29. Gordon S. Elie Metchnikoff: father of natural immunity. *Eur J Immunol.* 2008;38:3257–64. <https://doi.org/10.1002/eji.200838855>.
30. Kaufmann SHE. Immunology’s coming of age. *Front Immunol.* 2019;10:684. <https://doi.org/10.3389/fimmu.2019.00684>.
31. Pittet MJ, Garris CS, Arlauckas SP, Weissleder R. Recording the wild lives of immune cells. *Sci Immunol.* 2018;3. <https://doi.org/10.1126/sciimmunol.aag0491>.
32. Hyun Y-M, Choe YH, Park SA, Kim M. LFA-1 (CD11a/CD18) and mac-1 (CD11b/CD18) distinctly regulate neutrophil extravasation through hotspots I and II. *Exp Mol Med.* 2019;51:1–13. <https://doi.org/10.1038/s12276-019-0227-1>.
33. Horsthemke M, Wilden J, Bachg AC, Hanley PJ. Time-lapse 3D imaging of phagocytosis by mouse macrophages. *J Vis Exp.* 2018; <https://doi.org/10.3791/57566>.
34. Lau D, Garçon F, Chandra A, Lechermann LM, Aloj L, Chilvers ER, et al. Intravital imaging of adoptive T-cell morphology, mobility and trafficking following immune checkpoint inhibition in a mouse melanoma model. *Front Immunol.* 2020;11:1514. <https://doi.org/10.3389/fimmu.2020.01514>.
35. Boulch M, Grandjean CL, Cazaux M, Bousso P. Tumor immunosurveillance and immunotherapies: a fresh look from intravital imaging. *Trends Immunol.* Elsevier Inc. 2019;40:1022–34. <https://doi.org/10.1016/j.it.2019.09.002>.
36. Rigler LG. The development of Roentgen diagnosis. *Radiology.* 1945;45:467–502. <https://doi.org/10.1148/45.5.467>.
37. Thomas AMK, Banerjee AK. *The history of radiology* [internet]. Oxford University Press; 2013. <https://doi.org/10.1093/med/9780199639977.001.0001>.
38. Kaye GWC. Wilhelm Conrad Röntgen: and the early history of the Roentgen rays. *Nature.* 1934;133:511–3. <https://doi.org/10.1038/133511a0>.
39. Tubiana M. Wilhelm Conrad Röntgen and the discovery of X-rays. *Bull Acad Natl Med.* 1996;180:97–108.
40. Franquet T. Imaging of pneumonia: trends and algorithms. *Eur Respir J.* 2001;18:196–208. <https://doi.org/10.1183/09031936.01.00213501>.
41. Han X, Fan Y, Alwalid O, Li N, Jia X, Yuan M, et al. Six-month follow-up chest CT findings after severe COVID-19 pneumonia. *Radiology.* 2021;299:E177–86. <https://doi.org/10.1148/radiol.2021203153>.
42. Allard AB, Buscombe J, Kidd DP. The role of gallium (Ga-67) scintigraphy in the diagnosis of sarcoidosis. *Mod Res Inflamm.* 2014;03:99–107. <https://doi.org/10.4236/mri.2014.33012>.
43. Margaritondo G. Henri Becquerel: serendipitous brilliance. *Phys World.* 2008;21:26–8. <https://doi.org/10.1088/2058-7058/21/06/32>.
44. Donald BM. Becquerel and the discovery of radioactivity: early concepts. *Semin Nucl Med.* 1996;26:145–54. [https://doi.org/10.1016/S0001-2998\(96\)80019-5](https://doi.org/10.1016/S0001-2998(96)80019-5).
45. Anniversary of the Discovery of Radium. *Nature.* 1938;142:637. <https://doi.org/10.1038/142637b0>.
46. Vallabhajosula S. *Molecular imaging* [internet]. Berlin, Heidelberg, Heidelberg: Springer Berlin Heidelberg; 2009. <https://doi.org/10.1007/978-3-540-76735-0>.

47. Front D, Israel O. Present state and future role of gallium-67 scintigraphy in lymphoma. *J Nucl Med.* 1996;37:530–2.
48. Kurdziel KA. The panda sign. *Radiology.* 2000;215:884–5. <https://doi.org/10.1148/radiology.215.3.r00jn31884>.
49. Signore A, Jamar F, Israel O, Buscombe J, Martin-Comin J, Lazzeri E. Clinical indications, image acquisition and data interpretation for white blood cells and anti-granulocyte monoclonal antibody scintigraphy: an EANM procedural guideline. *Eur J Nucl Med Mol Imaging.* 2018;45:1816–31. <https://doi.org/10.1007/s00259-018-4052-x>.
50. Jamar F, Buscombe J, Chiti A, Christian PE, Delbeke D, Donohoe KJ, et al. EANM/SNMMI Guideline for 18 F-FDG use in inflammation and infection. *J Nucl Med.* 2013;54:647–58. <https://doi.org/10.2967/jnumed.112.112524>.
51. Lau D, Lechermann LM, Gallagher FA. Clinical translation of neutrophil imaging and its role in cancer. *Mol Imaging Biol.* 2021; <https://doi.org/10.1007/s11307-021-01649-2>.
52. Summers C, Singh NR, White JF, Mackenzie IM, Johnston A, Solanki C, et al. Pulmonary retention of primed neutrophils: a novel protective host response, which is impaired in the acute respiratory distress syndrome. *Thorax.* 2014;69:623–9. <https://doi.org/10.1136/thoraxjnl-2013-204742>.
53. Tregay N, Begg M, Cahn A, Farahi N, Povey K, Madhavan S, et al. Use of autologous 99m technetium-labelled neutrophils to quantify lung neutrophil clearance in COPD. *Thorax.* 2019;74:659–66. <https://doi.org/10.1136/thoraxjnl-2018-212509>.
54. Maratou E, Dimitriadis G, Kollias A, Boutati E, Lambadiari V, Mitrou P, et al. Glucose transporter expression on the plasma membrane of resting and activated white blood cells. *Eur J Clin Investig.* 2007;37:282–90. <https://doi.org/10.1111/j.1365-2362.2007.01786.x>.
55. Kim I-J, Lee JS, Kim S-J, Kim Y-K, Jeong YJ, Jun S, et al. Double-phase 18F-FDG PET-CT for determination of pulmonary tuberculoma activity. *Eur J Nucl Med Mol Imaging.* 2008;35:808–14. <https://doi.org/10.1007/s00259-007-0585-0>.
56. Spier BJ, Perlman SB, Reichelderfer M. FDG-PET in inflammatory bowel disease. *Q J Nucl Med Mol Imaging.* 2009;53:64–71.
57. Czernin J, Fanti S, Meyer PT, Allen-Auerbach M, Hacker M, Sathekge M, et al. Nuclear medicine operations in the times of COVID-19: strategies, precautions, and experiences. *J Nucl Med.* 2020;61:626–9. <https://doi.org/10.2967/jnumed.120.245738>.
58. Kist de Ruijter L, van de Donk PP, Hooiveld-Noeken JS, et al. Whole-body CD8+ T cell visualization before and during cancer immunotherapy: a phase 1/2 trial. *Nat Med.* 2022;28:2601–10. <https://doi.org/10.1038/s41591-022-02084-8>.
59. LaSalle T, Austin EE, Rigney G, Wehrenberg-Klee E, Nesti S, Larimer B, et al. Granzyme B PET imaging of immune-mediated tumor killing as a tool for understanding immunotherapy response. *J Immunother Cancer.* 2020;8:e000291. <https://doi.org/10.1136/jitc-2019-000291>.
60. Niemeijer AN, Leung D, Huisman MC, Bahce I, Hoekstra OS, van Dongen GAMS, et al. Whole body PD-1 and PD-L1 positron emission tomography in patients with non-small-cell lung cancer. *Nat Commun.* 2018;9:1–5. <https://doi.org/10.1038/s41467-018-07131-y>.
61. Duck F. ‘The electrical expansion of quartz’ by Jacques and Pierre Curie. *Ultrasound.* 2009;17:197–203. <https://doi.org/10.1179/174227109X12500830049951>.
62. Murphy A, Nadrjanski M. Physical principles of ultrasound [internet]. *Radiopaediaorg* Radiopaediaorg. 2010; <https://doi.org/10.53347/rID-8663>.
63. Tam AL, Lim HJ, Wistuba II, Tamrazi A, Kuo MD, Ziv E, et al. Image-guided biopsy in the era of personalized cancer care: proceedings from the Society of Interventional Radiology Research Consensus Panel. *J Vasc Interv Radiol.* 2016;27:8–19. <https://doi.org/10.1016/j.jvir.2015.10.019>.
64. Sheth RA, Murthy R, Hong DS, Patel S, Overman MJ, Diab A, et al. Assessment of image-guided intratumoral delivery of immunotherapeutics in patients with cancer. *JAMA Netw Open.* 2020;3:e207911. <https://doi.org/10.1001/jamanetworkopen.2020.7911>.

65. Joiner JB, Pylyayeva-Gupta Y, Dayton PA. Focused ultrasound for immunomodulation of the tumor microenvironment. *J Immunol.* 2020;205:2327–41. <https://doi.org/10.4049/jimmunol.1901430>.
66. Robert B, Yzet T, Regimbeau JM. Radiologic drainage of post-operative collections and abscesses. *J Visc Surg.* 2013;150:S11–8. <https://doi.org/10.1016/j.jviscsurg.2013.05.005>.
67. Men S, Akhan O, K orođlu M. Percutaneous drainage of abdominal abscess. *Eur J Radiol.* 2002;43:204–18. [https://doi.org/10.1016/S0720-048X\(02\)00156-0](https://doi.org/10.1016/S0720-048X(02)00156-0).
68. Supino MC, Buonsenso D, Scateni S, Scialanga B, Mesturino MA, Bock C, et al. Point-of-care lung ultrasound in infants with bronchiolitis in the pediatric emergency department: a prospective study. *Eur J Pediatr.* 2019;178:623–32. <https://doi.org/10.1007/s00431-019-03335-6>.
69. Milojevic I, Lemma K, Khosla R. Ultrasound use in the ICU for interventional pulmonology procedures. *J Thorac Dis.* 2021;13:5343–61. <https://doi.org/10.21037/jtd-19-3564>.
70. Subramaniam S, Bober J, Chao J, Zehtabchi S. Point-of-care ultrasound for diagnosis of abscess in skin and soft tissue infections. Carpenter CR, editor. *Acad Emerg Med.* 2016;23:1298–306. <https://doi.org/10.1111/acem.13049>.
71. Edelman RR. The history of MR imaging as seen through the pages of radiology. *Radiology.* 2014;273:S181–200. <https://doi.org/10.1148/radiol.14140706>.
72. McRobbie DW, Moore EA, Graves MJ, Prince MR. MRI from picture to proton. 2nd ed. Cambridge: Cambridge University Press; 2006. <https://doi.org/10.1017/CBO9780511545405>.
73. Gallagher FA. An introduction to functional and molecular imaging with MRI. *Clin Radiol The Royal College of Radiologists.* 2010;65:557–66. <https://doi.org/10.1016/j.crad.2010.04.006>.
74. Lau D, McLean MA, Priest AN, Gill AB, Scott F, Patterson I, et al. Multiparametric MRI of early tumor response to immune checkpoint blockade in metastatic melanoma. *J Immunother Cancer.* 2021;9:e003125. <https://doi.org/10.1136/jitc-2021-003125>.
75. Huhn K, Engelhorn T, Linker RA, Nagel AM. Potential of sodium MRI as a biomarker for neurodegeneration and neuroinflammation in multiple sclerosis. *Front Neurol.* 2019;10. <https://doi.org/10.3389/fneur.2019.00084>.
76. Biller A, Pflugmann I, Badde S, et al. Sodium MRI in multiple sclerosis is compatible with intracellular sodium accumulation and inflammation-induced hyper-cellularity of acute brain lesions. *Sci Rep.* 2016;6:31269. <https://doi.org/10.1038/srep31269>.
77. McAteer MA, Akhtar AM, von zur Muhlen C, Choudhury RP. An approach to molecular imaging of atherosclerosis, thrombosis, and vascular inflammation using microparticles of iron oxide. *Atherosclerosis.* 2010;209:18–27. <https://doi.org/10.1016/j.atherosclerosis.2009.10.009>.
78. Blezer ELA, Deddens LH, Kooij G, Drexhage J, van der Pol SMA, Reijkerk A, et al. In vivo MR imaging of intercellular adhesion molecule-1 expression in an animal model of multiple sclerosis. *Contrast Media Mol Imaging.* 2015;10:111–21. <https://doi.org/10.1002/cmmi.1602>.
79. Bulte JWM, Shakeri-Zadeh A. In vivo MRI tracking of tumor vaccination and antigen presentation by dendritic cells. *Mol Imaging Biol.* 2021; <https://doi.org/10.1007/s11307-021-01647-4>.
80. Chapelin F, Capitini CM, Ahrens ET. Fluorine-19 MRI for detection and quantification of immune cell therapy for cancer. *J Immunother Cancer.* 2018;6:105. <https://doi.org/10.1186/s40425-018-0416-9>.
81. Kim HS, Woo J, Lee JH, Joo HJ, Choi Y, Kim H, et al. In vivo tracking of dendritic cell using MRI Reporter Gene, Ferritin. Mattei F, editor. *PLoS One.* 2015;10:e0125291. <https://doi.org/10.1371/journal.pone.0125291>.
82. Iordanova B, Goins WF, Clawson DS, Hitchens TK, Ahrens ET. Quantification of HSV-1-mediated expression of the ferritin MRI reporter in the mouse brain. *Gene Ther.* 2013;20:589–96. <https://doi.org/10.1038/gt.2012.70>.

Nuclear Imaging of Inflammation



George Keeling and Francis Man

Abstract Nuclear imaging can be a powerful tool for imaging inflammation, for research and clinical use. Nuclear imaging methods allow noninvasive visualization of biochemical processes with very high sensitivity, often before the appearance of clinical symptoms. In the clinic, nuclear imaging is used for the diagnosis of many conditions including vascular inflammatory diseases, inflammatory bowel diseases, musculoskeletal diseases, and infections. However, significant issues remain, particularly in terms of specificity of the currently approved radiotracers toward different causes of inflammation. In this chapter, we aim to familiarize the reader with nuclear imaging modalities and their application to inflammatory diseases in clinical and preclinical settings. We first describe the basic principles of single-photon emission tomography (SPECT) and positron emission tomography (PET) and their benefits and limitations compared with other types of imaging, and describe several types of radiotracers. We then describe the main clinical uses of nuclear imaging applied to inflammation and new targets for radiotracer development that have shown promise in preclinical research.

Keywords PET · SPECT · Radiotracer · Inflammation · Molecular imaging · Whole-body imaging

G. Keeling
School of Biomedical Engineering & Imaging Sciences, King's College London, London, UK

F. Man (✉)
School of Biomedical Engineering & Imaging Sciences, King's College London, London, UK
Institute of Pharmaceutical Science, King's College London, London, UK
Present Address: GE HealthCare, Pollards Wood, Chalfont St Giles, UK
e-mail: francis.man@kcl.ac.uk

1 Introduction to Nuclear Imaging

Inflammation is a process that occurs as a response to a variety of stimuli, from physical injury to infection or arterial calcification. Detecting, locating, and diagnosing inflammation are an important challenge in the clinic, and nuclear imaging can be a key addition to the clinical toolbox, helping, for example, to differentiate sterile inflammation from infection as this impacts treatment.

Nuclear imaging can be broadly split into two techniques: single-photon emission computed tomography (SPECT) and positron emission tomography (PET). Both of these techniques share the working principle of the injection of a radioactive compound (the tracer), the emissions from which can be detected with very high sensitivity from outside the body. The main advantages of using nuclear imaging modalities are their very high sensitivity, very high depth of penetration (noninvasive imaging), the possibility of accurately quantifying signals, their translational aspect (i.e., the ability to perform preclinical and clinical imaging with the same tracer), and the fact that the signal reflects a biochemical process rather than structural changes in the body.

In this chapter, we first provide a brief introduction to the concepts of nuclear imaging and radiotracers,¹ along with some practical considerations for researchers who might be interested in using nuclear imaging for studying inflammation. We then highlight some of the nuclear imaging techniques currently used for the imaging of inflammation, emerging techniques that are still being established in the clinic, and some of the more recent targets and radiotracers that are still in preclinical stages of development but may lead to the exploration of new frontiers in imaging inflammation in years to come.

1.1 Basic Principles of PET and SPECT

Scintigraphy, SPECT, and PET consist in generating an image from gamma rays (photons) emitted by a radionuclide. For scintigraphy and SPECT, a direct gamma-emitting radionuclide, such as technetium-99m, is incorporated into the administered compound. The gamma rays emitted as the radionuclide decays pass through the body and are detected by a gamma camera. In scintigraphy, a single gamma camera is used to make a two-dimensional map of the location of the radioactivity. This technique is still in widespread use today because of its relatively low cost and simplicity. Images are often taken from both the front and back of the patient to improve organ delineation. In SPECT, two or more gamma cameras are made to

¹Note: The nomenclature of radioactive compounds in the literature is inconsistent and often incorrect. In this chapter, we have endeavored to follow the nomenclature guidelines outlined by Coenen et al. [224], and therefore the nomenclature we use in this chapter may not be identical to the original literature.

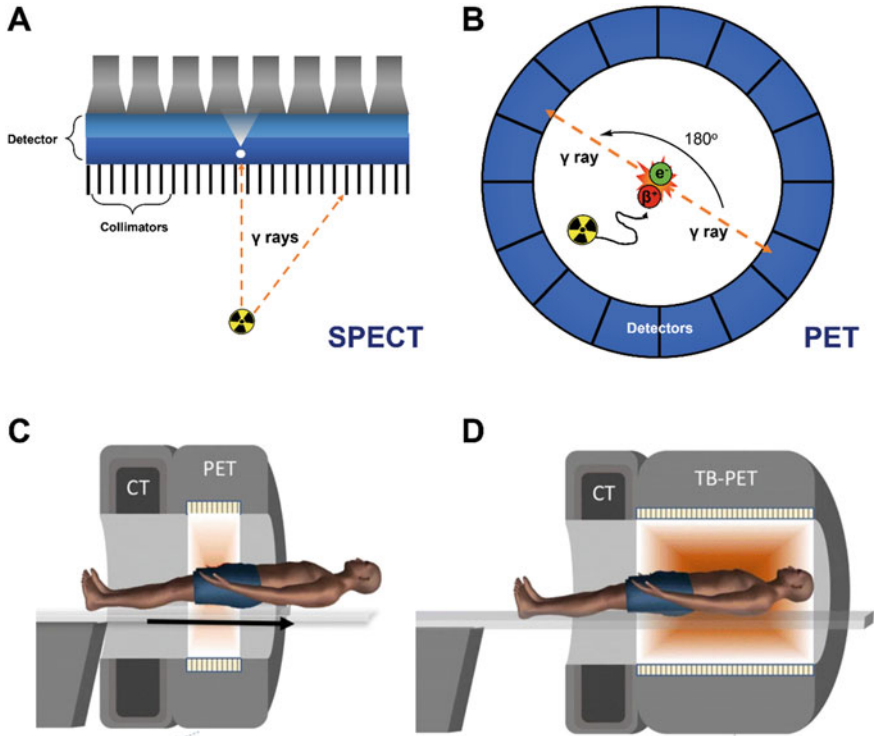


Fig. 1 Schematic representation of the principle of detection of radioactivity by SPECT and PET cameras. (a) In a typical SPECT scanner, there are two flat gamma cameras, positioned on either side of the patient and rotated around the patient during image acquisition. (b) A PET camera consists of detectors arranged in a static ring to detect pairs of gamma rays emitted from the annihilation event. Reproduced from Man et al. [1] with permission. (c, d) Schematic representation of conventional (c) and total-body (d) PET/CT scanners showing the array of detectors arranged around the patient. Modified with permission, © 2020, Vandenberghe et al. [2] (CC-BY-4.0 license, <http://creativecommons.org/licenses/by/4.0/>)

rotate around the patient, allowing for three-dimensional visualization of the location of the radionuclide and hence the compound into which it is incorporated. The gamma camera gantry typically consists of two flat wide camera heads, which are held on opposite sides of the patient. Each camera head consists of lead parallel or pinhole collimators to filter out gamma rays that are not parallel to the pinholes; a thallium-doped sodium-iodide (NaI(Tl)) crystal array, which produces visible light when struck by a gamma ray; a light guide, which improves the uniformity of light collection as a function of position; and an array of photomultiplier tubes (PMT), which convert the incident light produced by the NaI(Tl) crystals to electrical signal which can interface with a computer (Fig. 1a). More recent models make use of electronic detectors based on semiconductor materials (e.g., cadmium-zinc telluride) and do not require PMTs, increasing sensitivity and improving energy resolution, i.e., the capacity to discriminate between gamma rays of different energies.

In contrast, PET consists of the detection of gamma rays emitted by the annihilation of a positron (β^+ particle) and an electron of similar energy. Emitted positrons travel a short distance in tissue—determined by the positron emission energy—before annihilating with an electron, converting their mass to energy in the form of two photons of 511 keV energy. These photons are released in diametrically opposite directions and detected quasi-simultaneously by an array of detectors arranged in a ring around the patient (Fig. 1b), creating a 3D map of the radioactivity. Although each detector operates in a similar manner to a camera head in a SPECT scanner, there is no need for collimators because the position of the annihilation event is calculated from the direction and timing of arrival of the 511 keV photons. Additionally, different scintillation crystals are used, with state-of-the-art scanners generally using lutetium orthosilicate (LSO), lutetium-yttrium orthosilicate (LYSO), or other lutetium-based scintillators (LBS), while many older scanner models use bismuth-germanium oxide (BGO) scintillators [3, 4]. In conventional scanners (both PET and SPECT), the field of view (FOV) of the camera is relatively narrow (10–30 cm in clinical scanners) and only covers a fraction of the patient. To acquire a whole-body image, the patient bed is moved through the gantry and images are acquired sequentially (Fig. 1c), meaning there is a time delay between the top and the bottom of the patient and therefore a loss of temporal information about tracer distribution. This is less of an issue when the focus is on imaging a particular organ (e.g., heart or brain). One of the most exciting developments in nuclear imaging in recent years is the advent of total-body PET, which has a much larger FOV that encompasses the whole body (Fig. 1d), allowing simultaneous imaging of the entire body rather than having to move the patient through the camera to acquire sequential images. This promises to increase sensitivity 40-fold, allowing the injection of lower doses, imaging at later time points, shorter scan times, and increased signal-to-noise ratio [2]. Total-body PET also allows for dynamic scanning of the whole body, potentially opening the doors to innovations in tracer design.

1.2 Benefits and Limitations of Nuclear Imaging

The differences between PET and SPECT lead to various advantages and disadvantages; however, both techniques have very high sensitivity (lower range of detectable tracer concentration: PET, 10^{-11} – 10^{-12} M; SPECT, 10^{-10} – 10^{-11} M) [5], meaning that the low amount of tracer required (PET: μg ; SPECT: μg – mg in a human) [6–8] is unlikely to affect the biological process being investigated and toxicity concerns are reduced. PET and SPECT have excellent capacity for signal quantification and very high tissue penetration, although Compton scattering of gamma rays by adipose tissue can cause image quality issues in obese patients [9]. These techniques are noninvasive, allowing repeated imaging limited only by absorbed dose, and the same tracers can often be used in animals and in patients, which is beneficial for clinical translation. Furthermore, nuclear imaging is inherently molecular, i.e., it reflects biochemical processes occurring in the body. These can be broad, relatively nonspecific processes such as changes in vascular

permeability, or much more targeted such as the activity of a specific enzyme or the expression of a particular protein on cells (see Sect. 1.3.2). This is particularly relevant for inflammation imaging, given the dynamic nature of inflammation and the large variety of cellular and molecular processes involved.

On the other hand, both techniques involve administration of a radioactive substance and therefore exposure to ionizing radiation for the patient as well as any staff involved in radiotracer preparation, administration, and patient care. PET imaging is more sensitive than SPECT: it is typically necessary to inject 10–100 μg of tracer or 100–200 MBq of radioactivity for a PET scan (numbers vary by tracer) [7, 8] but 100–1000 μg of tracer or 700–1000 MBq of radioactivity with SPECT [6]. This stems from the detection of two photons at the same time in PET, meaning that individual photons with no counterpart can be ignored (electronically collimated). SPECT on the other hand uses physical collimators (lead blocks with narrow channels through which photons can pass), which block photons approaching the gamma cameras from all but a 90° angle corresponding to the location of the patient, meaning much of the signal is lost and only approximately 0.01% is actually detected, while in PET this value can reach 10% (values from Siemens technical specifications of state-of-the-art SPECT and PET scanners, respectively) [10, 11].

At time of writing, PET has finer spatial resolution in state-of-the-art clinical scanners than SPECT (~0.8 mm and 5 mm, respectively) [10, 11], although PET has a fundamental limit to its spatial resolution while SPECT does not, and so with further technological developments, SPECT may overtake PET in higher resolution. The best resolution possible in PET is determined by the distance travelled by the positron before annihilation, as the location of the annihilation is what is detected, rather than the nuclear decay event which releases the positron. The distance travelled by the positron depends on its energy and thus on the radionuclide, but a typical mean range of 1–3 mm can be expected [12], and therefore the 0.8 mm spatial resolution enabled by the scanner may not be achievable in practice. In modern preclinical scanners, there is less difference in spatial resolution between SPECT and PET, with submillimeter resolutions achievable for both techniques.

In SPECT, gamma rays are also filtered on the basis of their energy, i.e., detectors are set to detect specific radionuclides based on their characteristic energy profiles. For example, $^{99\text{m}}\text{Tc}$ is detected with an energy window centered around the 140 keV peak, and ^{111}In can be detected using one or two windows centered at 171 and 245 keV, respectively (Table 1). This also means that a SPECT camera can image multiple radionuclides and therefore radiotracers, simultaneously, to follow multiple processes in parallel. This is useful in inflammation when looking at the expression of a specific marker, to correct for increased blood flow that may cause nonspecific increase of radiotracer uptake at the target location. In contrast, with PET, all gamma rays emitted from positron annihilation events have 511 keV energy; therefore, it is not possible to distinguish between positron-emitting radionuclides, and only one radionuclide at a time can be imaged by PET using current scanners. It is possible to use several PET tracers in short succession (as a single imaging session for the patient) if the ones used first have short half-lives, for example, using [^{15}O]H $_2$ O (^{15}O has a half-life of 2.04 min) to image perfusion, followed a few minutes later by an

Table 1 Selection of radionuclides commonly used in medical imaging and their principal physical characteristics and production methods

Radionuclide	Half-life	Scanner type	Main emissions (abundance)	Production method
Carbon-11	20 min	PET	β^+ (99.6%)	Cyclotron: $^{14}\text{N}(p,\alpha)^{11}\text{C}$
Fluorine-18	110 min	PET	β^+ (96.7%)	Cyclotron: $^{18}\text{O}(p,n)^{18}\text{F}$
Copper-64	12.7 h	PET	β^+ (18%), β^- (38%)	Cyclotron: $^{64}\text{Ni}(p,n)^{64}\text{Cu}$
Gallium-67	78.2 h	SPECT	γ : 93 keV (38%), 184 keV (21%), 300 keV (16%)	Cyclotron: $^{68}\text{Zn}(p,2n)^{67}\text{Ga}$
Gallium-68	68 min	PET	β^+ (89%)	$^{68}\text{Ge}/^{68}\text{Ga}$ generator
Zirconium-89	78.4 h	PET	β^+ (23%)	Cyclotron: $^{89}\text{Y}(p,n)^{89}\text{Zr}$
Technetium-99m	6.02 h	SPECT	γ : 140 keV (98.6%), 142 keV (1.4%)	$^{99}\text{Mo}/^{99\text{m}}\text{Tc}$ generator
Indium-111	67.9 h	SPECT	γ : 245 keV (94.0%), 171 keV (90.2%)	Cyclotron: $^{112}\text{Cd}(p,2n)^{111}\text{In}$
Iodine-123	13.2 h	SPECT	γ : 159 keV (83.2%)	Cyclotron: $^{124}\text{Xe}(p,x)^{123}\text{Xe} \rightarrow ^{123}\text{I}$
Iodine-124	100.2 h	PET	β^+ : 1532 keV (11.4%), 2135 keV (10.3%)	Cyclotron: $^{124}\text{Te}(p,n)^{124}\text{I}$, $^{125}\text{Te}(p,2n)^{124}\text{I}$, $^{126}\text{Te}(p,3n)^{124}\text{I}$

^{18}F -based radiotracer. PET scanners able to discriminate between several PET radionuclides based on the energy of “prompt” gamma rays (i.e., co-emitted with the positron) have recently been developed, but these are not yet in widespread use.

Radionuclide imaging techniques only provide information about the location and amount of radioactivity and do not provide anatomical information on their own. For this reason, both PET and SPECT are commonly paired with computed tomography (CT), which provides anatomical context and can be used for attenuation correction as well. CT involves the use of a gantry comprised of an X-ray source tube on one side of the patient and detectors on the other side. This rotates around the patient, collecting a series of 2D views to generate a 3D image of the body based on tissue density, allowing excellent visualization of dense tissues such as bones and some soft tissue contrast as well. This CT scan adds to the total ionizing radiation dose received by the patient. An alternative to CT is the use of magnetic resonance imaging (MRI). MRI does not use ionizing radiation and can give better soft tissue contrast than CT. Both have similar spatial resolution, with Siemens quoting their state-of-the-art scanners to have 0.2 and 0.25 mm spatial resolution for MRI and CT, respectively [13, 14]. The combination of PET or SPECT with MRI is more recent and has yet to gain much popularity in the clinic due to several disadvantages, including the longer acquisition time of MRI compared to CT, the increased costs, and the difficulties with using MRI for attenuation correction [15].

1.3 Radiotracers: Radionuclides, Targeting Moieties, and Practical Considerations

Conceptually, radiotracers can be considered as being made of an imaging moiety (the radionuclide) and a targeting moiety and optionally a linker between the two. Sometimes the imaging moiety is the same as the targeting moiety, for example, with iodine-131 and technetium-99m pertechnetate ($[\text{}^{99\text{m}}\text{Tc}]\text{TcO}_4^-$), which are selectively taken up by the sodium-iodide symporter (NIS) and are used for thyroid, salivary gland, and stomach imaging, or $[\text{}^{18}\text{F}]\text{NaF}$ which simply exploits the natural affinity of fluoride anions for uncapped hydroxyapatite bone minerals. The linker can be a complex structure or a simple covalent bond, such as the carbon-fluorine bond in $[\text{}^{18}\text{F}]\text{fluorodeoxyglucose}$ ($[\text{}^{18}\text{F}]\text{FDG}$) (Fig. 2). In this section, we briefly describe some of the radionuclides used for nuclear imaging and the main categories of radiotracers based on their chemical structure. We also provide a few practical considerations for researchers who wish to add nuclear imaging to their investigations. Most of these are not specific to imaging of inflammation and are also applicable to other therapeutic areas.

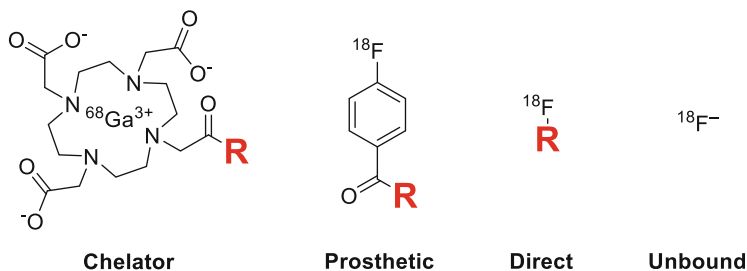


Fig. 2 Examples of different radiolabelling approaches. The chelator example shows a representative structure although metal-ligand bonds have been omitted for clarity. R = targeting moiety or carrier molecule (e.g., small molecule, peptide, antibody, polymer, nanoparticle, etc.)

1.3.1 Radionuclides

The vast majority of nuclear imaging is conducted with a dozen different radionuclides, with physical half-lives ranging from about a minute to several days (Table 1).

For imaging purposes, the radionuclides used are relatively short-lived, the most commonly used being technetium-99m ($t_{1/2} = 6.02$ h) for SPECT and fluorine-18 ($t_{1/2} = 110$ min) for PET. This means that in the vast majority of cases, the tracer has to be prepared on the day and, in the case of the shorter-lived radionuclides, cannot be stored for more than a few hours. For this reason, it is important to have a reliable supply of radionuclide, and the radiochemistry required for synthesizing tracers should be fast, high-yielding, robust, and require as little direct input from the radiopharmacist as possible to minimize the dose to the operator. For more details on the technical aspects of radiopharmacy, we refer the reader to an excellent textbook [16].

The radiochemistry for incorporating most metallic radionuclides is often fast complexation chemistry, which may be performed using kits: preprepared vials of nonradioactive excipients to which the radionuclide is added, heated if necessary, and allowed to react with as few adjustments as possible. It is this simplicity—in addition to its convenient half-life and gamma emissions which are low energy but easily detectable—that has led to technetium-99m, a metallic radionuclide, being the workhorse of nuclear imaging for decades. Radiometallation reactions generally require fewer steps than typical nonmetallic radiosyntheses—such as fluorine-18 or iodine radiolabelling reactions—which may be performed using automated synthesis modules to reduce the radiation dose to the operator as well as the scope for operator error. However, further chemical modification of the targeting moiety is generally required to allow metal chelation, with large chelators (multidentate ligands) being conjugated to the moiety responsible for localization of the probe. Modifications for incorporating nonmetallic radionuclides, on the other hand, tend to be minimal and in some cases radiotracers can be chemically identical to drugs or naturally occurring chemicals. Whether metallic or nonmetallic radionuclides are more appropriate depends on a number of factors, both within the design of the

radiopharmaceutical and in terms of preferences and resources of individual operators, clinicians, or institutions.

A popular radiometal for PET imaging is gallium-68. Gallium-68 has a shorter half-life than fluorine-18 (68 min vs. 110 min)—meaning the speed and yield of radiosynthesis takes on even greater importance—and a different production method. Fluorine-18 is produced in a cyclotron, a particle accelerator typically requiring a large, dedicated room, which is capable of producing large amounts of fluorine-18, which can be used locally or shipped over short distances. In the case of shorter-lived cyclotron-produced radionuclides such as carbon-11 ($t_{1/2} = 20$ min), the radionuclide must be produced on-site, and the scope for shipping to other sites is virtually zero. Gallium-68 however is produced in a generator, a solid-phase extraction system that allows gallium-68 to be chemically separated from its long-lived parent radionuclide germanium-68 ($t_{1/2} = 271$ days). This means that smaller quantities of radioactivity (typically enough for 1–5 PET scans, although this varies depending on tracer, generator model, generator usage, and protocol) can be eluted from the generator every few hours by nonexpert users. This is one of the most reliable sources of radioactivity and is not prone to mechanical issues that can affect cyclotrons. Typical generators are also far smaller than cyclotrons and can be integrated into most radiopharmacies without the need for major structural investment. However, the amount of radioactivity received is much smaller than a cyclotron, and the lifetime of a $^{68}\text{Ge}/^{68}\text{Ga}$ generator (roughly 1 year) means that the cost of buying generators over the lifetime of a cyclotron (20+ years) can be substantial. It is also important to ensure a reliable supply of generators. There were well-documented shortages of ^{99}Mo , the parent isotope of $^{99\text{m}}\text{Tc}$, in 2009–2010, which crippled the supply of the most popular radionuclide in nuclear imaging [17]. This led to a global shortage of $^{99}\text{Mo}/^{99\text{m}}\text{Tc}$ generators, which only have a clinical lifetime of about 1 week, meaning severe disruption to many nuclear medicine departments worldwide.

A closely related field to nuclear imaging is radionuclide therapy, which makes use of radionuclides that primarily emit α -particles, β -particles, and Auger electrons, which are far more damaging to tissues than gamma rays. These radionuclides can often be attached to targeting moieties using the same methods as for gamma- or positron-emitting radionuclides. For example, the same chelators (e.g., DOTA, NOTA, DTPA) can be used for the α -particle emitters ^{177}Lu and ^{225}Ac as for the positron emitter ^{68}Ga , meaning it is possible to “swap” an imaging radionuclide for a therapeutic radionuclide on the same targeting backbone and to use both radiotracers as a pair with nearly identical pharmacokinetics. This combination of diagnostic imaging and (radionuclide) therapy is called theranostics. The main applications of theranostics are currently in oncology [18], but radionuclide therapy also exists for certain inflammatory diseases, for example, radiosynoviorthesis is a procedure that employs radionuclides (^{90}Y , ^{169}Er , ^{186}Re , $^{117\text{m}}\text{Sn}$, etc.) to destroy macrophages in inflamed joints [19], and there are therefore potential applications of theranostics in inflammation as well.

Choosing the Right Radionuclide From a clinical perspective, radionuclides with a shorter half-life would seem preferable, in order to reduce the radiation dose to the patient. However, the half-life should also match the pharmacokinetic properties of the radiotracer, so that sufficient activity remains present for imaging after the radiotracer has accumulated at the target location. As a rule of thumb, tracers with larger molecular weight circulate for longer before accumulating at their target site. Small-molecule tracers and those based on peptides or antibody fragments tend to have shorter circulation times and will generally give good target-to-background ratios within an hour, so shorter-lived radionuclides can be used, while IgG antibody-based tracers or “stealthy” nanoparticles may take 2-3 days to localize at the target site, requiring the use of longer-lived radionuclides. These longer-lived tracers will typically have a half-life of a few days, e.g., indium-111 (for SPECT, $t_{1/2} = 2.8$ days), gallium-67 (for SPECT, $t_{1/2} = 3.3$ days), or zirconium-89 (for PET, $t_{1/2} = 3.3$ days). The choice of radionuclide also affects image quality: gamma rays with lower energies (e.g., technetium-99m, 140 keV) provide better spatial resolution than those with higher energies, such as indium-111 or gallium-67 (Table 1); similarly, positrons with lower energies travel shorter distances in tissue before annihilation, and there is therefore lower uncertainty around the position of the emitting nucleus [20]. In practice, the choice of radionuclide is also restricted by availability, as not all radionuclides are available in every nuclear imaging facility. Radionuclides with half-lives of a few hours or more can be shipped from the production center and used elsewhere, and those available from generators also require less infrastructure than those produced in a cyclotron. Preclinical studies with a translational aim should consider using radionuclides that are more widely available in the clinic.

1.3.2 Radiotracers: Structural Classes

One major benefit of nuclear imaging when investigating inflammation is its versatility. Virtually any molecule can be radiolabelled in order to detect subtle changes in the microenvironment in any part of the body noninvasively, and this opens many doors for evaluating inflammation. To date, the approaches toward imaging inflammation have followed three main strategies:

Firstly, labelling of a chemical which will be taken up by the immune cells at the site of inflammation. This uptake can be due to metabolic changes, or the upregulation of certain receptors, or the increased occurrence of certain types of immune cells at the site of inflammation.

Secondly, imaging other conditions correlate with inflammation—this can also be metabolic changes but may include conditions such as vascular calcification.

Finally, the labelling of larger entities such as cells, colloids, or nanoparticles, which will accumulate either actively or passively at the site of inflammation. An example would be the extraction, radiolabelling, and reinjection of immune cells, to look for sites of active cell recruitment.

Small Molecules Small-molecule radiotracers for inflammation are typically ligands for receptors or substrates for enzymes upregulated during inflammation. [^{18}F]FDG is a prime example, as it mimics the chemical structure of glucose (Fig. 3a) and is taken up by glucose transporters (GLUT) in metabolically active cells, including activated leukocytes at sites of inflammation (see Sect. 2.1). Another example is [^{11}C]DPA-713, which is a selective ligand with low nanomolar affinity for the translocator protein (TSPO; see Sect. 3.1.1). For small molecules, it is often preferable to use the direct radiolabelling approach (Fig. 2) to avoid affecting the affinity of the ligand for its target. Carbon-11 is an excellent radionuclide in this respect as it can replace a carbon atom (e.g., in a methyl or methoxy group) with no impact on the chemical structure. However, its short half-life makes it less convenient to use, as procedures (radiolabelling, administration, and imaging) must be carried out very quickly and only short-term imaging (1–2 h after administration) is possible. Fluorine-18 and radioisotopes of iodine can often be incorporated into small-molecule ligands with limited impact on binding affinity and pharmacokinetics or even no impact if the original structure already contains fluorine or iodine atoms. The potential of small-molecule radiotracers for imaging is also reflected in the increasing availability of chemical methods for direct radiolabelling [21, 22]. Alternatively, some small-molecule radiotracers are not specifically targeted and are used primarily for their pharmacokinetic characteristics. For example, diethylenetriamine pentaacetic acid (DTPA) is a small hydrophilic molecule with rapid renal clearance that is a good chelator for radiometals such as $^{99\text{m}}\text{Tc}$ and ^{111}In . [$^{99\text{m}}\text{Tc}$]Tc-DTPA (Fig. 3b) has long been used in the clinic to evaluate renal function and, in aerosol form, to evaluate lung ventilation/perfusion and epithelial

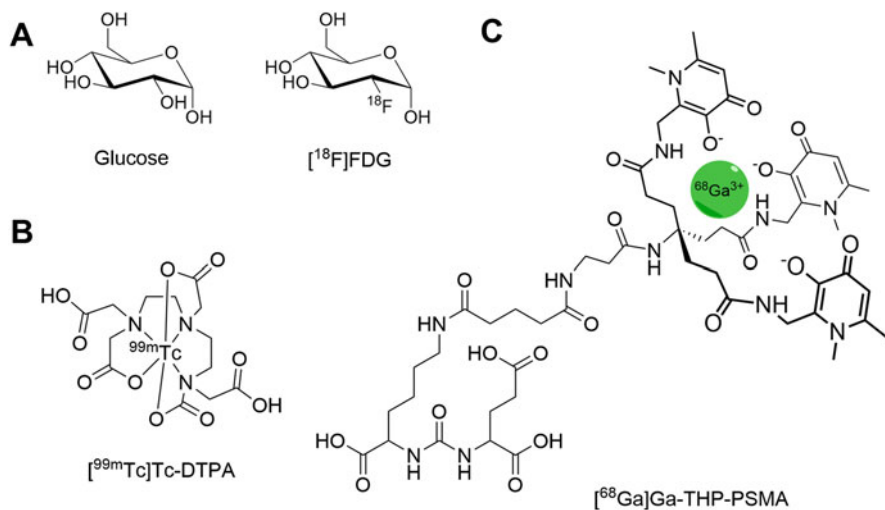


Fig. 3 (a) Chemical structures of glucose (in its α -pyranose form) and its radiolabelled analogue [^{18}F]FDG. (b) Proposed structure of [$^{99\text{m}}\text{Tc}$]Tc-DTPA. (c) Structure of THP-PSMA, a conjugate of PSMA which can be radiolabelled with the short-lived positron emitter gallium-68

permeability. More recently, [^{99m}Tc]Tc-DTPA has been shown to detect early changes (2 h after injury) in the blood-brain barrier (BBB) permeability in a rat model of stroke [23].

Conversely, hexamethylpropyleneamine oxime (HMPAO) readily crosses the BBB due to its lipophilicity and has high first-pass extraction in the brain (80%). In addition to leukocyte radiolabelling (see below), [^{99m}Tc]Tc-HMPAO is used for brain perfusion imaging, e.g., in acute stroke, chronic brain ischaemia, and traumatic brain injury but also inflammatory diseases such as viral encephalitis and Behcet's disease [24]. More recently, it has been used to evaluate lung inflammation in rats [25].

Peptides Peptides are interesting platforms to develop radiotracers because of their high affinity for certain biological targets and their versatility in terms of functionalization. Chelators or prosthetic groups can be added to peptide sequences by selectively incorporating these groups (i.e., site-specific labelling) in positions that do not interfere with binding or by adding linkers to increase the distance between the binding site and the imaging moiety. Typical examples include radiolabelled derivatives of the somatostatin analogue octreotide such as DOTA-TATE and DOTA-TOC, Arg-Gly-Asp (RGD) peptide derivatives that bind to integrins, and radiolabelled peptide ligands for prostate-specific membrane antigen (PSMA) (Fig. 3c). Care must still be taken to ensure the radiolabel does not interfere too much with target binding and pharmacokinetic properties, especially for small peptides and larger chelators or prosthetic groups. For further details on radiolabelled peptides and their applications, we refer the reader to the review by Jackson et al. [26].

Antibodies and Antibody Fragments Antibodies are highly attractive and extensively used platforms for radiotracer development and nuclear imaging because of their exquisite binding affinity and target specificity. Antibodies are relatively simple to radiolabel using bifunctional chelators or prosthetic groups that react with amine or thiol groups present on the side chains of the protein sequence; however, this approach does not allow for precise control of the number and location of radiolabels added. Because of the small size of the imaging moieties (~ 0.5 – 1 kDa each, with typically one to ten radiolabels per antibody molecule) relative to full-size antibodies (150–200 kDa), radiolabelling generally has little impact on antibody affinity and pharmacokinetic properties, although this should be verified during development. Most commonly, IgG-class antibodies are used, which have relatively long circulation times and biological half-lives. Therefore, imaging needs to be delayed (typically by 24–48 h) to allow for the radiolabelled antibody to accumulate at the target location and clear from the circulation to reduce background signal. Consequently, radionuclides with sufficiently long half-lives are required. In practice, this also means that the patient/subject is irradiated for a longer period of time, and in the clinic, the patient is required to attend twice (first for the injection and then for the scan). Although antibodies can be radiolabelled with ^{99m}Tc and ^{64}Cu , imaging 24 h after administration is the practical limit with these radionuclides. ^{111}In is more suitable for imaging long-circulating antibodies, and recent years have seen a

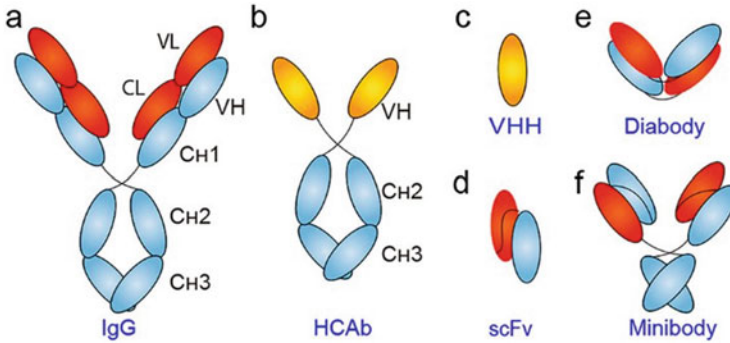


Fig. 4 Schematic structures of antibodies and antibody fragments. Antibodies (a) and antibody fragments (b-f) are typically radiolabelled by conjugating them to bifunctional chelators that can react with amine or thiol groups on the protein chain. Reproduced from Wei et al. [29] with permission. IgG: immunoglobulin G; HCAb: heavy-chain-only antibody; VHH: single-domain antibody, also known as nanobody; scFv: single-chain variable fragment

significant increase in the use of ^{89}Zr for PET imaging of antibody-based radiotracers (“immunoPET”), mostly in oncology [27]. Examples of radiolabelled antibodies used in the clinic include the anti-granulocyte monoclonal antibodies [$^{99\text{m}}\text{Tc}$]Tc-sulesomab (LeukoScan[®]), [$^{99\text{m}}\text{Tc}$]Tc-besilesomab (Scintimun[®]), the anti-HER2 [^{89}Zr]Zr-trastuzumab, and various radiolabelled derivatives of the anti-CD20 rituximab. For a more detailed overview of antibodies used for inflammation imaging, we direct the reader to the review by Lee et al. [28]. To solve the issue of long circulation and slow accumulation, antibody fragments with lower molecular weights such as single-chain Fv, minibodies, diabodies, or nanobodies (Fig. 4) have also seen increased use in preclinical research [29]. These fragments have much faster clearance and can typically be imaged within 0.5–4 h of administration. Thus, radionuclides with shorter half-lives (e.g., ^{68}Ga , ^{18}F) can be used. Another advantage of engineered antibody fragments is the possibility to perform site-specific labelling, i.e., having precise control over the location of the radionuclide to avoid impairing the affinity of the probe for its target. Finally, it is often claimed (even by us at the beginning of this chapter) that because of the high sensitivity of nuclear imaging, “tracer doses” of radiolabelled compounds pose very little risk to the subject. In the case of antibodies, however, the exquisite potency of some of these molecules means that even tracer doses can have unwanted biological effects [30] and should be used with caution.

Macromolecules: Colloids and Micro-/Nanoparticles Macromolecular structures such as protein aggregates, lipid micelles, liposomes, inorganic polymers, and metallic micro- or nanoparticles are also often used for nuclear imaging, as they are versatile platforms that can be functionalized with a wide variety of imaging reporters (radionuclides, fluorescent dyes, MR contrast agents) and targeting moieties and can additionally be loaded with therapeutic drugs (Fig. 5). Among the older examples are [$^{99\text{m}}\text{Tc}$]Tc-macroaggregated albumin (MAA), which is not a targeted radiotracer but simply follows the blood flow and is used for lung perfusion imaging,

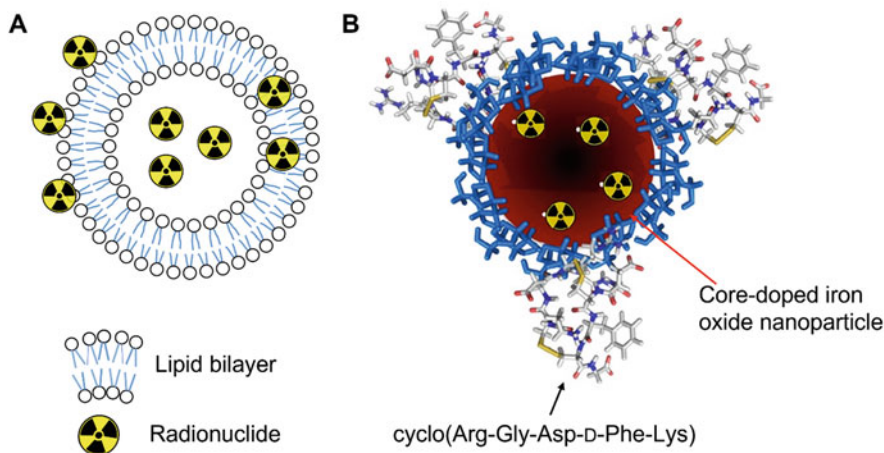


Fig. 5 Radiolabelled nanoparticles. (a) Schematic structure of a radiolabelled liposome, showing the phospholipid bilayer and radionuclides present in the aqueous compartment, within the membrane and on the liposome surface. The location of the radiolabel depends on the radiotracer and radiolabelling method; see [1]. (b) Schematic structure of a core-doped radiolabelled iron oxide nanoparticle (IONP), in which the metallic radionuclide is embedded within the iron core. Nanoparticles can additionally be surface-functionalized, in this example with a dextran coating (blue) to enable covalent linkage to a cyclic RGD peptide derivative for integrin $\alpha_v\beta_3$ targeting. Superparamagnetic IONPs can also be detected by MRI. Adapted with permission from Pellico et al. [32], © 2016 John Wiley & Sons

and [^{99m}Tc]Tc-sulfur colloid (Technecoll[®]), which is used for sentinel lymph node detection, bone marrow imaging and liver imaging. As a general rule, micro- and nanoparticles are taken up by phagocytic cells and tend to accumulate in phagocyte-rich organs such as the liver and spleen, and therefore radiolabelled particle-based tracers tend to give high background signal in these organs. Various strategies exist to affect the biodistribution of particles, for example, coating the surface with molecules that “mask” the particles from phagocytes or with antibodies to target the particles toward cells expressing specific markers. For a comprehensive overview of radiolabelled liposomes and nanoparticles and their use in medical imaging, we direct the reader to recent reviews [1, 31].

Radiolabelled Cells Cells, and particularly immune cells in the context of inflammation, can be radiolabelled and used for nuclear imaging, making use of the intrinsic homing capabilities of leukocytes toward sites of inflammation and infection. Radiolabelled leukocytes are currently the gold standard method for nuclear imaging of infections [33] (see Sect. 2.1.6). The procedure involves taking the patient’s blood, isolating leukocytes (or more specific subpopulations), incubating them with a lipophilic radiotracer that crosses the cell membrane (either [^{111}In]In-oxine or [^{99m}Tc]Tc-HMPAO in current clinical practice), removing any unbound radiotracer, and injecting them back into the patient. The downside of this approach is that the whole procedure takes several hours and involves risk to the operator due

to both radiation and manipulation of blood. In preclinical research, it is also impractical to isolate sufficient numbers of leukocytes from mice. Alternatively, cells can be engineered to express reporter genes that enable indirect radiolabelling, e.g., using NIS to image cells with [^{99m}Tc]TcO $_4^-$ or [^{18}F]BF $_4^-$, although this is not currently used in routine clinical practice. Cell radiolabelling has been used since the 1970s with relatively few improvements since, but recent developments in cell therapies have led to renewed efforts, particularly in trying to shift toward PET imaging. In addition to leukocytes for infection imaging, the use of stem cells to treat chronic inflammatory diseases [34] is also an area that could greatly benefit from nuclear imaging. For further details on cell radiolabelling, we invite the reader to consult our recent review [35].

1.3.3 Multimodal and Multi-Tracer Imaging

It is possible to use multimodal tracers, i.e., imaging probes that are detectable by more than one imaging modality, in order to maximize the advantages of each modality. For example, a dual PET/MRI tracer could have both the sensitivity of a PET tracer, to rapidly locate multiple sites of accumulation in the body, and the high spatial resolution of MRI (which is less suited to whole-body scanning) to “zoom in” to the area of interest and provide a more precise image that might enable surgical planning [36]. Alternatively, a PET/fluorescent tracer could allow highly sensitive imaging on completely different scales, from whole-body distribution to subcellular localization. The combination of radiotracers with fluorescent probes is increasingly explored in oncology, as it allows sensitive detection and mapping of tumor sites, followed by fluorescence-guided surgery [37]. Withana et al. demonstrated one such example for the imaging of atherosclerosis in mice, with an activated macrophage-targeting probe that contained both a fluorescent dye and a chelator for ^{64}Cu [38]. This allowed the noninvasive visualization of atherosclerotic plaque by PET, *in vivo* fluorescence imaging, and *ex vivo* imaging by confocal microscopy.

Multiple tracers can be used in combination to study different processes associated with inflammation. This is an established procedure in pulmonary medicine, as lung ventilation/perfusion (V/Q) scans are performed with one radiotracer as an inhaled gas (e.g., ^{81m}Kr , ^{133}Xe) or aerosol ([^{99m}Tc]Tc-DTPA) to image ventilation and another radiotracer (e.g., [^{99m}Tc]Tc-MAA) injected intravenously to image lung perfusion. This is possible with SPECT and scintigraphy because radionuclides can be separated by their characteristic gamma energies. With PET tracers, this is more challenging, although PET and SPECT could be used in parallel. Recently, Bocan et al. used in parallel the translocator protein (TSPO; see Sect. 3.1.1) radiotracer [^{18}F]DPA-714 to study neuroinflammation, [^{18}F]FMISO to investigate hypoxia, an ^{18}F -labelled caspase-3-substrate to detect apoptosis, [^{18}F]albumin to evaluate vascular (BBB) integrity, and [^{18}F]FDG to evaluate glucose metabolism, all in one model of viral encephalitis [39]. Note that the tracers were administered into separate groups of mice: indeed, it is not possible to image multiple ^{18}F -labelled tracers simultaneously as the signals (511 keV gamma rays) reaching the detector would be

identical. The tracers could potentially be administered sequentially if enough time was given between the injections (e.g., a 12-hour wait in the case of ^{18}F , which has a half-life of 110 min, would allow the first dose to decay by nearly two orders of magnitude). Alternatively, combinations of radiotracers with different half-lives could be used. For example, Chen et al. recently proposed that the use of [^{11}C] PBR28 (for TSPO-mediated imaging of macrophages) and [^{18}F]FDG (for neutrophil-driven glucose consumption) could be a way of distinguishing acute viral infection from chronic inflammation [40]. The short half-life of ^{11}C would allow both tracers to be administered on the same day, shortening the procedure. We expect this type of multi-tracer study to become more easily feasible and more common with the increasing availability of highly sensitive total-body PET scanners.

1.3.4 Practical Considerations for Preclinical Nuclear Imaging of Inflammation

Radiotracers need to be validated *in vitro* before use in animal models of inflammation. An important consideration is that radionuclides constantly emit radiation and cannot be “switched off”; consequently, radiotracers produce signal after administration until the radionuclide has sufficiently decayed or been eliminated. Notably, this means radioactive impurities and metabolites also contribute to the signal and may confound the results by generating false-positive spots on the image. The first step toward obtaining a good image, i.e., specific to the inflammatory process of interest, is to have a radiotracer with sufficient stability in its biological environment. This is typically evaluated *in vitro* by incubating the radiotracer in serum, but users may wish to consider additional assays to replicate, for example, the protease-rich environment of inflamed tissues. Peptide-based radiotracers are particularly sensitive to proteases, and numerous strategies have been devised to improve their stability, such as cyclization or the use of unnatural amino acids [41]. Note that, conversely, proteases can be exploited as targets for activatable radiotracers [42]. Tracers based on a chelated radiometal can be subject to transchelation, i.e., exchange of the radiometal with metal-binding proteins such as transferrin or ferritin, whereas fluorinated or iodinated radiotracers can be subject to dehalogenation. For radiolabelled cells, the radionuclide may be released from the cell over time. In either case, this results in the separation of the radionuclide from its targeting moiety and the appearance of nonspecific signal. Stability is achieved through proper radiotracer design, such as the use of radiometal-chelator pairs with high affinity.

The second step for good image quality is to have tracers with high radiochemical purity, i.e., aiming to ensure the only radioactive species in the product is the radiotracer. This is achieved by optimizing the radiolabelling and purification conditions and is generally evaluated by radiochromatography methods. *In vivo*, radiotracer instability can be determined by analyzing blood samples but also by unexpected patterns in images: for example, the appearance of radioactivity in the kidneys after administration of a radiotracer expected to have primarily hepatobiliary

metabolism or accumulation (such as radiolabelled antibodies, nanoparticles) suggests the radionuclide is no longer attached to the main molecule or this molecule has fragmented.

Specificity and affinity of the radiotracer for its intended target also needs to be evaluated where relevant. Particularly for smaller molecules, radiolabelling through the introduction of bifunctional chelators or prosthetic groups can have detrimental effects on their binding affinity. One recent example in the context of inflammation is provided by Kondo et al., who found that using a *N*-succinimidyl 4- ^{18}F fluorobenzoate prosthetic group reduced the affinity of their tracer for matrix metalloproteinases (MMPs; see Sect. 3.2.6) by one to two orders of magnitude compared to the parent compound, whereas the 4-nitrophenyl 2- ^{18}F fluoropropionate preserved affinity [43]. Mild radiolabelling conditions (rapid, room temperature, mild pH) are also preferable in order to preserve affinity, especially for peptide and protein-based radiotracers.

Initial *in vivo* experiments should be conducted in healthy animals to establish the normal distribution kinetics of the radiotracer. For earlier time points (typically from 0–60 min after administration), dynamic imaging can provide detailed analysis of radiotracer distribution across multiple organs (depending on the field of view and size of the subject) and with high temporal resolution. Usually, this is done by capturing initially very short frames (sometimes less than 10 s) [44] and progressively increasing frame duration. At later time points (hours or days after administration, depending on radiotracer, but usually not beyond three to four half-lives of the radionuclide), static images can be acquired with longer acquisition times (0.5–2 h) to compensate for radionuclide decay. The noninvasive and quantitative nature of nuclear imaging is an immense advantage here, as they allow subjects to be imaged repeatedly and the images can be used to generate time-activity curves from which pharmacokinetic models can be derived. Once the radiotracer's kinetics are better known, imaging can be limited to a smaller number of time points that are more relevant to the disease model. If repeated imaging over the course of disease is desired, it is important to wait sufficiently long (or use radiotracers with shorter half-lives) between two tracer administrations and scans to prevent overlap. In preclinical studies, radiotracer uptake in a given region is often expressed as percentage of injected radioactivity (%ID) per unit of volume (e.g., %ID/mL) or tissue weight (%ID/g) when measured *ex vivo*. In patients, uptake is more frequently expressed as standardized uptake values (SUV), corresponding to the ratio of tissue radioactivity concentration (e.g., MBq/mL) to administered activity (MBq), divided by body weight. In both cases, all measures are corrected for decay to the same time point.

Another point to consider is the relatively limited spatial resolution of nuclear imaging (compared to MRI and X-ray) and how it can affect measures in certain models, particularly in smaller animals such as mice. When volumes of interest are smaller than the resolution of the camera, the images can show an apparent increase in the volume from which the activity originates, leading to an apparent decrease in activity in the real source area (partial volume effect) and an increase in activity in neighboring regions (spillover). Consequently, it can be difficult to precisely locate

the source of activity. Virtanen et al. highlighted this problem with radiotracers targeting vascular adhesion protein 1 (VAP-1; see Sect. 3.2.8) in atherosclerosis, pointing out the difficulty of measuring uptake in small atherosclerotic lesions in the aortic arch in mice because of the activity in the blood pool, whereas in rats the aortic arch is much larger and image-based quantification is more reliable [45]. Therefore, although that mouse model of atherosclerosis is a standard one and appropriate from a biological perspective, it is less ideal from a nuclear imaging perspective. That study also illustrated the impact of the choice of radionuclide, as the images from the ^{68}Ga -labelled tracer appeared blurrier than those from the ^{18}F -labelled tracer, which could be explained by the higher positron energy of ^{68}Ga (mean energy 0.89 MeV) compared to ^{18}F (mean energy 0.25 MeV). In preclinical studies, quantification of radioactivity in organs is generally confirmed by ex vivo biodistribution (measuring individual organs in a liquid scintillation counter), which is extremely sensitive but negates the advantage of noninvasive imaging. It is highly recommended at the final experimental time point but may not be ethically justified for intermediate time points. Autoradiography on tissue slices can provide information on the spatial distribution of radioactivity. For targeted radiotracers, providing evidence of target presence (or lack thereof) by histological methods or flow cytometry is also good practice.

Finally, experimental conditions can also have an impact on the final image. Fueger et al. conducted an important study evaluating the effect of handling, diet, and anesthesia on [^{18}F]FDG uptake in mice [46]. It was shown that warming and fasting the mice reduced the uptake of [^{18}F]FDG in brown adipose tissue and thereby improved tumor visualization. It was also found that isoflurane had no effect on [^{18}F]FDG uptake by tumors whereas ketamine/xylazine caused hyperglycemia. In the brain, different anesthetic agents affected the regional distribution of [^{18}F]FDG [47]. For studies of cardiac inflammation, ketamine/xylazine is useful to reduce background signal of [^{18}F]FDG in the myocardium, whereas for other models it is preferable to use isoflurane which has a much lower effect on [^{18}F]FDG uptake. Similar results were observed with [^{18}F]FLT in tumor and inflammation models [48]. The anesthetic agent must therefore be chosen carefully and adapted to the study model.

2 Clinical Nuclear Imaging of Inflammation

2.1 *Current Uses and Tracers*

Nuclear imaging techniques have been used for identifying inflammation at least since the 1970s, when scintigraphy with [^{67}Ga]Ga-citrate was identified to be useful in detecting inflammatory lesions in cancer patients [49]. By the end of the decade, its uses had spread to the imaging of a wide variety of inflammatory processes and were not limited to oncological applications [50]. Since then, a wide variety of imaging probes have been developed and adapted for the imaging of inflammation in

a plethora of patient populations. Nuclear imaging is used in the diagnosis of numerous inflammatory conditions, including non-infectious conditions such as atherosclerosis, inflammatory bowel diseases (IBD), sarcoidosis and large vessel vasculitis, as well as infection-related inflammation such as infective endocarditis, prosthetic joint infections, osteomyelitis, and tuberculosis [33, 51]. Nuclear imaging can provide vital information for diagnosis, monitoring therapy, exclusion of other causes, guide for biopsy, and discrimination between active and residual disease [51]. Table 2 summarizes the principal radiotracers used for nuclear imaging of inflammatory diseases in the clinic.

One of the most widely used radiotracers in nuclear medicine is [^{18}F] fluorodeoxyglucose ([^{18}F]FDG), an analogue of glucose used in PET imaging. [^{18}F]FDG is taken up in the same way as glucose, via glucose transporters (GLUT), with particularly high uptake in more metabolically active areas [52]. Like glucose, upon entry into the cell, [^{18}F]FDG is phosphorylated by hexokinase to give [^{18}F]FDG-6-phosphate. At this point, the difference in structure compared to glucose—the 2-hydroxyl group of glucose is substituted with fluorine-18—means that the subsequent rearrangement of the glucose-6-phosphate to fructose-6-phosphate by phosphoglucose isomerase cannot occur, effectively trapping [^{18}F]FDG-6-phosphate at that stage of metabolism and trapping it within the cell, causing a gradual accumulation of [^{18}F]FDG-6-phosphate in the most metabolically active cells [53]. There are several reasons for the popularity of [^{18}F]FDG, but this ability to detect such a simple change has led to [^{18}F]FDG being the most used PET tracer worldwide and one of the most versatile radiotracers developed to date. The primary use of [^{18}F]FDG is in imaging cancer, where the increased energy demands of rapidly replicating cells lead to accumulation of the tracer in many tumors [53]. One of the main drawbacks of [^{18}F]FDG use is that organs that are already metabolically active, particularly the heart and brain, will have high background signal [52]. Another drawback is the versatility of the tracer; because glucose consumption by cells is upregulated in many different situations, it is challenging to determine the underlying cause of increased uptake [52, 54].

Aside from organs with high physiological glucose metabolism and tumors, the main reason for [^{18}F]FDG accumulation is inflammation. Indeed, the recruitment and activation of macrophages, neutrophils, and other cells leads to a locally increased demand for glucose [52]. Many studies have been conducted on the uses of [^{18}F]FDG for the imaging of various manifestations of inflammation.

In the remainder of this section, we provide a few examples of the main uses of radiotracers in the clinic across a range of inflammatory conditions, as an overview of how nuclear medicine can be used currently and the directions it may take. For more details, we refer the reader to a comprehensive review by Casali et al. which discusses the many applications of [^{18}F]FDG PET/CT in the imaging of inflammation and infection [55].

Table 2 Examples of radiotracers used in the clinic for nuclear imaging of inflammation

Radiotracer	Mechanism of action/ target	Inflammatory diseases
[¹⁸ F]FDG	Glucose transporters (metabolically active cells)	IBD, atherosclerosis, arteritis, infections, arthritis, infections, neuroinflammation
[⁶⁷ Ga]Ga-citrate	Transferrin (iron metabolism)	Infections
[¹⁸ F]NaF	Hydroxyapatite	Atherosclerosis, bone infections, arthritis
[^{99m} Tc]Tc-sulfur colloid, [^{99m} Tc]Tc-macroaggregated albumin	Passive (vascular permeability)	Infections
Radiolabelled leukocytes ([¹¹¹ In]In-oxine, [^{99m} Tc]Tc- HMPAO)	Leukocyte accumulation at sites of inflammation and infection	Infections, gastrointestinal inflammation
Anti-granulocyte antibodies ([^{99m} Tc]Tc-sulesomab, [^{99m} Tc] Tc-besilesomab)		Infections
[^{99m} Tc]Tc-MDP and other bisphosphonates	Hydroxyapatite and other calcium minerals	Atherosclerosis
[¹¹ C]PK11195, [¹¹ C]DPA-713, [¹¹ C]PBR28, [¹⁸ F]DPA-714, [¹⁸ F]GE-180	Translocator protein (TSPO)	Neuroinflammation
[⁶⁸ Ga]Ga-DOTA-TATE, [⁶⁸ Ga] Ga-DOTA-TOC, [⁶⁸ Ga]Ga- DOTA-NOC	Somatostatin receptors (SSTR)	Atherosclerosis
[⁶⁸ Ga]Ga-pentixafor	CXCR4	Atherosclerosis

2.1.1 Inflammation in the Gastrointestinal Tract

An example of the application of [¹⁸F]FDG in the imaging of inflammation is in the investigation of IBD, although specific protocols are yet to be defined [55]. [¹⁸F]FDG can be used for diagnosing IBD as well as discriminating between the two subtypes—Crohn's disease (CD) and ulcerative colitis (UC)—depending on the location of the uptake [55, 56]. [¹⁸F]FDG uptake primarily in the rectum with a single continuous area of uptake is indicative of UC, while CD can involve any part of the gastrointestinal (GI) tract, particularly the distal small bowel and terminal ileum, and uptake typically manifests itself as discontinuous patches [56]. However, as with its use in atherosclerosis, the applications of [¹⁸F]FDG in IBD are not without their drawbacks. Physiological uptake of [¹⁸F]FDG in the GI tract can always be expected due to the ongoing peristaltic muscle contractions; when this uptake is moderate to high, it may obscure IBD [54]. Additionally, patients who take metformin will typically have significantly increased [¹⁸F]FDG uptake in the GI tract [54].

Radiolabelled white blood cells (WBCs; see Sect. 2.1.6) are a well-established technique in nuclear imaging of many types of inflammation and infection. An

example of where this type of imaging can be applied is in CD, where WBCs are recruited to the inflamed intestine and accumulate in the mucosa [57]. A review of imaging of Crohn's disease by Gatta et al. discusses the advantages of radiolabelled WBCs compared to other nuclear imaging techniques as well as other imaging modalities [58], illustrating their point with the example shown in Fig. 6.

2.1.2 Cardiovascular Inflammation

Studies on cardiovascular inflammation have examined the ability of [^{18}F]FDG to detect the formation of atherosclerotic plaques. Pro-inflammatory M1 macrophages have an increased glycolytic rate compared to anti-inflammatory M2 macrophages, meaning that [^{18}F]FDG is theoretically better-suited to the detection of the early phases of inflammation rather than its resolution [59]. However, the high background uptake of [^{18}F]FDG in the heart means that there are complications in determining what uptake is disease-related and what uptake is physiologically normal [54]. The interpretation of such data can be further complicated by conditions such as chemotherapy-induced vascular inflammation or large artery inflammatory vascular diseases [52], in which inflammation plays a role in the absence atherosclerosis, meaning that [^{18}F]FDG uptake cannot always conclusively detect atherosclerosis.

Caution may be required when interpreting the reason for increased areas of [^{18}F]FDG uptake; however, various studies have explored ways to simplify this process while gaining additional information. One such way is the combination of imaging techniques. An example of this is when using [^{18}F]FDG for the imaging of atherosclerosis, a condition that is often accompanied by the presence of extraosseous calcification [60]. Microcalcifications (<50 μm) and larger sheet-like macrocalcifications (>3 mm) form as the plaque develops. Microcalcifications are associated with earlier stages of plaque development and have been reported to indicate plaque instability, while macrocalcification may develop later and stabilize the lesion [61]. As previously mentioned, PET imaging is normally performed in conjunction with CT, which is able to detect larger calcifications, and colocalization

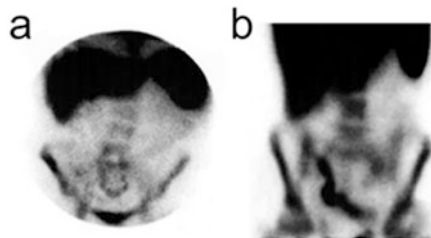


Fig. 6 Scintigraphy of Crohn's disease patients administered with [$^{99\text{m}}\text{Tc}$]Tc-HMPAO-labelled WBCs. (a) No inflammatory activity. (b) Severe inflammatory activity. Reproduced from [58] under CC-BY-3.0 license (<http://creativecommons.org/licenses/by/3.0/>). © 2012, Gatta et al.

of [^{18}F]FDG PET signal with the dense calcifications can be an indicator of inflammation-mediated uptake of [^{18}F]FDG in atherosclerotic plaques. CT may be unable to detect smaller calcifications, and instead bone-targeting radiotracers can be used for the detection of the microscopic calcium minerals present in plaques [62]. The most commonly used bone imaging agents are bisphosphonate (BP)-based SPECT tracers such as [$^{99\text{m}}\text{Tc}$]Tc-MDP; however, for imaging extraosseous calcification, the only agent in clinical use is ^{18}F -labelled sodium fluoride ([^{18}F]NaF) [63]. Bisphosphonates and [^{18}F]NaF also bind to the bone and are widely used for the imaging of metabolic bone conditions, which include inflammatory conditions such as osteomyelitis [64].

A study by Derlin et al. investigated the use of both [^{18}F]FDG and [^{18}F]NaF PET/CT imaging for the detection of atherosclerotic plaques [65]. [^{18}F]NaF showed higher target-to-background ratio than [^{18}F]FDG (2.3 ± 0.7 vs. 1.5 ± 0.3), but [^{18}F]FDG detected more lesions (124 vs. 105 with [^{18}F]NaF). 77.1% of the lesions detected with [^{18}F]NaF colocalized with arterial calcification (detected by CT), while only 14.5% of [^{18}F]FDG-detected lesions were colocalized with arterial calcification. The authors also highlighted that only 6.5% of detected lesions showed uptake with both tracers, hypothesizing that [^{18}F]FDG was detecting atherosclerosis at an earlier stage when inflammation is most active and calcifications are small, while [^{18}F]NaF was primarily detecting the larger calcifications also detected by CT at later stages of plaque development, by which point inflammation had subsided and therefore so had [^{18}F]FDG uptake. This trend has been contradicted in other works covered in a thorough review by Høilund-Carlsen et al. [66], with [^{18}F]NaF being reported as having higher uptake in macrocalcifications (at earlier stages of plaque development), suggesting further study of combining imaging techniques is warranted. This highlights the potential of combining imaging techniques (or combining radiotracers in this case) to provide complementary information.

At a preclinical level, much research into imaging calcification is ongoing, with many examples of [^{18}F]NaF imaging as well as the development of BP-based PET tracers for imaging calcification [67], which target calcification by a different mechanism of action. BPs bind by coordination of the phosphonate group with calcium ions, while fluoride selectively substitutes with the hydroxyl ions in the hydroxyapatite lattice to give fluorapatite and is therefore likely to offer different information, although the utility of this type of imaging as a proxy for inflammation remains to be explored.

Another PET tracer that has found relatively widespread use in the clinic is [^{68}Ga]Ga-DOTA-TATE, a radiolabelled derivative of the somatostatin analogue octreotide with high affinity for somatostatin receptor subtype-2 (SSTR2), which is upregulated in activated macrophages [52]. Much like [^{18}F]FDG, [^{68}Ga]Ga-DOTA-TATE has found its primary clinical application in oncology [68]. SSTR2 is highly expressed in neuroendocrine tumors, and [^{68}Ga]Ga-DOTA-TATE imaging can be used for the detection of primary sites and metastases, restaging in follow-up in patients with known disease, and selection of patients with metastatic disease for somatostatin-targeted radionuclide therapy [68]. SSTR2 is abundant on the membrane of activated macrophages, offering the opportunity to image inflammation due to the

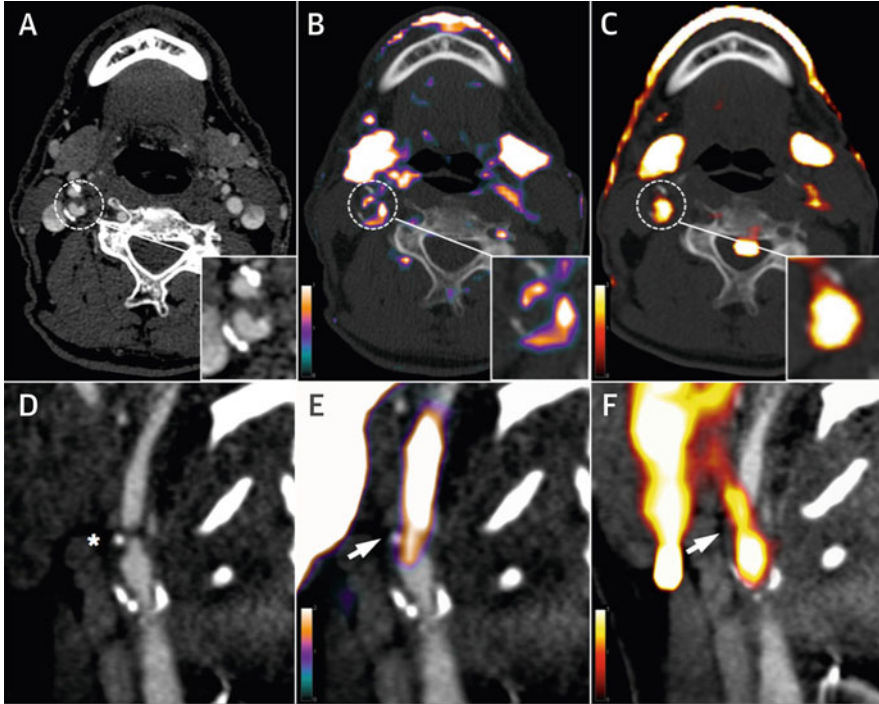


Fig. 7 PET imaging of atherosclerosis with $[^{68}\text{Ga}]\text{Ga-DOTATATE}$ and $[^{18}\text{F}]\text{FDG}$. Views from a 66-year-old man (top, axial plane) and a 70-year-old man (bottom, sagittal plane), both of whom had transient ischemic attacks resulting from right internal carotid artery lesions with intense culprit plaque inflammation (hatched circles in **a–c** and */arrows in **d–f**). (**a** and **d**) CT. (**b** and **e**) PET/CT imaging with $[^{68}\text{Ga}]\text{Ga-DOTATATE}$. (**c** and **f**) PET/CT imaging with $[^{18}\text{F}]\text{FDG}$. Reproduced from [69] under CC-BY-4.0 license. © 2017, Tarkin et al.

accumulation of activated macrophages at those sites [52]. Tarkin et al. compared $[^{68}\text{Ga}]\text{Ga-DOTA-TATE}$ to $[^{18}\text{F}]\text{FDG}$ for the PET imaging of inflammation leading to atherosclerotic plaques in 42 patients, with the conclusion that $[^{68}\text{Ga}]\text{Ga-DOTA-TATE}$ was better able to differentiate between high-risk and low-risk plaques than $[^{18}\text{F}]\text{FDG}$ (Fig. 7) [69]. It was also mentioned that in 64% of $[^{18}\text{F}]\text{FDG}$ images, the results were not interpreted due to high background uptake of $[^{18}\text{F}]\text{FDG}$ in the myocardium, whereas all $[^{68}\text{Ga}]\text{Ga-DOTA-TATE}$ images were able to be interpreted.

Other SSTR2-targeting tracers also exist, with $[^{68}\text{Ga}]\text{Ga-DOTA-NOC}$ (which has affinity to other somatostatin receptors as well as SSTR2) and $[^{68}\text{Ga}]\text{Ga-DOTA-TOC}$ in clinical use for the imaging of neuroendocrine tumors. Using a different radiometal is another option which has been examined. The most notable example of this is $[^{64}\text{Cu}]\text{Cu-DOTA-TATE}$, which, instead of gallium-68, is radiolabelled with longer-lived, cyclotron-produced positron emitter copper-64 ($t_{1/2} = 12.7$ h). A comparison of $[^{68}\text{Ga}]\text{Ga-DOTA-TOC}$ to $[^{64}\text{Cu}]\text{Cu-DOTA-TATE}$ in cancer patients

found that there was a significant correlation between cardiovascular risk scores and [^{64}Cu]Cu-DOTA-TATE uptake, whereas no such correlation was found for [^{68}Ga]Ga-DOTA-TOC [70].

A relatively recent PET tracer to reach the clinic is [^{68}Ga]Ga-pentixafor. Like both [^{18}F]FDG and [^{68}Ga]Ga-DOTA-TATE, its primary use in the clinic has been for the imaging of cancer. [^{68}Ga]Ga-pentixafor is a cyclopentapeptide with high affinity for the chemokine receptor CXCR4, which is upregulated in many types of cancer, and increased expression is associated with cancer proliferation, migration, and survival [71]. CXCR4 is highly expressed on several immune cells, particularly macrophages and T lymphocytes, and plays a role in the trafficking of immune cells [72]. Therefore, in a similar manner to [^{68}Ga]Ga-DOTA-TATE, this is a tracer that can identify inflammation on the working principle of detecting the accumulation of macrophages (and other immune cells). The key difference is that SSTR2, targeted by [^{68}Ga]Ga-DOTA-TATE, is upregulated on activated macrophages, while CXCR4 is highly expressed on all macrophages, thus reducing its specificity for macrophages involved in the inflammatory process. This uptake across macrophages means [^{68}Ga]Ga-pentixafor may be expected to lead to similar imaging results as those obtained with [^{18}F]FDG, which also accumulates at sites of inflammation primarily due to the increased number of macrophages present. However, a 2020 study by Kircher et al. found that [^{68}Ga]Ga-pentixafor was able to identify more atherosclerotic lesions than [^{18}F]FDG while also highlighting that there was a weak correlation between [^{68}Ga]Ga-pentixafor and [^{18}F]FDG uptake on a lesion-to-lesion basis [73].

2.1.3 Neuroinflammation

Neuroinflammation is the primary mechanism of defense of the central nervous system (CNS) against pathogens, toxic substances, and traumatic injury and plays a major role in neurodegenerative diseases, including multiple sclerosis, amyotrophic lateral sclerosis, Alzheimer's disease, and Parkinson's disease. [^{18}F]FDG, despite its physiologically high uptake in the brain, is also a useful radiotracer for certain neuroinflammatory diseases, as the patterns of uptake in the inflamed brain differ from those of healthy patients and can show areas of either increased or decreased uptake, corresponding to hyper- or hypometabolism associated with different underlying mechanisms and stages of disease [74]. [^{18}F]FDG is useful in diagnosing autoimmune encephalitis [74], but also for neurodegenerative diseases, which often have an inflammatory component [75, 76].

Translocator protein (TSPO) has long been used as a major biomarker for neuroinflammation, as its expression in microglia and astrocytes is highly upregulated in inflammatory conditions [77]. Over the last 30 years, multiple generations of radiotracers have been developed to image TSPO, and many are used in the clinic, including [^{11}C]PK11195 (first generation), [^{11}C]DPA-713, [^{11}C]PBR28, [^{18}F]DPA-714 (second generation), and [^{18}F]GE-180 (third generation), to name only a few of the more common ones [77]. Notably, tracers for

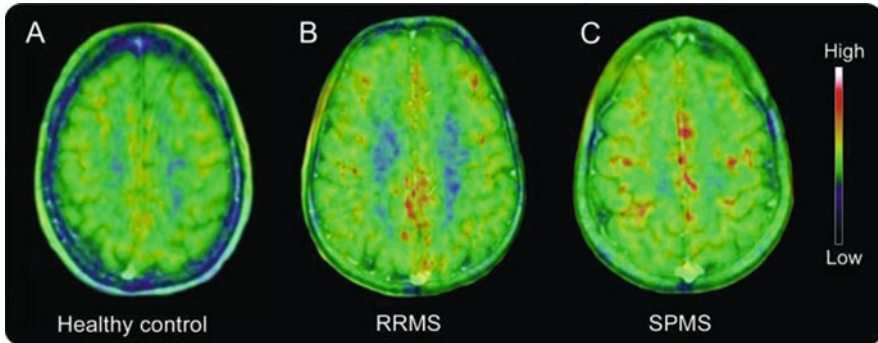


Fig. 8 PET imaging of TSPO in multiple sclerosis. Summed [^{11}C]PK11195 PET images co-registered and fused with 1.5 T MRI at the cortical level for (a) a healthy 40-year-old woman (cortical GM PK BP_{ND}: 0.061); (b) a 46-year-old man with a 12-year history of relapsing-remitting multiple sclerosis (RRMS) (cortical GM PK BP_{ND}: 0.121); and (c) a 46-year-old woman with secondary progressive multiple sclerosis (SPMS) (cortical GM PK BP_{ND}: 0.198). GM PK BP_{ND}: gray matter [^{11}C]PK11195 binding potential of the specifically bound radioligand relative to the nondisplaceable radioligand in tissue. Adapted from Politis et al. [78]. © 2012, American Academy of Neurology

neuroinflammatory diseases tend to be small molecules radiolabelled with ^{11}C and ^{18}F , as larger molecules (e.g., antibodies that are commonly used for cancer imaging) have difficulty crossing the blood-brain barrier (BBB).

An example of the utility of TSPO-targeting tracers in examining patients with neuroinflammation comes from a study by Politis et al. in which multiple sclerosis (MS) patients were imaged using [^{11}C]PK11195 PET fused with MRI [78]. The MRI was used to identify gray matter which was used to calculate the binding potential of [^{11}C]PK11195 in the gray matter (GM PK BP_{ND}). Patients with more severe MS showed higher GM PK BP_{ND} than patients with less severe MS or healthy controls (Fig. 8). A further example comes a more recent study by Ricigliano et al. in which patients with multiple sclerosis were imaged with [^{18}F]DPA-714—in combination with MR imaging to determine the volume of the choroid plexuses—and showed increased PET signal in the choroid plexuses of patients with MS compared to healthy control participants [79]. These results indicate a role of the choroid plexuses in the pathophysiology of MS, although whether these are triggers for MS or secondary effects was not determined. Another recent study by Fleischer et al. [80] with MR imaging alone was in agreement with the conclusions of Ricigliano et al. that the choroid plexuses are an interesting imaging target for MS patients. This provides an indication of the way in which a combination of different imaging techniques could be a useful addition to the clinical toolbox as well as an indication of the potential future directions of nuclear imaging in neuroinflammation.

The plethora of radiotracers developed can be explained first by the high scientific value of radiotracers for CNS diseases (due to the difficulty of studying the brain with invasive methods) and by the various shortcomings of the successive

generations of tracers. For example, [^{11}C]PK11195 suffers from low signal-to-noise ratio and requires an on-site cyclotron for production; second-generation tracers (often labelled with ^{18}F) have revealed the existence of polymorphism in the TSPO gene that leads to high interindividual variability in radiotracer affinity. Third-generation tracers have sought to address this issue by binding to TSPO regardless of various polymorphisms. While binding being less affected by TSPO polymorphism has been associated with increased sensitivity in detection of microglial activation in mice [81], a direct comparison study of third-generation [^{18}F]GE-180 and second-generation [^{11}C]PBR28 showed that [^{18}F]GE-180 demonstrated considerably worse BBB penetration as well as difficulties in kinetic modelling compared to [^{11}C]PBR28 [82]. There is therefore a continued need to improve nuclear imaging of TSPO so as to benefit more patients [83]. Recent innovations and developments in TSPO imaging are discussed in Sect. 3.1.1.

2.1.4 Musculoskeletal Diseases

Musculoskeletal diseases present an interesting opportunity for nuclear imaging [84]. The highly sensitive whole-body imaging allows not only for diagnosis of identified areas of inflammation such as arthritic joints but also incidental findings such as subclinical arthritic joints which may be more easily treated. Nonetheless, nuclear imaging has yet to become a standard technique in diagnosis of musculoskeletal diseases.

The majority of studies have used [^{18}F]FDG to probe for macrophage infiltration or used alternative markers of arthritis as an indirect way of imaging inflammation, such as using [^{18}F]NaF to image areas of high mineral turnover in the skeleton, a characteristic of osteoarthritis. A study by Al-Zaghal et al. imaged both healthy subjects and subjects with a history of chest pain with [^{18}F]FDG and [^{18}F]NaF. They found uptake of both tracers in the knees showed positive correlation with body mass index, although they did not have sufficient clinical data to determine whether there was correlation between tracer uptake and inflammation [85]. Another comparative study compared [^{18}F]FDG with [^{68}Ga]Ga-NOTA-PRGD2 [86], a tracer with high affinity toward $\alpha_v\beta_3$ -integrin, a biomarker for angiogenesis which is present in rheumatoid arthritis. In this study, the authors found that [^{68}Ga]Ga-NOTA-PRGD2 uptake showed better correlation with disease severity than [^{18}F]FDG. Furthermore, they found that upon therapeutic intervention, there was significant correlation between changes of [^{68}Ga]Ga-NOTA-PRGD2 uptake and changes in the clinical condition of the patients. An example of nuclear imaging in RA is shown in Fig. 9 [54]. This shows [^{18}F]FDG PET/CT scans of two patients, one with known RA but suspected infection (although no infectious foci were found, the RA signal in the shoulders and hips is clear) and the other with no serum biomarkers for RA but a distinctive symmetrical pattern of inflammation of the small joints in the hands, which is typical of RA.

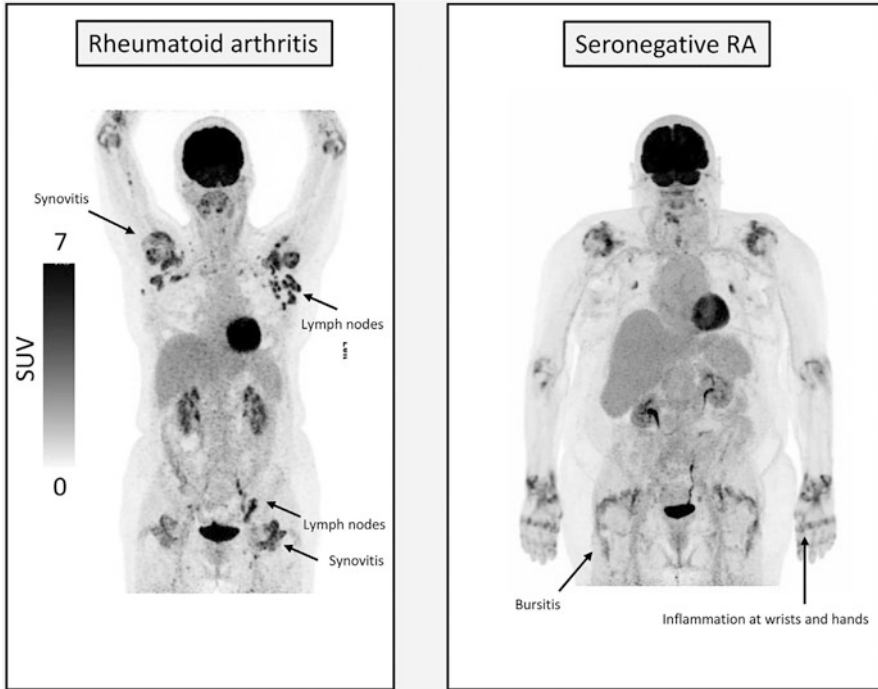


Fig. 9 [^{18}F]FDG PET imaging of rheumatoid arthritis. In the left panel, a 45-year-old woman with known RA underwent [^{18}F]FDG PET/CT due to suspected infection. No infectious foci were found, but RA was clearly active with avid [^{18}F]FDG uptake in the shoulders, elbows, and hips. Reactive local lymph nodes were also visible in the axillae and along the pelvic arteries. The right column shows a 67-year-old man with negative biomarkers for RA. However, [^{18}F]FDG uptake was rounded and avid in the shoulder region, and both wrists and finger joints were involved indicating a tentative diagnosis of seronegative (or elderly onset) RA. Adapted from [54] (CC-BY-4.0 license). © 2021, Pijl et al.

2.1.5 Fever of Unknown Origin (FUO)

Some of the first examples of [^{18}F]FDG imaging in inflammatory conditions were to identify the causes of fever of unknown origin. Initially, foci caused by inflammation and infection were considered false positives and seen as a drawback of [^{18}F]FDG imaging. The versatility of [^{18}F]FDG can also be advantageous in that it gives [^{18}F]FDG the ability to detect many conditions or to rule out a large number of conditions in the case of a negative scan. This is of particular use in FUO, which has more than 200 recognized causes [87], although the causes can be grouped into four main categories: infection, malignancies, noninfectious inflammatory diseases, and miscellaneous [88]. [^{18}F]FDG is able to detect infection, malignancies, and noninfectious inflammatory diseases due to the increased glucose demand. It is therefore the preferred option when likelihood of infection is considered low and can be used to rule out many possible conditions in a single scan. If likelihood of

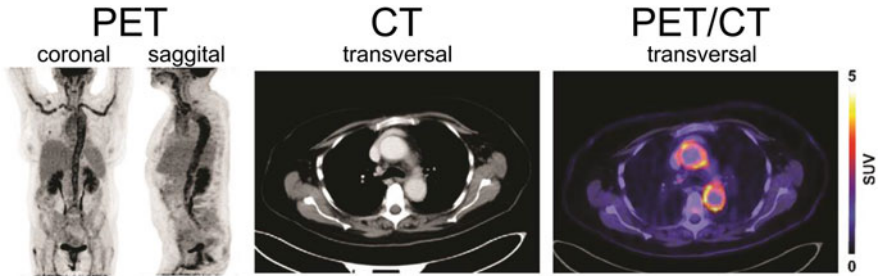


Fig. 10 Using nuclear imaging to investigate fevers of unknown origin. Representative coronal, sagittal, and transversal [^{18}F]FDG PET/CT images of a patient presenting with recurrent FUO for 3 months and increasing C-reactive protein levels. [^{18}F]FDG PET shows inflammation of the large vessels consistent with Takayasu's arteritis. Adapted from [89] (CC-BY-4.0 license). © 2021, Iking et al.

infection is considered high, infection-specific imaging agents such as [$^{99\text{m}}\text{Tc}$]Tc-HMPAO would be preferred [55]. An example of using [^{18}F]FDG to investigate FUO, in which a PET/CT scan of a patient with FUO revealed the underlying condition to be vascular inflammation (arteritis), is shown in Fig. 10.

2.1.6 Infection Imaging

Inflammation is a physiological response to infections, and therefore several radiotracers that are used for inflammation imaging are also used in the context of infectious diseases. In infections, both the pathogen and the inflammatory response can be imaged, but in clinical practice the latter is more commonly used, either with radiotracers that accumulate due to the locally increased vascular permeability or with radiotracers more specific to the infiltration and activation of immune cells at the site of infection. One of the oldest tracers used in nuclear imaging of infection and inflammation is [^{67}Ga]Ga-citrate [49]. Gallium-67 reaches the site of infection passively via the increased permeability of the capillary network. In aqueous media, gallium metal is found primarily in the +3 oxidation state, where it acts in a similar manner to iron(III). The [^{67}Ga]Ga-citrate complex is relatively unstable in the blood, and approximately 90% of the gallium-67 will dissociate and bind to transferrin. Upon reaching the site, the complex dissociates and the unbound gallium-67 is bound by lactoferrin—a protein overexpressed as part of the inflammatory response—and bacterial siderophores, reducing the chance of efflux away from the site of infection [90]. However, gallium-67 is not an ideal radionuclide for imaging because of its excessively long half-life and poor spatial resolution, and for these reasons, it has largely been replaced in the clinic by other radiotracers such as [^{18}F]FDG and radiolabelled leukocytes [91].

Scintigraphy with autologous radiolabelled WBC has been used since the late 1970s for imaging infections. This method is based on the fact that neutrophils, which typically represent 50–70% of circulating leukocytes, actively migrate toward

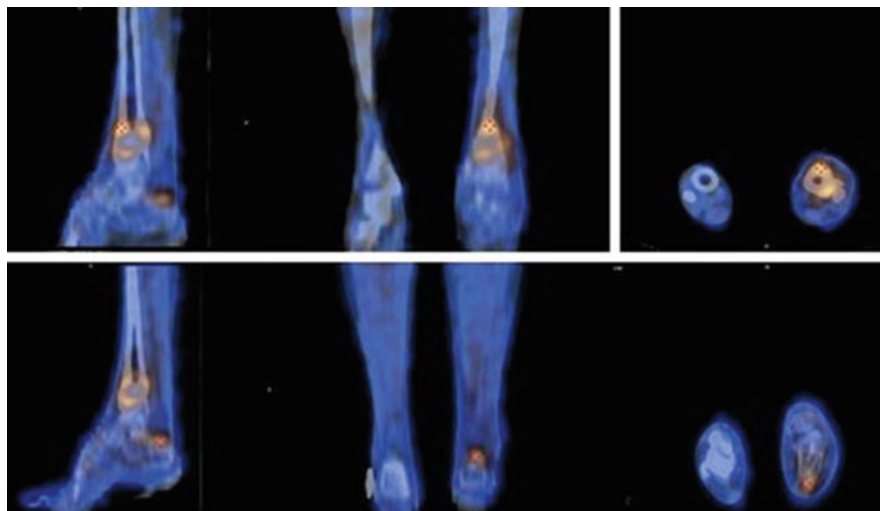


Fig. 11 Radiolabelled WBC for infection imaging. Sagittal (*left*), coronal (*middle*), and transaxial (*right*) SPECT/CT images of a patient with post-traumatic osteomyelitis of the left tibia. A focal site of increased [^{99m}Tc]Tc-HMPAO-labelled WBC uptake is evident at the distal tibia; a smaller additional focus of [^{99m}Tc]Tc-HMPAO-labelled WBC uptake is also evident at the tibial-calcaneal joint. Reproduced from Erba & Israel [64] with permission. © 2014, Italian Association of Nuclear Medicine and Molecular Imaging

sites of infection. Thus, radioactive cells accumulating at a site of infection generate a “hot spot” on a scan. Although numerous labelling methods exist [35], in the clinic WBCs are mostly radiolabelled *ex vivo* using the ionophoric complexes [^{111}In]In-oxine and [^{99m}Tc]Tc-HMPAO (hexamethylpropyleneamine oxime). Oxine and HMPAO each form a small, uncharged, lipophilic complex with their respective radiometal that is able to traverse the cell membrane. Upon entering a cell, the metastable complex dissociates, effectively trapping the radionuclide in the cell. In practice, a small volume (typically ≤ 60 mL) of blood is drawn from the patient, and the WBCs are isolated and then mixed with the radiotracer. After washing the cells to remove unbound radiotracer, the labelled cells are then reinjected into the patient and tracked, allowing the visualization of recruitment and accumulation of WBCs.

Despite the age of this technique, scintigraphy and SPECT/CT with radiolabelled WBC remain to this date the gold standard imaging method for many infectious diseases. Radiolabelled WBCs are typically indicated for the diagnosis, monitoring, and treatment response evaluation of bone or soft tissue infections, such as osteomyelitis (Fig. 11), spondylodiscitis, prosthetic joint infections, postoperative infections, diabetic foot infections, infective endocarditis, and bacterial pneumonia [33]. Because of the need to extract, radiolabel, and reinject the patient’s cells, the process is more time-consuming and complex than for other radiotracers; however, the good performance of radiolabelled WBC as diagnostic agents has kept them relevant. For diagnosing diabetic foot infections, for example, radiolabelled WBC imaging using [^{111}In]In-oxine and [^{99m}Tc]Tc-HMPAO has shown sensitivities of

75–100% and 86–93%, respectively, and specificities of 69–89% and 80–98%, respectively [64].

Another way of imaging leukocytes in infection is to use radiolabelled antibodies, for example, [^{99m}Tc]Tc-sulesomab or [^{99m}Tc]Tc-besilesomab. These antibodies bind selectively to granulocytes, meaning the imaging theoretically shows areas of increased granulocyte concentration, similar to radiolabelled WBC imaging methods [92]. Radiolabelled antibodies offer several practical advantages over WBC labelling methods: there is no need to extract, handle, and label blood, which could present increased radiation dose and risk of infection toward the operator. The performance of [^{99m}Tc]Tc-sulesomab has been compared to radiolabelled WBCs in many studies with results generally found to be similar, although sensitivity could vary depending on the condition being investigated [93, 94].

[^{18}F]FDG PET, based on the increased glycolytic activity of infiltrating leukocytes, has also shown good performance in diagnosing osteomyelitis and soft tissue infections, although differentiating between the two (which is important for treatment) is not always easy and there is a lack of standardized interpretation criteria for [^{18}F]FDG PET/CT images in these indications [55]. In contrast, [^{18}F]FDG PET does not perform as well as radiolabelled leukocytes for prosthetic joint infections [55]. [^{18}F]FDG has the potential to be used to monitor infectious/inflammatory diseases such as dengue, where the viremia correlates poorly with the actual course and outcome of the disease [95].

Finally, the development of pathogen-specific radiotracers is an active area of research that has been gathering pace in recent years. One of the most promising developments in our opinion is that of 2-deoxy-2- [^{18}F]fluoro-D-sorbitol ([^{18}F]FDS), a radiotracer specific for bacteria of the *Enterobacteriales* order (including major pathogens of the *Enterobacter*, *Escherichia*, *Klebsiella*, *Salmonella*, and *Yersinia* genera), which has moved from preclinical stages into several clinical trials with highly encouraging results [96]. A notable advantage of [^{18}F]FDS is its ease of preparation, as it is synthesized in a one-step reduction from [^{18}F]FDG, and therefore it could be easily manufactured in any PET facility already using [^{18}F]FDG [97]. Just like mammalian cells, microbes can be imaged by exploiting specific enzymes and transporter pathways (e.g., carbohydrate metabolism in the case of [^{18}F]FDS, iron uptake mechanisms with radiolabelled siderophores, beta-lactamases with radiolabelled antibiotics) or cell surface markers (e.g., specific glycans or lipids). For further details on pathogen-specific nuclear imaging, we refer the reader to recent reviews [98–100].

2.2 Challenges and Recent Developments

2.2.1 Increasing Specificity

Despite the usefulness of existing radiotracers in imaging of inflammation, there remains considerable room for improvement. Radiolabelled leukocytes are more

complex to use than other tracers because of the blood handling aspects that require additional time and precautions. [^{18}F]FDG is widely available, convenient, and highly versatile, but its relative lack of specificity is a double-edged sword. Indeed, it is unable to discriminate on its own between cancer, sterile inflammation, and infection. Postsurgical situations are a case in point: the wound-healing process involves an influx of inflammatory cells and fibroblast activation, and there is a risk of infection, especially if grafts are involved, that would also lead to leukocyte recruitment. As both cases would lead to an increase in [^{18}F]FDG uptake, it is important to differentiate between a physiological reaction that will subside and a nascent infection that needs to be tackled as early as possible. Acute infection tends to give focal and intense uptake, but low-grade infection and sterile inflammation are more difficult to differentiate [54]. Typical causes of false-positive [^{18}F]FDG PET/CT images in suspected inflammatory diseases, even years after the causative event, include tumors, recent bone fractures, postoperative inflammation, degenerative diseases, and synthetic grafts (foreign body reaction). False negatives can be caused by low-grade inflammation or infection masked by antibiotic or anti-inflammatory therapy (e.g., steroids), small lesions, and hyperglycemia [55]. Kidney and liver failure can also lead to higher background signal and confound results [54].

[^{18}F]FDG also has high uptake in healthy organs (heart, brain, muscle after effort), which makes it difficult to visualize signal changes due to inflammatory processes. For those organs especially, radiotracers with a higher target-to-background ratio are required. Furthermore, [^{18}F]FDG protocols often require several hours of fasting before the scan to reduce background signal and improve image quality, yet there are a number of situations where this is not achievable (e.g., noncompliant patients, diabetic patients, intensive care or emergency situations) [101]. Thus, radiotracers that are less sensitive to biochemical parameters and require shorter preparation times would also be beneficial alternatives. Attempts to replace [^{18}F]FDG with ^{68}Ga -based radiotracers that do not have endogenous uptake in the heart were not successful [102]. Despite this limitation, [^{18}F]FDG has been successfully used to image cardiac inflammation in animal models of myocardial infarction, using xylazine and ketamine to reduce background uptake of [^{18}F]FDG [103, 104]. With this uptake suppression protocol, [^{18}F]FDG was also used to predict the efficacy of cardiac induced stem cells as a treatment for myocardial infarction [105].

There is therefore a need to develop radiotracers for inflammatory and infectious diseases with an increased specificity for inflammatory processes, ideally the ability to further discriminate between different types of inflammation, improved pharmacokinetic and pharmacodynamic properties that lead to images with better contrast and allow dynamic assessment of inflammation, and preferably using radionuclides that are widely available and convenient to use to ensure that as many patients as possible can benefit. In Sect. 3 we describe several receptors, signalling pathways, and metabolic processes that could lead to more specific imaging of inflammation.

2.2.2 Quantification and Multimodal Imaging

For a long time, there were no universally recognized criteria for the diagnosis of inflammatory conditions using [^{18}F]FDG PET or other tracers. In clinical practice, radiotracer uptake is evaluated by a variety of methods. Visual analysis by trained specialists is the simplest method, scoring, for example, the signal intensity in the area of interest in comparison with the intensity in a reference organ where uptake is expected to be relatively constant. For example, Meller et al. defined a four-point scale to evaluate large vessel vasculitis, where grade 0 represents no uptake, grade I is vascular uptake lower than the liver, grade II is uptake similar to the liver, and grade III is higher vascular uptake than in the liver [106]. Other criteria can include the shape of the area with uptake, the focal or diffuse nature of the signal, and the number of uptake areas, depending on the nature of the disease. Qualitative analysis of images can be sufficient, although it can also lead to ambiguity. Recent efforts have aimed at standardizing the criteria in order to provide nuclear medicine physicians with clearer guidelines for diagnosis and treatment. Semiquantitative scoring methods based on SUV values (see Sect. 1.3.4) have also been developed, taking, for example, SUV values to calculate a target-to-background ratio and setting thresholds above which a diagnosis is established. For example, in their guide on the use of [^{18}F]FDG PET/CT for imaging infection and inflammation, Signore et al. indicate that in IBD imaging, in addition to qualitative analysis, if the maximum standardized uptake value (SUV_{max}) of the bowel is greater than that of the liver, it is suggestive of IBD [51]. However, truly quantitative criteria are not yet established. To date, the closest example is the use of [^{18}F]FDG in imaging spine infections, where an $\text{SUV}_{\text{max}} > 3$ has been identified as an indication of spine infection, although this is not yet an established standard.

A further challenge is that much of current practice relies on additional imaging data from other modalities, such as CT or MRI. These techniques provide anatomic detail at a level that PET and SPECT cannot provide and can inform on the involvement of bone or specific soft tissues. It is often necessary to interpret two different images within the context of each other. This can cause greater variance of interpretation by different users and can further complicate the quest for standardized criteria for diagnosis. Practical difficulties complicate this matter yet more, as issues with co-registration or imaging artifacts due to patient motion or other interference can present barriers in the way of standardized image interpretation. While the use of multiple modalities presents some challenges, these are offset by the extra information provided. For example, MRI is the standard imaging approach for spinal infections, and therefore a combined PET/MRI approach can address the shortcomings of each separate method to provide some of the most complete information available. Even if criteria are established, it has to be understood what has caused any detected abnormal uptake. This involves differentiating between infection, inflammation, and other causes of increased signal, such as oncological uptake of [^{18}F]FDG. One method for this is dual time-point imaging with [^{18}F]FDG, in which the uptake is compared at two time points postinjection. The principle is that glucose

metabolism varies depending on the underlying condition, where higher retention would be expected in malignant tumors than in infection or inflammation [54]. Nonetheless, differentiation between conditions remains challenging. As mentioned in Sect. 1.3.3, using multiple radiotracers could help with differentiation. Dynamic imaging may also bring improvements, as it can be used to determine the metabolic rate and thus potentially differentiate between conditions. Currently, dynamic imaging has to be focused on the main area of interest because of the limited axial FOV of cameras, but with the development of total-body PET, it may become a more common option for differential diagnosis. Independently of technological advances, a key part of differentiating between causes of radiotracer uptake is good knowledge of the patient's medical history. Past surgeries, bone fractures, tumors, diabetes, various medications, and kidney and liver failure can all yield misleading results and should be taken into account when interpreting imaging data. For this reason, information sharing between healthcare providers is crucial.

2.2.3 Radiomics

Radiomics consists in an ensemble of quantitative image analysis methods, enabled by recent developments in computational methods including machine-learning algorithms. This relatively novel field is expected to assist the development of inflammation imaging by extracting further information from medical images than might be visible to the human eye. For example, rather than simply measuring radiotracer uptake in a given volume, radiomics can analyze in finer detail the 3D distribution of activity within an organ or indicate features such as the granularity or texture of an image. Notably, radiomic analysis can be performed on any imaging modality and correlate data obtained from multiple modalities including nuclear imaging, MRI, and CT [107]. To date, PET radiomics have mostly been applied in oncology, and for MR and CT imaging of inflammation, and there are only limited reports of PET radiomics in inflammatory diseases [108–110]. The development of PET radiomics could conceivably improve the performance of existing tracers, especially [^{18}F] FDG, in distinguishing inflammation from other diseases.

3 Recent Developments in Preclinical Nuclear Imaging of Inflammation

In this section, we describe a number of relatively recent, mostly preclinical studies (i.e., from ~2014 onward) of radionuclide-based molecular imaging of inflammation that demonstrate progress in some of these aspects (see Table 3). Through this broad but by no means exhaustive selection, we intend to show that nuclear imaging can potentially be used to provide *in vivo* evidence of any signalling pathway or

Table 3 A selection of radiotracers used in preclinical models of inflammation

Target	Cell type	Radiotracer	Disease model
Translocator protein (TSPO)	Microglia, astrocytes	[¹¹ C]PK11195, DPA-713, DPA-714, [¹⁸ F]GE-180, [¹¹ C]PBR28, [¹⁸ F]FEDAC, [¹⁸ F]FEPPA, [¹⁸ F]FDG	Multiple sclerosis, amyotrophic lateral sclerosis, Alzheimer's, Parkinson's
Folate receptor β	Activated macrophages	[¹⁸ F]fluoro-PEG-folate, [¹⁸ F]AIF-NOTA-folate, [¹⁸ F]F-aza-5-methyltetrahydrofolate	Rheumatoid arthritis, atherosclerosis, myocarditis
Hypoxia	Activated macrophages and neutrophils	[¹⁸ F]fluoromisonidazole, [⁶⁴ Cu]Cu-ATSM, [⁶⁴ Cu]Cu-CTS	Atherosclerosis, sarcoidosis, rheumatoid arthritis
Aldehydes	Fibrotic tissue	[¹⁸ F]NA ₃ BF ₃	LPS-induced systemic inflammation
Iron metabolism	Neutrophils, bacteria	[⁶⁸ Ga]Ga-citrate, radiolabelled siderophores	Bacterial and fungal infections
Fibroblast activation protein (FAP)	Activated fibroblasts	[⁶⁸ Ga]Ga-FAPI-04	<i>(Exploratory clinical studies)</i> Arthritis, cirrhosis, myocardial infarction
CD80/86	Macrophages, dendritic cells	[¹¹¹ In]In-DOTA-belatacept, [⁶⁴ Cu]Cu-NODAGA-abatacept	Atherosclerosis, LPS-induced skin inflammation
Mannose receptor (MMR/CD206)	Macrophages, dendritic cells, hepatic and lymphatic endothelial cells	2-deoxy-2-[¹⁸ F]fluoro-D-mannose, ^{99m} Tc/ ¹¹¹ In-labelled DTPA-tilmanocept, [⁶⁸ Ga]Ga-NOTA-MMR nanobody	Atherosclerosis, myocarditis, neuroinflammation (traumatic brain injury)
Scavenger receptor A1	Activated macrophages	[⁸⁹ Zr]Zr-maleyl-albumin	Atherosclerosis
Galectin-3	M2 macrophages	[⁸⁹ Zr]Zr-DFO-galectin-3-F(ab') ₂ antibody	Atherosclerosis
Chemokine receptors	Monocytes, macrophages (CCR2, CCR5, CXCR4), neutrophils (CXCR1, CXCR2), T cells (CXCR4), endothelial cells (CXCR4)	[⁶⁸ Ga]Ga-pentixafor, ⁶⁸ Ga/ ⁶⁴ Cu-labelled ECL1i, ECL1i-targeted gold nanoparticles, ⁶⁴ Cu-labelled D-ala-peptide T-amide nanoparticles, [^{99m} Tc]Tc-interleukin-8, ⁶⁴ Cu-labelled α MIP-II-targeted nanoparticles	Acute lung injury, heart transplantation, vascular inflammation: atherosclerosis, ischemia-reperfusion, aortic aneurysm
Cell-adhesion molecules	Macrophages, lymphocytes, platelets, activated endothelial cells, sickle cells	Radiolabelled RGD peptides, ⁶⁴ Cu-labelled integrin β_7 antibodies, [⁶⁸ Ga]Ga-aquibepirin, [⁶⁴ Cu]Cu-LLP2A, [⁶⁸ Ga]Ga-fucoidan, [^{99m} Tc]Tc-	Rheumatoid arthritis, myocarditis, colitis, sickle-cell disease, atherosclerosis, ischemic stroke, aortic aneurysm

(continued)

Table 3 (continued)

Target	Cell type	Radiotracer	Disease model
		fucoidan microparticles, [¹¹¹ In]In-DOTA-butylamino-NorBIRT, radiolabelled VCAM-1 nanobodies, ^{99m} Tc-labelled ICAM-1 microbubbles	
Matrix metalloproteinases	Neutrophils, macrophages, lymphocytes, chondrocytes, epithelial cells	[^{99m} Tc]Tc-RP805, [^{99m} Tc]Tc-RYM1, [⁸⁹ Zr]Zr-pro-MMP-9 F(ab') ₂ antibody, ^{99m} Tc-labelled MMP-12 inhibitors, ¹⁸ F-labelled MMP-9/12 inhibitors	Lung inflammation, aortic aneurysm, fibrosis
T cell and B cell lineage markers, metabolic pathways	T cells (CD3, CD4, CD8, OX40), B cells (CD20)	[¹⁸ F]F-AraG, [⁸⁹ Zr]Zr-DFO-CD4 diabody, [⁸⁹ Zr]Zr-DFO-CD3 antibody, [⁶⁴ Cu]Cu-DOTA-OX40 antibody, ⁸⁹ Zr/ ⁶⁴ Cu-labelled rituximab	GvHD, arthritis, colitis, autoimmune encephalomyelitis, viral infection (influenza A)
VAP-1	Endothelial cells	¹²³ I-labelled VAP-1 antibodies, ⁶⁸ Ga-labelled peptides, [⁶⁸ Ga]Ga-DOTA-Siglec-9	Arthritis, lung inflammation

biological process involved in inflammation and is therefore a powerful tool to demonstrate on a whole-body level what has been discovered on a cellular level.

3.1 Metabolic Pathways Involved in Inflammation

3.1.1 Translocator Protein (TSPO) Ligands

Neuroinflammation is the primary mechanism of defense of the CNS against pathogens, toxic substances, and traumatic injury, as it plays a major role in neurodegenerative diseases including multiple sclerosis, amyotrophic lateral sclerosis, Alzheimer's disease, and Parkinson's disease. TSPO has long been used as a major biomarker for neuroinflammation, as its expression in microglia and astrocytes is highly upregulated in inflammatory conditions [77]. Over the last 30 years, multiple generations of radiotracers have been developed to image TSPO, and many are used in the clinic, including [¹¹C]PK11195 (first generation), [¹¹C]DPA-713, [¹⁸F]DPA-714 (second generation), and [¹⁸F]GE-180 (third generation), to name only a few of the more common ones [77]. Notably, tracers for

neuroinflammatory diseases tend to be small molecules radiolabelled with ^{11}C and ^{18}F , as larger molecules (e.g., antibodies that are commonly used for cancer imaging) have difficulty crossing the blood-brain barrier. The plethora of radiotracers developed can be explained first by the high scientific value of radiotracers for CNS diseases (due to the difficulty of studying the brain with invasive methods) and by the various shortcomings of the successive generations of tracers. For example, [^{11}C]PK11195 suffers from low signal-to-noise ratio and requires an on-site cyclotron for production; second-generation tracers (often labelled with ^{18}F) have revealed the existence of polymorphism in the TSPO gene that leads to high interindividual variability in radiotracer affinity. There is therefore a continued need to improve nuclear imaging of TSPO so as to benefit more patients [83]. Recently, TSPO imaging has also been used for peripheral inflammation. Uptake of [^{18}F]DPA-714 in the joints of arthritic rats, due to the expression of TSPO on infiltrating macrophages, correlated with disease severity [111]. Radioiodinated TSPO ligands ([^{125}I]DPA-713 and [^{124}I]DPA for SPECT and PET imaging, respectively) were used to image tuberculosis-associated inflammation and the response to antibiotic treatment in a mouse model of pulmonary tuberculosis [112, 113] (Fig. 12a). In a rat model of acute lung injury, [^{18}F]FEDAC was used to show the expression of TSPO on bronchial epithelial cells and bronchus-associated lymphoid tissue [114] (Fig. 12b), and in a mouse model of malaria-associated acute respiratory distress syndrome, [^{18}F]FEPPA uptake in the lungs correlated with blood levels of *Plasmodium berghei*. Finally, in a mouse model of Sendai virus infection, [^{11}C]PBR28 proved to be more specific than [^{18}F]FDG in imaging M2 macrophage-driven chronic lung inflammation [40]. Given this non-exhaustive list of examples, the future of TSPO imaging by PET is promising not only for neuroinflammation but in many other diseases and especially lung inflammation.

3.1.2 Amino Acid Metabolism: LAT1

Tracers targeting amino acid pathways are an alternative to [^{18}F]FDG for nuclear imaging. For example, system L amino acid transporters, in particular LAT1, have proven to be better targets to discriminate between cancerous and inflamed tissue. Novel tracers 2-[^{18}F]-2-fluoroethyl-L-phenylalanine (2-[^{18}F]FELP) [115] and (S)-2-amino-3-[3-(2-[^{18}F]fluoroethoxy)-4-iodophenyl]-2-methylpropanoic acid (^{18}F -FIMP) [116] have been found to distinguish tumors from inflamed tissue better than [^{18}F]FDG, [^{11}C]Met, or [^{18}F]FET, but this is because they preferentially accumulate in tumors (which often overexpress LAT1) and therefore they would be more useful for excluding the presence of inflammation than for specifically imaging inflammation. However, LAT1 is also a marker of T cell activation and thus could be useful in imaging T cell activity, whether in the context of inflammatory (e.g., autoimmune) diseases or for cancer immunotherapies or T cell-based therapies where T cell activation at the target location is actually a positive sign and can manifest as pseudoprogression on [^{18}F]FDG scans [117]. Similarly, immune checkpoint inhibitors used in oncology can cause severe immune-related adverse effects (irAEs) [118],

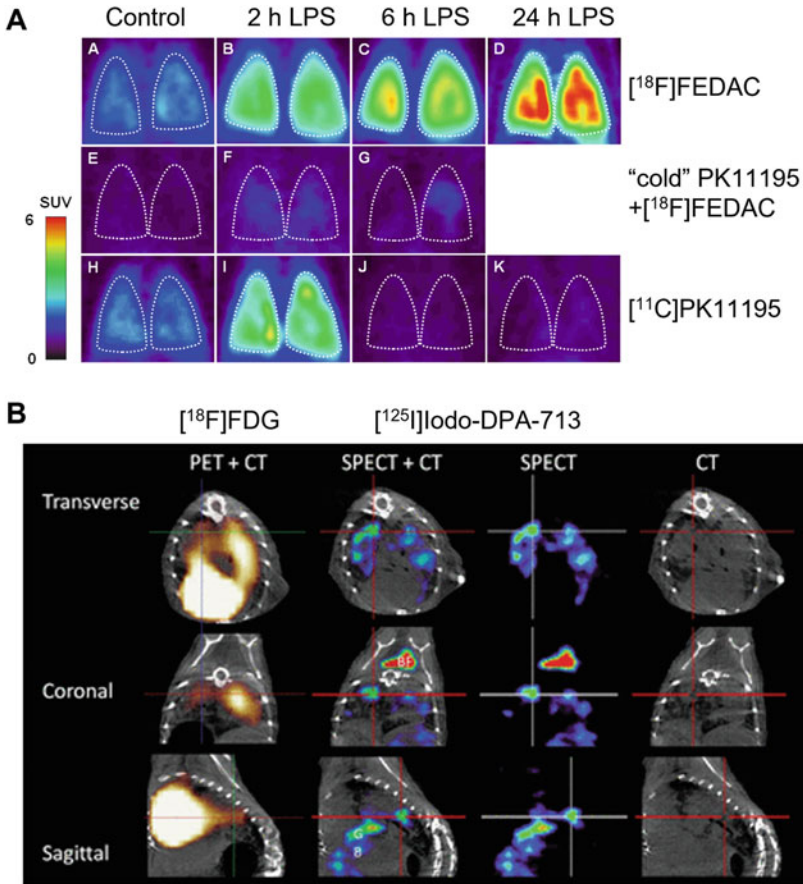


Fig. 12 Novel tracers for TSPO imaging of lung inflammation. (a) Representative coronal PET lung images acquired 0–30 min after injection of radiotracer in rats, at various time points after intratracheal administration of bacterial lipopolysaccharide (LPS). The images in the second line show tracer specificity, with TSPO blocked by nonradioactive PK11195. $[^{18}\text{F}]\text{FEDAC}$ was more sensitive than $[^{11}\text{C}]\text{PK11195}$ for TSPO imaging. Adapted with permission, © 2012, Hatori et al. [114]. (b) $[^{18}\text{F}]\text{FDG}$ PET/CT and $[^{125}\text{I}]\text{iodo-DPA-713}$ SPECT/CT images of C3HeB/FeJ mice infected with *M. tuberculosis*. Discrete areas of $[^{125}\text{I}]\text{iodo-DPA-713}$ SPECT signal are noted in the lungs of the infected mouse. The SPECT signal colocalizes with the tuberculosis lesion seen on CT (crosshair). The $[^{18}\text{F}]\text{FDG}$ PET signal is more diffuse, with intense signal noted in the heart, obscuring the pericardiac regions. $[^{125}\text{I}]\text{iodo-DPA-713}$ SPECT signal is also noted in the brown fat (BF) in the coronal view. Adapted with permission, © 2013, Foss et al. [112]

and although this hypothesis appears not to have been tested to date, imaging LAT1 may also be a way to detect irAEs. Approaches for specific imaging of T cells are discussed in Sect. 3.2.7.

3.1.3 Folate Receptor β

The folate metabolic pathway is fundamental for cells, and its dysregulation is involved in many diseases. Folate receptors (FRs) have long been targets for therapeutic and diagnostic agents, because of the frequent overexpression of FR- α on cancer cells [119] and FR- β specifically on activated macrophages [120]. This specificity makes FR- β a good target to develop (radio)tracers for diseases with significant macrophage involvement. While numerous radiolabelled folate analogues have been developed and used in the clinic, many of them bind to both α and β isoforms of FR [120]. One of the more recent FR-targeting radiotracers, [^{18}F] fluoro-PEG-folate, has recently been used in the clinic to image RA and provided better contrast than the TSPO tracer [^{11}C]PK11195 [121]. [^{18}F]fluoro-PEG-folate binds to both α and β isoforms and thus may also be useful for cancer imaging, but presumably without the ability to distinguish tumors from inflammation. [^{18}F]AlF-NOTA-folate is another example of radiotracer that has been shown to image FR- β in models of atherosclerosis (Fig. 13) [122] and myocarditis [123], but its affinity for FR- α has, to our knowledge, not been reported. To lift this ambiguity, efforts have been made to develop isoform-selective radiotracers for FRs, such as the recently developed 6*S* isomer of [^{18}F]F-aza-5-methyltetrahydrofolate (6*S*-5MTHF), which showed high uptake in FR- α -positive tumors and very low uptake in FR- β -positive tumors [124]. To the best of our knowledge, radiotracers with selectivity for FR- β over FR- α have not been reported to date but would have potential to be highly discriminating agents to image inflammatory diseases.

3.1.4 Imaging Hypoxia

Tissue hypoxia is associated with several inflammatory diseases. Among other factors, the infiltration of activated immune cells increases local consumption of oxygen. For example, macrophage-rich zones in atherosclerotic plaque are hypoxic [125], and so are granulomas in sarcoidosis [126]. Thus, imaging hypoxia could be a way of detecting certain inflammatory lesions. Radiotracers for imaging hypoxia are primarily used in oncology, but applications in cardiovascular and inflammatory diseases have recently emerged [127]. The lead radiotracer for hypoxia is [^{18}F] fluoromisonidazole ([^{18}F]FMISO), used clinically for cancer imaging for over 25 years [128]. [^{18}F]FMISO has been shown to detect atherosclerotic lesions in rabbits [129] and cardiac sarcoidosis in patients [130] (Fig. 14), and its uptake in inflamed joints correlated well with clinical symptoms in a mouse model of rheumatoid arthritis [131]. Other hypoxia tracers with potential to detect and monitor inflammatory diseases include those of the thiosemicarbazone family, such as [^{64}Cu] Cu-ATSM [132] and [^{64}Cu]Cu-CTS [133].

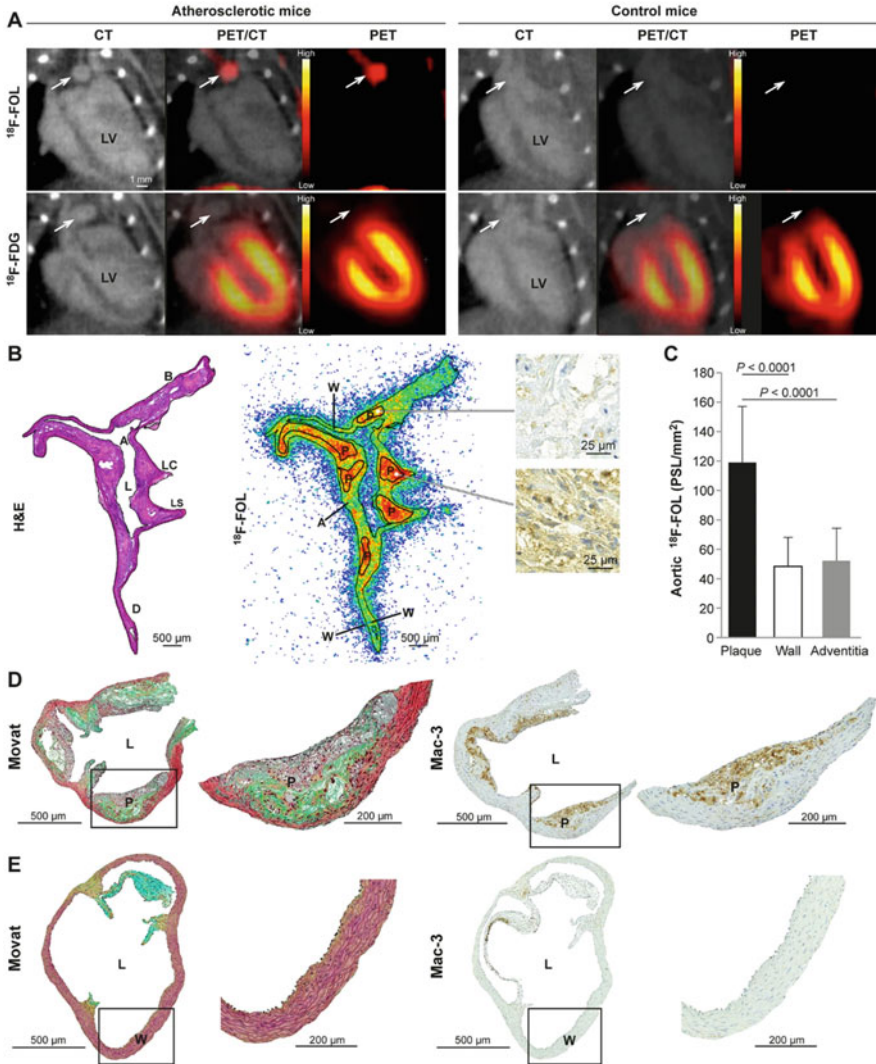


Fig. 13 Imaging folate receptors in atherosclerosis. (a) Representative coronal PET/CT images of atherosclerotic LDLR^{-/-} ApoB^{100/100} and healthy C57BL/6 N control mice administered [¹⁸F]AIF-NOTA-folate (¹⁸F-FOL) or [¹⁸F]FDG PET/CT. Note the low uptake of [¹⁸F]AIF-NOTA-folate in the heart. White arrows denote the aortic arch. LV: left ventricle. (b) Left: hematoxylin-eosin (H&E) staining of a longitudinally sectioned atherosclerotic mouse aorta. A: arch, AA: ascending aorta, B: brachiocephalic artery, D: descending thoracic aorta, L: lumen, LC: left common carotid artery, LS: left subclavian artery. Middle: superimposed ¹⁸F-FOL ex vivo autoradiograph and H&E staining, with black lines representing the tissue contour and regions of interest. P: plaques (excluding media); W: healthy vessel wall (no lesion formation); A: adventitia (mainly adipose tissue around the aorta). Right: Mac-3 immunohistochemical staining corresponding to a plaque with low (top) or high (bottom) ¹⁸F-FOL uptake. (c) Quantification of ¹⁸F-FOL binding on the ex vivo autoradiography of atherosclerotic mice aorta. PSL/mm² = photostimulated luminescence per mm² normalized for injected radioactivity dose. Adapted from [122], © 2018 Silvola et al. (CC-BY-4.0 license)

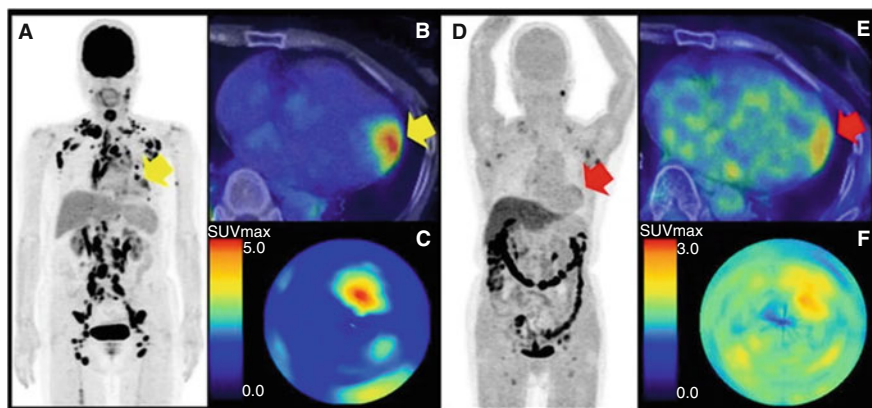


Fig. 14 Imaging cardiac sarcoidosis with [^{18}F]FMISO. [^{18}F]FDG (a–c) and [^{18}F]FMISO (d–f) PET/CT images: MIP image, fusion image, and polar map image of a patient with metastatic papillary thyroid cancer. This patient fasted for more than 18 h prior to [^{18}F]FDG administration to suppress the physiological uptake of [^{18}F]FDG in the myocardium. (a) Multiple areas of [^{18}F]FDG uptake are visible, making it difficult to distinguish metastases from sarcoidosis lesions. (d) [^{18}F]FMISO showed focal uptake in some of the [^{18}F]FDG-positive lymph nodes (d). In addition, a focal uptake of [^{18}F]FDG (yellow arrow; SUV_{max} 5.1) was detected at the anterolateral wall, indicating active inflammatory change associated with sarcoidosis (b, c). [^{18}F]FMISO PET also showed the abnormal uptake (red arrow; SUV_{max} 2.8) in the same cardiac region (e, f). Adapted from [130] with permission. © 2016, American Society of Nuclear Cardiology

3.1.5 Aldehyde Radiotracers

An emerging class of PET tracers which may reach the clinic in coming years is aldehyde-reactive PET tracers. These tracers bear functional groups such as oxyamines or hydrazines which can chemoselectively react with aldehydes. Aldehydes are a rare functional group in the healthy body, as their high chemical reactivity toward alcohols and amines makes them short-lived [134]. Aldehydes are, however, more abundant in systems under oxidative stress [135, 136]. They can be produced by the reaction of reactive oxygen species with amines (such as the side chain of the amino acid lysine) or by enzymatic action such as that of lysyl oxidase (LOX), which also oxidizes lysine to allysine [136]. LOX is upregulated during the formation of fibrotic tissue (fibrogenesis), where the side chains of lysine in collagen are oxidized to aldehydes, which then react with neighboring collagen fibrils to form a covalent cross-link [137]. The ability to image these aldehydes has been hypothesized to be used to stage disease progression of fibrotic diseases and monitor response to therapy [138]. It has also been suggested that aldehydic load—the concentration of aldehydes within the body or areas of the body—may in the future be adopted as a biomarker of inflammatory pathology [139]. Aldehyde-reactive PET tracers have been tested in preclinical models of bleomycin-induced lung fibrosis [140] and lipopolysaccharide (LPS)-induced systemic inflammation [139], demonstrating the aldehyde reactivity of the probes tested in these studies. In the study of an

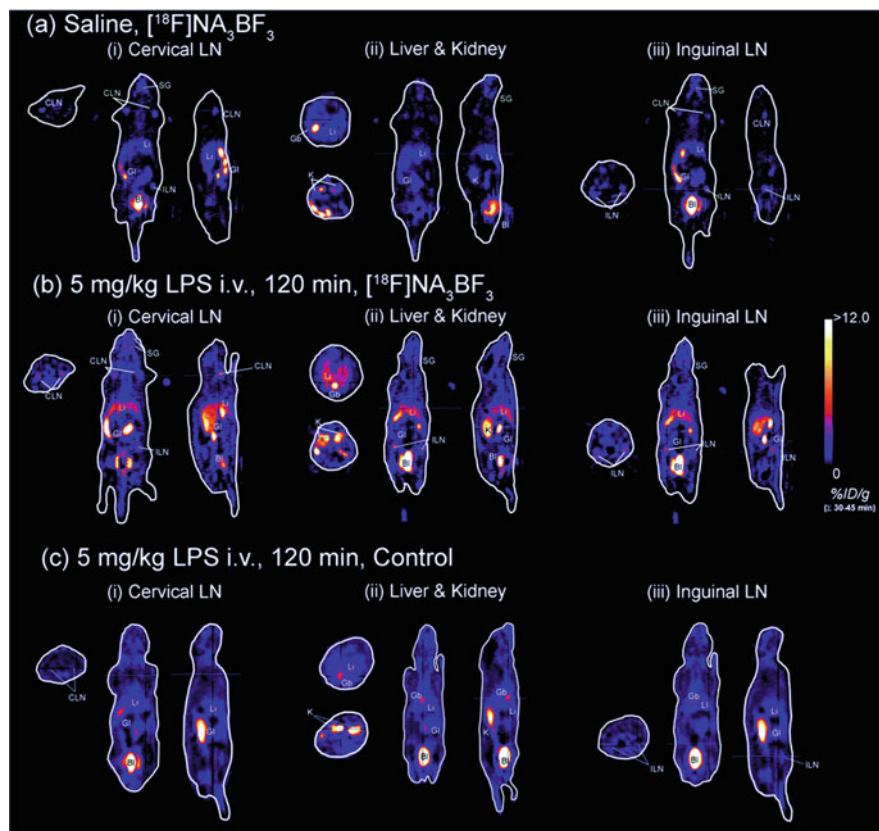


Fig. 15 PET/CT imaging of aldehydes in a systemic inflammation model. The uptake of $[^{18}\text{F}]\text{NA}_3\text{BF}_3$ increases in the liver, kidney, and lymph nodes following LPS-induced systemic inflammation. Orthogonal views of representative mice showing the differential uptake of $[^{18}\text{F}]\text{NA}_3\text{BF}_3$ 2 h following i.v. treatment with saline (a) or $5\text{ mg}\cdot\text{kg}^{-1}$ LPS (b) or of control probe (with no specific affinity for aldehydes) following $5\text{ mg}\cdot\text{kg}^{-1}$ LPS (c). CLN cervical lymph node, SG salivary gland, Li liver, GI gastrointestinal tract, ILN inguinal lymph node, K kidney, Bl bladder. Adapted from Kirby et al. [139] with permission. © 2019, The Royal Society of Chemistry

^{18}F -labelled hydrazine-functionalized tracer— $[^{18}\text{F}]\text{NA}_3\text{BF}_3$ —in a model of systemic inflammation, increased tracer uptake in the liver, kidneys, and lymph nodes was observed (Fig. 15) [139], with the lymphoid response matching reports that lymphocyte apoptosis and various pro-inflammatory signals can occur soon after LPS injection [141–143]. However, it was demonstrated more recently by dos Santos Ferreira et al. that a hydrazine-functionalized probe for MRI showed weak contrast enhancement in animals with inflammation but minimal fibrogenesis, and strong contrast enhancement in highly fibrogenic tissue [144]. This indicates that the probe tested, and indeed possibly all aldehyde-reactive probes, may image fibrogenesis—or other causes of aldehyde production—as a proxy of inflammation, but are not imaging inflammation itself. These studies were conducted in genetically

modified mouse models, and the clinical applicability of the conclusions has yet to be tested. Nonetheless, this indicates that caution may be necessary when interpreting results in terms of inflammation and that perhaps the use of this type of tracer in conjunction with another that detects inflammation by a different mechanism may be preferable.

3.1.6 Radioactive Gallium in the Host-Pathogen Fight over Iron

Iron is an essential trace metal for the vast majority of living organisms, and microbes have evolved multiple mechanisms to acquire iron from their environment, including their hosts, for example, by secreting siderophores or hijacking host ferroproteins [145]. In response, immune cells secrete iron-binding proteins, for example, lactoferrin and neutrophil lipocalin, to sequester iron from microbes. This competition over iron has been exploited since the 1970s to image infection-related inflammation by scintigraphy/SPECT with [^{67}Ga]Ga-citrate [91]. Indeed, gallium(III) has very similar physicochemical properties to iron(III), and therefore iron chelators very often have good affinity for gallium as well. Citrate being a relatively weak chelator for gallium, the administered Ga^{3+} ions are rapidly transchelated in the blood by transferrin, which accumulates at sites of infection through increased vascular permeability. There, gallium is sequestered by other chelators such as host lactoferrin and lipocalin, which are then either directly taken up by microbes or have the gallium “stolen” by bacterial or fungal siderophores with even higher affinity. Thus, radioactive gallium can detect both the pathogen and the host response to infection. Although [^{67}Ga]Ga-citrate has now been mostly replaced by other radiotracers, the increasing availability of gallium-68, which has much better imaging properties, has led to a reconsideration of the use of gallium citrate and other chelators for imaging infection and inflammation, such as deferoxamine [146]. Some pathogen species also secrete specific siderophores that are not taken up by other species, and these can be repurposed as pathogen-specific imaging agents [147]. However, citrate and deferoxamine appear more promising because they are more easily obtained and have already been used in the clinic and their safety profile is known, thus providing a more rapid pathway to clinical translation.

3.2 Adhesion Molecules and Intercellular Signalling Pathways

3.2.1 Fibroblast Activation Protein (FAP)

FAP is a transmembrane di-peptidyl protease overexpressed primarily on activated fibroblasts, with relatively little expression in healthy tissue. Activated fibroblasts are found mostly at sites of injury and are involved in tissue repair, but cancer cells also actively recruit fibroblasts that then participate in tissue remodelling, tumor

invasiveness, and immune evasion [148]. Overexpression of FAP has been observed in many types of cancer [149]. This has led to FAP becoming one of the most promising targets for radiotracer development in oncology in recent years, and the number of clinical studies using radiolabelled FAP inhibitors is rapidly growing [150, 151]. FAP has also been shown to be elevated in inflammatory diseases such as arthritis [152], cirrhosis [153], and systemic sclerosis [154]; thus, it is reasonable to expect it will be a useful target for imaging inflammation. This is supported by a few recent preclinical studies in myocardial infarction models and clinical case reports showing uptake of radiolabelled FAP inhibitors in arthritic joints and cirrhotic livers [155].

3.2.2 Antigen-Presenting Cell Activation Markers: CD80/CD86

The co-stimulatory molecules CD80 and CD86, involved in the activation of T cells, are found primarily on antigen-presenting cells (APCs) such as dendritic cells and macrophages and are often used in research as APC activation markers. Blocking the interaction between CD80/CD86 and CD28 prevents the activation of T cells, and this strategy has been used therapeutically [156], for example, with the clinically approved drugs belatacept and abatacept, which are indicated for the prophylaxis and treatment of kidney graft rejection and arthritic diseases (e.g., rheumatoid arthritis and psoriatic arthritis), respectively. Therefore, CD80/86 may also be interesting targets for imaging inflammation. Both belatacept and abatacept have been the subject of recent studies, in which ^{111}In -labelled belatacept was evaluated in a mouse model of atherosclerosis as well as human samples of atherosclerotic carotid plaque [157], and ^{64}Cu -labelled abatacept was evaluated in a mouse model of LPS-induced local inflammation (Fig. 16) [158]. Interestingly, although the accumulation of ^{111}In -belatacept was observed in atherosclerotic plaque areas, not all lipid-rich areas were detected, and the *in vivo* images were difficult to interpret because of high radioactivity associated with circulating radiotracer in the myocardium and large vessels. This is likely due to the long circulation time of belatacept, a feature often desirable for therapeutic applications but less so for imaging purposes where rapid clearance of unbound radiotracer is preferred in order to obtain higher target-to-background ratios and better contrast. ^{64}Cu -abatacept was also able to image inflammation, but the shorter half-life of ^{64}Cu (12.7 h) meant that by the time the radiotracer distribution had equilibrated (48 h), the remaining activity was low. The same group have attempted to develop ^{11}C -labelled small-molecule ligands of CD80 to circumvent the long circulation time of the antibody-based tracers, but the *in vivo* performance of the lead candidate was reportedly not satisfying due to unfavorable pharmacokinetic properties [159].

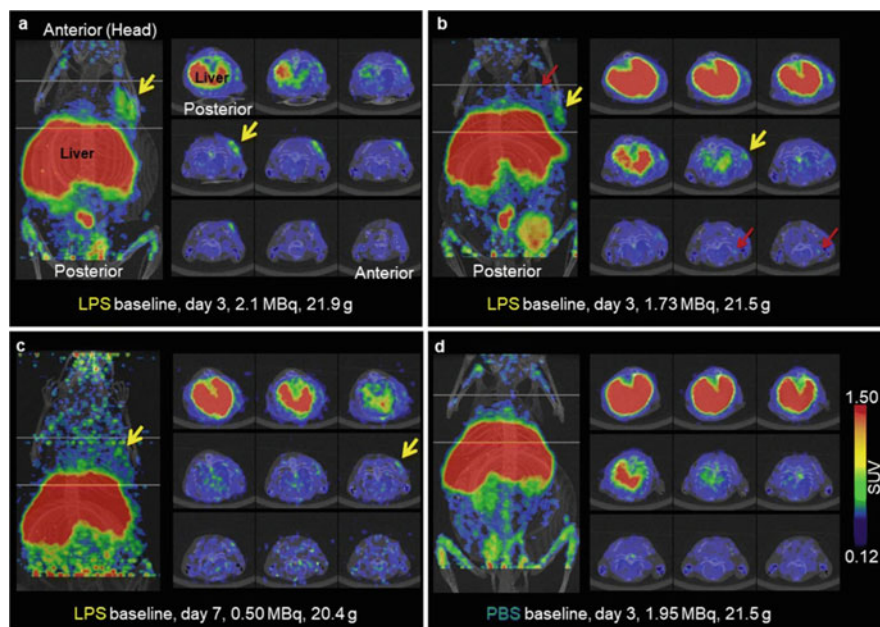


Fig. 16 Imaging CD80/CD86 in LPS-induced inflammation. Maximal-intensity projection PET/CT images of C57BL/6 mice 48 h after i.v. administration of ^{64}Cu -NODAGA-abatacept, showing increased radiotracer uptake in inflamed areas. Mice were inoculated with a Matrigel plug containing LPS (a–c) or PBS (d) subcutaneously on the right shoulder, 3 days (a, b, d) or 7 days (c) before the scan. The nine segments are MIPs of five adjacent axial slices each; segments are shown from posterior (top left) to anterior (bottom right). Yellow arrows indicate tracer accumulation in the region of inoculation. Red arrows indicate tracer accumulation in the region of lymph nodes. Dose in MBq at scan start and body weight as indicated. Adapted from [158], © 2020, Taddio et al. (CC-BY-4.0 license)

3.2.3 Macrophage Activation Marker: Mannose Receptor/CD206

The mannose receptor, CD206, is a scavenger receptor that is considered a marker of the M2 macrophage phenotype, although it is also found on dendritic cells and hepatic and lymphatic endothelial cells. It has been investigated as a target for imaging probes in oncology because the infiltration of CD206-positive macrophages in the tumor microenvironment is associated with poor prognosis [160], and CD206⁺ macrophages have also been reported in the fibrous cap of unstable atherosclerotic plaque [161] although their exact role in this setting is still unclear. The latter study was performed by PET imaging of rabbits using an ^{18}F -labelled derivative of mannose, 2-deoxy-2- ^{18}F fluoro-D-mannose (^{18}F FDM). However, clinical imaging of CD206 is more commonly performed with $^{99\text{m}}\text{Tc}$ -tilmanocept, a radiotracer that was approved by the FDA in 2013 for sentinel lymph node detection and is a macromolecule composed of a dextran backbone conjugated to 12 to 20 mannose

residues for CD206 targeting and 3 to 8 DTPA moieties to chelate ^{99m}Tc [162].² Tilmanocept also appears to be useful for inflammation imaging, having been used, for example, in a mouse model of traumatic brain injury to image neuroinflammation [163]. Interestingly, in the latter study, tilmanocept was also conjugated to the near-infrared fluorescent dye IRDye[®] 800CW, allowing *ex vivo* analysis of tissues by fluorescence microscopy. The DTPA moieties of tilmanocept also allow it to be conjugated with other radionuclides, for example, Varasteh et al. used ^{111}In -labelled tilmanocept to detect atherosclerotic plaque lesions in ApoE-knockout mice [164]. Tilmanocept has recently been used in the clinic to evidence the presence of CD206⁺ macrophages in atherosclerotic plaque in HIV-infected patients [165] and therefore appears to be a promising novel tracer for atherosclerosis and potentially for other inflammatory diseases.

The mannose receptor has also been targeted with radiolabelled nanobodies, which are single variable domains of heavy-chain antibodies originally found in camelids. Nanobodies are much smaller in size (12–15 kDa) than full antibodies, which endows them with a much more rapid clearance from blood and mainly renal excretion. These properties have made them highly interesting scaffolds to develop imaging probes [166]. The fast pharmacokinetic profile of nanobodies makes them a good match for radionuclides with short half-lives, for example, a ^{68}Ga -labelled anti-CD206 nanobody was able to detect small atherosclerotic plaque in an ApoE-knockout mouse model [167, 168] (Fig. 17). Finally, mannosylated human serum albumin (MSA) has been used to target CD206-positive cells in a rat model of myocarditis [169].

Similar approaches targeting activated macrophages include ^{89}Zr -labelled maleylated human serum albumin (targeting the scavenger receptor SR-A1) [170] and the imaging of M2 macrophages with a ^{89}Zr -labelled F(ab')₂ antibody fragment directed against galectin-3 [171].

3.2.4 Chemokine Receptors

Chemokine receptors play important roles in controlling the recruitment of immune cells in inflammation and are therefore interesting targets to develop radiotracers for inflammation. In addition to the CXCR4-targeting radiotracer [^{68}Ga]Ga-pentixafor previously discussed in Sect. 2.1, other chemokine signalling pathways have been explored recently for nuclear imaging purposes. Chemokine receptor type 2 (CCR2), for example, is involved in the recruitment of pro-inflammatory monocytes to sites of injury [172], and a CCR2-binding peptide conjugated to a DOTA chelator (DOTA-ECL1i) for radiolabelling with ^{64}Cu or ^{68}Ga has been shown to detect the

²Because of variability in the length of the dextran backbone as well as the conjugation method, the exact number of mannose and DTPA moieties cannot be precisely controlled, and the final product is actually a mixture of molecules. This is common when labelling macromolecules such as proteins and carbohydrates.

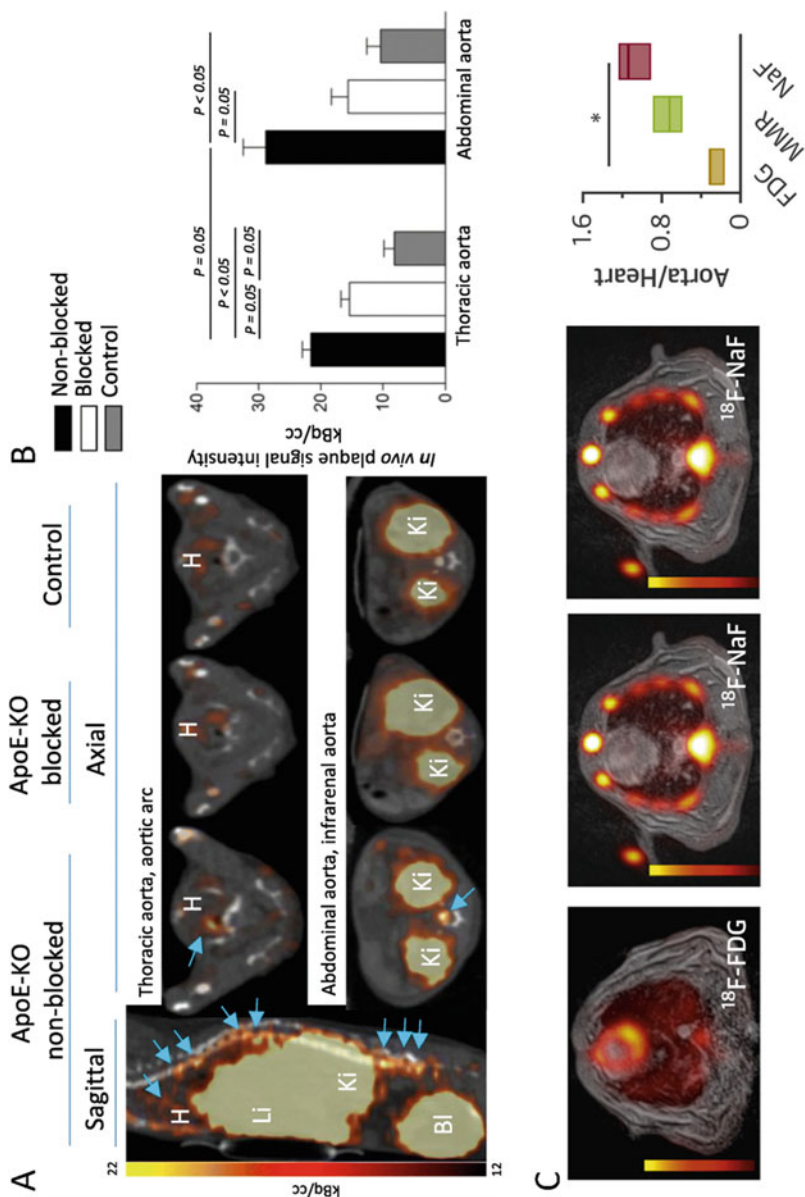


Fig. 17 Imaging of atherosclerosis with a macrophage mannose receptor (MMR)-targeting nanobody radiotracer. (a) *In vivo* PET/CT images from ApoE-KO non-blocked, blocked, and control mice acquired 1 h after administration of [^{68}Ga]Ga-NOTA-MMR nanobody. Note the intense focal signals in the atherosclerotic plaques of ApoE-KO non-blocked mice (blue arrows). In contrast, no focal uptake was detected in the aortas of ApoE-KO mice after blocking

recruitment of monocytes to inflammation sites in rodent models of acute lung injury [173], heart transplantation [174], atherosclerosis [175], and abdominal aortic aneurysm inflammation [176], with results suggesting that radiotracer uptake also correlates with disease severity. Interestingly, this tracer was able to provide positive contrast in the heart in an ischemia-reperfusion injury model, whereas the ischemic region appeared as a low-uptake region on [^{18}F]FDG scans (Fig. 18) [177]. Although this CCR2-targeting peptide has also been used to functionalize gold nanoparticles in order to prepare a multivalent radiotracer with extended pharmacokinetics [178], the results with the small peptide radiotracer have been sufficiently encouraging to warrant a clinical trial (NCT04217057) to image CCR2⁺ cell infiltration in head-and-neck cancer [179], which appears to be ongoing at the time of publication. The chemokine receptor CCR5 has also been imaged in ApoE^{-/-} atherosclerotic mice, using ^{64}Cu -labelled organic nanoparticles functionalized with a CCR5-specific peptide [180]. Rather notably, radiotracer uptake in atherosclerotic lesions diminished when ApoE expression was re-established, showing that it could be used to monitor response to treatment. $^{99\text{m}}\text{Tc}$ -labelled interleukin-8 (IL-8/CXCL8), a strong neutrophil chemoattractant, has also shown encouraging results for clinical SPECT imaging of inflammatory bowel disease [181].

Considering the promiscuity of chemokine receptors, an alternative approach might be to use somewhat less selective ligands as radiotracers, as illustrated by the example of ^{64}Cu -labelled nanoparticles conjugated to viral macrophage inflammatory protein II (vMIP-II) that are able to bind multiple chemokine receptors and could detect atherosclerotic plaque in mice [182]. It was subsequently found that the vMIP-II targeting sequence preferentially binds to CXCR4 expressed on endothelial cells and thus vMIP-II-based radiotracers could be a way of identifying areas of injured endothelium in atherosclerosis [183].

The wide variety of macrophage phenotypes means there are numerous markers than can serve as imaging targets. In the case of vascular inflammation, a common issue in the preclinical studies mentioned here is the small size of the vessels and lesions and the proximity to the myocardium, which make it all the more important to have tracers with high affinity, rapid clearance, and good imaging resolution. Affinity and clearance rate depend on the chemical structure of the targeting moiety,



Fig. 17 (continued) with an excess amount of non-labelled NOTA-MMR nanobody or in the aortas of control mice. The upper threshold is reduced in order to reveal focal uptake, which resulted in exaggerated abdominal area signals. H: heart; Li: liver; Ki: kidney; Bl: bladder. **(b)** Plaque signal intensities were quantified in thoracic and abdominal aorta using axial PET/CT images. **(a, b)** Reproduced from [164], © 2019, Varasteh et al. (CC-BY-4.0 license). **(c)** Representative fused PET/MR images of atherosclerotic rabbits after 8 months on a high-fat diet; administered [^{18}F]FDG (3 h p.i.), [^{68}Ga]Ga-NOTA-MMR nanobody (2 h p.i.), and [^{18}F]NaF (1.5 h p.i.); and associated aorta-to-heart ratios. [^{18}F]NaF had the highest ratio due to its low uptake in cardiac tissue, followed by [^{68}Ga]Ga-NOTA-MMR and [^{18}F]FDG, whose uptake in the myocardium was relatively high despite a 4-hour fasting protocol before injection. Adapted from [168] with permission, © 2019, Senders et al.

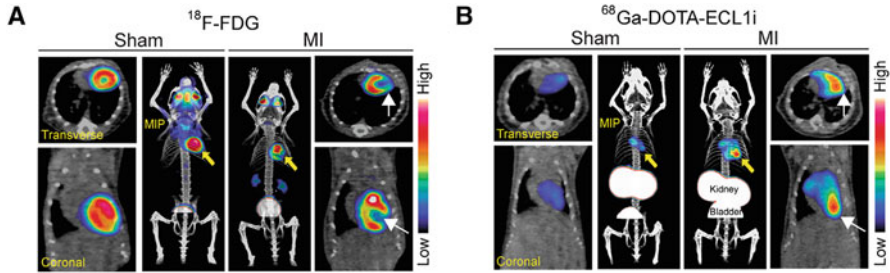


Fig. 18 Imaging of CCR2 receptors using [^{68}Ga]Ga-DOTA-ECL1i in a mouse model of closed-chest ischemia-reperfusion (IR) injury. **(a)** Representative [^{18}F]FDG PET/CT images obtained 5 days after 90 min of IR injury identifying the infarct region in mice that underwent IR injury (myocardial infarction [MI]) compared with sham controls. Transverse, coronal, and maximal-intensity projected (MIP) views are shown, and white arrows denote the infarct area. **(b)** Representative PET/CT images showing regional accumulation of [^{68}Ga]Ga-DOTA-ECL1i signal in the infarct and border zone 4 days after IR injury. Yellow arrows identify tracer uptake in hearts that underwent IR injury compared with sham controls. White arrows denote the infarct area as determined by [^{18}F]FDG imaging. Adapted from Heo et al. [177] with permission. © 2019, Wolters Kluwer Health

whereas the resolution depends on the radionuclide employed, highlighting the importance of good tracer design to obtain exploitable images.

3.2.5 Cell-Adhesion Molecules (CAMs): Integrins and Selectins

Integrins are transmembrane proteins that play important mechanical and signal transducing roles by linking the cytoskeleton with the extracellular matrix [184]. They are key actors in cell migration and tissue development and remodelling, and in the context of inflammation they are particularly involved in leukocyte migration [185]. Other CAMs such as selectins and Ig-like CAMs (e.g., ICAM-1, VCAM-1) are ligands for integrins and are also involved in leukocyte migration. Therefore, integrins, selectins, and other CAMs are interesting targets for molecular imaging of inflammation. One of the earliest strategies for imaging integrins is to use RGD peptide analogues, as the RGD sequence is common to many extracellular matrix (ECM) proteins and binds preferentially to integrin $\alpha_v\beta_3$. This has been used in the clinic primarily for imaging tumor angiogenesis with tracers such as [^{18}F]F-galacto-RGD, [^{18}F]fluciclatide, [$^{99\text{m}}\text{Tc}$]Tc-maraciclatide, and others [186], as well as in various vascular diseases, rheumatoid arthritis [187], and recently myocarditis [188]. There have been recent efforts to specifically target other integrin classes, most often through the use of monoclonal antibodies or antibody fragments. For example, integrin $\alpha_4\beta_7$ is involved in recruiting lymphocytes to the gut, but a ^{64}Cu -labelled antibody fragment targeting the broader β_7 family was found better for imaging colitis than a more specific antibody against $\alpha_4\beta_7$ [189]. Targeting integrin $\alpha_5\beta_1$ has been suggested to be more specific than $\alpha_v\beta_3$ for imaging rheumatoid arthritis (Fig. 19) [190].

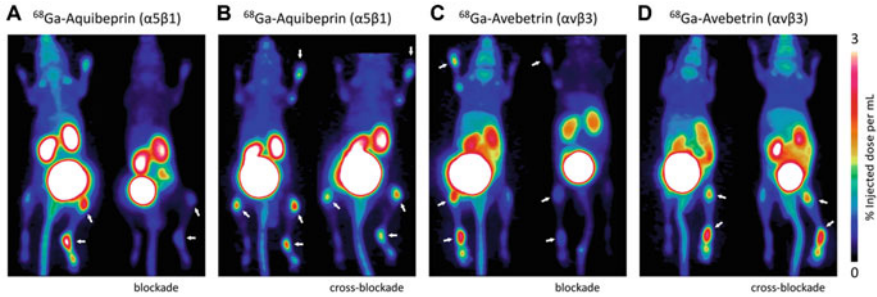


Fig. 19 Specific imaging of integrins $\alpha_5\beta_1$ and $\alpha_V\beta_3$ in arthritic mice. (a, b) $\alpha_5\beta_1$ integrin PET using [^{68}Ga]Ga-aquibepirin. (c, d) $\alpha_V\beta_3$ -integrin PET using [^{68}Ga]Ga-avebetrin. Each image shows two independent scans of the same mouse (different animals are shown in a–d). Arthritic joints are indicated by the arrows. The saturation of the receptor binding capacity by co-injection of a large dose (30 nmol) of unlabelled compound (blockade) resulted in a virtually complete reduction of the uptake in arthritic joints for both tracers, confirming the specificity of the PET imaging (a, c). The cross-blockade experiments confirmed the subtype selectivity of $\alpha_5\beta_1$ - and $\alpha_V\beta_3$ -integrin PET: the co-injection of 30 nmol avebetrin did not substantially affect the $\alpha_5\beta_1$ integrin imaging with [^{68}Ga]Ga-aquibepirin, while the minuscule reduction of the signal is likely related to a residual $\alpha_5\beta_1$ activity (39 nM) of avebetrin (b). The co-injection of 30 nmol aquibepirin did not affect $\alpha_V\beta_3$ -integrin imaging with [^{68}Ga]Ga-avebetrin (d). Reproduced from [190] with permission. © 2019 Notni et al. (CC-BY-4.0 license)

A ^{64}Cu -labelled peptide targeting integrin $\alpha_4\beta_1$ (VLA-4), which is overexpressed in sickle reticulocytes, was used to image LPS-induced hyper-adhesion of circulating cells in a mouse model of sickle-cell disease (Fig. 20), a phenomenon that leads to occlusions of the microvasculature and to ischemia-reperfusion injury [191]). A recent comparison of radiotracers for plaque imaging provided some interesting results: ^{111}In -labelled tracers targeting the integrin LFA-1 and folate receptors were shown to be better for overall plaque detection than tracers targeting SSTR2, whereas the latter were better at differentiating advanced plaque from early plaque [192]. Vascular cell-adhesion molecule 1 (VCAM-1) has also proven to be a promising target for imaging atherosclerotic plaque, most recently using nanobodies radiolabelled with $^{99\text{m}}\text{Tc}$, ^{18}F , and ^{64}Cu [193–195], and could potentially complement current imaging of atherosclerotic lesions with [^{18}F]FDG and [^{18}F]NaF [168]. $^{99\text{m}}\text{Tc}$ -labelled, ICAM-1-targeted microbubbles could detect peritonitis in rats [196]. P- and E-selectin are overexpressed by activated endothelial cells and, for P-selectin, by platelets. Both contribute to the adhesion of leukocytes to the inflamed endothelial wall and this has made them targets for imaging cardiovascular inflammation [197]. For example, $^{99\text{m}}\text{Tc}$ -labelled microparticles functionalized with fucoidan, which binds to P-selectin, were used to detect aortic aneurysm by SPECT [198], and ^{68}Ga -labelled fucoidan could image acute ischemic stroke [199] and vulnerable plaque [200]. Overall, the diversity of molecules involved in the different steps of the leukocyte recruitment cascade provides many targets for radiotracer development that can be used to image inflammation, and in some cases it may be possible to achieve specific imaging of certain inflammatory diseases.

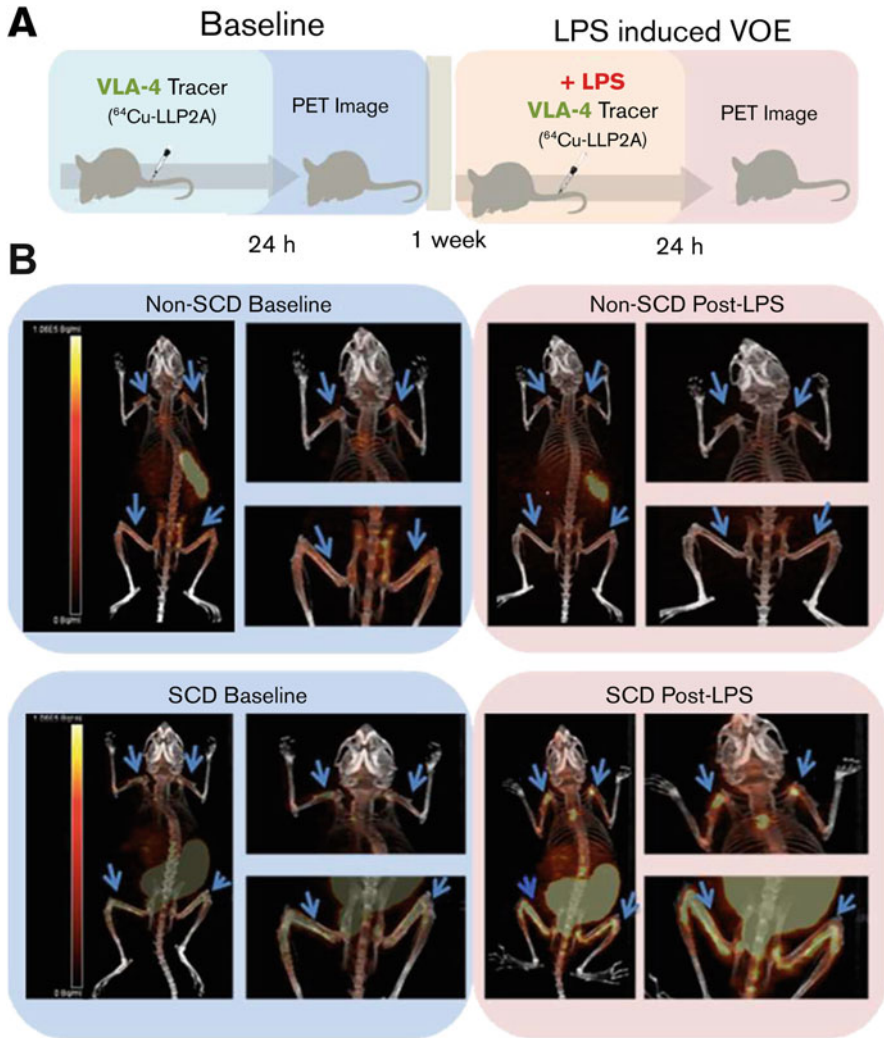


Fig. 20 Imaging integrin $\alpha_4\beta_1$ in a mouse model of sickle-cell disease (SCD). (a) Experimental design: SCD and non-SCD mice were imaged at baseline, and after 1 week they were injected intravenously with LPS and [⁶⁴Cu]Cu-LLP2A. LPS induces endothelial activation, promoting vaso-occlusive episodes (VOE). (b) Representative PET/CT images of SCD and non-SCD mice 24 h after injection of [⁶⁴Cu]Cu-LLP2A at baseline and post-LPS challenge. There are distinct differences between VLA-4 expression in SCD and non-SCD mice post-LPS in the humeri and femurs (blue arrows). Reproduced from Perkins et al. [191]. © 2020, American Society of Hematology

3.2.6 Matrix Metalloproteinases

Matrix metalloproteinases (MMPs) are a family of calcium-dependent, zinc-containing proteases that degrade extracellular matrix (ECM) components such as

collagens and fibronectins, as well as cell surface receptors, chemokines and cytokines. They participate in many physiological processes and are also well known for their role in cancer progression and the regulation of inflammation [201]. MMPs have long been investigated as targets for drug and diagnostic agent development [202]. Recently, the pan-MMP inhibitors [^{99m}Tc]Tc-RP805 and [^{99m}Tc]Tc-RYM1 were investigated in mouse models of lung inflammation [203] and abdominal aortic aneurysm [204], respectively. In both models, radiotracer uptake in the inflamed organs correlated well with MMP-12 activity, *MMP12* gene expression, and macrophage content. Further developments led to the synthesis of a radiotracer with higher specificity toward MMP-12, but it is not yet apparent whether this increased specificity results in better imaging of MMP-associated inflammation than with pan-MMP radiotracers [205]. A different, ^{18}F -labelled inhibitor of MMP-2, MMP-9, MMP-12 and MMP-13 was able to detect lung inflammation in a mouse model of cigarette smoke-induced COPD [43]. On the other hand, specific imaging of MMP-9 with an ^{89}Zr -labelled F(ab')₂ fragment in a mouse model of colonic fibrosis showed that high MMP-9 expression was a marker of fibrosis rather than inflammation [206]. Incidentally, that radiotracer also revealed the unexpected presence of kidney fibrosis in that model, further demonstrating the value of whole-body imaging techniques.

3.2.7 Radionuclide Imaging of T Cells and B Cells in Inflammation

The role of T cells in combating cancer and the advent of immunotherapy have driven many of the recent approaches to develop T cell-specific radiotracers, to understand, for example, the degree of T cell infiltration in tumors and the precise subtypes of infiltrating T cells, to demonstrate the efficacy of checkpoint inhibitors, or to distinguish tumor progression from pseudoprogression [29]. However, it is well known that various subsets of T cells are key players in many inflammatory and autoimmune diseases, including rheumatoid arthritis, asthma, graft-versus-host disease (GvHD), inflammatory bowel diseases, ischemic stroke, etc., and therefore radiotracers that can specifically image the presence or function of T cells in tissue could also be useful in these diseases.

One approach for T cell imaging is to use lineage markers. For example, a ^{89}Zr -labelled anti-CD3 antibody was used to image the accumulation of human T cells in a humanized mouse model of GvHD (Fig. 21a) [207], and CD4⁺ T cells were detected in the colons of mice using a radiolabelled anti-CD4 diabody in a model of dextran sodium sulfate-induced colitis [208]. More specific subsets have also been studied, for example, the specific imaging of activated T cells with a ^{89}Zr -labelled OX40-targeting antibody was able to detect GvHD before the onset of clinical symptoms in mice, and radiotracer uptake correlated with disease severity [209]. Recent PET studies using CD8-targeting diabodies and nanobodies have also shown the recruitment of CD8⁺ T cells in models of oncolytic herpes virus simplex therapy [210] and influenza A infection (Fig. 21b) [211], suggesting that this type of T cell imaging may have applications for other infectious diseases. An

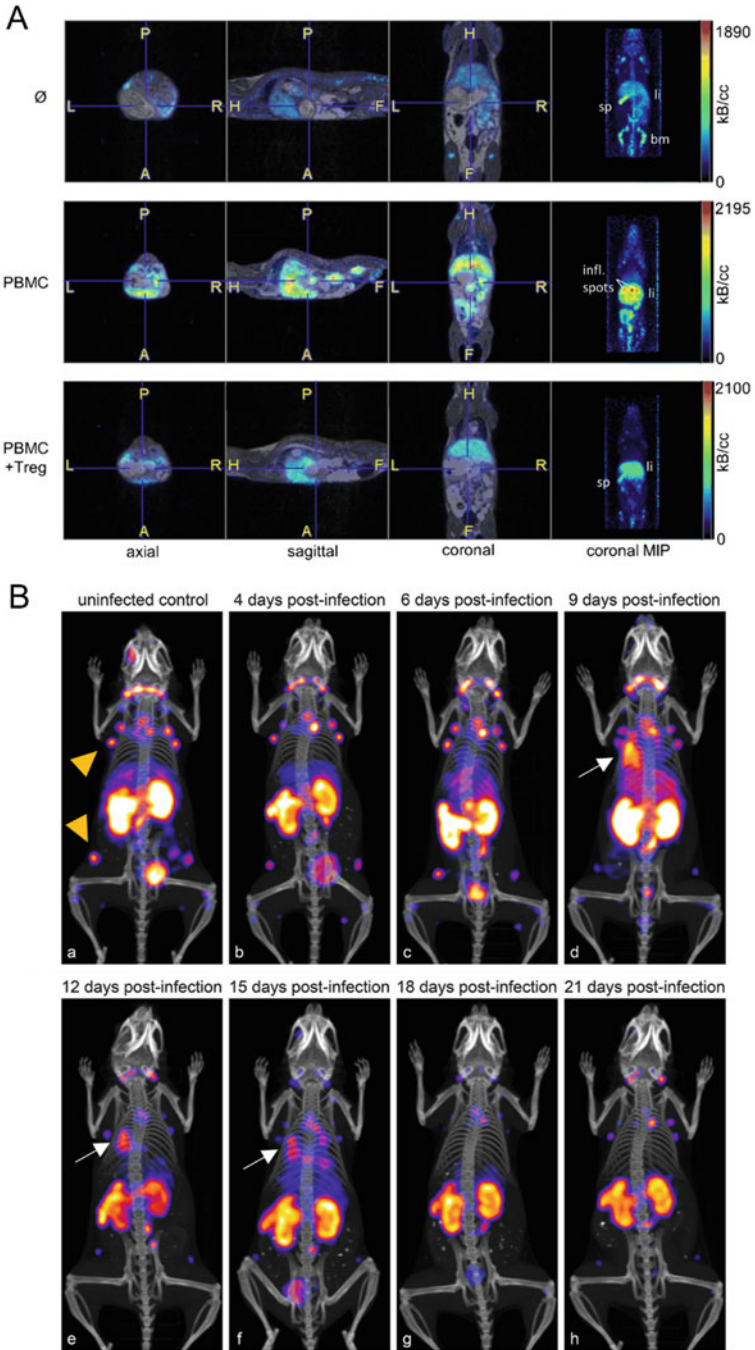


Fig. 21 PET imaging of T cells with CD3 and CD8 antibodies. (a) CD3-PET/MRI shows the efficiency of regulatory T cells (Treg) in preventing GvHD induction, evidenced by the reduced CD3-PET signal in the liver and spleen after administration of Treg. NSG mice were engrafted with 50×10^6 PBMC \pm Treg. Nineteen days later, mice received ^{89}Zr -labelled CD3 monoclonal

alternative approach is to exploit enzymes that are upregulated in activated T cells, for example, deoxycytidine kinase and deoxyguanosine kinase, which were targeted with 2'-[^{18}F]fluoro-9- β -D-arabinofuranosylguanine ([^{18}F]F-AraG) and showed high uptake in the cervical lymph nodes in a mouse model of acute GvHD [212] and in inflamed paws in adjuvant-induced arthritis [213]. Imaging of activated CD8⁺ and NK cells can also be performed by exploiting the enzymatic activity of the cytotoxic enzymes they release, as recently demonstrated with a ^{64}Cu -labelled propeptide containing a motif allowing specific recognition and cleavage by granzyme B [214]. Upon engagement of the target cell, cytotoxic lymphocytes secrete granzyme B which cleaves the propeptide, releasing a radiolabelled peptide that binds to nearby phospholipid bilayers (cell membranes). This approach was able to image responsiveness to immune checkpoint inhibitor therapy in cancer models and to image LPS-induced lung inflammation in mice, showing that it could have broad applicability [214].

For B cell imaging, many studies have been conducted using radiolabelled versions of the clinically approved anti-CD20 antibody rituximab (reviewed by Iodice et al. [215]). Recently, ^{64}Cu -labelled rituximab was used to image B cells in the brains of humanized mice with experimental autoimmune encephalomyelitis [30]. ^{89}Zr -labelled rituximab was also shown to have predictive value for response to treatment in patient with rheumatoid arthritis, with significantly higher uptake of ^{89}Zr -labelled rituximab in patients showing clinical response to rituximab over 24 weeks compared to nonresponders [216].

3.2.8 Vascular Adhesion Protein-1 (VAP-1)

Vascular adhesion protein-1 is a protein involved in leukocyte adhesion that is abundantly expressed on the surface of inflamed endothelial cells and has been shown to be interesting both as a biomarker of inflammation and as a target as for the development of anti-inflammatory drugs and imaging probes [217]. VAP-1 has been imaged directly in various models of inflammation with ^{123}I -labelled antibodies [218] and ^{68}Ga -labelled peptides [219], but recent studies have focused on using radiolabelled derivatives of one of the endogenous ligands of VAP-1, sialic acid-binding immunoglobulin-like lectin 9 (Siglec-9). [^{68}Ga]Ga-DOTA-Siglec-9 showed comparable uptake to [^{18}F]FDG in a rabbit model of arthritis [220], was able to



Fig. 21 (continued) antibody. 24 h p.i. PET/MRI of untreated (upper panel), PBMC-engrafted (middle panel), and PBMC + Treg-treated mice (lower panel) was performed. Adapted from Pektor et al. [195] with permission. © 2019, Springer-Verlag GmbH. **(b)** CD8⁺ T cells transiently accumulate in the lungs (white arrows) and mediastinal lymph nodes (orange arrowheads) of influenza A virus (IAV)-infected mice between 6 and 15 days postinfection (dpi). Representative immuno-PET images of IAV WSN/33-infected mice injected with a ^{89}Zr -labelled nanobody targeting CD8 α (^{89}Zr -VHH-X118-PEG₂₀) on the indicated dpi. Adapted from [199] under CC-BY license, © 2021, Rothlauf et al.

detect *Borrelia burgdorferi*-induced arthritis (Lyme disease) in mice [221], and could detect *S. aureus* soft tissue infection but not osteomyelitis in pigs [222]. It was also possible to use this radiotracer in a pig model of acute respiratory distress syndrome (ARDS), but accurately measuring radiotracer uptake was complicated by the high uptake in healthy animals and the need to correct for tissue perfusion [223].

4 Conclusion and Perspectives

Through the clinical and preclinical examples presented in this chapter, we hope to have convinced the reader of the utility of radionuclide-based molecular imaging for studying inflammation. The noninvasive and highly sensitive nature of nuclear imaging modalities, combined with a high depth of penetration, is considerable advantage and allows these techniques to diagnose diseases as well as monitor treatments and responses to treatments. Molecular imaging provides a way of visualizing biochemical processes that occur in inflammation, often at earlier stages than through imaging methods based on structural alterations. The wide variety of tracer scaffolds and radionuclides provides flexibility of design and means that radiotracers can be prepared relatively easily once a target has been found for a given biological process. Of the extensive list of tracers and targets presented in this chapter, only a small fraction have reached the clinic to date. In our view, this shows that the full potential of nuclear imaging has yet to be exploited for inflammatory and infectious diseases. The outlook is bright, and future progress in this field will likely come from a combination of improved instrumentation and increased radiotracer specificity. This increased specificity will in turn provide better insights into the sequence of events taking place in the inflammatory response, assisting the development of better anti-inflammatory drugs and helping clinicians in making therapeutic decisions.

Acknowledgments The authors are grateful to the reviewers for their valuable input to this chapter.

Compliance with Ethical Standards Funding: This work was supported by the EPSRC program for next generation molecular imaging and therapy with radionuclides (EP/S032789/1), the Wellcome EPSRC Centre for Medical Engineering at KCL [grant number WT 203148/Z/16/Z], the King's College London & Imperial College London EPSRC Centre for Doctoral Training in Medical Imaging [EP/L015226/1], the KCL/UCL Comprehensive Cancer Imaging Centre funded by CRUK and EPSRC in association with the MRC and DoH (England), the Medical Research Council Confidence in Concepts scheme, the Experimental Cancer Medicine Centre at KCL, the KHP/KCL CRUK Cancer Centre, a Wellcome Trust Multiuser Equipment Grant: A multiuser radioanalytical facility for molecular imaging and radionuclide therapy research [212885/Z/18/Z], the National Institute for Health Research (NIHR) Biomedical Research Centre based at Guy's and St Thomas' NHS Foundation Trust and KCL [grant number IS-BRC-1215-20006], the MRC Doctoral Training Programme, and the Research England Confidence in Collaboration scheme. This research was funded in whole, or in part, by the Wellcome Trust [WT 03148/Z/16/Z][212885/Z/18/Z]. The views expressed are those of the authors and not necessarily those of the NHS, the

NIHR, or the Department of Health. Francis Man has received salary support from the Sackler Institute of Pulmonary Pharmacology at King's College London.

Conflict of Interest: Francis Man is an employee and shareholder of GE HealthCare. The views expressed are his own and not necessarily those of GE HealthCare. George Keeling has no conflict of interest to declare.

Ethical approval: No studies with human participants or animals were directly involved in the writing of this chapter.

References

1. Man F, Gawne PJ, de Rosales TMR. Nuclear imaging of liposomal drug delivery systems: a critical review of radiolabelling methods and applications in nanomedicine. *Adv Drug Deliv Rev.* 2019;143:134–60. <https://doi.org/10.1016/j.addr.2019.05.012>.
2. Vandenberghe S, Moskal P, Karp JS. State of the art in total body PET. *EJNMMI Phys.* 2020;7:35. <https://doi.org/10.1186/s40658-020-00290-2>.
3. Hueso-González F, Biegun AK, Dendooven P, Enghardt W, Fiedler F, Golnik C, et al. Comparison of LSO and BGO block detectors for prompt gamma imaging in ion beam therapy. *J Instrum.* 2015;10:P09015. <https://doi.org/10.1088/1748-0221/10/09/P09015>.
4. Jiang C, Deen. Sensors for positron emission tomography applications. *Sensors.* 2019;19:5019. <https://doi.org/10.3390/s19225019>.
5. James ML, Gambhir SS. A molecular imaging primer: modalities, imaging agents, and applications. *Physiol Rev.* 2012;92:897–965. <https://doi.org/10.1152/physrev.00049.2010>.
6. IAEA. Technetium-99m radiopharmaceuticals: manufacture of kits. Vienna: International Atomic Energy Agency; 2008.
7. Pandit-Taskar N, Postow MA, Hellmann MD, Harding JJ, Barker CA, O'Donoghue JA, et al. First-in-humans imaging with Zr-89-Df-IAB22M2C anti-CD8 Minibody in patients with solid malignancies: preliminary pharmacokinetics, biodistribution, and lesion targeting. *J Nucl Med.* 2020;61:512–9. <https://doi.org/10.2967/jnumed.119.229781>.
8. Hofman MS, Eu P, Jackson P, Hong E, Binns D, Iravani A, et al. Cold kit for prostate-specific membrane antigen (PSMA) PET imaging: phase 1 study of ⁶⁸Ga-tris(Hydroxypyridinone)-PSMA PET/CT in patients with prostate cancer. *J Nucl Med.* 2018;59:625–31. <https://doi.org/10.2967/jnumed.117.199554>.
9. Uppot RN. Technical challenges of imaging & image-guided interventions in obese patients. *Br J Radiol.* 2018;20170931. <https://doi.org/10.1259/bjr.20170931>.
10. Siemens Healthineers. Biograph Vision. 2020. <https://www.siemens-healthineers.com/en-uk/molecular-imaging/pet-ct/biograph-vision>
11. Siemens Healthineers. Symbia Intevo Bold. 2020. <https://www.siemens-healthineers.com/en-uk/computed-tomography/dual-source-ct/somatom-force>
12. Conti M, Eriksson L. Physics of pure and non-pure positron emitters for PET: a review and a discussion. *EJNMMI Phys.* 2016;3:8. <https://doi.org/10.1186/s40658-016-0144-5>.
13. Siemens Healthineers. MAGNETOM Terra. 2019. <https://www.siemens-healthineers.com/en-uk/magnetic-resonance-imaging/7t-mri-scanner/magnetom-terra>
14. Siemens Healthineers. SOMATOM Force. 2020. <https://www.siemens-healthineers.com/molecular-imaging/xspect/symbia-intevo-bold>
15. Ward RD, Amorim B, Li W, King J, Umutlu L, Groshar D, et al. Abdominal and pelvic ¹⁸F-FDG PET/MR: a review of current and emerging oncologic applications. *Abdom Radiol.* 2021;46:1236–48. <https://doi.org/10.1007/s00261-020-02766-2>.
16. Theobald T. In: Theobald T, editor. Sampson's textbook of Radiopharmacy. Pharmaceutical Press; 2010.
17. Ruth TJ. The shortage of technetium-99m and possible solutions. *Annu Rev Nucl Part Sci.* 2020;70:77–94. <https://doi.org/10.1146/annurev-nucl-032020-021829>.

18. Langbein T, Weber WA, Eiber M. Future of Theranostics: an outlook on precision oncology in nuclear medicine. *J Nucl Med*. 2019;60:13S–9S. <https://doi.org/10.2967/jnumed.118.220566>.
19. Kampen WU, Boddenberg-Pätzold B, Fischer M, Gabriel M, Klett R, Konijnenberg M, et al. The EANM guideline for radiosynoviorthesis. *Eur J Nucl Med Mol Imaging*. 2022;49:681–708. <https://doi.org/10.1007/s00259-021-05541-7>.
20. Sánchez-Crespo A, Andreo P, Larsson SA. Positron flight in human tissues and its influence on PET image spatial resolution. *Eur J Nucl Med Mol Imaging*. 2004;31:44–51. <https://doi.org/10.1007/s00259-003-1330-y>.
21. Dahl K, Halldin C, Schou M. New methodologies for the preparation of carbon-11 labeled radiopharmaceuticals. *Clin Transl Imaging*. 2017;5:275–89. <https://doi.org/10.1007/s40336-017-0223-1>.
22. Ajenjo J, Destro G, Cornelissen B, Gouverneur V. Closing the gap between ¹⁹F and ¹⁸F chemistry. *EJNMMI Radiopharm Chem*. 2021;6:33. <https://doi.org/10.1186/s41181-021-00143-y>.
23. Szigeti K, Horváth I, Veres DS, Martinecz B, Lénárt N, Kovács N, et al. A novel SPECT-based approach reveals early mechanisms of central and peripheral inflammation after cerebral ischemia. *J Cereb Blood Flow Metab*. 2015;35:1921–9. <https://doi.org/10.1038/jcbfm.2015.174>.
24. Kapucu ÖL, Nobili F, Varrone A, Booi J, Vander Borgh T, Någren K, et al. EANM procedure guideline for brain perfusion SPECT using ^{99m}Tc-labelled radiopharmaceuticals, version 2. *Eur J Nucl Med Mol Imaging*. 2009;36:2093–102. <https://doi.org/10.1007/s00259-009-1266-y>.
25. Audi SH, Clough AV, Haworth ST, Medhora M, Ranji M, Densmore JC, et al. ^{99m}Tc-Hexamethylpropyleneamine oxime imaging for early detection of acute lung injury in rats exposed to hyperoxia or lipopolysaccharide treatment. *Shock*. 2016;46:420–30. <https://doi.org/10.1097/SHK.0000000000000605>.
26. Jackson IM, Scott PJH, Thompson S. Clinical applications of radiolabeled peptides for PET. *Semin Nucl Med*. 2017;47:493–523. <https://doi.org/10.1053/j.semnuclmed.2017.05.007>.
27. Heskamp S, Raavé R, Boerman O, Rijpkema M, Goncalves V, Denat F. ⁸⁹Zr-Immuno-positron emission tomography in oncology: state-of-the-art ⁸⁹Zr radiochemistry. *Bioconjug Chem*. 2017;28:2211–23. <https://doi.org/10.1021/acs.bioconjchem.7b00325>.
28. Lee HJ, Ehlerding EB, Cai W. Antibody-based tracers for PET/SPECT imaging of chronic inflammatory diseases. *Chembiochem*. 2019;20:422–36. <https://doi.org/10.1002/cbic.201800429>.
29. Wei W, Rosenkrans ZT, Liu J, Huang G, Luo Q-Y, Cai W. ImmunoPET: concept, design, and applications. *Chem Rev*. 2020;120:3787–851. <https://doi.org/10.1021/acs.chemrev.9b00738>.
30. James ML, Hoehne A, Mayer AT, Lechtenberg K, Moreno M, Gowrishankar G, et al. Imaging B cells in a mouse model of multiple sclerosis using ⁶⁴Cu-rituximab PET. *J Nucl Med*. 2017;58:1845–51. <https://doi.org/10.2967/jnumed.117.189597>.
31. Pellico J, Gawne PJ, de Rosales TMR. Radiolabelling of nanomaterials for medical imaging and therapy. *Chem Soc Rev*. 2021;50:3355–423. <https://doi.org/10.1039/DOCS00384K>.
32. Pellico J, Ruiz-Cabello J, Saiz-Alfía M, del Rosario G, Caja S, Montoya M, et al. Fast synthesis and bioconjugation of ⁶⁸Ga core-doped extremely small iron oxide nanoparticles for PET/MR imaging. *Contrast Media Mol Imaging*. 2016;11:203–10. <https://doi.org/10.1002/cmmi.1681>.
33. Signore A, Jamar F, Israel O, Buscombe J, Martin-Comin J, Lazzeri E. Clinical indications, image acquisition and data interpretation for white blood cells and anti-granulocyte monoclonal antibody scintigraphy: an EANM procedural guideline. *Eur J Nucl Med Mol Imaging*. 2018;45:1816–31. <https://doi.org/10.1007/s00259-018-4052-x>.
34. Sargent A, Miller RH. MSC therapeutics in chronic inflammation. *Curr Stem Cell Rep*. 2016;2:168–73. <https://doi.org/10.1007/s40778-016-0044-6>.
35. Gawne PJ, Man F, Blower PJ, de Rosales TMR. Direct cell radiolabeling for in vivo cell tracking with PET and SPECT imaging. *Chem Rev*. 2022;122:10266–318. <https://doi.org/10.1021/acs.chemrev.1c00767>.

36. Savolainen H, Volpe A, Phinikaridou A, Douek M, Fruhwirth G, de Rosales RTM. 68Ga-sienna+ for PET-MRI guided sentinel lymph node biopsy: synthesis and preclinical evaluation in a metastatic breast cancer model. *Nano*. 2019;3:255–65. <https://doi.org/10.7150/ntno.34727>.
37. Vargas SH, Ghosh SC, Azhdarinia A. New developments in dual-labeled molecular imaging agents. *J Nucl Med*. 2019;60:459–65. <https://doi.org/10.2967/jnumed.118.213488>.
38. Withana NP, Saito T, Ma X, Garland M, Liu C, Kosuge H, et al. Dual-modality activity-based probes as molecular imaging agents for vascular inflammation. *J Nucl Med*. 2016;57:1583–90. <https://doi.org/10.2967/jnumed.115.171553>.
39. Bocan TM, Stafford RG, Brown JL, Akuoku Frimpong J, Basuli F, Hollidge BS, et al. Characterization of brain inflammation, apoptosis, hypoxia, blood-brain barrier integrity and metabolism in Venezuelan Equine Encephalitis Virus (VEEV TC-83) exposed mice by in vivo positron emission tomography imaging. *Viruses*. 2019;11:1052. <https://doi.org/10.3390/v11111052>.
40. Chen DL, Agapov E, Wu K, Engle JT, Solingapuram Sai KK, Arentson E, et al. Selective imaging of lung macrophages using [11C]PBR28-based positron emission tomography. *Mol Imaging Biol*. 2021;23:905–13. <https://doi.org/10.1007/s11307-021-01617-w>.
41. Evans BJ, King AT, Katsifis A, Matesic L, Jamie JF. Methods to enhance the metabolic stability of peptide-based PET radiopharmaceuticals. *Molecules*. 2020;25:2314. <https://doi.org/10.3390/molecules25102314>.
42. Wang C, Keliher E, Zeller MWG, Wojtkiewicz GR, Aguirre AD, Buckbinder L, et al. An activatable PET imaging radioprobe is a dynamic reporter of myeloperoxidase activity in vivo. *Proc Natl Acad Sci*. 2019;116:11966–71. <https://doi.org/10.1073/pnas.1818434116>.
43. Kondo N, Temma T, Aita K, Shimochi S, Koshino K, Senda M, et al. Development of matrix metalloproteinase-targeted probes for lung inflammation detection with positron emission tomography. *Sci Rep*. 2018;8:1347. <https://doi.org/10.1038/s41598-018-19890-1>.
44. Yang Z, Zan Y, Zheng X, Hai W, Chen K, Huang Q, et al. Dynamic FDG-PET imaging to differentiate malignancies from inflammation in subcutaneous and in situ mouse model for non-small cell lung carcinoma (NSCLC). Tagliabue E, editor. *PLoS One*. 2015;10:e0139089. <https://doi.org/10.1371/journal.pone.0139089>.
45. Virtanen H, Silvola JMU, Autio A, Li X-G, Liljenbäck H, Hellberg S, et al. Comparison of 68Ga-DOTA-Siglec-9 and 18F-Fluorodeoxyribose-Siglec-9: inflammation imaging and radiation dosimetry. *Contrast Media Mol Imaging*. 2017;2017:1–10. <https://doi.org/10.1155/2017/7645070>.
46. Fueger BJ, Czernin J, Hildebrandt I, Tran C, Halpern BS, Stout D, et al. Impact of animal handling on the results of 18F-FDG PET studies in mice. *J Nucl Med*. 2006;47:999–1006.
47. Bascuñana P, Thackeray JT, Bankstahl M, Bengel FM, Bankstahl JP. Anesthesia and preconditioning induced changes in mouse brain [18F]FDG uptake and kinetics. *Mol Imaging Biol*. 2019;21:1089–96. <https://doi.org/10.1007/s11307-019-01314-9>.
48. Fuchs K, Kukuk D, Mahling M, Quintanilla-Martinez L, Reischl G, Reutershan J, et al. Impact of anesthetics on 3'-[18F]Fluoro-3'-deoxythymidine ([18F]FLT) uptake in animal models of cancer and inflammation. *Mol Imaging*. 2013;12:7290.2012.00042. <https://doi.org/10.2310/7290.2012.00042>.
49. Lavender JP, Lowe J, Barker JR, Burn JI, Chaudhri MA. Gallium 67 citrate scanning in neoplastic and inflammatory lesions. *Br J Radiol*. 1971;44:361–6. <https://doi.org/10.1259/0007-1285-44-521-361>.
50. Staab EV, McCartney WH. Role of gallium 67 in inflammatory disease. *Semin Nucl Med*. 1978;8:219–34. [https://doi.org/10.1016/S0001-2998\(78\)80030-0](https://doi.org/10.1016/S0001-2998(78)80030-0).
51. Signore A, Casali M, Lauri C. An easy and practical guide for imaging infection/inflammation by [18F]FDG PET/CT. *Clin Transl Imaging*. 2021;9:283–97. <https://doi.org/10.1007/s40336-021-00435-y>.

52. Bartlett B, Ludewick HP, Lee SL, Verma S, Francis RJ, Dwivedi G. Imaging inflammation in patients and animals: focus on PET imaging the vulnerable plaque. *Cell*. 2021;10:2573. <https://doi.org/10.3390/cells10102573>.
53. Martin J, Saleem N. 18F-FDG PET-CT scanning and diabetic patients. *Nucl Med Commun*. 2014;35:1197–203. <https://doi.org/10.1097/MNM.000000000000197>.
54. Pijl JP, Nienhuis PH, Kwee TC, Glaudemans AWJM, Slart RHJA, Gormsen LC. Limitations and pitfalls of FDG-PET/CT in infection and inflammation. *Semin Nucl Med*. 2021;51:633–45. <https://doi.org/10.1053/j.semnuclmed.2021.06.008>.
55. Casali M, Lauri C, Altini C, Bertagna F, Cassarino G, Cistaro A, et al. State of the art of 18F-FDG PET/CT application in inflammation and infection: a guide for image acquisition and interpretation. *Clin Transl Imaging*. 2021;9:299–339. <https://doi.org/10.1007/s40336-021-00445-w>.
56. Chandler MB, Zeddun SM, Borum ML. The role of positron emission tomography in the evaluation of inflammatory bowel disease. *Ann N Y Acad Sci*. 2011;1228:59–63. <https://doi.org/10.1111/j.1749-6632.2011.06032.x>.
57. Catalano O, Maccioni F, Lauri C, Auletta S, Dierckx R, Signore A. Hybrid imaging in Crohn's disease: from SPECT/CT to PET/MR and new image interpretation criteria. *Q J Nucl Med Mol Imaging*. 2018;62:40. <https://doi.org/10.23736/S1824-4785.17.03053-9>.
58. Gatta G, Di Grezia G, Di Mizio V, Landolfi C, Mansi L, De Sio I, et al. Crohn's disease imaging: A review. *Gastroenterol Res Pract*. 2012;2012:1–15. <https://doi.org/10.1155/2012/816920>.
59. Joseph P, Tawakol A. Imaging atherosclerosis with positron emission tomography. *Eur Heart J*. 2016;37:2974–80. <https://doi.org/10.1093/eurheartj/ehw147>.
60. Ahmed M, McPherson R, Abruzzo A, Thomas SE, Gorantla VR. Carotid artery calcification: what we know so far. *Cureus*. 2021;13. <https://doi.org/10.7759/cureus.18938>.
61. Cardoso L, Weinbaum S. Microcalcifications, their genesis, growth, and biomechanical stability in fibrous cap rupture. In: Fu B, Wright N, editors. *Mol Cell Tissue Eng Vasc Syst Adv Exp Med Biol*, vol. 1097. Cham: Springer; 2018. p. 129–55. https://doi.org/10.1007/978-3-319-96445-4_7.
62. Irkle A, Vesey AT, Lewis DY, Skepper JN, Bird JLE, Dweck MR, et al. Identifying active vascular microcalcification by 18F-sodium fluoride positron emission tomography. *Nat Commun*. 2015;6:7495. <https://doi.org/10.1038/ncomms8495>.
63. Tzolos E, Dweck MR. 18F-sodium fluoride (18F-NaF) for imaging microcalcification activity in the cardiovascular system. *Arterioscler Thromb Vasc Biol*. 2020;40:1620–6. <https://doi.org/10.1161/ATVBAHA.120.313785>.
64. Erba PA, Israel O. SPECT/CT in infection and inflammation. *Clin Transl Imaging*. 2014;2:519–35. <https://doi.org/10.1007/s40336-014-0092-9>.
65. Derlin T, Tóth Z, Papp L, Wisotzki C, Apostolova I, Habermann CR, et al. Correlation of inflammation assessed by 18F-FDG PET, active mineral deposition assessed by 18F-fluoride PET, and vascular calcification in atherosclerotic plaque: A dual-tracer PET/CT study. *J Nucl Med*. 2011;52:1020–7. <https://doi.org/10.2967/jnumed.111.087452>.
66. Høiland-Carlsen PF, Sturek M, Alavi A, Gerke O. Atherosclerosis imaging with 18F-sodium fluoride PET: state-of-the-art review. *Eur J Nucl Med Mol Imaging*. 2020;47:1538–51. <https://doi.org/10.1007/s00259-019-04603-1>.
67. Keeling GP, Sherin B, Kim J, San Juan B, Grus T, Eykyn TR, et al. [68Ga]ga-THP-pam: A bisphosphonate PET tracer with facile Radiolabeling and broad calcium mineral affinity. *Bioconjug Chem*. 2021;32:1276–89. <https://doi.org/10.1021/acs.bioconjchem.0c00401>.
68. Virgolini I, Ambrosini V, Bomanji JB, Baum RP, Fanti S, Gabriel M, et al. Procedure guidelines for PET/CT tumour imaging with 68Ga-DOTA-conjugated peptides: 68Ga-DOTA-TOC, 68Ga-DOTA-NOC, 68Ga-DOTA-TATE. *Eur J Nucl Med Mol Imaging*. 2010;37:2004–10. <https://doi.org/10.1007/s00259-010-1512-3>.

69. Tarkin JM, Joshi FR, Evans NR, Chowdhury MM, Figg NL, Shah AV, et al. Detection of atherosclerotic inflammation by ⁶⁸Ga-DOTATATE PET compared to [¹⁸F]FDG PET imaging. *J Am Coll Cardiol*. 2017;69:1774–91. <https://doi.org/10.1016/j.jacc.2017.01.060>.
70. Malmberg C, Ripa RS, Johnbeck CB, Knigge U, Langer SW, Mortensen J, et al. ⁶⁴Cu-DOTATATE for noninvasive assessment of atherosclerosis in large arteries and its correlation with risk factors: head-to-head comparison with ⁶⁸Ga-DOTATOC in 60 patients. *J Nucl Med*. 2015;56:1895–900. <https://doi.org/10.2967/jnumed.115.161216>.
71. Philipp-Abbrederis K, Herrmann K, Schottelius M, Eiber M, Gerngroß C, Pietschmann E, et al. [⁶⁸Ga]Pentixafor: A novel PET tracer for imaging CXCR4 status in patients with multiple myeloma. *Blood*. 2014;124:2014. <https://doi.org/10.1182/blood.V124.21.2014.2014>.
72. Pawig L, Klasen C, Weber C, Bernhagen J, Noels H. Diversity and inter-connections in the CXCR4 chemokine receptor/ligand family: molecular perspectives. *Front Immunol*. 2015;6:429. <https://doi.org/10.3389/fimmu.2015.00429>.
73. Kircher M, Tran-Gia J, Kemmer L, Zhang X, Schirbel A, Werner RA, et al. Imaging inflammation in atherosclerosis with CXCR4-directed ⁶⁸Ga-Pentixafor PET/CT: correlation with ¹⁸F-FDG PET/CT. *J Nucl Med*. 2020;61:751–6. <https://doi.org/10.2967/jnumed.119.234484>.
74. Bordonne M, Chawki MB, Doyen M, Kas A, Guedj E, Tyvaert L, et al. Brain ¹⁸F-FDG PET for the diagnosis of autoimmune encephalitis: a systematic review and a meta-analysis. *Eur J Nucl Med Mol Imaging*. 2021;48:3847–58. <https://doi.org/10.1007/s00259-021-05299-y>.
75. van Waarde A, Marcolini S, de Deyn PP, Dierckx RAJO. PET agents in dementia: an overview. *Semin Nucl Med*. 2021;51:196–229. <https://doi.org/10.1053/j.semnuclmed.2020.12.008>.
76. Nobili F, Arbuz J, Bouwman F, Drzezga A, Agosta F, Nestor P, et al. European Association of Nuclear Medicine and European Academy of neurology recommendations for the use of brain ¹⁸F-fluorodeoxyglucose positron emission tomography in neurodegenerative cognitive impairment and dementia: Delphi consensus. *Eur J Neurol*. 2018;25:1201–17. <https://doi.org/10.1111/ene.13728>.
77. Werry EL, Bright FM, Piguot O, Ittner LM, Halliday GM, Hodges JR, et al. Recent developments in TSPO PET imaging as A biomarker of neuroinflammation in neurodegenerative disorders. *Int J Mol Sci*. 2019;20:3161. <https://doi.org/10.3390/ijms20133161>.
78. Politis M, Giannetti P, Su P, Turkheimer F, Keihaninejad S, Wu K, et al. Increased PK11195 PET binding in the cortex of patients with MS correlates with disability. *Neurology*. 2012;79:523–30. <https://doi.org/10.1212/WNL.0b013e3182635645>.
79. Ricigliano VAG, Morena E, Colombi A, Tonietto M, Hamzaoui M, Poirion E, et al. Choroid plexus enlargement in inflammatory multiple sclerosis: 3.0-T MRI and translocator protein PET evaluation. *Radiology*. 2021;301:166–77. <https://doi.org/10.1148/radiol.2021204426>.
80. Fleischer V, Gonzalez-Escamilla G, Ciolac D, Albrecht P, Küry P, Gruchot J, et al. Translational value of choroid plexus imaging for tracking neuroinflammation in mice and humans. *Proc Natl Acad Sci*. 2021;118. <https://doi.org/10.1073/pnas.2025000118>.
81. James ML, Belichenko NP, Shuhendler AJ, Hoehne A, Andrews LE, Condon C, et al. [¹⁸F]GE-180 PET detects reduced microglia activation after LM11A-31 therapy in a mouse model of Alzheimer’s disease. *Theranostics*. 2017;7:1422–36. <https://doi.org/10.7150/thno.17666>.
82. Zanotti-Fregonara P, Pascual B, Rizzo G, Yu M, Pal N, Beers D, et al. Head-to-head comparison of ¹¹C-PBR28 and ¹⁸F-GE180 for quantification of the translocator protein in the human brain. *J Nucl Med*. 2018;59:1260–6. <https://doi.org/10.2967/jnumed.117.203109>.
83. Vivash L, O’Brien TJ. Imaging microglial activation with TSPO PET: lighting up neurologic diseases? *J Nucl Med*. 2016;57:165–8. <https://doi.org/10.2967/jnumed.114.141713>.
84. Chaudhari AJ, Raynor WY, Gholamrezanezhad A, Werner TJ, Rajapakse CS, Alavi A. Total-body PET imaging of musculoskeletal disorders. *PET Clin*. 2021;16:99–117. <https://doi.org/10.1016/j.cpet.2020.09.012>.
85. Al-Zaghal A, Yellanki DP, Ayubcha C, Werner TJ, Høiland-Carlsen PF, Alavi A. CT-based tissue segmentation to assess knee joint inflammation and reactive bone formation assessed by

- 18F-FDG and 18F-NaF PET/CT: effects of age and BMI. *Hell J Nucl Med.* 2018;21:102–7. <https://doi.org/10.1967/s002449910801>.
86. Zhu Z, Yin Y, Zheng K, Li F, Chen X, Zhang F, et al. Evaluation of synovial angiogenesis in patients with rheumatoid arthritis using 68Ga-PRGD2 PET/CT: a prospective proof-of-concept cohort study. *Ann Rheum Dis.* 2014;73:1269–72. <https://doi.org/10.1136/annrheumdis-2013-204820>.
87. Arnow PM, Flaherty JP. Fever of unknown origin. *Lancet.* 1997;350:575–80. [https://doi.org/10.1016/S0140-6736\(97\)07061-X](https://doi.org/10.1016/S0140-6736(97)07061-X).
88. Kan Y, Wang W, Liu J, Yang J, Wang Z. Contribution of 18F-FDG PET/CT in a case-mix of fever of unknown origin and inflammation of unknown origin: a meta-analysis. *Acta Radiol.* 2019;60:716–25. <https://doi.org/10.1177/0284185118799512>.
89. Iking J, Staniszewska M, Kessler L, Klose JM, Lückerath K, Fendler WP, et al. Imaging inflammation with positron emission tomography. *Biomedicine.* 2021;9:212. <https://doi.org/10.3390/biomedicines9020212>.
90. Ayesa SL, Schembri GP. Is 67gallium dead? A retrospective review of 67gallium imaging in a single tertiary referral Centre. *Nucl Med Commun.* 2021;42:378–88. <https://doi.org/10.1097/MNM.0000000000001342>.
91. Xu T, Chen Y. Research Progress of [68Ga]Citrate PET's utility in infection and inflammation imaging: a review. *Mol Imaging Biol.* 2020;22:22–32. <https://doi.org/10.1007/s11307-019-01366-x>.
92. Gratz S, Schipper ML, Dörner J, Höffken H, Becker W, Kaiser JW, et al. LeukoScan for imaging infection in different clinical settings. *Clin Nucl Med.* 2003;28:267–76. <https://doi.org/10.1097/01.RLU.0000057613.86093.73>.
93. Palestro CJ, Glaudemans AWJM, Dierckx RAJO. Multiagent imaging of inflammation and infection with radionuclides. *Clin Transl Imaging.* 2013;1:385–96. <https://doi.org/10.1007/s40336-013-0041-z>.
94. Palestro CJ. Radionuclide imaging of osteomyelitis. *Semin Nucl Med.* 2015;45:32–46. <https://doi.org/10.1053/j.semnuclmed.2014.07.005>.
95. Kalimuddin S, Xie W, Watanabe S, Tham JY, Sam H, Chan KWK, et al. 18F-fluorodeoxyglucose positron emission tomography as a window into human dengue pathophysiology. *Antivir Res.* 2021;185:104991. <https://doi.org/10.1016/j.antiviral.2020.104991>.
96. Ordóñez AA, Wintaco LM, Mota F, Restrepo AF, Ruiz-Bedoya CA, Reyes CF, et al. Imaging Enterobacteriales infections in patients using pathogen-specific positron emission tomography. *Sci Transl Med.* 2021;13. <https://doi.org/10.1126/scitranslmed.abe9805>.
97. Mota F, De Jesus P, Jain SK. Kit-based synthesis of 2-deoxy-2-[18F]-fluoro-d-sorbitol for bacterial imaging. *Nat Protoc.* 2021;16:5274–86. <https://doi.org/10.1038/s41596-021-00613-2>.
98. Polvoy I, Flavell RR, Rosenberg OS, Ohliger MA, Wilson DM. Nuclear imaging of bacterial infection: the state of the art and future directions. *J Nucl Med.* 2020;61:1708–16. <https://doi.org/10.2967/jnumed.120.244939>.
99. Ankrah AO, Sathekge MM, Dierckx RAJO, Glaudemans AWJM. Radionuclide imaging of fungal infections and correlation with the host Defense response. *J Fungi.* 2021;7:407. <https://doi.org/10.3390/jof7060407>.
100. Auletta S, Varani M, Horvat R, Galli F, Signore A, Hess S. PET radiopharmaceuticals for specific bacteria imaging: a systematic review. *J Clin Med.* 2019;8:197. <https://doi.org/10.3390/jcm8020197>.
101. Pijl JP, Londema M, Kwee TC, Nijsten MWN, Slart RHJA, Dierckx RAJO, et al. FDG-PET/CT in intensive care patients with bloodstream infection. *Crit Care.* 2021;25:133. <https://doi.org/10.1186/s13054-021-03557-x>.
102. Thackeray JT, Bankstahl JP, Wang Y, Korf-Klingebiel M, Walte A, Wittneben A, et al. Targeting post-infarct inflammation by PET imaging: comparison of 68Ga-citrate and 68Ga-

- DOTATATE with 18F-FDG in a mouse model. *Eur J Nucl Med Mol Imaging*. 2015;42:317–27. <https://doi.org/10.1007/s00259-014-2884-6>.
103. Lee WW, Marinelli B, van der Laan AM, Sena BF, Gorbatov R, Leuschner F, et al. PET/MRI of inflammation in myocardial infarction. *J Am Coll Cardiol*. 2012;59:153–63. <https://doi.org/10.1016/j.jacc.2011.08.066>.
104. Thackeray JT. PET assessment of immune cell activity and therapeutic monitoring following myocardial infarction. *Curr Cardiol Rep*. 2018;20:13. <https://doi.org/10.1007/s11886-018-0955-1>.
105. Vasudevan P, Gaebel R, Doering P, Mueller P, Lemcke H, Stenzel J, et al. 18F-FDG PET-based imaging of myocardial inflammation predicts a functional outcome following transplantation of mESC-derived cardiac induced cells in a mouse model of myocardial infarction. *Cell*. 2019;8:1613. <https://doi.org/10.3390/cells8121613>.
106. Meller J, Strutz F, Siefker U, Scheel A, Sahlmann CO, Lehmann K, et al. Early diagnosis and follow-up of aortitis with [18F]FDG PET and MRI. *Eur J Nucl Med Mol Imaging*. 2003;30:730–6. <https://doi.org/10.1007/s00259-003-1144-y>.
107. van Timmeren JE, Cester D, Tanadini-Lang S, Alkadhi H, Baessler B. Radiomics in medical imaging—“how-to” guide and critical reflection. *Insights Imaging*. 2020;11:91. <https://doi.org/10.1186/s13244-020-00887-2>.
108. Chen Z-W, Tang K, Zhao Y-F, Chen Y-Z, Tang L-J, Li G, et al. Radiomics based on fluoro-deoxyglucose positron emission tomography predicts liver fibrosis in biopsy-proven MAFLD: a pilot study. *Int J Med Sci*. 2021;18:3624–30. <https://doi.org/10.7150/ijms.64458>.
109. Chen L, Liu K, Zhao X, Shen H, Zhao K, Zhu W. Habitat imaging-based 18F-FDG PET/CT radiomics for the preoperative discrimination of non-small cell lung cancer and benign inflammatory diseases. *Front Oncol*. 2021;11:759897. <https://doi.org/10.3389/fonc.2021.759897>.
110. Watanabe S, Hirata K, Manabe O, Kobayashi K, Furuya S, Tamaki N, et al. A radiomics approach to discriminate lung cancer from pneumonia on FDG PET-CT. *J Nucl Med*. 2018;59(S1):1353.
111. Pottier G, Bernards N, Dollé F, Boisgard R. [18F]DPA-714 as a biomarker for positron emission tomography imaging of rheumatoid arthritis in an animal model. *Arthritis Res Ther*. 2014;16:R69. <https://doi.org/10.1186/ar4508>.
112. Foss CA, Harper JS, Wang H, Pomper MG, Jain SK. Noninvasive molecular imaging of tuberculosis-associated inflammation with radioiodinated DPA-713. *J Infect Dis*. 2013;208:2067–74. <https://doi.org/10.1093/infdis/jit331>.
113. Ordonez AA, Pokkali S, DeMarco VP, Klunk M, Mease RC, Foss CA, et al. Radioiodinated DPA-713 imaging correlates with bactericidal activity of tuberculosis treatments in mice. *Antimicrob Agents Chemother*. 2015;59:642–9. <https://doi.org/10.1128/AAC.04180-14>.
114. Hatori A, Yui J, Yamasaki T, Xie L, Kumata K, Fujinaga M, et al. PET imaging of lung inflammation with [18F]FEDAC, a radioligand for translocator protein (18 kDa). Gelovani JG, editor. *PLoS One*. 2012;7:e45065. <https://doi.org/10.1371/journal.pone.0045065>.
115. Verhoeven J, Baguet T, Piron S, Pauwelyn G, Bouckaert C, Descamps B, et al. 2-[18F]FELP, a novel LAT1-specific PET tracer, for the discrimination between glioblastoma, radiation necrosis and inflammation. *Nucl Med Biol*. 2020;82–83:9–16. <https://doi.org/10.1016/j.nucmedbio.2019.12.002>.
116. Nozaki S, Nakatani Y, Mawatari A, Shibata N, Hume WE, Hayashinaka E, et al. 18F-FIMP: a LAT1-specific PET probe for discrimination between tumor tissue and inflammation. *Sci Rep*. 2019;9:15718. <https://doi.org/10.1038/s41598-019-52270-x>.
117. Aide N, Hicks RJ, Le Tourneau C, Lheureux S, Fanti S, Lopci E. FDG PET/CT for assessing tumour response to immunotherapy. *Eur J Nucl Med Mol Imaging*. 2019;46:238–50. <https://doi.org/10.1007/s00259-018-4171-4>.
118. Dougan M. Understanding and overcoming the inflammatory toxicities of immunotherapy. *Cancer Immunol Res*. 2020;8:1230–5. <https://doi.org/10.1158/2326-6066.CIR-20-0372>.

119. Boss SD, Ametamey SM. Development of folate receptor–targeted PET radiopharmaceuticals for tumor imaging—a bench-to-bedside journey. *Cancers (Basel)*. 2020;12:1508. <https://doi.org/10.3390/cancers12061508>.
120. Muller C. Folate based radiopharmaceuticals for imaging and therapy of cancer and inflammation. *Curr Pharm Des*. 2012;18:1058–83. <https://doi.org/10.2174/138161212799315777>.
121. Verweij NJF, Yaqub M, Bruijnen STG, Pieplensbosch S, ter Wee MM, Jansen G, et al. First in man study of [18F]fluoro-PEG-folate PET: a novel macrophage imaging technique to visualize rheumatoid arthritis. *Sci Rep*. 2020;10:1047. <https://doi.org/10.1038/s41598-020-57841-x>.
122. Silvola JMU, Li X-G, Virta J, Marjamäki P, Liljenbäck H, Hytönen JP, et al. Aluminum fluoride-18 labeled folate enables in vivo detection of atherosclerotic plaque inflammation by positron emission tomography. *Sci Rep*. 2018;8:9720. <https://doi.org/10.1038/s41598-018-27618-4>.
123. Jahandideh A, Uotila S, Stähle M, Virta J, Li X-G, Kytö V, et al. Folate receptor β -targeted PET imaging of macrophages in autoimmune myocarditis. *J Nucl Med*. 2020;61:1643–9. <https://doi.org/10.2967/jnumed.119.241356>.
124. Guzik P, Fang H-Y, Deberle LM, Benešová M, Cohrs S, Boss SD, et al. Identification of a PET radiotracer for imaging of the folate receptor- α : A potential tool to select patients for targeted tumor therapy. *J Nucl Med*. 2021;62:1475–81. <https://doi.org/10.2967/jnumed.120.255760>.
125. Hultén LM, Levin M. The role of hypoxia in atherosclerosis. *Curr Opin Lipidol*. 2009;20:409–14. <https://doi.org/10.1097/MOL.0b013e3283307be8>.
126. Piotrowski WJ, Kiszalkiewicz J, Pastuszak-Lewandoska D, Górski P, Antczak A, Migdalska-Sęk M, et al. Expression of HIF-1A/VEGF/ING-4 Axis in pulmonary sarcoidosis. In: Pokorski M, editor. *Noncommunicable Dis*. Cham: Springer; 2015. p. 61–9. https://doi.org/10.1007/5584_2015_144.
127. Pell VR, Baark F, Mota F, Clark JE, Southworth R. PET imaging of cardiac hypoxia: hitting hypoxia where it hurts. *Curr Cardiovasc Imaging Rep*. 2018;11:7. <https://doi.org/10.1007/s12410-018-9447-3>.
128. Rajendran JG, Krohn KA. F-18 Fluoromisonidazole for imaging tumor hypoxia: imaging the microenvironment for personalized cancer therapy. *Semin Nucl Med*. 2015;45:151–62. <https://doi.org/10.1053/j.semnuclmed.2014.10.006>.
129. Mateo J, Izquierdo-García D, Badimon JJ, Fayad ZA, Fuster V. Noninvasive assessment of hypoxia in rabbit advanced atherosclerosis using 18F-fluoromisonidazole positron emission tomographic imaging. *Circ Cardiovasc Imaging*. 2014;7:312–20. <https://doi.org/10.1161/CIRCIMAGING.113.001084>.
130. Manabe O, Hirata K, Shozo O, Shiga T, Uchiyama Y, Kobayashi K, et al. 18F-fluoromisonidazole (FMISO) PET may have the potential to detect cardiac sarcoidosis. *J Nucl Cardiol*. 2017;24:329–31. <https://doi.org/10.1007/s12350-016-0495-2>.
131. Fuchs K, Kuehn A, Mahling M, Guenthoer P, Hector A, Schwenck J, et al. In vivo hypoxia PET imaging quantifies the severity of arthritic joint inflammation in line with overexpression of hypoxia-inducible factor and enhanced reactive oxygen species generation. *J Nucl Med*. 2017;58:853–60. <https://doi.org/10.2967/jnumed.116.185934>.
132. Nie X, Laforest R, Elvington A, Randolph GJ, Zheng J, Voller T, et al. PET/MRI of hypoxic atherosclerosis using 64Cu-ATSM in a rabbit model. *J Nucl Med*. 2016;57:2006–11. <https://doi.org/10.2967/jnumed.116.172544>.
133. Medina RA, Mariotti E, Pavlovic D, Shaw KP, Eykyn TR, Blower PJ, et al. 64Cu-CTS: A promising radiopharmaceutical for the identification of low-grade cardiac hypoxia by PET. *J Nucl Med*. 2015;56:921–6. <https://doi.org/10.2967/jnumed.114.148353>.
134. Ahmed Laskar A, Younus H. Aldehyde toxicity and metabolism: the role of aldehyde dehydrogenases in detoxification, drug resistance and carcinogenesis. *Drug Metab Rev*. 2019;51:42–64. <https://doi.org/10.1080/03602532.2018.1555587>.
135. Wood PL, Khan MA, Moskal JR. The concept of “aldehyde load” in neurodegenerative mechanisms: cytotoxicity of the polyamine degradation products hydrogen peroxide, acrolein,

- 3-aminopropanal, 3-acetamidopropanal and 4-aminobutanal in a retinal ganglion cell line. *Brain Res.* 2007;1145:150–6. <https://doi.org/10.1016/j.brainres.2006.10.004>.
136. O'Brien PJ, Siraki AG, Shangari N. Aldehyde sources, metabolism, molecular toxicity mechanisms, and possible effects on human health. *Crit Rev Toxicol.* 2005;35:609–62. <https://doi.org/10.1080/10408440591002183>.
137. Pinnell SR, Martin GR. The cross-linking of collagen and elastin: enzymatic conversion of lysine in peptide linkage to alpha-amino adipic-delta-semialdehyde (allysine) by an extract from bone. *Proc Natl Acad Sci.* 1968;61:708–16. <https://doi.org/10.1073/pnas.61.2.708>.
138. Chen HH, Waghorn PA, Wei L, Tapias LF, Schühle DT, Rotile NJ, et al. Molecular imaging of oxidized collagen quantifies pulmonary and hepatic fibrogenesis. *JCI Insight.* 2017;2:1–9. <https://doi.org/10.1172/jci.insight.91506>.
139. Kirby A, Suchý M, Brouwer A, Shuhendler A. Mapping aldehydic load in vivo by positron emission tomography with [18F]NA3BF3. *Chem Commun.* 2019;55:5371–4. <https://doi.org/10.1039/C9CC01831J>.
140. Wahsner J, Désogère P, Abston E, Graham-O'Regan KA, Wang J, Rotile NJ, et al. 68Ga-NODAGA-indole: an Allysine-reactive positron emission tomography probe for molecular imaging of pulmonary fibrogenesis. *J Am Chem Soc.* 2019;141:5593–6. <https://doi.org/10.1021/jacs.8b12342>.
141. Norimatsu M, Ono T, Aoki A, Ohishi K, Takahashi T, Watanabe G, et al. Lipopolysaccharide-induced apoptosis in swine lymphocytes in vivo. *Infect Immun.* 1995;63:1122–6. <https://doi.org/10.1128/iai.63.3.1122-1126.1995>.
142. Norimatsu M, Ono T, Aoki A, Ohishi K, Tamura Y. In-vivo induction of apoptosis in murine lymphocytes by bacterial lipopolysaccharides. *J Med Microbiol.* 1995;43:251–7. <https://doi.org/10.1099/00222615-43-4-251>.
143. Wang J, Wang H, Zhu R, Liu Q, Fei J, Wang S. Anti-inflammatory activity of curcumin-loaded solid lipid nanoparticles in IL-1 β transgenic mice subjected to the lipopolysaccharide-induced sepsis. *Biomaterials.* 2015;53:475–83. <https://doi.org/10.1016/j.biomaterials.2015.02.116>.
144. dos Santos FD, Arora G, Gieseck RL, Rotile NJ, Waghorn PA, Tanabe KK, et al. Molecular magnetic resonance imaging of liver fibrosis and fibrogenesis is not altered by inflammation. *Investig Radiol.* 2021;56:244–51. <https://doi.org/10.1097/RLI.0000000000000737>.
145. Ganz T. Iron and infection. *Int J Hematol.* 2018;107:7–15. <https://doi.org/10.1007/s12185-017-2366-2>.
146. Petrik M, Umlaufova E, Raclavsky V, Palyzova A, Havlicek V, Pfister J, et al. 68Ga-labelled desferrioxamine-B for bacterial infection imaging. *Eur J Nucl Med Mol Imaging.* 2021;48:372–82. <https://doi.org/10.1007/s00259-020-04948-y>.
147. Petrik M, Pfister J, Misslinger M, Decristoforo C, Haas H. Siderophore-based molecular imaging of fungal and bacterial infections—current status and future perspectives. *J Fungi.* 2020;6:73. <https://doi.org/10.3390/jof6020073>.
148. Kalluri R. The biology and function of fibroblasts in cancer. *Nat Rev Cancer.* 2016;16:582–98. <https://doi.org/10.1038/nrc.2016.73>.
149. Kratochwil C, Flechsig P, Lindner T, Abderrahim L, Altmann A, Mier W, et al. 68Ga-FAPI PET/CT: tracer uptake in 28 different kinds of cancer. *J Nucl Med.* 2019;60:801–5. <https://doi.org/10.2967/jnumed.119.227967>.
150. Calais J. FAP: the next billion Dollar nuclear Theranostics target? *J Nucl Med.* 2020;61:163–5. <https://doi.org/10.2967/jnumed.119.241232>.
151. Sollini M, Kirienko M, Gelardi F, Fiz F, Gozzi N, Chiti A. State-of-the-art of FAPI-PET imaging: a systematic review and meta-analysis. *Eur J Nucl Med Mol Imaging.* 2021;48:4396–414. <https://doi.org/10.1007/s00259-021-05475-0>.
152. Croft AP, Campos J, Jansen K, Turner JD, Marshall J, Attar M, et al. Distinct fibroblast subsets drive inflammation and damage in arthritis. *Nature.* 2019;570:246–51. <https://doi.org/10.1038/s41586-019-1263-7>.

153. Levy MT, McCaughan GW, Abbott CA, Park JE, Cunningham AM, Müller E, et al. Fibroblast activation protein: a cell surface dipeptidyl peptidase and gelatinase expressed by stellate cells at the tissue remodelling interface in human cirrhosis. *Hepatology*. 1999;29:1768–78. <https://doi.org/10.1002/hep.510290631>.
154. Dorst DN, van Caam APM, Vitters EL, Walgreen B, Helsen MMA, Klein C, et al. Fibroblast activation protein targeted photodynamic therapy selectively kills activated skin fibroblasts from systemic sclerosis patients and prevents tissue contraction. *Int J Mol Sci*. 2021;22:12681. <https://doi.org/10.3390/ijms222312681>.
155. Dendl K, Koerber SA, Kratochwil C, Cardinale J, Finck R, Dabir M, et al. FAP and FAPI-PET/CT in malignant and non-malignant diseases: a perfect symbiosis? *Cancers (Basel)*. 2021;13:4946. <https://doi.org/10.3390/cancers13194946>.
156. Zhang Q, Vignali DAA. Co-stimulatory and co-inhibitory pathways in autoimmunity. *Immunity*. 2016;44:1034–51. <https://doi.org/10.1016/j.immuni.2016.04.017>.
157. Meletta R, Müller Herde A, Dennler P, Fischer E, Schibli R, Krämer SD. Preclinical imaging of the co-stimulatory molecules CD80 and CD86 with indium-111-labeled belatacept in atherosclerosis. *EJNMMI Res*. 2016;6:1. <https://doi.org/10.1186/s13550-015-0157-4>.
158. Taddio MF, Castro Jaramillo CA, Runge P, Blanc A, Keller C, Talip Z, et al. In vivo imaging of local inflammation: monitoring LPS-induced CD80/CD86 upregulation by PET. *Mol Imaging Biol*. 2021;23:196–207. <https://doi.org/10.1007/s11307-020-01543-3>.
159. Taddio MF, Mu L, Castro Jaramillo CA, Bollmann T, Schmid DM, Muskalla LP, et al. Synthesis and structure–affinity relationship of small molecules for imaging human CD80 by positron emission tomography. *J Med Chem*. 2019;62:8090–100. <https://doi.org/10.1021/acs.jmedchem.9b00858>.
160. Debacker JM, Gondry O, Lahoutte T, Keyaerts M, Huvenne W. The prognostic value of CD206 in solid malignancies: a systematic review and meta-analysis. *Cancers (Basel)*. 2021;13:3422. <https://doi.org/10.3390/cancers13143422>.
161. Tahara N, Mukherjee J, de Haas HJ, Petrov AD, Tawakol A, Haider N, et al. 2-deoxy-2-[18F] fluoro-d-mannose positron emission tomography imaging in atherosclerosis. *Nat Med*. 2014;20:215–9. <https://doi.org/10.1038/nm.3437>.
162. Surasi DS, O'Malley J, Bhambhani P. 99mTc-Tilmanocept: A novel molecular agent for lymphatic mapping and sentinel lymph node localization. *J Nucl Med Technol*. 2015;43:87–91. <https://doi.org/10.2967/jnmt.115.155960>.
163. Chen W, Barback CV, Wang S, Hoh CK, Chang EY, Hall DJ, et al. A receptor-binding radiopharmaceutical for imaging of traumatic brain injury in a rodent model: [99mTc]Tc-tilmanocept. *Nucl Med Biol*. 2021;92:107–14. <https://doi.org/10.1016/j.nucmedbio.2020.02.013>.
164. Varasteh Z, Hyafil F, Anizan N, Diallo D, Aid-Launais R, Mohanta S, et al. Targeting mannose receptor expression on macrophages in atherosclerotic plaques of apolipoprotein E-knockout mice using 111In-tilmanocept. *EJNMMI Res*. 2017;7:40. <https://doi.org/10.1186/s13550-017-0287-y>.
165. Zanni MV, Toribio M, Wilks MQ, Lu MT, Burdo TH, Walker J, et al. Application of a novel CD206+ macrophage-specific arterial imaging strategy in HIV-infected individuals. *J Infect Dis*. 2017;215:1264–9. <https://doi.org/10.1093/infdis/jix095>.
166. Lecocq Q, De Vlaeminck Y, Hanssens H, D'Huyvetter M, Raes G, Goyvaerts C, et al. Theranostics in immuno-oncology using nanobody derivatives. *Theranostics*. 2019;9:7772–91. <https://doi.org/10.7150/thno.34941>.
167. Varasteh Z, Mohanta S, Li Y, López Armbruster N, Braeuer M, Nekolla SG, et al. Targeting mannose receptor expression on macrophages in atherosclerotic plaques of apolipoprotein E-knockout mice using 68Ga-NOTA-anti-MMR nanobody: non-invasive imaging of atherosclerotic plaques. *EJNMMI Res*. 2019;9:5. <https://doi.org/10.1186/s13550-019-0474-0>.
168. Senders ML, Hernot S, Carlucci G, van de Voort JC, Fay F, Calcagno C, et al. Nanobody-facilitated multiparametric PET/MRI phenotyping of atherosclerosis. *JACC Cardiovasc Imaging*. 2019;12:2015–26. <https://doi.org/10.1016/j.jcmg.2018.07.027>.

169. Lee S-P, Im H-J, Kang S, Chung S-J, Cho YS, Kang H, et al. Noninvasive imaging of myocardial inflammation in myocarditis using ⁶⁸Ga-tagged mannosylated human serum albumin positron emission tomography. *Theranostics*. 2017;7:413–24. <https://doi.org/10.7150/thno.15712>.
170. Ahmed M, Tegnebratt T, Tran TA, Lu L, Damberg P, Gisterå A, et al. Molecular imaging of inflammation in a mouse model of atherosclerosis using a Zirconium-89-Labeled probe. *Int J Nanomedicine*. 2020;15:6137–52. <https://doi.org/10.2147/IJN.S256395>.
171. Varasteh Z, De Rose F, Mohanta S, Li Y, Zhang X, Miritsch B, et al. Imaging atherosclerotic plaques by targeting Galectin-3 and activated macrophages using (89Zr)-DFO- Galectin3-F (ab')₂ mAb. *Theranostics*. 2021;11:1864–76. <https://doi.org/10.7150/thno.50247>.
172. Shi C, Pamer EG. Monocyte recruitment during infection and inflammation. *Nat Rev Immunol*. 2011;11:762–74. <https://doi.org/10.1038/nri3070>.
173. Liu Y, Gunsten SP, Sultan DH, Luehmann HP, Zhao Y, Blackwell TS, et al. PET-based imaging of chemokine receptor 2 in experimental and disease-related lung inflammation. *Radiology*. 2017;283:758–68. <https://doi.org/10.1148/radiol.2016161409>.
174. Heo GS, Bajpai G, Li W, Luehmann HP, Sultan DH, Dun H, et al. Targeted PET imaging of chemokine receptor 2-positive monocytes and macrophages in the injured heart. *J Nucl Med*. 2021;62:111–4. <https://doi.org/10.2967/jnumed.120.244673>.
175. Li W, Luehmann HP, Hsiao H-M, Tanaka S, Higashikubo R, Gauthier JM, et al. Visualization of monocytic cells in regressing atherosclerotic plaques by intravital 2-photon and positron emission tomography-based imaging—brief report. *Arterioscler Thromb Vasc Biol*. 2018;38:1030–6. <https://doi.org/10.1161/ATVBAHA.117.310517>.
176. English SJ, Sastriques SE, Detering L, Sultan D, Luehmann H, Arif B, et al. CCR2 positron emission tomography for the assessment of abdominal aortic aneurysm inflammation and rupture prediction. *Circ Cardiovasc Imaging*. 2020;13. <https://doi.org/10.1161/CIRCIMAGING.119.009889>.
177. Heo GS, Kopecky B, Sultan D, Ou M, Feng G, Bajpai G, et al. Molecular imaging visualizes recruitment of inflammatory monocytes and macrophages to the injured heart. *Circ Res*. 2019;124:881–90. <https://doi.org/10.1161/CIRCRESAHA.118.314030>.
178. Liu Y, Li W, Luehmann HP, Zhao Y, Detering L, Sultan DH, et al. Noninvasive imaging of CCR2+ cells in ischemia-reperfusion injury after lung transplantation. *Am J Transplant*. 2016;16:3016–23. <https://doi.org/10.1111/ajt.13907>.
179. NCT04217057: Imaging CCR2 Receptors With ⁶⁴Cu-DOTA-ECL1i in Head and Neck Cancer. <https://clinicaltrials.gov/ct2/show/NCT04217057>.
180. Detering L, Abdilla A, Luehmann HP, Williams JW, Huang L-H, Sultan D, et al. CC chemokine receptor 5 targeted nanoparticles imaging the progression and regression of atherosclerosis using positron emission tomography/computed tomography. *Mol Pharm*. 2021;18:1386–96. <https://doi.org/10.1021/acs.molpharmaceut.0c01183>.
181. Aarntzen EHJG, Hermesen R, Drenth JPH, Boerman OC, Oyen WJG. ^{99m}Tc-CXCL8 SPECT to monitor disease activity in inflammatory bowel disease. *J Nucl Med*. 2016;57:398–403. <https://doi.org/10.2967/jnumed.115.165795>.
182. Luehmann HP, Detering L, Fors BP, Pressly ED, Woodard PK, Randolph GJ, et al. PET/CT imaging of chemokine receptors in inflammatory atherosclerosis using targeted nanoparticles. *J Nucl Med*. 2016;57:1124–9. <https://doi.org/10.2967/jnumed.115.166751>.
183. Baba O, Huang L-H, Elvington A, Szpakowska M, Sultan D, Heo GS, et al. CXCR4-binding positron emission tomography tracers link monocyte recruitment and endothelial injury in murine atherosclerosis. *Arterioscler Thromb Vasc Biol*. 2021;41:822–36. <https://doi.org/10.1161/ATVBAHA.120.315053>.
184. Kechagia JZ, Ivaska J, Roca-Cusachs P. Integrins as biomechanical sensors of the microenvironment. *Nat Rev Mol Cell Biol*. 2019;20:457–73. <https://doi.org/10.1038/s41580-019-0134-2>.
185. Herter J, Zarbock A. Integrin regulation during leukocyte recruitment. *J Immunol*. 2013;190:4451–7. <https://doi.org/10.4049/jimmunol.1203179>.

186. Gaertner FC, Kessler H, Wester H-J, Schwaiger M, Beer AJ. Radiolabelled RGD peptides for imaging and therapy. *Eur J Nucl Med Mol Imaging*. 2012;39:126–38. <https://doi.org/10.1007/s00259-011-2028-1>.
187. Chen H, Niu G, Wu H, Chen X. Clinical application of Radiolabeled RGD peptides for PET imaging of integrin $\alpha v \beta 3$. *Theranostics*. 2016;6:78–92. <https://doi.org/10.7150/thno.13242>.
188. Jahandideh A, Stähle M, Virta J, Li X-G, Liljenbäck H, Moisio O, et al. Evaluation of [^{68}Ga] Ga-NODAGA-RGD for PET imaging of rat autoimmune myocarditis. *Front Med*. 2021;8. <https://doi.org/10.3389/fmed.2021.783596>.
189. Dearing JLJ, Daka A, Veiga N, Peer D, Packard AB. Colitis ImmunoPET: defining target cell populations and optimizing pharmacokinetics. *Inflamm Bowel Dis*. 2016;22:529–38. <https://doi.org/10.1097/MIB.0000000000000677>.
190. Notni J, Gassert FT, Steiger K, Sommer P, Weichert W, Rummeny EJ, et al. In vivo imaging of early stages of rheumatoid arthritis by $\alpha 5 \beta 1$ -integrin-targeted positron emission tomography. *EJNMMI Res*. 2019;9:87. <https://doi.org/10.1186/s13550-019-0541-6>.
191. Perkins LA, Nyiranshuti L, Little-Ihrig L, Latoche JD, Day KE, Zhu Q, et al. Integrin VLA-4 as a PET imaging biomarker of hyper-adhesion in transgenic sickle mice. *Blood Adv*. 2020;4:4102–12. <https://doi.org/10.1182/bloodadvances.2020002642>.
192. Meester EJ, de Blois E, Krenning BJ, van der Steen AFW, Norenberg JP, van Gaalen K, et al. Autoradiographical assessment of inflammation-targeting radioligands for atherosclerosis imaging: potential for plaque phenotype identification. *EJNMMI Res*. 2021;11:27. <https://doi.org/10.1186/s13550-021-00772-z>.
193. Broisat A, Tozczek J, Dumas LS, Ahmadi M, Bacot S, Perret P, et al. $^{99\text{m}}\text{Tc}$ -cAbVcAM1-5 imaging is a sensitive and reproducible tool for the detection of inflamed atherosclerotic lesions in mice. *J Nucl Med*. 2014;55:1678–84. <https://doi.org/10.2967/jnumed.114.143792>.
194. Bala G, Blykers A, Xavier C, Descamps B, Broisat A, Ghezzi C, et al. Targeting of vascular cell adhesion molecule-1 by ^{18}F -labelled nanobodies for PET/CT imaging of inflamed atherosclerotic plaques. *Eur Hear J Cardiovasc Imaging*. 2016;17:1001–8. <https://doi.org/10.1093/ehjci/jev346>.
195. Bridoux J, Neyt S, Debie P, Descamps B, Devoogdt N, Cleeren F, et al. Improved detection of molecular markers of atherosclerotic plaques using sub-Millimeter PET imaging. *Molecules*. 2020;25:1838. <https://doi.org/10.3390/molecules25081838>.
196. Ahmed M, Gustafsson B, Aldi S, Dusart P, Egri G, Butler LM, et al. Molecular imaging of a new multimodal microbubble for adhesion molecule targeting. *Cell Mol Bioeng*. 2019;12:15–32. <https://doi.org/10.1007/s12195-018-00562-z>.
197. Perkins LA, Anderson CJ, Novelli EM. Targeting P-selectin adhesion molecule in molecular imaging: P-selectin expression as a valuable imaging biomarker of inflammation in cardiovascular disease. *J Nucl Med*. 2019;60:1691–7. <https://doi.org/10.2967/jnumed.118.225169>.
198. Bonnard T, Yang G, Petiet A, Ollivier V, Haddad O, Arnaud D, et al. Abdominal aortic aneurysms targeted by functionalized polysaccharide microparticles: a new tool for SPECT imaging. *Theranostics*. 2014;4:592–603. <https://doi.org/10.7150/thno.7757>.
199. Israel I, Fluri F, Örbom A, Schadt F, Buck AK, Samnick S. Positron emission tomography and autoradiography imaging of P-selectin activation using ^{68}Ga -fucoidan in photothrombotic stroke. *Curr Neurovasc Res*. 2018;15:55–62. <https://doi.org/10.2174/1567202615666180319152007>.
200. Li X, Bauer W, Israel I, Kreissl MC, Weirather J, Richter D, et al. Targeting P-selectin by Gallium-68-labeled fucoidan positron emission tomography for noninvasive characterization of vulnerable plaques. *Arterioscler Thromb Vasc Biol*. 2014;34:1661–7. <https://doi.org/10.1161/ATVBAHA.114.303485>.
201. Nissinen L, Kähäri V-M. Matrix metalloproteinases in inflammation. *Biochim Biophys Acta Gen Subj*. 2014;1840:2571–80. <https://doi.org/10.1016/j.bbagen.2014.03.007>.
202. Rangasamy G, Ortín C, Zapico R, et al. Molecular imaging probes based on matrix metalloproteinase inhibitors (MMPi). *Molecules*. 2019;24:2982. <https://doi.org/10.3390/molecules24162982>.

203. Golestani R, Razavian M, Ye Y, Zhang J, Jung J-J, Toczek J, et al. Matrix metalloproteinase–targeted imaging of lung inflammation and remodeling. *J Nucl Med.* 2017;58:138–43. <https://doi.org/10.2967/jnumed.116.176198>.
204. Toczek J, Ye Y, Gona K, Kim H-Y, Han J, Razavian M, et al. Preclinical evaluation of RYM1, a matrix metalloproteinase–targeted tracer for imaging aneurysm. *J Nucl Med.* 2017;58:1318–23. <https://doi.org/10.2967/jnumed.116.188656>.
205. Gona K, Toczek J, Ye Y, Sanzida N, Golbazi A, Boodagh P, et al. Hydroxamate-based selective macrophage elastase (MMP-12) inhibitors and radiotracers for molecular imaging. *J Med Chem.* 2020;63:15037–49. <https://doi.org/10.1021/acs.jmedchem.0c01514>.
206. Dmochowska N, Tieu W, Keller MD, Hollis CA, Campaniello MA, Mavrangelos C, et al. ⁸⁹Zr-pro-MMP-9 F(ab')₂ detects colitis induced intestinal and kidney fibrosis. *Sci Rep.* 2020;10:20372. <https://doi.org/10.1038/s41598-020-77390-7>.
207. Pektor S, Schlöder J, Klasen B, Bausbacher N, Wagner D-C, Schreckenberger M, et al. Using immuno-PET imaging to monitor kinetics of T cell-mediated inflammation and treatment efficiency in a humanized mouse model for GvHD. *Eur J Nucl Med Mol Imaging.* 2020;47:1314–25. <https://doi.org/10.1007/s00259-019-04507-0>.
208. Freise AC, Zettlitz KA, Salazar FB, Tavaré R, Tsai W-TK, Chatziioannou AF, et al. Immuno-PET in inflammatory bowel disease: imaging CD4-positive T cells in a murine model of colitis. *J Nucl Med.* 2018;59:980–5. <https://doi.org/10.2967/jnumed.117.199075>.
209. Alam IS, Simonetta F, Scheller L, Mayer AT, Murty S, Vermesh O, et al. Visualization of activated T cells by OX40-ImmunoPET as a strategy for diagnosis of acute graft-versus-host disease. *Cancer Res.* 2020;80:4780–90. <https://doi.org/10.1158/0008-5472.CAN-20-1149>.
210. Kasten BB, Houson HA, Coleman JM, Leavenworth JW, Markert JM, Wu AM, et al. Positron emission tomography imaging with ⁸⁹Zr-labeled anti-CD8 cys-diabody reveals CD8+ cell infiltration during oncolytic virus therapy in a glioma murine model. *Sci Rep.* 2021;11:15384. <https://doi.org/10.1038/s41598-021-94887-x>.
211. Rothlauf PW, Li Z, Pishesha N, Xie YJ, Woodham AW, Bousbaine D, et al. Noninvasive immuno-PET imaging of CD8+ T cell behavior in influenza A virus-infected mice. *Front Immunol.* 2021;12. <https://doi.org/10.3389/fimmu.2021.777739>.
212. Ronald JA, Kim B-S, Gowrishankar G, Namavari M, Alam IS, D'Souza A, et al. A PET imaging strategy to visualize activated T cells in acute graft-versus-host disease elicited by allogeneic hematopoietic cell transplant. *Cancer Res.* 2017;77:2893–902. <https://doi.org/10.1158/0008-5472.CAN-16-2953>.
213. Franc BL, Goth S, MacKenzie J, Li X, Blecha J, Lam T, et al. In vivo PET imaging of the activated immune environment in a small animal model of inflammatory arthritis. *Mol Imaging.* 2017;16:153601211771263. <https://doi.org/10.1177/1536012117712638>.
214. Zhao N, Bardine C, Lourenço AL, Wang Y, Huang Y, Cleary SJ, et al. In vivo measurement of granzyme proteolysis from activated immune cells with PET. *ACS Cent Sci.* 2021;7:1638–49. <https://doi.org/10.1021/acscentsci.1c00529>.
215. Iodice V, Laganà B, Lauri C, Capriotti G, Germano V, D'Amelio R, et al. Imaging B lymphocytes in autoimmune inflammatory diseases. *Q J Nucl Med Mol Imaging.* 2014;58:258–68.
216. Buijnen S, Tsang-A-Sjoe M, Raterman H, Ramwadhoebe T, Vugts D, van Dongen G, et al. B-cell imaging with zirconium-89 labelled rituximab PET-CT at baseline is associated with therapeutic response 24 weeks after initiation of rituximab treatment in rheumatoid arthritis patients. *Arthritis Res Ther.* 2016;18:266. <https://doi.org/10.1186/s13075-016-1166-z>.
217. Salmi M, Jalkanen S. Vascular adhesion Protein-1: A cell surface amine oxidase in translation. *Antioxid Redox Signal.* 2019;30:314–32. <https://doi.org/10.1089/ars.2017.7418>.
218. Autio A, Vainio PJ, Sulamo S, Mali A, Vainio J, Saanijoki T, et al. Preclinical evaluation of a Radioiodinated fully human antibody for in vivo imaging of vascular adhesion Protein-1–positive vasculature in inflammation. *J Nucl Med.* 2013;54:1315–9. <https://doi.org/10.2967/jnumed.113.120295>.

219. Autio A, Henttinen T, Sipilä HJ, Jalkanen S, Roivainen A. Mini-PEG spacing of VAP-1-targeting ^{68}Ga -DOTAVAP-P1 peptide improves PET imaging of inflammation. *EJNMMI Res.* 2011;1:10. <https://doi.org/10.1186/2191-219X-1-10>.
220. Virtanen H, Autio A, Siitonen R, Liljenbäck H, Saanijoki T, Lankinen P, et al. ^{68}Ga -DOTA-Siglec-9—a new imaging tool to detect synovitis. *Arthritis Res Ther.* 2015;17:308. <https://doi.org/10.1186/s13075-015-0826-8>.
221. Siitonen R, Pietikäinen A, Liljenbäck H, Käkälä M, Söderström M, Jalkanen S, et al. Targeting of vascular adhesion protein-1 by positron emission tomography visualizes sites of inflammation in *Borrelia burgdorferi*-infected mice. *Arthritis Res Ther.* 2017;19:254. <https://doi.org/10.1186/s13075-017-1460-4>.
222. Jødal L, Roivainen A, Oikonen V, Jalkanen S, Hansen SB, Afzelius P, et al. Kinetic modelling of [^{68}Ga]Ga-DOTA-Siglec-9 in porcine osteomyelitis and soft tissue infections. *Molecules.* 2019;24:4094. <https://doi.org/10.3390/molecules24224094>.
223. Retamal J, Sørensen J, Lubberink M, Suarez-Sipmann F, Borges JB, Feinstein R, et al. Feasibility of (^{68}Ga)-labeled Siglec-9 peptide for the imaging of acute lung inflammation: a pilot study in a porcine model of acute respiratory distress syndrome. *Am J Nucl Med Mol Imaging.* 2016;6:18–31.
224. Coenen HH, Gee AD, Adam M, Antoni G, Cutler CS, Fujibayashi Y, et al. Consensus nomenclature rules for radiopharmaceutical chemistry—setting the record straight. *Nucl Med Biol.* 2017;55:v–xi. <https://doi.org/10.1016/j.nucmedbio.2017.09.004>.

Magnetic Resonance Imaging of Neuroinflammation



Vanessa A. Johanssen, Niloufar Zarghami, and Nicola R. Sibson

Abstract Magnetic resonance imaging is a powerful tool in preclinical research of diseases with associated neuroinflammation, as it allows high-resolution imaging without harmful ionizing radiation. The development of targetable iron oxide contrast agents, such as microparticles of iron oxide (MPIO), has greatly enhanced molecular MRI for superior detection of target molecules. Cell adhesion molecules (CAMs) are upregulated early in neuroinflammation on the luminal side of activated endothelial cells within the blood-brain barrier, making them a highly accessible target. Targeting MPIO with CAM antibodies has improved the early detection of neuropathologies in preclinical models, as well as providing further insight into disease progression and mechanisms. This chapter highlights the uses of molecular MRI, specifically CAM-targeted MPIO, for investigating multiple sclerosis, stroke, epilepsy, and brain cancer and how the advances made in these preclinical models have the potential to be transferred to other neuropathologies and tissues.

Keywords Magnetic resonance imaging · Molecular imaging · Preclinical MRI · Neuroinflammation · Endothelial activation · Cell adhesion molecules · MPIO · Multiple sclerosis · Stroke · Epilepsy · Brain cancer

1 Introduction

Magnetic resonance imaging (MRI) allows high-resolution imaging without the use of harmful ionizing radiation, making it well suited for longitudinal studies [1]. It is particularly advantageous for imaging of the central nervous system (CNS), because it can generate three-dimensional images of soft tissue at high resolution. MRI is

V. A. Johanssen · N. R. Sibson (✉)

Department of Oncology, University of Oxford, Radiobiology Research Institute, Churchill Hospital, Oxford, UK

e-mail: nicola.sibson@oncology.ox.ac.uk

N. Zarghami

Astellas Pharma Canada, Markham, ON, Canada

based on the acquisition of signals from protons, for the most part in tissue water, which they emit after application of a radiofrequency pulse within a magnetic field. Molecular MRI uses targeted probes (contrast agents) that alter the properties of the proton signal and, hence, alter the contrast of the targeted tissue, thus enabling indirect visualization of specific molecular targets [2].

Inflammation is the body's natural response to heal an injury or fight pathogens or reaction to disease such as cancer, heart disease, diabetes, asthma, and neurodegeneration. In the CNS, as part of this reaction, pro-inflammatory stimuli activate endothelial cells of the blood-brain barrier (BBB), leading to overexpression of cell adhesion molecules [3]. Cell adhesion molecules (CAMs) are transmembrane proteins that span from the intracellular space to the extracellular space of the cell plasma membrane [4]. Their extracellular domain interacts with specific ligands, which can be located on other cells or the extracellular matrix [4]. In particular, the expressed CAMs can bind circulating leukocytes, initiating their extravasation to sites of injury or disease. The extravasation of leukocytes across the BBB and ensuing inflammatory response is an early and fundamental response in numerous and diverse CNS disorders, such as multiple sclerosis, stroke, epilepsy, and brain tumors.

In this book chapter, we will focus primarily on CAMs upregulated in neuroinflammation, which can be harnessed for highly sensitive molecular imaging with MRI. While the majority of molecular MRI research, to date, has focused on neuropathologies, much of what will be discussed has the potential to be translated to other diseases, tissues, and organs.

1.1 MRI

Magnetic resonance imaging (MRI) utilizes nonionizing radiation, making it a safe and noninvasive modality for imaging inflammation. While both the spatial resolution and signal-to-noise ratio of MRI can be considered moderate (e.g. ca. 50 μm isotropic resolution with high-field MRI), it confers notable benefits over other imaging techniques for soft-tissue resolution, yielding detailed images of the brain, spinal cord, nerves, muscles, ligaments, and tendons. Moreover, the signal intensity can be amplified using higher magnetic field strengths, contrast agents, and hyperpolarization of nuclei [5]. Furthermore, since MRI is both well established for preclinical investigations and widely used in the clinic, any advances at the preclinical stage are highly translatable.

MRI systems use a strong external magnetic field (B_0) which causes tissue and water protons in the body to align with the magnetic field (the z -axis). Radiofrequency (RF) and gradient pulses are temporarily applied, stimulating the protons and spinning them out of alignment with B_0 into the transverse or x - y plane. Turning off the RF pulse causes the protons to de-phase and realign with the magnetic field, releasing energy while doing so, which is detectable within the RF coil sensors in the scanner. This signal is transformed to create the structural MR

images we are familiar with. The signal can be processed in a number of different ways to gather further functional and metabolic information. Protons in different tissues, or different structures within tissues, de-phase and realign at differing rates. These “relaxation rates” reflect how the protons interact both with their physical environment (spin-lattice or longitudinal relaxation time; T1) and with other neighboring protons (spin-spin or transverse relaxation time; T2). The magnetic field, however, is inhomogeneous, which also shortens the spin-spin relaxation time. The observed T2 with this inhomogeneity is known as T2*. Contrast in MR images can be achieved by changing the pulse sequence and gradient pulse timing parameters to exploit these different relaxation rates. While intrinsic contrast can produce detailed tissue images, exogenous contrast agents that alter the relaxation times of the dephasing protons can enhance structural differences and highlight pathological features.

1.2 Molecular MRI

MRI contrast agents can be categorized as T1 or T2 contrast agents. T1-based contrast agents are paramagnetic ion complexes, which shorten the *longitudinal* relaxation time of the surrounding water [6]. The most commonly used T1 agent is gadolinium diethylenetriaminepentaacetic acid, Gd-DTPA, which has been used extensively to measure vessel perfusion and permeability changes [7, 8]; for example, breakdown of the BBB associated with the inflammatory process.

T2-based contrast agents decrease *transverse* relaxation times by creating a local magnetic field effective enough to de-phase the transverse magnetism. Most T2-based contrast agents are iron oxide particles with a superparamagnetic core of nanocrystalline magnetite (Fe_3O_4) and/or maghemite ($\gamma\text{-Fe}_2\text{O}_3$), surrounded by a polymer shell. The term “T2 contrast agent” has extensively been used for iron oxide particles in the literature and is followed in this chapter; however, it should be noted that these particles manifest greater T2* properties and it is this contrast mechanism that is typically exploited for detection [9]. The coating of the iron oxide particle is important for biocompatibility and functionality such as targeting. These iron oxide particles are classified into three groups based on their hydrodynamic size: ultrasmall superparamagnetic iron oxide (USPIO; 20–50 nm hydrodynamic diameter), superparamagnetic iron oxide (SPIO; 50–150 nm hydrodynamic diameter), and microparticles of iron oxide (MPIO; 1–5 μm hydrodynamic diameter). The accumulation of iron oxide particles appears as dark or hypointense regions on T2*/T2-weighted MR images.

In molecular MRI, a contrast agent is targeted to a suitable marker of the disease. Targeted gadolinium-based contrast agents have been developed for some pathologies; however, the sensitivity of these agents remains very low [10–12]. More recently, targeted iron oxide particles have become more popular for molecular MRI, and, of these, MPIO have proven to be the most effective [9, 13, 14]. MPIO are the largest iron oxide particles, and their greater mass in turn generates greater

magnetic field distortion and contrast effects, extending up to ~ 50 times their physical size. This phenomenon is known as the “blooming artifact,” enabling *in vivo* detection of MPIO at low concentrations [15]; as low as ~ 50 pg of iron loaded into a single metastatic cell has been imaged at a field strength of 1.5 T [16], hence the superiority of MPIO over smaller iron oxide particles.

For effective molecular imaging, the marker being targeted needs to be specific and upregulated enough for the imaging needs, with low-level basal expression. The marker must also have an appropriate targeting ligand, such as an antibody, peptide, or other motifs, that will have strong, specific binding affinities to the target. The MRI contrast agent needs to be readily functionalized with the chosen targeting moiety, and, importantly, the target must be readily accessible or have technological means to become accessible to the contrast agent. Finally, a short half-life is highly advantageous to reduce background contrast effects, which in turn enables pre- and post-contrast imaging within the same imaging session. To this end, MPIO have demonstrated significant benefits over USPIO, with a half-life of approximately 1.2 min compared to 16.5 h for USPIO [9], while also reducing the potential for passive, nonspecific accumulation in pathological regions of BBB breakdown.

2 Molecular MRI to Reveal Inflammation in the Brain

Inflammation in the central nervous system is now recognized as a classical feature in various neurological diseases, such as multiple sclerosis (MS), stroke, cancer, neurodegeneration, and epilepsy. The inflammatory response has been exploited for molecular imaging to identify and treat these diseases. The CNS, previously believed to be “immune-privileged,” has an extensive network for interplay with the immune system. In normal conditions, endothelial cells, which are the main component of the BBB, are in a state of quiescence and, for the most part, block the migration of immune cells into the CNS. As part of the CNS immune response, glial cells release pro-inflammatory cytokines, and chemokines are released in the circulation. This release of pro-inflammatory molecules triggers the activation of endothelial cells and, consequently, upregulation of CAMs on the luminal side of the BBB, which engage immune cells at the site of inflammation [17]. The process of leukocyte passage across the vascular endothelium is a multistage process, which includes tethering, rolling, firm adhesion, arrest, and extravasation across the vessel wall. Within this process, distinct classes of CAMs (e.g., selectins, integrins) facilitate different elements [18, 19] (Fig. 1).

As a consequence of their expression on the luminal surface of endothelial cells, CAMs provide an easily reached marker of a disease site. This endoluminal expression is particularly important in the brain, as the specialized BBB prevents extravasation of such agents from the circulation into the brain parenchyma. Indeed, even in the case of a permeable BBB, penetration of larger (e.g., micron-sized) particles into the brain is minimal. Thus, with a target that is accessible to agents within the bloodstream, such as CAMs, there is no size restriction for the MRI contrast agent.

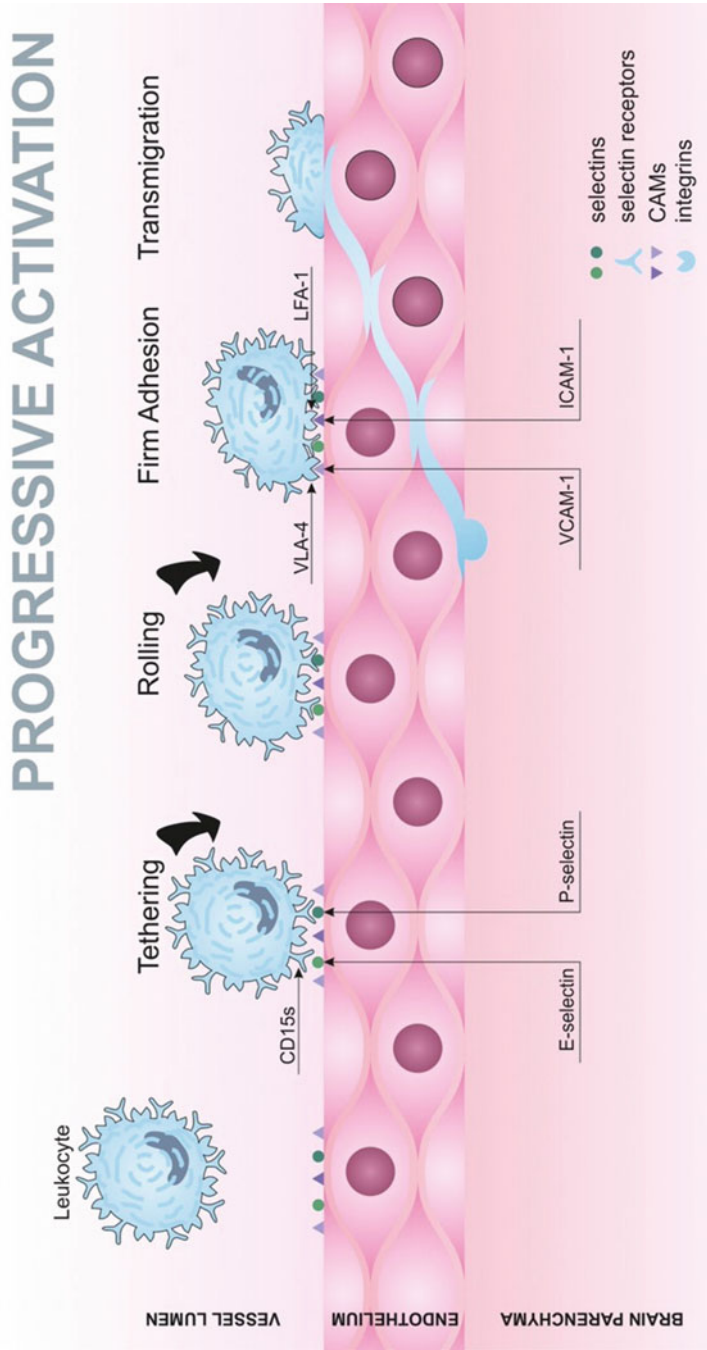


Fig. 1 Schematic illustrating the process of leukocyte extravasation across the vascular endothelium. Within this process, distinct classes of CAMs, expressed on the luminal surface of endothelial cells, facilitate different elements: selectins (e.g., E-selectin/CD15s) regulate the initial stages of capture and rolling along the endothelium, while integrin-ligand interactions (e.g., VLA-4/VCAM-1) support firm adhesion and arrest, followed by transendothelial diapedesis

Importantly, it has been shown that targeted MPIO do not trigger a response like endogenous leukocytes when they bind to adhesion molecules [20].

The demonstration that CAMs upregulated on activated endothelial cells could be used as a target for molecular MRI was first accomplished *in vivo* using a gadolinium-based contrast agent containing a sialyl Lewis^X (sLe^X) mimetic moiety that enabled it to bind to the adhesion molecule E-selectin [11]. However, the contrast was low and a move to iron oxide contrast agents was pursued. Although studies utilizing a range of iron oxide particles (from USPIO to MPIO) have been reported, as discussed above, recent work has demonstrated empirically that MPIO are the most sensitive iron oxide particles for preclinical work in the mouse brain [9]; these confer a high payload of contrast per particle, together with high multivalency in the targeting ligand and rapid clearance from the blood pool [9, 13, 14].

VCAM-1-targeted MPIO were first trialed in mouse models of acute neuroinflammation, induced by intrastriatal injection of the cytokine, interleukin-1 beta (IL-1 β) [21]. After endothelial activation from the cytokine, MPIO conjugated with anti-VCAM-1 antibodies (VCAM-MPIO) were injected intravenously and detected using T2*-weighted MRI. Focal hypointensities were observed in the hemisphere of the cytokine injection, indicating specific and sensitive detection of VCAM-1-expressing vessels (Fig. 2). This proof-of-concept study launched further research into CAM-targeted MPIO in numerous neuroinflammatory disease models, as discussed below.

2.1 Multiple Sclerosis

Multiple sclerosis (MS) is a chronic autoimmune neurological disease [22]. It is defined by inflammation, axonal injury, neuronal loss, and demyelinating lesions in the white matter and the cortex [23]. Clinically, MS is defined by periods of relapse (rise of symptoms) and remission (decline of symptoms) [24]. Disease progression can be monitored by quantifying the spatiotemporal lesion load through T2-weighted imaging for plaques and T1-weighted, gadolinium-enhanced, active lesions where BBB or blood-cerebrospinal fluid barrier breakdown has occurred [25], although it is acknowledged that these events reflect “tip of the iceberg” with respect to overall brain disease burden. At the same time, circulating adhesion molecules have been found to be increased in patients with MS compared to healthy controls [26], and upregulation of CAMs, specifically on the cerebral endothelium, has been demonstrated [27, 28]. On this basis, an array of molecular MRI methods targeting CAMs have been developed to (i) diagnose and stage MS in preclinical models [29–34], (ii) monitor response to therapy [31], and (iii) predict relapse and remission [35].

E- and P-selectin are two CAMs that are upregulated as part of the inflammatory response and are key to the initial rolling phase of leukocytes along the endothelium through carbohydrate binding interactions [36, 37] (Fig. 1). Glyconanoparticles (GNP), with high Fe-content, collectively targeting endothelial markers E-/P-

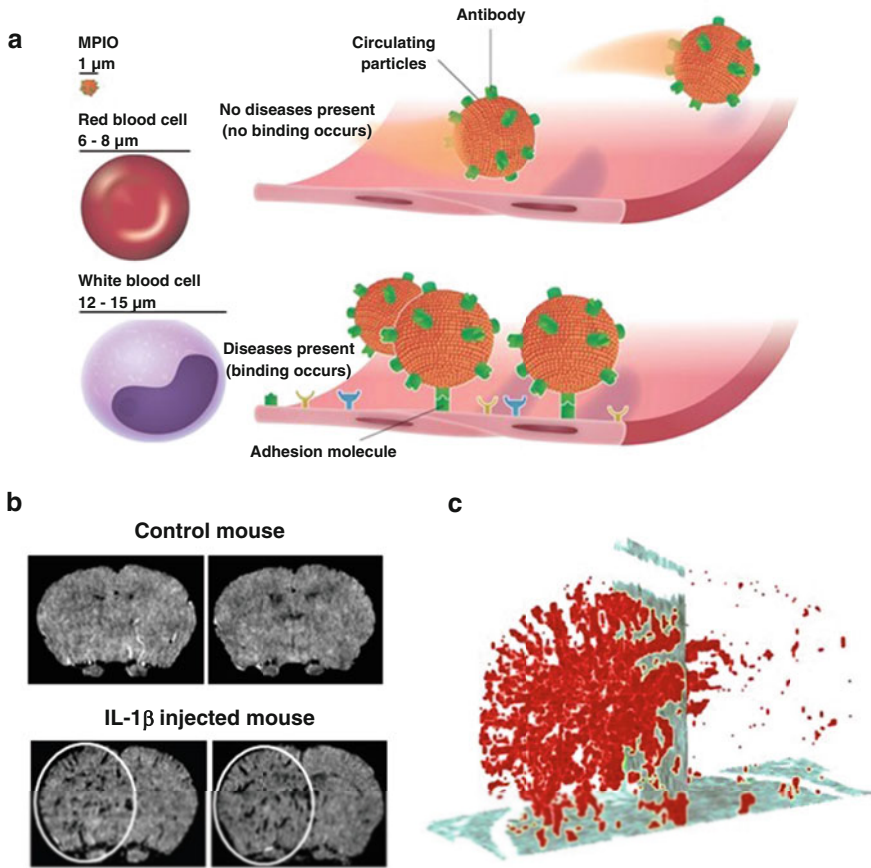


Fig. 2 Proof-of-principle VCAM-MPIO binding to activated endothelium. **(a)** Schematic illustrating concept of antibody targeting iron oxide microparticles to a specific molecular epitope on activated endothelium. Note that, although micron-sized, these microparticles are still markedly smaller than circulating red and white blood cells. Modified from Serres et al. [5] with permission. © 2014, Springer. **(b)** Representative images from mice injected unilaterally in the left striatum with interleukin-1 β (IL-1 β). Top images are from a control mouse injected with VCAM-1 antibody prior to VCAM-MPIO administration, blocking VCAM-MPIO binding. Both mice were subsequently injected intravenously with VCAM-MPIO. MPIO-induced hypointensities are only evident in the left hemisphere of the mouse injected without prior blocking (white circles), reflecting specific VCAM-MPIO binding. **(c)** 3D rendering of VCAM-MPIO-induced hypointensities in a mouse injected unilaterally with IL-1 β . Modified from McAteer et al. [21] with permission. © 2007, Nature Publishing Group

selectin by conjugation with the glycan ligand sialyl Lewis^X (GNP-sLe^X), were able to detect acute inflammation induced by intrastriatal cytokine injection and, also, presymptomatic focal inflammation in a rat model of experimental autoimmune encephalitis (EAE) [34], the classical experimental model of MS. In a more recent study, P-selectin was exclusively targeted for greater specificity of inflammation in

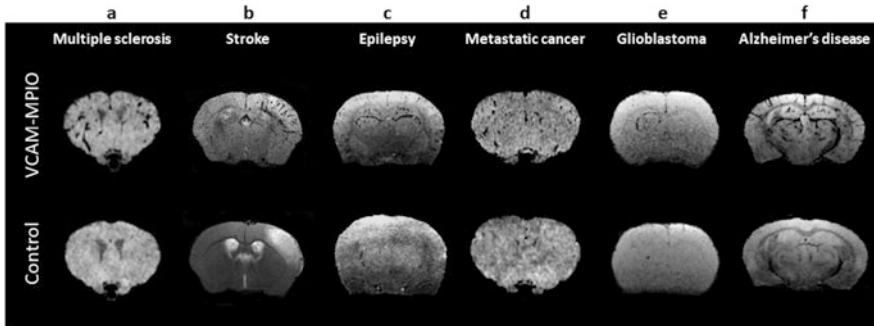


Fig. 3 Examples of VCAM-MPIO binding and detection of inflammation in different mouse models of neurological disease. Representative images of VCAM-MPIO binding and detection of inflammation in mouse models of (a) multiple sclerosis, (b) stroke, (c) epilepsy, (d) metastatic cancer, (e) glioblastoma, and (f) Alzheimer's disease. Selected T2*-weighted images from each model show focal hypointense areas (black) corresponding to VCAM-MPIO binding. (a) In the multiple sclerosis, EAE model at day 15, hypointensities can be seen throughout the brain, but with noticeably greater binding in the cerebellum and hindbrain. Few or no hypointensities were evident in EAE mice injected with control IgG-MPIO. (b) The stroke model (transient middle cerebral artery occlusion induced by intra-arterial injection of thrombin) shows hypointensities restricted to the ischemic area as highlighted by comparison to the T2W control image, in which this is evident as an area of hyperintensity. (c) Localized VCAM-1 expression is also evident in the epilepsy model (23 hours post-pilocarpine injection) and is restricted to the choroid plexus, periventricular organs, hippocampus, and pial vessels of the cerebral cortex. Few or no hypointensities were evident in mice injected with control IgG-MPIO post-pilocarpine. (d) In the metastatic cancer model (day 13 post-induction), hypointensities are evident throughout the brain compared to naïve control mice injected with VCAM-MPIO. (e) In the U87MG rat glioblastoma model, VCAM-MPIO hypointensities reveal the intrastriatal tumor margin, while minimal hypointensities are evident in rats injected with control IgG-MPIO. (f) Hypointensities are evident throughout the brain in a mouse model of Alzheimer's disease (aged APP/PS1) in mice injected with VCAM-MPIO, compared to those injected with control IgG-MPIO, revealing neuroinflammation in this model. (a) Reproduced from Serres et al. [32] with permission. © 2011, FASEB. (b) Adapted from Gauberti et al. [44] with permission. © 2013, American Heart Association. (c) Reproduced from Duffy et al. [53] with permission. © 2012, Elsevier. (d) Reproduced from Serres et al. [54] with permission. © 2012, National Academy of Sciences. (e) Reproduced from Cheng et al. [55] under CC-BY license. © 2022, Cheng et al. (f) Reproduced from Montagne et al. [56] with permission. © 2012, Elsevier

the spinal cord [35]. In preclinical EAE models, MPIO- α P-selectin not only detected the presymptomatic inflammatory response, but also enabled prediction of relapses in asymptomatic and remissions in symptomatic animals [35]. If translated to the clinic, these findings could help identify the most effective times for prophylactic treatment before the onset of symptoms.

Presymptomatic inflammation has also been successfully imaged in a mouse EAE model with VCAM-1-targeted MPIO [31, 32]. The inflammatory events were detected throughout the brain in regions without BBB breakdown, in particular the cerebellum and hindbrain, and correlated histologically with upregulation of VCAM-1 and leukocyte infiltration [32] (Fig. 3a). Moreover, the onset of disease was detected with VCAM-1-targeted molecular MRI, at a time when EAE mice

could not be distinguished from their control littermates on the basis of behavioral scoring [32]. Thus, this approach is highly sensitive to the early presence of inflammatory disease, when it is otherwise undetectable either by conventional imaging or standard behavioral readouts. The VCAM-MPIO-induced hypointensities also correlated with disease relapse, with reduced signal coinciding with disease treatment [31].

Intercellular adhesion molecule 1 (ICAM-1) is also upregulated early in lesion formation both in MS [38] and in the preclinical EAE model [39]. As for the above studies, ICAM-1 antibody functionalized MPIO were shown to detect upregulated ICAM-1 and, consequently, disease progression in the brains of EAE mice [29]. Comparable to VCAM-1, upregulated ICAM-1 expression in EAE pathology could be disconnected from BBB integrity. Thus, ICAM-1 is another promising CAM target for early diagnosis of MS lesions using molecular MRI.

2.2 *Stroke*

Inflammation plays a fundamental role in the pathophysiology of stroke, with a variety of supporting evidence including the prevention of repeated vascular incidents by anti-inflammatory therapeutics [40]. Markers of inflammation, including the adhesion molecule, ICAM-1, have been found clinically to predict future atrial fibrillation events [41]. Molecular MRI has the capacity to provide further insight into the pathophysiological inflammatory events in preclinical models of stroke and the potential to monitor stroke pathogenesis and treatment strategies in the clinic. Studies of molecular MRI in animal stroke models have targeted a number of different CAMs, including E-selectin [34], P-selectin [42], VCAM-1 [43, 44], and ICAM-1 [45, 46].

The first molecular MRI studies in preclinical models of stroke used the same GNP-sLe^X, to target E-/P-selectin, as described above in EAE rats [34]. GNP-sLe^X were found to visually detect damage not only at the primary ischemic site, but also where secondary damage was evident, importantly without BBB breakdown [34]. In a comparable study the same year, magnetic nanoparticles targeted to P-selectin, specifically, with a P-selectin-binding peptide (MNP-PBP) were also found to uncover endothelial activation in a mouse model of stroke by middle cerebral artery occlusion, in the very early stages of lesion evolution [42]. Moreover, in a mouse model of transient ischemic attack (TIA), a risk factor for stroke and currently a diagnostic obstacle in clinical practice, P-selectin-targeted MPIO revealed affected vasculature despite an absence of brain infarction on MRI [47]. Strikingly, P-selectin molecular MRI could discriminate between two mouse models of TIA mimics, migraine (intraperitoneal injection of nitroglycerin) and epilepsy (intraperitoneal injection of kainite) [47]. In clinical practice, this would be a significant advancement for positive and selective MRI-based diagnosis of TIA and the prescription of preventative therapies in patients at risk of stroke.

Targeting VCAM-1 for molecular MRI has revealed more about the inflammatory response of stroke [44] (Fig. 3b). Imaging using VCAM-MPIO has demonstrated that there is not only the detectable ischemic core lesion, usually visualized by diffusion-weighted imaging, but also a more widespread area of VCAM-1 expression (25% vs. 3% total brain volume), associated with inflammatory processes, at an acute stage of ischemic lesion pathology [43]. This region has been termed the “inflammatory penumbra” [48], and it has been shown that anti-inflammatory therapeutics can reduce brain injury in ischemic stroke [44, 49]. In line with these preclinical data, VCAM-1 has been found to be overexpressed at the site of the cerebral infarct in patients with acute cerebral ischemia at the time of thrombectomy; increased VCAM-1 levels were predictive of infarct volume and edema volume [50]. These findings suggest that molecular MRI, targeting VCAM-1 in preclinical stroke models, may be an effective approach to monitoring immunomodulatory treatments, such as statins or cyclooxygenase inhibitors [44].

In preclinical stroke models, ICAM-1 is also highly upregulated on the brain endothelium subacutely after stroke [51] and has been found to be elevated in patients with acute ischemic stroke [52]. On this basis, ICAM-1 was explored as an alternative target for molecular MRI in preclinical models [45]. Both gadolinium chelate-containing liposomes and MPIO contrast agents were functionalized with anti-ICAM-1 antibodies and their efficacy for imaging stroke-associated ICAM-1 upregulation assessed. However, specific imaging *in vivo* was only produced by ICAM-1-targeted MPIO, and not the ICAM-1-targeted liposomes containing gadolinium chelate. This study further highlights MPIO as a potent molecular MRI contrast agent and supports its superiority over gadolinium-based agents for target-specific imaging. Deddens et al. further optimized the ICAM-1-targeted MPIO to image not only activated vessels but also activated leukocytes in stroke pathophysiology. Importantly, it was found that imaging with the ICAM-1-targeted MPIO did not detrimentally alter the pathophysiology of stroke in preclinical models [46].

2.3 *Epilepsy*

Epilepsy refers to chronic neurological disorders exemplified by the occurrence of spontaneous periodic seizures [57, 58]. As with other neurological disorders, it is becoming apparent that inflammation is also an important feature of epilepsy, either before its onset causing increased excitability [57, 59, 60] or as a result of seizures [57, 58, 61]. Further, neuroinflammation may play a role in drug-resistant epilepsy [62]. Elucidating the pathophysiological role of neuroinflammation in epilepsy will help with identifying biomarkers, developing therapies, and stratifying patients for personalized therapeutics [58]. Moreover, up to 30% of patients with focal epilepsy syndromes have no visual pathology on MRI [63–65], emphasizing the beneficial role that molecular MRI could bring to this field.

In an established mouse model of epilepsy, induced by intraperitoneal pilocarpine, evidence of endothelial activation has been found, demonstrated by

upregulation of several CAMs including P-selectin, ICAM-1, and VCAM-1 [66]. The highest levels of CAM expression were found 24 hours post seizure, and they were still upregulated 7 days later [66]. This observation was developed further in a rat model of status epilepticus, and acute inflammatory events were observed postepileptic activity using VCAM-MPIO and T2*-weighted MRI [53]. Maximal contrast, indicating VCAM-1 upregulation, was evident in areas of the brain showing significant epileptic activity, such as the periventricular organs, hippocampus, and cerebral cortex (Fig. 3c). Importantly, no significant changes were observed on T2-weighted images without contrast agent, again highlighting the ability of VCAM-1-targeted molecular MRI to expose injury/inflammation earlier than conventional imaging. This study emphasizes how molecular MRI can improve our understanding of the pathological sequelae in epilepsy.

2.4 Brain Cancer

Cancer is a group of diseases characterized by cellular changes that cause abnormal, uncontrolled cell division and growth [67]. Growth goes beyond normal boundaries and can spread to other organs (metastasis). The most common brain cancer in adults is secondary cancer, or metastasis, from the lung, breast, and melanoma [68, 69], with a dismal prognosis of very low 6-month survival rates [70]. Two MRI sequences are routinely used for the detection of brain metastases in the clinic: firstly, T1-weighted imaging together with (un-targeted) gadolinium-based contrast agents to show BBB disruption and, secondly, a T2-weighted fluid attenuated inversion recovery (T2W-FLAIR) sequence, which reveals peri-tumoral edema [71]. These images, however, will only detect metastases that are large enough (>2–5 mm in diameter) to cause BBB breakdown, by which time they are frequently beyond effective therapy. There is a clear need, therefore, for an imaging modality that has the ability to detect smaller, earlier brain tumors.

Tumors are pathologically associated with infiltrating immune cells, and endothelial activation is an early event in the evolution of brain metastasis. Evidence suggests that, as for leukocyte recruitment to disease sites, tumor cells use CAMs to promote their extravasation into the secondary tissue site [72–74]. Soluble factors secreted by brain metastatic cancer cells activate endothelial cells [75], priming them for binding and rolling of the cancer cells by the selectin family [76]. The role of 12 CAMs and their ligands in early stages of breast cancer brain metastasis formation has been investigated [77], and both E-selectin and VCAM-1 were highly upregulated on the cerebral endothelium, while their ligands were upregulated on metastatic tumor cells. Moreover, blocking specific CAMs (e.g., VLA-4, ALCAM) reduced the number of tumors seeding to the brain [77].

Molecular MRI of endothelial activation, using VCAM-MPIO, has been found to reveal metastatic brain tumors, as small as 1000 cells, throughout the brain in a systemically induced model of the disease [54] (Fig. 3d). When translated to clinical imaging resolutions, this detection threshold would be 2–3 orders of magnitude

smaller than can be achieved by standard clinical imaging methods currently (10^7 – 10^8 cells) [54]. VCAM-targeted MRI has been shown to detect brain micrometastases in a number of xenograft models, including human breast carcinoma (MDA-MB-231-Br-GFP), lung adenocarcinoma (SEBTA-001), and melanoma (H1_DL2) [78], indicating that this approach to brain metastasis detection is effective across multiple primary tumor types.

Activated leukocyte cell adhesion molecule (ALCAM) has also been successfully used as a target with functionalized MPIO to detect brain micrometastases. ALCAM has been shown to specifically localize at the intercellular junctions between endothelial cells and is thought to play a pivotal role in the extravasation of monocytes, T cells and B cells in neurological disease [79–81]. In mice bearing breast, melanoma, or lung brain metastases, ALCAM was found to be upregulated early in tumor establishment, and ALCAM-MPIO enabled detection of brain micrometastases by MRI before any BBB breakdown [82]. Although the sensitivity of ALCAM-MPIO for metastasis detection was slightly lower than previously found for VCAM-1-targeted MPIO [82], the overall sensitivity for detection of endothelial ALCAM, per se, was very high (80–90%). Given that ALCAM has been shown to be upregulated on the cerebrovascular endothelium in several neuroinflammatory diseases, including EAE, MS, and stroke, ALCAM-targeted MRI may find a more important application in the detection and monitoring of other neurological diseases.

As noted above, a further CAM that has been shown to be strongly associated with endothelial activation in breast cancer brain metastasis is E-selectin [77] and is thought to be a mediator of metastasis from various primary tumor types [83]. In vitro, E-selectin and its ligand sLe^X (CD15s) have been found to facilitate adhesion between human non-small cell lung cancer tumor cells and endothelial cells [84]. As discussed in previous sections, a number of molecular MRI agents targeting E-selectin have been developed previously using either Gd-DTPA [11, 85] or glyconanoparticles [34] as the contrast moiety and sLe^X (or mimetic) as the targeting ligand. Although these have been tested in a number of neuroinflammatory models, none have proven as potent as the VCAM-1-, ICAM-1-, and ALCAM-targeted agents described above, in which antibodies have been used to target the ligand. This lower sensitivity may reflect the transient nature of the E-selectin/sLe^X interaction, which occurs during the rolling stage of the leukocyte adhesion cascade. Consequently, using its natural ligand, sLe^X, may not be the optimal approach for in vivo imaging of E-selectin. Moreover, sLe^X is also a carbohydrate ligand for P-selectin; thus, specific and sensitive detection of E-selectin alone may not be feasible with this technique. Jefferson et al. provided an alternative strategy by developing an antibody-based E-selectin-targeted MRI contrast agent [20]. In that study, high binding efficacy of the E-selectin-MPIO was confirmed under physiologically relevant shear stresses in vitro. In light of these results and developments in the production of high-affinity antibodies, a similar antibody-MPIO conjugate (E-sel-MPIO) was recently tested in vivo, in both neuroinflammatory and brain metastasis models [86]. In the latter study, E-selectin was shown to be upregulated on tumor-associated vasculature of brain metastases from breast, melanoma, and lung primary tumor types (unpublished data, Fig. 4a, b). Expression of E-selectin

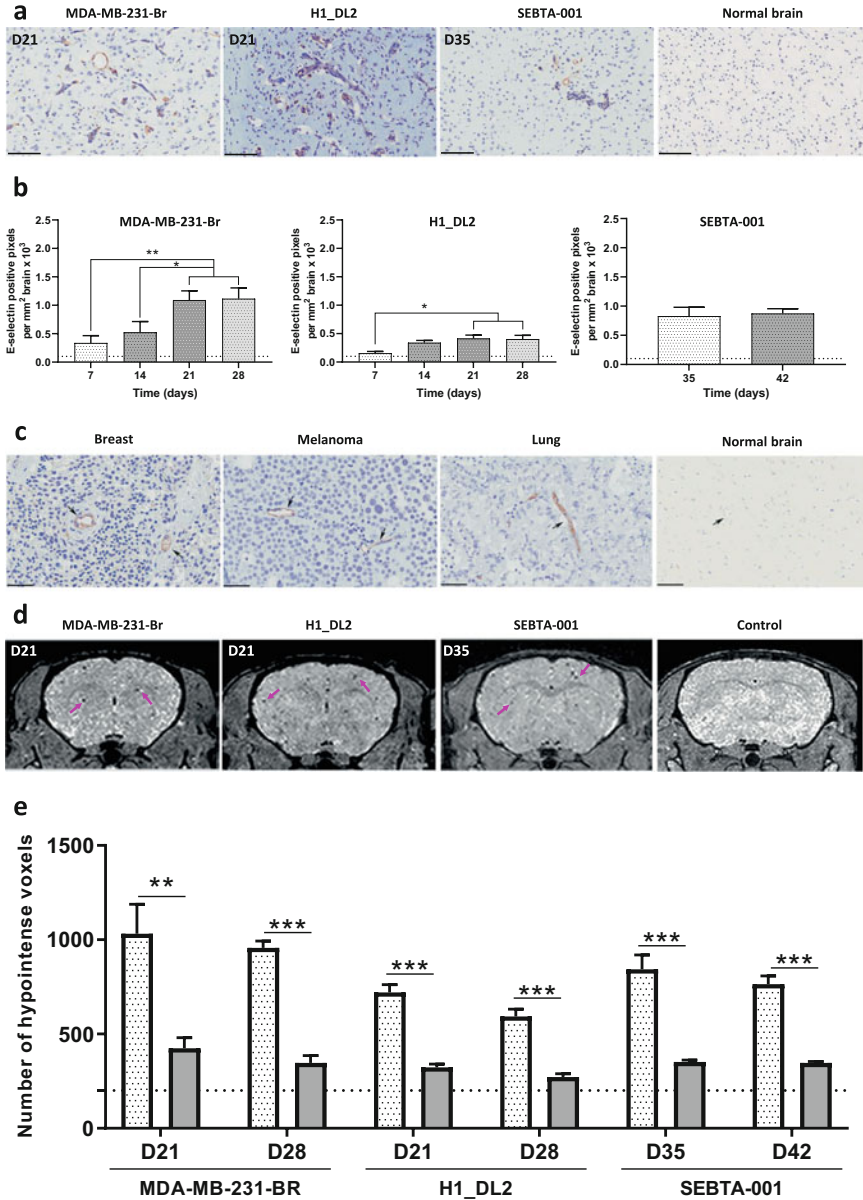


Fig. 4 E-selectin expression in brain metastasis and as a target for molecular MRI. (a) E-selectin expression (brown staining) associated with brain metastases was evident in all models—MDA-MB-231-Br (breast carcinoma), H1_DL2 (melanoma), and SEBTA-001 (lung adenocarcinoma)—but negligible in normal brain tissue. Scale bars = 100 μ m. (b) Graphs showing the time course of E-selectin upregulation for MDA-MB-231-Br, H1_DL2, and SEBTA-001 models ($n > 20$ tumors per time point; mean \pm SEM). Dashed line denotes baseline expression of E-selectin in naïve mouse brain ($n = 2$). * $p < 0.05$, ** $p < 0.01$. (c) E-selectin staining (brown) from human brain metastasis

was also found on tumor-associated blood vessels in postmortem human brain metastasis biopsies from breast, melanoma, and lung primary tumors (unpublished data, Fig. 4c). E-selectin-targeted molecular MRI was found to be more sensitive than ALCAM, but not VCAM-1, targeted molecular MRI, for the detection of brain metastases in all models (unpublished data, Fig. 4d, e and Table 1), with the smallest tumor detected having a volume of 4.7×10^{-5} μL , approximately 30–40 cells [87], in the breast cancer brain metastasis model [86].

Expanding on these results and previous work using VCAM-1 as the target, Zarghami and colleagues also investigated the potential for increasing the sensitivity of molecular MRI through a dual-targeted strategy [86]. It is still not clear whether distinctive classes of CAMs are involved at each step of the adhesion process or whether there is an active synergy between CAMs for these sequential steps. The detection of any neuropathology, including brain metastasis, by targeting a single adhesion molecule depends highly on the binding specificity, pharmacokinetics, target biodistribution, and stage of pathology. It was hypothesized, therefore, that targeting more than one CAM simultaneously would enhance detection, by increasing the number of potential binding sites and accounting for heterogeneity in expression of each individual target. Using mouse models of brain metastasis, it was found that concurrent intravenous administration of both VCAM-MPIO and E-selectin-MPIO increased the sensitivity for detection of brain micrometastases for all three types of primary cancer—breast, melanoma, and lung—to 91%, 75%, and 90% of tumors detected, respectively (unpublished data, Fig. 5 and Table 1) [86]. Thus, dual or even triple targeting may prove to be the most sensitive approach to detection of early disease, not only in brain metastasis but also in other neurological diseases. In a clinical setting, the dismal prognosis of patients suffering metastatic spread to the brain largely reflects the lack of early detection and consequent limited treatment approaches. Detecting these early inflammatory events in metastatic brain cancer

Fig. 4 (continued) biopsies from breast, melanoma, and lung primary cancer. E-selectin expression on cerebral vessels (black arrows) in close proximity to tumor cells was evident for all cases studied ($n = 2$ patients for each primary, $n = 2$ sections each patient). No E-selectin activated vessels (black arrow indicating cerebral vessel, $n = 2$ sections) were detected in normal human brain tissue. Counterstain (blue) = cresyl violet. Scale bars = 50 μm . **(d)** Detection of brain micrometastases using E-selectin-MPIO. Representative T2*-weighted coronal images from MGE3D datasets. Prominent focal hypointense (black) foci corresponding to binding of E-selectin-MPIO were evident in mice injected with MDA-MB-231-Br or H1_DL2 cells at day 21 and SEBTA-001 cells at day 35 after tumor cell injection. Examples of hypointense foci are indicated with pink arrows on each slice. Minimal hypointense foci were detected in the tumor-bearing animals injected intravenously with IgG-MPIO; representative control image shown from a SEBTA-001 bearing mouse injected with control IgG-MPIO on day 42. **(e)** Graph showing quantitation of the number of hypointense voxels for each tumor model over time ($n = 5$ per group; mean \pm SEM). A significant difference was evident between tumor-bearing mice injected with E-selectin-MPIO (dotted bars) and IgG-MPIO (gray bars) at all time points in all three models; $**p < 0.01$, $***p < 0.001$. Dashed line denotes background hypointense voxels detected in naïve mice injected with E-selectin-MPIO ($n = 2$). Data from authors' previously unpublished studies

Table 1 Sensitivity of targeted adhesion molecule MRI contrast agents in detection of brain micrometastases

Target adhesion molecule	Brain metastasis model	Tumors detected
VCAM-1	MDA-MB-231-Br	82%
ALCAM	MDA-MB-231-Br	82%
E-selectin	MDA-MB-231-Br	83%
VCAM-1 + E-selectin	MDA-MB-231-Br	91%
VCAM-1	H1_DL2	72%
ALCAM	H1_DL2	54%
E-selectin	H1_DL2	66%
VCAM-1 + E-selectin	H1_DL2	75%
VCAM-1	SEBTA-001	89%
ALCAM	SEBTA-001	68%
E-selectin	SEBTA-001	72%
VCAM-1 + E-selectin	SEBTA-001	90%

using molecular MRI approaches, before any pathological changes are evident by current imaging modalities, would greatly improve therapeutic outcome.

Although the majority of molecular MRI studies in brain cancer to date have focused on earlier diagnosis of micrometastatic (secondary) tumors, a very recent study addressed the question of improving detection of tumor margins in more established tumors. Current clinical neuroimaging techniques for characterizing brain tumors are limited in their capacity to detect the invasive margin, and, despite optimal local therapy, tumor cell invasion into normal brain parenchyma frequently results in recurrence in patients with solid tumors. Therefore, accurate knowledge of the extent of the tumor margin is required for optimal treatment planning. In the study by Cheng et al., VCAM-1-targeted MRI was shown to better detect brain tumor margins in mouse models of breast cancer brain metastasis, glioblastoma (Fig. 3e), and medulloblastoma, than conventional MRI methods [55]. The results of this study suggest that use of VCAM-1-targeted MRI, in combination with other MRI methods, for improved delineation of the tumor-brain interface could significantly improve the management of both primary and secondary brain tumors.

3 Extension of Molecular MRI to Other Diseases and Tissues

In the above sections, we have highlighted specific CNS diseases in which molecular MRI has been applied successfully, in a number of different studies, to uncover regions of inflammation at early stages of disease in preclinical models. Despite the ubiquitous nature of the target, the different spatial distribution of hypointensities enables disease specification/differentiation. These approaches, therefore, have the potential to span other neurological conditions in which there is an inflammatory response. Neuroinflammation is a well-established hallmark in neurodegenerative

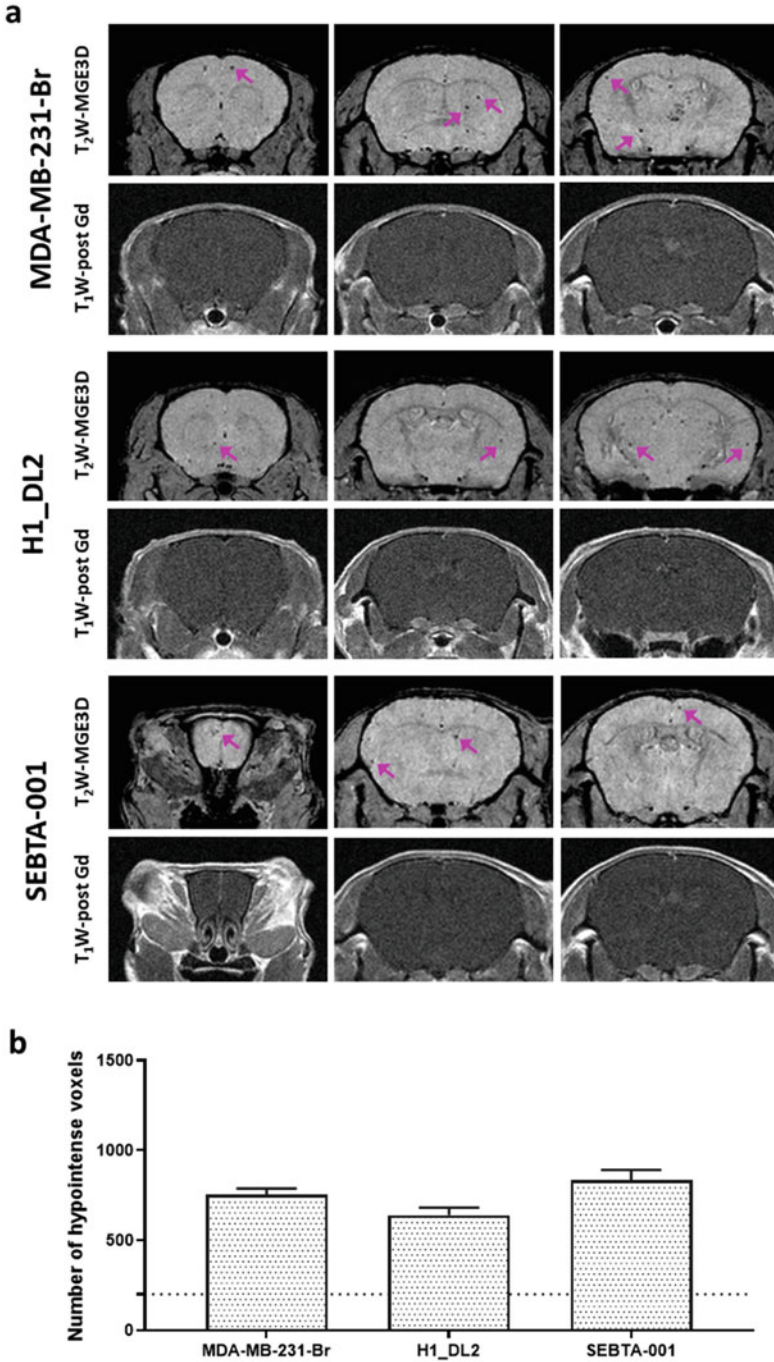


Fig. 5 Detection of brain metastases using a dual-targeted (VCAM–/E-selectin-MPIO) MRI approach. (a) Representative T_2^*W coronal images from MGE3D datasets and the corresponding post-gadolinium T_1W images. Hypointense (black) foci corresponding to binding of VCAM–/E-

disease, for example, Alzheimer's disease (AD) [88]. AD is an age-related condition typified by gradual cognitive decline and dementia. Neuroinflammation in AD is associated with a microglial response to extracellular amyloid plaques and intracellular neurofibrillary tangles [89]. Identifying early stages of neuroinflammation could, therefore, help to uncover the existence of these plaques and tangles and, speculatively, treat the disease early. Neuroinflammatory associated endothelial activation has been detected in AD patients [90]. To date, however, only one study has investigated exploiting the upregulation of CAMs in APP/PS1 mice, a mouse model of AD. VCAM-MPIO were found to reveal upregulation of VCAM-1 and, hence, inflammation in the brains of aged APP/PS1 mice [56] (Fig. 3f). Strikingly, the significant cerebrovascular inflammation was associated with AD like amyloid deposits [56]. The therapeutic impact of unmasking cerebrovascular inflammation through molecular MRI in a mouse model of AD is significant and warrants further investigation.

The greatest known risk factor for AD, and other CNS disorders, is increasing age [91]. In a study by Montagne and colleagues, VCAM-1-targeted MPIO were found to reveal significant hypointensities in aged mice (24-month-old) compared to young (3-month-old) mice [56]. Risk factors of CNS disorders also include systemic inflammation, and Montagne et al. further demonstrated that systemic challenges, such as peripheral injection of lipopolysaccharide (1 mg/kg), acute hyperglycemia (3 g/kg), and acute ethanol intoxication (4 g/kg) in mice, all induced significant VCAM-1-MPIO hypointensities in the brain [56]. This study further demonstrates the sensitivity of VCAM-1-targeted MPIO to unmask neuroinflammation before symptoms manifest.

In an acute setting of neuroinflammation, infection is another potential CNS pathology that is difficult to detect with imaging at an early time point. In a mouse model of cerebral malaria (CM), von Zur Muhlen et al. were able to demonstrate that MPIO targeted to activated platelets could detect platelets adhering to the cerebrovascular endothelium before any pathology was detectable with conventional MRI [92]. Not only did their finding have positive implications for diagnostic imaging, but it also enabled further insight into the pathology of CM, demonstrating that platelet binding was principally driven by the cytokine TNF, in this model. These findings highlight the multifaceted benefits that molecular MRI can achieve in a research model. Further, MPIO targeted to platelets may be used to detect other, non-CNS pathologies involving platelets, including platelet-containing thrombi [93, 94] and myocarditis [95].



Fig. 5 (continued) selectin-MPIO were evident in mice injected with MDA-MB-231-Br or H1_DL2 cells at day 21 and SEBTA-001 cells at day 42 after tumor cell injection. Examples of hypointense foci are indicated with pink arrows. Note that no BBB breakdown is evident on post-gadolinium T1W images at sites of MPIO binding. **(b)** Graph showing quantitation of the number of hypointense voxels for each tumor model ($n = 4-5$ per group; mean \pm SEM). Dashed line denotes background hypointense voxels detected in naïve mice injected with VCAM-/E-selectin-MPIO ($n = 2$). Data from authors' previously unpublished studies

The notable success of detecting pathologies in the CNS with preclinical molecular MRI undoubtedly makes it appealing to try to transfer this technology to other tissue/organs. To date, molecular MRI with targeted MPIO has been successfully applied preclinically in models of diabetes mellitus [96], atherosclerosis [97], renal ischemia reperfusion injury [98], acute kidney injury [96], tumor angiogenesis [13], and intestinal mucosal inflammation [99]. These various studies highlight the promising capabilities of such molecular imaging methods, including imaging multiple organs in one imaging session. Indeed, in a comprehensive study by Belliere and colleagues, this was achieved with endothelial activation mapping of the kidneys, heart, and brain, using VCAM-MPIO in mouse models of sepsis, acute kidney injury, diabetes mellitus, and aging [96].

It is to be noted, however, that MPIO are not suitable for all organs in the body. For example, imaging the liver or spleen will not work as the MPIO are very efficiently cleared from circulation by these organs [98] with a half-life of 1.2 min [9]. The sequestration of MPIO reduces the background signal of these organs and, thus, confounds the detection of target-specific contrast effects. The lungs are also a difficult target organ for MPIO-based molecular MRI due to their low intrinsic signal [100], which will make it difficult to see iron-induced hypointensities. Consequently, different contrast moieties may be needed for some organs. Further, it is important to note that there are pathologies in the brain, such as microbleeds [101], that can produce T2*-weighted hypointensities and, therefore, potential false positives. However, a number of preclinical [102, 103] and clinical [104] studies have demonstrated that normobaric hyperoxia can restore hypoperfusion, potentially negating these effects for molecular imaging. This approach has been demonstrated specifically with VCAM-MPIO in a mouse model of intracranial hemorrhage [102].

4 Future Perspective

Identifying immunological biomarkers and developing tools such as CAM-targeted MPIO potentially enable identification of molecular changes in disease that may drive the development of new immunotherapy drugs. Moreover, combination of these imaging agents with relevant therapeutics, to yield a theranostic agent, could enable delivery of drugs and radioactive substances very specifically to disease sites, as already demonstrated for VCAM-1-targeted alpha-particle therapy [105].

Large particles, such as MPIO, have significant advantages over their smaller counterparts (USPIO), including rapid circulatory half-life (<1–2 min) [9, 13] and high contrast per particle, both of which enhance the detection of target-specific binding. At the same time, high ligand valency increases the likelihood of target binding. Furthermore, as MPIO are greater than 500 nm in diameter, they are likely to have improved “margination” [106], i.e. be pushed toward the vessel wall by gravitational forces [107], and, therefore, have increased wall adhesion compared to nanoparticles, as found by computational modeling and in vitro studies [108–111]. Currently, however, the MPIO that have been used preclinically are not

suitable for clinical translation owing to their accumulation and persistence in the liver and spleen. While next-generation biocompatible and biodegradable, contrast-enhancing particles, based on poly(lactide-co-glycolide) or cellulose constructs, have been developed for *in vivo* cell labeling and tracking studies [112], these have not yet translated to human use. Recently, however, it has been shown that MPIO can be generated from multiple iron oxide nanoparticles coupled covalently through peptide linkers that are designed to be cleaved by intracellular macrophage proteases [113]. On clearance primarily to the resident macrophages in the liver (Kupffer cells), these multimeric MPIO (mMPIO) are rapidly degraded, thus overcoming the most significant obstacle to clinical translation. These mMPIO have also been ligand-targeted and shown to enable detection of inflammation *in vivo* [113]. These results are promising and may pave the way to molecular MRI in the clinic.

A further consideration for clinical translation of MPIO is the relatively high dose of agent required as compared to tracers for other molecular imaging modalities, such as positron emission tomography (PET). With regard to iron toxicity *per se*, excessive therapy with parenteral iron can lead to excess storage of iron with the possibility of iatrogenic hemosiderosis, but this is at considerably higher doses than the likely clinical dose of VCAM-MPIO (1–2 mg/kg iron). Given the very rapid clearance of MPIO from the circulation and uptake by Kupffer cells in the liver, for particles designed to be rapidly degraded, the primary source of potential cytotoxicity would be the nanoparticles released within lysosomes. Several studies have examined the cytotoxic potential of different types of iron nanoparticles with a range of surface coatings and have generally found low or no cytotoxicity associated with these nanoparticles until very high exposure levels. Nevertheless, although preliminary toxicology studies in mice have been performed for VCAM-MPIO with no adverse effects noted [113], formal toxicology studies in animals would be required before these agents can progress to Phase I safety and pharmacokinetic clinical trials in humans.

5 Conclusions

Molecular MRI is a rapidly evolving field, as evidenced not only by the improvements in imaging of molecular contrast agents *per se* that we have seen over the last decade or so, but also the expansion in both molecular targets and pathologies that have been reported. To identify an appropriate molecular target for inflammation imaging, it must be easily accessible, specific to the inflammation process, and exhibit low basal expression levels [114]. In this chapter, we have highlighted how CAMs fit these criteria and have been employed as targets to functionalize MRI contrast agents for imaging inflammation and disease. In principle, a variety of targeting moieties can be used for such molecular contrast agents, including antibodies, antibody fragments, peptides, and carbohydrates, although to date the greatest success has been realized with antibody-targeted agents. While we have

focused primarily on endothelial CAMs as targets for molecular MRI, and indeed they have received the most attention to date, it is important to note that these are not the only inflammatory markers that can be targeted. Studies have shown that it is also possible to image inflammatory cells, such as leukocytes, and activated platelets, and thus additional indicators of inflammation are within reach. The ability to image different inflammatory and other disease-related molecules *in vivo* will not only improve our ability to detect and diagnose disease but will also greatly expand our understanding of the roles that these molecules play in different diseases and potentially enable stratification of patient treatment.

Compliance with Ethical Standards Funding: The authors of this chapter were funded by the Medical Research Council (MR/V005995/1), Cancer Research UK (C5255/A15935), the CRUK & EPSRC Cancer Imaging Centre in Oxford (C5255/A16466), and a Radcliffe Scholarship from the University College, Oxford, UK.

Conflict of Interest: The authors have no conflicts of interest to declare.

Ethical approval: All animal experiments were approved by the University of Oxford Clinical Medicine Ethics Review Committee and the UK Home Office (Animals [Scientific Procedures] Act 1986) and conducted in accordance with the University of Oxford Policy on the Use of Animals in Scientific Research, the ARRIVE Guidelines, and Guidelines for the Welfare and Use of Animals in Cancer Research (Workman et al. Guidelines for the welfare and use of animals in cancer research. *British Journal of Cancer* 2010; 1555–1557).

References

- McRobbie DW, Moore EA, Graves MJ, Prince MR. MRI from picture to proton. 2nd ed. Cambridge: Cambridge University Press; 2006. <https://doi.org/10.1017/CBO9780511545405>.
- Gauberti M, Martinez de Lizarrondo S. Molecular MRI of neuroinflammation: time to overcome the translational roadblock. *Neuroscience*. 2021;474:30–6. <https://doi.org/10.1016/j.neuroscience.2021.08.016>.
- Serhan CN, Ward PA, Gilroy DW, editors. Fundamentals of inflammation. Cambridge: Cambridge University Press; 2010.
- Darnell JE, Lodish H, Berk A, Zipursky L, Matsudaira P, Baltimore D. Molecular cell biology. 4th ed. New York, NY: W.H. Freeman & Co; 2000.
- Serres S, O'Brien ER, Sibson NR. Imaging angiogenesis, inflammation, and metastasis in the tumor microenvironment with magnetic resonance imaging. In: Koumenis C, Hammond E, Giaccia A, editors. Tumor microenvironment cell stress. New-York, USA: Springer; 2014. p. 263–83. https://doi.org/10.1007/978-1-4614-5915-6_12.
- Helm L, Morrow JR, Bond CJ, Camiato F, Botta M, Braun M, et al. Chapter 2. Gadolinium-based Contrast Agents. 2017. p. 121–242. <https://doi.org/10.1039/9781788010146-00121>.
- Runge VM, Clanton JA, Price AC, Wehr CJ, Herzer WA, Partain CL, et al. The use of GD DTPA as a perfusion agent and marker of blood-brain barrier disruption. *Magn Reson Imaging*. 1985;3:43–55. [https://doi.org/10.1016/0730-725X\(85\)90008-6](https://doi.org/10.1016/0730-725X(85)90008-6).
- Lohrke J, Frenzel T, Endrikat J, Alves FC, Grist TM, Law M, et al. 25 years of contrast-enhanced MRI: developments, current challenges and future perspectives. *Adv Ther*. 2016;33: 1–28. <https://doi.org/10.1007/s12325-015-0275-4>.
- Zarghami N, Khrapitchev AA, Perez-Balderas F, Sarmiento Soto M, Larkin JR, Bau L, et al. Optimization of molecularly targeted MRI in the brain: empirical comparison of sequences and particles. *Int J Nanomedicine*. 2018;13:4345–59. <https://doi.org/10.2147/IJN.S158071>.

10. Obermeier B, Daneman R, Ransohoff RM. Development, maintenance and disruption of the blood-brain barrier. *Nat Med.* 2013;19:1584–96. <https://doi.org/10.1038/nm.3407>.
11. Sibson NR, Blamire AM, Bernades-Silva M, Laurent S, Boutry S, Muller RN, et al. MRI detection of early endothelial activation in brain inflammation. *Magn Reson Med.* 2004;51:248–52. <https://doi.org/10.1002/mrm.10723>.
12. Artemov D, Mori N, Ravi R, Bhujwala ZM. Magnetic resonance molecular imaging of the HER-2/neu receptor. *Cancer Res.* 2003;63:2723–7.
13. Melemenidis S, Jefferson A, Ruparelia N, Akhtar AM, Xie J, Allen D, et al. Molecular magnetic resonance imaging of angiogenesis in vivo using polyvalent cyclic RGD-iron oxide microparticle conjugates. *Theranostics.* 2015;5:515–29. <https://doi.org/10.7150/thno.10319>.
14. Yang Y, Yang Y, Yanasak N, Schumacher A, Hu TC-C. Temporal and noninvasive monitoring of inflammatory-cell infiltration to myocardial infarction sites using micrometer-sized iron oxide particles. *Magn Reson Med.* 2010;63:33–40. <https://doi.org/10.1002/mrm.22175>.
15. Shapiro EM, Skrtic S, Sharer K, Hill JM, Dunbar CE, Koretsky AP. MRI detection of single particles for cellular imaging. *Proc Natl Acad Sci.* 2004;101:10901–6. <https://doi.org/10.1073/pnas.0403918101>.
16. Heyn C, Ronald JA, Ramadan SS, Snir JA, Barry AM, MacKenzie LT, et al. In vivo MRI of cancer cell fate at the single-cell level in a mouse model of breast cancer metastasis to the brain. *Magn Reson Med.* 2006;56:1001–10. <https://doi.org/10.1002/mrm.21029>.
17. Nourshargh S, Alon R. Leukocyte migration into inflamed tissues. *Immunity.* 2014;41:694–707. <https://doi.org/10.1016/j.immuni.2014.10.008>.
18. Ley K, Laudanna C, Cybulsky MI, Nourshargh S. Getting to the site of inflammation: the leukocyte adhesion cascade updated. *Nat Rev Immunol.* 2007;7:678–89. <https://doi.org/10.1038/nri2156>.
19. Muller WA. Getting leukocytes to the site of inflammation. *Vet Pathol.* 2013;50:7–22. <https://doi.org/10.1177/0300985812469883>.
20. Jefferson A, Ruparelia N, Choudhury RP. Exogenous microparticles of iron oxide bind to activated endothelial cells but, unlike monocytes, do not trigger an endothelial response. *Theranostics.* 2013;3:428–36. <https://doi.org/10.7150/thno.5895>.
21. McAteer MA, Sibson NR, von zur Muhlen C, Schneider JE, Lowe AS, Warrick N, et al. In vivo magnetic resonance imaging of acute brain inflammation using microparticles of iron oxide. *Nat Med.* 2007;13:1253–8. <https://doi.org/10.1038/nm1631>.
22. Compston A, Coles A. Multiple sclerosis. *Lancet.* 2008;372:1502–17. [https://doi.org/10.1016/S0140-6736\(08\)61620-7](https://doi.org/10.1016/S0140-6736(08)61620-7).
23. Lucchinetti CF, Popescu BFG, Bunyan RF, Moll NM, Roemer SF, Lassmann H, et al. Inflammatory cortical demyelination in early multiple sclerosis. *N Engl J Med.* 2011;365:2188–97. <https://doi.org/10.1056/NEJMoa1100648>.
24. Lassmann H. Pathogenic mechanisms associated with different clinical courses of multiple sclerosis. *Front Immunol.* 2019;9. <https://doi.org/10.3389/fimmu.2018.03116>.
25. Trip SA, Miller DH. Imaging in multiple sclerosis. *J Neurol Neurosurg Psychiatry.* 2005;76:iii11–8. <https://doi.org/10.1136/jnnp.2005.073213>.
26. Hartung H-P, Reiners K, Archelos JJ, Michels M, Seeltrayers P, Heidenreich F, et al. Circulating adhesion molecules and tumor necrosis factor receptor in multiple sclerosis: correlation with magnetic resonance imaging. *Ann Neurol.* 1995;38:186–93. <https://doi.org/10.1002/ana.410380210>.
27. Cannella B, Raine CS. The adhesion molecule and cytokine profile of multiple sclerosis lesions. *Ann Neurol.* 1995;37:424–35. <https://doi.org/10.1002/ana.410370404>.
28. Kuwahara H, Nishina K, Yokota T. Blood-brain barrier: a novel therapeutic target in multiple sclerosis. *Clin Exp Neuroimmunol.* 2015;6:129–38. <https://doi.org/10.1111/cen3.12212>.
29. Blezer ELA, Deddens LH, Kooij G, Drexhage J, van der Pol SMA, Reijkerkerk A, et al. In vivo MR imaging of intercellular adhesion molecule-1 expression in an animal model of multiple sclerosis. *Contrast Media Mol Imaging.* 2015;10:111–21. <https://doi.org/10.1002/cmmi.1602>.

30. Gauberti M, Montagne A, Quenault A, Vivien D. Molecular magnetic resonance imaging of brain-immune interactions. *Front Cell Neurosci.* 2014;8. <https://doi.org/10.3389/fncel.2014.00389>.
31. Mardiguian S, Serres S, Ladds E, Campbell SJ, Wilainam P, McFadyen C, et al. Anti-IL-17A treatment reduces clinical score and VCAM-1 expression detected by in vivo magnetic resonance imaging in chronic relapsing EAE ABH mice. *Am J Pathol.* 2013;182:2071–81. <https://doi.org/10.1016/j.ajpath.2013.02.029>.
32. Serres S, Mardiguian S, Campbell SJ, McAteer MA, Akhtar A, Krapitchev A, et al. VCAM-1-targeted magnetic resonance imaging reveals subclinical disease in a mouse model of multiple sclerosis. *FASEB J.* 2011;25:4415–22. <https://doi.org/10.1096/fj.11-183772>.
33. Towner RA, Smith N, Zalles M, Morris S, Toliver M, Saunders D, et al. ELTD1 as a biomarker for multiple sclerosis: pre-clinical molecular-targeted studies in a mouse experimental autoimmune encephalomyelitis model. *Mult Scler Relat Disord.* 2021;49:102786. <https://doi.org/10.1016/j.msard.2021.102786>.
34. van Kasteren SI, Campbell SJ, Serres S, Anthony DC, Sibson NR, Davis BG. Glycananoparticles allow pre-symptomatic in vivo imaging of brain disease. *Proc Natl Acad Sci.* 2009;106:18–23. <https://doi.org/10.1073/pnas.0806787106>.
35. Fournier AP, Quenault A, Martinez de Lizarrondo S, Gauberti M, Defer G, Vivien D, et al. Prediction of disease activity in models of multiple sclerosis by molecular magnetic resonance imaging of P-selectin. *Proc Natl Acad Sci.* 2017;114:6116–21. <https://doi.org/10.1073/pnas.1619424114>.
36. Sathiyadan K, Coisne C, Enzmann G, Deutsch U, Engelhardt B. PSGL-1 and E/P-selectins are essential for T-cell rolling in inflamed CNS microvessels but dispensable for initiation of EAE. *Eur J Immunol.* 2014;44:2287–94. <https://doi.org/10.1002/eji.201344214>.
37. Carrithers MD, Visintin I, Kang SJ, Janeway CA. Differential adhesion molecule requirements for immune surveillance and inflammatory recruitment. *Brain.* 2000;123:1092–101. <https://doi.org/10.1093/brain/123.6.1092>.
38. Sobel RA, Mitchell ME, Fondren G. Intercellular adhesion molecule-1 (ICAM-1) in cellular immune reactions in the human central nervous system. *Am J Pathol.* 1990;136:1309–16.
39. Cannella B, Cross AH, Raine CS. Upregulation and coexpression of adhesion molecules correlate with relapsing autoimmune demyelination in the central nervous system. *J Exp Med.* 1990;172:1521–4. <https://doi.org/10.1084/jem.172.5.1521>.
40. Kelly PJ, Lemmens R, Tsvigoulis G. Inflammation and stroke risk: a new target for prevention. *Stroke.* 2021;52:2697–706. <https://doi.org/10.1161/STROKEAHA.121.034388>.
41. Conen D, Ridker PM, Everett BM, Tedrow UB, Rose L, Cook NR, et al. A multimarker approach to assess the influence of inflammation on the incidence of atrial fibrillation in women. *Eur Heart J.* 2010;31:1730–6. <https://doi.org/10.1093/eurheartj/ehq146>.
42. Jin AY, Tuor UI, Rushforth D, Filfil R, Kaur J, Ni F, et al. Magnetic resonance molecular imaging of post-stroke neuroinflammation with a P-selectin targeted iron oxide nanoparticle. *Contrast Media Mol Imaging.* 2009;4:305–11. <https://doi.org/10.1002/cmmi.292>.
43. Hoyte LC, Brooks KJ, Nagel S, Akhtar A, Chen R, Mardiguian S, et al. Molecular magnetic resonance imaging of acute vascular cell adhesion molecule-1 expression in a mouse model of cerebral ischemia. *J Cereb Blood Flow Metab.* 2010;30:1178–87. <https://doi.org/10.1038/jcbfm.2009.287>.
44. Gauberti M, Montagne A, Marcos-Contreras OA, Le Béhot A, Maubert E, Vivien D. Ultra-sensitive molecular MRI of vascular cell adhesion molecule-1 reveals a dynamic inflammatory penumbra after strokes. *Stroke.* 2013;44:1988–96. <https://doi.org/10.1161/STROKEAHA.111.000544>.
45. Deddens LH, van Tilborg GAF, van der Toorn A, van der Marel K, Paulis LEM, van Bloois L, et al. MRI of ICAM-1 upregulation after stroke: the importance of choosing the appropriate target-specific particulate contrast agent. *Mol Imaging Biol.* 2013;15:411–22. <https://doi.org/10.1007/s11307-013-0617-z>.

46. Deddens LH, van Tilborg GAF, van der Marel K, Hunt H, van der Toorn A, Viergever MA, et al. In vivo molecular MRI of ICAM-1 expression on endothelium and leukocytes from subacute to chronic stages after experimental stroke. *Transl Stroke Res.* 2017;8:440–8. <https://doi.org/10.1007/s12975-017-0536-4>.
47. Quenault A, Martinez de Lizarondo S, Etard O, Gauberti M, Orset C, Haelewyn B, et al. Molecular magnetic resonance imaging discloses endothelial activation after transient ischaemic attack. *Brain.* 2017;140:146–57. <https://doi.org/10.1093/brain/aww260>.
48. Gauberti M, De Lizarondo SM, Vivien D. The “inflammatory penumbra” in ischemic stroke: From clinical data to experimental evidence. *Eur Stroke J.* 2016;1:20–7. <https://doi.org/10.1177/2396987316630249>.
49. Spera PA, Ellison JA, Feuerstein GZ, Barone FC. IL-10 reduces rat brain injury following focal stroke. *Neurosci Lett.* 1998;251:189–92. [https://doi.org/10.1016/S0304-3940\(98\)00537-0](https://doi.org/10.1016/S0304-3940(98)00537-0).
50. Maglinger B, Sands M, Frank JA, McLouth CJ, Trout AL, Roberts JM, et al. Intracranial VCAM1 at time of mechanical thrombectomy predicts ischemic stroke severity. *J Neuroinflammation.* 2021;18:109. <https://doi.org/10.1186/s12974-021-02157-4>.
51. Zhang R-L, Chopp M, Zaloga C, Zhang ZG, Jiang N, Gautam SC, et al. The temporal profiles of ICAM-1 protein and mRNA expression after transient MCA occlusion in the rat. *Brain Res.* 1995;682:182–8. [https://doi.org/10.1016/0006-8993\(95\)00346-R](https://doi.org/10.1016/0006-8993(95)00346-R).
52. Shyu K-G, Chang H, Lin C-C. Serum levels of intercellular adhesion molecule-1 and E-selectin in patients with acute ischaemic stroke. *J Neurol.* 1997;244:90–3. <https://doi.org/10.1007/s004150050055>.
53. Duffy BA, Choy M, Riegler J, Wells JA, Anthony DC, Scott RC, et al. Imaging seizure-induced inflammation using an antibody targeted iron oxide contrast agent. *NeuroImage.* 2012;60:1149–55. <https://doi.org/10.1016/j.neuroimage.2012.01.048>.
54. Serres S, Soto MS, Hamilton A, McAteer MA, Carbonell WS, Robson MD, et al. Molecular MRI enables early and sensitive detection of brain metastases. *Proc Natl Acad Sci.* 2012;109:6674–9. <https://doi.org/10.1073/pnas.1117412109>.
55. Cheng VWT, de Pennington N, Zakaria R, Larkin JR, Serres S, Sarkar M, et al. VCAM-1-targeted MRI improves detection of the tumor-brain interface. *Clin Cancer Res.* 2022;OF1–12. <https://doi.org/10.1158/1078-0432.CCR-21-4011>.
56. Montagne A, Gauberti M, Macrez R, Jullienne A, Briens A, Raynaud J-S, et al. Ultra-sensitive molecular MRI of cerebrovascular cell activation enables early detection of chronic central nervous system disorders. *NeuroImage.* 2012;63:760–70. <https://doi.org/10.1016/j.neuroimage.2012.07.018>.
57. Amhaoul H, Staelens S, Dedeurwaerdere S. Imaging brain inflammation in epilepsy. *Neuroscience.* 2014;279:238–52. <https://doi.org/10.1016/j.neuroscience.2014.08.044>.
58. Vezzani A, Balosso S, Ravizza T. Neuroinflammatory pathways as treatment targets and biomarkers in epilepsy. *Nat Rev Neurol.* 2019;15:459–72. <https://doi.org/10.1038/s41582-019-0217-x>.
59. Pauletti A, Terrone G, Shekh-Ahmad T, Salamone A, Ravizza T, Rizzi M, et al. Targeting oxidative stress improves disease outcomes in a rat model of acquired epilepsy. *Brain.* 2019;142:e39. <https://doi.org/10.1093/brain/awz130>.
60. Ravizza T, Gagliardi B, Noé F, Boer K, Aronica E, Vezzani A. Innate and adaptive immunity during epileptogenesis and spontaneous seizures: evidence from experimental models and human temporal lobe epilepsy. *Neurobiol Dis.* 2008;29:142–60. <https://doi.org/10.1016/j.nbd.2007.08.012>.
61. Aronica E, Crino PB. Inflammation in epilepsy: clinical observations. *Epilepsia.* 2011;52:26–32. <https://doi.org/10.1111/j.1528-1167.2011.03033.x>.
62. Bogdanović RM, Syvänen S, Michler C, Russmann V, Eriksson J, Windhorst AD, et al. (R)-[¹¹C]PK11195 brain uptake as a biomarker of inflammation and antiepileptic drug resistance: evaluation in a rat epilepsy model. *Neuropharmacology.* 2014;85:104–12. <https://doi.org/10.1016/j.neuropharm.2014.05.002>.

63. Li LM, Fish DR, Sisodiya SM, Shorvon SD, Alsanjari N, Stevens JM. High resolution magnetic resonance imaging in adults with partial or secondary generalised epilepsy attending a tertiary referral unit. *J Neurol Neurosurg Psychiatry*. 1995;59:384–7. <https://doi.org/10.1136/jnnp.59.4.384>.
64. Cascino GD, Jack CR, Parisi JE, Sharbrough FW, Hirschorn KA, Meyer FB, et al. Magnetic resonance imaging-based volume studies in temporal lobe epilepsy: pathological correlations. *Ann Neurol*. 1991;30:31–6. <https://doi.org/10.1002/ana.410300107>.
65. Peixoto-Santos JE, de Carvalho LED, Kandratavicius L, Diniz PRB, Scanduzzi RC, Coras R, et al. Manual hippocampal subfield segmentation using high-field MRI: impact of different subfields in hippocampal volume loss of temporal lobe epilepsy patients. *Front Neurol*. 2018;9 <https://doi.org/10.3389/fneur.2018.00927>.
66. Fabene PF, Mora GN, Martinello M, Rossi B, Merigo F, Ottoboni L, et al. A role for leukocyte-endothelial adhesion mechanisms in epilepsy. *Nat Med*. 2008;14:1377–83. <https://doi.org/10.1038/nm.1878>.
67. WHO. World Health Organization Health Topics Cancer. 2021;
68. Achrol AS, Rennert RC, Anders C, Soffiatti R, Ahluwalia MS, Nayak L, et al. Brain metastases. *Nat Rev Dis Prim*. 2019;5:5. <https://doi.org/10.1038/s41572-018-0055-y>.
69. Steeg PS. The blood–tumour barrier in cancer biology and therapy. *Nat Rev Clin Oncol*. 2021;18:696–714. <https://doi.org/10.1038/s41571-021-00529-6>.
70. Stelzer KJ. Epidemiology and prognosis of brain metastases. *Surg Neurol Int*. 2013;4:192. <https://doi.org/10.4103/2152-7806.111296>.
71. Mehrabian H, Detsky J, Soliman H, Sahgal A, Stanisz GJ. Advanced magnetic resonance imaging techniques in Management of Brain Metastases. *Front Oncol*. 2019;9. <https://doi.org/10.3389/fonc.2019.00440>.
72. Khatib AM, Kontogiannea M, Fallavollita L, Jamison B, Meterissian S, Brodt P. Rapid induction of cytokine and E-selectin expression in the liver in response to metastatic tumor cells. *Cancer Res*. 1999;59:1356–61.
73. Läubli H, Borsig L. Selectins as mediators of lung metastasis. *Cancer Microenviron*. 2010;3: 97–105. <https://doi.org/10.1007/s12307-010-0043-6>.
74. Vidal-Vanaclocha F, Fantuzzi G, Mendoza L, Fuentes AM, Anasagasti MJ, Martín J, et al. IL-18 regulates IL-1 β -dependent hepatic melanoma metastasis via vascular cell adhesion molecule-1. *Proc Natl Acad Sci*. 2000;97:734–9. <https://doi.org/10.1073/pnas.97.2.734>.
75. Carbonell WS, Ansorge O, Sibson N, Muschel R. The vascular basement membrane as “soil” in brain metastasis. Cordes N, editor. *PLoS One*. 2009;4:e5857. <https://doi.org/10.1371/journal.pone.0005857>.
76. Strell C, Entschladen F. Extravasation of leukocytes in comparison to tumor cells. *Cell Commun Signal*. 2008;6:10. <https://doi.org/10.1186/1478-811X-6-10>.
77. Soto MS, Serres S, Anthony DC, Sibson NR. Functional role of endothelial adhesion molecules in the early stages of brain metastasis. *Neuro-Oncology*. 2014;16:540–51. <https://doi.org/10.1093/neuonc/not222>.
78. Cheng VWT, Soto MS, Khrapitchev AA, Perez-Balderas F, Zakaria R, Jenkinson MD, et al. VCAM-1–targeted MRI enables detection of brain micrometastases from different primary Tumors. *Clin Cancer Res*. 2019;25:533–43. <https://doi.org/10.1158/1078-0432.CCR-18-1889>.
79. Lyck R, Lécuyer M-A, Abadier M, Wyss CB, Matti C, Rosito M, et al. ALCAM (CD166) is involved in extravasation of monocytes rather than T cells across the blood–brain barrier. *J Cereb Blood Flow Metab*. 2017;37:2894–909. <https://doi.org/10.1177/0271678X16678639>.
80. Masedunskas A, King JA, Tan F, Cochran R, Stevens T, Sviridov D, et al. Activated leukocyte cell adhesion molecule is a component of the endothelial junction involved in transendothelial monocyte migration. *FEBS Lett*. 2006;580:2637–45. <https://doi.org/10.1016/j.febslet.2006.04.013>.

81. Michel L, Grasmuck C, Charabati M, Lécuyer M-A, Zandee S, Dhazez T, et al. Activated leukocyte cell adhesion molecule regulates B lymphocyte migration across central nervous system barriers. *Sci Transl Med*. 2019;11. <https://doi.org/10.1126/scitranslmed.aaw0475>.
82. Zarghami N, Soto MS, Perez-Balderas F, Khrapitchev AA, Karali CS, Johansen VA, et al. A novel molecular magnetic resonance imaging agent targeting activated leukocyte cell adhesion molecule as demonstrated in mouse brain metastasis models. *J Cereb Blood Flow Metab*. 2021;41:1592–607. <https://doi.org/10.1177/0271678X20968943>.
83. Burdick MM, Henson KA, Delgadillo LF, Choi YE, Goetz DJ, Tees DFJ, et al. Expression of E-selectin ligands on circulating tumor cells: cross-regulation with cancer stem cell regulatory pathways? *Front Oncol*. 2012;2. <https://doi.org/10.3389/fonc.2012.00103>.
84. Jassam S, Maheraly Z, Smith J, Ashkan K, Roncaroli F, Fillmore H, et al. CD15s/CD62E interaction mediates the adhesion of non-small cell lung cancer cells on brain endothelial cells: implications for cerebral metastasis. *Int J Mol Sci*. 2017;18:1474. <https://doi.org/10.3390/ijms18071474>.
85. Barber PA, Foniok T, Kirk D, Buchan AM, Laurent S, Boutry S, et al. MR molecular imaging of early endothelial activation in focal ischemia. *Ann Neurol*. 2004;56:116–20. <https://doi.org/10.1002/ana.20162>.
86. Zarghami N. Novel molecular MRI approaches to the detection of brain metastasis. University of Oxford; 2019.
87. Ren X, Ghassemi P, Babahosseini H, Strobl JS, Agah M. Single-cell mechanical characteristics analyzed by multiconstriction microfluidic channels. *ACS Sensors*. 2017;2:290–9. <https://doi.org/10.1021/acssensors.6b00823>.
88. Leng F, Edison P. Neuroinflammation and microglial activation in Alzheimer disease: where do we go from here? *Nat Rev Neurol*. 2021;17:157–72. <https://doi.org/10.1038/s41582-020-00435-y>.
89. Heppner FL, Ransohoff RM, Becher B. Immune attack: the role of inflammation in Alzheimer disease. *Nat Rev Neurosci*. 2015;16:358–72. <https://doi.org/10.1038/nrn3880>.
90. Grammas P. Neurovascular dysfunction, inflammation and endothelial activation: implications for the pathogenesis of Alzheimer's disease. *J Neuroinflammation*. 2011;8:26. <https://doi.org/10.1186/1742-2094-8-26>.
91. Feigin VL, Vos T, Alahdab F, Amit AML, Bärnighausen TW, Beghi E, et al. Burden of neurological disorders across the US from 1990–2017. *JAMA Neurol*. 2021;78:165. <https://doi.org/10.1001/jamaneurol.2020.4152>.
92. von zur Muhlen C, Sibson NR, Peter K, Campbell SJ, Wilainam P, Grau GE, et al. A contrast agent recognizing activated platelets reveals murine cerebral malaria pathology undetectable by conventional MRI. *J Clin Invest*. 2008; <https://doi.org/10.1172/JCI33314>.
93. von zur Muhlen C, Peter K, Ali ZA, Schneider JE, McAteer MA, Neubauer S, et al. Visualization of activated platelets by targeted magnetic resonance imaging utilizing conformation-specific antibodies against glycoprotein IIb/IIIa. *J Vasc Res*. 2009;46:6–14. <https://doi.org/10.1159/000135660>.
94. von zur Muhlen C, von Elverfeldt D, Moeller JA, Choudhury RP, Paul D, Hagemeyer CE, et al. Magnetic resonance imaging contrast agent targeted toward activated platelets allows in vivo detection of thrombosis and monitoring of thrombolysis. *Circulation*. 2008;118:258–67. <https://doi.org/10.1161/CIRCULATIONAHA.107.753657>.
95. Maier A, Braig M, Jakob K, Bienert T, Schäper M, Merkle A, et al. Molecular magnetic resonance imaging of activated platelets allows noninvasive detection of early myocarditis in mice. *Sci Rep*. 2020;10:13211. <https://doi.org/10.1038/s41598-020-70043-9>.
96. Belliere J, Martinez de Lizarrondo S, Choudhury RP, Quenault A, Le Béhot A, Delage C, et al. Unmasking silent endothelial activation in the cardiovascular system using molecular magnetic resonance imaging. *Theranostics*. 2015;5:1187–202. <https://doi.org/10.7150/thno.11835>.
97. McAteer MA, Schneider JE, Ali ZA, Warrick N, Bursill CA, von zur Muhlen C, et al. Magnetic resonance imaging of endothelial adhesion molecules in mouse atherosclerosis

- using dual-targeted microparticles of iron oxide. *Arterioscler Thromb Vasc Biol.* 2008;28:77–83. <https://doi.org/10.1161/ATVBAHA.107.145466>.
98. Akhtar AM, Schneider JE, Chapman SJ, Jefferson A, Digby JE, Mankia K, et al. In vivo quantification of VCAM-1 expression in renal ischemia reperfusion injury using non-invasive magnetic resonance molecular imaging. Fadini GP, editor. *PLoS One.* 2010;5:e12800. <https://doi.org/10.1371/journal.pone.0012800>.
99. Fournier AP, Martinez de Lizarondo S, Rateau A, Gerard-Brisou A, Waldner MJ, Neurath MF, et al. Ultrasensitive molecular imaging of intestinal mucosal inflammation using leukocyte-mimicking particles targeted to MAdCAM-1 in mice. *Sci Transl Med.* 2020;12. <https://doi.org/10.1126/scitranslmed.aaz4047>.
100. Biederer J. General requirements of MRI of the lung and suggested standard protocol. In: Kauczor H-U, Wielpütz M, editors. *MRI Lung.* Cham: Springer International Publishing; 2017. p. 1–20. https://doi.org/10.1007/174_2017_98.
101. Chesebro AG, Amarante E, Lao PJ, Meier IB, Mayeux R, Brickman AM. Automated detection of cerebral microbleeds on T2*-weighted MRI. *Sci Rep.* 2021;11:4004. <https://doi.org/10.1038/s41598-021-83607-0>.
102. Gaberel T, Gakuba C, Hebert M, Montagne A, Agin V, Rubio M, et al. Intracerebral hematomas disappear on T2*-weighted images during normobaric oxygen therapy. *Stroke.* 2013;44:3482–9. <https://doi.org/10.1161/STROKEAHA.113.002045>.
103. Goulay R, Drieu A, Di Palma C, Pro-Sistiaga P, Delcroix N, Chazalviel L, et al. Modification of apparent intracerebral hematoma volume on T2 * –weighted images during normobaric oxygen therapy may contribute to false diagnosis. *J Clin Neurosci.* 2018;52:105–8. <https://doi.org/10.1016/j.jocn.2018.01.046>.
104. Chen Z, Ding J, Wu X, Bao B, Cao X, Wu X, et al. Safety and efficacy of normobaric oxygenation on rescuing acute intracerebral hemorrhage-mediated brain damage—a protocol of randomized controlled trial. *Trials.* 2021;22:93. <https://doi.org/10.1186/s13063-021-05048-4>.
105. Corroyer-Dulmont A, Valable S, Falzone N, Frelin-Labalme A-M, Tietz O, Toutain J, et al. VCAM-1 targeted alpha-particle therapy for early brain metastases. *Neuro-Oncology.* 2020;22:357–68. <https://doi.org/10.1093/neuonc/noz169>.
106. Cooley M, Sarode A, Hoore M, Fedosov DA, Mitragotri S, Sen GA. Influence of particle size and shape on their margination and wall-adhesion: implications in drug delivery vehicle design across nano-to-micro scale. *Nanoscale.* 2018;10:15350–64. <https://doi.org/10.1039/C8NR04042G>.
107. Gentile F, Curcio A, Indolfi C, Ferrari M, Decuzzi P. The margination propensity of spherical particles for vascular targeting in the microcirculation. *J Nanobiotechnol.* 2008;6:9. <https://doi.org/10.1186/1477-3155-6-9>.
108. Charoenphol P, Mocherla S, Bouis D, Namdee K, Pinsky DJ, Eniola-Adefeso O. Targeting therapeutics to the vascular wall in atherosclerosis—carrier size matters. *Atherosclerosis.* 2011;217:364–70. <https://doi.org/10.1016/j.atherosclerosis.2011.04.016>.
109. Charoenphol P, Onyskiw PJ, Carrasco-Teja M, Eniola-Adefeso O. Particle-cell dynamics in human blood flow: implications for vascular-targeted drug delivery. *J Biomech.* 2012;45:2822–8. <https://doi.org/10.1016/j.jbiomech.2012.08.035>.
110. Lee T-R, Choi M, Kopacz AM, Yun S-H, Liu WK, Decuzzi P. On the near-wall accumulation of injectable particles in the microcirculation: smaller is not better. *Sci Rep.* 2013;3:2079. <https://doi.org/10.1038/srep02079>.

111. Fish MB, Banka AL, Braunreuther M, Fromen CA, Kelley WJ, Lee J, et al. Deformable microparticles for shuttling nanoparticles to the vascular wall. *Sci Adv.* 2021;7. <https://doi.org/10.1126/sciadv.abe0143>.
112. Nkansah MK, Thakral D, Shapiro EM. Magnetic poly(lactide- co -glycolide) and cellulose particles for MRI-based cell tracking. *Magn Reson Med.* 2011;65:1776–85. <https://doi.org/10.1002/mrm.22765>.
113. Perez-Balderas F, van Kasteren SI, Aljabali AAA, Wals K, Serres S, Jefferson A, et al. Covalent assembly of nanoparticles as a peptidase-degradable platform for molecular MRI. *Nat Commun.* 2017;8:14254. <https://doi.org/10.1038/ncomms14254>.
114. Wijesurendra RS, Jefferson A, Choudhury RP. Target: ligand interactions of the vascular endothelium. Implications for molecular imaging in inflammation. *Integr Biol.* 2010;2:467–82. <https://doi.org/10.1039/c0ib00022a>.

Ultrasound Imaging in Inflammation Research



Matthew Muller, Jonathan R. Lindner, and Matthew W. Hagen

Abstract Ultrasound is a well-established and widely used tool for both clinical diagnosis and preclinical research. In this chapter, we review the physics behind and applications of 2D, Doppler, and contrast-enhanced ultrasound. Our focus will be the research applications of contrast-enabled molecular imaging of inflammatory mediators as a tool for understanding atherosclerosis and ischemic memory. We will also cover the use of ultrasound in the diagnosis of and research on inflammatory conditions including rheumatoid arthritis and renal failure. Our work and others' demonstrate the continued place of ultrasound at the cutting edge of biomedical practice and research.

Keywords Contrast ultrasound · Microbubbles · Molecular imaging · Ultrasound

1 Introduction

Ultrasound is a versatile noninvasive medical imaging approach that is used extensively to measure tissue or organ structure, function, and blood flow. Advantages that ultrasound has over other advanced imaging modalities such as MRI and CT include the low cost of services, the speed of imaging protocols, and safety. In this chapter, we will discuss some of the approaches used to image ultrasound through anatomic imaging or acoustic characterization of tissue content or by the ultrasound

M. Muller · M. W. Hagen
Knight Cardiovascular Institute, Oregon Health & Science University, Portland, OR, USA

J. R. Lindner (✉)
Knight Cardiovascular Institute, Oregon Health & Science University, Portland, OR, USA
Oregon National Primate Research Center, Oregon Health & Science University, Portland, OR, USA

Robert M. Berne Cardiovascular Research Center, University of Virginia Health System, Charlottesville, VA, USA

Cardiovascular Division, University of Virginia Health System, Charlottesville, VA, USA
e-mail: jlindner@virginia.edu

detection of acoustically active contrast agents that have been specifically designed to assess the molecular and cellular signatures of inflammation within the vascular compartment. We will also highlight some examples of where ultrasound-based imaging of inflammation is likely to be impactful in clinical care.

1.1 *Ultrasound Physics*

Ultrasound is characterized by the fluctuation of pressures that travel through a tissue at frequencies above the audible range. These pressure fluctuations are produced by a transducer housing piezoelectric elements. For most 2D and Doppler ultrasound imaging systems used in medicine, these elements are fired in specific sequences to produce focused or steered “lines” of ultrasound to cover a defined 3D volume. The acoustic field is divided into three planes illustrated in Fig. 1: axial,

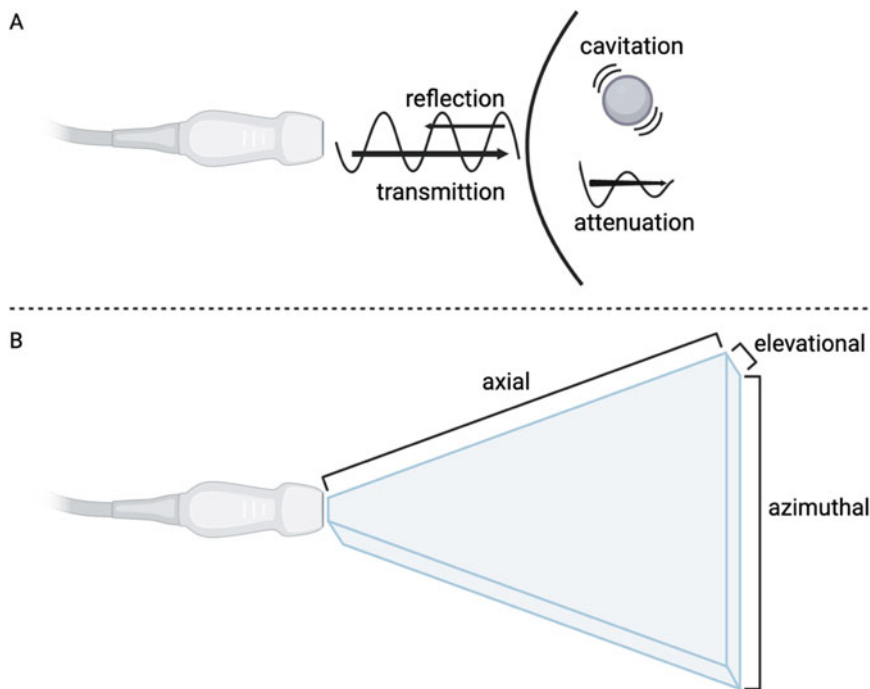


Fig. 1 (a) An illustration of ultrasound physics at a surface defined by a difference in acoustic impedance. The ultrasound wave is partially reflected and backscattered, as well as transmitted through the media. Some ultrasound energy will be attenuated and absorbed. Ultrasound that encounters microbubble contrast agents causes cavitation. (b) The axial, azimuthal, and elevational planes of an ultrasound image are shown. In 2D imaging, the elevational planes are compounded to create a 2D image along the axial and azimuthal dimensions. For 3D imaging, the elevational pulses are rastered sequentially

azimuthal (lateral), and elevational [1]. The axial plane is parallel to the ultrasound direction, while the azimuthal plane defines the width of each ultrasound line used to produce an image. The elevational plane describes the “thickness” of the ultrasound line or plane. The elevational volume is generally compounded to produce a 2D display. 3D imaging is generally accomplished by rastering sequential 2D planes or complex protocols for retrospective beam forming from large transmit volumes.

Diagnostic ultrasound is conventionally transmitted in frequencies in the MHz scale [2]. Ultrasound power is quantified by mechanical index (MI) defined by the peak negative acoustic pressure of the ultrasound wave divided by the square root of the transmission frequency. This is an important variable in determining the safety and usage of ultrasound. As ultrasound pressure waves travel through a medium, some of their energy is attenuated and absorbed, and some of the energy is reflected back (Fig. 1), particularly at boundaries between areas of differing acoustic impedances, which is determined by the density and speed of sound through the media. Relative extremes in acoustic impedance, such as solids (bone) or gasses, can cause shadowing by limiting acoustic transmission [1]. Ultrasound that is reflected at a relative difference in acoustic impedance is partially reflected and backscattered. Backscattered ultrasound is received by the ultrasound transducer and processed to create an image using the difference of the transmitted ultrasound compared to the backscattered signal.

1.2 *Ultrasound Modalities*

B-mode ultrasound imaging involves sending out several lines of ultrasound to produce a 2D image based on the location and strength of the returning echo signal. Information on B-mode imaging is influenced not only by tissue characteristics but also ultrasound settings such as power (acoustic amplitude), frequency, pulse duration (cycle number), dynamic focusing, gain, post-processing algorithms, and transducer characteristics such as aperture. Figure 2 shows B-mode imaging of the LV outflow leading into the aortic arch in a nonhuman primate.

Doppler ultrasound can be subdivided into multiple categories, the most common of which are pulsed-wave (PW) Doppler, continuous wave (CW) Doppler, and color Doppler. Doppler modalities are based on the Doppler effect. When an ultrasound wave encounters a moving target such as flowing blood, its frequency is shifted depending on the directionality of the flow [3]. Flow away from the transducer and origin of ultrasound propagation will result in a decrease in ultrasound frequency, whereas blood flow toward a transducer and point of propagation will increase ultrasound frequency. Knowing the initial frequency of the ultrasound, this basic principle allows us to determine the flow velocity in the vector component that is in line with the ultrasound transducer.

PW Doppler allows for velocity measurements at a specific user-chosen axial and lateral region within an ultrasound field. This chosen location is named the volume or gate, and only flow through this region will be quantified [4]. This is

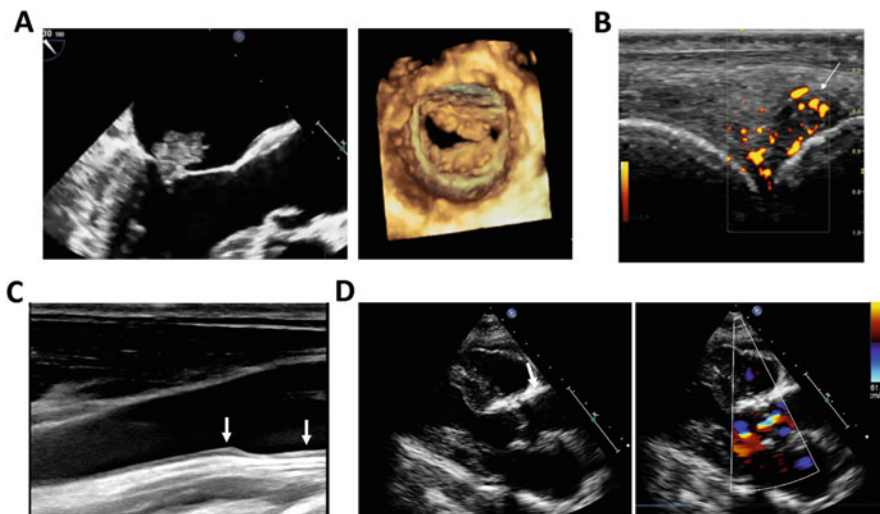


Fig. 2 B-mode and Doppler ultrasound imaging of inflammatory conditions. **(a)** Images illustrating thromboinflammatory “marantic” abnormalities of the mitral valve secondary to systemic lupus erythematosus (Libman-Sacks endocarditis). These lesions are manifest as either a focal mass (arrow) on the anterior mitral leaflet on 2D transesophageal echo (left panel) or diffuse nodular thickening of the valve seen on 3D imaging (right panel). **(b)** Two-dimensional ultrasound and power-harmonic Doppler imaging of a metacarpophalangeal joint illustrating synovial thickening and hyperemia in arthritis (image courtesy of Dr. Catherine Bakewell, MD). **(c)** Long-axis 2D ultrasound imaging showing intimal media thickening and early plaque formation at the carotid bifurcation and proximal external carotid artery. **(d)** Transthoracic echocardiography in the parasternal long-axis view showing post-radiation inflammatory and fibrotic changes of the basal septum (arrow), aortic valve, and proximal aorta which appear echo bright (left panel) and secondary aortic insufficiency from valve involvement on color Doppler imaging illustrated by retrograde flow at the aortic valve (right panel). Images © 2022, The Authors

accomplished by sending out short pulses of ultrasound to allow each pulse to return to the probe. Color Doppler is essentially a color display of PW Doppler ensembles, with a heat map applied according to Doppler velocities. It is used when spatial assessments of flow velocities and directions are needed (Fig. 2). CW Doppler is performed differently than PW Doppler. Instead of sending out small pulses of ultrasound to analyze a specific region, continuous Doppler relies on continuous transmission and receipt of ultrasound by neighboring groups of transducer elements. CW Doppler allows for a much larger range of velocities to be detected than PW Doppler [4]. However due to the absence of pulses (i.e., pulse-echo), spatial localization of velocities in the axial direction is not possible with CW such that this technology is used to measure maximal or peak velocities along the imaging line. Power-harmonic Doppler is a technology designed to evaluate blood flow in more distal small arteries. Accordingly, it has been proposed for detection of inflammation-related hyperemia. This technique relies on analyzing the difference in a returning packet of pulses and displaying the corresponding difference in intensity on 2D. Photoacoustic imaging has also been investigated for inflammation

imaging whereby acoustic energy produced by optical absorption from light energy (e.g., in the near-infrared frequency range) can reveal abnormalities in tissue perfusion or oxygenation [5, 6].

There has been increasing interest in using B-mode ultrasound to reveal and quantify tissue mechanical characteristics. While these applications have traditionally been targeted to detect tissue fibrosis, there is hope that they would also be able to detect tissue responses involved in early inflammation including edema. Early approaches to tissue characterization included acoustic backscatter imaging which integrates all returning frequency and amplitudes. New approaches have been developed such as acoustic radiation force imaging or shear-wave elastography that rely on the ultrasound imaging of the tissue deformation responses to a high-amplitude low-frequency pulse of sound.

Contrast-enhanced ultrasound (CEU) relies on the use of microbubbles with ultrasound. Ultrasound contrast agent microbubbles (MBs) are composed of lipid, protein (albumin), or biocompatible polymer shells and are filled with high molecular weight inert gases such as perfluorocarbons or sulfur hexafluoride. MBs used in humans typically range in diameter from 0.5 to 5 μm , permitting their intravenous injection and unimpeded passage through the pulmonary, coronary, and peripheral microcirculation [7, 8]. Signal generation from these agents occurs through stable cavitation, as shown in Fig. 3a, b, or inertial cavitation with the pressure peaks and nadirs of the ultrasound field [9, 10]. Both stable and inertial cavitation result in signal emission at harmonic frequencies, while only inertial cavitation results in the immediate destruction of the agent [10–12]. There are several applications for CEU in inflammation imaging. The first relies on the use of CEU perfusion imaging to assess inflammation-related hyperemia. The contrast improvement provided by CEU in apical four-chamber images in a patient with ischemic cardiomyopathy is shown in Fig. 3c. The other approach is CEU cellular or molecular imaging whereby inflammation imaging can be achieved through either nonspecific interactions between MBs and inflammatory cells or the development of targeted MBs that bear ligands against specific molecular markers or mediators of the innate or adaptive immune response.

2 B-Mode and Doppler Ultrasound Imaging of Inflammation

2.1 Renal B-Mode and Doppler Ultrasound Imaging

Ultrasound (B-mode, Doppler) is a routinely used technique to evaluate renal pathology. In chronic kidney disease, B-mode is used to visualize the morphology of the renal cortex, medulla, collecting systems, the presence of cysts, and the echogenicity of segmented components. Echogenicity is used to identify plaque or tissue structures through segmentation [14, 15]. Images are often taken to measure

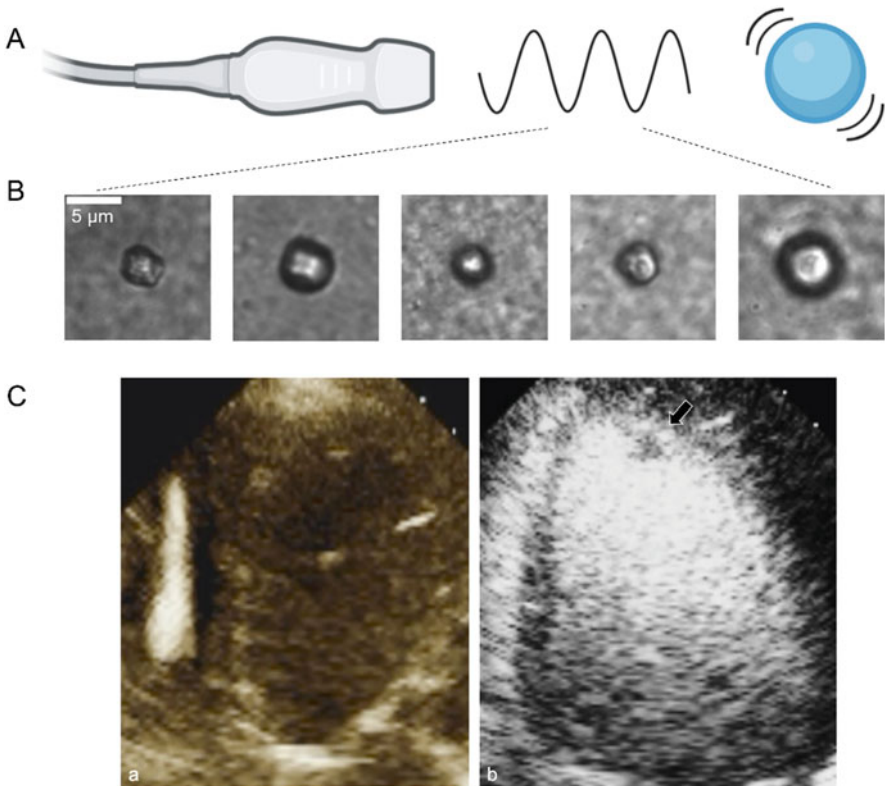


Fig. 3 Contrast-enhanced ultrasound methods. (a) schematic showing pressure peaks and nadirs during ultrasound which result in compression and expansion (oscillation) of gas-filled microbubbles which can be viewed by high-speed microscopy (b) during the different ultrasound pressure phases (images courtesy of David Giraud). (c) Intracardiac thrombus in a 58-year-old woman with known ischemic cardiomyopathy. Apical four-chamber view prior to microbubble administration (*left*) shows poor visualization of the left ventricular cavity, and following microbubble administration (*right*), the image clearly identifies a left ventricular apical thrombus (black arrow) associated with an akinetic segment seen during real-time imaging. (b) © 2022, The Authors. (c) Adapted from [13] with permission. © 2021, Kutty et al.

longitudinal diameter and cortical thickness to evaluate morphology and any irreversible damage to the renal cortex [16]. In parallel, color Doppler and spectral Doppler can be used to evaluate vascularization and vascular function within the kidney. Increased renal resistance can be an indicator of the severity of chronic kidney diseases [17, 18], including those caused by inflammatory conditions.

The use of ultrasound with acute renal failure is more limited than chronic renal failure. It is more selectively used to rule out urinary obstruction in acute renal failure [19]. In patients with acute tubular necrosis or suspected acute tubular necrosis, the kidney can appear to be within the normal range, but still edematous or inflamed [19, 20]. Severe renal allograft rejection can be diagnosed with ultrasound through

major changes in kidney size, changes in kidney echogenicity, and reductions in blood flow [19, 21]. B-mode ultrasound allows for detection of allograft swelling, morphologic changes, and loss of corticomedullary differentiation. Renal blood flow can be quantified with Doppler measurements [22]. Resistance indexes can be a useful metric to determine the vascular resistance and compliance of an allograft as well as a useful indicator of allograft outcome [23].

Ultrasound can be effective in differentiating and diagnosing cystic renal disease. Renal cysts are thought to develop within tubules through inflammatory processes such as infiltration of interstitium with mononuclear inflammatory cells or interstitial fibrosis [24]. Ultrasound can be used to identify autosomal dominant polycystic kidney disease in the absence of genotyping [25, 26]. Additionally, ultrasound can be used to identify inflamed or hemorrhagic cysts [19].

2.2 Rheumatoid Arthritis Imaging

Recognizing early indications of rheumatoid arthritis can have significant influences on the outcomes of patients with this inflammatory disorder [27]. Rheumatoid arthritis treatment has significantly benefitted from ultrasound modalities to diagnose and monitor the pathology. Diagnoses of rheumatoid arthritis can employ B-mode imaging, pulsed-wave Doppler, and color Doppler modalities. These can allow sonographers and clinicians to visualize the extent of synovitis, tenosynovitis, and bone erosion, which can serve as indicators of early or relapsing rheumatoid arthritis [28].

Synovitis can be identified using B-mode and Doppler modalities mainly in the metacarpal phalangeal joints. B-mode images allow for identification of synovitis and tenosynovitis due to the echogenic differences of tissue, interstitial fluids, and joints. Doppler modalities can identify hyperperfusion associated with inflammation [29]. According to the guidelines of the EULAR Outcome Measurements in Rheumatology US task force, findings indicating synovial hypertrophy are vital in identification of synovitis and tenosynovitis. Within the last few years, ultrasound detection of synovitis in the proximal and distal wrist interphalangeal joints, the metatarsophalangeal joints, and foot interphalangeal joints has shown to be more effective than clinical examination [6, 30]. Recently, it has been shown that synovitis and tenosynovitis serve as strong predictors of disease-modifying antirheumatic drugs (DMARDs) tapering failure in patients with chronic rheumatoid arthritis [31].

Bone erosion is commonly seen in rheumatoid arthritis and as such acts as an important target for therapeutics such as DMARDs. Ultrasound can be used to visualize bony cortex discontinuity in joints due to the differences in echogenicity of bone to surrounding tissue and fluids [32]. Discontinuity in two perpendicular planes clinically identifies the presence of bone erosion [32]. Presence of bone erosion on ultrasound evaluation after discontinuation of DMARDs predicts the relapse of rheumatoid arthritis and weakly predicts relapse after discontinuation of methotrexate in a 12-month window [33, 34].

Recently, photoacoustic imaging (see the dedicated chapter in this book) has shown promise as a noninvasive technique to recognize rheumatoid arthritis in human and preclinical trials [35, 36]. Photoacoustic imaging can effectively map 2D and 3D morphology of cartilage, synovium, vascularity, and bone tissue within human peripheral joints [37]. Additionally, it can detect clinically evident synovitis and hemodynamic properties of rheumatoid arthritis in humans. More validation is required for the efficacy of photoacoustic imaging in a clinical setting [6, 37].

2.3 *Plaque Imaging*

Based on its safety, low cost, and widespread availability, ultrasound has been used extensively in the clinical setting to assess plaque development in arteries that are easily visualized with current technology. The most common anatomic locations include the carotid arteries, the aorta, and proximal limb conduit arteries. At its most basic level, ultrasound is used to measure plaque severity in terms of dimension, which reflects inflammation-related intimal-medial hyperplasia. Indices that are measured include lumen encroachment by diameter or area narrowing, Doppler-derived pressure gradients caused by increased resistance, and plaque area or volume which takes into account outward vascular remodeling. More advanced methods have been developed that are able to reveal plaque composition through differences in acoustic characteristics of fibrous, necrotic, and calcified tissues and abnormalities in the mechanical properties of the arterial wall.

Historically, B-mode imaging of plaque size has been useful for determining when plaque is present, which influences decisions on pharmacologic therapy for primary prevention, or when arterial narrowing becomes severe enough to explain symptoms or justify procedural intervention. However, the degree of stenosis or plaque volume does not entirely reflect the atherothrombotic potential of plaque which is strongly influenced by inflammatory phenotype. Correlates between plaque composition and grayscale values within the bandpass filter range have been established for both catheter-based intravascular ultrasound (IVUS) and external ultrasound imaging. In general, low echogenicity is associated with high-lipid content or necrosis, while high echogenicity with far-field attenuation tends to signify calcification [38–42]. Using postmortem histology as a training tool, radiofrequency spectral pattern-recognition algorithms have been trained to distinguish fibrous, fibrofatty, necrotic or lipid-rich, and calcified regions that can be displayed as a high-resolution color map (Fig. 4a) [41–44]. This approach, termed IVUS virtual histology (IVUS-VH), has shown efficacy in predicting secondary major adverse cardiovascular events following acute coronary syndrome, notably often in non-culprit arteries identified as low risk by angiography [45–47]. Photoacoustic imaging alone, which can detect lipid content, or in conjunction with leukocyte-targeted photoacoustic probes, has also been used in clinical or preclinical studies to assess plaque content.

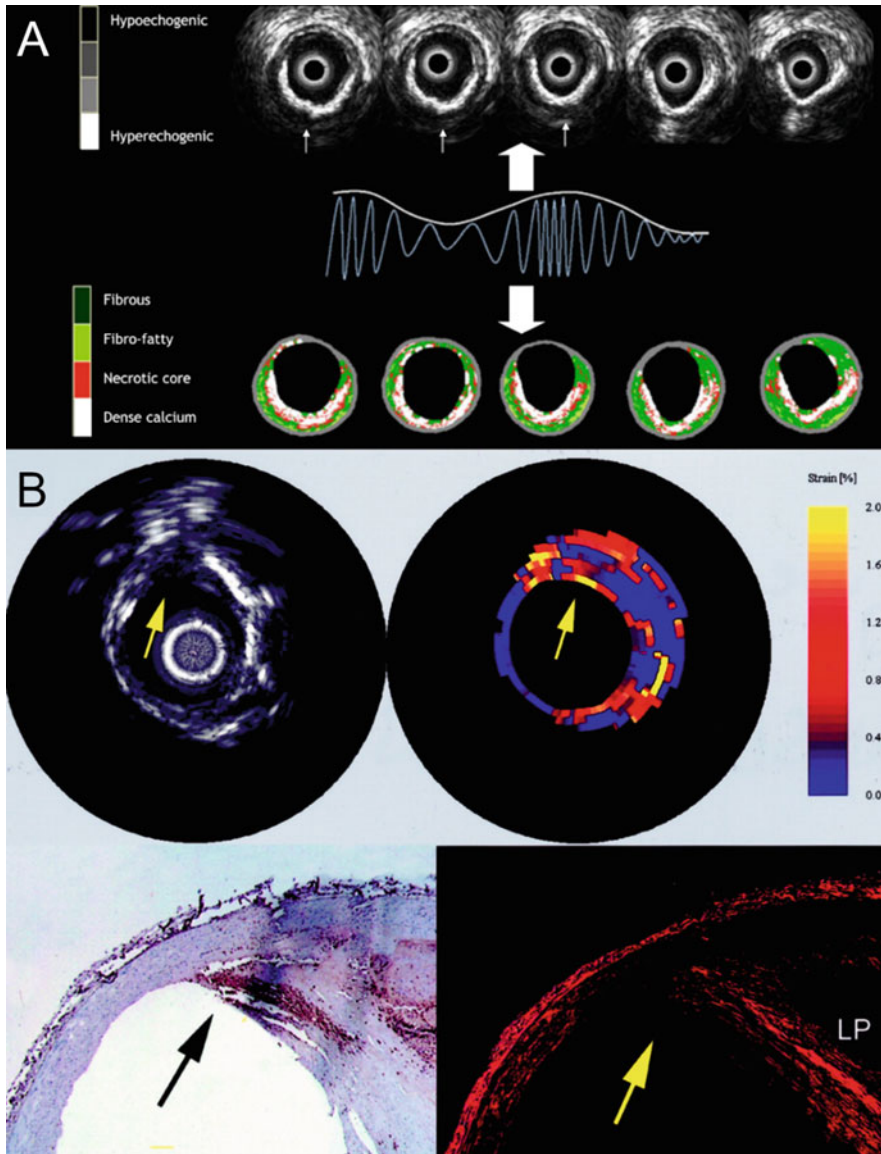


Fig. 4 Examples of “virtual histology” approaches to evaluating atherosclerotic plaque content, including necrotic and inflammatory core, using intravascular ultrasound. **(a)** Intravascular ultrasound with the raw B-mode images shown at the top (catheter denoted by the central circular object) and the color-coded virtual histology images characterizing plaque content below. Thin white arrows at the top show acoustic shadowing by calcium deposits. **(b)** Strain imaging during systole to detect abnormal mechanical properties of the vessel wall caused by plaque inflammation. Intravascular ultrasound raw data (*top left*) and corresponding map of time-domain strain information during the systolic phase (*top right*) and corresponding immunohistochemistry for macrophages (*bottom left*, dark purple areas) and smooth muscle actin (*bottom right*) illustrating increased strain in an area with high macrophage content. **(a)** modified from [44] with permission; © 2011, Gogas et al.; **(b)** modified from Schaar et al. [50] with permission. © 2003, Wolters Kluwer Health

A vessel's dynamic geometric response to biologic forces can also provide information on atherosclerotic plaque phenotype. Ultrasound has high temporal resolution, meaning that when used in conjunction with real-time measurements of vascular pressures, the elastic properties of a vessel, which change predictably during the course of plaque development based on inflammatory remodeling of the matrix, can be determined. Transmural spatial maps of elastic properties, i.e., elastography, can be obtained by speckle tracking patterns starting at the lumen boundary [48–50] (Fig. 4b).

3 Contrast-Enhanced Ultrasound (CEU) Molecular Imaging

CEU molecular imaging is accomplished using MBs which are retained in tissues based on their ability to bind to molecular targets. This targeting can be accomplished through two general approaches. The first, relatively simple approach relies on nonspecific retention of MBs through their binding to activated endothelial cells or leukocytes. The mechanisms driving this interaction include opsonization, the deposition of serum complement proteins onto the MB surface which in turn trigger leukocyte and endothelial complement receptors [51–53]. MB interaction with cells can be controlled by tuning the net charge and presence of polymeric surfactants (such as polyethylene glycol) making up the bubble surface. The presence of phosphatidylserine, a phospholipid on the outer leaflet of cell membranes that acts as a signal of senescence or apoptosis, in the MB shell can enhance attachment to activated cells through opsonization [53]. Nonspecific interactions with activated leukocytes and endothelial cells can be leveraged for general detection of the presence of inflammatory states rather than the specific targeting of any specific molecular pathway.

The second approach consists in the specific targeting of MBs, accomplished through the conjugation of specific ligands (antibodies, peptides, glycoproteins, small molecules, etc.) to the MB surface. The surface density of targeting ligands can affect attachment efficacy [54]. The binding properties of these agents under various shear stress conditions have been examined by flow chamber evaluation of MB attachment to activated cultured endothelial cells [54–57], which demonstrate an inverse relationship between endothelial attachment and shear force. Most agents have been designed with a ligand surface density on the scale of thousands per μm^2 of MB shell surface area, generally well above that needed for maximum binding at microcirculatory shear stresses (<2 dyne/cm²). Factors influencing MB adhesion to target molecules are illustrated in Fig. 5.

Studies have confirmed that the signal generated from MBs is not substantially influenced by their attachment to target cells or even their internalization by phagocytosis [58, 59]; therefore, they can be imaged using settings similar to those used for conventional CEU. Molecular imaging with CEU is generally carried out through

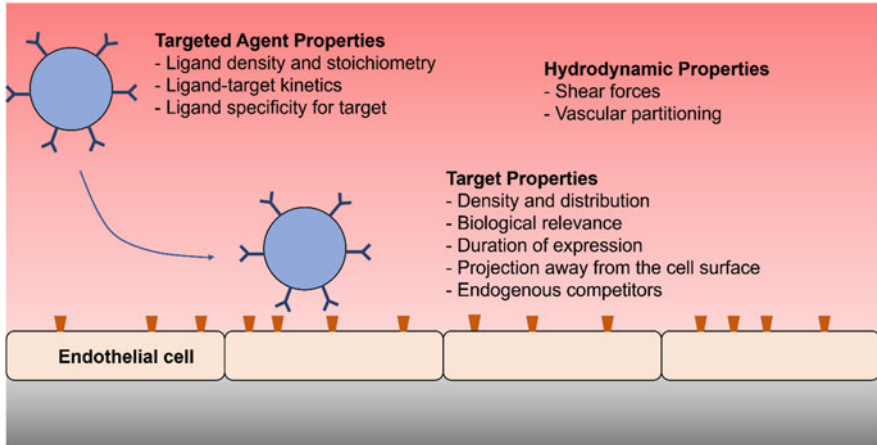


Fig. 5 Factors influencing the efficiency of molecular targeting with intravascular nanoscale or microscale agents

delivery of an intravenous bolus of MB and registering tissue retention in one of two ways. The first involves simply measuring tracer intensity in tissue 5–10 min after delivery when the majority of freely circulating MBs have been cleared from the blood pool. The specificity of this approach is further enhanced by after-the-fact background subtraction, accomplished by destroying all MBs in an ROI and measuring the returning residual blood pool signal [60]. An alternative method involves the use of transfer kinetics to evaluate the retention fraction. In this method, video intensity is measured constantly after bolus delivery allowing deconvolution of two curves: one which rises and decays with the blood pool and one which rises and plateaus representing retained tracer [61]. The latter approach is useful in settings when differences in tissue perfusion over time or between conditions affect the decay kinetics of the adjacent blood pool.

3.1 CEU Molecular Imaging of Cardiovascular Inflammation

The detection of mild or chronic inflammation with CEU has generally been performed by the administration of MBs bearing antibodies or other ligands to endothelial cell adhesion molecules. Agents used to image inflammation with CEU include those targeted to selectins, ICAM-1, VCAM-1, and MAdCAM-1 (Fig. 6) [54, 57, 60, 62]. Thromboinflammation and thrombosis are studied using MBs targeted to portions of von Willebrand factor, platelet GP1b α , fibrin, and tissue factor [62–67].

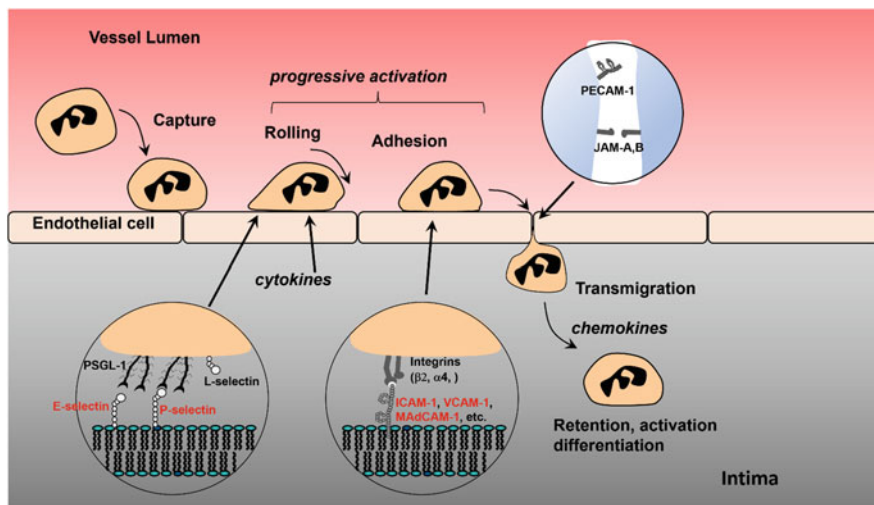


Fig. 6 Illustration of the sequential cellular and molecular events involved in the capture, rolling, adhesion, and extravascular emigration of innate immune cells. Some of the endothelial adhesion molecules that have been targeted by ultrasound molecular imaging probes are highlighted in red and include E- and P-selectin, intercellular adhesion molecule-1 (ICAM-1), vascular cell adhesion molecule-1 (VCAM-1), and mucosal vascular addressin cell adhesion molecule-1 (MAdCAM-1). JAM, junctional adhesion molecules; PECAM-1, platelet-endothelial cell adhesion molecule-1; PSGL-1, P-selectin glycoprotein ligand-1

3.1.1 Ischemic Memory

The diagnosis of patients with acute coronary syndromes is usually dependent on medical history, serologic markers such as troponins, and echocardiogram. It is widely recognized that many patients do not present with classical angina symptoms, and many who are suffering acute coronary syndromes do not have detectable changes on echocardiogram [68]. Diagnostic tools sensitive to the presence and spatial extent of recently resolved myocardial ischemia would improve the care of patients suspected of having unstable coronary syndromes.

Imaging postischemic inflammation has been proposed as a method for ultrasound-based imaging of recent ischemia. Early approaches used MBs targeted to endothelial P-selectin because it is rapidly externalized from secretory granules in response to only mild ischemia and because upregulation can persist for hours following injury (Fig. 7) [69–71]. The ability of P-selectin targeted microbubbles to adhere and produce robust CEU signal enhancement in postischemic tissue was first demonstrated following renal ischemia-reperfusion in mice [60]. Subsequently it has been shown that MBs targeted to P-selectin by surface conjugation of either selective antibodies or glycoprotein analogous to P-selectin glycoprotein ligand-1 (PSGL-1) produce robust myocardial signal enhancement in rats, mice, and nonhuman primates after brief myocardial ischemia [72–75]. Studies in canine and

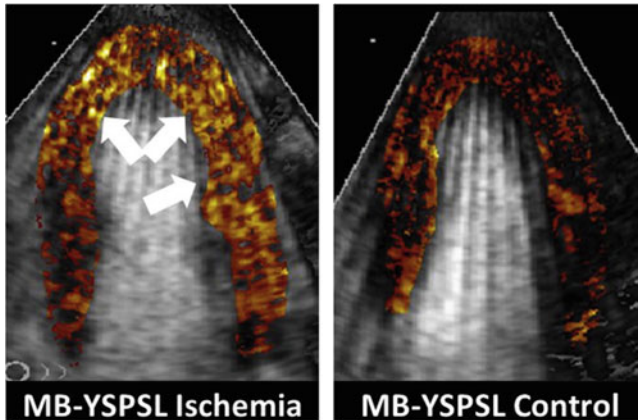


Fig. 7 Molecular imaging of endothelial P-selectin with myocardial contrast echocardiography and targeted microbubbles bearing a recombinant form of PSGL-1 (MB-YSPSL) shows myocardial enhancement in the postischemic territory of a rhesus macaque undergoing ischemia-reperfusion injury. Arrows denote regions of enhancement in the postischemic risk area. Right image is from an animal not undergoing ischemia. Modified with permission from Davidson et al. [74]. © 2014, American Society of Echocardiography

murine models of myocardial ischemia-reperfusion have alternatively shown that MBs with phosphatidylserine are as effective as those targeted against P-selectin [76, 77]. This opsonization-based approach has been shown to be feasible for detection of recent ischemia in humans [78].

3.1.2 Atherosclerosis

The pathophysiology of atherosclerosis is complex and changes over the several decades of disease development. However, a process common in both early disease development and late complications involves vascular inflammation [79]. The ability to directly image inflammatory processes may provide clinical utility for detection of high risk at an early stage or for stratifying patients with known advanced disease to specific anti-inflammatory therapies. Molecular imaging of pro-inflammatory pathways may also be useful for the development of drugs to either palliate advanced high-risk atherosclerotic lesions or arrest disease at an early time point. CEU molecular imaging is particularly useful for the noninvasive assessment of endothelial pro-inflammatory changes, such as the expression of the leukocyte adhesion molecules described above, given the unique capability of MBs to detect molecules actively expressed within the vascular lumen. Although there are many potential targets for molecular imaging in atherosclerosis that could be useful for clinical or research purposes, the target must be governed by the intended clinical use and the stage of disease. For example, the assessment of future risk of progressive disease in an individual without known disease is likely to rely on the detection of early inciting

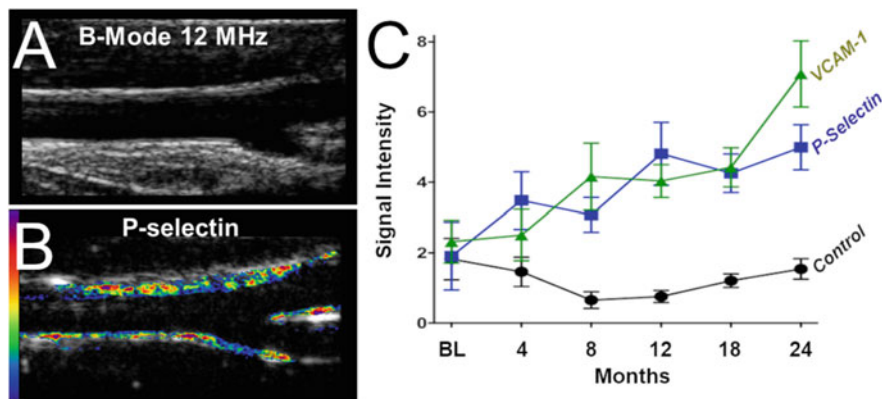


Fig. 8 Molecular imaging of early endothelial inflammation during atherogenesis in a nonhuman primate model of diet-induced obesity and inflammation. (a) Example of a 2D B-mode image of a carotid artery after 2 years of high-fat diet and (b) corresponding background-subtracted color-coded intensity overlay of molecular imaging signal after intravenous injection of microbubbles targeted to P-selectin showing intense endothelial signal enhancement. (c) Quantitative data (mean \pm SEM) of background-subtracted video intensity for P-selectin (blue) and VCAM-1 (green) targeted microbubbles from the carotid artery at baseline (BL) and at incremental intervals after initiating a high-fat diet. Modified with permission from Chadderdon et al. [81]. © 2013, American Heart Association

events such as oxidative stress, lipid accumulation, or endothelial cell adhesion molecule expression. Detection of the “vulnerable plaque” or “vulnerable patient” in advanced disease could include targets within the plaque that are not accessible to currently used MB constructs which are restricted to the blood pool.

For the detection of aggressive atherogenesis, CEU molecular imaging of adhesion molecules such as selectins, ICAM-1, and VCAM-1 has been applied in murine disease models [62, 80]. These molecules are involved in the recruitment of innate immune cells into plaque. Thus, they have been found to provide some of the earliest markers for detecting the onset of aggressive atherogenesis [80]. Carotid CEU molecular imaging of P-selectin and VCAM-1 performed in nonhuman primates has been shown to detect the onset of early-stage endothelial activation in response to high-lipid diet prior to any change in carotid intima-media thickness (Fig. 8) [81]. CEU molecular imaging is also able to detect prothrombotic vascular events associated with acute vascular injury, such as exposed fibrin or tissue factor or platelet aggregation [62, 63, 65]. However, the clinical utility of strategies for imaging individual “vulnerable plaques” remains undecided. Recently, molecular imaging of excess endothelial von Willebrand factor and secondary vascular platelet adhesion has provided new evidence for the role of platelet adhesion as a driver of early atherogenesis, in accelerated plaque growth after an ischemic event, and in chemotherapy-related arterial events [66, 82, 83]. This approach to atherosclerosis has not only provided a better understanding of the pathophysiology of aggressive

atherosclerotic disease but has been used to evaluate the efficacy of new therapies as well [66, 83, 84].

Increasingly, it is recognized that inflammation and thrombosis are interrelated processes that potentiate each other. Accordingly, molecular imaging signal of either vascular fibrin deposition or platelet adhesion has been shown to correlate well with plaque inflammation status. Fibrin-targeted agents have been shown to produce enhancement not only in areas of vascular mechanical injury but also on ventricular thrombi in large animal models [62, 85]. For example, lipid nanodroplets targeted to fibrin or to glycoprotein IIb/IIIa (GPIIb/IIIa) detectable by high frequency ultrasound have been shown to colocalize with regions of plaque development in animal models of atherosclerosis [62]. Ultrasound signal enhancement from MBs targeted to platelet GPIIb α and von Willebrand factor has been detected in very early stages of atherogenesis at the time of fatty streak formation, and high signal enhancement has been shown to reflect unstable plaque phenotype in terms of underlying inflammatory status and likelihood for rapid plaque progression [82–84].

3.2 Organ-Specific Applications of CEU Molecular Imaging

Renal molecular imaging has been used in animal models to identify antibody-mediated rejection of renal allografts. Complement component C4d can be an early indicator of antibody-mediated rejection [86]. Accordingly, molecular imaging can be used to determine C4d distribution in renal grafts with a linear relationship between ultrasound molecular imaging signal and C4d deposition on graft histology [87]. Beyond antibody-mediated rejection, ultrasound can be used to track adoptive T-cell activity in a rat model of allograft transplant rejection through molecular imaging targeted to CD3, CD4, and CD8 [88]. The ability to evaluate T-cell activity in allograft transplant rejection is a promising approach for quick and specific assessment of allograft rejection.

Similarly, there is emerging work evaluating the use of CEU molecular imaging for the assessment of hepatic microvascular injury. ICAM-1 was targeted in a rabbit model of hepatic ischemia-reperfusion injury [89], and VCAM-1 was targeted in a swine ex vivo assessment of vascular injury resulting from storage conditions often used in organ transplant settings [90].

There is also important work happening in the development of molecular imaging tools for the diagnosis and treatment evaluation of many kinds of solid organ carcinomas. In the kidney, nanobubbles targeted to renal cell carcinoma-associated antigen G250 were able to differentiate benign from malignant tumors in vitro [91]. In the case of pancreatic ductal adenocarcinoma (PDAC), a disease whose substantial lethality is due in large part to its difficulty to detect in operable stages, Thy-1 has been identified as a PDAC-specific neovessel marker. Multiple studies in murine transgenic PDAC models have shown potential diagnostic value in CEU molecular imaging [92–94]. While not as disease-specific, many groups are also exploring the use of VEGFR-2 as a CEU molecular imaging target of neovascular

angiogenesis. VEGFR-2 targeting has been demonstrated for both diagnosis and antiangiogenic therapeutic assessment in animal models of renal cell carcinoma [95, 96], PDAC [97], and hepatocellular carcinomas [98].

3.3 Limitations and Benefits Compared to Other Molecular Imaging Approaches

CEU molecular imaging is one of a slate of existing modalities capable of noninvasively identifying the presence or expression of specific cell types, molecules, or receptors (Fig. 9). Other technologies that can be used include MRI, PET, and SPECT. The utility of all forms of molecular imaging is affected by their spatial and temporal resolution, risk-benefit ratio of clinical use, and the time and expense associated with clinical use. Contextually, CEU represents a technique with a good

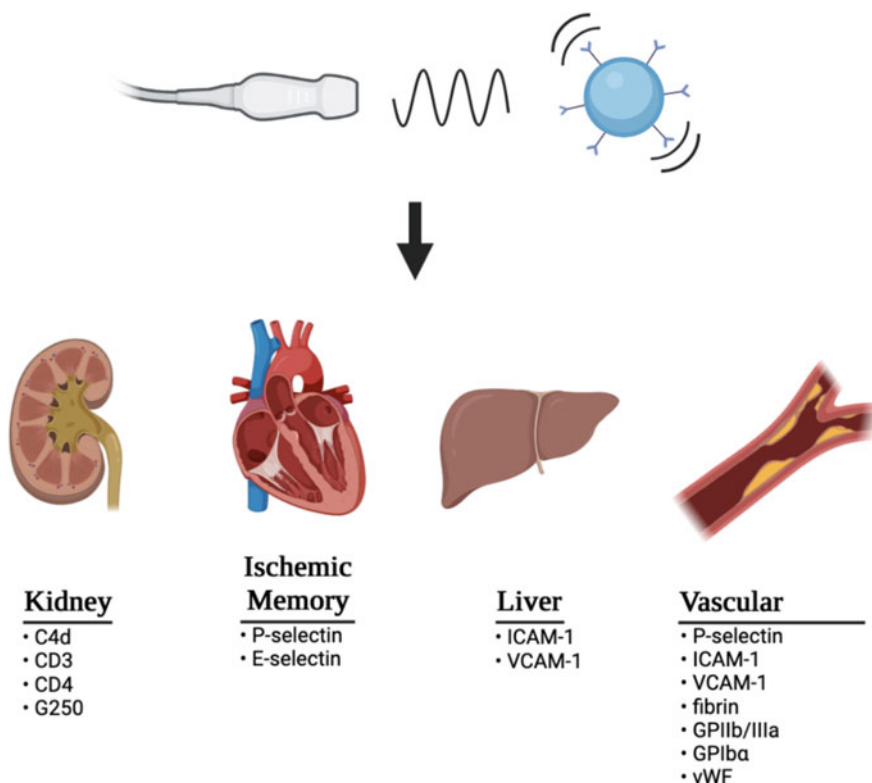


Fig. 9 Illustration of some of the intravascular targets that have been used for research in inflammation imaging through contrast-enhanced ultrasound molecular imaging. Targets are divided into three main categories: adaptive and innate immune cells, endothelial cells, and thromboinflammation

balance between spatial resolution and sensitivity and has practical advantages with respect to cost and throughput. Ultrasound frequency is proportional to the tissue depth penetration but inversely proportional to the spatial resolution. Given this relationship, it is important to selectively choose a frequency based on the application and anatomy desired [99]. However, CEU also has several limitations even for cardiovascular-specific applications. MBs are limited to the vascular compartment and cannot access ischemic regions. Unfortunately many markers that could be used to stratify the thromboembolic risk of advanced atherosclerotic plaques, such as markers of subendothelial oxidative stress, are inaccessible to MBs. Additionally, one should be cognizant of the risks associated with MBs, as mild to moderate adverse events have been reported in low percentages of cases [100, 101].

4 Conclusion

Ultrasound has been a foundational tool in modern cardiovascular medicine and continues to be at the cutting edge of preclinical research into inflammation-related pathology. In this chapter we described the principles that enable ultrasound to function with high temporal resolution and an advantageous safety profile in the clinic. We focused on the applications of ultrasound to vascular diseases, including the acoustic mapping of plaques in atherosclerosis, and the regulation of inflammatory mediators by molecular imaging. Other sites of inflammatory pathology, including the kidneys and joints, were also discussed. Finally, we conclude with a frank discussion of the strengths and weaknesses of ultrasound compared to other currently available medical imaging modalities.

Compliance with Ethical Standards Funding: Dr. Lindner is supported by grants R01-HL078610, R01-HL130046, and P51-OD011092 from the National Institutes of Health (NIH), Bethesda, MD, and grant 18-18HCFBP_2-0009 from NASA.

Conflict of Interest: The authors have no conflicts of interest to declare.

Ethical approval: Images obtained from human subjects were acquired during studies approved by the Institutional Review Board of Oregon Health and Science University.

References

1. Bushberg JT, Seibert JA Jr, Boone EMLJM. The essential physics of medical imaging. 3rd ed. Third, Nor. Philadelphia: LWW; 2011.
2. Wettlaufer J. Physical principles of medical imaging. 2nd ed. Radiology, vol. 200. Radiological Society of North America; 1996. p. 504. <https://doi.org/10.1148/radiology.200.2.504>.
3. Pellett AA, Kerut EK. The doppler equation. Echocardiography. 2004;21:197–8. <https://doi.org/10.1111/j.0742-2822.2004.03146.x>.
4. Baker DW, Rubenstein SA, Lorch GS. Pulsed doppler echocardiography: principles and applications. Am J Med. 1977;63:69–80. [https://doi.org/10.1016/0002-9343\(77\)90119-X](https://doi.org/10.1016/0002-9343(77)90119-X).

5. Lee C, Jeon M, Kim C. Photoacoustic imaging in nanomedicine. In: Hamblin MR, Avci P, editors. *Appl Nanosci Photomed*. Elsevier; 2015. p. 31–47. <https://doi.org/10.1533/9781908818782.31>.
6. van den Berg PJ, Daoudi K, Bernelot Moens HJ, Steenbergen W. Feasibility of photoacoustic/ultrasound imaging of synovitis in finger joints using a point-of-care system. *Photo-Dermatology*. 2017;8:8–14. <https://doi.org/10.1016/j.pacs.2017.08.002>.
7. Jayaweera AR, Edwards N, Glasheen WP, Villanueva FS, Abbott RD, Kaul S. In vivo myocardial kinetics of air-filled albumin microbubbles during myocardial contrast echocardiography. Comparison with radiolabeled red blood cells. *Circ Res*. 1994;74:1157–65. <https://doi.org/10.1161/01.RES.74.6.1157>.
8. Lindner JR, Song J, Jayaweera AR, Sklenar J, Kaul S. Microvascular rheology of Definity microbubbles after intra-arterial and intravenous administration. *J Am Soc Echocardiogr*. 2002;15:396–403. <https://doi.org/10.1067/mje.2002.117290>.
9. Kaufmann BA, Wei K, Lindner JR. Contrast echocardiography. *Curr Probl Cardiol*. 2007;32:51–96. <https://doi.org/10.1016/j.cpcardiol.2006.10.004>.
10. de Jong N, Hoff L, Skotland T, Bom N. Absorption and scatter of encapsulated gas filled microspheres: theoretical considerations and some measurements. *Ultrasonics*. 1992;30:95–103. [https://doi.org/10.1016/0041-624X\(92\)90041-J](https://doi.org/10.1016/0041-624X(92)90041-J).
11. Qin S, Caskey CF, Ferrara KW. Ultrasound contrast microbubbles in imaging and therapy: physical principles and engineering. *Phys Med Biol*. 2009;54:R27–57. <https://doi.org/10.1088/0031-9155/54/6/R01>.
12. Seol S-H, Davidson BP, Belcik JT, Mott BH, Goodman RM, Ammi A, et al. Real-time contrast ultrasound muscle perfusion imaging with intermediate-power imaging coupled with acoustically durable microbubbles. *J Am Soc Echocardiogr*. 2015;28:718–726.e2. <https://doi.org/10.1016/j.echo.2015.02.002>.
13. Kutty S, Biko DM, Goldberg AB, Quartermain MD, Feinstein SB. Contrast-enhanced ultrasound in pediatric echocardiography. *Pediatr Radiol*. 2021;51:2408–17. <https://doi.org/10.1007/s00247-021-05119-3>.
14. Grønholdt M-LM, Nordestgaard BG, Schroeder TV, Vorstrup S, Sillesen H. Ultrasonic Echolucent carotid plaques predict future strokes. *Circulation*. 2001;104:68–73. <https://doi.org/10.1161/hc2601.091704>.
15. Petersen C, Peçanha PB, Venneri L, Pasanisi E, Pratali L, Picano E. The impact of carotid plaque presence and morphology on mortality outcome in cardiological patients. *Cardiovasc Ultrasound*. 2006;4:16. <https://doi.org/10.1186/1476-7120-4-16>.
16. Meola M, Samoni S, Petrucci I. Imaging in chronic kidney disease. *Ultrasound imaging acute chronic kidney dis*. Karger Publishers; 2016. p. 69–80. <https://doi.org/10.1159/000445469>.
17. Bigé N, Lévy PP, Callard P, Faintuch J-M, Chigot V, Jousselin V, et al. Renal arterial resistive index is associated with severe histological changes and poor renal outcome during chronic kidney disease. *BMC Nephrol*. 2012;13:139. <https://doi.org/10.1186/1471-2369-13-139>.
18. Sugiura T, Wada A. Resistive index predicts renal prognosis in chronic kidney disease. *Nephrol Dial Transplant*. 2009;24:2780–5. <https://doi.org/10.1093/ndt/gfp121>.
19. O'Neill WC. Renal relevant radiology: use of ultrasound in kidney disease and nephrology procedures. *Clin J Am Soc Nephrol American Society of Nephrology*. 2014;9:373–81. <https://doi.org/10.2215/CJN.03170313>.
20. Nomura G, Kinoshita E, Yamagata Y, Koga N. Usefulness of renal ultrasonography for assessment of severity and course of acute tubular necrosis. *J Clin Ultrasound*. 1984;12:135–9. <https://doi.org/10.1002/jcu.1870120304>.
21. O'Neill WC, Baumgarten DA. Ultrasonography in renal transplantation. *Am J Kidney Dis*. 2002;39:663–78. <https://doi.org/10.1053/ajkd.2002.31978>.
22. Thölking G, Schuette-Nuetgen K, Kentrup D, Pawelski H, Reuter S. Imaging-based diagnosis of acute renal allograft rejection. *World J Transplant*. 2016;6:174. <https://doi.org/10.5500/wjt.v6.i1.174>.

23. Naesens M, Heylen L, Lerut E, Claes K, De Wever L, Claus F, et al. Intrarenal resistive index after renal transplantation. *N Engl J Med.* 2013;369:1797–806. <https://doi.org/10.1056/NEJMoa1301064>.
24. Grantham JJ. Pathogenesis of renal cyst expansion: opportunities for therapy. *Am J Kidney Dis.* 1994;23:210–8. [https://doi.org/10.1016/S0272-6386\(12\)80974-7](https://doi.org/10.1016/S0272-6386(12)80974-7).
25. Pei Y, Obaji J, Dupuis A, Paterson AD, Magistroni R, Dicks E, et al. Unified criteria for ultrasonographic diagnosis of ADPKD. *J Am Soc Nephrol.* 2009;20:205–12. <https://doi.org/10.1681/ASN.2008050507>.
26. Lee J, Darcy M. Renal cysts and urinomas. *Semin Intervent Radiol.* 2011;28:380–91. <https://doi.org/10.1055/s-0031-1296080>.
27. Heidari B. Rheumatoid arthritis: early diagnosis and treatment outcomes. *Caspian J Intern Med.* 2011;2:161–70.
28. Naredo E, Bonilla G, Gamero F, Uson J, Carmona L, Laffon A. Assessment of inflammatory activity in rheumatoid arthritis: a comparative study of clinical evaluation with grey scale and power Doppler ultrasonography. *Ann Rheum Dis.* 2005;64:375–81. <https://doi.org/10.1136/ard.2004.023929>.
29. Newman JS, Adler RS, Bude RO, Rubin JM. Detection of soft-tissue hyperemia: value of power doppler sonography. *Am J Roentgenol.* 1994;163:385–9. <https://doi.org/10.2214/ajr.163.2.8037037>.
30. Hubac J, Gilson M, Gaudin P, Clay M, Imbert B, Carpentier P. Ultrasound prevalence of wrist, hand, ankle and foot synovitis and tenosynovitis in systemic sclerosis, and relationship with disease features and hand disability. *Jt Bone Spine.* 2020;87:229–33. <https://doi.org/10.1016/j.jbspin.2020.01.011>.
31. Massignan Á, da Silva M, Chakr R, Bueno P, de Andrade N, Brenol CV. Synovitis and tenosynovitis on ultrasound as predictors of DMARD tapering failure in patients with long-standing rheumatoid arthritis in clinical remission or low disease activity. *J Ultrasound Med.* 2021;40:2549–59. <https://doi.org/10.1002/jum.15640>.
32. Wakefield RJ, Gibbon WW, Conaghan PG, O'Connor P, McGonagle D, Pease C, et al. The value of sonography in the detection of bone erosions in patients with rheumatoid arthritis: a comparison with conventional radiography. *Arthritis Rheum.* 2000;43:2762–70. [https://doi.org/10.1002/1529-0131\(200012\)43:12%3C2762::aid-anr16%3E3.0.co;2-#](https://doi.org/10.1002/1529-0131(200012)43:12%3C2762::aid-anr16%3E3.0.co;2-#).
33. Kawashiri S, Fujikawa K, Nishino A, Okada A, Aramaki T, Shimizu T, et al. Ultrasound-detected bone erosion is a relapse risk factor after discontinuation of biologic disease-modifying antirheumatic drugs in patients with rheumatoid arthritis whose ultrasound power Doppler synovitis activity and clinical disease activity are well. *Arthritis Res Ther.* 2017;19:108. <https://doi.org/10.1186/s13075-017-1320-2>.
34. Sundin U, Sundlister NP, Aga A-B, Sexton J, Nordberg LB, Hammer HB, et al. Value of MRI and ultrasound for prediction of therapeutic response and erosive progression in patients with early rheumatoid arthritis managed by an aggressive treat-to-target strategy. *RMD Open BMJ Specialist Journals.* 2021;7:e001525. <https://doi.org/10.1136/rmdopen-2020-001525>.
35. Chamberland DL, Wang X, Roessler BJ. Photoacoustic tomography of carrageenan-induced arthritis in a rat model. *J Biomed Opt.* 2008;13:011005. <https://doi.org/10.1117/1.2841028>.
36. Rajian JR, Shao X, Chamberland DL, Wang X. Characterization and treatment monitoring of inflammatory arthritis by photoacoustic imaging: a study on adjuvant-induced arthritis rat model. *Biomed Opt Express.* 2013;4:900. <https://doi.org/10.1364/BOE.4.000900>.
37. Jo J, Tian C, Xu G, Sarazin J, Schioppa E, Gandikota G, et al. Photoacoustic tomography for human musculoskeletal imaging and inflammatory arthritis detection. *Photo-Dermatology.* 2018;12:82–9. <https://doi.org/10.1016/j.pacs.2018.07.004>.
38. Takiuchi S, Rakugi H, Honda K, Masuyama T, Hirata N, Ito H, et al. Quantitative ultrasonic tissue characterization can identify high-risk atherosclerotic alteration in human carotid arteries. *Circulation.* 2000;102:766–70. <https://doi.org/10.1161/01.CIR.102.7.766>.
39. Sano K, Kawasaki M, Ishihara Y, Okubo M, Tsuchiya K, Nishigaki K, et al. Assessment of vulnerable plaques causing acute coronary syndrome using integrated backscatter

- intravascular ultrasound. *J Am Coll Cardiol*. 2006;47:734–41. <https://doi.org/10.1016/j.jacc.2005.09.061>.
40. Nair A, Kuban BD, Tuzcu EM, Schoenhagen P, Nissen SE, Vince DG. Coronary plaque classification with intravascular ultrasound radiofrequency data analysis. *Circulation*. 2002;106:2200–6. <https://doi.org/10.1161/01.CIR.0000035654.18341.5E>.
 41. Nair A, Kuban BD, Obuchowski N, Vince DG. Assessing spectral algorithms to predict atherosclerotic plaque composition with normalized and raw intravascular ultrasound data. *Ultrasound Med Biol*. 2001;27:1319–31. [https://doi.org/10.1016/S0301-5629\(01\)00436-7](https://doi.org/10.1016/S0301-5629(01)00436-7).
 42. Nasu K, Tsuchikane E, Katoh O, Vince DG, Virmani R, Surmely J-F, et al. Accuracy of in vivo coronary plaque morphology assessment. *J Am Coll Cardiol*. 2006;47:2405–12. <https://doi.org/10.1016/j.jacc.2006.02.044>.
 43. König A, Klauss V. Virtual histology. *Heart*. 2007;93:977–82. <https://doi.org/10.1136/hrt.2007.116384>.
 44. Gogas BD, Farooq V, Serruys PW, García-García HM. Assessment of coronary atherosclerosis by IVUS and IVUS-based imaging modalities: progression and regression studies, tissue composition and beyond. *Int J Cardiovasc Imaging*. 2011;27:225–37. <https://doi.org/10.1007/s10554-010-9791-0>.
 45. Stone GW, Maehara A, Lansky AJ, de Bruyne B, Cristea E, Mintz GS, et al. A prospective natural-history study of coronary atherosclerosis. *N Engl J Med*. 2011;364:226–35. <https://doi.org/10.1056/NEJMoa1002358>.
 46. Calvert PA, Obaid DR, O’Sullivan M, Shapiro LM, McNab D, Densem CG, et al. Association between IVUS findings and adverse outcomes in patients with coronary artery disease. *JACC Cardiovasc Imaging*. 2011;4:894–901. <https://doi.org/10.1016/j.jcmg.2011.05.005>.
 47. Cheng JM, García-García HM, de Boer SPM, Kardys I, Heo JH, Akkerhuis KM, et al. In vivo detection of high-risk coronary plaques by radiofrequency intravascular ultrasound and cardiovascular outcome: results of the ATHEROREMO-IVUS study. *Eur Heart J*. 2014;35:639–47. <https://doi.org/10.1093/eurheartj/eh4484>.
 48. Ophir J, Céspedes I, Ponnekanti H, Yazdi Y, Li X. Elastography: a quantitative method for imaging the elasticity of biological tissues. *Ultrason Imaging*. 1991;13:111–34. <https://doi.org/10.1177/016173469101300201>.
 49. Maurice RL, Brusseau É, Finet G, Cloutier G. On the potential of the Lagrangian speckle model estimator to characterize atherosclerotic plaques in endovascular elastography: in vitro experiments using an excised human carotid artery. *Ultrasound Med Biol*. 2005;31:85–91. <https://doi.org/10.1016/j.ultrasmedbio.2004.07.009>.
 50. Schaar JA, de Korte CL, Mastik F, Strijder C, Pasterkamp G, Boersma E, et al. Characterizing vulnerable plaque features with intravascular elastography. *Circulation*. 2003;108:2636–41. <https://doi.org/10.1161/01.CIR.0000097067.96619.1F>.
 51. Lindner JR, Coggins MP, Kaul S, Klibanov AL, Brandenburger GH, Ley K. Microbubble persistence in the microcirculation during ischemia/reperfusion and inflammation is caused by integrin- and complement-mediated adherence to activated leukocytes. *Circulation*. 2000;101:668–75. <https://doi.org/10.1161/01.CIR.101.6.668>.
 52. Anderson D, Tsutsui J, Xie F, Radio S, Porter T. The role of complement in the adherence of microbubbles to dysfunctional arterial endothelium and atherosclerotic plaque. *Cardiovasc Res*. 2007;73:597–606. <https://doi.org/10.1016/j.cardiores.2006.11.029>.
 53. Lindner JR, Song J, Xu F, Klibanov AL, Singbartl K, Ley K, et al. Noninvasive ultrasound imaging of inflammation using microbubbles targeted to activated leukocytes. *Circulation*. 2000;102:2745–50. <https://doi.org/10.1161/01.CIR.102.22.2745>.
 54. Bachmann C, Klibanov AL, Olson TS, Sonnenschein JR, Rivera-Nieves J, Cominelli F, et al. Targeting mucosal Addressin cellular adhesion molecule (MAdCAM)-1 to noninvasively image experimental Crohn’s disease. *Gastroenterology*. 2006;130:8–16. <https://doi.org/10.1053/j.gastro.2005.11.009>.
 55. Kaufmann BA, Sanders JM, Davis C, Xie A, Aldred P, Sarembok II, et al. Molecular imaging of inflammation in atherosclerosis with targeted ultrasound detection of vascular cell adhesion

- Molecule-1. *Circulation*. 2007;116:276–84. <https://doi.org/10.1161/CIRCULATIONAHA.106.684738>.
56. Weller GER, Villanueva FS, Klibanov AL, Wagner WR. Modulating targeted adhesion of an ultrasound contrast agent to dysfunctional endothelium. *Ann Biomed Eng*. 2002;30:1012–9. <https://doi.org/10.1114/1.1513565>.
 57. Villanueva FS, Jankowski RJ, Klibanov S, Pina ML, Alber SM, Watkins SC, et al. Microbubbles targeted to intercellular adhesion Molecule-1 bind to activated coronary artery endothelial cells. *Circulation*. 1998;98:1–5. <https://doi.org/10.1161/01.CIR.98.1.1>.
 58. Lankford M, Behm CZ, Yeh J, Klibanov AL, Robinson P, Lindner JR. Effect of microbubble ligation to cells on ultrasound signal enhancement. *Investig Radiol*. 2006;41:721–8. <https://doi.org/10.1097/01.rli.0000236825.72344.a9>.
 59. Dayton PA, Chomas JE, Lum AFH, Allen JS, Lindner JR, Simon SI, et al. Optical and acoustical dynamics of microbubble contrast agents inside neutrophils. *Biophys J*. 2001;80:1547–56. [https://doi.org/10.1016/S0006-3495\(01\)76127-9](https://doi.org/10.1016/S0006-3495(01)76127-9).
 60. Lindner JR, Song J, Christiansen J, Klibanov AL, Xu F, Ley K. Ultrasound assessment of inflammation and renal tissue injury with microbubbles targeted to P-selectin. *Circulation*. 2001;104:2107–12. <https://doi.org/10.1161/hc4201.097061>.
 61. Carr CL, Qi Y, Davidson B, Chadderdon S, Jayaweera AR, Belcik JT, et al. Dysregulated selectin expression and monocyte recruitment during ischemia-related vascular remodeling in diabetes mellitus. *Arterioscler Thromb Vasc Biol*. 2011;31:2526–33. <https://doi.org/10.1161/ATVBAHA.111.230177>.
 62. Hamilton AJ, Huang S-L, Warnick D, Rabbat M, Kane B, Nagaraj A, et al. Intravascular ultrasound molecular imaging of atheroma components in vivo. *J Am Coll Cardiol*. 2004;43:453–60. <https://doi.org/10.1016/j.jacc.2003.07.048>.
 63. Schumann PA, Christiansen JP, Quigley RM, McCreery TP, Sweitzer RH, Unger EC, Lindner JR, et al. Targeted-microbubble binding selectively to GPIIb/IIIa receptors of platelet thrombi. *Investig Radiol*. 2002;37:587–93. <https://doi.org/10.1097/00004424-200211000-00001>.
 64. Lanza GM, Abendschein DR, Hall CS, Scott MJ, Scherrer DE, Houseman A, et al. In vivo molecular imaging of stretch-induced tissue factor in carotid arteries with ligand-targeted nanoparticles. *J Am Soc Echocardiogr*. 2000;13:608–14. <https://doi.org/10.1067/mje.2000.105840>.
 65. Wang X, Hagemeyer CE, Hohmann JD, Leitner E, Armstrong PC, Jia F, et al. Novel single-chain antibody-targeted microbubbles for molecular ultrasound imaging of thrombosis. *Circulation*. 2012;125:3117–26. <https://doi.org/10.1161/CIRCULATIONAHA.111.030312>.
 66. Latifi Y, Moccetti F, Wu M, Xie A, Packwood W, Qi Y, et al. Thrombotic microangiopathy as a cause of cardiovascular toxicity from the BCR-ABL1 tyrosine kinase inhibitor ponatinib. *Blood*. 2019;133:1597–606. <https://doi.org/10.1182/blood-2018-10-881557>.
 67. Ozawa K, Packwood W, Varlamov O, Qi Y, Xie A, Wu MD, et al. Molecular imaging of VWF (von Willebrand factor) and platelet adhesion in postischemic impaired microvascular reflow. *Circ Cardiovasc Imaging*. 2018;11:e007913. <https://doi.org/10.1161/CIRCIMAGING.118.007913>.
 68. Pope JH, Aufderheide TP, Ruthazer R, Woolard RH, Feldman JA, Beshansky JR, et al. Missed diagnoses of acute cardiac ischemia in the emergency department. *N Engl J Med*. 2000;342:1163–70. <https://doi.org/10.1056/NEJM200004203421603>.
 69. McEver RP, Beckstead JH, Moore KL, Marshall-Carlson L, Bainton DF. GMP-140, a platelet alpha-granule membrane protein, is also synthesized by vascular endothelial cells and is localized in Weibel-Palade bodies. *J Clin Invest*. 1989;84:92–9. <https://doi.org/10.1172/JCI114175>.
 70. Bevilacqua MP, Nelson RM. Selectins. *J Clin Invest*. 1993;91:379–87. <https://doi.org/10.1172/JCI116210>.
 71. Chukwuemeka AO, Brown KA, Venn GE, Chambers DJ. Changes in P-selectin expression on cardiac microvessels in blood-perfused rat hearts subjected to ischemia-reperfusion. *Ann Thorac Surg*. 2005;79:204–11. <https://doi.org/10.1016/j.athoracsur.2004.06.105>.

72. Kaufmann BA, Lewis C, Xie A, Mirza-Mohd A, Lindner JR. Detection of recent myocardial ischaemia by molecular imaging of P-selectin with targeted contrast echocardiography. *Eur Heart J*. 2007;28:2011–7. <https://doi.org/10.1093/eurheartj/ehm176>.
73. Villanueva FS, Lu E, Bowry S, Kilic S, Tom E, Wang J, et al. Myocardial ischemic memory imaging with molecular echocardiography. *Circulation*. 2007;115:345–52. <https://doi.org/10.1161/CIRCULATIONAHA.106.633917>.
74. Davidson BP, Chadderdon SM, Belcik JT, Gupta S, Lindner JR. Ischemic memory imaging in nonhuman primates with echocardiographic molecular imaging of selectin expression. *J Am Soc Echocardiogr*. 2014;27:786–93.e2. <https://doi.org/10.1016/j.echo.2014.03.013>.
75. Davidson BP, Kaufmann BA, Belcik JT, Xie A, Qi Y, Lindner JR. Detection of antecedent myocardial ischemia with multiselectin molecular imaging. *J Am Coll Cardiol*. 2012;60:1690–7. <https://doi.org/10.1016/j.jacc.2012.07.027>.
76. Christiansen JP, Leong-Poi H, Klibanov AL, Kaul S, Lindner JR. Noninvasive imaging of myocardial reperfusion injury using leukocyte-targeted contrast echocardiography. *Circulation*. 2002;105:1764–7. <https://doi.org/10.1161/01.CIR.0000015466.89771.E2>.
77. Mott B, Packwood W, Xie A, Belcik JT, Taylor RP, Zhao Y, et al. Echocardiographic ischemic memory imaging through complement-mediated vascular adhesion of phosphatidylserine-containing microbubbles. *JACC Cardiovasc Imaging*. 2016;9:937–46. <https://doi.org/10.1016/j.jcmg.2015.11.031>.
78. Davidson BP, Hodovan J, Layoun ME, Golwala H, Zahr F, Lindner JR. Echocardiographic ischemic memory molecular imaging for point-of-care detection of myocardial ischemia. *J Am Coll Cardiol*. 2021;78:1990–2000. <https://doi.org/10.1016/j.jacc.2021.08.068>.
79. Libby P, Ridker PM, Hansson GK. Inflammation in atherosclerosis. *J Am Coll Cardiol*. 2009;54:2129–38. <https://doi.org/10.1016/j.jacc.2009.09.009>.
80. Kaufmann BA, Carr CL, Belcik JT, Xie A, Yue Q, Chadderdon S, et al. Molecular imaging of the initial inflammatory response in atherosclerosis. *Arterioscler Thromb Vasc Biol*. 2010;30:54–9. <https://doi.org/10.1161/ATVBAHA.109.196386>.
81. Chadderdon SM, Belcik JT, Bader L, Kirigiti MA, Peters DM, Kievit P, et al. Proinflammatory endothelial activation detected by molecular imaging in obese nonhuman primates coincides with onset of insulin resistance and progressively increases with duration of insulin resistance. *Circulation*. 2014;129:471–8. <https://doi.org/10.1161/CIRCULATIONAHA.113.003645>.
82. Shim CY, Liu YN, Atkinson T, Xie A, Foster T, Davidson BP, et al. Molecular imaging of platelet–endothelial interactions and endothelial von Willebrand Factor in early and mid-stage atherosclerosis. *Circ Cardiovasc Imaging*. 2015;8:e002765. <https://doi.org/10.1161/CIRCIMAGING.114.002765>.
83. Moccetti F, Brown E, Xie A, Packwood W, Qi Y, Ruggeri Z, et al. Myocardial infarction produces sustained proinflammatory endothelial activation in remote arteries. *J Am Coll Cardiol*. 2018;72:1015–26. <https://doi.org/10.1016/j.jacc.2018.06.044>.
84. Liu Y, Davidson BP, Yue Q, Belcik T, Xie A, Inaba Y, et al. Molecular imaging of inflammation and platelet adhesion in advanced atherosclerosis effects of antioxidant therapy with NADPH oxidase inhibition. *Circ Cardiovasc Imaging*. 2013;6:74–82. <https://doi.org/10.1161/CIRCIMAGING.112.975193>.
85. Hamilton A, Huang S-L, Warnick D, Stein A, Rabbat M, Madhav T, et al. Left ventricular thrombus enhancement after intravenous injection of echogenic immunoliposomes. *Circulation*. 2002;105:2772–8. <https://doi.org/10.1161/01.CIR.0000017500.61563.80>.
86. Cohen D, Colvin RB, Daha MR, Drachenberg CB, Haas M, Nickenleit V, et al. Pros and cons for C4d as a biomarker. *Kidney Int*. 2012;81:628–39. <https://doi.org/10.1038/ki.2011.497>.
87. Liao T, Zhang Y, Ren J, Zheng H, Zhang H, Li X, et al. Noninvasive quantification of intrarenal allograft C4d deposition with targeted ultrasound imaging. *Am J Transplant*. 2019;19:259–68. <https://doi.org/10.1111/ajt.15105>.
88. Grabner A, Kentrup D, Mühlmeister M, Pawelski H, Biermann C, Bettinger T, et al. Noninvasive imaging of acute renal allograft rejection by ultrasound detection of microbubbles

- targeted to T-lymphocytes in rats. *Ultraschall der Medizin – Eur J Ultrasound*. 2015;37:82–91. <https://doi.org/10.1055/s-0034-1385796>.
89. Xie F, Li Z-P, Wang H-W, Fei X, Jiao Z-Y, Tang W-B, et al. Evaluation of liver ischemia-reperfusion injury in rabbits using a nanoscale ultrasound contrast agent targeting ICAM-1. Gracia-sancho J, editor. *PLoS One*. 2016;11:e0153805. <https://doi.org/10.1371/journal.pone.0153805>.
90. Xie F, Zhang S-H, Cheng J, Wang H-W, Fei X, Jiao Z-Y, et al. Evaluation of hepatic vascular endothelial injury during liver storage by molecular detection and targeted contrast-enhanced ultrasound imaging. *IUBMB Life*. 2016;68:51–7. <https://doi.org/10.1002/iub.1459>.
91. Yu Z, Hu M, Li Z, Dan X, Zhu L, Guo Y, et al. Anti-G250 nanobody-functionalized nanobubbles targeting renal cell carcinoma cells for ultrasound molecular imaging. *Nanotechnology*. 2020;31:205101. <https://doi.org/10.1088/1361-6528/ab7040>.
92. Abou-Elkacem L, Wang H, Chowdhury SM, Kimura RH, Bachawal SV, Gambhir SS, et al. Thy1-targeted microbubbles for ultrasound molecular imaging of pancreatic ductal adenocarcinoma. *Clin Cancer Res*. 2018;24:1574–85. <https://doi.org/10.1158/1078-0432.CCR-17-2057>.
93. Bam R, Daryaei I, Abou-Elkacem L, Vilches-Moure JG, Meuillet EJ, Lutz A, et al. Toward the clinical development and validation of a Thy1-targeted ultrasound contrast agent for the early detection of pancreatic ductal adenocarcinoma. *Investig Radiol*. 2020;55:711–21. <https://doi.org/10.1097/RLI.0000000000000697>.
94. Foygel K, Wang H, Machtaler S, Lutz AM, Chen R, Pysz M, et al. Detection of pancreatic ductal adenocarcinoma in mice by ultrasound imaging of thymocyte differentiation antigen 1. *Gastroenterology*. 2013;145:885–94.e3. <https://doi.org/10.1053/j.gastro.2013.06.011>.
95. Rojas JD, Lin F, Chiang Y-C, Chytil A, Chong DC, Bautch VL, et al. Ultrasound molecular imaging of VEGFR-2 in clear-cell renal cell carcinoma tracks disease response to antiangiogenic and notch-inhibition therapy. *Theranostics*. 2018;8:141–55. <https://doi.org/10.7150/thno.19658>.
96. Wei S, Fu N, Sun Y, Yang Z, Lei L, Huang P, et al. Targeted contrast-enhanced ultrasound imaging of angiogenesis in an orthotopic mouse tumor model of renal carcinoma. *Ultrasound Med Biol*. 2014;40:1250–9. <https://doi.org/10.1016/j.ultrasmedbio.2013.12.001>.
97. Korpanty G, Carbon JG, Grayburn PA, Fleming JB, Brekken RA. Monitoring response to anticancer therapy by targeting microbubbles to tumor vasculature. *Clin Cancer Res*. 2007;13:323–30. <https://doi.org/10.1158/1078-0432.CCR-06-1313>.
98. Baron Toaldo M, Salvatore V, Marinelli S, Palamà C, Milazzo M, Croci L, et al. Use of VEGFR-2 targeted ultrasound contrast agent for the early evaluation of response to sorafenib in a mouse model of hepatocellular carcinoma. *Mol Imaging Biol*. 2015;17:29–37. <https://doi.org/10.1007/s11307-014-0764-x>.
99. Lucas VS, Burk RS, Creehan S, Grap MJ. Utility of high-frequency ultrasound. *Plast Surg Nurs*. 2014;34:34–8. <https://doi.org/10.1097/PSN.0000000000000031>.
100. Hu C, Feng Y, Huang P, Jin J. Adverse reactions after the use of SonoVue contrast agent. *Medicine (Baltimore)*. 2019;98:e17745. <https://doi.org/10.1097/MD.00000000000017745>.
101. Dijkmans P, Visser C, Kamp O. Adverse reactions to ultrasound contrast agents: is the risk worth the benefit? *Eur J Echocardiogr*. 2005;6:363–6. <https://doi.org/10.1016/j.euje.2005.02.003>.

Whole-Body Chemiluminescence and Fluorescence Imaging of Inflammation



Jen-Chieh Tseng and Jeffrey D. Peterson

Abstract This chapter focuses on the application of optical imaging methods to visualize inflammation in living animals. Optical imaging has several advantages as it operates without any involvement of ionizing radiation or strong magnetic fields. Optical imaging uses nonradioactive probes that produce chemiluminescent or fluorescent light signals in the visible, far-red, or near-infrared (NIR) range of the electromagnetic spectrum. To visualize inflammation at the tissue level, high molecular weight probes can be used to produce fluorescent contrast in the inflamed tissues by taking advantage of the enhanced permeability and retention (EPR) effect. In addition to this general, but rather less selective, approach, the chapter discusses the more specific and mechanistic imaging strategies that specifically target several unique biological aspects of inflammatory processes at the cellular and enzyme levels. These unique aspects include the inflammatory phagocytes that produce reactive oxygen species (ROS), and the tissue-remodeling proteases present in the inflamed tissues. Once activated, specific probes can produce visible or NIR luminescent signals that can be quantified for assessing inflammatory responses. Although visible light is subject to scattering and attenuation in the tissue, fluorescent probes that use NIR light sources have improved tissue penetration allowing generation of 3D tomographic images.

Keywords Inflammation · Chemiluminescence · Fluorescence · Inflammatory phagocytes · Reactive oxygen species (ROS)

J.-C. Tseng (✉) · J. D. Peterson
PerkinElmer, Inc., Hopkinton, MA, USA
e-mail: jen-chieh.tseng@perkinelmer.com

1 Introduction and Background

1.1 Significance of Imaging Inflammation in Animal Models

Inflammation is a fundamental biological aspect of many human diseases. It is the body's natural defense mechanism in response to physical damage, microbial infection, and other tissue insults [1]. In addition, inflammatory processes are known to be associated with various noninfectious pathological conditions such as cancer [2] and neurodegenerative diseases [3]. Although ubiquitously observed in many human diseases, inflammation is an intricate and highly regulated dynamic process that evolves over time, involving the collaboration of many different types of cells. The process typically begins with resolving microbial infection and clearance of damaged tissue and cell debris at early stages. The goals of inflammation later shift to promoting tissue regeneration, restructure, and its eventual repair. As inflammation is an intricate, dynamic, and collective phenomenon involving many cellular players, it is virtually impossible to study inflammation without the use of living subjects as research models. Animal inflammation models provide closer representations of human diseases, and noninvasive molecular imaging provides a means to follow the dynamic changes in target tissues.

Molecular imaging methods that specifically target cells that drive inflammatory responses can be very useful for inflammation research, but the selection of effective imaging strategies requires extensive knowledge of inflammation biology. Several types of immune cells are involved in inflammation and, among them, phagocytes are particularly important during tissue inflammatory responses. These specialized leukocytes include granulated neutrophils, phagocytic monocytes, and macrophages. All three cell types are considered major professional phagocytic cells for their unique capability to engulf and digest invading microbes or tissue debris. In addition to their phagocytic capability, each of these cell types is equipped with specific enzymatic tools to exert their necessary inflammatory functions at different stages of inflammation. These unique enzymatic tools can also help them communicate and coordinate with other immune and somatic cells to achieve their inflammation-specific objectives. Since tissue inflammation is largely mediated by neutrophils and monocytes/macrophages, many inflammatory imaging methods have been developed by specifically targeting these phagocytes. This review will begin with an in-depth discussion of critical cellular players in inflammation and the proteases, enzymes, and other factors important in their inflammatory effector functions. The attention will then focus on recent noninvasive chemiluminescence imaging (CLI) and fluorescence imaging (FLI) strategies that exploit these unique inflammatory features and functions for noninvasive, real-time assessment of inflammation and treatment.

1.2 *Unique Cell Biology of Inflammation: Phagocytes*

Polymorphonuclear neutrophils are the most abundant granulocytes circulating in the blood stream, and these cells are the first phagocytic cells responding to tissue insults and microbial infection. At this initial stage of inflammation, damage-associated molecular patterns (DAMPs) released by somatic cells attract neutrophils to the site [4]. One of the neutrophil's primary functions is to inactivate and kill invading microbes. The ability to phagocytose and eliminate invading microorganisms is critical for host defense. Neutrophils can ingest pathogens into phagosomes, which have an acidic, nutrient-deprived environment. In addition, phagosomes can fuse with special granules that contain proteases and antimicrobial peptides, and, more importantly, these specialized compartments can produce highly toxic levels of reactive oxygen species (ROS) for direct killing of pathogens (mostly bacteria) engulfed within. Besides this direct killing mechanism, neutrophils release proteases stored in their granules to modify the extracellular milieu or regulate other cell functions. In general, neutrophils are the first line of inflammatory phagocytes attracted to an injury site, where they perform their function and then undergo programmed cell death [5].

Circulating monocytes are another type of phagocyte that traffic via the blood stream to peripheral tissues in both homeostasis and inflammation. One unique feature of monocytes is their capability to differentiate into macrophages. When a monocyte enters a damaged tissue through the blood vessel, a process known as leukocyte chemotaxis and extravasation, it undergoes a series of changes to become a macrophage [6]. The maturation from monocyte to macrophage is triggered by local growth factors, such as pro-inflammatory cytokines and microbial products. Monocyte recruitment and maturation are critical for inflammation, and they contribute to effective control and clearance of bacterial, protozoal, fungal, and viral infections. It is worth noting that although there are stationary "resting" macrophages within healthy tissues, most macrophages that accumulate at diseased sites are functionally and biologically different and typically derived from circulating monocytes.

Once differentiated, mature and active macrophages can express cyclooxygenase-2 (COX-2) that produces prostaglandins [7]. Prostaglandins are locally acting, paracrine lipid mediators that promote vasodilation and inhibit the aggregation of blood platelets. Since prostaglandins are potent inflammatory triggers, specific COX-2 inhibitors have been developed for modulating inflammatory responses [8], although some show cardiotoxicity and significant safety concerns. Macrophages also express several other unique genes to facilitate their inflammatory functions. To cope with high-energy demand after maturation, macrophages express higher levels of folate receptor to increase folate uptake [9]. As the macrophages play an important role in tissue repair, they express several types of integrins on the plasma membrane to interact with the surrounding milieu and tissue scaffolds [10, 11]. In addition, macrophages can restructure tissue frameworks by secreting

many types of proteases specifically targeting components of the extracellular matrix (ECM) [12, 13].

Macrophages are also professional phagocytes, with an individual macrophage capable of digesting more than 100 bacteria during its life span. Similar to neutrophils, macrophages can ingest pathogens by engulfing them into phagosomes, which then fuse with lysosomes to form phagolysosomes. Intracellular phagolysosomes in macrophages contain enzymes and toxic reactive oxygen species (ROS) to digest and destroy their targets [14]. In addition to producing ROS in the intracellular compartments, activated macrophages can assemble ROS-producing machinery on the plasma membrane and release ROS into the nearby extracellular space. These ROS not only inactivate external targets directly but can also serve as chemical signals to coordinate with other cells [15]. However, unlike neutrophils which are short-lived and mostly die in the early stages of inflammation, macrophages survive longer in the body and are important regulators of inflammation at later stages. In addition to ingesting invading pathogens, macrophages are highly specialized in the removal of dying or dead cells and cellular debris. Thus, neutrophils and macrophages play their roles at different temporal stages of inflammation. In a typical bacterial infection scenario, neutrophils are attracted to the site of infection, where they perform their function, die, and are ultimately phagocytosed by the macrophages.

Compared to other somatic and stromal cells, phagocytes are specialized granulocytes with unique biochemical capabilities. They perform their inflammatory functions, either as effectors or regulators, by utilizing these unique enzymes or small mediator molecules. Given tissue inflammation is largely mediated by neutrophils and monocytes/macrophages, these cells and their biochemical armament could serve as possible targets for inflammation imaging. In the following sections, we will discuss how we can take advantage of these immune cell characteristics for noninvasively studying and quantifying inflammatory processes. In particular, the discussion will focus on phagocyte enzymes that are involved in ROS production and inflammatory proteases for zymogen activation.

1.3 Unique Inflammatory Enzymes for ROS Production

First, phagocytes have the capability to produce high levels of ROS. Activated phagocytes generate these highly reactive, oxygen-derived small molecules at sufficient levels to directly eliminate invading bacteria. However, at lower levels, ROS can also serve as signaling molecules to surrounding tissue. Superoxide ($O_2^{\cdot-}$) is the primary source of many downstream ROS, and in both neutrophils and macrophages, the phagocyte NADPH oxidase (Phox) is the major source of tightly controlled superoxide production [15]. Phox has multiple components/subunits and its activity can be regulated by its assembly. The major components include a membrane-bound heterodimer cytochrome b_{558} as the enzyme core, and several cytosolic regulatory subunits, including $p67^{phox}$, $p47^{phox}$, $p40^{phox}$, and Rac

[15]. Cytochrome b_{558} is a heterodimer protein consisting of subunit CYBA and CYBB. CYBB is a highly glycosylated transmembrane subunit of Phox (also known as $p91^{phox}$ and NOX2). More importantly, CYBB is the essential subunit which carries out the primary redox chain reaction from the cytosolic electron donor, NADPH, to the electron acceptor, oxygen, on the outside of the membrane [15]. Upon stimulation and activation, phagocytes assemble the complete Phox enzyme complex by recruiting cytosolic regulatory components (p67/p47/p40 and the GTPase Rac) to the membrane-bound cytochrome b_{558} core.

Interestingly, different phagocytes have different final assembly locations of Phox. At the initial stage of tissue damage and inflammation, neutrophils can consume high levels of oxygen to produce various ROS in the phagosome for their microbe-killing activities, a phenomenon called respiratory burst [16]. In resting neutrophils, most of the cytochrome b_{558} (CYBA/CYBB) is located in the membrane of intracellular storage granules, and only a small fraction is present in the plasma membrane [17]. Upon phagocytosis of opsonized bacteria, cytochrome b_{558} and all necessary regulatory subunits are transported to phagosomes where they are assembled into complete, active holoenzymes [15]. The enzyme complex is strategically placed on the granular membrane to release high levels of superoxide into the intragranular space of phagosomes. Of note, there are also several other enzymes in the phagosomes to further convert superoxide to various downstream ROS, greatly potentiating its toxicity toward microbes. For example, hydrogen peroxide (H_2O_2), another major ROS for killing bacteria, can be generated by spontaneous dismutation of superoxide particularly at low pH within phagosomes. Alternatively, but to a lesser extent, hydrogen peroxide production can be facilitated by superoxide dismutase (SOD) [15]. Hydrogen peroxide can be further converted to other downstream antimicrobial ROS such as hypochlorous acid (HOCl) in the presence of myeloperoxidase (MPO) [18]. Thus, the respiratory burst is a phenomenon of neutrophils using phagosomal enzymes such as Phox and MPO to rapidly convert high levels of oxygen into a variety of toxic ROS.

On the other hand, macrophages are known to produce extracellular ROS, but at a lower level. When macrophages emerge as secondary responders at sites of inflammation, they play various regulatory roles and small, reactive ROS serve as signaling molecules. One of the primary functions of macrophages is to coordinate with other cell types to achieve tissue repair. The ROS generated by macrophages at later stages of inflammation have multiple regulatory functions, including tissue remodeling, new vessel formation, and reepithelialization [19]. Therefore, unlike in neutrophils, cytochrome b_{558} in macrophages is mostly found in the plasma membrane with low levels present in the intracellular compartments [20], to serve as a recycling pool of the enzyme core [21]. Furthermore, macrophages show low levels of MPO expression in intracellular vesicles that are not sufficient for high-level hypochlorous acid production as seen in neutrophils [22]. Thus, neutrophils use Phox to produce high levels of internal ROS for direct microbe killing, while macrophages use Phox to generate lower levels of external superoxide predominantly for regulatory functions [20].

1.4 Unique Inflammatory Proteases

In addition to ROS-related enzymes, phagocytes produce and/or secrete various proteases to facilitate their antimicrobial, tissue remodeling, and other inflammatory functions. For example, neutrophil elastase is a serine proteinase stored within specialized neutrophil lysosomes, called azurophil granules. When released from activated neutrophils, neutrophil elastase has a direct antimicrobial function. It is known to degrade the outer membrane protein A (OmpA) of *E. coli* as well as other virulence bacterial factors found in *Shigella*, *Salmonella*, and *Yersinia* [23]. In addition to elastin, neutrophil elastase has a broad substrate range beyond what its name suggests. The enzyme can hydrolyze other protein components of the extracellular matrix, including aggrecan, fibronectin, the triple-helix structure of type III and IV collagens, and the cross-linkage regions of type I, II, and V collagens [24]. It has been shown that neutrophil elastase is present in considerable concentrations outside of the neutrophil at sites of chronic inflammation, and its serine proteinase activity has been linked to the pathologic processes of a variety of inflammatory diseases, including idiopathic pulmonary fibrosis, rheumatoid arthritis, adult respiratory distress syndrome, and cystic fibrosis. Released neutrophil elastase may regulate inflammation by digesting and processing various inflammation-promoting factors in the extracellular matrix, an idea supported by recent studies showing the involvement of neutrophil elastase in degenerative and inflammatory disorders [25].

Matrix metalloproteinases (MMPs) are another class of protease commonly associated with tissue inflammation. MMPs are zinc-dependent endopeptidases produced by many cell types, including lymphocytes and granulocytes, but in particular by activated macrophages [13]. Macrophages secrete a broad range of MMPs, and these specialized phagocytes represent a major source of MMPs in chronic inflammatory lesions such as granulomas [26]. Like many proteases with potent regulatory functions, MMP activities are carefully controlled. They are initially synthesized as inactive proenzymes (zymogens) with a pro-peptide domain that must be removed before the enzyme is active. For example, pro-MMPs can be activated by neutrophil elastase [27]. MMPs are capable of degrading a wide range of extracellular matrix proteins, and thus they play important roles in various physiological and pathological processes involving tissue remodeling. MMP activities are associated with morphogenesis, angiogenesis, tissue repair, cirrhosis, arthritis, and metastasis. More interestingly, the roles of MMPs are not only limited to tissue remodeling, as they also modulate the immune response by cleaving cytokines and chemokines to control leukocyte migration. In turn, cytokines and chemokines activated and released by MMPs can control surrounding cell behavior such as cell proliferation, migration (adhesion/dispersion), differentiation, angiogenesis, apoptosis, and host defense [28]. They can also control cell death by specific cleavage of cell surface receptors and the release of apoptotic ligands (such as the Fas ligand). Therefore, it is not surprising that MMPs have been found to be involved in many human diseases. Studies indicate that MMP-2 and MMP-9 are particularly important in cancer metastasis [29], while MMP-1 is thought to be important in rheumatoid arthritis and osteoarthritis [30].

Cathepsins (Cat) belong to a family of proteases commonly found in all animals as well as most other organisms, and some of them are implicated in inflammatory responses. There are approximately a dozen members of this family, and they are categorized by their structure, catalytic mechanism, and which proteins they cleave [31]. Currently, the cathepsin family includes two serine proteases (Cat A, Cat G), two aspartic proteases (Cat D, Cat E), and 11 lysosomal cysteine proteases (Cat B, C, F, H, K, L, O, S, V, X, and W). Like many proteases, cathepsins are initially synthesized as inactive proenzymes that need to be proteolytically processed for activation [32]. Many cathepsins become activated at the low pH found in lysosomes, and as a result, most Cat activities are observed intracellularly and, in particular, within these organelles. However, there are secretory cathepsins that operate extracellularly. One of the important examples is Cat K, a cysteine protease that is known to be secreted into the extracellular space by osteoclasts to facilitate bone resorption. Furthermore, macrophages secrete Cat K in inflamed tissues, and so can some fibroblasts and epithelial cells, albeit to a lesser degree [12]. Monocyte-derived macrophages express and secrete Cat K after 6 or 12 days of differentiation [12, 33]. In addition, a variety of cysteine cathepsins are key regulatory proteases in inflammation [34]. Cat B, C, F, H, and L are also known to be expressed by macrophages. In macrophages and microglia, cysteine Cat S is initially present within the cells; however, upon phagocyte activation, Cat S activity is released extracellularly [35]. Furthermore, antigen-presenting cells (APCs), including dendritic cells (DCs) and B lymphocytes, are known to express Cat S [36].

1.5 Advantages of Whole-Body Optical Imaging for Inflammation Research

In inflamed tissue, many biochemical, physiological, and pathological processes occur, as does communication or crosstalk between many cellular players, making it rather difficult to reproduce such environments *in vitro*. Furthermore, inflammation is not a simple, static phenomenon that can be characterized by a simple endpoint measurement. It is a dynamic process evolving with time as different immune cells enter, exit, and/or die at inflammatory sites. Thus, it is necessary to use living animal models for inflammation research, with research tools that can capture the dynamic nature of inflammation. However, using animals for research presents several challenges, including the acquisition of repeated measurements of the animal model in a longitudinal observation. Traditionally, histological techniques are the gold standard for detecting the presence of inflammatory phagocytes in tissues. However, as tissue collection typically requires animal termination, histological approaches are not capable of following inflammation processes in the same animals over time. In addition, histological methods generally require much higher number of animals in a cohort, which is especially true when engaging in a longitudinal study involving many sample-collecting timepoints. Therefore, histological methods are

questionable from an animal welfare point of view and also too costly for longitudinal studies, and they are typically used only for endpoint assessment.

In this regard, noninvasive molecular imaging techniques have several advantages that can greatly help researchers to better understand the inflammatory processes in living subjects. Currently, there are several imaging methods available for imaging inflammation in living animals. These methods include optical imaging (chemiluminescence or fluorescence, in the visible and near-infrared range), positron emission tomography (PET), single-photon emission computed tomography (SPECT), magnetic resonance imaging (MRI), X-ray-based computed tomography (CT), and ultrasound (US). Each method has its strengths and can be used to visualize certain, but not all, aspects of tissue inflammation in living animals. Nevertheless, the noninvasive nature of these technologies makes it possible to combine more than one of these imaging modalities into an animal study for a more comprehensive view of disease progression.

Optical imaging has several advantages over the nonoptical imaging methods. Unlike PET or SPECT that detect high-energy, short-wavelength radiation emitted from unstable radioactive isotopes, optical methods use stable, safe, and nonradioactive probes that produce light signals in the visible, far-red, or near-infrared (NIR) range (400–800 nm) of the electromagnetic spectrum. This means that optical imaging does not require dedicated space and special shielding for safety; therefore, optical imaging instruments are much less regulated and are more accessible for researchers (with less shielding needed for fluorescence excitation lasers). *In vivo* optical imaging instruments are generally less expensive than PET, SPECT, and MRI imagers, and most optical imaging probes generally are less expensive than radioactive tracers. Thus, optical modalities have lower operational expenses and are more easily accessible for researchers. In addition, optical imaging can provide quantitative assessment of biological changes. Although MRI, CT, and US are highly useful modalities for anatomical and functional visualization, it is not easy to use them for quantitative assessment of unique inflammatory cells or biological processes, even with the help of contrast-modulating agents. On the other hand, optical imaging data can be easily quantified since inflammatory target signals can be calculated in terms of photoemission from the inflamed tissues, and in tomographic optical imaging, it is also possible to quantify the amount of localized probes in terms of molar concentrations or total nanomoles or picomoles. The scope of this review will focus on the strengths of optical imaging methods and discuss imaging strategies that take advantage of unique and specific inflammatory ROS enzymes and proteases for imaging inflammation in living animals.

Of note, since optical imaging operates in the visible and NIR spectral range (400–800 nm), the scattering of light limits its spatial resolution to slightly below a millimeter [37]. Further, as visible light in the 400–600 nm range can be significantly attenuated by hemoglobin, optical imaging methods operating in the visible light spectrum have detection depth typically less than 10 mm. Fortunately, the tissue penetration of optical signals can be greatly improved by using NIR light sources (700–800 nm or above) and fluorescent probes. The use of fluorescent probes has

another advantage over the radioactive tracers, as their distribution in the target tissues can be further validated by fluorescence microscopy.

1.6 Chemiluminescence Imaging (CLI) and Fluorescence Imaging (FLI): An Overview

In vivo optical imaging techniques can be generally categorized by the mode of light excitation: chemiluminescence imaging (CLI) or fluorescence imaging (FLI). The main difference between CLI and FLI is the energy source for photon generation. CLI uses chemical compounds as the energy source [38], whereas FLI utilizes excitatory light as the energy source. As external excitatory light sources have much higher-energy output, FLI typically requires shorter exposure time and less pixel binning during image acquisition. On the other hand, since CLI uses injected chemical compounds as the energy sources, the CLI light signals are much dimmer in comparison. Therefore, to improve imaging sensitivity, CLI generally requires longer exposure and larger binning which makes the images more pixelated in presentation.

FLI can measure a broad variety of physiological endpoints with a variety of biologically targeted or enzyme-activatable fluorescent probes. Nevertheless, the use of FLI in living animals can be limited by tissue auto-photoluminescence at certain wavelengths due to the inherent short Stokes shifts (~20–40 nm) of most dyes [39]. CLI has certain advantages over FLI. Without the need for excitation light, CLI has lower background signal and thus can often yield higher signal-to-noise (S/N) ratios and better sensitivity. Bioluminescence imaging (BLI) is a unique type of CLI imaging that utilizes specific enzyme-substrate pairs (e.g., luciferase-luciferin) to further improve signal strength and specificity [40, 41]. However, the potential of BLI for in vivo application in inflammation imaging is limited due to the need for ectopic expression of luciferase in the inflamed tissues and restricted by a rather small selection of compatible luciferase-luciferin pairs [42, 43]. Thus, this review will focus mostly on CLI imaging for inflammation using chemical compounds.

2 Imaging Inflammation Using ROS-Sensitive Chemiluminescent Compounds

2.1 Small Chemiluminescent Compounds

Since inflammation is a multistep in vivo process involving a variety of specialized inflammatory cells and enzymes, molecular imaging methods specifically targeting these unique features would allow noninvasive, accurate assessment of inflammation

status in a longitudinal manner. The CLI strategies for inflammation imaging mainly take advantage of the unique ROS enzymes in inflammatory phagocytes. These enzymes can produce superoxide and its downstream reactive oxygen species that can react with CLI compounds. Many small chemiluminescent compounds have been widely used in laboratories as chemical assays to detect different types of ROS. One of the most important examples is luminol ($C_8H_7N_3O_2$, MW = 177.2). Luminol can react with hydrogen peroxide (H_2O_2) to generate blue chemiluminescence. However, the luminol-based chemiluminescence reaction requires the presence of a catalyst such as a peroxidase to promote light production. Other small CLI probes such as lucigenin ($C_{28}H_{22}N_4O_6$, bis-N-methylacridinium nitrate, MW = 510.5) [44] and methylated *Cypridina* luciferin analogs ($C_{14}H_{14}ClN_3O_2$, MCLA hydrochloride, MW = 291.7) are commonly used in laboratories as well. They are specific chemiluminescence compounds for the detection of superoxide anions (O_2^-) and singlet oxygen (1O_2) in vitro and ex vivo [45]. However, unlike luminol, lucigenin and MCLA can react with ROS and produce chemiluminescence without the presence of a peroxidase. In addition, it is worth noting that these small chemiluminescent compounds, luminol, lucigenin, and *Cypridina* luciferin analogs, all produce light in the blue region of visible light at around 450 nm, which has limited tissue penetration due to strong absorbance by heme in this spectral region. Figure 1 summarizes these small CLI compounds (luminol, lucigenin, and MCLA) and their reaction requirements for light production.

Despite the extensive use of small CLI compounds for in vitro assays, their potential for in vivo imaging of superficial sites of inflammation was only recently examined. With their specific affinity for ROS, these chemiluminescence compounds were tested for in vivo inflammation imaging and found to react with inflammatory ROS to generate inflammation-specific chemiluminescence in living animals. More importantly, they demonstrated acceptable pharmacological properties and were generally well tolerated when injected into mice. Luminol and its derivative L-012 ($C_{13}H_8ClN_4O_2$, sodium salt) are capable of generating blue chemiluminescence in several animal models of inflammation [46–48]. Lucigenin can also produce chemiluminescent signal; however, further investigation indicates luminol and lucigenin target different inflammatory phagocytes and have different light-producing mechanisms in the used animal models. Interestingly, it has been shown that luminol bioluminescence in vivo is mediated by neutrophils, while lucigenin bioluminescence is mediated by macrophages [49]. Such a difference makes it possible to use luminol and lucigenin imaging to distinguish early and late phases of inflammation [49]. Since these small compounds are commercially available and relatively inexpensive, they can be readily translated to many inflammation imaging applications in small animals. Figure 2 illustrates the difference in phagocyte imaging mechanisms of these two small CLI compounds. This pair of compounds allows differential visualization of neutrophils and macrophages in a noninvasive manner, thus allowing the longitudinal assessment of these cell populations both in the acute and chronic phases of inflammation.

Two factors determine the different specificities of these two compounds toward phagocytes. The first factor is the difference in membrane permeability. Luminol

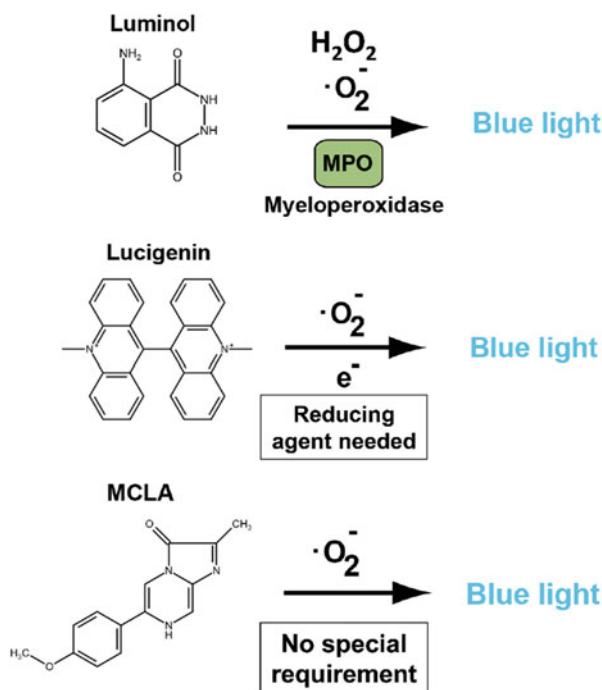


Fig. 1 Mechanism of small chemiluminescence probes for ROS detection and imaging in living animals. Luminol, lucigenin, and the methylated *Cypridina* luciferin analog (MCLA) are small CLI probes capable of producing blue chemiluminescence in response to ROS. Luminol reacts with superoxide or hydrogen peroxide (H_2O_2). However, luminol chemiluminescence requires a catalyst such as a peroxidase to promote light production. In living animals, myeloperoxidase (MPO) is responsible for this catalytic role. Other small CLI compounds such as lucigenin and the methylated *Cypridina* luciferin analog (MCLA hydrochloride) can react with the superoxide anion ($\cdot\text{O}_2^-$) and singlet oxygen ($^1\text{O}_2$) without any peroxidase. However, lucigenin chemiluminescence requires a reducing agent for its activation. In biological systems, NADH or NADPH are the typical reducing agents for lucigenin activation

(MW = 177.2) is a small uncharged molecule that can easily penetrate both the plasma membrane and the membrane of intracellular vesicles (such as phagosomes). On the other hand, lucigenin is a larger molecule (MW = 510.5) with two positive charges, making it much less membrane-permeable. The second and more critical factor is the difference in subcellular locations in neutrophils and macrophages where the Phox holoenzyme assembles.

Although both luminol and lucigenin depend on Phox to provide superoxide anion ($\text{O}_2^{\cdot-}$), in living subjects, luminol bioluminescence also relies on peroxidase activity to catalyze the light-emitting reaction [46, 49]. Prior studies have indicated that myeloperoxidase (MPO) is the peroxidase responsible for luminol luminescence in vivo. In neutrophils (or monocytes), high levels of MPO are found in the intracellular vesicles (phagosomes), where most of the Phox is present [18]. As a result, luminol bioluminescence is preferentially generated within phagosomes of activated neutrophils (or monocytes, to a lesser extent). Interestingly, as acute

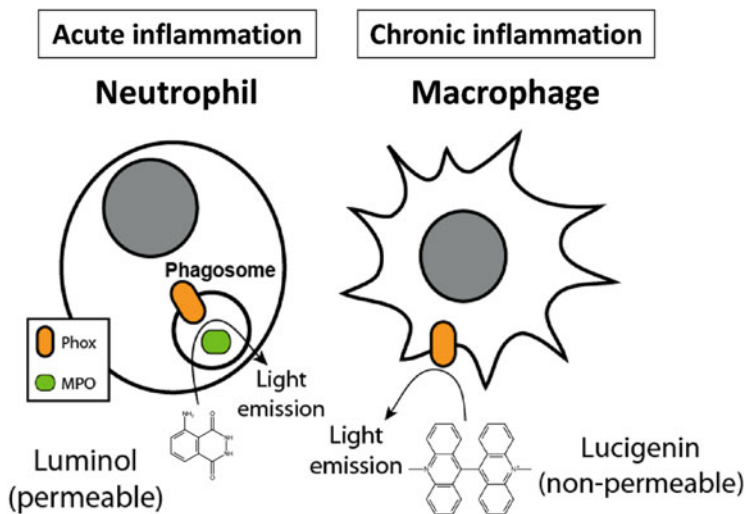


Fig. 2 Phagocyte NADPH oxidase (Phox) is the major source of superoxide produced in inflammatory phagocytes. Phagocyte NADPH oxidase has multiple components and is responsible for the CLI luminescence observed in living animals. Upon activation, granulocytes such as neutrophils assemble Phox in the membrane of intracellular storage granules. Neutrophils (granulocytes) also express high levels of myeloperoxidase (MPO) in the granules. In contrast, activated macrophages assemble Phox in the plasma membrane after activation. The difference in subcellular locations of Phox holoenzyme assembly enables the use of luminol and lucigenin to image specific phagocyte populations. Luminol is a small uncharged molecule that can easily penetrate both plasma membrane and membrane of intracellular vesicles in the neutrophils, where MPO is also present. On the other hand, lucigenin is a larger molecule with two positive charges, making it much less membrane-permeable and therefore it can be used for imaging plasma membrane-bound Phox activity in macrophages

inflammation is mostly mediated by neutrophils, the fact that MPO activity is predominantly present in neutrophils makes luminol ideal for imaging early inflammatory responses. Therefore, luminol is not suitable for monitoring late-phase or chronic inflammation, in which neutrophils are believed to play a lesser role in comparison to macrophages.

On the other hand, lucigenin is more specific for imaging macrophage activity in animal inflammation models [49]. After maturation from circulating monocytes, macrophages in the tissue tend to lose most of their MPO activity [22], and thus cannot be effectively visualized using luminol. Lucigenin can react with extracellular ROS produced by macrophages in chronically inflamed tissues to produce chemiluminescence. Unlike neutrophils, whose Phox activities are mostly in the intracellular granules, macrophages assemble Phox in the plasma membrane after activation [20]. Therefore, the membrane-impermeable lucigenin selectively interacts with superoxide produced by macrophage Phox in the extracellular space and produces CLI signals indicative of late-stage inflammation.

Figure 3 demonstrates the use of these two CLI compounds to distinguish between early and late stages in a murine skin inflammation model. Local and

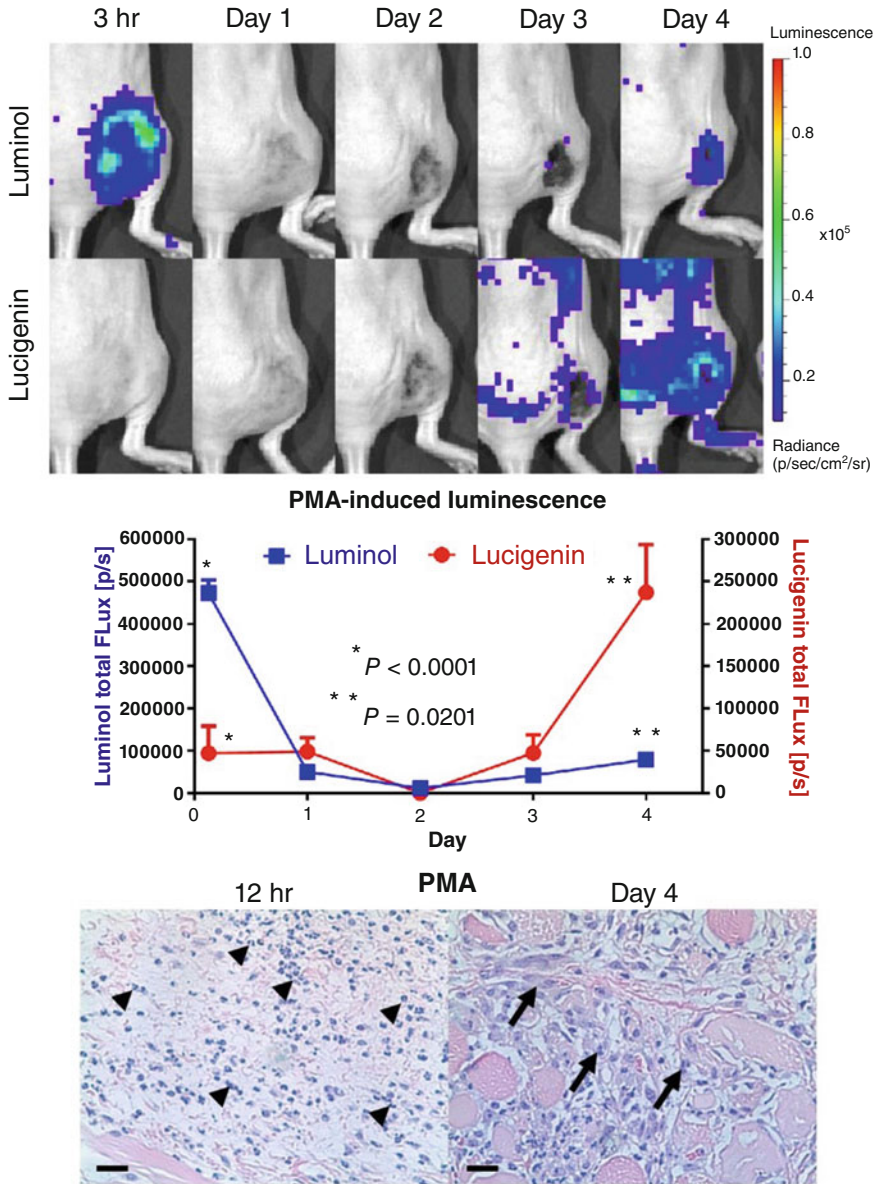
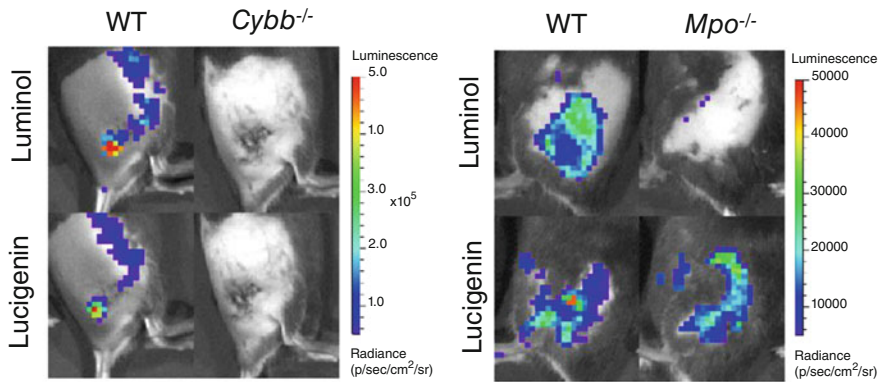


Fig. 3 Luminol and lucigenin image different stages of inflammation responses. Subcutaneous injection of phorbol 12-myristate 13-acetate (PMA) causes rapid skin irritation and inflammation. Daily imaging (top) of both lucigenin and luminol bioluminescence was performed for 4 days. Using an IVIS® Spectrum imaging system, significant luminol chemiluminescence from the injection sites were observed as early as 3 h after PMA injection, while very low lucigenin luminescence was observed. However, from day 3 onward, as wound contraction and scar formation were visible, a steady increase of lucigenin bioluminescence was observed (middle graph). These results suggest that luminol bioluminescence is associated with the acute phase of

superficial inflammation can be induced by subcutaneous injection of phorbol 12-myristate 13-acetate (PMA), a potent protein kinase C (PKC) activator capable of causing rapid skin irritation and inflammation. The preferential affinity of luminol for neutrophils makes it ideal for visualizing acute inflammation, whereas very low lucigenin luminescence is observed at this early stage. However, as macrophages move into the inflamed skin tissue to orchestrate wound repair and scar formation, lucigenin luminescence prevails at this later inflammatory stage. Further mechanistical studies using *Cybb* or *Mpo* knockout mice have demonstrated the different chemiluminescence mechanisms of these two CLI compounds. Although both luminol and lucigenin need Phox as the superoxide source, lucigenin does not require a peroxidase such as MPO to produce light (Fig. 4). The chemiluminescence reaction of lucigenin involves two key steps [50]. The first step is single-electron reduction of lucigenin (LC^{++}) to form lucigenin cation radical ($LC^{+\cdot}$). The second step is for the radical intermediate to react with superoxide anion ($O_2^{\cdot-}$) to produce light. Superoxide by itself is not able to reduce lucigenin. It has been demonstrated that an additional reducing agent, such as NADH or NADPH, is required for ex vivo measurement of superoxide anion level in tissue homogenates [51]. In living tissues, plasma membrane-bound Phox in macrophages can facilitate both steps by single-electron reduction of extracellular lucigenin using intracellular NADPH as an electron donor and provide superoxide to complete the chemiluminescent reaction, making it ideal for imaging macrophages (Fig. 4). One concern regarding the use of lucigenin for CLI is its possible redox cycling, a phenomenon that typically occurs when lucigenin is used to measure ROS in vitro or ex vivo. In this alternative mechanism, the lucigenin cation radical ($LC^{+\cdot}$) intermediate, instead of reacting with superoxide to produce light, may reduce oxygen (O_2) to produce artificial superoxide ($O_2^{\cdot-}$) [47]. However, redox cycling is not likely to happen in live animals since living tissues have rather low oxygen pressure (~ 10 mmHg, compared with ~ 150 mmHg in the atmosphere). In living tissues, the positively charged radicals would have much higher affinity for endogenous superoxide anion ($O_2^{\cdot-}$, with a negative charge opposite to $LC^{+\cdot}$) than for the uncharged oxygen (O_2) [51]. The fact that macrophage Phox generates both lucigenin cation radical ($LC^{+\cdot}$) and superoxide anion ($O_2^{\cdot-}$) in the vicinity of extracellular space greatly facilitates lucigenin chemiluminescence and therefore makes lucigenin a selective CLI compound for macrophage imaging.

Fig. 3 (continued) inflammation, whereas lucigenin bioluminescence is preferentially associated with the late phases of inflammation. Skin samples collected at 12 h and 4 days after PMA injection show different phagocyte presence (bottom row) in the inflamed tissue according to H&E staining (scale bar: 20 μ m). At the early stage (12 h), granulocytes, mostly neutrophils, are the predominate phagocytes. On the other hand, macrophages are the dominant type at a late inflammation stage (day 4). Images shown are original data from a related published study [49]



Magnetically purified splenocytes

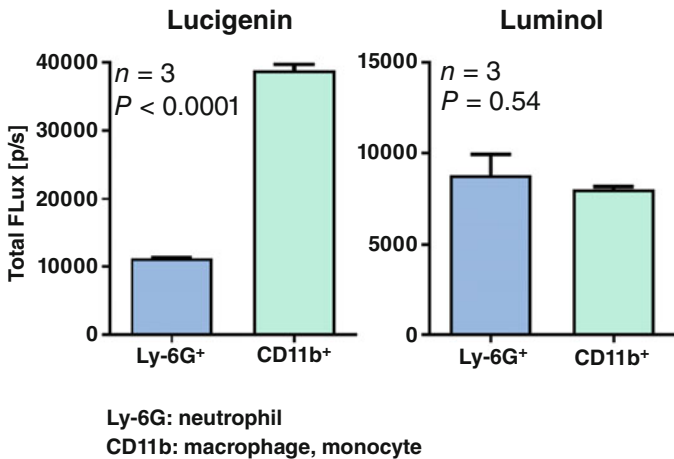


Fig. 4 Mechanistic studies of luminol and lucigenin chemiluminescence using knockout mice. Inflammatory CLI was performed in *Cybb*^{-/-} and *Mpo*^{-/-} mice to examine the roles of Phox and MPO in chemiluminescence produced by lucigenin and luminol. CYBB is the key component of Phox holoenzyme. *Top row*: in one study, surgical skin wounds were made in both WT and *Cybb*^{-/-} mice and imaging of both CLI compounds was performed 4 days later. Using an IVIS® Spectrum imaging system, very low CLI signals of both lucigenin and luminol were observed in *Cybb*^{-/-} animals, indicating that Phox is necessary for both lucigenin and luminol bioluminescence. In another set of studies, local tissue inflammation was induced by subcutaneous (s.c.) injection of PMA into wild-type (WT) and *Mpo*^{-/-} mice. Acute-phase luminol luminescence signals were acquired 3 h after PMA injection, and late-stage lucigenin chemiluminescence was visualized 3 days after PMA injection. MPO deficiency greatly affected luminol bioluminescence, especially in the early phase of inflammation, while lucigenin bioluminescence did not depend upon MPO activity. *Bottom row*: magnetically purified Ly-6G⁺ neutrophils and CD11b⁺ macrophages/monocytes were stimulated with PMA *in vitro*. The CD11b⁺ cells produced higher lucigenin bioluminescence than Ly-6G⁺ cells, indicating that macrophages and/or monocytes preferentially activate lucigenin. In contrast, luminol bioluminescence showed no significant difference between

2.2 *Energy Transfer Luminescence Imaging Using Small CLI Substrates as Energy Sources*

Small CLI compounds in general have good signal-to-noise ratios (S/N) for visualizing inflammatory processes in living animals. However, an immediate drawback of using these small CLI compounds for animal imaging is that their light emissions are mostly in the blue range (~450 nm). Several strategies have been pursued to make them emit light of longer wavelengths to improve tissue penetration. The general concept is to use small CLI compounds as the energy sources, and upon reacting with ROS, the chemical energy is transferred to a nearby acceptor fluorophore to generate red-shifted light emission [52]. There are two types of energy transfer strategies: chemiluminescence resonance energy transfer (CRET) and chemically initiated electron-exchange luminescence (CIEEL). Both energy transfer strategies attempt to address the blue color issue by combining the strength of both chemiluminescence and fluorescence imaging. CIEEL, like CRET, also uses chemical energy stored within CLI compounds to generate proximity-dependent luminescence. Nevertheless, these two techniques are fundamentally different in their energy transfer mechanisms and therefore have different application scenarios.

CRET has a Förster (resonance) energy transfer mechanism as used in fluorescence resonance energy transfer (FRET). The Förster resonance energy transfer mechanism is based on dipole-dipole coupling and thus requires spectral overlap between the energy donor's emission and the recipient's absorbance spectra for efficient energy transfer and subsequent light emission. Therefore, the recipient is typically a fluorescent dye whose excitation wavelength matches well with the donor CLI compound's emission wavelength, but capable of emitting red-shifted light. In theory, the operational distance for Förster energy transfer is 10–100 Å [53], and therefore CRET can be used to visualize larger molecule interaction such as protein-to-protein or protein-to-nucleic acid *in vitro*. Several ROS-sensing small microbeads or nanoparticles have been developed and are commonly used for *in vitro* binding assays and applications [54]. For *in vivo* CRET applications, luminol-based ROS imaging strategies have been used to visualize inflammation in deep tissues [55]. In addition, as luminol emits blue chemiluminescence upon activation, it is suitable for pairing with NIR quantum dots or nanoparticles (conjugated or in free form) that efficiently absorb blue light for imaging deep tissue inflammation [55].

Figure 5 illustrates a CRET imaging strategy to visualize phagocyte ROS production using microbeads specifically designed for amplified luminescence proximity homogeneous assay (ALPHA) technology. These ALPHA acceptor beads can

Fig. 4 (continued) Ly-6G⁺ and CD11b⁺ cells, suggesting that MPO was present in both cell types. Together, these results suggest that lucigenin bioluminescence is not mediated by neutrophils, as is the case for luminol. Images shown are original data from a related published study [49]

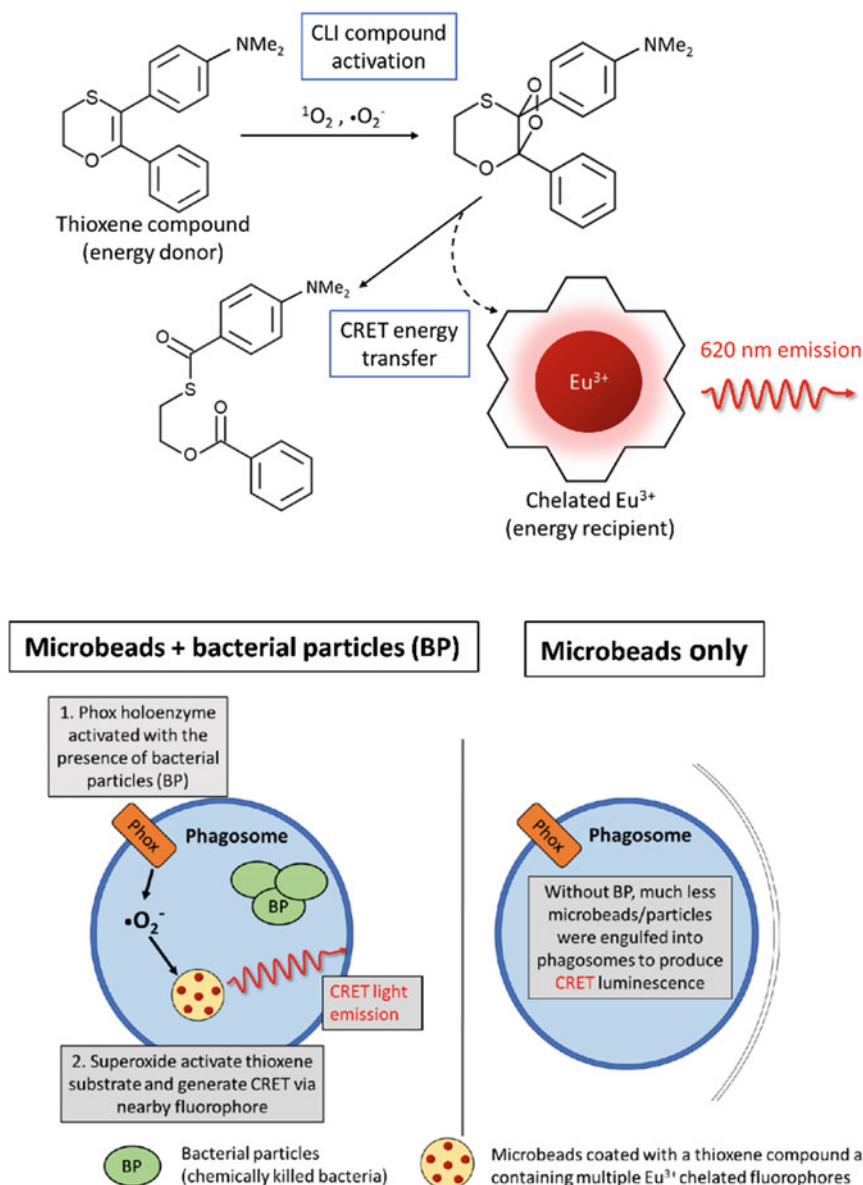


Fig. 5 Thioxene/europium microbeads produce CRET luminescence in response to ROS produced by phagocytes. The amplified luminescence proximity homogeneous assay (ALPHA) acceptor microbeads are coated with thioxene compounds that serve as the energy donor. *Top row:* the thioxene compound can react with singlet oxygen or superoxide anion to form a high-energy intermediate. To ensure efficient energy transfer and CRET light production, the bead is embedded with several europium (III) chelate complexes acting as energy recipients that emit red CRET light at ~620 nm. *Bottom row:* to image inflammatory ROS produced by phagocytes, the microbeads can be mixed with chemically killed *Staphylococcus aureus* bacterial particles (BP) to trigger efficient

produce luminescence in response to ROS such as the superoxide anion and singlet oxygen [54]. The microbeads are about 250 nm in diameter and have a chemiluminescent thioxene coating that serves as the CLI energy source to react with ROS. In addition, embedded within the beads are multiple europium (III) chelate complexes that serve as CRET energy recipients. In this configuration, energy transfer between the ROS-activated small CLI chemical compound (thioxene) and the energy recipient (chelated Eu^{3+}) is ensured. In living animals, locally injected ROS-sensing microbeads can detect ROS produced downstream of Phox in phagocytes. Figure 6 demonstrates the use of these beads to visualize red CRET light signals produced by inflammatory phagocytes. However, their application in *in vivo* imaging is rather limited, mostly due to the larger size of the microbeads or nanoparticles in comparison to small CLI substrates. The large size of microparticles make them less ideal for systemic delivery, and therefore they are mostly used for imaging local inflammation, for example, in bacterial infection models [56].

Similar footpad inflammation studies were performed on WT and *Cybb*^{-/-} mice. As CYBB is the critical catalytic subunit for Phox function, mice lacking CYBB cannot produce high levels of superoxide in the phagosomes, and very little CRET light signals were observed in the *Cybb*^{-/-} footpads inoculated with both ALPHA microbeads and BPs. These results indicate phagosome Phox is responsible for the Alpha microbead CRET light signals in this inflammation model.

Other Förster energy transfer strategies, such as bioluminescence resonance energy transfer (BRET), also use chemical energy stored within luciferins to generate proximity-dependent luminescence. The major difference between CRET and BRET is how the small high-energy chemical molecules (either CLI compounds or luciferins) are activated. CRET relies on ROS to trigger CLI substrate activation, while BRET requires specific luciferase enzymes to release the energy stored within luciferins. Since BRET is also based on the Förster energy transfer mechanism, it has similar operational distance (10–100 Å) and spectral requirement between the energy donor (in this case, a luciferin) and the recipient. Thus, it is also possible to use BRET to visualize interactions between larger molecules. In laboratories, BRET has been adapted for microscopic imaging of protein-protein interactions in living cells using luciferase/photoluminescent protein pairs such as *Renilla* luciferase/YFP. However, *in vivo* applications of BRET for whole-animal imaging have been hindered by the need for exogenous introduction of chimeric target proteins, and by tissue attenuation of blue-green light signal [57, 58]. To improve tissue penetration, *Renilla* luciferase has been conjugated with quantum dots and polymer

Fig. 5 (continued) uptake of both the microbeads and BPs into the phagosome (lower left). Once inside the phagosome, superoxide produced by Phox can activate the thioxene compound and transfer its energy to the embedded fluorescent recipients for CRET light emission. In the absence of BP (lower right), fewer microbeads are engulfed into phagosomes and only very low CRET signals are detected

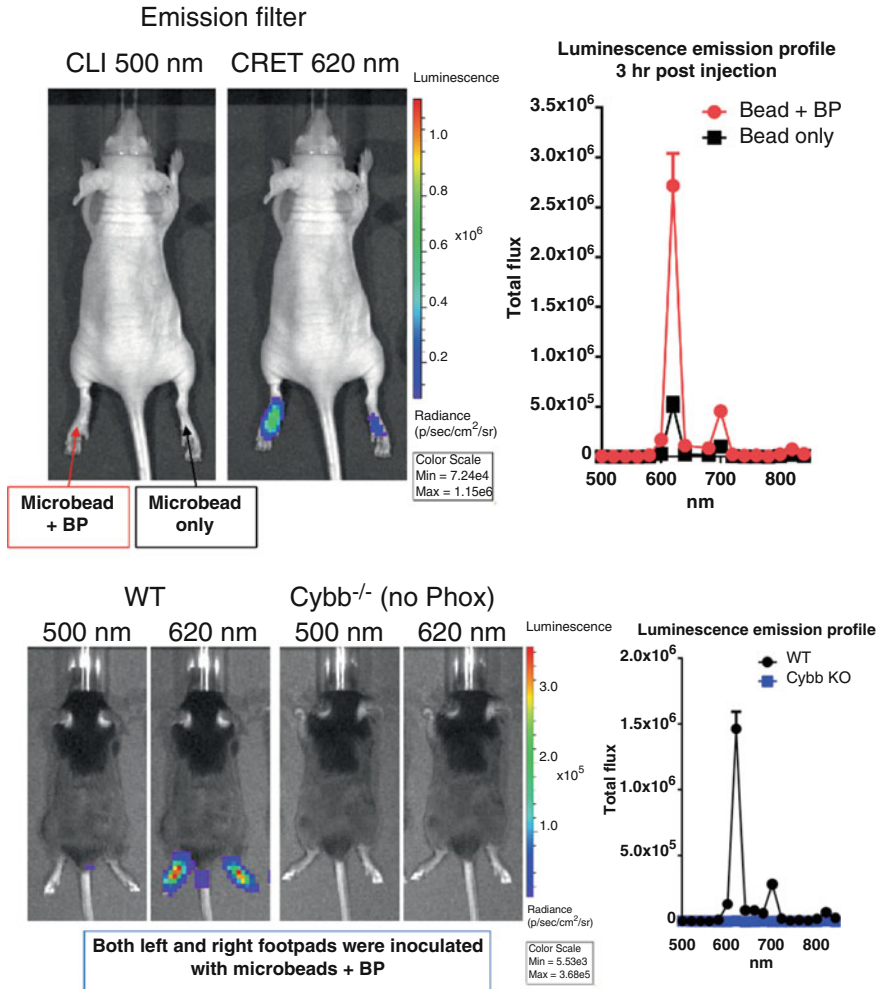


Fig. 6 In vivo CRET energy transfer imaging using ROS-sensitive thioxene/europium microbeads. In this example, ALPHA acceptor microbeads were mixed with chemically killed *Staphylococcus aureus* bacterial particles (BP) prior to subcutaneous injection into the left hind footpad. The bacterial component ensures efficient uptake of both the BP and microbeads (left hind footpad). Once inside the phagosome, superoxide produced by Phox can activate the microbeads to produce CRET light emission which can be readily visualized using the IVIS® Spectrum imaging system. In the absence of BP (right hind footpad), fewer microbeads were engulfed into phagosomes and only low CRET signals were observed. Interestingly, spectral analysis of the emitted luminescence showed red light of 620 nm wavelength which was the major light emission without significant blue light emission, indicating efficient CRET energy transfer of ALPHA microbeads in this footpad inflammation model. Images shown are original data from an unpublished study

nanoparticles to generate far-red or NIR BRET luminescence [59, 60]. These limitations make BRET a more challenging approach for *in vivo* inflammation imaging.

Another energy transfer strategy for inflammation imaging is based on chemically initiated electron-exchange luminescence (CIEEL). Unlike Förster energy transfer, CIEEL energy transfer mechanism does not require spectral overlap between the energy donor (e.g., small chemical compounds, luciferin) and the fluorescent recipient. Instead, CIEEL has a charge-exchange mechanism that requires wave function overlap for direct intermolecular electron transfer between the donor and the recipient. Therefore, CIEEL operates in a much shorter length scale ($<10 \text{ \AA}$) than CRET/BRET. In other words, the CIEEL energy transfer is initiated by direct intermolecular collision between the chemical energy donor and the fluorescent recipient molecules [61–63]. If such short-range interaction can be achieved, CIEEL has an appealing advantage over CRET: CIEEL does not require spectral overlap between the energy donor and the recipient. Although CIEEL is not governed by spectral compatibility, efficient energy transfer is largely determined by the accessibility of the donor and the recipient for intermolecular collision. Therefore, CIEEL energy transfer imaging could take advantage of a broader repertoire of fluorescent probes for customizable biological readouts. It is also possible to use the same small compound as the energy source to drive a variety of fluorescent recipients for CIEEL luminescence at different colors.

The best studied example of CIEEL is the glow stick. Commercially available glow sticks utilize peroxyoxalates, such as bis-2,4,6-(trichlorophenyl)-oxalate (TCPO), as the chemical energy source. Figure 7 illustrates the general CIEEL mechanisms using small chemical compounds as energy sources. After snapping a glow stick, TCPO in the inner tube reacts with hydrogen peroxide in the outer tube to produce 1,2-dioxetanedione, a high-energy intermediate [61, 62]. In the absence of any energy recipient, the high-energy intermediate fragments into two molecules of carbon dioxide and releases its chemical energy as UV emission or heat dissipation. However, in the presence of a fluorescent recipient in the near vicinity, the chemical energy can be transferred via formation of a charge-transfer complex of the intermediate and the fluorescent recipient [63]. Thus, glow stick luminescence is fundamentally different from Förster-based CRET or FRET [53, 64]. Using the same chemical substrate TCPO as the energy source, it is possible to manufacture glow sticks in a wide range of colors as the color is solely determined by the fluorescent recipient added into the tubes.

Since CIEEL is a hybrid mechanism of chemiluminescence and fluorescence and can produce red-shifted luminescence for better tissue penetration, CIEEL was also investigated for its potential applications in live animal imaging. As many small chemiluminescent substrates are known to react with ROS while still having good biodistribution characteristics, it is feasible to develop a viable CIEEL strategy for imaging tissue inflammation in living animals. Nevertheless, a critical challenge would be on the fluorescent energy recipient side. Since CIEEL requires close proximity of the chemical energy donor and the fluorescent recipient to ensure efficient energy transfer and light production, any ROS-sensing CIEEL strategy would need to achieve specific accumulation of both the ROS-sensing chemical

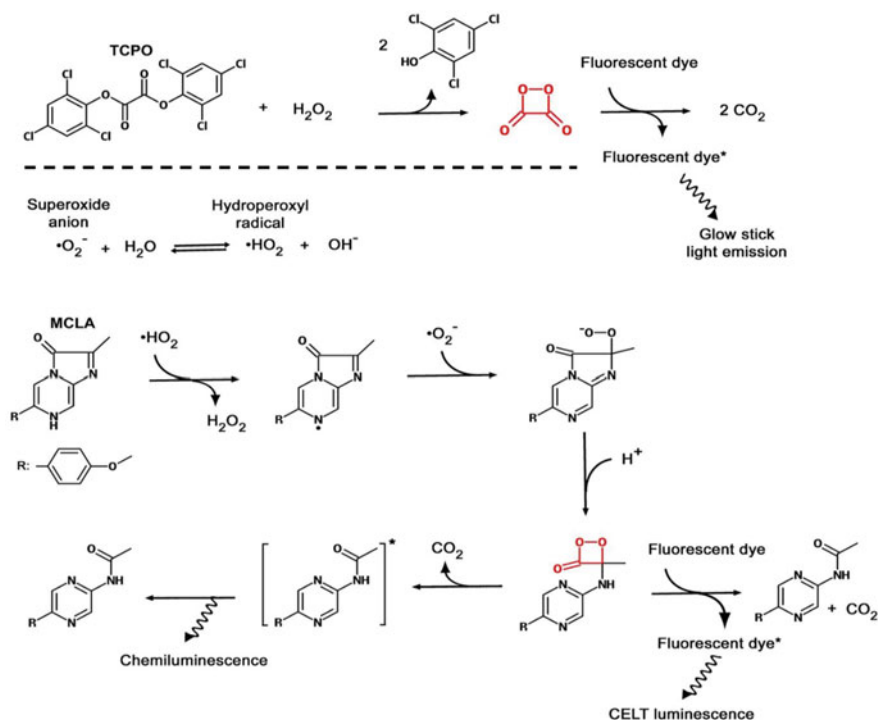


Fig. 7 Glow stick chemistry and CIEEL energy transfer mechanism of MCLA. Common commercially available glow sticks utilize TCPO as the energy source to produce CIEEL energy transfer luminescence. TCPO reacts with hydrogen peroxide to produce 1,2-dioxetanedione (in red), a high-energy intermediate. In the presence of a fluorescent recipient, the chemical energy can be transferred via formation of a charge-transfer complex of the intermediate and the fluorescent recipient. If no fluorescent recipient is present, the high-energy intermediate self-decomposes into two molecules of carbon dioxide and releases its energy as UV emission or heat dissipation. The color of a glow stick is solely determined by the fluorescent recipient, making it possible to produce glow sticks in a variety of colors using the same chemical substrate. However, TCPO is not water soluble and therefore it is not suitable for biological applications. MCLA is a methylated *Cypridina* luciferin analog that has several properties suitable for *in vivo* applications. The compound is small and has no net charge, allowing for penetration of both plasma membrane and membranes of subcellular organelles. Importantly, MCLA readily reacts with superoxide or its downstream ROS derivatives such as the hydroperoxyl radical to form a high-energy 1,2-dioxetane intermediate capable of CIEEL energy transfer in a mechanism similar to TCPO

energy donor and the fluorescent energy recipient at the same microscopic localization. This is a rather difficult task to achieve in living animals.

To overcome the proximity issue, a straightforward approach for CIEEL is to pack the chemical donor together with the fluorescent recipient in microbeads or nanoparticles. This will ensure activated chemical compounds have sufficient opportunity to collide and transfer their energy to fluorescent dyes. In a sense, this strategy is very similar to using miniaturized glow sticks for ROS imaging. *In vivo* imaging

using these miniature glow sticks in living subjects has also been tested and good progress has been made for inflammation imaging. For example, although the poor solubility of TCPO prohibits its direct application in *in vivo* imaging, Lee et al. have demonstrated that nanoparticles formulated from peroxyoxalate polymer and a fluorescent dye were capable of sensing hydrogen peroxide and generating far-red CIEEL luminescence in living animals [65]. Similarly, other types of small peroxyoxalate-based chemiluminescent substrates that are sensitive to ROS and singlet oxygen have been packed into larger polymer-based nanoparticles or microbeads for CIEEL applications.

An alternative CIEEL strategy to achieve concentrated co-localization of both the donor and recipient is to take advantage of the naturally formed small ROS-producing cellular compartments. In inflamed tissues, one of the suitable compartments is the phagosome in stimulated phagocytes. For the choice of CLI energy donor for this CIEEL strategy, in addition to having good ROS reactivity, the substrate also needs to be small and membrane-permeable to reach intracellular phagosomes. In this regard, TCPO is not suitable for this strategy due to its poor water solubility. Luminol, despite its usefulness for imaging of MPO activity, seems to have a very unstable intermediate state and thus is more suitable for CRET [66]. MCLA, on the other hand, has several characteristics suitable for *in vivo* CIEEL applications [45]. MCLA is a *Cypridina* luciferin analog and has good solubility and stability in aqueous solution. Importantly, this substrate can readily react with superoxide or its downstream ROS derivatives [67] to form a high-energy 1,2-dioxetane intermediate similar to TCPO (Fig. 7). MCLA is uncharged and relatively small (MW = 291.7), enabling it to penetrate both the plasma membrane and membranes of subcellular organelles. Additionally, MCLA does not undergo redox cycling when reacting with ROS. The *in vivo* proof of concept for this subcellular compartment CIEEL imaging strategy is shown in Fig. 8. Phox-specific CIEEL light can be produced by selective targeting of ROS-producing phagosomes by fluorescent dyes. These highly accumulated fluorescent dyes then serve as CIEEL energy recipients for MCLA [68]. Interestingly, MCLA CIEEL imaging can also be used to visualize other organelles that produce endogenous ROS. For example, by using mitochondria-targeting fluorescent dyes, it is possible to visualize ROS produced in mitochondria during oxidative phosphorylation. Besides CIEEL imaging of ROS production, this strategy could be extended to visualize other endogenous hydrolytic enzyme activities in living animals by replacing ROS-sensitive substrates with substrates that can be activated by specific enzymes [69]. Several metastable 1,2-dioxetane compounds have been engineered with protective groups to prevent their activation. These protective groups can be removed by hydrolytic enzymes such as β -galactosidase and alkaline phosphatase [61]. Once activated with a suitable enzyme, the chemical energy within the activated substrate can be transferred to a nearby fluorescent recipient via the CIEEL mechanism.

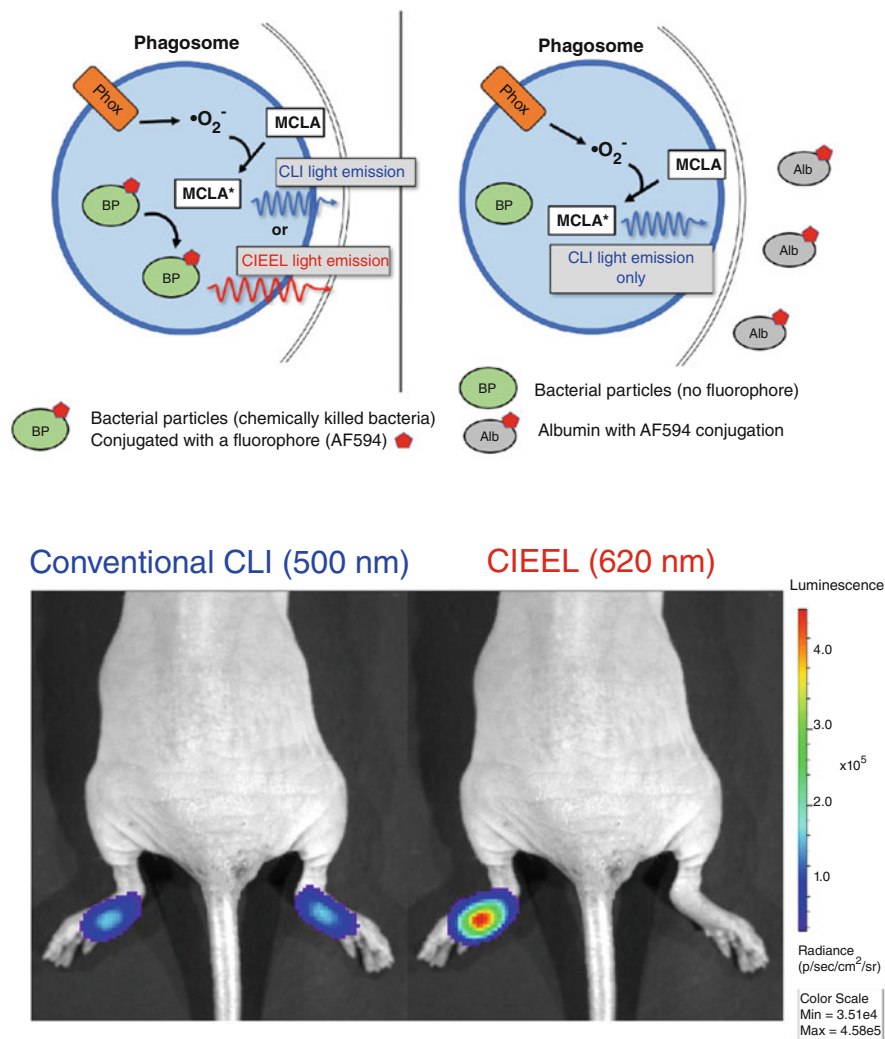


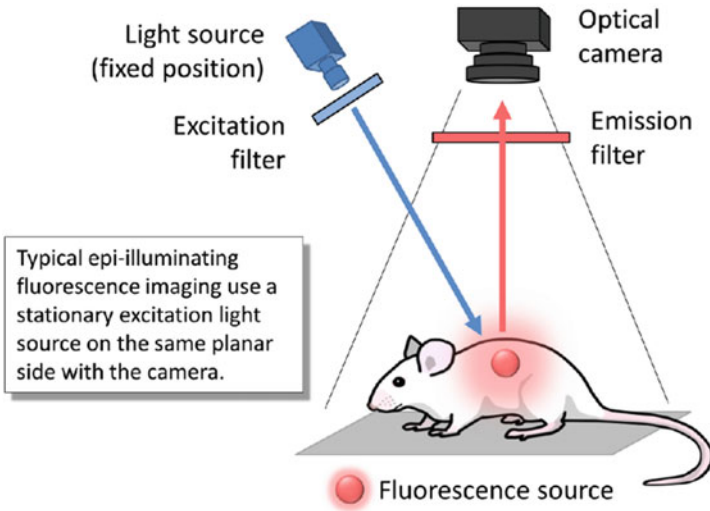
Fig. 8 In vivo CIEEL inflammation imaging using small fluorophores as energy recipient. *Top row*: in this set of footpad inflammation study, we tested whether MCLA is capable of CIEEL energy transfer to the fluorescent recipients conjugated to the bacterial particles (BP). *Bottom row*: subcutaneous injection of Alexa Fluor 594-labeled bacterial particles (BP-AF594) in the left footpads triggered rapid phagocyte accumulation and phagosome ROS production. As controls, the right footpads received a mixture of unconjugated BP and Alexa Fluor 594-labeled albumin (BP + Alb-AF594). As albumin is a common serum protein lacking pathogenic molecular signatures, the phagocytes preferentially engulfed BioParticles but not the Alb-AF594 conjugates. In the footpads receiving BP-AF594, we observed good CIEEL emission (620 nm) using the IVIS[®] Spectrum imaging system after intravenous delivery of MCLA, indicative of high levels of energy transfer to the AF594 moiety. In contrast, control footpads only produced conventional blue chemiluminescence (500 nm) but very low CIEEL emission from the AF594 moiety on Alb-AF594 (620 nm). Images shown are original data from an unpublished study

3 Noninvasive Fluorescence Imaging for Tissue Inflammation

In comparison to CLI, fluorescence imaging (FLI) is a more mature technology that has been widely used for preclinical small animal imaging [70]. Instead of using chemical energy stored within low molecular weight substrates, FLI uses an external light source to excite the fluorophore. Therefore, FLI has a simpler, robust, and straightforward workflow making it more flexible when choosing the right fluorescent probes to suit the research need. It is also possible to perform multicolor imaging on the same animal using probes of different fluorescent wavelengths. The spectral range of FLI is limited by background signals observed from two major sources: tissue autofluorescence at visible wavelengths (peaking at ~500 nm) and interfering mouse chow fluorescence (primarily due to chlorophyll and peaking at ~680 nm). Fortunately, these interfering background signals can be mostly avoided by using NIR-shifted fluorophores and by feeding mice low-fluorescence chow. Therefore, the optimal FLI operates in the range from red to NIR spectra (650–850 nm). Another consideration is the inherent short Stokes shift (~20–40 nm) of most dyes that can modestly decrease fluorescent output due to the requirement of filtering out the emission/excitation overlap [39]. Nevertheless, since the power output for the excitation light is tunable, FLI techniques have a more intense signal output than small chemical compound-based CLI in general. Of note, since modern FLI operates in the red or NIR spectra, it is not hindered by the blue chemiluminescence issue associated with small CLI compounds; recent developments and advances in optical imaging reagents and instrumentation have made FLI more attractive for deep tissue imaging than CLI. This advantage also makes FLI techniques more likely to be translated into clinical use. Various red and NIR fluorescent probes are commercially available for imaging small animals. In addition to planar 2D images, when combined with sufficiently strong excitation light sources such as NIR lasers or halogen lamps coupled with NIR filters, FLI offers sufficient tissue penetration and probe excitation in small laboratory animals to generate 3D tomography images. For example, fluorescent molecular tomography (FMT®) systems that are equipped with strong transilluminating NIR lasers are capable of deeper tissue penetration and faster 3D reconstruction for whole-body imaging in small laboratory animals. Schematic diagrams explaining the difference between the conventional 2D planar and 3D tomographic FLI imaging techniques are provided in Fig. 9.

Aside from imaging instrumentation, the accessibility of a wide range of fluorescent probes also plays a key role in the success of FLI. Traditionally, FLI probes are designed to directly bind/target specific biological markers and pathological features involved in tissue inflammation. The smaller, fluorescently active moiety can be conjugated to a larger targeting agent such as a peptide or protein (antibody). In a sense, FLI probes behave like drugs or therapeutic biologicals of comparable sizes, and their pharmacokinetic and pharmacodynamic properties need to be considered

2D epi-illuminating fluorescence imaging



3D trans-illuminating fluorescence imaging

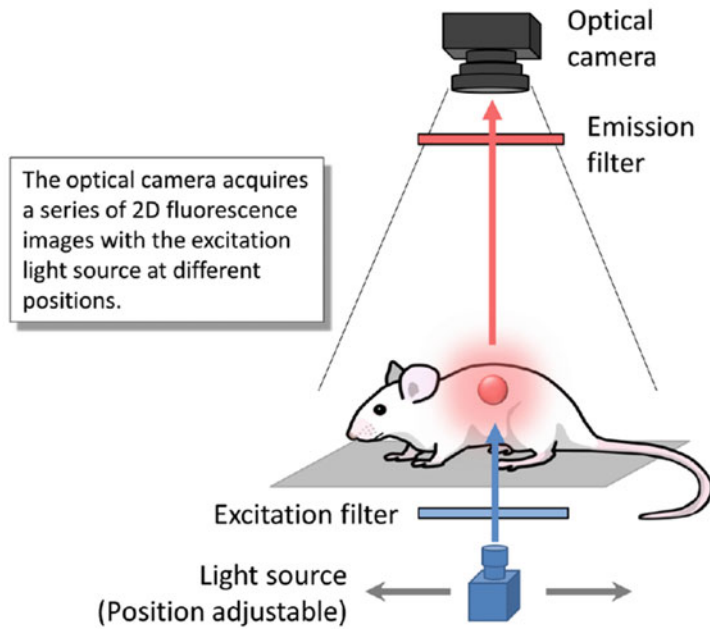


Fig. 9 Instrumental schematics of 2D and 3D FLI imaging. There are two types of FLI imaging for small laboratory animals. The first type is the conventional 2D epi-illumination FLI (*top*). In this configuration, both the excitation light source and the camera are on the same planar side with respect to the animal subject. The advantage of using a stationary epi-illumination light source is to

for successful in vivo imaging applications. In the following sections, we will discuss the major FLI probe design strategies for inflammation imaging.

3.1 Targeting Enhanced Vascular Permeability at Inflamed Sites

One of the hallmarks of local inflammation is tissue swelling (edema), characterized by excess fluid buildup in the injured tissues. This phenomenon is caused by local inflammatory signals such as prostaglandins which increase vascular permeability to facilitate leukocyte infiltration and erythema formation. In addition to cellular extravasation, vascular leakiness and tissue swelling result in enhanced permeability and retention (EPR) for large molecules with sizes greater than 16 kDa [71]. Several fluorescent probes and nanoparticles have been developed to systemically visualize leaky vasculature and have been widely used to visualize edema and vascular leakiness in inflamed tissues [72]. Figure 10 illustrates the polymer-based and nanoparticle-based designs of FLI probes for vascular and inflammation imaging. Typically, these probes differ in size and can have a variety of blood half-lives and speed of extravasation into tissue, though longer circulation times facilitate leakage into sites of chronic swelling and inflammation. Therefore, this type of vascular FLI probe can be injected into animals and imaged immediately to visualize general tissue vasculature in both healthy and diseased tissues. After a period of incubation, the probes will extravasate and accumulate in the inflamed tissues to generate inflammation-specific signals. Figure 11 demonstrates the use of these two types of FLI probes for imaging inflammation in a mouse model of arthritis. Of note, this class of probe does not target a specific molecular feature (e.g., enzymes, markers) in the inflamed tissue, and the accumulation is based on increased vascular permeability, although non-targeting nanoparticles can be further engulfed by macrophages [73]. Nevertheless, these probes can be used not only to systemically scan the whole

Fig. 9 (continued) cast the excitation light over multiple animal subjects and therefore increase operational throughput. However, as excitation light is spread over a larger area, planar 2D FLI is typically not suitable for imaging fluorescent targets deeper than 5 mm. The second and more advanced type is 3D transillumination FLI (*bottom*). Unlike conventional 2D FLI, the excitation light source is placed on the opposite site of the imaging plane and under the animal subject with respect to the camera. Of note, the transilluminating light source is not stationary. For a typical 3D FLI imaging, the light source needs to be placed at various positions near the fluorescent target, and the positional variation of fluorescent signal is the basis for 3D tomographic reconstruction. The advantage of this configuration is better tissue penetration as the intense focal excitation source is placed underneath the subject and close to the fluorescent target. For example, the laser-based FMT system can have tissue penetration in the range of 30–40 mm depending upon the laser power and NIR wavelength. However, as multipoint excitation is required, tomography 3D FLI is generally slower and has lower throughput than the planar 2D FLI, requiring algorithmic reconstruction

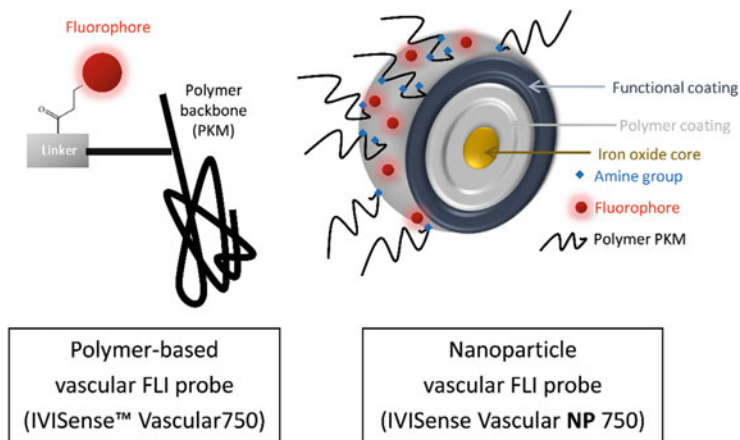


Fig. 10 Design schematics of circulating vascular FLI probes. Polymer-based fluorescent probes (*left*) and nanoparticle-based (*right*) FLI probes with good blood pool stability can be used to visualize general tissue vasculature in both healthy and diseased tissues. Interestingly, after a period of incubation, these probes will extravasate and selectively accumulate in the edematous tissues since local inflammatory signals cause increased vascular leakiness. For example, a polymer-based vascular FLI probe, IVISense Vascular 750 (also reported as AngioSense® 750), has a long polymer backbone that serves as a pharmacokinetic modifier (PKM) for enhanced blood stability. A NIR fluorophore can be chemically conjugated to the backbone via a linker. Another vascular FLI probe design is based on nanoparticles. For example, a nanoparticle vascular FLI probe, IVISense Vascular NP 750 (also reported as AngioSpark® 750), has a metal oxide core and contains layers of polymer and functional coating. To enhance its blood stability, the surface is modified with polymer PKMs. In addition, the fluorescent signals are generated by NIR fluorophores conjugated to the surface functional coating. The PKM modification prolongs the particles' circulation time without affecting their intense NIR fluorescence. Although neither FLI probe targets a specific inflammatory molecular feature (enzymes, markers), both are selectively retained within the inflamed sites due to the unique pathological feature in inflamed tissues (e.g., leaky vasculature and erythema). Nevertheless, their selective retention in inflamed tissues makes it possible to systemically scan the whole body to pinpoint the inflammation sites

body to pinpoint inflammation sites but also to provide a quantitative means of assessing their inflammation status.

3.2 Selective Binding and Targeting of Inflammatory Protein Markers

This is the most straightforward and robust design concept for inflammation FLI probes: designing a fluorescent probe that is capable of direct interaction and binding to a specific inflammatory marker. Targeted fluorescent probes can be delivered systemically into animals to bind upregulated inflammatory markers, thereby accumulating at sites of disease. Figure 12 illustrates three examples taking advantage of

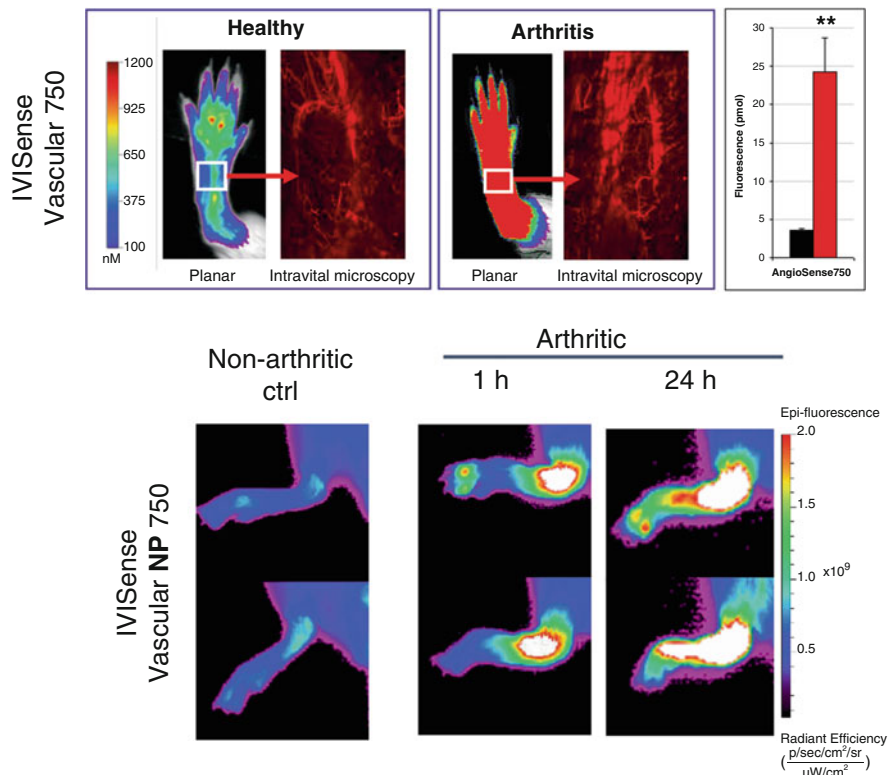


Fig. 11 FLI of vascular leakiness associated with inflammation in an arthritis mouse model. Collagen antibody-induced arthritis (CAIA) was induced by antibody cocktail injection, and mice with CAIA arthritis were used in this set of studies. Increased vascular permeability in the arthritic tissues was visualized by polymer-based FLI probes (IVISense Vascular 750, *top*) and nanoparticles (IVISense Vascular NP 750, *bottom*). Both FLI probes with good blood pool stability can be injected into animals and visualize general tissue vasculature in both healthy and diseased tissues. After systemic delivery of IVISense Vascular 750, 2D planar FLI and intravital microscopy were performed immediately to confirm enhanced vasculature development in the CAIA footpads. The 2D FLI signals can be quantified for a more accurate assessment of the inflammation status (** $P < 0.01$). The presence of IVISense Vascular 750 in vasculature was also validated by intravital microscopy (arrows). In another set of studies, IVISense Vascular NP 750 nanoparticles were systemically injected into non-arthritic and CAIA mice. The mice were imaged at 1 and 24 h after nanoparticle injection. Significantly increased inflammatory FLI signals were observed at 1 h in the CAIA footpads, where fluorescent signals further increased at 24 h after more particles extravasated and were retained in the inflamed tissue. Selective extravasation and retention of nanoparticle signals in the inflamed tissues is largely caused by increased vascular leakiness. Images shown are original data from unpublished studies

known ligand interactions with their inflammation biomarkers. This type of probe can also be used *in vitro* for imaging cells and for *ex vivo* imaging of tissues to validate specific targeting in animals.

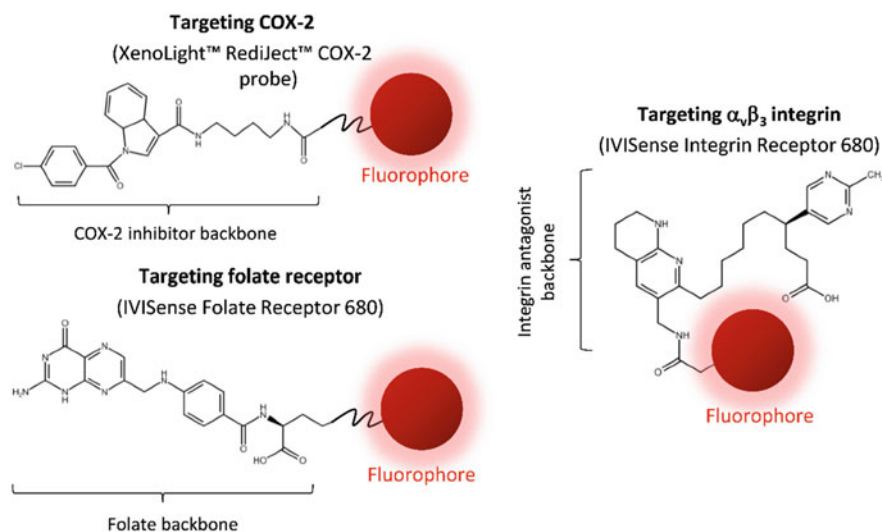


Fig. 12 FLI probe designs for direct targeting inflammatory markers. FLI probes can be designed to directly interact and bind to specific inflammatory markers. This can be achieved by using known small moieties that specifically interact and bind to the protein targets. For example, small COX-2 inhibitors that show excellent specificity and binding affinity can be used as targeting backbones to which a NIR fluorescent moiety is chemically linked (XenoLight™ RediJect™ COX-2 probe). Similar strategies can be used to produce a FLI probe directly targeting folate receptors or integrin $\alpha_v\beta_3$ by taking advantage of their known binding partners, folate (IVISense Folate Receptor 680, also reported as FolateRSense™ 680) or an RGD mimetic $\alpha_v\beta_3$ antagonist (IVISense Integrin Receptor 680, also reported as IntegriSense™ 680)

One of the best examples of this strategy is cyclooxygenase-2 (COX-2)-targeting fluorescent probes. COX-2 is an attractive biomarker for inflammation. Although COX-2 expression is also found in a healthy tissue, its expression in macrophages is highly upregulated in inflamed and malignant tissues [74]. COX-2 is a cytosolic enzyme that catalyzes the conversion of arachidonate, an essential fatty acid, to prostaglandins, which are involved in modulating vessel permeability and inflammatory responses. COX-2 expression is typically low or undetectable in most healthy tissues. However, COX-2 activity at sites of inflammation is highly upregulated. COX-2 has also been shown to play a central role in tumorigenesis in various carcinomas. Figure 13 demonstrates the use of a COX-2-targeting probe for FLI of tumor-associated COX-2 expression.

Because of its critical role in promoting inflammation, inhibition of COX-2 can provide relief from symptoms of inflammation and pain. Several small COX-2 inhibitors have been developed as nonsteroidal anti-inflammatory drugs (NSAIDs) that show excellent specificity and binding affinity. Taking advantage of these small inhibitors as backbones, a series of COX-2-specific fluorescent probes were designed and synthesized. A red or NIR fluorescent moiety (such as rhodamine) can be chemically linked to the targeting moiety that is based on the inhibitor backbone. Although the final structure (Fig. 12) is larger than the original inhibitor

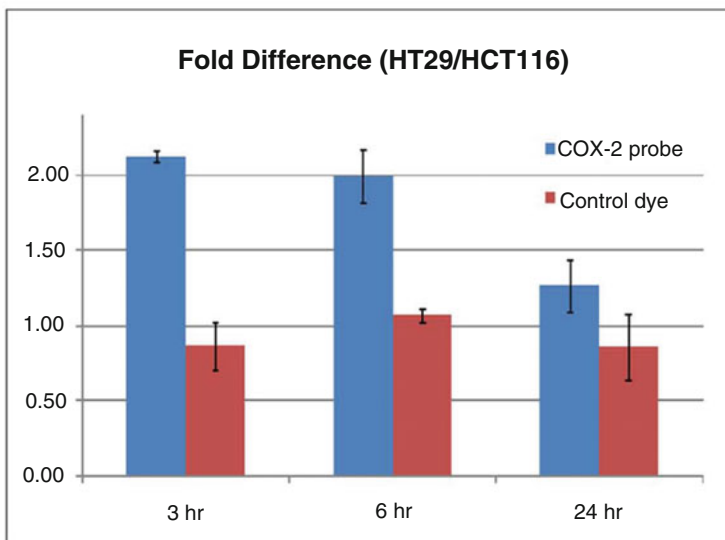
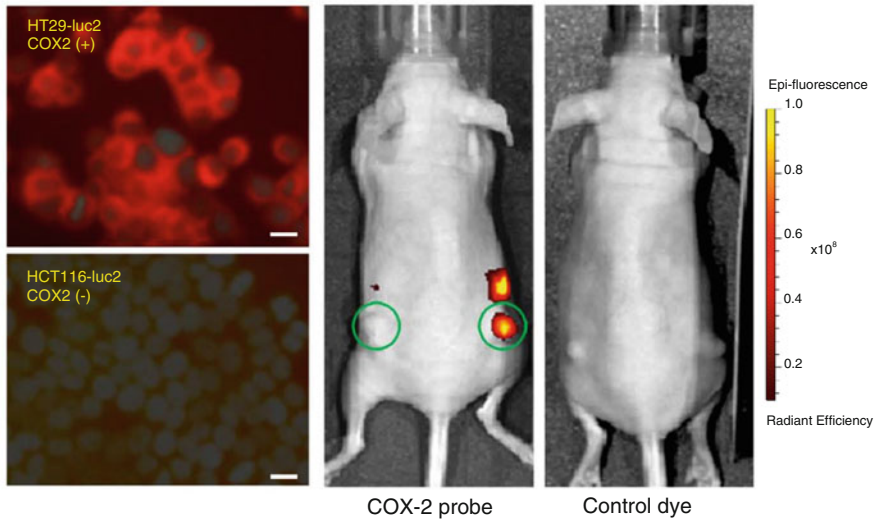


Fig. 13 Direct targeting of COX-2 expression in cancer cells. Cyclooxygenase-2 (COX-2) is an inflammatory biomarker known to be expressed in macrophages as well as in malignant tumors. In cultured cells (*top left*), a COX-2-specific FLI targeting probe (XenoLight RediJect COX-2 probe) can bind to the COX-2-positive HT29 cells, but not to HCT116 cells (scale bar: 10 μ m). IVIS® Spectrum imaging (*top right*) of mice bearing both a subcutaneous HT29 tumor (right flank) and a HCT116 tumor (left flank) revealed specific COX-2 targeting only in the COX-2-positive HT29 tumors. A control dye lacking the COX-2 targeting moiety showed low fluorescence in both tumors (*bottom graph*; mean \pm s.e.m.). Images shown are original data from an unpublished study

backbone, the endogenous substrate of COX-2, arachidonate, is a long-chain fatty acid, and therefore the enzyme is able to accommodate the elongated fluorescent moiety without losing much of its binding affinity and specificity.

Similar design strategies can be adopted to target other inflammation-specific proteins/markers that have well-characterized “activity pockets” for the targeting moiety to interact and bind. The goal of this generalized strategy is to conjugate a fluorescent dye to the targeting moiety in such a way that the dye does not interfere with the targeting moiety’s physical interaction with the activity pocket. For enzymes, the targeting moieties can be their substrates or specific inhibitors. For surface receptors, the targeting moieties can be its ligand or specific antagonists. Appropriate spacer groups or linkers may be needed between the dye and targeting moiety in order to prevent steric hindrance during binding. For instance, folic acid has emerged as a good direct targeting ligand backbone for inflammation FLI. Folate receptors (FRs) have three isoforms (α , β , γ) in humans, and their expression is mostly restricted to inflammatory macrophages and cancer cells to accommodate the increased energy consumption and metabolism of these cells [9]. Specific fluorescent imaging probes have been developed to image arthritis and acute lung inflammation mouse models [75, 76]. The success of this particular design strategy is due to the facts that folate is a relatively small (MW = 441.4) and linear molecule and that its binding pocket in FRs is large enough to accommodate the additional fluorophore with minimal detrimental effects on binding affinity. In fact, similar conjugation schemes have been used to deliver anticancer drugs for selective targeting of tumor cells with high levels of FR expression. After specific binding to cell surface FR, the fluorescent or drug conjugates are internalized via endocytosis which further enhances fluorescent contrast. In principle, this design strategy is not specific to FRs and has been extended to target other cell surface receptors that are known for their recycling and trafficking between the plasma membrane surface and the intracellular endomembrane systems [77, 78].

Some types of integrins are also good imaging targets for inflammation imaging. Integrins are a family of $\alpha\beta$ heterodimeric receptors that comprise 24 $\alpha\beta$ pairs with multiple conformations and interact with a wide variety of components in the extracellular matrix (ECM). They can modulate their binding affinity through conformational switches. As they bridge the extracellular matrix and intracellular cytoskeleton, integrins play critical roles in bidirectional signaling across the plasma membranes involved in many biological processes, such as inflammation, angiogenesis, cell survival, and tumorigenesis [79]. Integrin $\alpha\beta$ dimers can be categorized into four classes: leukocyte, collagen-binding, Arg-Gly-Asp (RGD)-binding, and laminin-binding. In particular, the RGD-binding integrin $\alpha v\beta 3$ is of great interest as it is involved in many inflammatory processes. Integrin $\alpha v\beta 3$ is known to be expressed on differentiated macrophages and angiogenic endothelial cells to regulate vascular permeability [10, 80]. Integrin $\alpha v\beta 3$ is also highly expressed on rapidly growing cells under pathological conditions such as cancer, while its expression is typically minimal on quiescent normal cells [81]. Therefore, integrin $\alpha v\beta 3$ is a good biomarker for imaging vascular inflammation using various probes and imaging modalities [11, 82–84]. Figure 14 illustrates the use of a fluorescent targeting probe

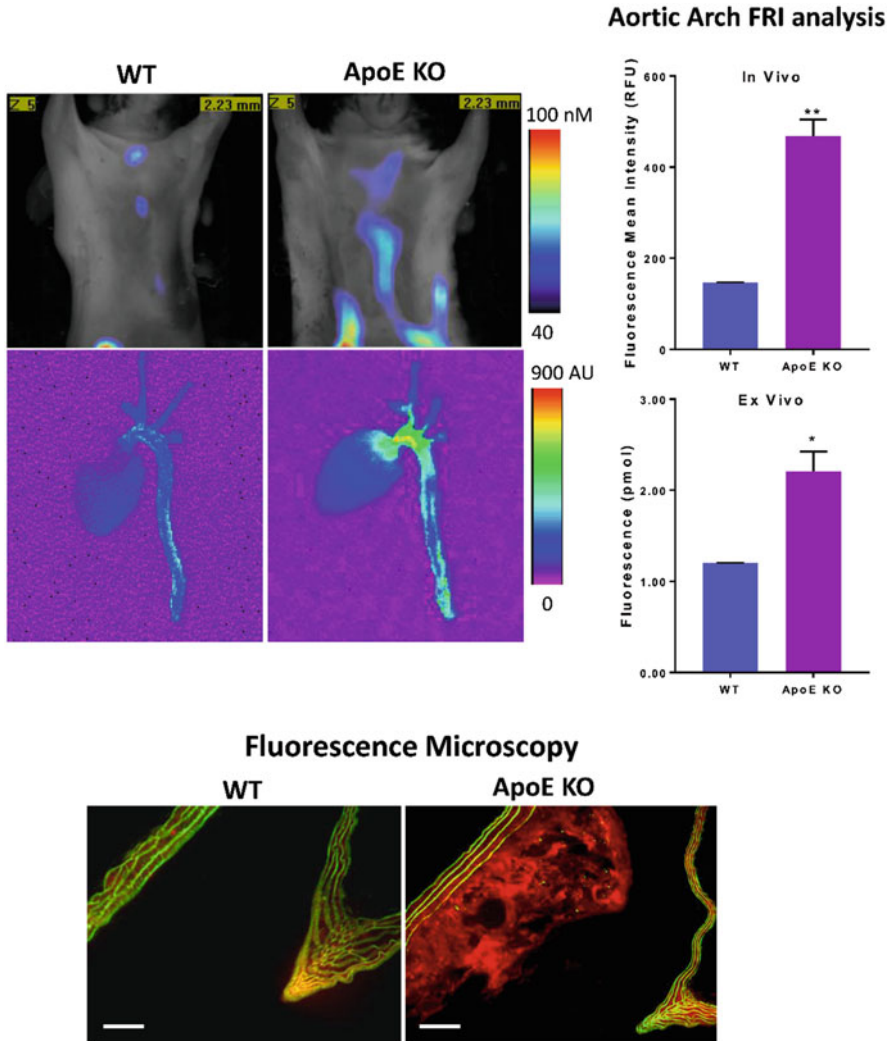


Fig. 14 Direct targeting of integrin expression in a mouse model of atherosclerosis. Atherosclerosis in ApoE^{-/-} male mice was induced by feeding with high cholesterol diet for 16–18 weeks. To visualize plaque formation in living animals, the ApoE^{-/-} and age-matching C57BL/6 wild-type mice were injected i.v. with 8 nmol of IVISense Integrin Receptor 680 probe, and specific integrin signals were imaged 48 h later (*top left panels*). Following imaging, mice were sacrificed and perfused with PBS. The heart, aortic arch, and descending aorta were excised and ex vivo 2D planar FLI were performed. In addition, the tissues were subject to fluorescence microscopy, and higher level of integrin expression (*bottom images*, in red) was observed in the aortic plaque in the ApoE^{-/-} mouse (scale bar: 100 μm). The green color represents the autofluorescence of collagen. Images shown are unpublished original data consistent with a related published study [85]

specific to integrin $\alpha\beta3$ to visualize chronic inflammation in the ApoE^{-/-} atherosclerosis mouse models [85]. In this example, the ApoE^{-/-} mice were maintained on high cholesterol diet for 16–18 weeks to induce atherosclerosis. Systemic delivery (i.v.) of IVISense Integrin Receptor 680 probe detected higher integrin levels in association with plaque formation in the ApoE^{-/-} mice. Subsequent ex vivo imaging and fluorescence microscopy studies confirmed the in vivo imaging findings.

3.3 ROS-Reactive Fluorescent Probes for Inflammation Imaging

In the previous sections, we discussed the use of small, ROS-reacting compounds to selectively target inflamed tissues for direct CLI imaging. Another parallel strategy for FLI is to use small compounds whose fluorescence properties can be “turned on” or altered by reacting with ROS in pathophysiological environment. For tissue and cell staining and microscopic imaging, several reaction-based fluorescent probes have been developed to visualize ROS and other reactive nitrogen and sulfur species [86]. In addition, ROS-sensing fluorescent probes have been widely used to image ROS production in plants to study their response to environmental and developmental changes [87]. Successful ROS sensing in living animals has been performed using a hydrocyanine-based fluorescent probe [88], and this strategy has shown promising proof-of-concept results for visualizing inflammatory ROS production and oxidative stress in rodent retina [89]. However, other classes of ROS-reacting FLI probes have had limited success since most of these ROS-reacting fluorescent probes operate in the green spectral range that is not ideal for imaging live animals. Green-fluorescent probes are still useful for superficial imaging, e.g., for image-guided surgery [90]. Nevertheless, some red ROS-sensing fluorescent imaging probes can be delivered locally to visualize inflammation caused by biomaterial implants in living subjects [91]. Their highly reactive nature makes them poorly stable after systemic injection into animals and might have long-term safety and toxicity implications. To address this, recent developments in ROS-sensing FLI have focused on polymer-based nanoparticles or liposome-based micelles to encapsulate the reactive dyes [92]. Semiconducting polymer dots (Pdots) have also shown promising results for ROS-sensing FLI of hypochlorous acid (HOCl) in mice [93].

3.4 Activatable Fluorescent Probes for Imaging Specific Inflammatory Protease Activity

Using protease-activated fluorescent probes is by far the most successful and widely used FLI strategy for inflammation imaging [94–96]. This strategy has several advantages over the blood-pool/edema, biomarker direct-binding, and

Table 1 Examples of peptide motifs that can be used to develop activatable probes specific for inflammatory proteases

Protease	Peptide motif
Neutrophil elastase	PMAVVQSV
Matrix metalloproteinase-2/-9 (MMP-2, MMP-9)	GPPGVVGEKGEQ
Cathepsin B (Cat B)	GFLG

ROS-sensing FLI probes. By selectively targeting unique protease activities such as neutrophil elastase, MMPs, and cathepsins (see Sect. 1.4 and Table 1) in inflamed tissues, protease-activated fluorescent probes have much higher specificity than the nonselective blood-pool/edema imaging probes. These probes also show lower background signal and thus better signal-to-noise ratios than “always-on” targeted probes, since probes in normal tissue that are not activated by protease activity do not emit fluorescent light.

Figure 15 illustrates the working principles of protease-activated fluorescent probes. This type of probe is designed to take advantage of the self-quenching property of fluorescent dyes: when two or more near-infrared fluorescent (NIRF) dyes are placed in close spatial proximity, the energy of absorbed excitation light is released in the form of heat due to energy transfer between the dye molecules. Figure 16 illustrates two fluorescent probe designs for imaging pan-cathepsin activity. The first design consists of a large polypeptide scaffold and multiple dye moieties (standard IVISense Pan Cathepsin 680, also reported as ProSense 680). By conjugating NIRF dyes to a long-circulating graft copolymer backbone consisting of poly-L-lysine, the proximity of the dyes to each other results in an internally quenched probe. However, in the presence of a suitable protease, the peptidyl backbone can be cleaved to release the fluorescent dyes. The separated, unquenched dyes are now capable of producing fluorescent signals. Therefore, the larger scaffold version has delayed but stronger fluorescence in response to the target protease activity. On the other hand, the small scaffold version (IVISense Pan Cathepsin 750 FAST, also reported as ProSense® 750 FAST) has a short but more enzyme-specific peptide linking only a pair of quenched fluorophores. The smaller size makes it faster for tissue delivery and penetration. In addition, the more unique and specific peptidyl sequence enables quicker digestion in response to protease activation. The peptidyl backbone can be further modified with a pharmacokinetic modifier (PKM) such as methoxy polyethylene glycol (mPEG) to fine-tune the probe’s biodistribution properties in living animals [94, 95].

This versatile platform makes it possible to design and produce a variety of protease-specific FLI probes. For example, several activatable probes have been developed to target proteases with significant roles in inflammation, including neutrophil elastase [97], matrix metalloproteinases [98], and cathepsins [99]. Examples of peptide motifs recognized by these proteases are provided in Table 1. Several studies have demonstrated the effectiveness of this strategy to image inflammatory protease activities in living subjects. For example, using this strategy, specific neutrophil elastase activity was noninvasively visualized in early atherosclerotic

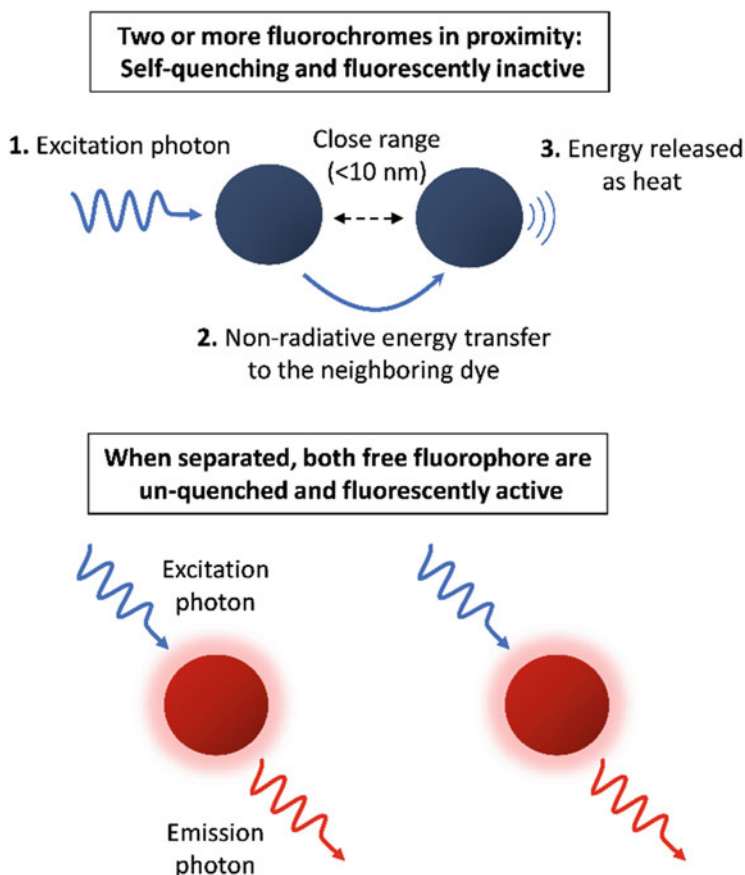


Fig. 15 Self-quenching of fluorescent dyes in close proximity. Fluorescent quenching can occur when two or more of the same fluorophores are in close proximity. As both molecules have the same excitation/emission spectral spectra, when they are in close range (<10 nm), the energy absorbed by one fluorophore can be non-radiatively transferred to the neighboring fluorophore. This type of dynamic quenching is based on the FRET mechanism. However, there is no emission from the recipient and the energy is eventually released as heat. Importantly, the quenching process is distance-dependent. When both fluorophores are separated and free of interference from each other, they are fluorescently active and capable of emitting light after excitation

lesions in a mouse model [100]. In an experimental murine asthma model, a pan-cathepsin activable FLI probe was used to detect eosinophils and monitor treatment responses to dexamethasone [101]. An MMP-specific FLI probe was able to detect early joint inflammation in a collagen antibody-induced arthritis (CAIA) mouse model [102]. Figures 17 and 18 show examples of successful FLI of various inflammatory protease activities in a similar CAIA mouse model [103]. Systemic whole-body imaging reveals strong NE activity in the joints of forepaws, knees, and hind paws (Fig. 17); the algorithms of the applied FMT system

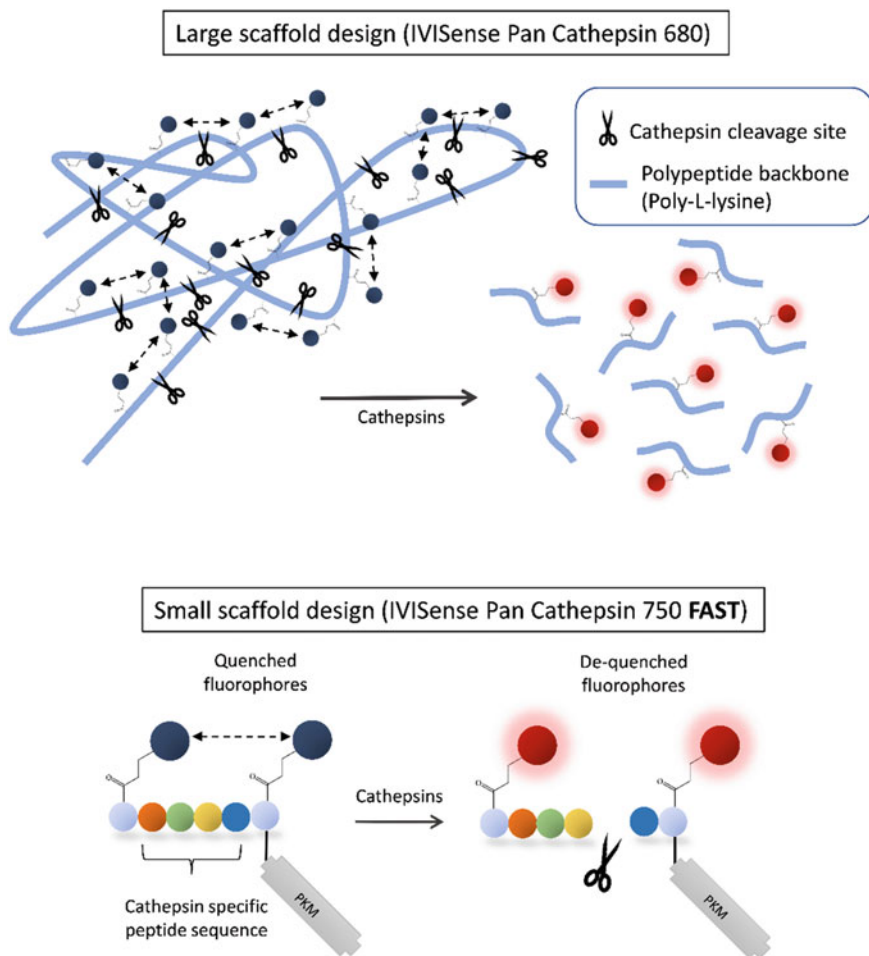
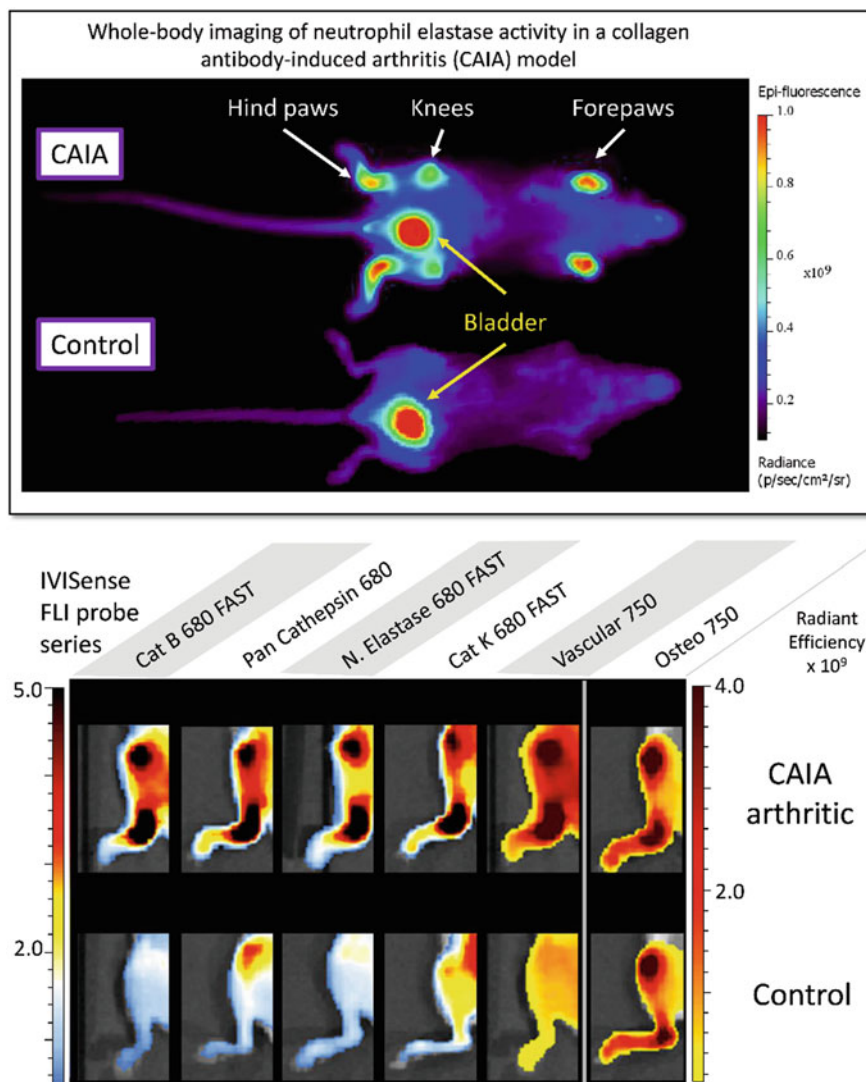


Fig. 16 Schematic diagrams of protease-activated FLI probes. Many fluorescent dyes are self-quenching and when two or more dyes are placed in spatial proximity, they do not emit fluorescent light. Taking advantage of this property, the quenched state can be achieved by linking two fluorescent dyes with a peptide scaffold that is susceptible to a specific protease activity. When the target protease is present, the scaffold is cleaved, and the released fluorescent dyes become fluorescently active. This strategy can be used to generate a variety of protease-sensing FLI probes by selecting different, target-specific peptide sequences. In addition, the pharmacokinetic characteristics can be fine-tuned with the length of the peptide scaffold or with PEG-based polymers (PKM, pharmacokinetic modifier). For example, depending on the length of the peptide scaffold, two versions of cathepsin-specific activatable probes can be prepared. The larger scaffold version (standard IVISense Pan Cathepsin 680, also reported as ProSense 680; *top*) has higher molecular weight and contains multiple dye moieties. Therefore, the larger scaffold version has delayed but stronger fluorescence in response to the target protease activity. On the other hand, the small scaffold version (IVISense Pan Cathepsin 750 FAST, also reported as ProSense[®] 750 FAST; *bottom*) has a short and more specific peptide linking only a pair of quenched fluorophores. This design makes it faster for tissue delivery and penetration, and therefore quicker to respond to protease activation. The short version also contains a pharmacokinetic modification such as mPEG to improve its blood stability and biological viability



allow for quantitative assessment of treatment responses in this CAIA model (Fig. 18).

4 Conclusion

Although in this review we have discussed CLI and FLI as two separate approaches for noninvasive optical imaging of tissue inflammation, in practice, modern optical imaging instruments are equipped with highly sensitive camera systems and high-performance filter sets and can simultaneously perform CLI and FLI on the same animal subject. The quantitative nature of both CLI and FLI makes optical imaging a highly valuable, complementary modality to CT, MRI, and ultrasound whose strengths are in anatomical and structural imaging. In addition to appropriate imaging instrumentation, the key to successful inflammation imaging is the luminescent probe. As both CLI and FLI probes take advantage of unique features at various levels in the inflamed tissues, they define the inflammatory target specificity and biological readouts. At the tissue level, FLI probes are available to target edema and vascular leakiness. At the cell level, different CLI substrates can be used to distinguish neutrophils and macrophages based on their preference for different ROS production sites. Most importantly, at the molecular level, specific FLI probes can detect inflammatory protease activities that are critical in modulating immune responses and shaping inflammation outcomes in living animals.

As summary, Table 2 compares the pros and cons of these two optical imaging approaches. The fundamental difference of CLI and FLI is the energy source for light production. As CLI substrates are very sensitive to ROS produced by the inflammatory phagocytes, they have shorter incubation times and therefore can rapidly produce light signals after systemic delivery into animals. FLI probes typically require longer incubation times as they have more drug-like pharmacodynamic properties after systemic delivery. In order to generate sufficient fluorescence contrast, a period of time is needed for the FLI probe to specifically interact and accumulate at the inflamed site, while free FLI probes in the normal tissues are washed out and excreted via the renal or hepatic pathways. For CLI, there is currently a limited selection of small chemical compounds available for inflammation imaging. Furthermore, CLI is mostly limited to imaging inflammation at shallow locations: as most CLI substrates produce blue light after reacting with ROS, they are not ideal for imaging deep tissue and generally not able to produce 3D tomography images. On the other hand, FLI is a more versatile approach capable of targeting a great variety of physiological changes (e.g., leaky vasculature and EPR) and unique inflammatory biomarkers such as secreted proteolytic enzymes and

Fig. 17 (continued) expected to have similar levels of bone mineral turnover. Images shown are from unpublished studies

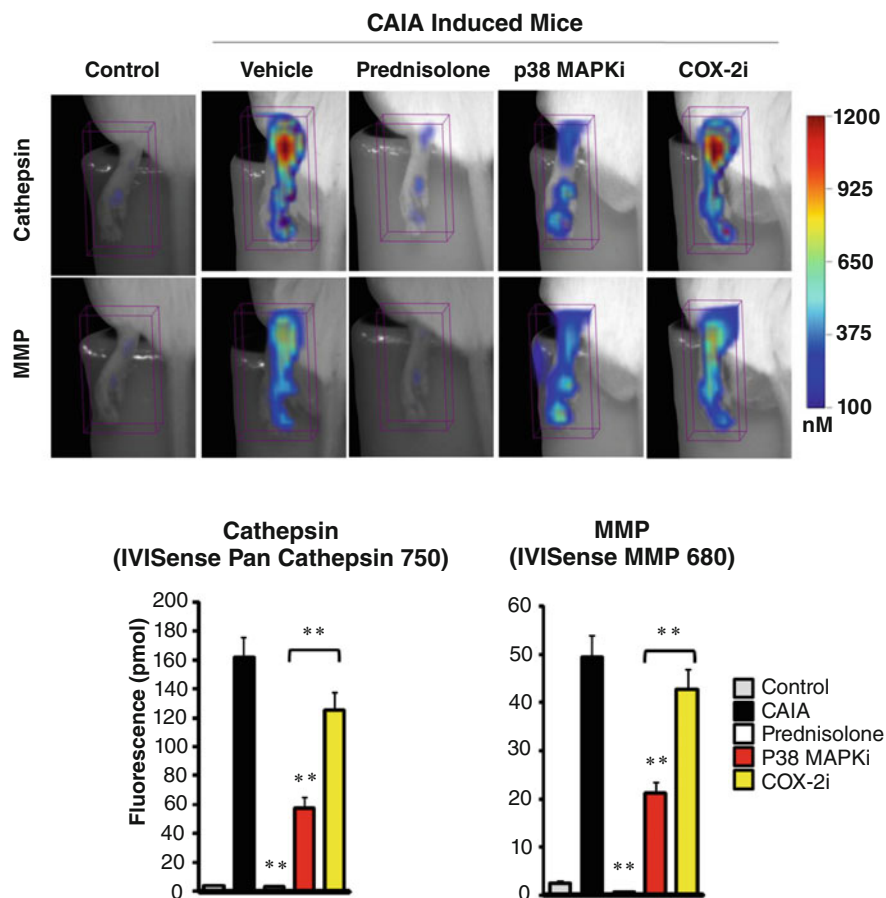


Fig. 18 Use of activatable FLI probes to image treatment responses in the CAIA arthritis model. The treatment responses of several anti-inflammatory drugs in the CAIA mouse model were visualized using the FMT® 4000 imaging system after systemic delivery of the pan-cathepsin (IVISense Pan Cathepsin 750) and MMP-specific (IVISense MMP 680, also reported as MMPsense™ 680) imaging probes (*top panels*). Three anti-inflammatory drugs were tested in this study: prednisolone and inhibitors against p38 MAPK (P38 MAPKi) and COX-2 (COX-2i). Control joints have very low cathepsin and MMP activities, while the CAIA joints have elevated levels of both inflammatory proteases. The FMT® system used in this experiment allows quantification and enables accurate assessment of drug responses (*lower panels*). In this example, prednisolone was the most effective therapy to suppress CAIA inflammation and protease activities. COX-2i only showed moderate anti-inflammatory effects in comparison to the untreated CAIA group (** $P < 0.01$, *t*-test). Images shown are original data from a related published study [103]

surface receptors. In particular, the most important advantage of FLI is that there are currently many NIR fluorescent probes available for deep tissue and 3D tomographic imaging. Table 3 summarizes all the FLI probes discussed in this chapter to provide a

Table 2 Comparison of CLI and FLI methods for inflammation imaging

Mode	Chemiluminescence (CLI)	Fluorescence (FLI)
Energy source	Chemical compounds activated by ROS	External excitation light
Advantages	<ul style="list-style-type: none"> • Highly sensitive to ROS produced by phagocytes • Fast reaction and light production after systemic delivery of small CLI substrates 	<ul style="list-style-type: none"> • Versatile strategies to target inflammatory targets • Various NIR fluorescent dyes with different wavelength for deep tissue and 3D tomography imaging • Simultaneously imaging multiple targets at different channels • High light signal output • Mechanistic imaging of inflammation (protease, ROS possible)
Disadvantages	<ul style="list-style-type: none"> • Fewer choices of CLI compounds • Lower luminescence output compared with FLI • Mostly limited to 2D planar imaging: blue light produced by small CLI substrates are not suitable for deep tissue imaging • CRET and CIEEL energy transfer methods further reduce signal production efficiency 	FLI probes have drug-like pharmacokinetic property, and therefore they require longer incubation time to circulate, interact, or activate in the inflamed tissues

broad overview of FLI imaging versatility and their potential applications in inflammation-related disease conditions such as cancer, arthritis, and atherosclerosis.

In the foreseeable future, with new discoveries and more knowledge obtained in inflammation biology, we expect great advances will be made in optical imaging. Recent proof-of-concept studies of CRET and CIEEL energy transfer nanoparticles greatly encourage the development of next-generation inflammation imaging probes. In return, these new probes could advance our understanding in this intricate, dynamic yet fundamental pathological process that is critical in so many human diseases.

Table 3 Selection of FLI probes mentioned and their applications

Type	Probe	Mechanism	Applications
Physiologic	IVISense Vascular750	IV circulation, EPR	Edema, cancer, arthritis, and other acute/chronic inflammation conditions
	IVISense Vascular NP 750	IV circulation, EPR	Vascular imaging of inflamed tissues by intravital microscopy
Targeted (direct-binding)	XenoLight RediJect COX-2 probe	COX-2 enzyme	Target upregulated COX-2 in cancer and other inflamed tissues
	IVISense Folate Receptor 680	Folate receptor	Tumor/inflammation metabolism marker; cancer, arthritis, and other acute/chronic inflammation conditions
	IVISense Integrin Receptor 680	Alpha V beta 3 integrin	Cancer (tumor and neo-vasculature), atherosclerosis (foam cells)
	IVISense Osteo 750	Hydroxyapatite	Bone turnover (growth and resorption): fracture healing, osteoporosis, arthritis, soft tissue calcification
Protease-activatable	IVISense Pan Cathepsin 680	Lysosomal pan-cathepsin activity	Cancer, arthritis, pulmonary neutrophilia/eosinophilia, atherosclerosis, general acute/chronic inflammation
	IVISense Pan Cathepsin 750 FAST	FAST version of Pan-Cathepsin, with faster kinetics and a broader imaging window	
	IVISense Cat B 680 FAST	Lysosomal cathepsin B activity	
	IVISense Cat K 680 FAST	Cathepsin K activity	Osteoclastic bone resorption, osteoporosis, soft tissue calcification, tumor-associated macrophages
	IVISense Neutrophil Elastase 680 FAST	Secreted neutrophil elastase activity	Pulmonary inflammation, acute neutrophilia, arthritis
	IVISense MMP 680	Secreted and membrane pan-matrix metalloprotease activity	Cancer, arthritis, pulmonary neutrophilia/eosinophilia, atherosclerosis, general acute/chronic inflammation

Note: The 680 and 750 indicate the emission wavelength of the fluorescent probe

Compliance with Ethical Standards Funding/Conflict of Interest: This work is sponsored by PerkinElmer Inc., and its R&D research division for developing advanced molecular imaging technologies. Both authors of this chapter (J.C. Tseng and J.D. Peterson) are employees of PerkinElmer Inc.

Ethical Approval: All animal research involved in this work followed the guidelines of PerkinElmer's Institutional Animal Care and Use Committee (IACUC). A research protocol (#01-0112) was approved for this study.

References

1. Medzhitov R. Origin and physiological roles of inflammation. *Nature*. 2008;454:428–35. <https://doi.org/10.1038/nature07201>.
2. Greten FR, Grivennikov SI. Inflammation and cancer: triggers, mechanisms, and consequences. *Immunity*. 2019;51:27–41. <https://doi.org/10.1016/j.immuni.2019.06.025>.
3. Fakhoury M. Inflammation in Alzheimer's disease. *Curr Alzheimer Res*. 2021;17:959–61. <https://doi.org/10.2174/156720501711210101110513>.
4. Roh JS, Sohn DH. Damage-associated molecular patterns in inflammatory diseases. *Immune Netw*. 2018;18. <https://doi.org/10.4110/in.2018.18.e27>.
5. Jones HR, Robb CT, Perretti M, Rossi AG. The role of neutrophils in inflammation resolution. *Semin Immunol*. 2016;28:137–45. <https://doi.org/10.1016/j.smim.2016.03.007>.
6. Martinez FO, Gordon S, Locati M, Mantovani A. Transcriptional profiling of the human monocyte-to-macrophage differentiation and polarization: new molecules and patterns of gene expression. *J Immunol*. 2006;177:7303–11. <https://doi.org/10.4049/jimmunol.177.10.7303>.
7. Tang T, Scambler TE, Smallie T, Cunliffe HE, Ross EA, Rosner DR, et al. Macrophage responses to lipopolysaccharide are modulated by a feedback loop involving prostaglandin E2, dual specificity phosphatase 1 and tristetraprolin. *Sci Rep*. 2017;7:4350. <https://doi.org/10.1038/s41598-017-04100-1>.
8. Zarghi A, Arfaei S. Selective COX-2 inhibitors: a review of their structure-activity relationships. *Iran J Pharm Res*. 2011;10:655–83.
9. Yi Y-S. Folate receptor-targeted diagnostics and therapeutics for inflammatory diseases. *Immune Netw*. 2016;16:337. <https://doi.org/10.4110/in.2016.16.6.337>.
10. Antonov AS, Antonova GN, Munn DH, Mivechi N, Lucas R, Catravas JD, et al. $\alpha\text{V}\beta\text{3}$ integrin regulates macrophage inflammatory responses via PI3 kinase/Akt-dependent NF- κB activation. *J Cell Physiol*. 2011;226:469–76. <https://doi.org/10.1002/jcp.22356>.
11. Mezu-Ndubuisi OJ, Maheshwari A. The role of integrins in inflammation and angiogenesis. *Pediatr Res*. 2021;89:1619–26. <https://doi.org/10.1038/s41390-020-01177-9>.
12. Dai R, Wu Z, Chu HY, Lu J, Lyu A, Liu J, et al. Cathepsin K: the action in and beyond bone. *Front Cell Dev Biol*. 2020;8. <https://doi.org/10.3389/fcell.2020.00433>.
13. Page-McCaw A, Ewald AJ, Werb Z. Matrix metalloproteinases and the regulation of tissue remodelling. *Nat Rev Mol Cell Biol*. 2007;8:221–33. <https://doi.org/10.1038/nrm2125>.
14. Canton J. Phagosome maturation in polarized macrophages. *J Leukoc Biol*. 2014;96:729–38. <https://doi.org/10.1189/jlb.1MR0114-021R>.
15. Bedard K, Krause K-H. The NOX family of ROS-generating NADPH oxidases: physiology and pathophysiology. *Physiol Rev*. 2007;87:245–313. <https://doi.org/10.1152/physrev.00044.2005>.
16. El-Benna J, Hurtado-Nedelec M, Marzaioli V, Marie J-C, Gougerot-Pocidalo M-A, Dang PM-C. Priming of the neutrophil respiratory burst: role in host defense and inflammation. *Immunol Rev*. 2016;273:180–93. <https://doi.org/10.1111/imr.12447>.
17. Stasia MJ. CYBA encoding p22phox, the cytochrome b558 alpha polypeptide: gene structure, expression, role and physiopathology. *Gene*. 2016;586:27–35. <https://doi.org/10.1016/j.gene.2016.03.050>.
18. Davies MJ, Hawkins CL. The role of myeloperoxidase in biomolecule modification, chronic inflammation, and disease. *Antioxid Redox Signal*. 2020;32:957–81. <https://doi.org/10.1089/ars.2020.8030>.

19. Jiang F, Zhang Y, Dusting GJ. NADPH oxidase-mediated redox Signaling: roles in cellular stress response, stress tolerance, and tissue repair. Sibley DR, editor. *Pharmacol Rev.* 2011;63: 218–42. <https://doi.org/10.1124/pr.110.002980>.
20. Fuhrman B, Shiner M, Volkova N, Aviram M. Cell-induced copper ion-mediated low density lipoprotein oxidation increases during in vivo monocyte-to-macrophage differentiation. *Free Radic Biol Med.* 2004;37:259–71. <https://doi.org/10.1016/j.freeradbiomed.2004.04.026>.
21. Ejlerskov P, Christensen DP, Beyaie D, Burritt JB, Paclat M-H, Gorchach A, et al. NADPH oxidase is internalized by Clathrin-coated pits and localizes to a Rab27A/B GTPase-regulated secretory compartment in activated macrophages. *J Biol Chem.* 2012;287:4835–52. <https://doi.org/10.1074/jbc.M111.293696>.
22. Kumar AP, Piedrafitra FJ, Reynolds WF. Peroxisome proliferator-activated receptor γ ligands regulate myeloperoxidase expression in macrophages by an estrogen-dependent mechanism involving the -463GA promoter polymorphism. *J Biol Chem.* 2004;279:8300–15. <https://doi.org/10.1074/jbc.M311625200>.
23. Stapels DA, Geisbrecht BV, Rooijackers SH. Neutrophil serine proteases in antibacterial defense. *Curr Opin Microbiol.* 2015;23:42–8. <https://doi.org/10.1016/j.mib.2014.11.002>.
24. Chua F, Laurent GJ. Neutrophil elastase: mediator of extracellular matrix destruction and accumulation. *Proc Am Thorac Soc.* 2006;3:424–7. <https://doi.org/10.1513/pats.200603-078AW>.
25. Garratt LW, Sutanto EN, Ling K-M, Looi K, Iosifidis T, Martinovich KM, et al. Matrix metalloproteinase activation by free neutrophil elastase contributes to bronchiectasis progression in early cystic fibrosis. *Eur Respir J.* 2015;46:384–94. <https://doi.org/10.1183/09031936.00212114>.
26. Elkington PT, Green JA, Friedland JS. Analysis of matrix metalloproteinase secretion by macrophages. 2009. p. 253–65. doi:https://doi.org/10.1007/978-1-59745-396-7_16.
27. Krotova K, Khodayari N, Oshins R, Aslanidi G, Brantly ML. Neutrophil elastase promotes macrophage cell adhesion and cytokine production through the integrin-Src kinases pathway. *Sci Rep.* 2020;10:15874. <https://doi.org/10.1038/s41598-020-72667-3>.
28. Laronha H, Caldeira J. Structure and function of human matrix metalloproteinases. *Cell.* 2020;9:1076. <https://doi.org/10.3390/cells9051076>.
29. Li H, Qiu Z, Li F, Wang C. The relationship between MMP-2 and MMP-9 expression levels with breast cancer incidence and prognosis. *Oncol Lett.* 2017; <https://doi.org/10.3892/ol.2017.6924>.
30. Burrage PS, Mix KS, Brinckerhoff CE. Matrix metalloproteinases: role in arthritis. *Front Biosci.* 2006;11:529. <https://doi.org/10.2741/1817>.
31. Yadati T, Houben T, Bitorina A, Shiri-Sverdlov R. The ins and outs of cathepsins: physiological function and role in disease management. *Cell.* 2020;9:1679. <https://doi.org/10.3390/cells9071679>.
32. Conus S, Simon H. Cathepsins and their involvement in immune responses. *Swiss Med Wkly.* 2010; <https://doi.org/10.4414/smw.2010.13042>.
33. Szulc-Dąbrowska L, Bossowska-Nowicka M, Struzik J, Toka FN. Cathepsins in bacteria-macrophage interaction: defenders or victims of circumstance? *Front Cell Infect Microbiol.* 2020;10. <https://doi.org/10.3389/fcimb.2020.601072>.
34. Jakoš T, Pišlar A, Jewett A, Kos J. Cysteine cathepsins in tumor-associated immune cells. *Front Immunol.* 2019;10. <https://doi.org/10.3389/fimmu.2019.02037>.
35. Fuchs N, Meta M, Schuppan D, Nuhn L, Schirmeister T. Novel opportunities for cathepsin S inhibitors in cancer immunotherapy by nanocarrier-mediated delivery. *Cell.* 2020;9:2021. <https://doi.org/10.3390/cells9092021>.
36. Montague-Cardoso K, Malcangio M. Cathepsin S as a potential therapeutic target for chronic pain. *Med Drug Discov.* 2020;7:100047. <https://doi.org/10.1016/j.medidd.2020.100047>.
37. Ntziachristos V, Ripoll J, Wang LV, Weissleder R. Looking and listening to light: the evolution of whole-body photonic imaging. *Nat Biotechnol.* 2005;23:313–20. <https://doi.org/10.1038/nbt1074>.

38. Roda A, Pasini P, Mirasoli M, Michelini E, Guardigli M. Biotechnological applications of bioluminescence and chemiluminescence. *Trends Biotechnol.* 2004;22:295–303. <https://doi.org/10.1016/j.tibtech.2004.03.011>.
39. Ntziachristos V, Bremer C, Weissleder R. Fluorescence imaging with near-infrared light: new technological advances that enable in vivo molecular imaging. *Eur Radiol.* 2003;13:195–208. <https://doi.org/10.1007/s00330-002-1524-x>.
40. Li S, Ruan Z, Zhang H, Xu H. Recent achievements of bioluminescence imaging based on firefly luciferin-luciferase system. *Eur J Med Chem.* 2021;211:113111. <https://doi.org/10.1016/j.ejmech.2020.113111>.
41. Contag CH, Bachmann MH. Advances in in vivo bioluminescence imaging of gene expression. *Annu Rev Biomed Eng.* 2002;4:235–60. <https://doi.org/10.1146/annurev.bioeng.4.111901.093336>.
42. Mezzanotte L, van 't Root M, Karatas H, Goun EA, CWGM L. In vivo molecular bioluminescence imaging: new tools and applications. *Trends Biotechnol.* 2017;35:640–52. <https://doi.org/10.1016/j.tibtech.2017.03.012>.
43. Zambito G, Chawda C, Mezzanotte L. Emerging tools for bioluminescence imaging. *Curr Opin Chem Biol.* 2021;63:86–94. <https://doi.org/10.1016/j.cbpa.2021.02.005>.
44. Dikalov S, Griendling KK, Harrison DG. Measurement of reactive oxygen species in cardiovascular studies. *Hypertension.* 2007;49:717–27. <https://doi.org/10.1161/01.HYP.0000258594.87211.6b>.
45. Bancirova M. Sodium azide as a specific quencher of singlet oxygen during chemiluminescent detection by luminol and Cypridina luciferin analogues. *Luminescence.* 2011;26:685–8. <https://doi.org/10.1002/bio.1296>.
46. Gross S, Gammon ST, Moss BL, Rauch D, Harding J, Heinecke JW, et al. Bioluminescence imaging of myeloperoxidase activity in vivo. *Nat Med.* 2009;15:455–61. <https://doi.org/10.1038/nm.1886>.
47. Kielland A, Blom T, Nandakumar KS, Holmdahl R, Blomhoff R, Carlsen H. In vivo imaging of reactive oxygen and nitrogen species in inflammation using the luminescent probe L-012. *Free Radic Biol Med.* 2009;47:760–6. <https://doi.org/10.1016/j.freeradbiomed.2009.06.013>.
48. Zhou J, Tsai Y-T, Weng H, Tang L. Noninvasive assessment of localized inflammatory responses. *Free Radic Biol Med.* 2012;52:218–26. <https://doi.org/10.1016/j.freeradbiomed.2011.10.452>.
49. Tseng J-C, Kung AL. In vivo imaging of inflammatory phagocytes. *Chem Biol.* 2012;19:1199–209. <https://doi.org/10.1016/j.chembiol.2012.08.007>.
50. Okajima T, Ohsaka T. Chemiluminescence of lucigenin by electrogenerated superoxide ions in aqueous solutions. *Luminescence.* 2003;18:49–57. <https://doi.org/10.1002/bio.706>.
51. Rezende F, Prior K-K, Löwe O, Wittig I, Strecker V, Moll F, et al. Cytochrome P450 enzymes but not NADPH oxidases are the source of the NADPH-dependent lucigenin chemiluminescence in membrane assays. *Free Radic Biol Med.* 2017;102:57–66. <https://doi.org/10.1016/j.freeradbiomed.2016.11.019>.
52. Shuhendler AJ, Pu K, Cui L, Uetrecht JP, Rao J. Real-time imaging of oxidative and nitrosative stress in the liver of live animals for drug-toxicity testing. *Nat Biotechnol.* 2014;32:373–80. <https://doi.org/10.1038/nbt.2838>.
53. Pfleger KDG, Eidne KA. Illuminating insights into protein-protein interactions using bioluminescence resonance energy transfer (BRET). *Nat Methods.* 2006;3:165–74. <https://doi.org/10.1038/nmeth841>.
54. Eglen RM, Reisine T, Roby P, Rouleau N, Illy C, Bossé R, et al. The use of AlphaScreen technology in HTS: current status. *Curr Chem Genomics.* 2008;1:2–10. <https://doi.org/10.2174/1875397300801010002>.
55. Zhang N, Francis KP, Prakash A, Ansaldi D. Enhanced detection of myeloperoxidase activity in deep tissues through luminescent excitation of near-infrared nanoparticles. *Nat Med.* 2013;19:500–5. <https://doi.org/10.1038/nm.3110>.

56. Hoshyar N, Gray S, Han H, Bao G. The effect of nanoparticle size on in vivo pharmacokinetics and cellular interaction. *Nanomedicine*. 2016;11:673–92. <https://doi.org/10.2217/nmm.16.5>.
57. Dragulescu-Andrasi A, Chan CT, De A, Massoud TF, Gambhir SS. Bioluminescence resonance energy transfer (BRET) imaging of protein–protein interactions within deep tissues of living subjects. *Proc Natl Acad Sci*. 2011;108:12060–5. <https://doi.org/10.1073/pnas.1100923108>.
58. Bhuckory S, Kays JC, Dennis AM. In vivo biosensing using resonance energy transfer. *Biosensors*. 2019;9:76. <https://doi.org/10.3390/bios9020076>.
59. So M-K, Xu C, Loening AM, Gambhir SS, Rao J. Self-illuminating quantum dot conjugates for in vivo imaging. *Nat Biotechnol*. 2006;24:339–43. <https://doi.org/10.1038/nbt1188>.
60. Xiong L, Shuhendler AJ, Rao J. Self-luminescing BRET-FRET near-infrared dots for in vivo lymph-node mapping and tumour imaging. *Nat Commun*. 2012;3:1193. <https://doi.org/10.1038/ncomms2197>.
61. Augusto FA, de Souza GA, de Souza Júnior SP, Khalid M, Baader WJ. Efficiency of electron transfer initiated chemiluminescence. *Photochem Photobiol*. 2013;89:1299–317. <https://doi.org/10.1111/php.12102>.
62. Rauhut MM. Chemiluminescence from concerted peroxide decomposition reactions. *Acc Chem Res*. 1969;2:80–7. <https://doi.org/10.1021/ar50015a003>.
63. Rauhut MM, Bollyky LJ, Roberts BG, Loy M, Whitman RH, Iannotta AV, et al. Chemiluminescence from reactions of electronegatively substituted aryl oxalates with hydrogen peroxide and fluorescent compounds. *J Am Chem Soc*. 1967;89:6515–22. <https://doi.org/10.1021/ja01001a025>.
64. Freeman R, Liu X, Willner I. Chemiluminescent and chemiluminescence resonance energy transfer (CRET) detection of DNA, metal ions, and aptamer–substrate complexes using Hemin/G-quadruplexes and CdSe/ZnS quantum dots. *J Am Chem Soc*. 2011;133:11597–604. <https://doi.org/10.1021/ja202639m>.
65. Lee D, Khaja S, Velasquez-Castano JC, Dasari M, Sun C, Petros J, et al. In vivo imaging of hydrogen peroxide with chemiluminescent nanoparticles. *Nat Mater*. 2007;6:765–9. <https://doi.org/10.1038/nmat1983>.
66. Bag S, Tseng J-C, Rochford J. A BODIPY-luminol chemiluminescent resonance energy-transfer (CRET) cassette for imaging of cellular superoxide. *Org Biomol Chem*. 2015;13:1763–7. <https://doi.org/10.1039/C4OB02413C>.
67. Kambayashi Y, Ogino K. Reestimation of Cypridina Luciferin Analogs (MCLA) as a chemiluminescence probe to detect active oxygen species—cautionary note for use of MCLA. *J Toxicol Sci*. 2003;28:139–48. <https://doi.org/10.2131/jts.28.139>.
68. Tseng J-C, Bailey D, Tupper T, Kung AL. Using glow stick chemistry for biological imaging. *Mol Imaging Biol*. 2014;16:478–87. <https://doi.org/10.1007/s11307-014-0721-8>.
69. Tseng J-C, Kung AL. In vivo imaging of endogenous enzyme activities using luminescent 1,2-dioxetane compounds. *J Biomed Sci*. 2015;22:45. <https://doi.org/10.1186/s12929-015-0155-x>.
70. Leblond F, Davis SC, Valdés PA, Pogue BW. Pre-clinical whole-body fluorescence imaging: review of instruments, methods and applications. *J Photochem Photobiol B Biol*. 2010;98:77–94. <https://doi.org/10.1016/j.jphotobiol.2009.11.007>.
71. Maeda H, Matsumura Y. EPR effect based drug design and clinical outlook for enhanced cancer chemotherapy. *Adv Drug Deliv Rev*. 2011;63:129–30. <https://doi.org/10.1016/j.addr.2010.05.001>.
72. Eaton VL, Vasquez KO, Goings GE, Hunter ZN, Peterson JD, Miller SD. Optical tomographic imaging of near infrared imaging agents quantifies disease severity and immunomodulation of experimental autoimmune encephalomyelitis in vivo. *J Neuroinflammation*. 2013;10:904. <https://doi.org/10.1186/1742-2094-10-138>.
73. Buono C, Anzinger JJ, Amar M, Kruth HS. Fluorescent pegylated nanoparticles demonstrate fluid-phase pinocytosis by macrophages in mouse atherosclerotic lesions. *J Clin Invest*. 2009;119:1373–81. <https://doi.org/10.1172/JCI35548>.

74. Uddin MJ, Crews BC, Blobaum AL, Kingsley PJ, Gorden DL, McIntyre JO, et al. Selective visualization of cyclooxygenase-2 in inflammation and cancer by targeted fluorescent imaging agents. *Cancer Res.* 2010;70:3618–27. <https://doi.org/10.1158/0008-5472.CAN-09-2664>.
75. Han W, Zaynagetdinov R, Yull FE, Polosukhin VV, Gleaves LA, Tanjore H, et al. Molecular imaging of folate receptor β -positive macrophages during acute lung inflammation. *Am J Respir Cell Mol Biol.* 2015;53:50–9. <https://doi.org/10.1165/rcmb.2014-0289OC>.
76. Chen W-T, Mahmood U, Weissleder R, Tung C-H. Arthritis imaging using a near-infrared fluorescence folate-targeted probe. *Arthritis Res Ther.* 2005;7:R310–7. <https://doi.org/10.1186/ar1483>.
77. Bridgewater RE, Norman JC, Caswell PT. Integrin trafficking at a glance. *J Cell Sci.* 2012;125:3695–701. <https://doi.org/10.1242/jcs.095810>.
78. Paul NR, Jacquemet G, Caswell PT. Endocytic trafficking of integrins in cell migration. *Curr Biol.* 2015;25:R1092–105. <https://doi.org/10.1016/j.cub.2015.09.049>.
79. Moreno-Layseca P, Icha J, Hamidi H, Ivaska J. Integrin trafficking in cells and tissues. *Nat Cell Biol.* 2019;21:122–32. <https://doi.org/10.1038/s41556-018-0223-z>.
80. Su G, Atakilit A, Li JT, Wu N, Bhattacharya M, Zhu J, et al. Absence of integrin $\alpha\beta3$ enhances vascular leak in mice by inhibiting endothelial cortical actin formation. *Am J Respir Crit Care Med.* 2012;185:58–66. <https://doi.org/10.1164/rccm.201108-1381OC>.
81. Laitinen I, Saraste A, Weidl E, Poethko T, Weber AW, Nekolla SG, et al. Evaluation of $\alpha\beta3$ integrin-targeted positron emission tomography tracer 18 F-Galacto-RGD for imaging of vascular inflammation in atherosclerotic mice. *Circ Cardiovasc Imaging.* 2009;2:331–8. <https://doi.org/10.1161/CIRCIMAGING.108.846865>.
82. Jenkins WS, Vesey AT, Vickers A, Neale A, Moles C, Connell M, et al. In vivo alpha-V beta-3 integrin expression in human aortic atherosclerosis. *Heart.* 2019;105:1868–75. <https://doi.org/10.1136/heartjnl-2019-315103>.
83. Razavian M, Marfatia R, Mongue-Din H, Tavakoli S, Sinusas AJ, Zhang J, et al. Integrin-targeted imaging of inflammation in vascular remodeling. *Arterioscler Thromb Vasc Biol.* 2011;31:2820–6. <https://doi.org/10.1161/ATVBAHA.111.231654>.
84. Ludwig BS, Kessler H, Kossatz S, Reuning U. RGD-binding integrins revisited: how recently discovered functions and novel synthetic ligands (re-)shape an ever-evolving field. *Cancers (Basel).* 2021;13:1711. <https://doi.org/10.3390/cancers13071711>.
85. Lin S-A, Patel M, Suresch D, Connolly B, Bao B, Groves K, et al. Quantitative longitudinal imaging of vascular inflammation and treatment by ezetimibe in apoE mice by FMT using new optical imaging biomarkers of cathepsin activity and $\alpha\beta3$ integrin. *Int J Mol Imaging.* 2012;2012:1–13. <https://doi.org/10.1155/2012/189254>.
86. Wu L, Sedgwick AC, Sun X, Bull SD, He X-P, James TD. Reaction-based fluorescent probes for the detection and imaging of reactive oxygen, nitrogen, and sulfur species. *Acc Chem Res.* 2019;52:2582–97. <https://doi.org/10.1021/acs.accounts.9b00302>.
87. Driever SM, Fryer MJ, Mullineaux PM, Baker NR. Imaging of reactive oxygen species in vivo. In: Pfannschmidt T, editor. *Plant signal transduct.* Totowa, NJ: Humana Press; 2009. p. 109–16. https://doi.org/10.1007/978-1-59745-289-2_7.
88. Kundu K, Knight SF, Willett N, Lee S, Taylor WR, Murthy N. Hydrocyanines: a class of fluorescent sensors that can image reactive oxygen species in cell culture, tissue, and in vivo. *Angew Chemie Int Ed.* 2009;48:299–303. <https://doi.org/10.1002/anie.200804851>.
89. Prunty MC, Aung MH, Hanif AM, Allen RS, Chrenek MA, Boatright JH, et al. In vivo imaging of retinal oxidative stress using a reactive oxygen species-activated fluorescent probe. *Investig Ophthalmol Vis Sci.* 2015;56:5862. <https://doi.org/10.1167/iovs.15-16810>.
90. Ito R, Kamiya M, Urano Y. Molecular probes for fluorescence image-guided cancer surgery. *Curr Opin Chem Biol.* 2022;67:102112. <https://doi.org/10.1016/j.cbpa.2021.102112>.
91. Suri S, Lehman SM, Selvam S, Reddie K, Maity S, Murthy N, et al. In vivo fluorescence imaging of biomaterial-associated inflammation and infection in a minimally invasive manner. *J Biomed Mater Res Part A.* 2015;103:76–83. <https://doi.org/10.1002/jbm.a.35162>.

92. Uusitalo LM, Hempel N. Recent advances in intracellular and in vivo ROS sensing: focus on nanoparticle and nanotube applications. *Int J Mol Sci.* 2012;13:10660–79. <https://doi.org/10.3390/ijms130910660>.
93. Wu L, Wu I-C, DuFort CC, Carlson MA, Wu X, Chen L, et al. Photostable Ratiometric Pd⁰ probe for in vitro and in vivo imaging of hypochlorous acid. *J Am Chem Soc.* 2017;139:6911–8. <https://doi.org/10.1021/jacs.7b01545>.
94. Funovics M, Weissleder R, Tung C-H. Protease sensors for bioimaging. *Anal Bioanal Chem.* 2003;377:956–63. <https://doi.org/10.1007/s00216-003-2199-0>.
95. Weissleder R, Tung C-H, Mahmood U, Bogdanov A. In vivo imaging of tumors with protease-activated near-infrared fluorescent probes. *Nat Biotechnol.* 1999;17:375–8. <https://doi.org/10.1038/7933>.
96. Wunder A, Tung C-H, Müller-Ladner U, Weissleder R, Mahmood U. In vivo imaging of protease activity in arthritis: a novel approach for monitoring treatment response. *Arthritis Rheum.* 2004;50:2459–65. <https://doi.org/10.1002/art.20379>.
97. Kossodo S, Zhang J, Groves K, Cuneo GJ, Handy E, Morin J, et al. Noninvasive in vivo quantification of neutrophil elastase activity in acute experimental mouse lung injury. *Int J Mol Imaging.* 2011;2011:1–11. <https://doi.org/10.1155/2011/581406>.
98. Akers WJ, Xu B, Lee H, Sudlow GP, Fields GB, Achilefu S, et al. Detection of MMP-2 and MMP-9 activity in vivo with a triple-helical peptide optical probe. *Bioconjug Chem.* 2012;23:656–63. <https://doi.org/10.1021/bc300027y>.
99. Chen X, Lee D, Yu S, Kim G, Lee S, Cho Y, et al. In vivo near-infrared imaging and phototherapy of tumors using a cathepsin B-activated fluorescent probe. *Biomaterials.* 2017;122:130–40. <https://doi.org/10.1016/j.biomaterials.2017.01.020>.
100. Glinzer A, Ma X, Prakash J, Kimm MA, Lohöfer F, Kosanke K, et al. Targeting elastase for molecular imaging of early atherosclerotic lesions. *Arterioscler Thromb Vasc Biol.* 2017;37:525–33. <https://doi.org/10.1161/ATVBAHA.116.308726>.
101. Korideck H, Peterson JD. Noninvasive quantitative tomography of the therapeutic response to dexamethasone in ovalbumin-induced murine asthma. *J Pharmacol Exp Ther.* 2009;329:882–9. <https://doi.org/10.1124/jpet.108.147579>.
102. Ibarra JM, Jimenez F, Martinez HG, Clark K, Ahuja SS. MMP-activated fluorescence imaging detects early joint inflammation in collagen-antibody-induced arthritis in CC-chemokine Receptor-2-null mice, in-vivo. *Int J Inflamm.* 2011;2011:1–6. <https://doi.org/10.4061/2011/691587>.
103. Peterson JD, LaBranche TP, Vasquez KO, Kossodo S, Melton M, Rader R, et al. Optical tomographic imaging discriminates between disease-modifying anti-rheumatic drug (DMARD) and non-DMARD efficacy in collagen antibody-induced arthritis. *Arthritis Res Ther.* 2010;12:R105. <https://doi.org/10.1186/ar3038>.

Photoacoustic Imaging in Inflammation Research



Jingqin Chen, Zhihua Xie, Liang Song, Xiaojing Gong, and Chengbo Liu

Abstract Photoacoustic (PA) imaging has emerged as a promising technique for real-time detection and diagnosis of pathologies related to inflammation owing to the deep penetration of the ultrasound waves and the high resolution of optical imaging. This chapter provides an overview on the latest developments on endogenous and exogenous probes used for PA imaging to evaluate the dynamics of inflammatory factors in inflammation-related diseases. We first review the label-free PA imaging of arthritis and Crohn's disease using hemoglobin as an endogenous probe to detect blood oxygenation saturation; we then focus on PA imaging assisted with three types of contrast agents for inflammation research: (1) activatable probes that respond to endogenous inflammatory stimuli, (2) probes targeted toward inflammation markers, and (3) direct cell labeling agents for PA imaging. Finally, we discuss the challenges and perspectives in developing further strategies for specific and sensitive PA imaging in inflammation research. This chapter is intended to provide a brief introduction to PA imaging and, through selected examples, to showcase how PA imaging can increase our understanding of inflammatory diseases, provide benefits in preclinical research studies, and pave the way for future clinical applications.

Keywords Photoacoustics · Molecular imaging · Inflammation · Tomography · Label-free imaging · Collagen · Hemoglobin

Jingqin Chen and Zhihua Xie contributed equally to this work

J. Chen · Z. Xie · L. Song · X. Gong (✉) · C. Liu (✉)
Research Center for Biomedical Optics and Molecular Imaging, Shenzhen Institute of Advanced Technology, CAS Key Laboratory of Health Informatics, Chinese Academy of Sciences, Shenzhen, China
e-mail: xj.gong@siat.ac.cn; cb.liu@siat.ac.cn

1 Introduction to Photoacoustic Imaging

Inflammation is a biological response to disturbed homeostasis in tissues, leading to the recruitment of blood-derived products such as plasma proteins, fluids, and leukocytes into the affected tissues [1, 2]. Changes in the local vascular system promote this recruitment, inducing vasodilation, increased vascular permeability, and increased blood flow [3–5]. In addition, redox imbalance and a large amount of reactive oxygen species (ROS) and pro-inflammatory chemokines (secreted by inflammatory cells, such as M1 macrophages and neutrophils) are present in most inflammatory microenvironments [1, 6, 7]. The main function of inflammation is to quickly destroy or isolate the potential source of disturbance, remove the damaged tissue, and then restore tissue homeostasis [8, 9]. Inflammation, if properly regulated, is considered adaptive. If not properly regulated, excess inflammation has devastating effects, leading to excessive collateral damage and occurrence of inflammation-related pathologies, such as rheumatoid arthritis, gout, diabetes, and arteriovenous diseases [10, 11]. Therefore, an accurate and sensitive detection of the inflammatory microenvironment is of great importance not only for the diagnosis and treatment of such diseases but also to gain a better understanding of the mechanisms characterizing the occurrence and development of diseases.

Traditional biomedical imaging plays an indispensable role in the diagnosis of inflammation [12, 13]. Clinically, magnetic resonance imaging (MRI), ultrasound (US) imaging, and X-ray computed tomography (CT) have a practically unlimited tissue penetration depth and allow the observation of structural changes of deep tissues, including vascular distribution, synovitis, and erosion [14, 15]. However, their imaging resolution is insufficient to observe subtle changes, neovessel formation, and molecular dynamics. US imaging can evaluate dynamic processes, providing high spatiotemporal resolution in imaging of anatomical structures, and high sensitivity in identifying blood flow [16, 17]. It is also easily available and affordable and is therefore widely used for the clinical evaluation of inflammatory diseases [18, 19]. However, because ultrasound imaging is more sensitive to high-speed blood flow and less sensitive to low flow rate circulation, inflammation is often missed because it tends to involve vasodilation with a low flow rate. In addition, US imaging cannot assess blood oxygen saturation, which is another important physiological indicator of inflammatory diseases [20].

Photoacoustic (PA) imaging is an emerging medical imaging technology that combines optical and ultrasound imaging [21]. Its imaging process typically starts with a short laser pulse fired at biological tissue. As photons propagate into the tissue, some are absorbed by biomolecules such as hemoglobin, nucleic acids (DNA, RNA), lipids, water, melanin, and cytochromes. The absorbed optical energy is then partially or completely converted into heat through non-radiative relaxation of the excited molecules (Fig. 1a). This heat generates a pressure wave that propagates in tissue as an ultrasound wave. The ultrasound wave is detected outside the tissue by an ultrasonic transducer to form an image that maps the original optical energy deposition inside the tissue [21, 22]. Because ultrasound waves scatter much less

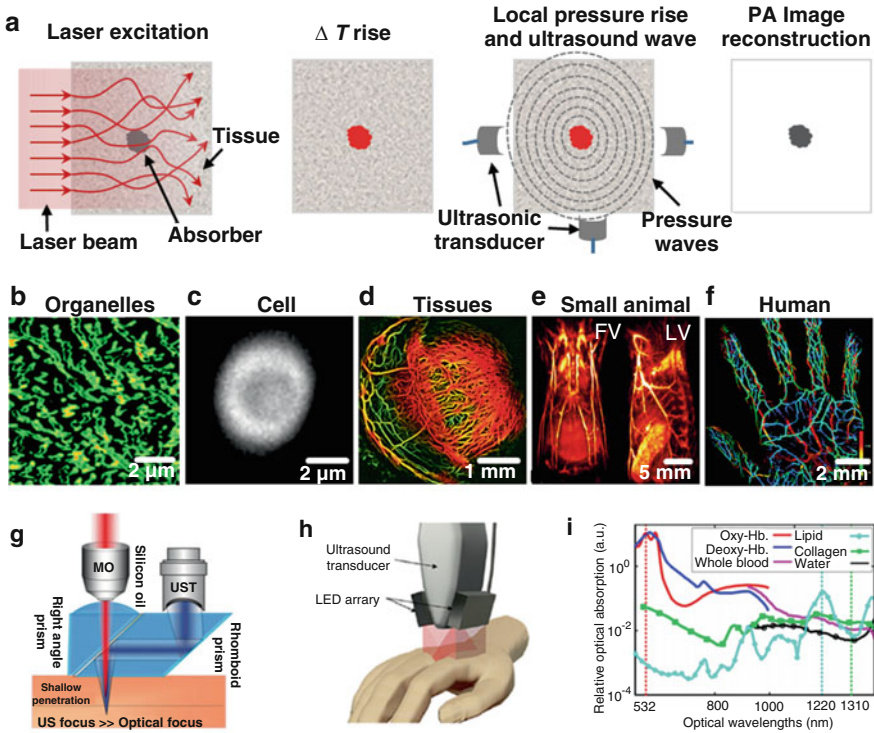


Fig. 1 Principle and applications of multi-scale photoacoustic imaging. **(a)** The physical principle of PA imaging. **(b–f)** PA images of **(b)** mitochondria in mouse embryonic fibroblasts; **(c)** a mouse red blood cell; **(d)** the vascular bed of a mouse eyeball; **(e)** whole-body PA image of a mouse; **(f)** major blood vessels in a human hand. **(g)** Schematic representation of a photoacoustic microscopy (PAM) system used for high-resolution imaging; **(h)** Schematic representation of a PA/ultrasound imaging handheld probe based on a linear-array ultrasound transducer; **(i)** Relative optical absorption spectra of major molecular components of biological tissues. **(a)** Adapted from [22] with permission, © 2016, Nature America. **(b)** Adapted from [26] with permission, © 2014, Danielli et al. (CC-BY 3.0 license, <https://creativecommons.org/licenses/by/3.0/>). **(c)** Adapted from [28] with permission, © 2013, Strohm et al. (CC-BY-NC-SA 3.0 license, <https://creativecommons.org/licenses/by-nc-sa/3.0/>). **(d)** Adapted from [29] with permission, © 2019, Zhao et al. (CC-BY 4.0 license, <https://creativecommons.org/licenses/by/4.0/>). **(e)** Adapted from [30] with permission, © 2017, Deán-Ben et al. (CC-BY 4.0 license). **(f)** Adapted from [31] with permission, © 2018, Matsumoto et al. (CC-BY 4.0 license). **(g)** Adapted from [24] with permission, © 2019, Steinberg et al. (CC-BY-NC-ND 4.0 license, <https://creativecommons.org/licenses/by-nc-nd/4.0/>); **(h)** Adapted from [32] with permission, © 2018, Jo et al. (CC-BY 3.0 license); **(i)** Reproduced from [33] with permission, © 2016, The Optical Society

than light in tissue, good contrast can be achieved from deeper inside the tissue. Based on this principle, PA imaging combines the advantages of optical and ultrasonic imaging, showing increased imaging depth, temporal resolution, and sensitivity compared with optical and ultrasound imaging [23–27]. To date, using endogenous absorbers such as hemoglobin as probes, PA imaging has been used to

capture images of organelles, cells, tissue, small animals, and blood vessels in the human hand (Fig. 1b–f) [26–31]. Therefore, information on vascular-related inflammation can be obtained through label-free PA imaging. In addition to PA imaging inflammation based on endogenous probes, advances in nanomaterial technology and chemistry have allowed inflammatory molecules in the tissue microenvironment to be detected with exogenous probes [27].

Note: in photoacoustic and ultrasound imaging systems, the physical device used to record the signal is often called a probe. Somewhat confusingly, acoustogenic contrast agents, i.e., molecules that can generate a PA/US signal, are also often called probes. Given the prevalence of both meanings in the literature, we have chosen to keep to common usages and clarify in the text where necessary. In this introductory section, “probe” refers to the physical device.

Photoacoustic imaging systems in various forms have been used, mainly divided into photoacoustic microscopy (PAM) and photoacoustic computed tomography (PACT). PAM uses low-energy (nJ to μ J), focused lasers for excitation and a single focused transducer for detection, providing PA imaging with high spatial resolution (lateral resolution: ~ 0.5 – $10\ \mu\text{m}$) but limited depth (a few millimeters) by point-to-point scanning (Fig. 1g). The lateral imaging resolution is defined by the size of either the focused light spot or the focused acoustic spot, allowing PA imaging with a high spatial resolution and offering detailed anatomical information about blood vessels, at the expense of a reduced depth of penetration. Because of the increase in spatial resolution, these techniques are called optical-resolution photoacoustic microscopy (OR-PAM) and acoustic-resolution photoacoustic microscopy (AR-PAM), respectively [34].

In contrast, PACT systems use transducer arrays for ultrasonic signal detection and higher-energy lasers for excitation (several to tens of mJ), acquiring PA signal at moderate lateral resolution ($>0.25\ \mu\text{m}$), but the use of low-frequency (1–10 MHz) ultrasound elements enables the detection of PA/US signals from deeper tissue (generally 5–6 cm) (Fig. 1h). However, using low ultrasound frequencies limits the lateral resolution of the images and makes it difficult to obtain detailed information on neovessels, such as the accurate anatomical formation of individual vessels. The imaging of inflammation through linear array-based PA systems (Fig. 1h) driven by commercial ultrasound units may provide many advantages and accelerate the acceptance into routine clinical practice of this novel imaging modality, especially with state-of-the-art ultrasound technologies such as probes with a large number of parallel channels facilitating real-time image acquisition and display. With a dual-modality arrangement, PA and ultrasound images of joints can also be obtained simultaneously, using the same system, resulting in naturally co-registered images. Since ultrasound is an established tool for musculoskeletal imaging, ultrasound images can be used to guide the PA procedure and help the interpretation of PA

images. Combined PA/ultrasound imaging based on linear-array ultrasound transducers has been widely applied to identify blood vessels in arthritic joints, both in animals and humans [35]. In recent years, linear-array PA/ultrasound systems (e.g., Vevo LAZR-X, LOIS/LOUISA-3D) have become commercially available and seen clinical application such as breast cancer diagnosis, sentinel lymph node detection, and malignant and benign thyroid nodule identification [36, 37].

PA imaging systems based on conventional US systems, such as the linear-array US probes mentioned above, have the advantage of being more readily translatable to the clinic and were therefore the first to be experimented and characterized. However, the PA images generated from these systems generally suffer from some distortion due to the limited view effect, especially at the edges of the field of view. This has encouraged the development of PA systems based on concave array transducers, which mitigate the problem of image distortion by providing a wider imaging angle. Concave array systems can only image a small region located at the center of the arc, and therefore, hybrid array-based PA/US probes have also been proposed to combine the advantages of the large field of view of linear-array systems and the wide imaging angle of concave array systems [38]. These hybrid array-based PA/US systems have been reported in disease detection, including inflammation, with great potential for clinical translation [37]. For further technical details about the various types of transducers and their respective advantages and disadvantages, we refer the readers to a review by Choi et al. [37].

Finally, spectroscopic PA imaging techniques such as multispectral optoacoustic tomography (MSOT) can exploit the unique absorption spectra of different endogenous chromophores to accurately quantify multiple molecular components by sequentially illuminating a tissue volume at multiple wavelengths [25]. For example, oxyhemoglobin (HbO), deoxyhemoglobin (Hb), and collagen have different absorption spectra (Fig. 1i), and therefore PA imaging can simultaneously assess hemoglobin and collagen contents in biological tissue [39], resulting in a useful tool for the characterization of multiple markers of inflammation. One of the strengths of PA imaging is its ability to provide absolute quantification of chromophores. For a description of the mathematical foundations of quantitative PA imaging, we refer the reader to the review by Cox et al. [40].

During spectroscopic PA imaging of a complex biological tissue, the intensity of the PA signals is proportional to the total optical energy absorption at the wavelengths at which the signals are acquired. The corresponding total optical absorption rate is calculated as in Eq. (1):

$$A_i = \sum_j c_j \mu_{ji} \quad (1)$$

where A_i is the total optical absorption rate at the wavelength i , which is proportional to the PA intensity (P_λ), μ_{ji} is the absorption coefficient of the molecular component j at the wavelength i , and c_j is the relative concentration of the molecular component j . Continuing the example above, HbO, Hb, and collagen are important molecular

components in the assessment of Crohn's disease (CD). Their individual concentrations in the imaged tissue can be derived from their contributions to the PA signal intensity using Eq. (2). The blood oxygenation (SpO_2) and the ratio between the concentrations of collagen and hemoglobin (Collagen/Hb) are obtained using Eqs. (3) and (4), respectively:

$$\begin{bmatrix} c_{HbO} \\ c_{Hb} \\ c_{Collagen} \end{bmatrix} = \begin{bmatrix} \mu_{HbO@l1} & \mu_{Hb@l1} & \mu_{collagen@l1} \\ \mu_{HbO@l2} & \mu_{Hb@l2} & \mu_{collagen@l2} \\ \mu_{HbO@l3} & \mu_{Hb@l3} & \mu_{collagen@l3} \end{bmatrix}^{-1} \times \begin{bmatrix} P_{l1} \\ P_{l2} \\ P_{l3} \end{bmatrix} \quad (2)$$

$$SpO_2 = \frac{c_{HbO}}{c_{HbO} + c_{Hb}} \quad (3)$$

$$Collagen/Hb = \frac{c_{collagen}}{c_{HbO} + c_{Hb}} \quad (4)$$

In this chapter, we provide a number of examples of the use of PA imaging in clinical and preclinical inflammation research. We first focus on label-free PA imaging and its use in visualizing angiogenesis and blood oxygenation saturation in inflammatory diseases such as arthritis and Crohn's disease. We then summarize several PA imaging strategies using specific exogenous acoustogenic probes for the inflammatory microenvironment, including reactive oxygen species (ROS), glutathione (GSH), carbon monoxide (CO), leukotriene A₄ (LTA₄H), cluster of differentiation 36 (CD36), interleukin-6 (IL-6), and inflammatory cells.

2 Label-Free Photoacoustic Imaging of Inflammation

Many endogenous biomolecules (e.g., lipids, bone, hemoglobin, DNA/RNA, water, melanin, cytochromes, etc.) are chromophores with characteristic light absorption wavelengths, enabling label-free PA imaging of various tissue components and moreover, the detection of diseases. For example, the PA imaging of lipids is widely reported as a method of detecting atherosclerosis [41], fatty liver diseases [42] and observing nerve activity [43]; variations in hydroxyapatite, hemoglobin, collagen, and lipid contents in bones have enabled the detection and monitoring of osteoporosis by PA imaging [44]; PA imaging of collagen has been used for musculoskeletal diseases such as Duchenne's myopathy [45]; PA imaging of hemoglobin is used for angiogenesis and tumors [46], and also inflammatory skin diseases [47]. Inflammatory diseases often involve changes in microcirculation, making PA imaging of hemoglobin and oxygen saturation especially useful to detect and evaluate inflammation (Table 1).

Table 1 Changes affecting blood vessels in inflammation and role of PA imaging in identifying these changes

Disease	Physiological process	Endogenous label	Photoacoustic imaging system	Selected references
Arthritis	Angiogenesis	<i>Hemoglobin</i>	Array-based PA system, single-transducer-based PA system	[48–51]
Colitis, sepsis	Impaired microcirculation	<i>Hemoglobin</i>	Single-transducer-based PA system	[52, 53]
Crohn's disease	Blood flow, oxygen saturation change	<i>SpO2</i>	Array-based PA system, single-transducer-based PA system	[33, 54–56]

2.1 Evaluation of Inflammation by Photoacoustic Imaging of Hemoglobin

Generally, the microenvironment of inflammation involves changes in the microcirculation, such as angiogenesis, impaired microcirculatory perfusion, or hyperperfusion due to vasodilation, depending on the phase of inflammation. Changes can generally be identified by imaging the vessels and evaluating blood flow rate in and around the inflamed area. Blood flowing in the vessels contains a variety of chromophores such as oxygenated hemoglobin and deoxygenated hemoglobin, both highly absorptive in the visible to near-infrared (NIR) spectral region (400–1200 nm) and capable of generating PA signals efficiently [57]. The optical contrast is intrinsically sensitive to tissue abnormalities and functions such as increased blood content due to angiogenesis and blood flow rate change due to hyperperfusion; therefore, PA imaging is an appropriate modality to obtain information on the morphology and number of vessels and blood flow, enabling the evaluation of the severity of inflammation.

Doppler ultrasound imaging is a mature clinical technology used for vascular imaging, obtaining blood flow information through vessels by bouncing ultrasonic waves off circulating red blood cells. It is a very useful imaging modality for the clinical diagnosis of vascular issues such as blood clots, decreased blood circulation, narrowing of arteries, etc. Although PA imaging relies on the detection of ultrasound signals, it differs significantly from clinical Doppler ultrasound imaging in three aspects. First, PA signal relies only on the presence of hemoglobin (or other chromophores), rather than the movement of erythrocytes that forms the basis of Doppler ultrasound imaging of circulation [21]. Second, the PA signal is less affected by the orientation of the blood vessel than the Doppler ultrasound signal [58]. Last but not least, a larger concentration of hemoglobin is present inside the vasculature than in the surrounding tissue, leading to more intense signal generation from the vessels, while in Doppler ultrasound imaging, erythrocytes produce a less intense signal than the surrounding tissue. These properties imply that slow blood flow in the synovial microvasculature can be easily detected by PA imaging. Thus, our hypothesis is that PA imaging can be particularly sensitive to early occurrence of inflammation.

Inflammatory arthritis, such as rheumatoid arthritis, is characterized by the proliferation of synovial tissue and the destruction of articular cartilage. Synovial angiogenesis is an important early symptom in the development and perpetuation of inflammatory arthritis [48]. Angiogenesis is the result of the combination of hypoxia and high metabolic demand, increasing the number of synovial vessels and leading to synovial infiltration and hyperplasia. The presence of hypervascularized synovial tissue is directly associated with disease activity [49], and PA imaging has been applied to the evaluation of arthritis by imaging the neovessels around the inflammatory area (Fig. 2).

Experiments using animal models of arthritis showed an increased intensity of the PA signal around the target joint affected by arthritis in comparison with the signal from a non-inflamed joint (Fig. 2a). The increased intensity in this chronic inflammation model is mainly due to angiogenesis in the inflamed tissues, demonstrated by histologic analysis of the arthritic joint (Fig. 2b). An increased PA signal can be observed even in subclinical arthritis (Fig. 2c), underlining the high sensitivity of PA imaging in the detection of arthritis. PA imaging can also reveal the network of vessels with high spatial resolution, showing the distorted vessel distribution induced by inflammation (Fig. 2d).

Photoacoustic microscopy has been applied to inflammatory diseases such as sepsis. Sepsis is a dysregulated inflammatory response to infection by bacteria, parasites, fungi, or viruses and is accompanied by clinical symptoms including fever, chills, accelerated heartbeat, and severe pain. Severe sepsis can lead to multiple organ dysfunction and has a high mortality rate. During sepsis, tissue damage is generally characterized by impaired microcirculatory perfusion correlated with systemic hemodynamic and oxygen transport indices. Sepsis is also anatomically associated with significant changes in existing vessels, including vessel number, tortuosity, etc. [60]. For example, changes in the microvasculature in a mouse model of lipopolysaccharide (LPS)-induced inflammation have been imaged by high-resolution PA microscopy, showing the evolution of the microvasculature over time in great detail. Anatomical characteristics of the vessels including vessel diameter, vessel ratio, and vessel intensity were accurately quantified to assess the severity of inflammation [53].

In addition to changes in the morphology and number of vessels, inflammation also affected the blood flow rate in the affected vessels. In this regard, monitoring the microcirculatory function by quantifying the blood flow rate may help the assessment of the severity of the inflammatory response and consequently allow the treatment of inflammation. Another method to evaluate blood flow rate is photoacoustic Doppler broadening of bandwidth, which is analogous to Doppler ultrasound and can additionally indicate the direction of the blood flow (Fig. 2e) [59]. This study by Yao et al. illustrates the feasibility of quantifying the blood flow rate in and around the area of inflammation area by PA imaging and the possibility of using PA imaging to perform a comprehensive, multi-parametric evaluation of inflammation severity.

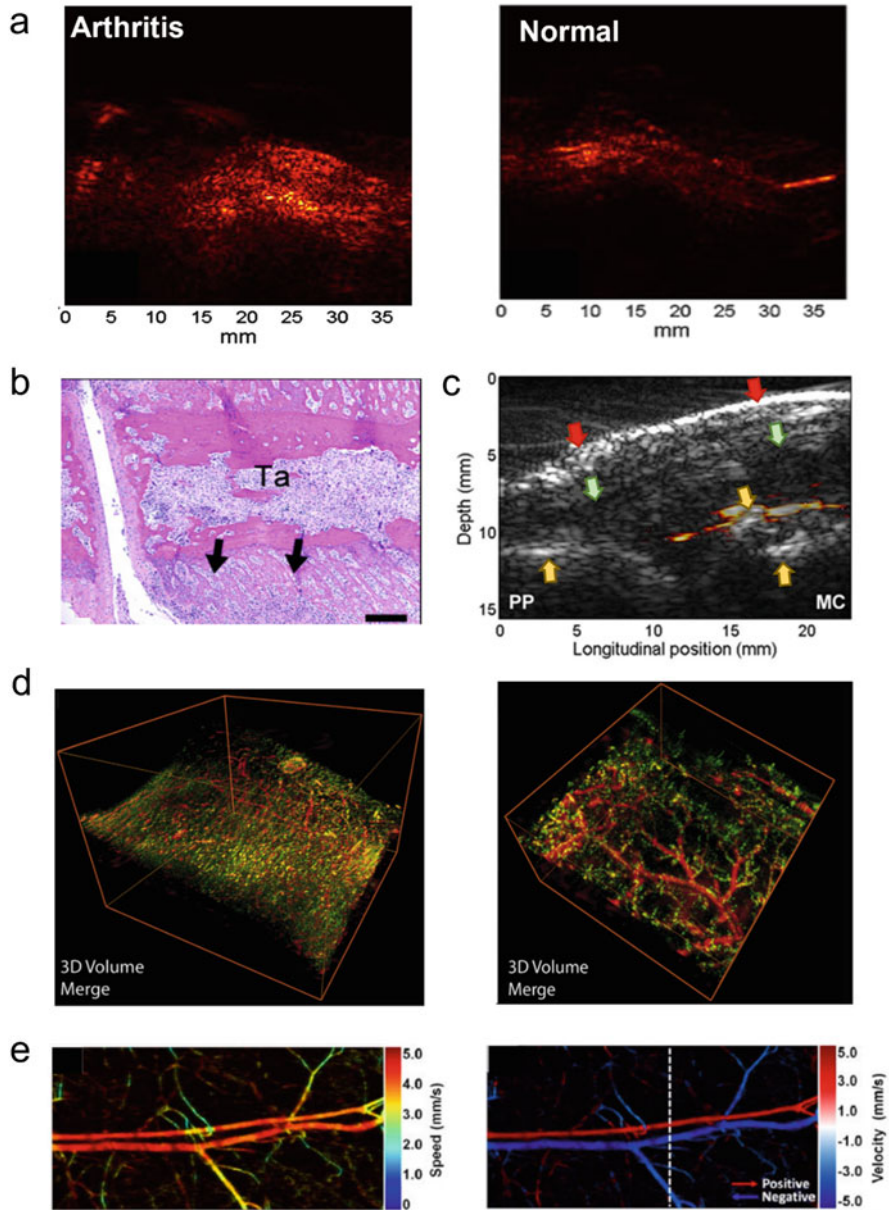


Fig. 2 (a) PA tomography image at 532 nm (for hemoglobin) of a rat ankle affected by arthritis (left) and normal rat ankle (right) [50]; (b) Microscopy image (hematoxylin and eosin staining) of arthritic rat tibiotarsal (ankle) joints; scale bar: 200 μ m; (c) Pseudo-color PA image superimposed on a grayscale ultrasound image of the second metacarpophalangeal joint of a human hand affected by arthritis, demonstrating the presence of active vascularity in the joint. Yellow arrow, bone; green arrow, tendon; red arrow, skin [51]; (d) Photoacoustic images of colon vessels in healthy mice (left) and mice with colitis (right) showing enlarged vasculature in the colon wall [52]; (e) Photoacoustic

2.2 *Label-Free Photoacoustic Imaging of Blood Oxygen Saturation and Collagen in Crohn's Disease*

Crohn's disease (CD) is an inflammatory bowel disease in which both inflammation and fibrosis cause the thickening of the bowel wall and the development of complications such as strictures in many patients [61]. The physiopathology of CD is characterized by obstructing intestinal strictures due to inflammation (with high levels of hemoglobin), fibrosis (high levels of collagen), or a combination of both, as shown in Fig. 3. The accurate characterization of strictures is fundamental for the monitoring and management of CD. Additionally, tissue hemoglobin (Hb) and oxygenated hemoglobin (HbO₂) content are also valuable markers of perfusion and inflammation in the gastrointestinal tract [52, 62]. Therefore, imaging techniques that can simultaneously assess Hb, HbO₂, collagen, and other markers of inflammation in the intestinal wall of patients with inflammatory bowel diseases provide a highly sensitive and reliable noninvasive way of assessing disease activity in great detail [63].

For example, Waldner et al. used MSOT to evaluate intestinal inflammation in a clinical trial in patients with CD [54]. The wavelengths of 700 nm, 730 nm, 760 nm, 800 nm, 850 nm, and 900 nm were used for PA signal generation and spectral analysis. A region of interest inside the intestinal wall of the terminal ileum or sigmoid colon was chosen to calculate individual parameters of MSOT such as hemoglobin and oxygen saturation. Figure 3b shows transabdominal MSOT images of the intestinal wall of CD patients in remission and with disease activity, respectively. The imaging results demonstrated that HbO₂ and sO₂ values increase steadily in correlation with disease activity. The use of spectroscopic PA imaging in animal models of CD has also been reported [55, 56]. The imaging results revealed an increase in the relative collagen/hemoglobin ratio in the animals with chronic CD compared to those with acute CD due to the deposition of extracellular collagen and decreased vascularity in the fibrotic intestinal stricture. In contrast, the animals with acute CD were characterized by higher oxygenated (850 nm) and deoxygenated (750 nm) hemoglobin and blood oxygenation levels than the animals with chronic CD due to the rich vascularity and blood supply secondary to the inflamed segment of intestine. The data sets acquired at the individual wavelengths were consistent with the increased collagen content and the reduced intra-tissue blood observed by histology in animals with chronic CD. The ratios derived from the measurements at the three wavelengths between collagen and hemoglobin contents were significantly

Fig. 2 (continued) images of blood vessels showing the flow rate (left) and flow direction (right) [59]. (a, b) Adapted from [50] with permission, © 2012, Rajian et al. (CC-BY 4.0 license). (c) Adapted from [51] with permission, © 2017, Jo et al. (CC-BY 4.0 license). (d) Adapted from [52] with permission, © 2018, The AGA Institute. (e) Adapted from [59] with permission, © 2018, The Optical Society

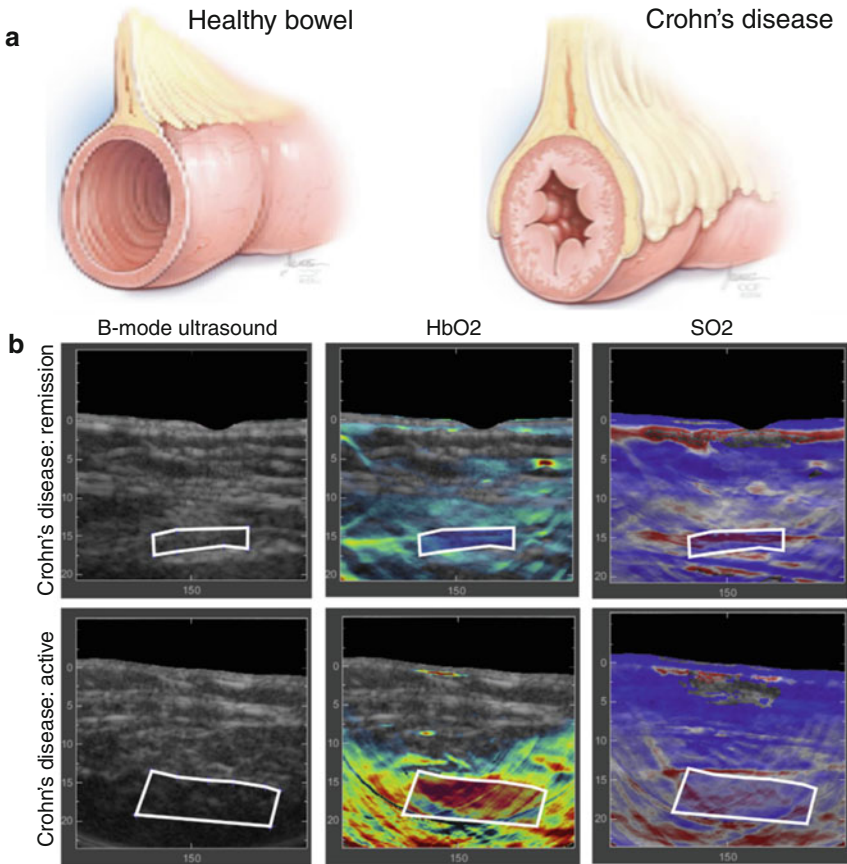


Fig. 3 (a) Schematic representation of a normal bowel (left) and small-bowel stricture in Crohn's disease (right), showing inflammation with thickening of the bowel wall and creeping fat [64]. (b) Representative images from multispectral optoacoustic tomography measurements of the intestinal wall of a patient with CD in remission (top line) and a patient with active CD (bottom line). The left column represents ultrasound images. The middle and right columns represent the ultrasound images co-registered with multispectral photoacoustic tomography data of oxygenated hemoglobin (HbO₂) and oxygen saturation (sO₂). The patient with active CD displays increased HbO₂ and sO₂ signals in the intestinal wall (white rectangle) [54]. (a) Reproduced from [64] with permission, © 2018, Crohn's & Colitis Foundation. (b) Adapted from [54] with permission, © 2016, the AGA Institute

different between the two conditions and could potentially be used as to predict clinical outcomes.

In summary, label-free PA imaging technologies hold great potential in observing anatomical changes in vessels and blood flow rate changes induced by inflammation, as well as other associated markers such as collagen content and angiogenesis. Oxygen saturation levels in tissue can also be quantified by PA imaging to evaluate

the severity of the inflammation. Numerous studies have demonstrated the capability of PA imaging to identify areas of inflammation and quantify inflammation severity. Based on the success of preclinical and early clinical studies, label-free PA imaging is expected to achieve more widespread clinical adoption in the near future.

3 Probe-Based Photoacoustic Imaging of Inflammation

Note: for the rest of this chapter, the word “probe” refers to acoustogenic molecules or macromolecular structures, rather than the physical device for signal acquisition.

In addition to the changes in blood flow and tissue oxygenation status mentioned above, the course of inflammatory diseases is characterized by changes in numerous inflammatory factors and in the cellular microenvironment. For example, oxidative stress, as a result of the imbalance between oxidants (e.g., ROS and RNS) and antioxidants (e.g., glutathione (GSH) and vitamin E), is involved in both acute and chronic inflammatory responses [6]. Carbon monoxide (CO), a by-product of heme catabolism by heme oxygenase, plays an effective anti-inflammatory role. Many inflammatory factors, including cell surface markers such as CD36 and cytokines (e.g., IL-6), are overexpressed, and there is large recruitment of inflammatory cells. These alterations provide important biomarkers for inflammation imaging that can be targeted with specific molecular probes for PA imaging.

A PA probe is composed of a signaling, or acoustogenic, moiety that absorbs light and generates heat, and a targeting moiety that allows the imaging of a specific biological process. The signaling moiety can be a small organic molecule, a metallic or semiconducting nanoparticle, or an organic nanoparticle [65]. The targeting moiety can be anything that targets a specific biological process or structure, such as a small molecule, a peptide, an aptamer, an antibody fragment, or a full protein. The two moieties can be linked through a covalent bond, through encapsulation in a nanoparticle, or via surface functionalization of a nanoparticle. As for any other imaging probe, a PA probe must have suitable biological properties such as an appropriate blood circulation time that allows its accumulation at the target location, the ability to cross biological barriers to reach its target, good affinity for its target, and low toxicity. In addition, an ideal PA probe will have the following properties: an intense (and preferably narrow) absorption peak in the NIR region to provide high sensitivity and avoid interference with endogenous chromophores, a low quantum yield (unlike fluorescent probes) so that the relaxation releases more heat, efficient conversion of heat to pressure waves, and high photostability for consistent imaging [21, 65]. In this section, we present selected examples of specific exogenous PA probes and targets for the detection of inflammation.

3.1 *Activatable Photoacoustic Probes Responsive to Inflammatory Stimuli*

3.1.1 **Reactive Oxygen Species (ROS)-Responsive Probes**

In biological organisms, maintaining adequate levels of ROS is essential for cell growth and differentiation, immune responses, and aging [66, 67]. Hydrogen peroxide (H_2O_2) is one of the key ROS molecules involved in the development of many diseases. Excessive H_2O_2 levels in the body can destroy the structure and function of proteins, causing tissue damage and leading to a variety of diseases including cancer, ischemia/reperfusion injury, and inflammation [68, 69]. Therefore, the development of effective, sensitive, and real-time quantitative H_2O_2 detection methods may allow the diagnosis of inflammation and help clarify the chemical mechanism underlying the development and progression of inflammation. Recently, several optical molecular sensing and imaging methods have been developed to detect H_2O_2 in vivo using sensitive and specific probes [70–72]. Fluorescence imaging is an established optical imaging method with high sensitivity, but there is significant light scatter that degrades the spatial resolution and limits the imaging depth, thus making difficult the detection of inflammation in deep lesions. This depth penetration issue can be solved by using PA imaging. For example, Chen et al. rationally designed the mitochondria-targeted near-infrared probe TPP-HCy-BOH for fluorescent and PA imaging of H_2O_2 in a mouse model of LPS-induced peritoneal inflammation. The comparison of fluorescence and PA images in this model demonstrates how PA imaging can improve on in vivo fluorescence imaging in localizing the source and distribution of inflammation [73]. Chen et al. developed a highly sensitive and specific PA nanoprobe to detect H_2O_2 , by simultaneously loading HRP and its substrate 2,2'-azino-bis(3-ethylbenzothiazoline-6-sulfonic acid) (ABTS) into liposome nanoparticles to obtain Lipo@HRP&ABTS [70] (Fig. 4a). In the presence of H_2O_2 , HRP converts the colorless ABTS into an oxidized form with strong near-infrared (NIR) absorption (Fig. 4b), enabling the PA detection of H_2O_2 at low micromolar concentrations. The authors used a bacterial infection model to induce cellular oxidative stress, autophagy, and necrocytosis in mice, which increases ROS production and activates inflammation (Fig. 4c), and used Lipo@HRP&ABTS as an H_2O_2 -responsive nanoprobe to accurately detect the H_2O_2 produced in response to the bacterial infection (Fig. 4d).

To further improve the depth penetration of PA imaging, probes with excitation peaks shifted further into the near-infrared region have been explored. Indeed, near-infrared light in the first region (NIR-I, 680–900 nm) has a shallower tissue penetration than near-infrared light in the second region (NIR-II, 900–2000 nm) due to the different scattering and absorption characteristics of light in different wavelength bands by biological tissues [74]. Therefore, NIR-II PA imaging has better potential for imaging inflammatory lesions located deeper inside the body. Ye et al. developed a novel silver-coated, palladium-tipped gold nanorod (Au–Pd@Ag NR) nanoprobe to detect H_2O_2 through ratiometric PA imaging [72]. The Ag shell shifts the

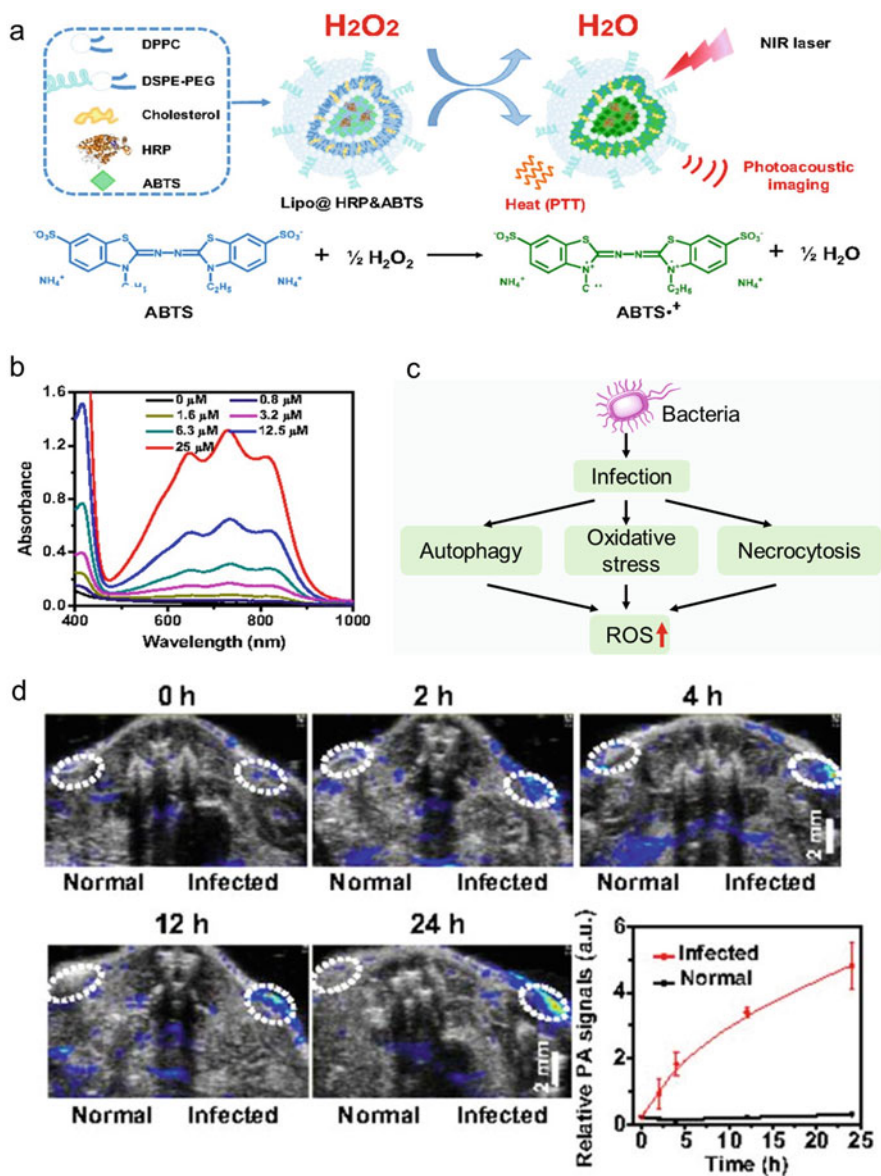


Fig. 4 (a) Schematic illustration showing the construction of Lipo@HRP&ABTS and its applications in H_2O_2 detection by PA imaging and H_2O_2 -activated photothermal therapy. (b) UV-vis-NIR absorbance spectra of Lipo@HRP&ABTS dispersed in buffers with different H_2O_2 concentrations. (c) Schematic illustration of bacterial infection-induced ROS increase. (d) In vivo PA images and PA signals at 800 nm from mice with bacterial infection, after injection of the H_2O_2 -responsive probe Lipo@HRP&ABTS. The infected regions and healthy regions injected with Lipo@HRP&ABTS are highlighted in dashed circles. (a, b, d) Adapted with permission from Chen et al. [70]

maximum absorption peak at ~ 1200 nm of these Au–Pd nanorods to 700 nm in the NIR-I region, which is extended to 1260 nm in the NIR-II region following its oxidation by H_2O_2 . Thus, ratiometric PA imaging at 1260 and 700 nm (PA1260/PA700) can be used to accurately quantify H_2O_2 , and this was applied in a mouse model of bacterial infection and abdominal inflammation, as well as in a rabbit model of osteoarthritis [72]. The NIR-II PA images of the probe activated by H_2O_2 accurately differentiated the inflamed tissue from healthy tissue. Therefore, these novel Au–Pd@Ag nanoparticles have diagnostic potential by precisely quantifying H_2O_2 in inflamed tissue. Additionally, considering that osteoarthritis in a rabbit is located much deeper than in a mouse, the ability to image osteoarthritis by PA in a rabbit model illustrates the merits of using NIR-II probes for PA imaging.

3.1.2 Reactive Oxygen Species/Glutathione-Responsive Probes

Sustained oxidative stress in the inflammatory microenvironment leads to the release of pro-inflammatory cytokines and metalloproteinases, and the activation of antioxidant protection mechanisms. H_2O_2 is the main ROS involved in the oxidation and reduction of protein thiols, and the glutathione redox pair (GSH/GSSG) is the main antioxidant protection system [75]. Therefore, the ability to quantify the redox status through the relative levels of ROS/GSH might provide a more accurate assessment of the inflammatory activity, compared to the detection of ROS alone.

Illustrating this approach, Gao et al. designed a probe to simultaneously image ROS and GSH in atherosclerotic plaque [76]. Atherosclerotic plaque disruption is the most frequent underlying cause of acute clinical events such as myocardial infarction and stroke. Plaque disruption is directly linked to inflammation, which causes important ROS production and disrupts redox homeostasis. Therefore, the ability to quantify plaque-specific redox status is highly desirable for the accurate assessment of plaque inflammatory activity and vulnerability, for stratification of patient risk and to gain a deeper understanding of the molecular mechanisms contributing to plaque instability. In this example, two fluorescent molecular probes, Cy-3- NO_2 for the detection of GSH and Mito-NIRHP for the monitoring of H_2O_2 , were constructed and then self-assembled with bovine serum albumin (BSA) to form a BSA-Cy-Mito PA nanoprobe for the detection of the redox levels in vivo, as shown in Fig. 5a [76]. This BSA-incorporated nanoprobe displayed excellent biocompatibility and prolonged the blood circulation time for optimal plaque targeting. It also showed strong GSH and H_2O_2 -dependent absorbance at 765 and 680 nm for the simultaneous PA detection of GSH/ H_2O_2 at low micromolar concentrations (Fig. 5b, c), with high specificity (Fig. 5d). For in vivo imaging of GSH/ H_2O_2 in atherosclerosis, BSA-Cy-Mito was administered to apolipoprotein E-deficient ($\text{ApoE}^{-/-}$) mice on a high-fat diet, and redox-related inflammation was detected accurately by the appearance of changes in GSH/ H_2O_2 PA signals in the abdominal aorta.

This nanoprobe also allowed to distinguish vulnerable plaque from stable plaque based on the difference in H_2O_2 content and redox status (Fig. 5e, f). Therefore, this

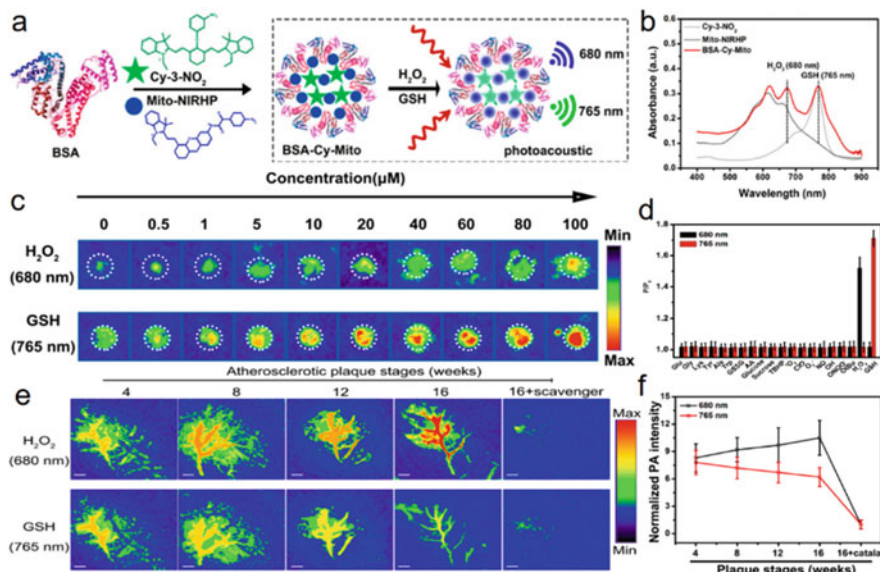


Fig. 5 (a) Structure of the GSH/H₂O₂-responsive nanoprobe BSA-Cy-Mito. (b) UV-vis-NIR absorption spectra of Cy-3-NO₂, Mito-NIRHP, and BSA-Cy-Mito in PBS (pH 7.4). (c) PA imaging of BSA-Cy-Mito nanoprobe (0.25 mg/mL) at different concentrations of H₂O₂ (upper panel) and GSH (lower panel). (d) Enhanced PA intensity (P/P_0) of BSA-Cy-Mito at 680 nm (black bars) and 765 nm (red bars) of various analytes. (e) Representative PA imaging of the abdominal aorta of plaque-bearing ApoE^{-/-} mice at different stages of plaque development, 2 h after the injection of BSA-Cy-Mito nanoprobe (10 mg/kg) or pretreated with a scavenger. The scavengers used were catalase (upper panel) and BSO (lower panel). Scale bar = 2 mm. (f) Normalized PA signal of an abdominal aorta in (e). Adapted with permission from Gao et al. [76]. © 2019, American Chemical Society

sensitive redox-responsive PA nanoprobe can be an effective tool for the prevention and treatment of diseases such as vascular plaque inflammation.

3.1.3 Carbon Monoxide-Responsive Probes

Carbon monoxide (CO) is a by-product of heme catabolism by heme oxygenase and possesses effective anti-inflammatory properties [77]. Low concentrations of CO differentially and selectively inhibit the expression of LPS-induced pro-inflammatory cytokines, including tumor necrosis factor- α (TNF- α), interleukin-1 β (IL-1 β), and macrophage inflammatory protein-1 β (MIP-1 β) both in vivo and in vitro, and increase the LPS-induced expression of the anti-inflammatory cytokine interleukin-10 (IL-10) [78]. CO has an important protective function against inflammatory diseases and therefore has a potential therapeutic use. Therefore, the development of convenient and accurate methods to measure changes in CO levels in complex biological systems in real time is a potential strategy for monitoring

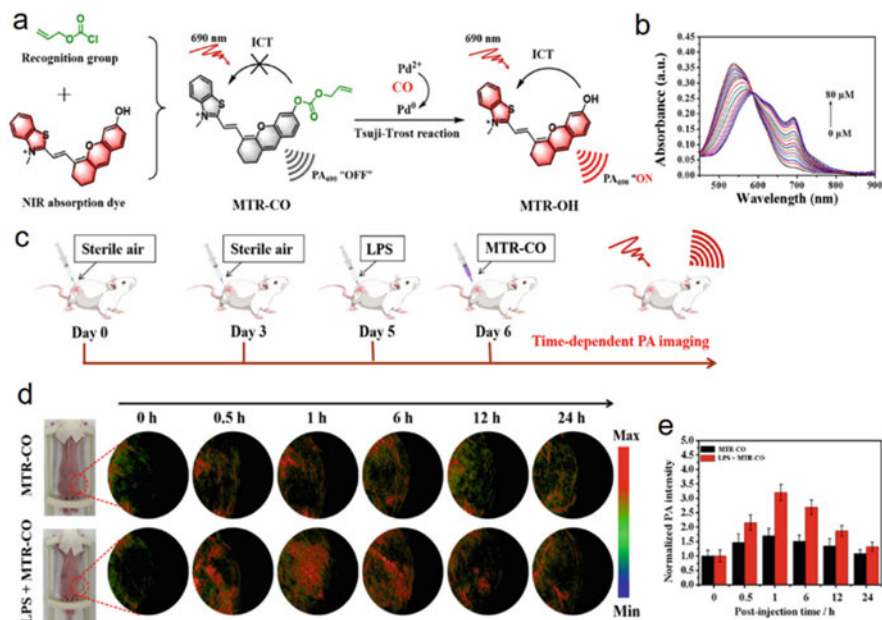


Fig. 6 (a) Rational design of the PA probe MTR-CO for the detection of carbon monoxide. (b) Absorption spectra of MTR-CO (10 μM) after the addition of 0–80 μM of the CO donor CORM-3. Time-dependent PA imaging monitoring the endogenous CO using the MTR-CO probe in vivo. (c) Schematic representation of the protocol used for PA imaging in vivo using MTR-CO in LPS-induced air pouch inflammation. (d) PA images of air pouch inflammation in a nude mouse before and after the subcutaneous injection of the MTR-CO probe (30 μM per mouse) for 0, 0.5, 1, 6, 12, and 24 h. The PA signal was collected under a pulsed laser at 690 nm. (e) Relative PA₆₉₀ intensity of the corresponding PA images in (d). Error bars represent the standard deviation of three separate measurements. Adapted with permission from Li et al. [82]. © 2021, American Chemical Society

inflammation. Conventional detection methods for CO are based on electrochemical analysis, gas chromatography, and chromogenic detection [79–81]. However, these techniques are not suitable for real-time, noninvasive imaging of endogenous CO in living organisms. Li et al. developed the first small-molecule PA probe (denoted as MTR-CO) for the sensitive and selective detection of CO [82]. This PA MTR-CO probe is composed of an allyl formate group (the responsive moiety) and a cyanine-like dye (the reporting moiety, MTR-OH) (Fig. 6a). The PA signal of MTR-CO is “off” because the allyl formate moiety masks the hydroxyl group of MTR-OH, preventing the intramolecular charge transfer that normally gives rise to PA signal. However, in the presence of CO and exogenous Pd²⁺, a Tsuji–Trost reaction occurs that selectively cleaves the allyl formate moiety, thus converting MTR-CO into MTR-OH, which results in the production of a strong near-infrared (NIR) absorbance peak (690 nm) and an intense PA signal (Fig. 6b). The injection of the MTR-CO probe and PdCl₂ in the murine air pouch inflammation model and the visualization using a PA tomography system at different time points revealed that the

mice treated with saline are characterized by a slight PA signal increase after the injection of MTR-CO at 1 h, followed by a slow decrease (Fig. 6c, d), indicating that the MTR-CO probe detects low levels of CO in mice, with the detection limit of CO calculated to be 0.66 μM . These results confirmed that MTR-CO could detect CO levels in mice in real time. In contrast, there was a larger increase in PA signal in the LPS-treated model (Fig. 6e), showing that excessive CO is produced in the LPS-induced mouse inflammation model. All these results indicate that MTR-CO can be used as an effective PA imaging probe to monitor the fluctuation of CO in a mouse inflammation model. However, as this method requires the administration of PdCl_2 , it is currently unclear whether it could be applied in humans. The safety of PA probes needs to be considered during their development to increase their translational potential.

3.1.4 Leukotriene A₄ Hydrolase-Responsive Probes

Leukotriene A₄ hydrolase (LTA₄H) is a bifunctional zinc enzyme that catalyzes the biosynthesis of leukotriene B₄ (LTB₄), a potent lipid chemoattractant involved in inflammation, immune responses, host defense against infection, and platelet-activating factor (PAF)-induced shock [83, 84]. Therefore, it is considered as a biomarker of inflammation in the body, and its detection could allow to distinguish normal tissues from inflamed tissues. On this basis, Wang et al. developed a near-infrared (NIR) fluorescent and PA dual-modality imaging probe, Cy-ASP, with high penetration depth and high selectivity to detect LTA₄H and effectively and noninvasively distinguish inflamed tissue from normal tissue [85]. The Cy-ASP probe uses a hemicyanine dye (Cy-NH₂) as the chromophore and the amide bond in the unnatural amino acid L-Asp-Bzl as the reaction site. L-Asp-Bzl is a specific substrate of LTA₄H; therefore, when the Cy-ASP probe reacts with LTA₄H, the amide bond between L-Asp-Bzl and Cy-NH₂ is specifically hydrolyzed by LTA₄H, releasing the Cy-NH₂ fluorophore. Upon release, the intramolecular charge transfer effect is restored, and Cy-NH₂ can emit intense fluorescence (Fig. 7a). Cy-ASP has been used to detect the activity of LTA₄H *in vivo* to detect the site of inflammation. The PA signal intensity of Cy-ASP in the liver of mice with chemically induced hepatic fibrosis and in the lung tissue of mice with pneumonia significantly increased over 30 minutes after injection showing the gradual conversion of the probe in the presence of LTA₄H (Fig. 7b–e). These results suggest that Cy-ASP could be a useful PA probe for imaging the activity of LTA₄H in deep tissues, which in turn allows to identify sites of inflammation in the body.

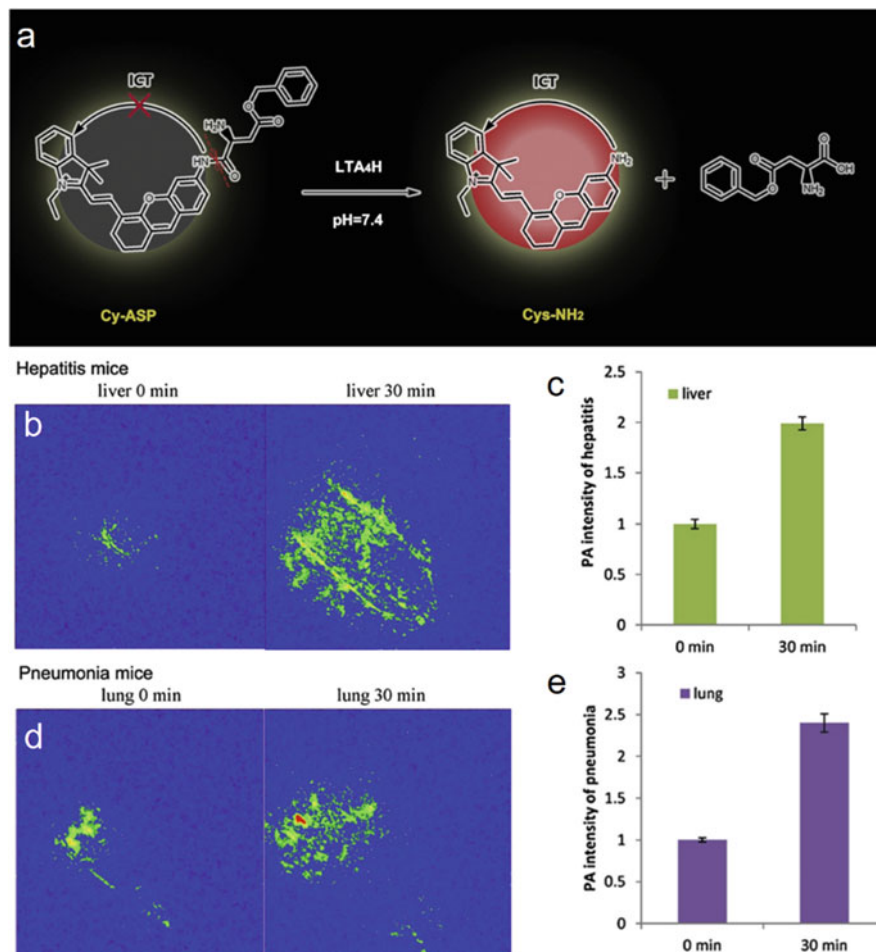


Fig. 7 (a) Activation mechanism of Cy-ASP for the detection of LTA₄H. (b) In vivo PA imaging of mice with hepatitis using Cy-ASP. (d) In vivo PA imaging of pneumonia mice using Cy-ASP. (c, e) Quantification of the PA intensity in panels (b) and (d), respectively. Adapted with permission from Wang et al. [85]. © 2019, Elsevier B.V

3.2 Photoacoustic Probe Targeted Toward Inflammation Markers

3.2.1 Photoacoustic Probes Targeted Toward CD36

Cluster of differentiation 36 (CD36) is a scavenger receptor of oxidized low-density lipoprotein (oxLDL) and a transmembrane glycoprotein found on many cell types including monocytes, macrophages, microvascular endothelial cells, adipocytes, and platelets. It is a marker of atherosclerotic inflammation, participating in the

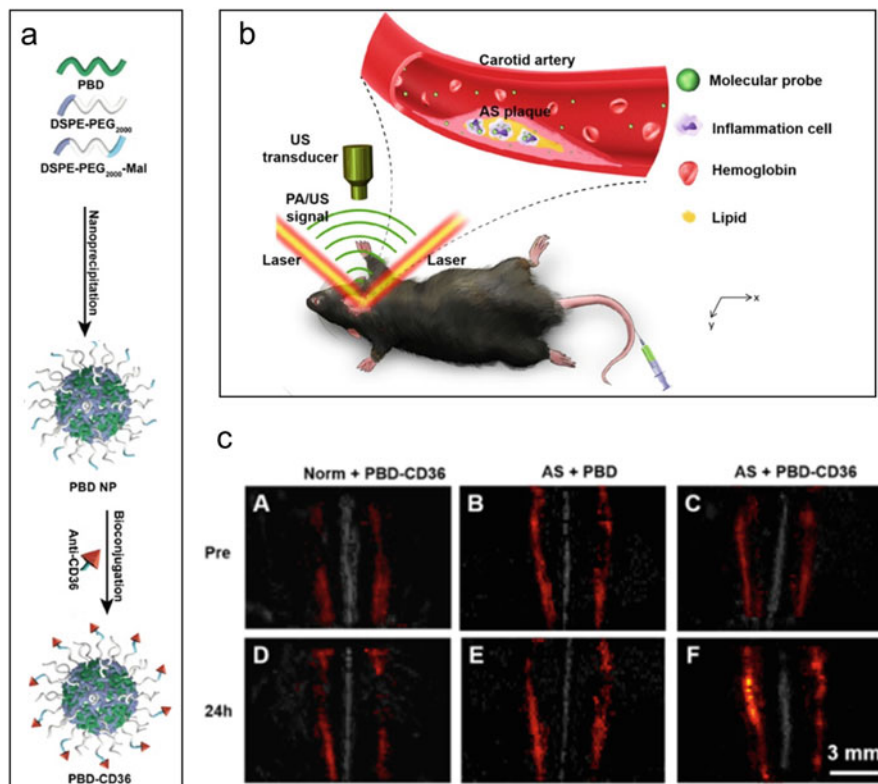


Fig. 8 (a) Schematic illustration of the preparation of PBD-CD36 targeted nanoparticles for PA imaging. (b) Schematic representation of the detection of carotid atherosclerotic inflammation. An excitatory light beam is directed onto the shaved mouse neck, generating a PA signal in the presence of PBD-CD36 nanoparticles, which is detected by an ultrasonic transducer. (c) Fused PA/US maximal amplitude projection (MAP) images of a normal mouse (A, D) and two atherosclerotic mice (B, C, E, F) before (A–C) and 24 h after (D–F) injection of the PBD-CD36, PBD, and PBD-CD36, respectively, showing the accumulation of the PBD-CD36 nanoparticles at atherosclerotic sites. Adapted from [88] with permission, © 2020, Xie et al. (CC-BY 4.0 license, <https://creativecommons.org/licenses/by/4.0>)

formation of the atherosclerotic arterial plaques by the uptake of oxLDL and triggering the signaling cascade of the inflammatory response [86, 87]. CD36 is therefore an interesting target to study the progression and the severity of atherosclerosis, and CD36-specific PA probes have been developed for the in vivo imaging of atherosclerotic inflammation. An anti-CD36 decorated semiconducting polymer nanoparticle (PBD-CD36 NP, Fig. 8a) was designed, using nanoparticles of PBD as the PA signal-generating moiety, conjugated to an anti-CD36 antibody for targeting of the atherosclerotic plaque [88]. The probe has an absorption wavelength of 1064 nm, i.e., in the NIR-II range. The efficient targeting of these nanoparticles (NPs) to inflammatory cells in atherosclerosis is a prerequisite for the obtention of an

inflammation-specific PA signal *in vivo*. *In vivo* PA images of the carotid arteries showed no evident PA signal enhancement in healthy mice, but an enhanced PA signal intensity was observed in the carotid arteries of mice with atherosclerosis plaque (Fig. 8b, c). Notably, this was only observed with the CD36-targeted nanoparticles and not with non-targeted nanoparticles and was associated with expression of CD36 (reflecting the inflammatory status) in the arteries. Histologic analysis of the arteries revealed the good efficiency of PBD-CD36 in specifically targeting inflammatory cells. These results demonstrate that targeting CD36 with acoustogenic nanoparticles allows the identification of atherosclerotic inflammation and the evaluation of atherosclerosis severity *in vivo* using PA imaging.

3.2.2 Photoacoustic Imaging of Arthritis Based on an IL-6 Targeted Probe

Pro-inflammatory cytokines such as IL-1, IL-6, and TNF- α overexpressed in serum and synovial fluid can result in the development of autoimmunity and tissue damage and induce rheumatoid arthritis (RA) [89]. Among these, IL-6 is an important pleiotropic cytokine affecting the biological activity of various cells including T cells, B cells, neutrophils, monocytes, and osteoclasts and is one of the most relevant targets in the treatment of RA [90, 91]. Therefore, the detection of IL-6 and its related factors could help stratify the risk of patients and provide a deeper understanding of the molecular mechanisms underlying RA. The inhibition of IL-6 and IL-6 receptor (IL-6R) is a strategy used in the clinic to alleviate the symptoms of RA. Tocilizumab (TCZ) is a clinically approved humanized monoclonal antibody that inhibits IL-6 signaling by competitively binding to IL-6R, consequently improving the severe symptoms of RA [92, 93]. Chen et al. synthesized polymer nano-PA probes (PNPs) with strong light absorption in the NIR-II region and good biocompatibility [94]. Tocilizumab was conjugated to PNPs to obtain TCZ-PNPs as an IL-6R-targeted theranostic agent for PA imaging and treatment of RA (Fig. 9a). TCZ-PNPs were effective in showing the inflamed forepaws of mice with collagen-induced arthritis. The intensity of the PA signal in the paw reflected the severity of inflammation. After administration of TCZ-PNPs, paws of normal mice showed very low PA signal (Fig. 9b, c), whereas mice with collagen-induced arthritis showed intense PA signal in the paw joint area on day 27 after first immunization. The PA signal gradually decreased over time after the administration of TCZ-PNPs, indicating a significant reduction in joint inflammation. The PA signal in the cartilage (blue arrow) and swollen tissue (yellow arrow) in the joint is clearly visible (Fig. 9c, dashed line) owing to the strong penetrating ability and high sensitivity of NIR-II PA molecular imaging. This work demonstrates the feasibility of specifically imaging IL-6 in RA, and TCZ-PNPs have strong potential to become a new theranostic tool for the diagnosis, real-time monitoring, and treatment of RA.

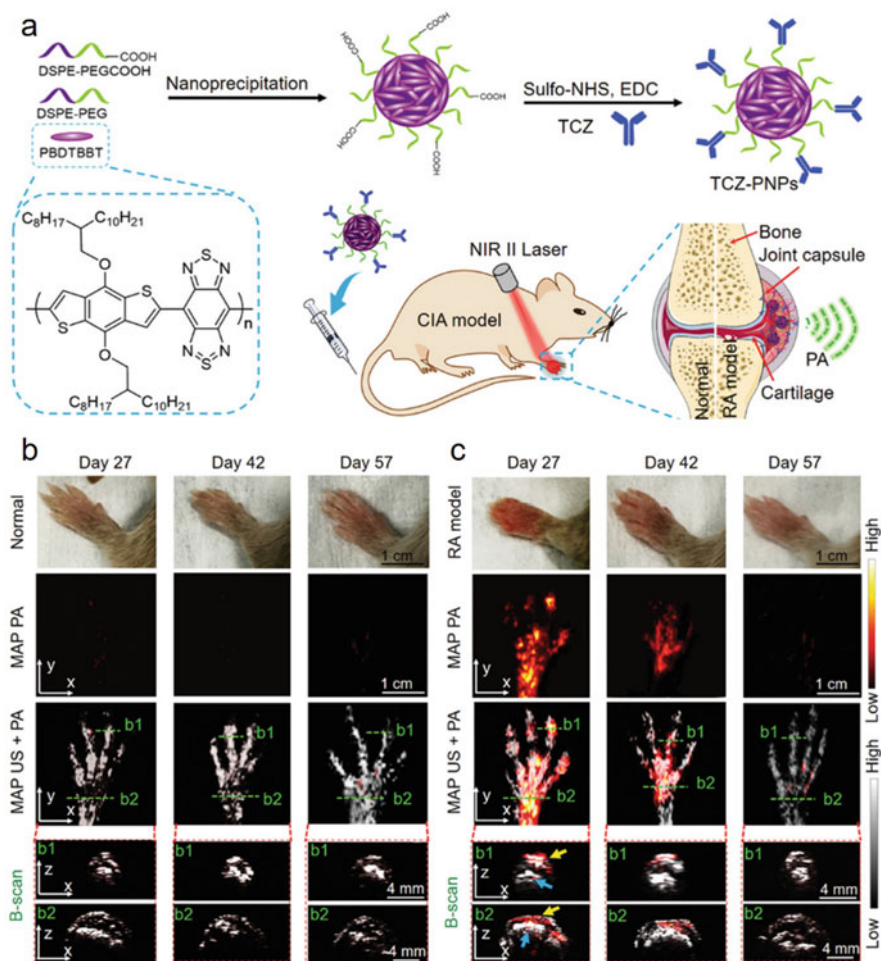


Fig. 9 (a) Schematic illustration of the preparation of TCZ-PNPs, a PA probe specific for IL-6, and its use for NIR-II PA imaging in a mouse model of RA using a 1064 nm laser. (b, c) Photographs and PA images of the forepaws in normal and TCZ-PNP-treated RA groups at day 27, 42, and 57 after the first immunization. The B-scan PA images correspond to the green dashed region. The yellow arrow indicates the swollen tissue, while the blue arrow indicates the cartilage tissue. Adapted from Chen et al. [94] with permission, © 2020, Wiley-VCH GmbH

3.3 Direct Labeling of Immune Cells for Photoacoustic Imaging of Inflammation

Among the immune responses that occur during inflammation, the activation and polarization of macrophages play a key role in the development, progression, and resolution of inflammation [95]. In particular, macrophages participate in multiple aspects of the regulation of inflammation, by removing damaged tissues and

pathogens through phagocytosis, secreting immunomodulatory cytokines and other factors, and regulating adaptive immunity through antigen presentation to lymphocytes [96]. Cell debris removal and tissue repair during acute or chronic inflammation also require the participation of other immune cells and stem cells [97]. Effective cell tracking methods that can elucidate the activation status and fate of individual cell types in inflammation would be highly beneficial to better understand disease mechanisms, develop treatments, and monitor patients. Immune cells can be tracked *in vivo* by incubation with cell-binding tracers, and this strategy, also known as direct cell labeling, is routinely used for fluorescence [98], MRI [99], and nuclear imaging [100], to achieve real-time monitoring of the cell fate. Cell tracking by PA imaging has also emerged in recent years, particularly for stem cell imaging where long-term tracking is desirable [101]. As an example of cell labeling for PA imaging, Li et al. rationally designed and synthesized the thiadiazoloquinoxaline-based semiconducting polymer p-BBT-TQP and encapsulated it with 1,2-distearoyl-*sn*-glycero-3-phosphoethanolamine-*N*-[methoxy(polyethylene glycol)-2000] (DSPE-PEG₂₀₀₀) and maleimide-functionalized DSPE-PEG₂₀₀₀-Mal to form water-dispersed nanoparticles [102]. The nanoparticles were then functionalized with a cell-penetrating peptide (Tat) to facilitate rapid labeling of cells. These Tat-BBT-TQP nanoparticles (Tat-BTNPs) were found to efficiently label macrophages, neutrophils, and mesenchymal stem cells through simple incubation (Fig. 10a, b). Labeled cells were intravenously injected into mice with an inflamed right ear and a non-inflamed left ear for *in vivo* PA tracking. Endogenous PA signals of hemoglobin in blood vessels of the ears were collected using a 532 nm excitation wavelength, showing the microstructure of the blood vessels and locating the inflammation site (Fig. 10c). The injected macrophages labeled with Tat-BTNPs were then monitored by pulsed laser irradiation at 840 nm. The PA signal from Tat-BTNP-labeled macrophages in the inflamed ear gradually increased from 1 to 24 hours after injection, while the signal in the normal ear remained low over the same period (Fig. 10d). The relative PA signal of Tat-BTNPs in the inflamed ears was significantly higher than in non-inflamed ears ($p < 0.0001$) from 6 to 24 h after administration of labeled macrophages, showing the homing and accumulation of these cells in the inflamed tissues over time (Fig. 10d). These results successfully prove that this strategy enables the tracking of macrophages in inflamed tissues with high spatial and temporal resolution, providing a new strategy for the study of immune cell trafficking in inflammation.

4 Conclusion and Prospects of Photoacoustic Imaging in Inflammation Research

Photoacoustic imaging offers many advantages over other biomedical imaging modalities, including a higher spatiotemporal resolution compared to nuclear and conventional ultrasound imaging, and a better imaging depth compared to optical

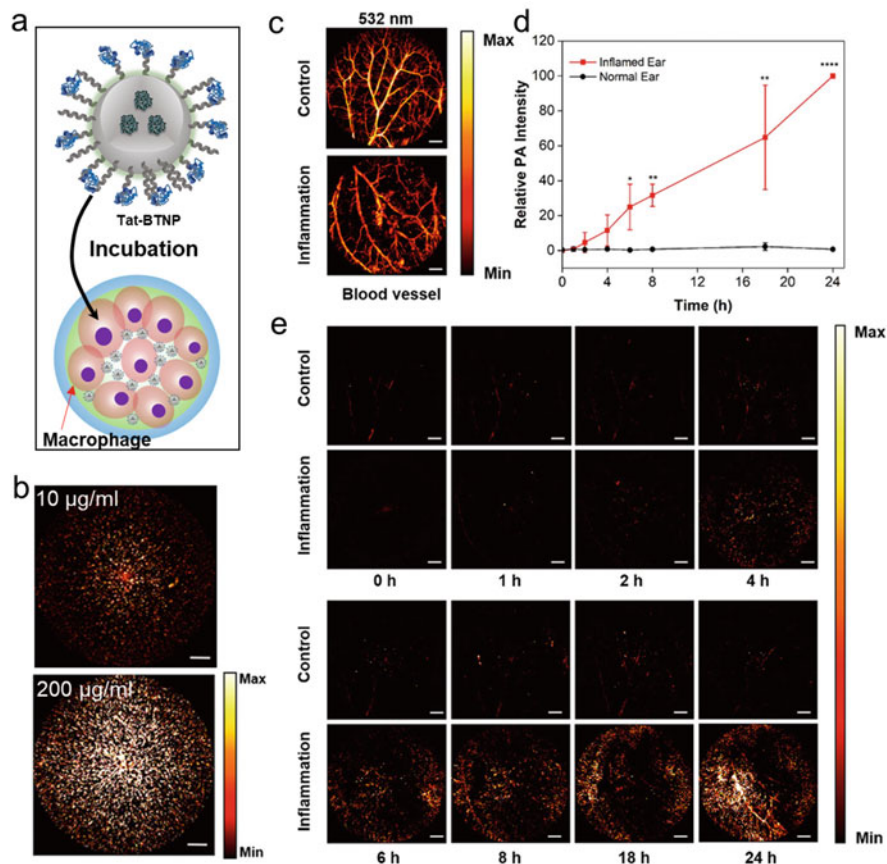


Fig. 10 (a) Cell labeling with Tat-BTNPs. (b) Representative in vitro PA image of macrophages after labeling by Tat-BTNPs at 10 and 200 $\mu\text{g}/\text{mL}$. The highest PA signal of the labeled macrophages was set at a relative intensity of 100%. Scale bar: 1 mm. (c) PA signals of hemoglobin in blood vessels at 532 nm excitation wavelength, revealing the vasculature of normal and inflamed mouse ears. (d) PA signals of Tat-BTNP-labeled macrophages (840 nm excitation) accumulated in the inflamed ear and collected after their intravenous injection. (e) Representative PA images of Tat-BTNP-labeled macrophages in a non-inflamed (upper row) and inflamed (lower row) ear. Scale bar: 1 mm. Adapted from Li et al. [102] with permission, © 2021 American Chemical Society

imaging. PA does not involve ionizing radiation, and PA systems are more portable than PET/SPECT or MRI scanners. These characteristics make PA imaging a promising tool for the diagnosis of inflammatory reactions or inflammatory lesions in the living body. In the development and progression of inflammation, changes in organ perfusion and blood oxygen saturation are two important characteristics that can be imaged, for example, using hemoglobin as an endogenous, label-free PA contrast agent. Label-free PA imaging can monitor the changes in vasodilation and angiogenesis in inflammatory diseases such as RA and CD. In addition, blood

oxygen saturation in the lesion can be detected by PA imaging based on the changes of the PA spectrum when oxygen binds and dissociates from hemoglobin.

Furthermore, changes in the inflammatory microenvironment such as increases in inflammatory factors and recruitment of immune cells are also characteristic. However, these inflammatory markers have no intrinsic chromophores for PA imaging; thus, they cannot be detected by label-free PA imaging and need to be functionalized or targeted with specific probes. Exogenous imaging probes have been developed to image various components of the intricate inflammatory microenvironment, which mainly include three categories: (1) activatable probes that respond to endogenous inflammatory stimuli such as ROS, GSH, CO, and LTA₄H, enabling highly sensitive and specific PA detection of these molecules; (2) antibody-based PA probes targeted toward inflammation markers such as IL-6 and CD36, which monitor the expression of these markers in the inflammatory lesions and evaluate the therapeutic effect on the inflammatory diseases; and (3) direct cell labeling agents for PA imaging of immune cells, which are used to locate sites of inflammation based on the homing properties of these immune cells. The above methods allow the dynamic monitoring of the levels of various factors related to the inflamed microenvironment with high sensitivity and specificity. Thus, they provide a noninvasive diagnostic strategy for the occurrence and development of inflammation. One important consideration for future developments is the biocompatibility of PA probes, particularly in the case of nanoparticle-based probes as nanoparticles tend to accumulate nonspecifically in the liver and spleen. This is a potential source of long-term toxicity, and nanoparticles made of biodegradable materials such as albumin [76] or cellulose [103] are likely to have better prospects of clinical translation.

With continuous improvements of the performance of PA imaging systems and increasing commercial availability, label-free PA imaging, which does not require exogenous probes, has a much lower barrier to clinical translation of inflammation diagnosis. On the other hand, the use of exogenous contrast agents could extend the applications of PA imaging and exploit additional mechanisms of inflammation once the safety of these probes has been established. Therefore, optimizing PA systems and enhancing the safety profile of PA probes will not only help the understanding of the occurrence and development mechanisms of inflammatory diseases but also promote their translation to the clinic.

Compliance with Ethical Standards Funding: This work was supported by grants from the National Natural Science Foundation of China (81801758 and 82172008), Chinese Academy of Sciences (YJKYYQ20190078 and GJJSTD20210003), National Key R&D Program of China (2020YFA0908800), CAS Key Laboratory of Health Informatics (2011DP173015), Guangdong Provincial Key Laboratory of Biomedical Optical Imaging (2020B121201010), and Science and Technology Innovation Fund of Shenzhen (JCYJ20190806150001764).

Conflict of Interest: The authors have no conflict of interest to declare.

Ethical Approval: No human or animal research was directly involved in the writing of this chapter.

References

1. Ashley NT, Weil ZM, Nelson RJ. Inflammation: mechanisms, costs, and natural variation. *Annu Rev Ecol Evol Syst.* 2012;43:385–406. <https://doi.org/10.1146/annurev-ecolsys-040212-092530>.
2. Medzhitov R. Origin and physiological roles of inflammation. *Nature.* 2008;454:428–35. <https://doi.org/10.1038/nature07201>.
3. Sprague AH, Khalil RA. Inflammatory cytokines in vascular dysfunction and vascular disease. *Biochem Pharmacol.* 2009;78:539–52. <https://doi.org/10.1016/j.bcp.2009.04.029>.
4. Pober JS, Sessa WC. Inflammation and the blood microvascular system. *Cold Spring Harb Perspect Biol.* 2015;7:a016345. <https://doi.org/10.1101/cshperspect.a016345>.
5. Elenkov IJ, Iezzoni DG, Daly A, Harris AG, Chrousos GP. Cytokine dysregulation, inflammation and well-being. *Neuroimmunomodulation.* 2005;12:255–69. <https://doi.org/10.1159/000087104>.
6. Mittal M, Siddiqui MR, Tran K, Reddy SP, Malik AB. Reactive oxygen species in inflammation and tissue injury. *Antioxid Redox Signal.* 2014;20:1126–67. <https://doi.org/10.1089/ars.2012.5149>.
7. Riesenberger S, Groetchen A, Siddaway R, Bald T, Reinhardt J, Smorra D, et al. MITF and c-Jun antagonism interconnects melanoma dedifferentiation with pro-inflammatory cytokine responsiveness and myeloid cell recruitment. *Nat Commun.* 2015;6:8755. <https://doi.org/10.1038/ncomms9755>.
8. Muñoz LE, Leppkes M, Fuchs TA, Hoffmann M, Herrmann M. Missing in action—the meaning of cell death in tissue damage and inflammation. *Immunol Rev.* 2017;280:26–40. <https://doi.org/10.1111/imr.12569>.
9. Wallach D, Kang T-B, Kovalenko A. Concepts of tissue injury and cell death in inflammation: a historical perspective. *Nat Rev Immunol.* 2014;14:51–9. <https://doi.org/10.1038/nri3561>.
10. Pawelec G, Goldeck D, Derhovanessian E. Inflammation, ageing and chronic disease. *Curr Opin Immunol.* 2014;29:23–8. <https://doi.org/10.1016/j.coi.2014.03.007>.
11. Hotamisligil GS. Inflammation, metaflammation and immunometabolic disorders. *Nature.* 2017;542:177–85. <https://doi.org/10.1038/nature21363>.
12. Mulder WJM, Jaffer FA, Fayad ZA, Nahrendorf M. Imaging and nanomedicine in inflammatory atherosclerosis. *Sci Transl Med.* 2014;6. <https://doi.org/10.1126/scitranslmed.3005101>.
13. Absinta M, Vuolo L, Rao A, Nair G, Sati P, Cortese ICM, et al. Gadolinium-based MRI characterization of leptomeningeal inflammation in multiple sclerosis. *Neurology.* 2015;85:18–28. <https://doi.org/10.1212/WNL.0000000000001587>.
14. MacRitchie N, Frleta-Gilchrist M, Sugiyama A, Lawton T, McInnes IB, Maffia P. Molecular imaging of inflammation - current and emerging technologies for diagnosis and treatment. *Pharmacol Ther.* 2020;211:107550. <https://doi.org/10.1016/j.pharmthera.2020.107550>.
15. Sun Y, Sobel ES, Jiang H. First assessment of three-dimensional quantitative photoacoustic tomography for in vivo detection of osteoarthritis in the finger joints. *Med Phys.* 2011;38:4009–17. <https://doi.org/10.1118/1.3598113>.
16. Zhu J, Rowland EM, Harput S, Riemer K, Leow CH, Clark B, et al. 3D super-resolution US imaging of rabbit lymph node vasculature in vivo by using microbubbles. *Radiology.* 2019;291:642–50. <https://doi.org/10.1148/radiol.2019182593>.
17. Deshpande N, Lutz AM, Ren Y, Foygel K, Tian L, Schneider M, et al. Quantification and monitoring of inflammation in murine inflammatory bowel disease with targeted contrast-enhanced US. *Radiology.* 2012;262:172–80. <https://doi.org/10.1148/radiol.11110323>.
18. Wang H, Machtaler S, Bettinger T, Lutz AM, Luong R, Bussat P, et al. Molecular imaging of inflammation in inflammatory bowel disease with a clinically translatable dual-selectin-targeted US contrast agent: comparison with FDG PET/CT in a mouse model. *Radiology.* 2013;267:818–29. <https://doi.org/10.1148/radiol.13122509>.

19. Machtaler S, Knieling F, Luong R, Tian L, Willmann JK. Assessment of inflammation in an acute on chronic model of inflammatory bowel disease with ultrasound molecular imaging. *Theranostics*. 2015;5:1175–86. <https://doi.org/10.7150/thno.13048>.
20. Castellon X, Bogdanova V. Chronic inflammatory diseases and endothelial dysfunction. *Aging Dis*. 2016;7:81. <https://doi.org/10.14336/AD.2015.0803>.
21. Beard P. Biomedical photoacoustic imaging. *Interface. Focus*. 2011;1:602–31. <https://doi.org/10.1098/rsfs.2011.0028>.
22. Wang LV, Yao J. A practical guide to photoacoustic tomography in the life sciences. *Nat Methods*. 2016;13:627–38. <https://doi.org/10.1038/nmeth.3925>.
23. Zhang J, Duan F, Liu Y, Nie L. High-resolution photoacoustic tomography for early-stage cancer detection and its clinical translation. *Radiol Imaging Cancer*. 2020;2:e190030. <https://doi.org/10.1148/rycan.2020190030>.
24. Steinberg I, Huland DM, Vermesh O, Frostig HE, Tummers WS, Gambhir SS. Photoacoustic. *Clin Imaging Photoacoustics*. 2019;14:77–98. <https://doi.org/10.1016/j.pacs.2019.05.001>.
25. Ntziachristos V, Razansky D. Molecular imaging by means of multispectral optoacoustic tomography (MSOT). *Chem Rev*. 2010;110:2783–94. <https://doi.org/10.1021/cr9002566>.
26. Danielli A, Maslov KI, Garcia-Uribe A, Winkler AM, Li C, Wang L, et al. Label-free photoacoustic nanoscopy. *J Biomed Opt*. 2014;19:1. <https://doi.org/10.1117/1.JBO.19.8.086006>.
27. Regensburger AP, Brown E, Krönke G, Waldner MJ, Knieling F. Optoacoustic imaging in inflammation. *Biomedicines*. 2021;9:483. <https://doi.org/10.3390/biomedicines9050483>.
28. Strohm EM, Berndl ESL, Kolios MC. High frequency label-free photoacoustic microscopy of single cells. *Photo-Dermatology*. 2013;1:49–53. <https://doi.org/10.1016/j.pacs.2013.08.003>.
29. Zhao H, Liu C, Li K, Chen N, Zhang K, Wang L, et al. Multiscale vascular enhancement filter applied to in vivo morphologic and functional photoacoustic imaging of rat ocular vasculature. *IEEE Photonics J*. 2019;11:1–12. <https://doi.org/10.1109/JPHOT.2019.2948955>.
30. Deán-Ben XL, Fehm TF, Ford SJ, Gottschalk S, Razansky D. Spiral volumetric optoacoustic tomography visualizes multi-scale dynamics in mice. *Light Sci Appl*. 2017;6:–e16247. <https://doi.org/10.1038/lsa.2016.247>.
31. Matsumoto Y, Asao Y, Yoshikawa A, Sekiguchi H, Takada M, Furu M, et al. Label-free photoacoustic imaging of human palmar vessels: a structural morphological analysis. *Sci Rep*. 2018;8:786. <https://doi.org/10.1038/s41598-018-19161-z>.
32. Jo J, Xu G, Zhu Y, Burton M, Sarazin J, Schiopu E, et al. Detecting joint inflammation by an LED-based photoacoustic imaging system: a feasibility study. *J Biomed Opt*. 2018;23:1. <https://doi.org/10.1117/1.JBO.23.11.110501>.
33. Lei H, Johnson LA, Liu S, Moons DS, Ma T, Zhou Q, et al. Characterizing intestinal inflammation and fibrosis in Crohn's disease by photoacoustic imaging: feasibility study. *Biomed Opt Express*. 2016;7:2837. <https://doi.org/10.1364/BOE.7.002837>.
34. Yao J, Wang LV. Photoacoustic microscopy. *Laser Photon Rev*. 2013;7:758–78. <https://doi.org/10.1002/lpor.201200060>.
35. Jo J, Tian C, Xu G, Sarazin J, Schiopu E, Gandikota G, et al. Photoacoustic tomography for human musculoskeletal imaging and inflammatory arthritis detection. *Photo-Dermatology*. 2018;12:82–9. <https://doi.org/10.1016/j.pacs.2018.07.004>.
36. Fatima A, Kratkiewicz K, Manwar R, Zafar M, Zhang R, Huang B, et al. Review of cost reduction methods in photoacoustic computed tomography. *Photo-Dermatology*. 2019;15:100137. <https://doi.org/10.1016/j.pacs.2019.100137>.
37. Choi W, Park E-Y, Jeon S, Kim C. Clinical photoacoustic imaging platforms. *Biomed Eng Lett*. 2018;8:139–55. <https://doi.org/10.1007/s13534-018-0062-7>.
38. Deán-Ben XL, Merčep E, Razansky D. Hybrid-array-based optoacoustic and ultrasound (OPUS) imaging of biological tissues. *Appl Phys Lett*. 2017;110:203703. <https://doi.org/10.1063/1.4983462>.
39. Laufer J, Delpy D, Elwell C, Beard P. Quantitative spatially resolved measurement of tissue chromophore concentrations using photoacoustic spectroscopy: application to the

- measurement of blood oxygenation and haemoglobin concentration. *Phys Med Biol.* 2007;52: 141–68. <https://doi.org/10.1088/0031-9155/52/1/010>.
40. Cox B, Laufer JG, Arridge SR, Beard PC. Quantitative spectroscopic photoacoustic imaging: a review. *J Biomed Opt.* 2012;17:061202. <https://doi.org/10.1117/1.JBO.17.6.061202>.
 41. Choi SSS, Mandelis A. Review of the state of the art in cardiovascular endoscopy imaging of atherosclerosis using photoacoustic techniques with pulsed and continuous-wave optical excitations. *J Biomed Opt.* 2019;24:1. <https://doi.org/10.1117/1.JBO.24.8.080902>.
 42. Xu G, Meng Z-X, Lin JD, Yuan J, Carson PL, Joshi B, et al. The functional pitch of an organ: quantification of tissue texture with photoacoustic Spectrum analysis. *Radiology.* 2014;271: 248–54. <https://doi.org/10.1148/radiol.13130777>.
 43. Bodea S-V, Westmeyer GG. Photoacoustic neuroimaging—perspectives on a maturing imaging technique and its applications in neuroscience. *Front Neurosci.* 2021;15. <https://doi.org/10.3389/fnins.2021.655247>.
 44. Feng T, Zhu Y, Morris R, Kozloff KM, Wang X. Functional photoacoustic and ultrasonic assessment of osteoporosis: a clinical feasibility study. *BME Front.* 2020;2020:1–15. <https://doi.org/10.34133/2020/1081540>.
 45. Regensburger AP, Fonteyne LM, Jüngert J, Wagner AL, Gerhalter T, Nagel AM, et al. Detection of collagens by multispectral optoacoustic tomography as an imaging biomarker for Duchenne muscular dystrophy. *Nat Med.* 2019;25:1905–15. <https://doi.org/10.1038/s41591-019-0669-y>.
 46. Diot G, Metz S, Noske A, Liapis E, Schroeder B, Ovsepien SV, et al. Multispectral optoacoustic tomography (MSOT) of human breast cancer. *Clin Cancer Res.* 2017;23:6912–22. <https://doi.org/10.1158/1078-0432.CCR-16-3200>.
 47. Aguirre J, Schwarz M, Garzorz N, Omar M, Buehler A, Eyerich K, et al. Precision assessment of label-free psoriasis biomarkers with ultra-broadband optoacoustic mesoscopy. *Nat Biomed Eng.* 2017;1:0068. <https://doi.org/10.1038/s41551-017-0068>.
 48. Stupack DG, Storgard CM, Cheres DA. A role for angiogenesis in rheumatoid arthritis. *Brazilian J Med Biol Res.* 1999;32:573–81. <https://doi.org/10.1590/S0100-879X1999000500011>.
 49. Szekanecz Z, Koch AE. Mechanisms of disease: angiogenesis in inflammatory diseases. *Nat Clin Pract Rheumatol.* 2007;3:635–43. <https://doi.org/10.1038/ncprheum0647>.
 50. Rajian JR, Girish G, Wang X. Photoacoustic tomography to identify inflammatory arthritis. *J Biomed Opt.* 2012;17:960131. <https://doi.org/10.1117/1.JBO.17.9.096013>.
 51. Jo J, Xu G, Cao M, Marquardt A, Francis S, Gandikota G, et al. A functional study of human inflammatory arthritis using photoacoustic imaging. *Sci Rep.* 2017;7:15026. <https://doi.org/10.1038/s41598-017-15147-5>.
 52. Knieling F, Gonzales Menezes J, Claussen J, Schwarz M, Neufert C, Fahlbusch FB, et al. Raster-scanning optoacoustic mesoscopy for gastrointestinal imaging at high resolution. *Gastroenterology.* 2018;154:807–809.e3. <https://doi.org/10.1053/j.gastro.2017.11.285>.
 53. Guo Z, Li Z, Deng Y, Chen S. Photoacoustic microscopy for evaluating a lipopolysaccharide-induced inflammation model in mice. *J Biophotonics.* 2019;12. <https://doi.org/10.1002/jbio.201800251>.
 54. Waldner MJ, Knieling F, Egger C, Morscher S, Claussen J, Vetter M, et al. Multispectral optoacoustic tomography in Crohn’s disease: noninvasive imaging of disease activity. *Gastroenterology.* 2016;151:238–40. <https://doi.org/10.1053/j.gastro.2016.05.047>.
 55. Zhu Y, Johnson LA, Huang Z, Rubin JM, Yuan J, Lei H, et al. Identifying intestinal fibrosis and inflammation by spectroscopic photoacoustic imaging: an animal study in vivo. *Biomed Opt Express.* 2018;9:1590. <https://doi.org/10.1364/BOE.9.001590>.
 56. Lei H, Johnson LA, Eaton KA, Liu S, Ni J, Wang X, et al. Characterizing intestinal strictures of Crohn’s disease in vivo by endoscopic photoacoustic imaging. *Biomed Opt Express.* 2019;10:2542. <https://doi.org/10.1364/BOE.10.002542>.
 57. Xu M, Wang LV. Photoacoustic imaging in biomedicine. *Rev Sci Instrum.* 2006;77:41101. <https://doi.org/10.1063/1.2195024>.

58. van den Berg PJ, Daoudi K, Bernelot Moens HJ, Steenbergen W. Feasibility of photoacoustic/ultrasound imaging of synovitis in finger joints using a point-of-care system. *Photo-Dermatology*. 2017;8:8–14. <https://doi.org/10.1016/j.pacs.2017.08.002>.
59. Yao J, Maslov KI, Shi Y, Taber LA, Wang LV. In vivo photoacoustic imaging of transverse blood flow by using Doppler broadening of bandwidth. *Opt Lett*. 2010;35:1419. <https://doi.org/10.1364/OL.35.001419>.
60. Lelubre C, Vincent J-L. Mechanisms and treatment of organ failure in sepsis. *Nat Rev Nephrol*. 2018;14:417–27. <https://doi.org/10.1038/s41581-018-0005-7>.
61. Torres J, Mehandru S, Colombel J-F, Peyrin-Biroulet L. Crohn's disease. *Lancet*. 2017;389:1741–55. [https://doi.org/10.1016/S0140-6736\(16\)31711-1](https://doi.org/10.1016/S0140-6736(16)31711-1).
62. Bhutiani N, Grizzle WE, Galandiuk S, Oтали D, Dryden GW, Egilmez NK, et al. Noninvasive imaging of colitis using multispectral optoacoustic tomography. *J Nucl Med*. 2017;58:1009–12. <https://doi.org/10.2967/jnumed.116.184705>.
63. Knieling F, Neufert C, Hartmann A, Claussen J, Urich A, Egger C, et al. Multispectral optoacoustic tomography for assessment of Crohn's disease activity. *N Engl J Med*. 2017;376:1292–4. <https://doi.org/10.1056/NEJMc1612455>.
64. Mao R, Kurada S, Gordon IO, Baker ME, Gandhi N, McDonald C, et al. The mesenteric fat and intestinal muscle Interface: creeping fat influencing stricture formation in Crohn's disease. *Inflamm Bowel Dis*. 2019;25:421–6. <https://doi.org/10.1093/ibd/izy331>.
65. Weber J, Beard PC, Bohndiek SE. Contrast agents for molecular photoacoustic imaging. *Nat Methods*. 2016;13:639–50. <https://doi.org/10.1038/nmeth.3929>.
66. Sena LA, Chandel NS. Physiological roles of mitochondrial reactive oxygen species. *Mol Cell*. 2012;48:158–67. <https://doi.org/10.1016/j.molcel.2012.09.025>.
67. Wittmann C, Chockley P, Singh SK, Pase L, Lieschke GJ, Grabher C. Hydrogen peroxide in inflammation: messenger, guide, and assassin. *Adv Hematol*. 2012;2012:1–6. <https://doi.org/10.1155/2012/541471>.
68. Lisanti MP, Martinez-Outschoorn UE, Lin Z, Pavlides S, Whitaker-Menezes D, Pestell RG, et al. Hydrogen peroxide fuels aging, inflammation, cancer metabolism and metastasis. *Cell Cycle*. 2011;10:2440–9. <https://doi.org/10.4161/cc.10.15.16870>.
69. Guo H, Aleyasin H, Dickinson BC, Haskew-Layton RE, Ratan RR. Recent advances in hydrogen peroxide imaging for biological applications. *Cell Biosci*. 2014;4:64. <https://doi.org/10.1186/2045-3701-4-64>.
70. Chen Q, Liang C, Sun X, Chen J, Yang Z, Zhao H, et al. H2O2-responsive liposomal nanoprobe for photoacoustic inflammation imaging and tumor theranostics via in vivo chromogenic assay. *Proc Natl Acad Sci*. 2017;114:5343–8. <https://doi.org/10.1073/pnas.1701976114>.
71. Zlitni A, Gowrishankar G, Steinberg I, Haywood T, Sam GS. Maltotriose-based probes for fluorescence and photoacoustic imaging of bacterial infections. *Nat Commun*. 2020;11:1250. <https://doi.org/10.1038/s41467-020-14985-8>.
72. Ye J, Li Z, Fu Q, Li Q, Zhang X, Su L, et al. Quantitative photoacoustic diagnosis and precise treatment of inflammation in vivo using activatable theranostic nanoprobe. *Adv Funct Mater*. 2020;30:2001771. <https://doi.org/10.1002/adfm.202001771>.
73. Chen X, Ren X, Zhang L, Liu Z, Hai Z. Mitochondria-targeted fluorescent and photoacoustic imaging of hydrogen peroxide in inflammation. *Anal Chem*. 2020;92:14244–50. <https://doi.org/10.1021/acs.analchem.0c03506>.
74. Chen J, Sedgwick AC, Sen S, Ren Y, Sun Q, Chau C, et al. Expanded porphyrins: functional photoacoustic imaging agents that operate in the NIR-II region. *Chem Sci*. 2021;12:9916–21. <https://doi.org/10.1039/D1SC01591E>.
75. D'Autréaux B, Toledano MB. ROS as signalling molecules: mechanisms that generate specificity in ROS homeostasis. *Nat Rev Mol Cell Biol*. 2007;8:813–24. <https://doi.org/10.1038/nrm2256>.

76. Gao W, Li X, Liu Z, Fu W, Sun Y, Cao W, et al. A redox-responsive self-assembled nanoprobe for photoacoustic inflammation imaging to assess atherosclerotic plaque vulnerability. *Anal Chem.* 2019;91:1150–6. <https://doi.org/10.1021/acs.analchem.8b04912>.
77. Foresti R, Bani-Hani MG, Motterlini R. Use of carbon monoxide as a therapeutic agent: promises and challenges. *Intensive Care Med.* 2008;34:649–58. <https://doi.org/10.1007/s00134-008-1011-1>.
78. Romão CC, Blättler WA, Seixas JD, Bernardes GJL. Developing drug molecules for therapy with carbon monoxide. *Chem Soc Rev.* 2012;41:3571. <https://doi.org/10.1039/c2cs15317c>.
79. Lee Y, Kim J. Simultaneous electrochemical detection of nitric oxide and carbon monoxide generated from mouse kidney organ tissues. *Anal Chem.* 2007;79:7669–75. <https://doi.org/10.1021/ac070814z>.
80. Heylen S, Martens JA. Progress in the chromogenic detection of carbon monoxide. *Angew Chemie Int Ed.* 2010;49:7629–30. <https://doi.org/10.1002/anie.201002569>.
81. Moragues ME, Esteban J, Ros-Lis JV, Martínez-Mañez R, Marcos MD, Martínez M, et al. Sensitive and selective chromogenic sensing of carbon monoxide via reversible axial CO coordination in binuclear rhodium complexes. *J Am Chem Soc.* 2011;133:15762–72. <https://doi.org/10.1021/ja206251r>.
82. Li W, Li R, Chen R, Liang X, Song W, Lin W. Activatable photoacoustic probe for in situ imaging of endogenous carbon monoxide in the murine inflammation model. *Anal Chem.* 2021;93:8978–85. <https://doi.org/10.1021/acs.analchem.1c01568>.
83. Thunnissen M, Nordlund P, Haeggström J. Crystal structure of human leukotriene A(4) hydrolase, a bifunctional enzyme in inflammation. *Nat Struct Mol Biol.* 2001;8:131–5. <https://doi.org/10.1038/84117>.
84. Szul T, Castaldi P, Cho MH, Blalock JE, Gaggari A. Genetic regulation of expression of leukotriene A4 hydrolase. *ERJ Open Res.* 2016;2:00058–2015. <https://doi.org/10.1183/23120541.00058-2015>.
85. Wang H, Xue K, Duan Z, Yang Y, He Z, Wu C, et al. A photoacoustic and fluorescence dual-mode probe for LTA4H imaging reveals inflammation site in murine. *Sensors Actuators B Chem.* 2019;286:243–9. <https://doi.org/10.1016/j.snb.2019.01.154>.
86. Razansky D, Harlaar NJ, Hillebrands JL, Taruttis A, Herzog E, Zeebregts CJ, et al. Multi-spectral photoacoustic tomography of matrix metalloproteinase activity in vulnerable human carotid plaques. *Mol Imaging Biol.* 2012;14:277–85. <https://doi.org/10.1007/s11307-011-0502-6>.
87. Sheedy FJ, Grebe A, Rayner KJ, Kalantari P, Ramkhalawon B, Carpenter SB, et al. CD36 coordinates NLRP3 inflammasome activation by facilitating intracellular nucleation of soluble ligands into particulate ligands in sterile inflammation. *Nat Immunol.* 2013;14:812–20. <https://doi.org/10.1038/ni.2639>.
88. Xie Z, Yang Y, He Y, Shu C, Chen D, Zhang J, et al. In vivo assessment of inflammation in carotid atherosclerosis by noninvasive photoacoustic imaging. *Theranostics.* 2020;10:4694–704. <https://doi.org/10.7150/thno.41211>.
89. Chen Z, Bozec A, Ramming A, Schett G. Anti-inflammatory and immune-regulatory cytokines in rheumatoid arthritis. *Nat Rev Rheumatol.* 2019;15:9–17. <https://doi.org/10.1038/s41584-018-0109-2>.
90. Schinnerling K, Aguilón JC, Catalán D, Soto L. The role of interleukin-6 signalling and its therapeutic blockage in skewing the T cell balance in rheumatoid arthritis. *Clin Exp Immunol.* 2017;189:12–20. <https://doi.org/10.1111/cei.12966>.
91. Beziere N, von Schacky C, Kosanke Y, Kimm M, Nunes A, Licha K, et al. Optoacoustic imaging and staging of inflammation in a murine model of arthritis. *Arthritis Rheumatol.* 2014;66:2071–8. <https://doi.org/10.1002/art.38642>.
92. Suzuki M, Hashizume M, Yoshida H, Mihara M. Anti-inflammatory mechanism of tocilizumab, a humanized anti-IL-6R antibody: effect on the expression of chemokine and adhesion molecule. *Rheumatol Int.* 2010;30:309–15. <https://doi.org/10.1007/s00296-009-0953-0>.

93. Hashizume M, Tan S-L, Takano J, Ohsawa K, Hasada I, Hanasaki A, et al. Tocilizumab, a humanized Anti-IL-6R antibody, as an emerging therapeutic option for rheumatoid arthritis: molecular and cellular mechanistic insights. *Int Rev Immunol*. 2015;34:265–79. <https://doi.org/10.3109/08830185.2014.938325>.
94. Chen J, Qi J, Chen C, Chen J, Liu L, Gao R, et al. Tocilizumab–conjugated polymer nanoparticles for NIR-II photoacoustic-imaging-guided therapy of rheumatoid arthritis. *Adv Mater*. 2020;32:2003399. <https://doi.org/10.1002/adma.202003399>.
95. Oishi Y, Manabe I. Macrophages in inflammation, repair and regeneration. *Int Immunol*. 2018; <https://doi.org/10.1093/intimm/dxy054>.
96. Ariel A, Maridonneau-Parini I, Rovere-Querini P, Levine JS, Mühl H. Macrophages in inflammation and its resolution. *Front Immunol*. 2012;3. <https://doi.org/10.3389/fimmu.2012.00324>.
97. Lee C-H, Choi EY. Macrophages and inflammation. *J Rheum Dis*. 2018;25:11. <https://doi.org/10.4078/jrd.2018.25.1.11>.
98. Birch GP, Campbell T, Bradley M, Dhaliwal K. Optical molecular imaging of inflammatory cells in interventional medicine—an emerging strategy. *Front Oncol Front Media SA*. 2019;9: 882. <https://doi.org/10.3389/fonc.2019.00882>.
99. Yang R, Sarkar S, Yong VW, Dunn JF. In vivo MR imaging of tumor-associated macrophages: the next frontier in cancer imaging. *Magn Reson Insights*. 2018;11: 1178623X1877197. <https://doi.org/10.1177/1178623X18771974>.
100. Gawne PJ, Man F, Blower PJ, de Rosales TMR. Direct cell radiolabeling for in vivo cell tracking with PET and SPECT imaging. *Chem Rev*. 2022;122:10266–318. <https://doi.org/10.1021/acs.chemrev.1c00767>.
101. James S, Neuhaus K, Murphy M, Leahy M. Contrast agents for photoacoustic imaging: a review of stem cell tracking. *Stem Cell Res Ther BioMed Central*. 2021;12:511. <https://doi.org/10.1186/s13287-021-02576-3>.
102. Li Z, Li T, Zhang C, Ni J-S, Ji Y, Sun A, et al. A multispectral photoacoustic tracking strategy for wide-field and real-time monitoring of macrophages in inflammation. *Anal Chem*. 2021;93:8467–75. <https://doi.org/10.1021/acs.analchem.1c00690>.
103. Jokerst JV, Van de Sompel D, Bohndiek SE, Gambhir SS. Cellulose nanoparticles are a biodegradable photoacoustic contrast agent for use in living mice. *Photo-Dermatology*. 2014;2:119–27. <https://doi.org/10.1016/j.pacs.2014.07.001>.

Imaging Inflammation by Intravital Microscopy



Marco De Donatis, Frédéric Fercoq, and Leo M. Carlin

Abstract The ability to visualise the biological processes involved in initiation and maintenance of inflammation is critical to our understanding of their context in pathophysiology. Intravital microscopy allows us to directly investigate leukocyte dynamics *in vivo*. Dynamic processes and effector functions can now synergistically be observed in live animal models and through indirect mechanistic experiments for a more complete picture. Thanks to intravital imaging, we now hold a detailed understanding of the leukocyte adhesion cascade, as well as mediators of effector cell migration and interactions with external pathogens. The combination of intravital microscopy and appropriate reporter models also allows the study of processes, such as sterile inflammation and aberrant modes of leukocyte trafficking, maintaining important tissue- and cell-specific detail. Importantly, intravital imaging also has the power to reveal behaviour, forcing us to refine long-held paradigms. From intravascular leukocyte functions to reverse transmigration and behaviour in non-blood fluids, intravital microscopy keeps pushing the boundaries of our understanding of inflammation. In this chapter, we give examples illustrating the role of intravital microscopy in describing canonical immunological processes, challenging established ideas and gathering insights into new paradigms by direct observation. We also discuss some of the technical challenges encountered during intravital imaging and how they are being overcome.

Keywords Intravital imaging · Light microscopy · Inflammation · Cell dynamics · *In vivo* · Leukocytes · Innate immunity

M. De Donatis · L. M. Carlin (✉)

Cancer Research UK Beatson Institute, Glasgow, UK

School of Cancer Sciences, University of Glasgow, Glasgow, UK

e-mail: leo.carlin@glasgow.ac.uk

F. Fercoq

Cancer Research UK Beatson Institute, Glasgow, UK

1 Introduction

A combined approach of direct imaging in live organisms together with more reductionist studies of *in vitro* or fixed tissue specimens has taken us a long way towards defining the molecular mechanisms that regulate inflammation. Some of the earliest observations of the innate immune response in action were made by intravital microscopy (IVM) of phagocytes [1]. In the intervening 125 or so years, we have been able to define the molecular details of certain paradigms for how inflammation responds to infection or physical injury (e.g. the leukocyte adhesion cascade), but excitingly, IVM often presents us with data that do not fit pre-existing ‘rules’ forcing us to refine our models to account for these behaviours.

We now know of circumstances where leukocytes crawl long distances on the luminal side of the endothelium with functional consequences that do not require extravasation [2–5], such as intravascular immunity and the orchestration of inflammation. Moreover, neutrophils have been shown to reverse transmigrate back into vessels as both a physiological [6] and pathological [7] response, or even lay trails of chemotactic ‘breadcrumbs’ for other cells [8]. The role of the aging endothelium itself in regulating (or dysregulating) these responses is also coming into sharper focus [9], due to the power of IVM when coupled with single-cell analysis. All these strikingly different behaviours, sometimes seemingly counterproductive to the host, are no doubt the product of the complex coevolution of our defences with microbes.

IVM allows us the opportunity to directly see the inflammatory response, spanning from microbial or sterile injury to cancer, in the context of a complete immune response. However, IVM is by no means a perfect methodology. Often only one or a handful of cell types can be observed, and the surgery required can severely limit not only the volume of tissue imaged but also the time over which measurements can be made. Sometimes, surgical preparations required for IVM may even account for some of the responses observed, requiring carefully designed experiments and interpretation. Therefore, it is important to put the information gained by IVM in the context of other techniques (as recently reviewed by Hor and Germain [10]) and to continue to make progress in tackling some of these technical challenges. However, many of the major technical limitations affecting early IVM studies have been overcome (Table 1). We are now able to image across a vast array of tissues and contexts and more is available in terms of both what we can image and how we can make sense of images (Fig. 1). In the following sections, we have therefore exemplified some of these recent advances in methods and understanding, with a focus on myeloid cell recruitment and lymphoid cell effector functions.

Table 1 Challenges in IVM and potential solutions

Major challenge	Solution(s)
Multiple cellular markers of interest	Fluorescence microscopy and fluorescent dyes, proteins and intrinsic fluorescence allow spectral/photophysical (e.g. fluorescence lifetime) multiplexing
Out-of-focus tissue fluorescence	Confocal techniques and multiphoton microscopy that reject out-of-focus light mechanically, deconvolve, or selectively excite just at the focus
Fast-moving behaviours	Sensitive optics and detectors, spinning-disk, resonance scanners, multi-line scanning approaches (cloud-scanner, Airyscan Fast) that allow high-speed acquisition (tens of frames per second). However, where the cells imaged are deep or reporters not bright, there might not be enough light available to image at more than one to two frames per second, limiting temporal resolution
Tissue movement (peristalsis, respiration, heartbeat)	Physical tissue immobilisation (pinning, gluing, clamping of permanent windows and holders, vacuum coverslip holders), gated acquisition, software image stabilisation
Turbid tissue-induced aberrations (in target tissue)	Adaptive optics
Highly scattering tissue obscures target tissue/process (e.g. adipose tissue in mammary glands)	Surgical preparation of target tissue
Processes occur over days or weeks	Repeat imaging of permanently installed imaging windows with fiducial markers

2 Leukocyte Migration to the Site of Inflammation: Imaging Trafficking in Intravascular (and Non-vascular) Spaces

In response to tissue inflammation, circulating leukocytes are recruited through a series of sequential and overlapping steps termed the leukocyte adhesion cascade. In this context, endothelial cells sense inflammatory cues coming from the inflamed tissue (such as histamine, platelet-activating factor, IL1- β and TNF) and become activated [11]. Endothelial cell activation drives important rearrangements of adhesion molecules on the luminal side of the blood vessel, particularly selectins and intercellular adhesion molecules (ICAMs). This event allows leukocytes to establish weak and transient tethering to the endothelial cells (slow rolling) followed by strong shear-resistant adhesions (firm adhesion) and translocation on the apical side of the endothelium (crawling) and finally exit through the endothelial barrier (transmigration). IVM is an essential tool for quantitative visualisation of the cellular and

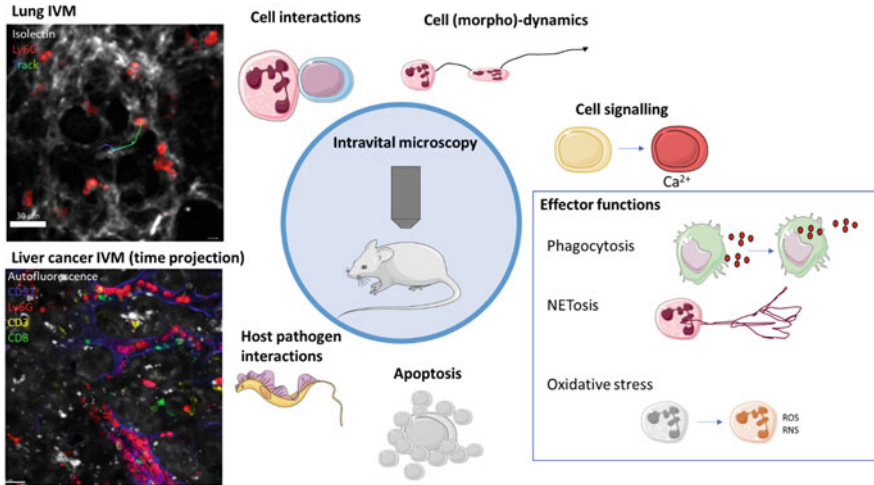


Fig. 1 Examples of application of intravital microscopy (IVM). IVM can be used to monitor not only localisation and behaviour but also function and mechanism. Top left panel: lung IVM image showing isolectin (white), neutrophils (Ly6G⁺ cells, red) and the movement of an individual neutrophil (green line) through the tissue. Bottom left panel: IVM image of liver cancer, showing neutrophils (Ly6G⁺ cells, red), endothelial cells (CD31⁺ cells, blue) and infiltrating lymphocytes (CD3⁺ cells, yellow; CD8⁺ cells, green). Original IVM images from the authors. Schematics: Servier Medical Art, licensed under a Creative Commons Attribution 3.0 Unported Licence

molecular mechanisms governing the leukocyte adhesion cascade during inflammation.

2.1 *Imaging Classical Leukocyte Rolling and Firm Adhesion*

In systemic postcapillary venules, leukocyte rolling is largely dependent on the weak and transient binding of P-, E- and L-selectins to their ligands. One of the first *in vivo* observations of the role of P-selectin in leukocyte rolling was provided by transmitted-light IVM of mesenteric venules in P-selectin-deficient mice [12]. The authors observed severe impairment of leukocyte rolling in deficient mice compared to wild-type (WT) controls and delayed neutrophil recruitment upon experimentally induced inflammation. A second study using IVM of the cremaster muscle of P-selectin-deficient mice reported similar results [13]. Furthermore, IVM studies defined the different kinetics that characterise P- and E-selectin-mediated rolling. Using TNF α -stimulated cremaster muscle of E- or P-selectin-deficient mice, P-selectin-mediated rolling was determined to be faster (17.1 $\mu\text{m/s}$) than E-selectin rolling (3.5 $\mu\text{m/s}$) [14].

The transition from rolling to firm adhesion is orchestrated by selectins and chemokine G-protein-coupled receptor (GPCR) signalling, which ultimately results

in integrin activation on leukocytes. Cooperation of E-selectin and chemokines in leukocyte rolling was shown by IVM of TNF α -stimulated cremaster muscle of E-selectin-deficient mice treated with pertussis toxin which blocks G α_i signalling downstream of GPCRs [15]. Extending this line of investigation, a combination of autoperfused flow chambers and IVM of thioglycolate-induced peritonitis was used to demonstrate that PSGL-1 and chemokine-GPCR signalling were both required for integrin activation [16]. Two integrins are primarily responsible for the firm adhesion phase, Mac-1 (α M β 2, CD11b/CD18) and LFA-1 (α L β 2, CD11a/CD18). Both integrins bind to ICAM-1 and ICAM-2, although evidence available today shows variability of contribution depending on mouse model, challenge type and leukocyte subset. Integrins exist in two main conformational states: a bent, inactive conformation characterised by low ligand affinity and an extended, active conformation characterised by high ligand affinity [17]. Conformational switching between the two states is driven by chemokine-GPCR signalling. IVM studies looking at MIP-2 (CCL3)-stimulated postcapillary venules dissected the role of Mac-1 and LFA-1 in neutrophil adhesion and transmigration [18]. LFA-1 (but not Mac-1)-deficient mice had a marked decrease in neutrophil adhesion compared to WT controls, whilst Mac-1-deficient neutrophils, although capable of adhesion, failed to transmigrate. Interestingly, the few LFA-1-deficient neutrophils that did adhere were able to transmigrate, indicating that Mac-1 can mediate transmigration in response to MIP-2. Furthermore, blocking of ICAM-1 (but not ICAM-2 or PECAM-1) inhibited neutrophil transmigration but not adherence [18].

It is now clear that the mechanisms governing leukocyte recruitment, motility and transmigration are cell- and tissue-specific. For instance, neutrophil (but not T cell) recruitment to the lungs seems to be independent of ICAM-1 and ICAM-2 in systemically lipopolysaccharide (LPS)-stimulated mice [19] and more reliant on physical entrapment mediated by cytoskeletal rearrangement [20, 21]. However, CD11b has been shown to be important for neutrophil crawling in lung capillaries [22]. Sphingosine-1-phosphate (S1P) inhibition in T cells impaired integrin-mediated adhesion in high endothelial venules (HEVs) for entry into peripheral lymphoid organs but not in Peyer's patches, indicating tissue specificity in integrin action [23]. In addition, recent IVM showed that tumour-associated HEVs (TA-HEVs) can be a major E- and P-selectin-dependent route for lymphocyte rolling and arrest in solid tumours [24].

2.2 Imaging Novel Leukocyte Trafficking Events

The leukocyte adhesion cascade is often viewed as a unidirectional process resulting in recruitment of circulating immune cells into the tissue. However, inflammatory stimuli provided by application of cytokines or ischemia/reperfusion have been noted by high-resolution IVM to result in disrupted neutrophil extravasation, termed reverse transmigration (rTEM), implicated in the dissemination of systemic inflammation [25]. Interestingly, other forms of neutrophil rTEM have been postulated to

provide a beneficial role in the resolution of inflammation following hepatic sterile injury, where neutrophils entered the lesions contributing to debris uptake and tissue healing before migrating back to the circulation [6] in a process perhaps analogous to the reverse migration observed in zebrafish neutrophils [26, 27].

To better address the potentially pathological, ‘disrupted-type’ rTEM, where cells do not move far enough away from the vessels for the type of photoactivation used to label cells in other contexts [6, 28], other labelling strategies are necessary. LysM-EGFP mice (bearing GFP⁺ neutrophils) were intravenously injected with a biotinylated anti-Ly6G (a major neutrophil marker) monoclonal antibody, followed by tissue infusion of far-red fluorescent (AF647)-streptavidin. This method successfully differentiated neutrophils that partially or completely migrated through the endothelial walls and thus could be labelled with the streptavidin-fluorophore (GFP⁺, AF647⁺) from neutrophils that remained on the luminal side (GFP⁺, AF647⁻) allowing their tracking [7]. Subsequent work from the same group showed that neutrophil rTEM increases in aged mice compared to young controls driven by mast cell-derived CXCL1 [9]. Using the biotinylated anti-Ly6G approach, the authors could directly show pathological ‘rTEM-experienced’ neutrophils accumulate in the lungs where they were implicated in exacerbation of vascular leakage and lung damage [9].

As noted above, leukocyte transmigration through the endothelial wall can represent the final step of the leukocyte adhesion cascade. IVM studies have been instrumental in revealing some of the molecular details of this process, e.g. the involvement of PECAM1 (or CD31) and CD99 on the endothelium. Interestingly, the role of PECAM1 and CD99 seems to be mouse strain-dependent. Cremaster IVM of IL-1 β -injected mice indicated that in FVB/N mice, treatment with anti-PECAM1 (but not anti-CD99) blocking antibody resulted in leukocyte arrest at the luminal side of blood vessels, indicating that PECAM1 acts upstream to CD99. Conversely, in C57BL/6 mice, both anti-PECAM1 and anti-CD99 blocking resulted in leukocyte arrest at the site between endothelial cells and basement membrane [29]. In addition to corroborating the role of PECAM1 and CD99 in the leukocyte migration process, this highlights the power of IVM for uncovering nuances in different mouse backgrounds important to our interpretation of other data generated in them. Endothelial cell autophagy in acutely inflamed postcapillary venules has also been identified as a regulator of neutrophil transmigration in IVM experiments [30]. Here, an inducible endothelium-restricted *Cdh5*-CreER^{T2};ATG5^{fl/fl} mouse model with a fluorescent reporter for recombination was used to directly compare in vivo neutrophil migration in WT and autophagy-deficient endothelial cells in the same venular segment. This approach showed that deficient autophagy causes PECAM1 accumulation at endothelial cell junctions, and this correlates with higher neutrophil extravasation. Thus, endothelial cell autophagy may have further ability to regulate inflammation or its resolution by controlling leukocyte extravasation [30].

Leukocyte adhesion and slow migration on the endothelium can also occur in the absence of inflammation particularly in specialised vasculatures like the liver sinusoids [5] and the glomeruli [3]. Ly6C^{low}, CCR2⁻, CX3CR1⁺ monocytes have been

demonstrated by IVM to transiently adhere to and migrate in blood vessels in the dermis, mesentery and peritubular capillaries in a steady state [2, 4]. Upon local TLR7 stimulation, this monocyte subset was shown to accumulate in the peritubular capillaries of the kidney and recruit neutrophils which mediated focal necrosis of endothelial cells with the monocytes clearing cellular debris [4]. This revealed that these cells, termed patrolling monocytes, whilst still in the lumen of blood vessels, can provide an important cell orchestration role more commonly associated with macrophages. Neutrophils and monocytes are also retained in non-inflamed glomerular blood vessels for seconds to minutes. Upon immune complex-driven inflammation in the glomerulus, neutrophils were shown to be retained longer and produce Nox2-dependent oxidants detected by appropriate probes [3] exemplifying the power of IVM to reveal both dynamic localisation and function simultaneously. Further work again implicated patrolling monocytes in the behaviour of glomerular neutrophils [31], adding to several reports implicating monocytes in general in regulating neutrophil behaviour, notably for this chapter including those employing IVM of the paw (arthritis) [32] and lung (ARDS) [33]. A further example of cooperation in intravascular immunity that could only be exposed by IVM is that during TNF α -induced inflammation, neutrophils migrate on the endothelium, whilst their extended ‘antenna-like’ uropod interacts with activated platelets in the blood via PSGL-1. In some contexts, both endothelial and platelet signals are necessary for neutrophils to transmigrate into the tissue and generate an inflammatory response [34].

Differently from leukocytes in the blood, peritoneal cavity macrophages appear to rely on shear flow and scavenger receptors rather than integrin pathways for recruitment to the inflamed site. The first direct visualisation of the cavity macrophage behaviour was obtained using spinning-disk confocal microscopy in a sterile thermal injury model of the liver. Topical application of anti-F4/80 antibody at the injury site revealed an F4/80^{hi} population accumulating 1 h post-injury, which were further phenotyped for the expression of GATA6 [35]. Interestingly, the study found that transmigration of GATA6⁺ macrophages is largely independent of chemokine and integrin signalling, and mediated by necrosis-derived ATP and CD44-hyaluronan binding [35]. Multiphoton imaging of mouse peritoneal cavities has also been performed directly through the intact peritoneal membrane to minimise potential surgically generated artefacts. Here, laser-induced peritoneal sterile injury caused free-floating GATA6⁺ macrophages to adhere to the injury within 1–15 min, followed by tethering of additional macrophages without any obvious chemotactic behaviour [36]. Administration of the scavenger receptor inhibitor polyinosinic acid resulted in decreased macrophage aggregation and prolonged tissue healing, indicating that peritoneal macrophages respond in a scavenger receptor-dependent manner leading to the formation of scar tissue and subsequent repair of the lesion [36]. IVM of the peritoneal cavity challenged with *Escherichia coli* revealed that here macrophages produce factor V and other clotting factors to initiate coagulation [37]. Formation of the clots trapped bacteria, whilst recruitment and adherence of additional cavity macrophages led to their clearance [37]. Finally, the peritoneal cavity is another site where macrophages influence neutrophil behaviour, as shown

by IVM of microlesions in the peritoneal serosa [38]. Here, nonmigratory resident macrophages covered and sequestered laser-induced necrotic debris before neutrophil recruitment, preventing swarming and subsequent inflammation. This mechanism, termed ‘cloaking’, is speculated to protect the tissue from neutrophil damage in steady-state condition [38].

3 Visualising the Inflammatory Response in Sterile Injury, Infection and Cancer

3.1 *Imaging Sterile Injury*

Sterile injury occurs when stimuli including trauma, auto/alloimmunity or organ necrosis cause release of danger-associated molecular patterns (DAMPs) to induce inflammatory responses in the absence of pathogens. This has been studied by IVM using models of confined injury in the dermis, revealing a stepwise regulated process consisting of detection by the scanning behaviour of neutrophils followed by their accumulation and clustering in large numbers [39]. Laser damage of the intact ear dermis demonstrated that this neutrophil swarming behaviour is LTB₄-dependent [40]. IVM in zebrafish and mice has been used to show that these swarms represent highly neutrophil self-coordinated and self-limiting behaviour proposed to then limit bacterial infiltration [41, 42]. In a model of hepatic focal laser injury, neutrophils also follow a cascade of events that is initially regulated by chemokines and integrins then switching to formyl peptides to allow entry deep into necrotic tissue [43]. IVM has also revealed cooperation between platelets and neutrophils early in this process where platelets adhered and covered the liver sinusoids for several hours providing a docking site for neutrophils [44]. Further dissection of the role of platelets in sterile injury comes from IVM of a model of transfusion-related acute lung injury (TRALI), where platelets covered the lung endothelium and LysM⁺ leukocytes after anti-MHC class I antibody injection, followed by retention of neutrophils [45]. Platelet-dependent neutrophil recruitment has also been observed in the high endothelial venules of the omentum in a thioglycolate-induced peritonitis model [46]. Here, a metabolite secreted by platelets and mast cells was shown to bind the GPCR GPR35 expressed on neutrophils, promoting transendothelial migration [46].

3.2 *Imaging Infection*

The immune system coevolved with microorganisms such as bacteria, viruses and parasites. IVM can be used to visualise microbial entrance and interaction with and clearance by leukocytes.

3.2.1 Bacterial Infections and Bacterial PAMPs

As mentioned above, IVM has been employed to investigate invariant natural killer T (iNKT) cells in the liver using CXCR6^{GFP+} transgenic mice, revealing a role in intravascular immune surveillance [5]. Spinning-disk IVM of *Streptococcus pneumoniae*-infected mice further showed that iNKT cell recruitment from the intravascular space to the interstitial space is regulated by neutrophil-derived CCL17 [47]. The lung is another site characterised by peculiar immunology, as the constant inhalation of non-sterile air requires a fine balance between pro- and anti-inflammatory signals. Thoracic suction windows allow lung imaging whilst preserving gas exchange and blood flow and limiting tissue motion [48, 49]. The usefulness of earlier thoracic windows used in rabbits and rats was substantially increased by miniaturising and refining them for use in mice with the highly characterised immune system and large reagent portfolio that they represent [48]. This is demonstrated by clear visualisation of increased neutrophil influx after intratracheal challenge with MIP-2 and LPS [48]. In addition to fluorescent reporter mice and antibodies, dyes have excellent utility when they can be introduced selectively. PKH26 dye aggregates that are directly phagocytosed by alveolar macrophages (AMs) upon administration to the lungs can be used to visualise AMs, tracking their behaviour upon bacterial infection [50]. Our own group has used mouse thoracic suction windows to observe interactions between NK cells, which are almost entirely intravascular in the lung, and neutrophils, in real time. Although these two cell types behave very differently in the alveolar capillaries, with NK cells generally much slower-moving or stationary, NK-neutrophil interactions that last from a few seconds up to several minutes could be readily observed. Extensive cell tracking analysis revealed that neutrophils that interact with NK cells move more slowly, and these kinetic differences could not be accounted for by the interaction time alone, suggesting different behaviour of these cells. Furthermore, LPS application in NK-cell-depleted mice led to more neutrophil accumulation in the lungs compared to the control, suggesting that in addition to their canonical roles, NK cells may regulate neutrophilic responses to bacterial PAMPs [51]. The spleen, a key immune organ, is also accessible by IVM [52]. In a study investigating *S. pneumoniae* distribution in the spleen, spinning-disk IVM was used to dissect the role of immature Ly6G-intermediate and mature Ly6G-high neutrophils [53]. Here, the Ly6G-high population was observed to be mobile and to take up *S. pneumoniae* bound to resident macrophages in the red pulp via the complement system. Conversely, splenic immature Ly6G-low neutrophils were static and transitioned towards a mature phenotype within 24 h after the infection [53]. The role of blood- and tissue-resident neutrophils in pathogen response was further investigated using IVM in the lung and spleen in models of systemic *E. coli* challenge [54]. In the lung, *E. coli* particles were captured from the circulation by endothelial cells and subsequently taken up by margined neutrophils, which then slowed down and formed *E. coli*-positive aggregates [54]. Similarly to the aforementioned *S. pneumoniae* model, neutrophil abundance did not increase in the

spleen, but instead neutrophils redistributed to the marginal zone, where they acted as the main cell type responsible for *E. coli* uptake and clearance.

Neutrophil extracellular traps (NETs) are composed of chromatin decorated with MPO, neutrophil elastase (NE), histones and other cytotoxic proteins. They have an important role in trapping and killing microbes, but they are also implicated in the onset of some pathologies. Although they have been extensively characterised in vitro, visualising NETs in tissues in vivo is more challenging. IVM of systemic *Staphylococcus aureus* infection showed that most bacteria are rapidly sequestered in the liver, inducing a strong neutrophil accumulation. The neutrophils then released NETs (characterised using markers for extracellular DNA, neutrophil elastase and histone H2) leading to liver injury mediated by neutrophil elastase activity. Interestingly, if treatment with DNases was able to efficiently remove DNA in vivo, it was not able to remove histones attached to vessel walls and did not fully prevent liver damage [55]. Similarly, IVM of a methicillin-resistant *Staphylococcus aureus* (MRSA) infection model showed that NETs are responsible for bacterial clearance in the lungs as well as alveolar-capillary damage [56]. Another study showed that in different mouse models of sepsis, NETs colocalised with activated intravascular thrombin and platelet aggregates, which promoted intravascular coagulation [57]. DNase infusion reduced coagulation, improved vascular perfusion and reduced organ damage. However, it is important to note that DNase has activity beyond its interaction with NETs, as recent platelet intravital work suggests that DNase I can also increase hydrolysis of ATP and ADP, which also act as mediators of inflammatory responses [58].

3.2.2 Viral Infection

Viruses are incapable of autonomous reproduction; therefore, they are forced to employ the cellular machinery of the host cell. The resulting response against infected cells has been extensively studied using IVM. However, when dealing with live animals infected with pathogenic viruses, caution is required to avoid spread of the infection to the operator. A good example protocol using high-efficiency particulate air (HEPA) filters, pressure masks and a Tyvek suit for operator protection has recently been published [59], but this work is possible in relatively few centres with the required expertise in both virus work and imaging. A great example of the impact of IVM in the study of viral infection is the recent observation of neutrophil-derived trails in the influenza-infected mouse trachea as mentioned in the opening paragraph of this chapter [8]. Upon viral infection, neutrophils rapidly but transiently infiltrate the trachea leaving behind CXCL12⁺ trails visible by multiphoton IVM. These trails persisted during infection and were shown to be essential to subsequent CD8 T migration in the infected tissue [8]. Underlining that specialised vasculatures like the lung and the liver have specialised immunobiology, adoptively transferred HBV antigen-specific CD8 T cells were shown to continuously crawl inside the liver sinusoids of mice infected with GFP-tagged hepatitis B virus until they get in close proximity to

antigen-expressing hepatocytes, where they can perform effector functions without needing to extravasate from the sinusoids [60].

3.2.3 Parasite Infection

Parasites have complex life cycles that can include multiple hosts/vectors, making them difficult to study *in vitro*. IVM and the use of fluorescent parasites can help understanding the different steps of infections and interactions with these hosts (reviewed by De Niz et al. [61]). In particular, the first steps of tissue invasion are hard to address in fixed tissues. *Leishmania major* is an intracellular parasite of macrophages transmitted by the sandfly. Multiphoton IVM of the ear using LysM-GFP reporter mice and RFP-expressing parasites showed early neutrophil infiltration at the injection site. Invading neutrophils were able to phagocytose *Leishmania* parasites, but these remained viable. Furthermore, viable parasites were released from apoptotic neutrophils close to macrophages (the definitive host cell), and therefore contributed to the progression of the disease, supporting the hypothesis of a ‘Trojan Horse’ role for neutrophils in *L. major* infection [62]. Multicellular parasites can also be imaged in their host using IVM. Filarial worms are transmitted into the skin by blood-feeding arthropods and migrate into their host before moulting and reproducing, but how they migrate from the skin to their final location is not well understood. Soon after their arrival in the dermis, infective larvae from *Litomosoides sigmodontis* enter pre-collecting lymphatics by mechanical disruption of their wall, causing lymphatic pathology [63, 64]. The larvae then follow lymphatic collectors unidirectionally towards the lymph node. Confirmation by IVM is still needed, but it is then thought that larvae join the blood circulation via the thoracic duct, enter the lungs and settle in the pleural cavity (their final destination) [65].

3.3 *Imaging the Tumour Microenvironment: Inflammation in Cancer*

IVM is also a crucial tool to understand immune cell dynamics in the tumour microenvironment (reviewed by Boulch et al. [66]). Our understanding of the intratumoural behaviour of neutrophils as well as their role in the metastatic cascade benefited greatly from IVM. Using fluorescent reporter mice, neutrophil infiltration was monitored in small intradermal tumour lesions for 6 days [67]. Interestingly, intratumoural neutrophils showed reduced motility compared to stromal ones. In addition, the blockade of CXCR2, a major chemotactic receptor for neutrophils, only transiently reduced intratumoural recruitment whilst it effectively inhibited the accumulation of neutrophils in stromal regions [67]. IVM experiments in the liver and in tumours located in the ear dermis showed that neutrophil extracellular traps, visualised by neutrophil elastase activity, can physically impair contact between

cytotoxic effector lymphocytes and tumour cells [68]. In addition to this ‘shielding’ effect of NETs, IVM imaging demonstrated a role for neutrophils and NETs in the metastatic cascade. Different studies using IVM have investigated neutrophil-dependent cancer cell adhesion to liver endothelium. After intra-arterial injection of H-59 cancer cells, cancer cells have been observed to adhere directly to arrested neutrophils [69, 70]. NETs had a similar effect by increasing circulating cancer cell adhesion to liver sinusoids implicated in increasing metastasis in models of lung and colon cancers [71]. More neutrophils and NETs appear in the lungs of mice intravenously injected with metastatic 4T1 breast cancer cells than those with non-metastatic 4T07 cells [72]. Excitingly, permanently implantable thoracic windows enable us to observe the same lung tissue over a period of weeks and therefore multiple stages of metastatic cascade even in spontaneously metastatic models [73, 74].

If IVM is an important tool to understand the biology of tumour and immune cells, it is also very useful to address the efficacy of therapeutic strategies. IVM has shown neutrophils can transport drug nanoparticles to tumours [75, 76], and it has also been used to visualise the effects of adoptive cellular therapy (ACT) *in situ* and analyse the morphodynamics of adoptively infused cells in tumours [77]. ACT aims to provide an abundant population of tumour-reactive T cells to increase antitumour immune responses by injection of *ex vivo* manipulated and expanded T cells. IVM has been used to monitor the infiltration of modified T cells over time and showed that the GTPase-activating protein RGS1 impairs T-cell infiltration into breast tumours [78]. Direct functional readouts are also possible by IVM: T-cell cytotoxicity by using fluorescent T cells and monitoring apoptosis with a Förster resonance energy transfer-based (FRET-based) reporter of caspase 3 activity has been demonstrated [79, 80]. In solid tumours, transfer of *in vitro*-activated OT-I T cells induced tumour regression through the direct action of the T cells on tumour cells, with minimal bystander effects [79]. However, the killing of tumour cells was very slow (6 h on average). Chimeric antigen receptor (CAR) T cells were used to treat the lung and bone marrow in a mouse model of B-cell lymphoma [80]. CAR T cells interacted with circulating tumour cells in the lungs where they formed large aggregates. This ‘trapping’ of CAR T cells in the lung altered their trafficking to the bone marrow (the tumour site). In the bone marrow, tumour apoptosis (monitored using the same FRET reporter as above) was much faster than that mentioned above as CAR T cells engaged, killed and detached from their targets within 25 min. Using the Twitch2B genetically encoded calcium reporter revealed functional heterogeneity within the cell population, as the interaction with tumour cells did not induce calcium signalling in some CAR T cells.

4 Conclusion and Future Perspectives

In the above sections, we have concentrated on examples of the new understanding of the regulation of inflammation in a plethora of pathogenic circumstances revealed by IVM and described some of the technical aspects of these studies where relevant or interesting. In each case, a compromise between the imaging method and the biological question must be achieved, and not all methods are equally applicable (Table 2). However, some of the most exciting recent advances in IVM are not only coming from the imaging technology itself (as reviewed by Giampetraglia and Weigel [81]), but from the way it is used. The computational power required for manipulation and analysis of huge datasets had until recently been hard to access for many researchers engaged in IVM, but recent advances in computing hardware and analytical tools including deep learning allow segmentation [82] and analysis and clustering of cellular spatial relations [83] in a way not unfamiliar to that exploited in -omics approaches. An exciting extension of this is to use those approaches to directly compare how cells move in different conditions, as elegantly recently demonstrated in the description of behavioural landscapes of inflammation [84].

On a more direct level, 3D printing and flexible materials are revolutionising how we perform the surgery necessary for IVM by allowing rapid prototyping of microscope mounts and preparation holders [49, 85, 86], some of which have enhanced

Table 2 Advantages and limitations of major IVM imaging approaches

Microscope technique	Advantage	Limitation
Wide field	Cheap/accessible	Depth, phototoxicity (can be mitigated by increasing sensitivity of detectors); resolution, particularly in z dimension
Laser-scanning confocal	Resolution, particularly in z dimension, very sensitive point detectors (e.g. GaAsP), spectral point detectors for multiplexing	Depth, phototoxicity (can be mitigated by increasing sensitivity of detectors)
Spinning-disk confocal	Fast, sensitive cameras can be used to limit phototoxicity	Depth, number of channels
Two-photon	Depth due to less scattering of long wavelengths, intrinsically confocal, pulsing makes time-domain fluorescence lifetime imaging upgrade accessible	Expensive, cannot increase sensitivity by sacrificing z resolution for light (by opening confocal pinhole, multiplexing can require multi-(line) lasers or optical parametric oscillator
Three-photon in short-wave infrared range	Even greater depth, can be combined with coherent anti-Stokes Raman spectroscopy for label-free imaging	Phototoxicity, cost of lasers
Light sheet	Very high speed across large volumes with isotropic resolution	Optical design often limits overall size of organisms (e.g. zebrafish and embryos fit between objectives but mice do not) or resolution

biocompatibility for longitudinal imaging [87, 88]. This may enable even better imaging of organs such as the lung that have been notoriously tricky to image in situ longitudinally, but are now being probed more fully [73, 74]. It must also be acknowledged that although they are often the best alternative due to their well-characterised immune systems and the availability of transgenic animals and reagents, imaging in mice has important limitations. Therefore, some of our ambitions must lie towards seeing these processes in other animal models that allow us to observe or recapitulate what is not visible in mice [89] and ultimately in humans [90, 91] with the incorporation of IVM into clinical trials (<https://clinicaltrials.gov/ct2/show/NCT03823144>).

It is clear that IVM continues to develop at an incredible pace and still has a lot to reveal about the processes mediating inflammation and how we can manipulate them.

Acknowledgements MDD, FF and LMC are grateful for the help from Judith Secklehner and John Mackey along with the light microscopy (FILM and BAIR) and animal units (CBS and BSU) at Imperial College London and the CRUK Beatson Institute with the imaging examples used in Fig. 1.

Compliance with Ethical Standards Funding: MDD, FF and LMC have received funding from Cancer Research UK (CRUK C596/A17196, A31287 and A23983) and Breast Cancer Now (2019DecPR1424).

Conflict of Interest: The authors have no conflicts of interest to declare.

Ethical approval: All experiments involving mice were performed in accordance with the UK Animal (Scientific Procedures) Act 1986, approved by the local animal welfare (AWERB) committees and conducted under UK Home Office licences.

References

1. Metchnikoff E. Lectures on the comparative pathology of inflammation delivered at the Pasteur Institute in 1891. Trench; 1893.
2. Auffray C, Fogg D, Garfa M, Elain G, Join-Lambert O, Kayal S, et al. Monitoring of blood vessels and tissues by a population of monocytes with patrolling behavior. *Science* (80-). 2007;317:666–70. <https://doi.org/10.1126/science.1142883>.
3. Devi S, Li A, Westhorpe CLV, Lo CY, Abeynaik LD, Snelgrove SL, et al. Multiphoton imaging reveals a new leukocyte recruitment paradigm in the glomerulus. *Nat Med*. 2013;19: 107–12. <https://doi.org/10.1038/nm.3024>.
4. Carlin LM, Stamatziades EG, Auffray C, Hanna RN, Glover L, Vizcay-Barrena G, et al. Nr4a1-dependent Ly6Clow monocytes monitor endothelial cells and orchestrate their disposal. *Cell*. 2013;153:362–75. <https://doi.org/10.1016/j.cell.2013.03.010>.
5. Geissmann F, Cameron TO, Sidobre S, Manlongat N, Kronenberg M, Briskin MJ, et al. Intravascular immune surveillance by CXCR6+ NKT cells patrolling liver sinusoids. Jenkins M, editor. *PLoS Biol*. 2005;3:e113. <https://doi.org/10.1371/journal.pbio.0030113>.
6. Wang J, Hossain M, Thanabalasuriar A, Gunzer M, Meininger C, Kubers P. Visualizing the function and fate of neutrophils in sterile injury and repair. *Science* (80-). 2017;358:111–6. <https://doi.org/10.1126/science.aam9690>.
7. Owen-Woods C, Joulia R, Barkaway A, Rolas L, Ma B, Nottebaum AF, et al. Local microvascular leakage promotes trafficking of activated neutrophils to remote organs. *J Clin Invest*. 2020;130:2301–18. <https://doi.org/10.1172/JCI133661>.

8. Lim K, Hyun Y-M, Lambert-Emo K, Capece T, Bae S, Miller R, et al. Neutrophil trails guide influenza-specific CD8 + T cells in the airways. *Science* (80-). 2015;349:aaa4352. <https://doi.org/10.1126/science.aaa4352>.
9. Barkaway A, Rolas L, Joulia R, Bodkin J, Lenn T, Owen-Woods C, et al. Age-related changes in the local milieu of inflamed tissues cause aberrant neutrophil trafficking and subsequent remote organ damage. *Immunity*. 2021;54:1494–510.e7. <https://doi.org/10.1016/j.immuni.2021.04.025>.
10. Hor JL, Germain RN. Intravital and high-content multiplex imaging of the immune system. *Trends Cell Biol*. 2021; <https://doi.org/10.1016/j.tcb.2021.11.007>.
11. Nourshargh S, Alon R. Leukocyte migration into inflamed tissues. *Immunity*. 2014;41:694–707. <https://doi.org/10.1016/j.immuni.2014.10.008>.
12. Mayadas TN, Johnson RC, Rayburn H, Hynes RO, Wagner DD. Leukocyte rolling and extravasation are severely compromised in P selectin-deficient mice. *Cell*. 1993;74:541–54. [https://doi.org/10.1016/0092-8674\(93\)80055-J](https://doi.org/10.1016/0092-8674(93)80055-J).
13. Ley K, Bullard DC, Arbonés ML, Bosse R, Vestweber D, Tedder TF, et al. Sequential contribution of L- and P-selectin to leukocyte rolling in vivo. *J Exp Med*. 1995;181:669–75. <https://doi.org/10.1084/jem.181.2.669>.
14. Kunkel EJ, Ley K. Distinct phenotype of E-selectin-deficient mice. *Circ Res*. 1996;79:1196–204. <https://doi.org/10.1161/01.RES.79.6.1196>.
15. Smith ML, Olson TS, Klaus L. CXCR2- and E-selectin-induced neutrophil arrest during inflammation in vivo. *J Exp Med*. 2004;200:935–9. <https://doi.org/10.1084/jem.20040424>.
16. Zarbock A, Lowell CA, Ley K. Spleen tyrosine kinase Syk is necessary for E-selectin-induced α L β 2 integrin-mediated rolling on intercellular adhesion molecule-1. *Immunity*. 2007;26:773–83. <https://doi.org/10.1016/j.immuni.2007.04.011>.
17. Luo B-H, Carman CV, Springer TA. Structural basis of integrin regulation and signaling. *Annu Rev Immunol*. 2007;25:619–47. <https://doi.org/10.1146/annurev.immunol.25.022106.141618>.
18. Phillipson M, Heit B, Colarusso P, Liu L, Ballantyne CM, Kubes P. Intraluminal crawling of neutrophils to emigration sites: a molecularly distinct process from adhesion in the recruitment cascade. *J Exp Med*. 2006;203:2569–75. <https://doi.org/10.1084/jem.20060925>.
19. Petrovich E, Feigelson SW, Stoler-Barak L, Hatzav M, Solomon A, Bar-Shai A, et al. Lung ICAM-1 and ICAM-2 support spontaneous intravascular effector lymphocyte entrapment but are not required for neutrophil entrapment or emigration inside endotoxin-inflamed lungs. *FASEB J*. 2016;30:1767–78. <https://doi.org/10.1096/fj.201500046>.
20. Conrad C, Yildiz D, Cleary SJ, Margraf A, Cook L, Schlomann U, et al. ADAM8 signaling drives neutrophil migration and ARDS severity. *JCI. Insight*. 2022;7. <https://doi.org/10.1172/jci.insight.149870>.
21. Lämmermann T, Bader BL, Monkley SJ, Worbs T, Wedlich-Söldner R, Hirsch K, et al. Rapid leukocyte migration by integrin-independent flowing and squeezing. *Nature*. 2008;453:51–5. <https://doi.org/10.1038/nature06887>.
22. Yipp BG, Kim JH, Lima R, Zbytniuk LD, Petri B, Swanlund N, et al. The lung is a host defense niche for immediate neutrophil-mediated vascular protection. *Sci Immunol*. 2017;2. <https://doi.org/10.1126/sciimmunol.aam8929>.
23. Halin C, Scimone ML, Bonasio R, Gauguet J-M, Mempel TR, Quackenbush E, et al. The SIP-analog FTY720 differentially modulates T-cell homing via HEV: T-cell-expressed SIP1 amplifies integrin activation in peripheral lymph nodes but not in Peyer patches. *Blood*. 2005;106:1314–22. <https://doi.org/10.1182/blood-2004-09-3687>.
24. Asrir A, Tardiveau C, Couderc J, Laffont R, Blanchard L, Bellard E, et al. Tumor-associated high endothelial venules mediate lymphocyte entry into tumors and predict response to PD-1 plus CTLA-4 combination immunotherapy. *Cancer Cell*. 2022;40:318–34.e9. <https://doi.org/10.1016/j.ccell.2022.01.002>.
25. Woodfin A, Voisin M-B, Beyrau M, Colom B, Caille D, Diapouli F-M, et al. The junctional adhesion molecule JAM-C regulates polarized transendothelial migration of neutrophils in vivo. *Nat Immunol*. 2011;12:761–9. <https://doi.org/10.1038/ni.2062>.

26. Mathias JR, Perrin BJ, Liu T-X, Kanki J, Look AT, Huttenlocher A. Resolution of inflammation by retrograde chemotaxis of neutrophils in transgenic zebrafish. *J Leukoc Biol.* 2006;80:1281–8. <https://doi.org/10.1189/jlb.0506346>.
27. Elks PM, van Eeden FJ, Dixon G, Wang X, Reyes-Aldasoro CC, Ingham PW, et al. Activation of hypoxia-inducible factor-1 α (Hif-1 α) delays inflammation resolution by reducing neutrophil apoptosis and reverse migration in a zebrafish inflammation model. *Blood.* 2011;118:712–22. <https://doi.org/10.1182/blood-2010-12-324186>.
28. Yoo SK, Huttenlocher A. Spatiotemporal photolabeling of neutrophil trafficking during inflammation in live zebrafish. *J Leukoc Biol.* 2011;89:661–7. <https://doi.org/10.1189/jlb.1010567>.
29. Sullivan DP, Watson RL, Muller WA. 4D intravital microscopy uncovers critical strain differences for the roles of PECAM and CD99 in leukocyte diapedesis. *Am J Physiol Circ Physiol.* 2016;311:H621–32. <https://doi.org/10.1152/ajpheart.00289.2016>.
30. Reglero-Real N, Pérez-Gutiérrez L, Yoshimura A, Rolas L, Garrido-Mesa J, Barkaway A, et al. Autophagy modulates endothelial junctions to restrain neutrophil diapedesis during inflammation. *Immunity.* 2021;54:1989–2004.e9. <https://doi.org/10.1016/j.immuni.2021.07.012>.
31. Finsterbusch M, Hall P, Li A, Devi S, Westhorpe CLV, Kitching AR, et al. Patrolling monocytes promote intravascular neutrophil activation and glomerular injury in the acutely inflamed glomerulus. *Proc Natl Acad Sci.* 2016;113:E5172–81. <https://doi.org/10.1073/pnas.1606253113>.
32. Wang B, Zinselmeyer BH, Runnels HA, LaBranche TP, Morton PA, Kreisel D, et al. In vivo imaging implicates CCR2+ monocytes as regulators of neutrophil recruitment during arthritis. *Cell Immunol.* 2012;278:103–12. <https://doi.org/10.1016/j.cellimm.2012.07.005>.
33. Maus UA, Waelsch K, Kuziel WA, Delbeck T, Mack M, Blackwell TS, et al. Monocytes are potent facilitators of alveolar neutrophil emigration during lung inflammation: role of the CCL2-CCR2 Axis. *J Immunol.* 2003;170:3273–8. <https://doi.org/10.4049/jimmunol.170.6.3273>.
34. Sreeramkumar V, Adrover JM, Ballesteros I, Cuartero MI, Rossaint J, Bilbao I, et al. Neutrophils scan for activated platelets to initiate inflammation. *Science (80-).* 2014;346:1234–8. <https://doi.org/10.1126/science.1256478>.
35. Wang J, Kubes P. A reservoir of mature cavity macrophages that can rapidly invade visceral organs to affect tissue repair. *Cell.* 2016;165:668–78. <https://doi.org/10.1016/j.cell.2016.03.009>.
36. Zindel J, Peiseler M, Hossain M, Deppermann C, Lee WY, Haenni B, et al. Primordial GATA6 macrophages function as extravascular platelets in sterile injury. *Science (80-).* 2021;371. <https://doi.org/10.1126/science.abe0595>.
37. Zhang N, Czepielewski RS, Jarjour NN, Erlich EC, Esaulova E, Saunders BT, et al. Expression of factor V by resident macrophages boosts host defense in the peritoneal cavity. *J Exp Med.* 2019;216:1291–300. <https://doi.org/10.1084/jem.20182024>.
38. Uderhardt S, Martins AJ, Tsang JS, Lämmermann T, Germain RN. Resident macrophages cloak tissue microlesions to prevent neutrophil-driven inflammatory damage. *Cell.* 2019;177:541–55. e17. <https://doi.org/10.1016/j.cell.2019.02.028>.
39. Ng LG, Qin JS, Roediger B, Wang Y, Jain R, Cavanagh LL, et al. Visualizing the neutrophil response to sterile tissue injury in mouse dermis reveals a three-phase cascade of events. *J Invest Dermatol.* 2011;131:2058–68. <https://doi.org/10.1038/jid.2011.179>.
40. Lämmermann T, Afonso PV, Angermann BR, Wang JM, Kastenmüller W, Parent CA, et al. Neutrophil swarms require LTB4 and integrins at sites of cell death in vivo. *Nature.* 2013;498:371–5. <https://doi.org/10.1038/nature12175>.
41. Poplimont H, Georgantzoglou A, Boulch M, Walker HA, Coombs C, Papaleonidopoulou F, et al. Neutrophil swarming in damaged tissue is orchestrated by connexins and cooperative calcium alarm signals. *Curr Biol.* 2020;30:2761–76.e7. <https://doi.org/10.1016/j.cub.2020.05.030>.

42. Kienle K, Glaser KM, Eickhoff S, Mihlan M, Knöpper K, Reátegui E, et al. Neutrophils self-limit swarming to contain bacterial growth in vivo. *Science* (80-). 2021;372. <https://doi.org/10.1126/science.abe7729>.
43. McDonald B, Pittman K, Menezes GB, Hirota SA, Slaba I, Waterhouse CCM, et al. Intravascular danger signals guide neutrophils to sites of sterile inflammation. *Science* (80-). 2010;330:362–6. <https://doi.org/10.1126/science.1195491>.
44. Slaba I, Wang J, Kolaczowska E, McDonald B, Lee W-Y, Kubes P. Imaging the dynamic platelet-neutrophil response in sterile liver injury and repair in mice. *Hepatology*. 2015;62:1593–605. <https://doi.org/10.1002/hep.28003>.
45. Cleary SJ, Kwaan N, Tian JJ, Calabrese DR, Mallavia B, Magnen M, et al. Complement activation on endothelium initiates antibody-mediated acute lung injury. *J Clin Invest*. 2020;130:5909–23. <https://doi.org/10.1172/JCI138136>.
46. De Giovanni M, Tam H, Valet C, Xu Y, Looney MR, Cyster JG. GPR35 promotes neutrophil recruitment in response to serotonin metabolite 5-HIAA. *Cell*. 2022;185:815–30.e19. <https://doi.org/10.1016/j.cell.2022.01.010>.
47. Thanabalasuriar A, Neupane AS, Wang J, Krummel MF, Kubes P. iNKT cell emigration out of the lung vasculature requires neutrophils and monocyte-derived dendritic cells in inflammation. *Cell Rep*. 2016;16:3260–72. <https://doi.org/10.1016/j.celrep.2016.07.052>.
48. Looney MR, Thornton EE, Sen D, Lamm WJ, Glenn RW, Krummel MF. Stabilized imaging of immune surveillance in the mouse lung. *Nat Methods*. 2011;8:91–6. <https://doi.org/10.1038/nmeth.1543>.
49. Headley MB, Bins A, Nip A, Roberts EW, Looney MR, Gerard A, et al. Visualization of immediate immune responses to pioneer metastatic cells in the lung. *Nature*. 2016;531:513–7. <https://doi.org/10.1038/nature16985>.
50. Neupane AS, Willson M, Chojnacki AK, Silva VE, Castanheira F, Morehouse C, Carestia A, et al. Patrolling alveolar macrophages conceal bacteria from the immune system to maintain homeostasis. *Cell*. 2020;183:110–25.e11. <https://doi.org/10.1016/j.cell.2020.08.020>.
51. Secklehner J, De Filippo K, Mackey JBG, Vuononvirta J, Raffo Iraolagoitia XL, McFarlane AJ, et al. Pulmonary natural killer cells control neutrophil intravascular motility and response to acute inflammation. *bioRxiv*. 2019:680611. <https://doi.org/10.1101/680611>.
52. Duarte D, Hawkins ED, Akinduro O, Ang H, De Filippo K, Kong IY, et al. Inhibition of endosteal vascular niche remodeling rescues hematopoietic stem cell loss in AML. *Cell Stem Cell*. 2018;22:64–77.e6. <https://doi.org/10.1016/j.stem.2017.11.006>.
53. Deniset JF, Surewaard BG, Lee W-Y, Kubes P. Splenic Ly6Ghigh mature and Ly6Gint immature neutrophils contribute to eradication of *S. pneumoniae*. *J Exp Med*. 2017;214:1333–50. <https://doi.org/10.1084/jem.20161621>.
54. Juzenaite G, Secklehner J, Vuononvirta J, Helbawi Y, Mackey JBG, Dean C, et al. Lung marginated and splenic murine resident neutrophils constitute pioneers in tissue-defense during systemic *E. coli* challenge. *Front Immunol*. 2021;12. <https://doi.org/10.3389/fimmu.2021.597595>.
55. Kolaczowska E, Jenne CN, Surewaard BGJ, Thanabalasuriar A, Lee W-Y, Sanz M-J, et al. Molecular mechanisms of NET formation and degradation revealed by intravital imaging in the liver vasculature. *Nat Commun*. 2015;6:6673. <https://doi.org/10.1038/ncomms7673>.
56. Lefrançois E, Mallavia B, Zhuo H, Calfee CS, Looney MR. Maladaptive role of neutrophil extracellular traps in pathogen-induced lung injury. *JCI Insight*. 2018;3. <https://doi.org/10.1172/jci.insight.98178>.
57. McDonald B, Davis RP, Kim S-J, Tse M, Esmo CT, Kolaczowska E, et al. Platelets and neutrophil extracellular traps collaborate to promote intravascular coagulation during sepsis in mice. *Blood*. 2017;129:1357–67. <https://doi.org/10.1182/blood-2016-09-741298>.
58. Carminita E, Crescence L, Brouilly N, Altié A, Panicot-Dubois L, Dubois C. DNase-dependent, NET-independent pathway of thrombus formation in vivo. *Proc Natl Acad Sci*. 2021;118. <https://doi.org/10.1073/pnas.2100561118>.

59. Ueki H, Wang I-H, Zhao D, Gunzer M, Kawaoka Y. Multicolor two-photon imaging of in vivo cellular pathophysiology upon influenza virus infection using the two-photon IMPRESS. *Nat Protoc.* 2020;15:1041–65. <https://doi.org/10.1038/s41596-019-0275-y>.
60. Guidotti LG, Inverso D, Sironi L, Di Lucia P, Fioravanti J, Ganzer L, et al. Immunosurveillance of the liver by intravascular effector CD8 + T cells. *Cell.* 2015;161:486–500. <https://doi.org/10.1016/j.cell.2015.03.005>.
61. De Niz M, Meehan GR, Brancucci NMB, Marti M, Rotureau B, Figueiredo LM, et al. Intravital imaging of host–parasite interactions in skin and adipose tissues. *Cell Microbiol.* 2019;21:e13023. <https://doi.org/10.1111/cmi.13023>.
62. Peters NC, Egen JG, Secundino N, Debrabant A, Kimblin N, Kamhawi S, et al. In vivo imaging reveals an essential role for neutrophils in leishmaniasis transmitted by sand flies. *Science* (80-). 2008;321:970–4. <https://doi.org/10.1126/science.1159194>.
63. Kilarski WW, Martin C, Pisano M, Bain O, Babayan SA, Swartz MA. Inherent biomechanical traits enable infective filariae to disseminate through collecting lymphatic vessels. *Nat Commun.* 2019;10:2895. <https://doi.org/10.1038/s41467-019-10675-2>.
64. Furlong-Silva J, Cross SD, Marriott AE, Pionnier N, Archer J, Steven A, et al. Tetracyclines improve experimental lymphatic filariasis pathology by disrupting interleukin-4 receptor–mediated lymphangiogenesis. *J Clin Invest.* 2021;131. <https://doi.org/10.1172/JCI140853>.
65. Karadjian G, Fercoq F, Pionnier N, Vallarino-Lhermitte N, Lefoulon E, Nieguitsila A, et al. Migratory phase of *Litomosoides sigmodontis* filarial infective larvae is associated with pathology and transient increase of S100A9 expressing neutrophils in the lung. Brehm K, editor. *PLoS Negl Trop Dis.* 2017;11:e0005596. <https://doi.org/10.1371/journal.pntd.0005596>.
66. Boulch M, Grandjean CL, Cazaux M, Bouso P. Tumor immunosurveillance and immunotherapies: a fresh look from intravital imaging. *Trends Immunol.* 2019;40:1022–34. <https://doi.org/10.1016/j.it.2019.09.002>.
67. Sody S, Uddin M, Grüneboom A, Görgens A, Giebel B, Gunzer M, et al. Distinct spatio-temporal dynamics of tumor-associated neutrophils in small tumor lesions. *Front Immunol.* 2019;10. <https://doi.org/10.3389/fimmu.2019.01419>.
68. Teixeira Á, Garasa S, Gato M, Alfaro C, Migueliz I, Cirella A, et al. CXCR1 and CXCR2 chemokine receptor agonists produced by tumors induce neutrophil extracellular traps that interfere with immune cytotoxicity. *Immunity.* 2020;52:856–71.e8. <https://doi.org/10.1016/j.immuni.2020.03.001>.
69. Spicer JD, McDonald B, Cools-Lartigue JJ, Chow SC, Giannias B, Kubes P, et al. Neutrophils promote liver metastasis via mac-1–mediated interactions with circulating tumor cells. *Cancer Res.* 2012;72:3919–27. <https://doi.org/10.1158/0008-5472.CAN-11-2393>.
70. McDonald B, Spicer J, Giannias B, Fallavollita L, Brodt P, Ferri LE. Systemic inflammation increases cancer cell adhesion to hepatic sinusoids by neutrophil mediated mechanisms. *Int J Cancer.* 2009;125:1298–305. <https://doi.org/10.1002/ijc.24409>.
71. Rayes RF, Mouhanna JG, Nicolau I, Bourdeau F, Giannias B, Rousseau S, et al. Primary tumors induce neutrophil extracellular traps with targetable metastasis-promoting effects. *JCI Insight.* 2019;4. <https://doi.org/10.1172/jci.insight.128008>.
72. Park J, Wysocki RW, Amoozgar Z, Maiorino L, Fein MR, Jorns J, et al. Cancer cells induce metastasis-supporting neutrophil extracellular DNA traps. *Sci Transl Med.* 2016;8:361ra138. <https://doi.org/10.1126/scitranslmed.aag1711>.
73. Entenberg D, Voiculescu S, Guo P, Borriello L, Wang Y, Karagiannis GS, et al. A permanent window for the murine lung enables high-resolution imaging of cancer metastasis. *Nat Methods.* 2018;15:73–80. <https://doi.org/10.1038/nmeth.4511>.
74. Borriello L, Coste A, Traub B, Sharma VP, Karagiannis GS, Lin Y, et al. Primary tumor associated macrophages activate programs of invasion and dormancy in disseminating tumor cells. *Nat Commun.* 2022;13:626. <https://doi.org/10.1038/s41467-022-28076-3>.
75. Naumenko V, Nikitin A, Garanina A, Melnikov P, Vodopyanov S, Kapitanova K, et al. Neutrophil-mediated transport is crucial for delivery of short-circulating magnetic nanoparticles to tumors. *Acta Biomater.* 2020;104:176–87. <https://doi.org/10.1016/j.actbio.2020.01.011>.

76. Chu D, Dong X, Zhao Q, Gu J, Wang Z. Photosensitization priming of tumor microenvironments improves delivery of nanotherapeutics via neutrophil infiltration. *Adv Mater.* 2017;29:1701021. <https://doi.org/10.1002/adma.201701021>.
77. Lau D, Garçon F, Chandra A, Lechermann LM, Aloj L, Chilvers ER, et al. Intravital imaging of adoptive T-cell morphology, mobility and trafficking following immune checkpoint inhibition in a mouse melanoma model. *Front Immunol.* 2020;11:1514. <https://doi.org/10.3389/fimmu.2020.01514>.
78. Huang D, Chen X, Zeng X, Lao L, Li J, Xing Y, et al. Targeting regulator of G protein signaling 1 in tumor-specific T cells enhances their trafficking to breast cancer. *Nat Immunol.* 2021;22:865–79. <https://doi.org/10.1038/s41590-021-00939-9>.
79. Breart B, Lemaître F, Celli S, Bouso P. Two-photon imaging of intratumoral CD8+ T cell cytotoxic activity during adoptive T cell therapy in mice. *J Clin Invest.* 2008;118:1390–7. <https://doi.org/10.1172/JCI34388>.
80. Cazaux M, Grandjean CL, Lemaître F, Garcia Z, Beck RJ, Milo I, et al. Single-cell imaging of CAR T cell activity in vivo reveals extensive functional and anatomical heterogeneity. *J Exp Med.* 2019;216:1038–49. <https://doi.org/10.1084/jem.20182375>.
81. Giampetraglia M, Weigelin B. Recent advances in intravital microscopy for preclinical research. *Curr Opin Chem Biol.* 2021;63:200–8. <https://doi.org/10.1016/j.cbpa.2021.05.010>.
82. Stringer C, Wang T, Michaelos M, Pachitariu M. Cellpose: a generalist algorithm for cellular segmentation. *Nat Methods.* 2021;18:100–6. <https://doi.org/10.1038/s41592-020-01018-x>.
83. Stoltzfus CR, Filipek J, Germ BH, Olin BE, Leal JM, Wu Y, et al. CytoMAP: a spatial analysis toolbox reveals features of myeloid cell organization in lymphoid tissues. *Cell Rep.* 2020;31:107523. <https://doi.org/10.1016/j.celrep.2020.107523>.
84. Crainiciuc G, Palomino-Segura M, Molina-Moreno M, Sicilia J, Aragones DG, Li JLY, et al. Behavioural immune landscapes of inflammation. *Nature.* 2022;601:415–21. <https://doi.org/10.1038/s41586-021-04263-y>.
85. Burkovskiy I, Lehmann C, Jiang C, Zhou J. Utilization of 3D printing for an intravital microscopy platform to study the intestinal microcirculation. *J Microsc.* 2016;264:224–6. <https://doi.org/10.1111/jmi.12437>.
86. Valet C, Magnen M, Qiu L, Cleary SJ, Wang KM, Ranucci S, et al. Sepsis promotes splenic production of a protective platelet pool with high CD40 ligand expression. *J Clin Invest.* 2022;132. <https://doi.org/10.1172/JCI153920>.
87. Jacquemin G, Benavente-Diaz M, Djaber S, Bore A, Dangles-Marie V, Surdez D, et al. Longitudinal high-resolution imaging through a flexible intravital imaging window. *Sci Adv.* 2021;7:eabg7663. <https://doi.org/10.1126/sciadv.abg7663>.
88. Maiorino L, Shevik M, Adrover JM, Han X, Georgas E, Wilkinson JE, et al. Longitudinal intravital imaging through clear silicone windows. *J Vis Exp.* 2022:e62757. <https://doi.org/10.3791/62757>.
89. Turner-Stokes T, Garcia Diaz A, Pinheiro D, Prendecki M, McAdoo SP, Roufosse C, et al. Live imaging of monocyte subsets in immune complex-mediated glomerulonephritis reveals distinct phenotypes and effector functions. *J Am Soc Nephrol.* 2020;31:2523–42. <https://doi.org/10.1681/ASN.2019121326>.
90. Fisher DT, Muhitch JB, Kim M, Doyen KC, Bogner PN, Evans SS, et al. Intraoperative intravital microscopy permits the study of human tumour vessels. *Nat Commun.* 2016;7:10684. <https://doi.org/10.1038/ncomms10684>.
91. Gabriel EM, Kim M, Fisher DT, Mangum C, Attwood K, Ji W, et al. A pilot trial of intravital microscopy in the study of the tumor vasculature of patients with peritoneal carcinomatosis. *Sci Rep.* 2021;11:4946. <https://doi.org/10.1038/s41598-021-84430-3>.

Spatial Transcriptomics in Inflammation: Dissecting the Immune Response in 3D in Complex Tissues



Kenneth Hu

Abstract Inflammatory responses in tissues in the contexts of infection, autoimmunity, and tumors display significant spatial heterogeneity. Understanding how the elements of the immune system are spatially organized and how this organization evolves over time can reveal important cell-cell communication that leads to resolution of tissue insults/injuries or, in the case of tumors or autoimmunity, lead to aberrant tissue states. Delineating how cell-cell communication affects tissue states requires the capability to link gene expression in cells to their spatial coordinates in the tissue and thus merge transcriptomic data with imaging. Here we explore the ever-evolving world of spatial transcriptomic approaches, consider their unique strengths, and finally discuss how some of them have been applied toward answering questions in the immunology space. We close by providing suggestions for researchers planning to incorporate spatial transcriptomics into their studies and possible future directions of this field.

Keywords Transcriptomics · Sequencing · Microscopy · Tissue biology · Inflammation · Immunity · Cell-cell communication · Tumor immunology

“The body is a cell state in which every cell is a citizen”—Rudolf Virchow

Ever since the emergence of the central dogma, biologists have sought to fully account for all the mRNA molecules a cell generates as an indicator of cell identity, response to stimuli, and associated functions. While this collection of total mRNA, known as the transcriptome, may not tell the full picture (e.g., considering the epigenome, surface proteome, and metabolome), it serves as an invaluable cell-profiling tool.

The dream of fully resolving the transcriptome seems ever closer to being reality, with the advent of first bulk RNA-Seq and then single-cell RNA Seq (scRNA-Seq) [1]. A staggering amount of information can now be compiled through multimodal

K. Hu (✉)

Department of Pathology, University of California, San Francisco, San Francisco, CA, USA
e-mail: kenneth.hu@ucsf.edu

assays on many thousands of single cells at a time with a combination of epigenome, transcriptome, and surface proteome all combined in a single assay [2].

However, humans, mice, and other metazoans are comprised of tissues, complex and heterogenous assemblies of cells and extracellular components bathed in interstitial fluid. Following from Rudolf Virchow's statement, where the citizens of a state reside and move to and from is of utmost importance in determining the functioning of that state. If we consider the levels of mRNA transcript "A" as analogous to "wealth", it would be of great interest to examine each citizen/cell's individual wealth as opposed to the gross domestic product of the state. This highlights the advances scRNA-Seq offers over more traditional bulk RNA-Seq measurements. However, a state, analogous to a tissue, occupies a physical space defined by boundaries, landmarks, geographical features, and population centers. Being able to place that individual wealth data in that physical space represents the promise of spatial transcriptomics (ST), revealing how the local neighborhood shapes the citizen and vice versa.

The process of inflammation, a dramatic coordination of cells and signals between them, represents a response to injury, insult, or infection which seeks to return the tissue to a state of homeostasis. Naturally, the fluxes of cell expression states, numbers, and signaling molecules must be spatially organized to achieve the necessary coordination. In this chapter, we will seek to first motivate the need for spatial transcriptomics to understand the immune response in multiple disease models with an emphasis on prior experimental work. Next, we will explore established and emerging technologies, their strengths and weaknesses, and how they can be best applied. Finally, we will explore how these technologies are being applied for discovery in immunology and where the field is going next, with a focus on computational techniques for extracting useful information from this high-dimensional data.

We will not aim to cover the sheer number of spatial transcriptomic methods, nor their technical details in this chapter. Instead, our focus will be on explaining how spatial transcriptomic information has allowed for new discoveries in systems immunology in a variety of tissue/disease contexts and where it can go from here. For technical discussions of the breadth of spatial technologies out there, readers are encouraged to explore a variety of comprehensive reviews [3–7]. We will instead try to categorize approaches, both new and old, into general classes with a focus on those technologies that have been applied to questions in immunology.

1 The Importance of Spatial Dimensions When Studying Immune Responses in Tissue

The complex signaling networks that govern immune system behavior in tissues are mediated by a number of mechanisms. Each of these mechanisms has an inherent length scale (range of effect) from the order of direct cell-cell contact to diffusion of

cytokines in tissues across hundreds of microns or tens of cell diameters [8]. Combined, these signaling mechanisms give rise to multicellular tissue organization and determine its homeostatic state [9] and response to perturbations such as inflammation and its resolution. As we will explore below, the spatial organization of immune cells is tightly linked to their activity and function in a variety of tissues. Thus, being able to link immune cell transcriptomic information to position will greatly advance our understanding of the immune system's components and their interactions.

1.1 Lymphoid Tissues: It's All About Space

If we focus our attention on lymphoid tissues such as lymph nodes and the spleen, the necessity of spatial organization in the immune response becomes immediately apparent [10]. The arrival and ultimate positioning of antigen-carrying dendritic cells from the periphery is intricately linked to their ability to present antigen and thus activate distinct subpopulations of T cells [11–13]. The coordination of multiple cell types during an immune response requires that the right cell type, in the right state be found in the right place at the right time, and this complex choreography has only begun to be deciphered. An example of this coordination can be found in the dendritic cell compartment in the lymph node, wherein cross-presenting conventional dendritic cells type 1 (cDC1) which serve as effective activators of CD8⁺ T cells can be found deep within the T cell zone. This stands in opposition to cDC2 cells which are thought to effectively present to CD4⁺ T cells through MHCII and reside on the periphery of the T cell zone [12, 14]. This spatial distribution has also been hypothesized to affect the uptake of antigen with less antigen available to cDC1 populations due to their more centralized positioning [11]. Concurrently, T lymphocytes skew in their distributions according to the most potent antigen-presenting cell (APC) type, i.e., CD4 more peripheral than CD8 T cells. A number of signaling mechanisms have been shown to drive these spatial patterns in cell distributions both at rest and during immunization, such as Ebi2 [14, 15], wherein a combination of ligand gradient ($7\alpha,25\text{-OHC}$) and receptor expression level tunes a given cell's localization. As the immune response is a dynamic process, localizations necessarily may shift, and indeed in the spleen, cDC2 cells use increased CCR7 expression upon antigen uptake to move centrally toward the T zone to make CD4 T-cDC2 interactions more likely [15]. Disruption of these signaling mechanisms alters cell localization patterns and results ultimately in a suboptimal response, again stressing the link between localization and function.

Other elements of the innate immune system are also found in distinct regions of the lymph node related to their function such as subcapsular sinus macrophages [16], natural killer (NK) cells [17, 18], and neutrophils [19]. Even the nonimmune components of the lymph node, including stromal cells, display distinct spatial organization relative to the medulla and B cell follicles [20].

The cellular choreography of lymphoid tissues serves as a powerful example for how multicellular structure arises from intercellular signaling. They also serve as

poignant examples of how structure then informs function, in this case the response to immunological perturbations.

1.2 Spatial Organization of Immune Cells in Nonlymphoid Tissues Is Vital to Their Function

Beyond lymphoid tissues, immune cells in the periphery often occupy specific niches closely related to their function in either surveillance or maintenance of the tissue. For example, Kupffer cells occupy a specific intravascular spatial niche in the liver, where signaling with neighboring stellate cells, endothelial cells, and hepatocytes guides their differentiation from monocytes [21]. Through close interactions with nonimmune cells, this population of immune cells is precisely localized in a specific intravascular niche within the liver, vital to its function [22].

The skin, as a barrier tissue, exhibits immune organization closely related to the many microanatomical layers that comprise the tissue [23]. Even hair follicles interact closely with immune populations, serving as foci for organization of immune responses to inflammatory perturbation in the skin [24]. Due to the variety of potentially inflammatory stimuli these barrier tissues face, the placement of distinct immune cells largely determines the progression of the immune response. For instance, Langerhans cells reside at homeostasis in close contact with keratinocytes in the epidermis and upon inflammation-inducing conditions, downregulate E-cadherin to promote their egress toward draining lymph nodes, trafficking antigen for presentation [25, 26]. This serves as yet another example of how cell-cell interactions (in this case a juxtacrine one) govern immune cell positioning in tissue and tie into their function at different stages of the immune response (surveillance vs. antigen trafficking).

Taken together, these examples underline how components of the immune system can be found across diverse tissue contexts, with their specific localizations governed by cell-cell communication and essential for their function. Thus, efforts to study the immune system's role in maintaining homeostasis in these diverse tissues will be greatly enabled by the merging of spatial information with transcriptomic.

1.3 Immune Cells in the Physical Space of the Tumor: Order from Chaos

Given the rise of cancer immunotherapy, there is naturally great interest in studying the state of the immune system in the tumor microenvironment (TME) [27] and what features of the immune infiltrate in tumor determine response to immune checkpoint blockade (ICB). The concept of immunologically “hot” tumors has emerged as a

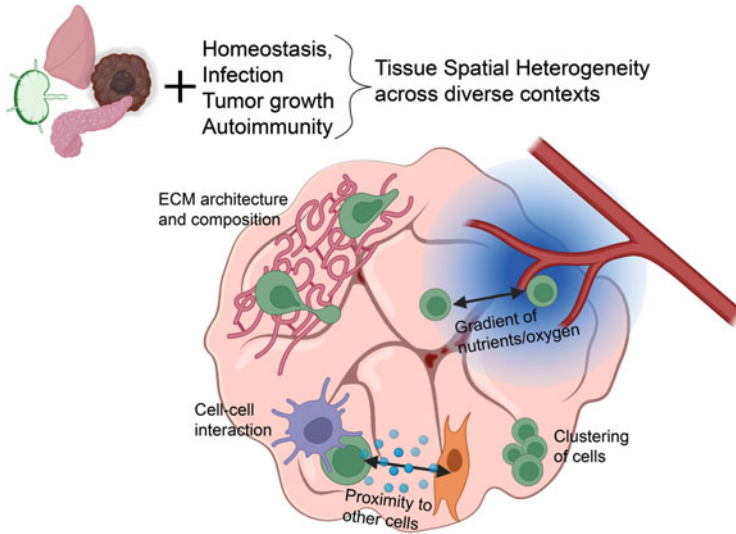


Fig. 1 Tissues, both at homeostasis and undergoing an inflammatory response due to injury or insult, exhibit spatial heterogeneity. Immune cells within these tissues encounter spatially varying stimuli and signaling. For example, cells may encounter altered ECM architecture and short- and long-range signals from other cell types and be distributed in different regions of the tumor mass (Figure made with BioRender)

paradigm to describe TMEs that are poised for optimal responses to ICB [28]; these tumors are characterized by greater infiltration of T cells and potent stimulatory antigen-presenting cells (APCs) such as conventional dendritic cells (cDCs) [29]. Conversely, “cold” tumors are characterized by a lack of T cell infiltration, an imbalance toward poorly stimulating or inhibitory myeloid cells, and exclusionary fibrosis mediated by stromal cells. Major questions remain:

- What mechanisms shape the progression of a hot versus a cold tumor?
- How can we refine our models of hot/cold tumor with spatial information?
- Can hot and cold regions exist within the same tumor?
- How does intratumoral spatial heterogeneity influence the response to ICB?

At first glance, the tumor represents chaos rather than order, a subversion of the regulatory pathways that are the basis of multicellular organization and harmony. However, emerging work has started to highlight surprising levels of spatial organization in the tumor including the immune compartment (Fig. 1). Because tumors repurpose existing mechanisms for tissue homeostasis and regeneration [30], perhaps it is not so surprising that tumors can generate their own unique tissue architecture with the formation of spatially heterogenous domains [31].

The presence of tertiary lymphoid structures (TLS) in tumors is one example of newly appreciated spatial organization in the TME and surrounding stroma. These aggregations of lymphocytes share many of the spatially organized features found in lymphoid tissues including T and B zones, but can be found in a variety of

chronically inflamed tissues including tumors [32]. Importantly, these structures serve as foci for proliferation and differentiation of T effector memory (T_{EM}) cells and plasma B cells, and their presence in the stroma surrounding tumors is strongly linked to good prognoses across solid tumor indications [33–35]. The mechanisms that lead to the de novo emergence of these structures involve many cell types, both immune and nonimmune and signaling molecules such as VEGFC, CCL19/21, and others possibly unexplored [32]. Because of the strong correlation with good outcomes to treatment, there is intense interest in deciphering the mechanisms behind the assembly of TLS.

While angiogenesis and the role of endothelial cells have been extensively studied in terms of tumor growth and metastases, recent work highlights the vasculature as an organizing center for tumor-infiltrating immune cells [36, 37]. The authors of these studies discovered distinct immune populations that resided in perivascular regions in the tumor which were poised to respond to ICB. In particular, Di Pilato et al. found that cytokine signaling through CXCR6 served a crucial role in positioning effector $CD8^+$ T cells to this specific niche where they received signals from a dendritic cell subpopulation that promoted their survival and persistence in the TME [36]. This provides yet another example of cell-cell communication leading to formation of a spatially organized immune compartment in the TME with implications for the anti-tumor response.

But what are the consequences of altered immune localization in the tumor and what relevance does it have for clinical prognoses? Already, major efforts have been made to profile the immune composition of human tumors across indications and treatment histories and to identify patterns of composition and their correlation to clinical outcomes [38–40]. Notably, these papers identified general classes of tumors defined by immune composition which go beyond simple “hot” and “cold” terminology. These efforts have been performed on dissociated tumors, collecting either bulk or single-cell RNA-Seq on single-cell suspensions.

However, there is ample evidence that applying a layer of spatial information on top of these compositional profiling approaches can improve our prognostic capabilities and reveal new mechanisms that explain resistance to ICB. Degree of immune infiltration and the positions of immune cells relative to each other and to tumor cells hold prognostic value [31, 41–47] and can have significant influences on the response to immunotherapies [48]. These studies have used a variety of spatial metrics including co-localization scores, proximity measurements, and cell neighborhood analyses to generate predictive stratification of human tumor samples. For example, Keren et al. used multiplexed ion beam imaging (MIBI) to show more favorable prognosis in triple-negative breast cancer (TNBC) samples with specific immune neighborhoods concentrated at the tumor edge as opposed to dispersed within the tumor mass [46]. Although the studies vary in assays and metrics used, they share a common theme in the refinement of prognostic scores with the addition of spatial information.

Taken together, it becomes apparent that architecture and higher-level organization found in healthy tissues can be at least partially recapitulated in the TME and highlight the need to understand not only the transcriptional state of immune cells,

but their physical position in tumor space. This understanding would then hold great prognostic value and could generate actionable targets for perturbing the spatial organization of the immune compartment in tumors to improve outcomes in cancer. Already several interventions and perturbations have been proposed for inducing spatial shifts in immune cells in the TME to achieve greater anti-tumor response. For example, degradation of collagen matrices at the tumor-stroma interface has been shown to enhance CD8⁺ T cell infiltration deeper into the tumor mass [49]. Vascular normalization (e.g., anti-VEGF blockade) has been shown to increase immune infiltration into the tumor and synergize with immune checkpoint blockade in tumor clearance [50]. Therapies can also act by altering the distribution of other cell types. For example, in a mouse model of pancreatic ductal adenocarcinoma (PDA), CD40 blockade induced macrophage accumulation in the tumor stroma, leading to a decrease in collagen deposition and disruption of the tumor stroma [51].

1.4 Spatial Aspects of Autoimmunity

On the other side of the coin, autoimmunity is often characterized by prolonged or inappropriate inflammation that damages healthy tissue leading to pathology. This self-targeting immune response also exhibits clear spatial heterogeneity in cell types and their states which determines the trajectory of pathology. For example, in type 1 diabetes, the stages of disease progression are marked by the accumulation of distinct immune cell populations in regions surrounding islets followed by increasing infiltration into the islet and eventual destruction of beta cells [52]. This progression of immune accumulation can also vary significantly between neighboring islets [53] leading us to ask what cell-cell signals govern the placement of immune populations and how this affects their ability to be polarized into an inflammatory or anti-inflammatory state. To do so requires the ability to study the state of these immune cells as a function of their position relative to the islets [54].

1.5 Summary: Capturing Spatial Information is Vital for Understanding Immunity

Hopefully the examples above demonstrate the importance of the spatial dimension in studying inflammatory and immune responses in a wide array of tissue types and pathologies. In the next section, we will imagine that we wish to understand the transcriptomic state of a cell to determine its identity or function. However, we also want to know where exactly that cell was in the tissue and, importantly, what is the state of other cells near and far from it. We may also have traditional imaging data marking tissue landmarks of interest such as clusters of a given cell type, vasculature, or ECM components, and we would like to know how cell transcript levels vary

as a function of distance to these landmarks. Keeping these questions in mind, we will review available methods to address this problem and the considerations we must keep in mind as we weigh each method.

2 The Spatial Transcriptomic Toolbox

This section will introduce the many methods for spatial transcriptomic profiling, both old and new. It is not meant to be a comprehensive catalog of all techniques, but rather a sampling of the major classes, touching upon principles and particular strengths. Techniques are covered in this section in the context of the discoveries they have enabled in the field of immunology.

2.1 *The Ever-Evolving Spatial Transcriptomic Toolbox*

2.1.1 Targeted Approaches

The earliest attempt at gaining spatial information on transcriptional states of cells has its roots in in situ hybridization technologies [55]. The field of spatial transcriptomics, fundamentally, is the marriage of transcriptional space which can range from 1 to tens of thousands of dimensions, within two- or three-dimensional physical space. Traditionally, characterization of physical space has been the purview of microscopy; in situ hybridization (ISH) seeks to make use of microscopy to directly visualize and quantify mRNA species in a biological sample. If proteins can be detected through specific binding by an antibody, so too can an RNA transcript by a fluorescently labeled reverse complementary probe.

From the beginning of fluorescence in situ hybridization (FISH) [56], major advancements have increased the number of targets able to be detected simultaneously and the sensitivity of detection. Single-molecule FISH used multiple short probes per target transcript to achieve signal amplification, allowing for single mRNAs to be detected [57]. In order to increase the number of mRNA species detected at a time, the fluorophores attached to these short probes can be varied, such that the unique combination of fluorophores defines an mRNA species, increasing the number of discernible targets with a limited set of fluorophores in what is known as spectral FISH [58].

The advent of multiplexed error-robust FISH (MERFISH) greatly expanded the number of simultaneously detectable mRNA species by several orders of magnitude. Instead of direct fluorescent probe binding to the mRNA target itself, the probe strands contain two overhang regions flanking the targeting region which are hybridized with fluorescently labeled readout probes. By alternating addition of fluorescently labeled probes and photobleaching, each detected mRNA is defined by presence and absence of signal for each round. In this way, mRNA species are

defined by a binary code (presence or absence of a fluorescent signal); with sufficient edit distance between codes, errors or dropouts in signal can be caught and correctly assigned [59]. In the latest iteration of MERFISH, the authors demonstrated detection of 10,050 targets with the ability to localize transcripts to subcellular compartments [60].

Sequential FISH uses cycles of probe hybridization and stripping via DNase treatment to define a sequential barcode. The first iteration of seqFISH managed to detect 249 individual mRNA targets [61]. However, by encapsulating this serial barcoding idea to one of four readout regions attached to a target-specific probe, the authors were able to create 60 pseudocolors (sequential barcodes) for seqFISH+ [62]. Because these pseudocolors are defined by presence/absence of signal in a round, this approach also deals with the issue of resolving mRNA molecules that become increasingly crowded with more and more detected targets. Ultimately, this approach allowed for simultaneous detection of 10,000 genes, approaching the scale of untargeted, whole-transcriptome approaches detailed below.

An early approach for mapping single-cell transcriptomes in 3D in zebrafish embryos by Satija et al. made use of a set of known landmark genes, with previously characterized spatial patterns of expression via FISH [63]. By querying the expression level of these landmark genes in each cell, and mapping to the previously determined probability landscape, the authors could infer the likelihood a given cell's position in 3D space. While a powerful technique in the embryo, this method necessarily required previously known landmark genes with geometrically ordered expression covering enough "degrees of freedom" for accurate mapping. While there is a wealth of such genes, e.g., morphogens, in the developing embryo, there are relatively few for other tissue contexts without well-defined geometry.

Performing traditional FISH on thick, 3D tissue samples becomes a challenge due to imaging and reagent penetration issues; these obstacles have been creatively tackled using strategies such as tissue clearing, expansion, and sequencing in situ. Spatially-resolved transcript amplicon readout mapping (STARMap) represents a combination of technologies that combines hybridization, amplification, and sequencing by ligation with error correction [64]. The set of issues that the authors sought to address using STARMap were difficulties in detecting target transcripts, amplifying signals, and reading out these signals out with in situ sequencing in 3D intact tissue (brain in their seminal publication). The first step in the solution was the generation of DNA amplicons from rolling-circle amplification based on target-specific probes, creating nanoballs containing many copies of a barcode associated with the target of interest. Critically, these nanoballs incorporate chemical moieties allowing their anchoring to a hydrogel support which permeates the tissue, thus allowing other cellular and tissue components to be stripped away, reminiscent of recent tissue clearing protocols [65]. The final piece of the puzzle is an innovative sequencing by ligation approach, sequencing with error-reduction by dynamic annealing and ligation (SEDAL), which addressed the issue of high error rate and background in other in situ sequencing approaches. Using this technique, the authors were able to demonstrate detection of 160 target transcripts in a 150-micron-thick

brain section, revealing neuronal clusters that serial 2D sectioning would have missed.

Combining both targeted and untargeted capabilities, ExSeq [66] is conceptually similar to STARMap mentioned above, but builds upon the expansion microscopy technique [67] to increase spacing between RNA molecules and provide greater physical accessibility to the reagents and enzymes necessary for fluorescence in situ sequencing or FISSEQ [68]. Crucially, the authors elute transcripts from the polymer for traditional next-generation sequencing (NGS), allowing better mapping of their short in situ reads. The targeted approach was demonstrated in visual cortex sections around $1 \times 1 \times 0.02$ mm targeting 42 genes. The authors went further and examined 297 genes of interest in a breast cancer metastasis in the liver, finding expression patterns in one cell type dependent on proximity to an expression pattern in another cell type. This kind of analysis represents a potentially powerful method for elucidating cell-cell interactions and the signaling pathways they act through.

2.1.2 “Whole” or “Untargeted” Transcriptome Capture Techniques

With the approaches described above (with the partial exception of ExSeq), although some offer tens of thousands of targets, they still require the selection of targets in advance and the generation of probes. In this section, we touch upon the exciting technological advancements that have allowed for capture of the whole transcriptome, either from single cells or cellular neighborhoods in tissues. The details and strategies are incredibly diverse in their execution; here we describe two general groupings: solid-phase capture and region-based selection techniques. Generally speaking, these techniques use a combination of nonselective capture of transcripts, reverse transcription, library construction, and next-generation sequencing (NGS) to quantify transcript levels in an unbiased manner.

Solid-Phase Capture

The core idea behind this group of techniques is first the construction of a solid support able to capture transcripts, usually through a classic poly-dT oligonucleotide. By varying a barcode sequence in the capture oligo over the capture area, a transcript captured and turned into cDNA during reverse transcription (RT) by the solid support can be mapped back to a position on the support and thus the tissue section placed against that support (Fig. 2).

One of the first exemplars of this family of techniques was the approach pioneered by Stahl et al. in which immobilized barcoded capture oligonucleotides were printed in 100-micron spots on a glass slide to capture mRNA transcripts in a tissue section overlaid on top, relying on the permeabilization of the tissue and diffusion of transcripts onto the slide [69]. This initial effort has since grown extensively, commercialized as the Visium spatial transcriptome solution from 10X Genomics, into the most widely used technology in this family. The latest

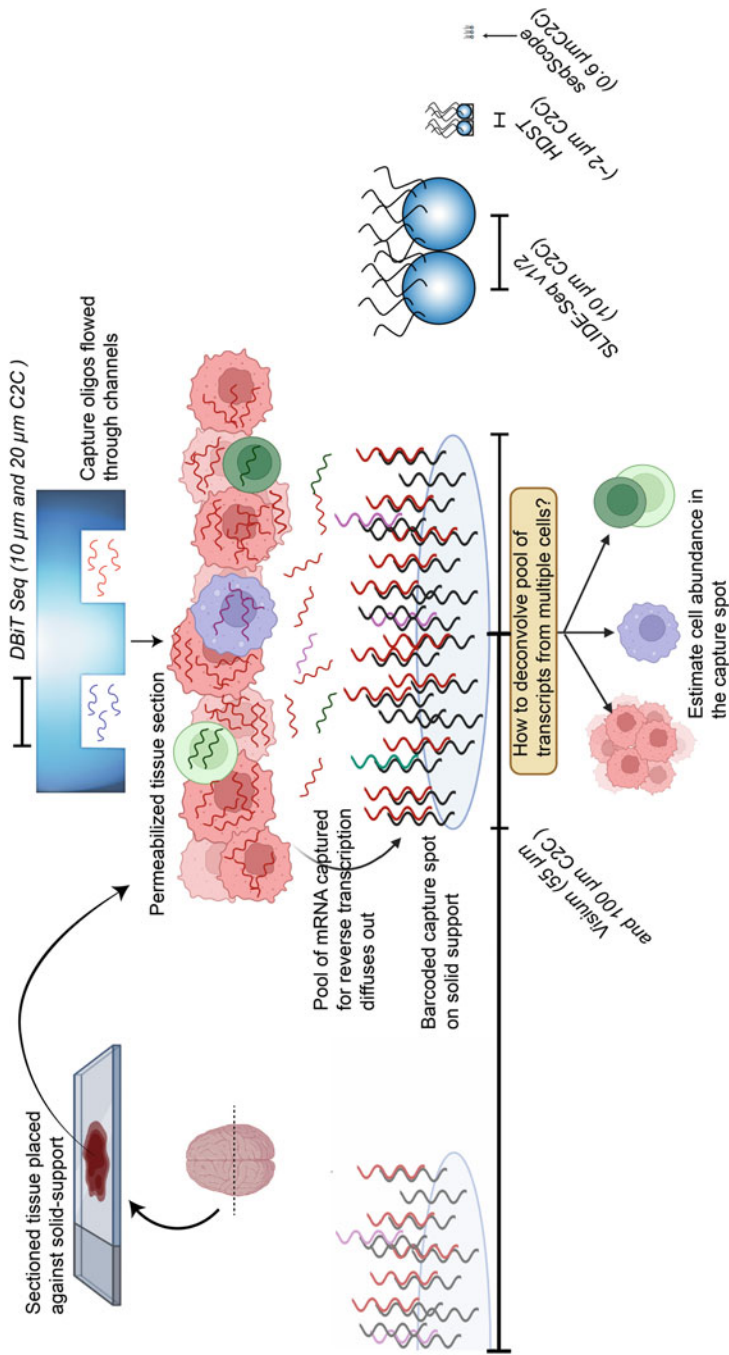


Fig. 2 Generalized schematic for solid-phase capture methods such as Visium, SLIDE-Seq, HDST, DBiT-Seq, and Seq-Scope. Generally speaking, these methods rely on capture of mRNA on physically partitioned barcoded capture oligonucleotides. For techniques such as Visium that encompass multiple cells, the pool of transcripts must be deconvolved to estimate cell-type abundances. Capture regions/beads/wells and cells (est. 10 μm max diameter) are shown to scale where possible, RNA molecules are not. C2C: center-center (Figure partially made with BioRender)

commercially available iteration boasts increased spatial resolution (55-micron spots with a 100-micron center-center distance) and greater transcript capture efficiency (Fig. 2) [70].

Variations on this idea can be found in SLIDE-Seq and SLIDE-SeqV2, its improved version [71, 72], in which an array of beads, each bearing its own barcoded capture oligonucleotide, serve as the solid support. Naturally, the size of the beads (10 μm) governs the spatial resolution of the approach.

Combining barcoded beads with an array of hexagonal microwells, high-definition spatial transcriptomics (HDST) [73] represents another development in the solid-support family. Seeking to improve the spatial resolution of the earlier spatial transcriptomics approach, the authors created an array of hexagonal wells, into which a slightly smaller bead (2 μm diameter) decorated with barcoded capture oligonucleotides is deposited. Naturally, the arrangement of barcoded beads is unknown a priori; thus, these approaches require accurate barcode sequencing of the bead arrays prior to use.

The latest development in solid-phase capture, Seq-Scope [74], creatively repurposes next-generation sequencing (NGS) flow cells to create a dense forest of randomly barcoded capture clusters similar to the clusters that form during the typical NGS workflow. This “organically” grown array of capture spots achieves exceedingly high spatial resolution, with a 0.5–0.8 μm separation between spots. This subcellular resolution even allows for identification of differential distribution of spliced and unspliced transcript variants as a function of nuclear localization (to see in scale with other approaches, see Fig. 2).

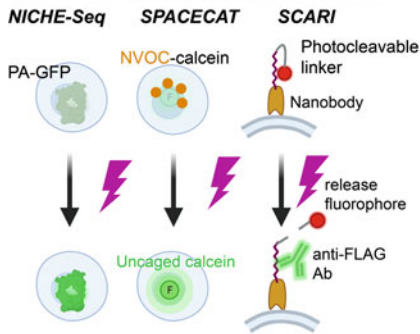
In a similar vein to Seq-Scope, PIXEL-Seq [75] also has its foundation in the organic growth of “colonies” to form clusters of barcoded capture oligonucleotides. However, this approach was performed on polyacrylamide gels which, the authors claim, allow for more uniform density of capture oligonucleotides. The resulting clusters are on the order of 1.17 microns, allowing again for subcellular spatial resolution.

DBiT-Seq meanwhile uses an ingenious microfluidic array to physically control the flow of barcoded RT primers over a tissue section, for in situ reverse transcription [76]. Clamping of the microfluidic array over the sample allows for barcoded RT primers to read out transcripts in the lane. By simply rotating the array by 90 degrees and performing a secondary amplification, the combination of two barcodes maps a given transcript to a x - y position in the section. The width of microchannels necessarily determines the capture region size and the spacing between them (50 and 10 μm sizes described). Although DBiT-Seq does not use a preexisting array of capture oligonucleotides, the microchannels effectively partition the tissue into a grid format; thus, we categorize them here.

Region-Based Selection

Another family of spatial transcriptomics techniques seeks to use tissue landmarks or features to inform selection of cells/transcripts for downstream analysis. One of the

Light-responsive chemical groups for selecting cells in ROI



Generalized workflows

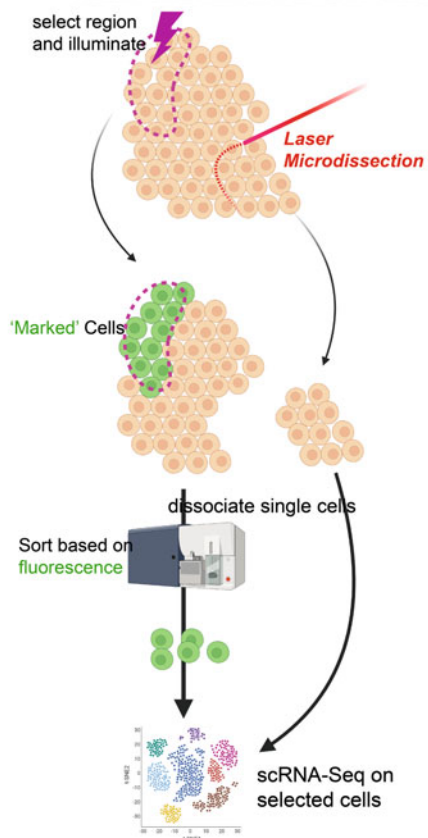


Fig. 3 Several strategies for light-based cell marking used in NICHE-Seq, SPACECAT, and SCARI. All three techniques rely on some fluorescent signal to differentiate marked cells for downstream sorting and scRNA-Seq. Laser capture microdissection physically removes a region for downstream processing, including scRNA-Seq (made with BioRender)

earliest methods in this class is the use of laser microdissection first described in 1996, in which a focused laser beam allows for physical removal of a region of interest from a tissue explant or section [77]. This region can then be processed downstream for a variety of assays including scRNA-Seq [78] such as in Geo-Seq (Fig. 3).

Light offers theoretically subcellular spatial resolution and modulating illumination has become technologically commonplace using several devices such as laser scanning confocal microscopes and digital micromirror devices (DMDs). The other part of this formula is the wide variety of chemical groups and fluorophores have been designed to react to illumination at specific wavelengths. By combining this chemistry with spatially modulated light illumination, these approaches allow for

arbitrary regions of interest (ROIs) to be defined, with cells in these regions somehow differentiated from those in the rest of the tissue (Fig. 3).

The first of such techniques, NICHE-Seq, utilizes photoactivatable GFP (PA-GFP) to mark cells of interest for downstream sorting based on fluorescence for processing via scRNA-Seq [79]. This of course necessitates the use of a genetically encoded PA-GFP in the cells of interest. In a similar vein, SPACECAT [80] uses cell-permeable dyes that upon photo-uncaging, become fluorescent, again allowing for sorting of selected cells. However, this approach does not require transgenic PA-GFP expression in the tissue/organism, which allowed the authors to explore different regions of human lung tumor biopsies. Additional chemistry could lead to orthogonal caged fluorophores that could be uncaged using different wavelengths or exhibit different fluorescent spectra, allowing for more than one ROI to be defined in the same tissue.

Along the lines of photo-uncaging, the developers of SCARI-Seq [81] made use of a photocaged FLAG-Tag attached to a cell-binding nanobody, which upon photocleavage, opens up the tag for recognition via a fluorescently labeled anti-FLAG antibody. Finally, ZipSeq directly links photo-uncaging to DNA barcoding by controlling the hybridization of a readout oligonucleotide (“ZipCode”) to a cell-anchored photocaged oligonucleotide [82]. By performing a cycle of spatially modulated illuminations and addition of distinct barcodes on top of a tissue section, the number of regions defined scales linearly with cycle number (Fig. 4). The ZipCodes hybridized to the cells are then read out alongside mRNA during common scRNA-Seq protocols, generating a parallel library for “regional demultiplexing.”

Nanostring’s GeoMX Digital Spatial Profiler (DSP) represents an interesting fusion of region-based selection and in situ hybridization approaches [83]. The protocol resembles in situ hybridization but the probe oligonucleotides contain a photocleavable linker attached to a barcode. After hybridization of a set of probes to a tissue section, ROIs can be illuminated, liberating the barcodes into solution which are collected for sequencing to quantify the levels of target transcripts within the ROI.

For this class of region-based approaches (NICHE, SPACECAT, SCARI, and ZipSeq), the selection of regions guided by some tissue architecture, geometry, or fluorescent signal is of utmost importance. To this end, the use of conventional fluorescence microscopy can provide guidance and landmarks for region definition. What these approaches lack in spatial resolution, they make up for in cellular resolution, however. Because these methods plug into existing scRNA-Seq workflows, they gain all the capabilities this workflow affords. Spatially variable gene expression can be confidently linked to a given cell type in tissue rather than relying on computational deconvolution required for other techniques such as Visium. Theoretically, these approaches can also harmonize with the growth of multimodal single-cell assays, combining single-cell gene expression, proteomics (e.g., CITE-Seq or REAP-Seq) [84], epigenome state, immune repertoire, and CRISPR screening [85].

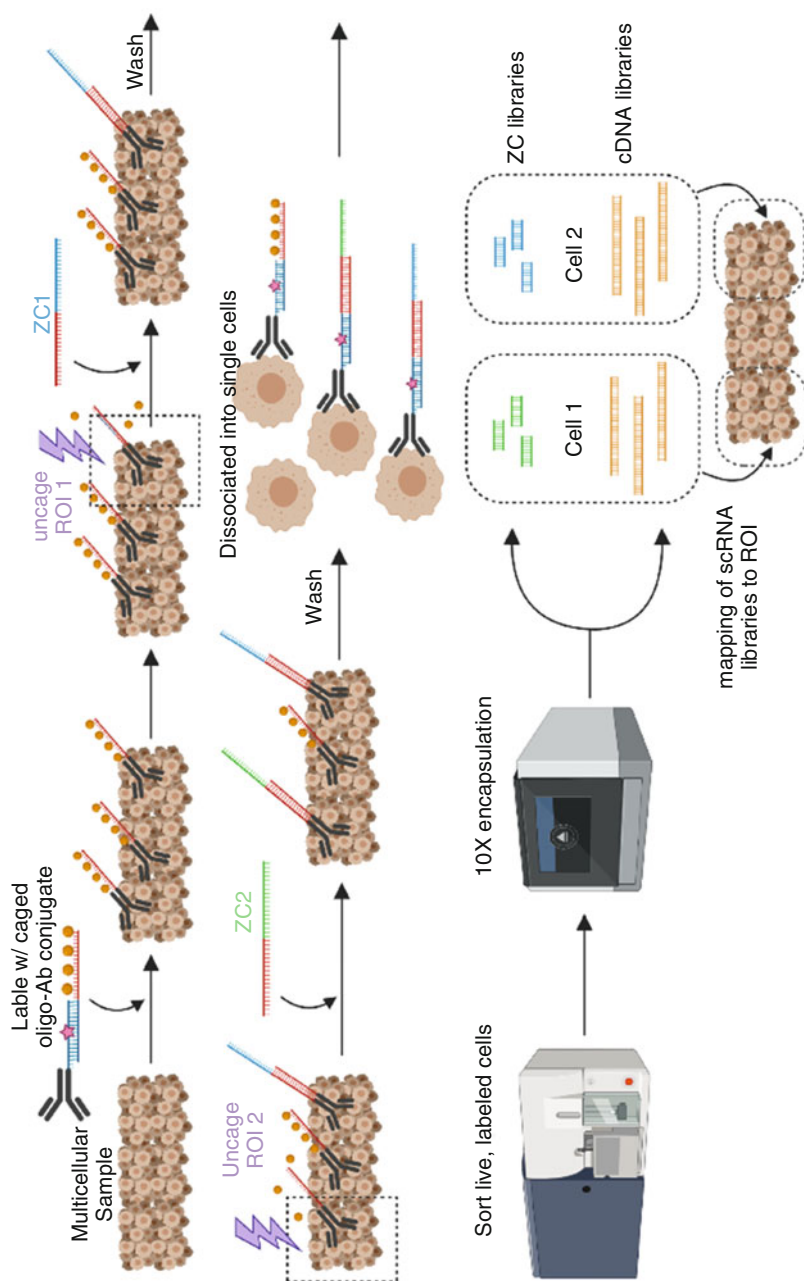


Fig. 4 Schematic of the ZipSeq workflow: a tissue section is stained with an antibody-oligo conjugate with a ssDNA overhang. This overhang is caged with 6-nitropiperonyloxyethyl (NPOM) protecting groups that prevent hybridization with complementary strand. A region of interest is selectively illuminated, removing NPOM groups. Then a complementary barcoded readout strand, or ZipCode (ZC), is added and allowed to hybridize to the now-exposed overhangs. Repetition of process scales up the number of regions defined linearly. Dissociated cells can then be run through commercially available droplet-based scRNA-

Combining Grids with “True” Single-Cell Transcriptomics

A promising middle ground that combines increased spatial resolution and “true” single-cell transcriptomic profiling makes use of an array of wells upon which a tissue section can be placed. Upon dissociation, cells fall into the wells (500 μm center-center) for permeabilization and first-round reverse transcription. By following with a combinatorial second round of barcoding, XYZeq [86] achieves single-cell transcriptomic capabilities mapped back to a grid of wells. In a further development, the authors of sci-Space [87] used a spotted grid of oligonucleotides ($\sim 140 \mu\text{m}$ with $\sim 220 \mu\text{m}$ center-center), but not to capture transcript, but rather label and thus spatially hash nuclei in a permeabilized tissue section. Following extraction of the nuclei and single-nuclei sequencing via sci-RNA-Seq [88], the authors were then able to use that hashing information to map a single nucleus transcriptome back to a grid coordinate. By iterating this spatial nucleus hashing over 14 serial sections, the authors were able to reconstruct cellular architecture and states in 3D for a mouse embryo.

Taken together, this impressive array of technologies and workflows represents the toolbox which immunologists will have to sift through in the coming years. We note that many of these approaches were tested and showed exemplary data for brain tissue. Because of the well-characterized spatial organization of the brain, this tissue is an ideal test bed to showcase the accuracy and precision of new spatial transcriptomic techniques. As these approaches emerge from their infancy and become more widespread, we will surely see their increased application toward questions in immunology.

2.2 Parameters to Consider

When considering the sheer number of approaches published and now commercially available for performing spatial transcriptomics, there are several parameters to be weighed in terms of utility for the question being asked. In this section, we will cover several of the most relevant parameters, compare approaches, and discuss their importance based on experimental context. As seen in Table 1, every approach features unique strengths while coming with its own set of considerations and caveats. Some of these “considerations” could be considered disadvantages or advantages depending on the context. For example, if examining a rare cell type, the fact that some approaches are performed on fixed or frozen sections may not be ideal as these cells cannot be sort-enriched prior to transcript capture and so rare cells

Fig. 4 (continued) Seq workflows to generate two parallel libraries: cDNA and ZipCode, allowing a single-cell transcriptome to be mapped to a region of interest using the ZipCode “hash.” Adapted from [82] with permission, © 2020 Hu et al.

Table 1 List of strengths and considerations for untargeted spatial transcriptomic approaches

Technique	Strengths	Considerations
Spatial transcriptomics (ST) [69] and Visium [70]	<ul style="list-style-type: none"> – Commercially available – Likely to see improvements in spatial resolution and capture efficiency – Can be performed on fresh/frozen and FFPE samples (with modifications) – Order of 10^4 UMI per spot 	<ul style="list-style-type: none"> – Capture spots in first iteration have resolution of $55 \mu\text{m}$ – Convolutes transcripts from all cells in capture region, potentially diluting out small/rare cell transcript contributions – Requires computational inference to assign cell proportions
HDST [73]	<ul style="list-style-type: none"> – Performed on frozen tissue sections – High spatial resolution ($2 \mu\text{m}$) allows for roughly single-cell resolution 	<ul style="list-style-type: none"> – Low UMI representation per cell (est. 175 for cell diameter of $10 \mu\text{m}$)
SLIDE-Seq v2 [72]	<ul style="list-style-type: none"> – Performed on frozen tissue sections – Moderate spatial resolution ($10 \mu\text{m}$) could represent mixture of cells but significantly less than Visium 	<ul style="list-style-type: none"> – Improved UMI/bead order of ~ 600/bead but still significantly less than other scRNA-Seq approaches assuming cell diameter of $10 \mu\text{m}$
DBiT-Seq [76]	<ul style="list-style-type: none"> – Performed on fixed, frozen tissue sections – Concurrent protein quantification through Ab-oligo conjugate staining – Average of $\sim 10^4$ UMI per $10 \mu\text{m}$ pixel, approaching droplet-based scRNA-Seq – Moderate spatial resolution ($10 \mu\text{m}$) could represent mixture of cells but significantly less than Visium 	<ul style="list-style-type: none"> – Mixture of cells in transcript pool per pixel
seq-Scope [74]	<ul style="list-style-type: none"> – Extremely high spatial resolution allowing for subcellular transcript localization – Est. $\sim 6\text{--}7$ UMI per micron and comparable UMI/cell in liver section to droplet-based scRNA-Seq – Starts with frozen tissue sections 	
SPACECAT [80]	<ul style="list-style-type: none"> – Pan-cell-type targeting permeant dye – Cells can be sorted for enrichment following – Plugs into scRNA-Seq pipelines (transcript capture efficiency dependent on workflow) 	<ul style="list-style-type: none"> – Only one demonstrated ROI per sample – Relies on penetration of reagent, – Possible UV phototoxicity – No frozen/FFPE solution
SCARI-Seq [81]	<ul style="list-style-type: none"> – Plugs into scRNA-Seq pipelines (transcript capture efficiency dependent on workflow) – Not reliant on genetically encoded reporter – Cells can be sorted for enrichment following 	<ul style="list-style-type: none"> – Requires penetration of labeling nanobody – Allows for selection of one region per sample – Targeting moiety must be adjusted for cell types of interest – No frozen/FFPE solution

(continued)

Table 1 (continued)

Technique	Strengths	Considerations
ZipSeq [82]	<ul style="list-style-type: none"> – Plugs into scRNA-Seq pipelines (transcript capture efficiency dependent on workflow) – Allows for definition of linearly scaling number of regions of interest per sample – Cells can be sorted for enrichment following 	<ul style="list-style-type: none"> – Requires penetration of labeling reagents – Targeting moiety must be adjusted for cell types of interest – UV (365 nm) could result in phototoxicity – No frozen/FFPE solution
NICHE-Seq [79]	<ul style="list-style-type: none"> – No reliance on tissue penetration of reagent (ROIs deeper in tissue) – Can utilize two-photon illumination for photoactivation – Plugs into scRNA-Seq pipelines (transcript capture efficiency dependent on workflow) – Cells can be sorted for enrichment following 	<ul style="list-style-type: none"> – Requires genetically encoded PA-GFP expression, precluding human samples – One ROI defined per sample – No frozen/FFPE solution
XYZeq [86]	<ul style="list-style-type: none"> – Performed on frozen tissue – Maintains single cell transcriptomes – Combinatorial indexing negates need for droplet-based scRNA-Seq kits 	<ul style="list-style-type: none"> – Lower spatial resolution (~500 μm) – UMIs/cell less than obtained through traditional scRNA-Seq (order of 10^3 UMI/cell)
sci-Space [87]	<ul style="list-style-type: none"> – Maintains single-nucleus resolution 	<ul style="list-style-type: none"> – Lower spatial resolution (146 μm diameter spots with 222 μm C2C) – Captures nuclei, resulting in limited transcript pool per cell ~2500 UMI/cell, however could allow for matching to scRNA-Seq data from paired sample

may be missed unless large expanses of tissue are assayed at great expense, so techniques performed on live tissues may be advantageous in this regard.

2.2.1 Targeted Versus Untargeted Approaches

Analogous to qPCR or microarrays, some spatial transcriptomic assays (e.g., FISH-based) are performed with a specific set of genes in mind (targeted). Meanwhile, another class of spatial assays resembles the nonspecific mRNA reverse transcription and sequencing via NGS (bulk RNA-Seq) which seeks to gain an “untargeted” view of transcriptome. Whether or not these workflows truly capture an unbiased quantification of all mRNA species in the cell is an ongoing issue, but the main idea is these approaches are not targeted toward any specific transcripts.

Recent advances in FISH-based methods have greatly increased the number of targets that can be detected per sample, increasing the tested order of magnitude from tens to thousands. For example, the authors of STARMap demonstrate the ability to detect 1020 transcript targets simultaneously which their clearing and error-correcting SEDAL sequencing enable [64]. The authors also note that this begins to reach the physical limit of resolution as the sheer number of detected transcripts begins to increase the density of signal, making resolution of individual amplicons more difficult. seqFISH and MERFISH have broken into the realm of tens of thousands of genes detected at a time, approaching the order of magnitude of genes often detected in scRNA-Seq [59, 62].

Working with preselected targets may be optimal depending on the question being investigated. If carefully curated for the question at hand, the gene sets available for several in situ technologies can effectively provide coverage for certain pathways of interest, with the added consideration that capturing and sequencing all mRNA in unbiased methods may not be a cost-effective method all the time. Many genes may not represent relevant sources of variability, such as housekeeping, cell cycle, mitochondrial, or ribosomal protein encoding transcripts. For practical considerations, this means occupying precious reads with genes outside of the scope of the study, crowding out reads from potential genes of interest (in effect wasted sequencing).

These approaches are not however in opposition or mutually exclusive; the cycle of target discovery, validation, and thus hypothesis generation could be neatly fulfilled by a combination of untargeted and targeted approaches. In this way, we can imagine all these technologies in an ecosystem whereby a tissue feature raises a question, leading to an untargeted approach directed at that region, followed by verification of hits via a targeted approach.

2.2.2 Lost in Reverse Transcription: Transcriptome Capture Efficiency

An important factor in whole-transcriptome capture or “untargeted” methods is the efficiency of transcript capture which translates downstream to the complexity or diversity of the cDNA library and is commonly measured by the number of unique molecular identifiers (UMI) per cell/spot/grid position. Importantly, this metric is distinguished from sequencing depth which depends on the degree of sampling from a library for sequencing. Low-complexity libraries from inefficient transcriptome capture cannot be rescued by increasing sequencing depth as UMIs begin to reoccur [89]. Below, our comparison of UMI counts should be considered in terms of orders of magnitude and taken with the caveat that UMI per unit area can highly vary due to tissue type and not solely technical considerations.

What are the consequences of low-read depth? Certain genes may experience considerable variability in their detection including “dropout” issues in which a transcript is undetected, possibly due to natural variability in transcript abundance or stochasticity in the capture and amplification [90, 91]. Lower capture rates will disproportionately impact these high dropout genes in downstream analyses.

The combination of limited mRNA capture rate and mixing of transcript contributions of all cells in tissues theoretically presents an issue for studying the immune system's activity in tissues. Immune cell representation in tissues, even inflamed ones, can be quite low compared to stromal/parenchymal cell populations. In immunologically "cold" tumors, which would be very valuable to characterize, this problem can become even worse. Compounding the issue is the highly variable RNA content of different cell types [92] depending on size and cell cycle phase. T cells have been reported to hold tenfold less transcript than much larger, cycling tumor cells [93]. When combined with their sparse distribution in a tumor setting, T cell originating transcripts are necessarily diluted by the presence of many larger, more transcriptionally abundant cells in their vicinity. Early attempts at whole-transcriptome capture suffered from low numbers of reads detected per spot, exacerbating the issue. For instance, the first iterations of SLIDE-Seq on average had 59 UMI per 10-micron bead [71] and spatial transcriptomics (ST) allowed for around 3×10^4 mean UMI per 100-micron spot (assuming 10-micron cell diameter, this translates to 300 UMI per cell). Meanwhile, HDST on average detected ~ 7 UMI per 2-micron well [73]. Extrapolating to a cell on the order of 10 microns in diameter, the estimate of 175 UMI per cell remains at least an order of magnitude less than that achieved by droplet-based scRNA-Seq workflows which already face significant dropout issues. Given the limitations in capture efficiency for untargeted spatial transcriptomic technologies, study of immune cell gene expression will likely run into difficulties when considering certain low-read-count genes.

However, new advances in capture chemistry and workflows have greatly increased the capture efficiencies of these technologies with SLIDE-Seq v2 increasing UMI per bead by ninefold in demonstrated tissues [72] and Visium (commercialized version of ST) to the order of tens of thousands UMIs per $55 \mu\text{m}$ spot. Meanwhile DBiT-Seq achieves a similar UMI representation with a significantly smaller "pixel" size of $10 \mu\text{m}$ [76]. Seq-Scope, with its extremely high resolution, manages to achieve a similar "area density" of UMIs as DBiT-Seq, with estimated UMI/cell approaching that of droplet-based scRNA-Seq [74].

Methods that make use of existing single-cell workflows, such as droplet-based ones, take advantage of the greater capture efficiency afforded by these techniques. Regional selection techniques, while affording low spatial resolution and often only a handful of selected regions, can nevertheless plug directly into scRNA-Seq workflows. While the actual number of UMIs and genes detected is heavily dependent on cell type, we can nevertheless make order of magnitude judgments in the relative efficiencies. Direct comparison of droplet-based assays from 10X Genomics with well-based Smart-Seq2 showed UMIs on the order of 10^4 and 10^6 per cell, respectively [94]. This provides a benchmark against which solid-phase capture techniques such as Visium, SLIDE-Seq, etc. can be compared.

Techniques such as XYZeq and sci-Space sit in a middle ground, preserving single-cell/nuclei transcriptomes with relatively high spatial resolution in a grid layout. XYZeq, while maintaining single-cell assignment of transcripts, displays on the order of 10^3 of UMI per cell. For large, RNA-rich cell lines such as HEK293T and NIH3T3 that the authors used, we would estimate a one order of magnitude

decrease compared to droplet-based scRNA-Seq methods. Because sci-Space captures single nuclei, it naturally suffers from comparably fewer UMIs than entire cells (order of 2500 UMIs). However, the authors posit that matching single-nuclei data with a paired scRNA-Seq dataset, more complete single-cell transcriptomes can be mapped back into the coordinates defined by sci-Space on nuclei [87]. Of course, capture efficiency is just one parameter when considering approaches and its importance varies with the aims of the study.

2.2.3 Spatial Resolution: How Low Can We Go?

Just as microscopy has evolved ever-increasing levels of spatial resolution, so too has the race for spatial transcriptomic technologies. Of course, *in situ* techniques such as smFISH/MERFISH/seqFISH can achieve unparalleled spatial resolution, theoretically limited by the ability to resolve signals originating from individual mRNA transcripts. With these techniques, researchers can describe precise subcellular localization of transcripts such as dendritic or axonal localizations in neurons. Super-resolution microscopy has been used to aid resolution of single mRNA molecules in a crowded cellular environment [58]. However, approaches such as seqFISH+ which use a binary ON/OFF barcode mitigate the issue, greatly reducing the number of fluorescent signals that must be resolved per frame, similar in concept to super-resolution techniques such as PALM and STORM [62].

Certain technologies are limited in their spatial resolution by the physical size of the capture spots or partitioning material as seen in Visium (55 micron), SLIDE-Seq (10 micron), XYZeq (500 micron), HDST (2 micron), and DBiT-seq (50 or 10 micron). Other technologies using light-based regional selection, such as ZipSeq, SPACE-CAT, and SCARI-Seq, are limited theoretically by the diffraction limit of light. However, “selecting” a single cell at a time for downstream sorting and sequencing is very low throughput and likely unfeasible, thus restricting these techniques to larger regions containing a more reasonable number of cells (e.g., 200-micron B follicles in ZipSeq [82]).

For most solid-support capture techniques, the question of spatial resolution is intimately linked to the question of what cell this transcript came from. Capture zones on the order of or larger than a typical cell face the issue of deconvolving the transcript contribution of a collection of cells within the capture zone (e.g., Visium). A considerable amount of computational effort is currently directed at dealing with the issue of untangling the mix of transcripts obtained (discussed below). Techniques such as XYZeq and sci-Space escape this conundrum, using physical partitioning or *in situ* barcoding of intact cells/nuclei, respectively. Techniques that achieve subcellular resolution such as Seq-Scope and PIXEL-Seq also avoid this issue, and using cell segmentation, users can partition detected reads as belonging to a given cell. This, of course, necessitates accurate cell segmentation which can depend on image quality, membrane marker used, and the tissue/cell types being considered [95]. For a sense of scale regarding capture regions, please refer to Fig. 2.

2.2.4 What Kind of Samples Can We Use?

Another important consideration is the type of sample that the method can use as input. For human tissues, this consideration takes on greater import as fresh tissue samples are necessarily difficult to obtain on-demand. Banking of specimens has several significant advantages, one being the ability to process a large number of banked samples simultaneously, removing potential batch effects. In addition, being able to tap into the extensive existing tissue banks is a major advantage. Many of the techniques covered, such as Visium, HDST, Seq-Scope, XYZeq, and others, can be applied to fresh frozen tissue sections. Meanwhile ZipSeq, NICHE-Seq, SPACE-Cat, and SCARI-Seq were demonstrated on live tissue sections.

Formalin-fixed paraffin-embedded (FFPE) samples represent a very stable storage solution for tissues with massive existing specimen banks. Extracted macromolecules (RNA/DNA/protein) have been shown to be stable for at least 12 years in FFPE samples [96]. However, the process of fixation itself along with storage temperatures is known to significantly impact the quality of extracted RNA from FFPE samples [97]. 10x Genomics has tackled spatial transcriptomics in FFPE samples using pairs of probes directed against the entire transcriptome which are ligated to form an intact probe. It is this hybridized probe strand that it ultimately captured by the standard Visium spot array, avoiding the need to liberate endogenous RNA strands cross-linked to proteins within the sample.

3 What Has Been Done with Spatial Transcriptomics in Studying Immunology?

Many of the “newer” technologies discussed have yet to be applied toward studying the immune system in situ, including inflamed tissues and tumor settings. Many of these techniques have been validated in brain tissue but are certainly ready to be applied to other tissues. In this section, we will cover what has been done with spatial transcriptomics in studying the immune system in situ and emphasize the strategies the studies used for integrating spatial transcriptomic data with other assays and using them to inform downstream hypothesis generation.

3.1 Skin Wound Healing

The healing skin wound undergoes phases of inflammation followed by repair and resolution. The anatomy of a full-thickness wound has x - y coordinates (inner and outer wound areas) as well as a z -dimension (dermal layers), making localization of gene expression essential for studying cellular coordination in this process. In a recent study, Visium was applied to cross sections from a healing skin wound to

reveal expression patterns at several timepoints following wounding. By using paired scRNA-Seq data, they were able to estimate the contribution and thus local abundance of four major fibroblast subpopulations [98]. Going further, the authors integrated scATAC-Seq data in order to impute the epigenetic state of fibroblasts as a function of spatial localization.

3.2 *The Tumor Microenvironment*

The tumor environment represents a spatially heterogeneous environment. With the advent of cancer immunotherapy, analyzing the state of immune cells and where they reside in the tumor space has become a major application for spatial transcriptomics [6]. Due to the accumulation of mutations during tumor development and outgrowth of clones, the tumor can represent a spatially heterogeneous landscape of genotypes. The selective pressure of the immune system leads to immunoediting of the tumor whereby tumor clones undergo antigenic escape [99]. Models of antigen escape sometimes use mosaic tumors formed from co-injection of antigen-positive/antigen-negative tumor lines [100]. SCARI-Seq made its debut selecting antigen-specific CD8⁺ T cells from antigen⁺ and antigen⁻ regions of such a mosaic tumor model to address the activity of the immune response in these regions. The authors found increased expression of soluble effector molecules from antigen-specific CD8⁺ T cells isolated from antigen⁺ regions vs antigen⁻ regions [81]. Given the ability of secreted cytokines, such as interferon gamma, to diffuse hundreds of microns beyond the site of secretion, spatial dissection of the borders between these regions would likely yield additional insights [100].

Recently, the meaning of tissue “atlases” has been revamped with the addition of the spatial dimension. Nieto et al. created a true tumor atlas by combining scRNA-Seq of tumor-infiltrating immune cells with data gained from Visium [101]. By using the NMF-based matrix decomposition technique SPOTLight [102], the authors were able to define several key immune subpopulations and impute the proportions of these cells within each capture spot. Using this information, the authors described co-localization of certain immune populations such as exhausted CD8⁺ T cells and C1QC-expressing macrophages. Similar to clustering of cells in scRNA-Seq analysis, spots can be clustered, defining distinct domains of the tumor with certain signature proportions. Visium has also been applied to cutaneous squamous cell carcinoma (cSCC) patient samples for identification of gene expression patterns localized to the leading edge of the tumor as identified via H & E staining [103]. The authors found an inflammatory signature localized to the edge, with co-localization of several immune cell populations including exhausted CD8⁺ T cells and regulatory T cells. Nagasawa S. et al. made use of Visium in studying gene expression as related to the structure of ductal carcinoma in situ (DCIS) [104]. Interestingly, the authors were able to link altered spatial patterns of gene expression to localization of mutant GATA3 transcripts, examining the sequenced 3' end of captured GATA3 transcripts

to find Visium spots containing cells with GATA3 variants, demonstrating a fusion of the genome and transcriptome information.

In a similar vein, the work from XYZeq also describes varying compositions of immune cell types relative to tumor core, surrounding stroma, and the margins between these regions in a model of MC38 colon adenocarcinoma metastasis in the liver [86]. The authors went further than just cell-type composition and were able to describe a gradient of gene expression as a function of proximity to tumor mass. Such spatially variable gene expression patterns showcase the power of spatial transcriptomics to align vectors in space with vectors of gene expression changes.

The PyMT mouse model is widely used genetically engineered mouse model in which insertion of an MMTV-PyMT (polyoma middle T antigen) cassette in the genome serves as an oncogene expressed in the mammary gland, resulting in spontaneous tumorigenesis that advances through stages mirroring those in patients [105]. ZipSeq, when applied to the mouse PyMT chOVA (mCherry-ovalbumin) breast cancer model, identified increasing differentiation of monocytes to macrophages correlating with increased tumor depth as well as an increased terminal exhaustion signature score in adoptively transferred OTI CD8⁺ T cells [82]. In a recent study in a B78 tumor model, ZipSeq again identified a spatially correlated increase in CD8⁺ T cell exhaustion with increasing monocyte-to-macrophage differentiation. Analysis of spatial patterns of gene expression suggests the role of *Csf1* and *Ccl3/4* expression by exhausted CD8⁺ T cells in driving this macrophage differentiation in the tumor interior [106].

Targeted FISH-based technologies serve as excellent methods for bridging the gap between scRNA-Seq and the imaging realm. scRNA-Seq is invaluable for identification of population heterogeneity, highlighting subpopulations with unique differentially expressed genes. However, finding these populations in space via immunofluorescent staining is not always trivial, given the lack of antibodies for many proteins and the potential mismatch between proteome and transcriptome [107, 108]. By “staining” for the transcripts of interest, we can gain a more direct translation from scRNA-Seq to imaging, and with a priori knowledge of a gene set such as gene signature defining a cell subpopulation, the probe panel can be optimally designed. For example, in the tumor immunology space, MERFISH was used with a 135-gene panel to demonstrate the proximity of macrophages to glioblastoma cells undergoing a transition to a mesenchymal-like state, supporting a model where macrophage-derived oncostatin M drives this process [109]. In another exciting development, Pelka et al. defined co-occurring gene programs being executed across immune cell types in patient colorectal samples, which they term “hubs.” Armed with the knowledge of the top-contributing genes to these programs of interest, the authors used an in situ hybridization approach to map the activation of these programs in tissue space relative to each other [110]. Understanding the spatial localization of these hubs allows for a tissue to be described as a mosaic of these multi-cell-type hubs, revealing the cell-cell communication axis that determines tissue state.

3.3 *Lymphoid Tissues*

Moving beyond tumor immunology, ZipSeq has been applied to spatially dissecting the lymph node at rest. Partitioning the lymph node into T and B zones using spatial barcodes revealed the expected biases in T and B cell compositions [82]. Using a higher-resolution second layer of photocaging allowed for a four-region delineation moving from the deep T cell zone to the B follicles, revealing finer details on the localization of subsets of T and B cells as well as rarer populations such as NK cells found predominantly in interfollicular regions. With this four-region definition, the authors describe spatial profiles of gene expression such as *Ccr7* and *Klf2* displaying a monotonic decrease moving out from the deep T cell zone into the B cell zone.

Still in the lymph node space, the authors of NICHE-Seq applied their photoactivation-based technique toward studying changes in cellular composition in distinct regions of the lymph node and spleen following infection with the lymphocytic choriomeningitis virus (LCMV) and the vesicular stomatitis virus (VSV). Infection with LCMV or VSV results in markedly different immune responses in the mouse, with stronger cell-mediated or humoral response, respectively. NICHE-Seq was applied to study the differences in the priming niches CD4⁺ T cells experienced in VSV and LCMV infections that propagate these divergent responses [111]. Photoactivated cells in the vicinity of fluorescently labeled antigen-specific CD4⁺ clusters in the lymph node were sorted for scRNA-Seq, which revealed an interferon response signature upregulated in niches during LCMV infection vs. VSV, leading to the hypothesis that timing of type I interferon is a deciding factor in CD4⁺ differentiation into a Tfh or Th1 fate. These NICHE-Seq studies highlight the capability of region-based selection to uncover spatially restricted gene expression patterns that ultimately inform downstream hypothesis generation. These studies also relied on selection of one set of ROIs based upon a fluorescent readout such as transgenically expressed GFP in CD4⁺ T cells in this example.

As mentioned above, in situ hybridization techniques serve as powerful tools for mapping the heterogenous clusters derived from scRNA-Seq experiments back to the tissue. For example, Xiang et al. used RNAscope to physically map lymphatic endothelial cell (LEC) subpopulations identified in a scRNA-Seq dataset to regions in the lymph node [112].

3.4 *Infectious Disease and Autoimmunity*

In the realm of infectious diseases, the emergence of SARS-CoV-2 raised new questions about the role of various actors in the immune system in balancing viral control with pathological tissue damage in the lung [113]. Using the DSP approach, Delorey et al. characterized the spatially heterogenous gene expression patterns found in SARS-CoV-2-infected lungs, using anatomical features and amount of

local SARS-CoV-2 RNA detected to define regions of interest [114]. Using this approach, the authors identified differentially expressed genes found in regions with high levels of SARS-CoV-2 RNA, including some with unknown functions in the immune response. In this example, spatial transcriptomics enabled discovery of potential targets for mechanistic follow-up using selection of regions based on fluorescent landmarks (SARS-CoV-2 RNA quantity), again highlighting the utility of pairing imaging with transcriptomics.

With regard to autoimmune inflammation, application of spatial transcriptomics (ST) technology to rheumatoid arthritis (RA) and spondyloarthritis patients allowed the authors of this study [115] to zoom in specifically into regions of increased immune infiltration visualized via H & E staining. In a follow-up publication, Hardt et al. used ST on synovial biopsies from RA patients to ask what tissue niches autoreactive memory B and plasma cells inhabit and what cell-cell interactions might generate these niches [116]. Again, demonstrating the utility of integrating scRNA-Seq with spatial data, the authors used gene signatures derived from scRNA-Seq to estimate cell-type frequencies across the tissue section, finding co-localization of plasma cells with CCR7⁺ T cells. Concurrently, CXCL12 reads were also spatially correlated with plasma cell signatures, suggesting a signaling axis driving the maintenance of these pro-plasma cell niches.

As seen in this sampling of recent published works, the range of spatial transcriptomic techniques have already begun to demonstrate their utility in answering questions in the immunology space. Importantly, as tools for discovery, these techniques have yielded actionable and verifiable candidate genes and cell types underlying tissue heterogeneity. It will be exciting to see what new discoveries continue to be made with wider adoption of spatial transcriptomic techniques.

4 We Have Our Data, Now What? How Do We Analyze Spatial Transcriptomic Data? And Where Can We Go from Here?

One way to analyze spatial transcriptomic data is to relate the patterns of expression to features of interest in the tissue. The big question remains: what are the relevant tissue features that we center our analysis around? In the examples we have covered so far, studies have used a combination of endogenous fluorescent reporters, H & E staining, and immunofluorescent staining to designate tissue features against which spatial expression data can be mapped to. However, as we explore below, there are marker-free analyses that work independently of any tissue features to identify patterns of gene expression.

When trying to make meaning of spatially resolved transcriptomics, analysis techniques can run the gamut, with a diverse set of software packages and algorithms for analysis. For example, Giotto represents an environment with multiple computational tools for discovery of genes with colocalized expression and thus shared

spatial patterns [117]. One example of the methods implemented by Giotto is spatial pattern recognition via kernels or SPARK which uses a Gaussian process regression to identify marker-free patterns of gene expression [118].

4.1 *Deconvolving Spatial Transcriptomes*

Capture techniques that are not single-cell in their resolution will require a computational backend to impute the individual cellular contributions to the “blended” transcriptome captured in a spot. The issue of disentangling the cellular contributions from spot-based transcript capture methods such as Visium has motivated a host of computational work-arounds [119]. One approach, SPOTLight, makes use of non-negative matrix factorization (NMF) which identifies sets of co-expressed genes and assigns a weight for these metagenes for every spot corresponding to the cell-type abundance. The metagenes in this context can be thought of as cell-type-specific signatures, a collection of genes that define a cell type.

Having a paired scRNA-Seq dataset can greatly help in this deconvolution as seen in Cell2location which uses the expression signature of clusters defined by scRNA-Seq to then estimate the abundance of each cell type in a Visium spot [120]. Using paired scRNA-Seq and Visium data from a human tonsil, the authors imputed cell-type abundances per spot. In order to decompose the array of cell abundances over space into a series of overlaid patterns, the authors then applied NMF to find groupings of cell types with shared spatial distributions. This marker-free approach was then able to identify spatial patterns that corresponded well with annotations on a paired H & E image (e.g., within or excluded from germinal centers). In a similar vein, robust cell-type decomposition (RCTD) uses scRNA-Seq and models each Visium spot’s count matrix as a linear combination of single-cell expression profiles with Poisson distributed numbers of observed counts for a gene [121]. In another approach, the authors used estimates of cell numbers from the paired H & E image and expression data from paired scRNA-Seq to subtract out contributions from cells other than fibroblasts to focus on their distribution [98].

4.2 *Extracting Cell-Cell Communication*

A major motivation behind spatial transcriptomic analysis of the immune system is the potential to elucidate signaling pathways for cell-cell communication that position immune cells and influence their expression state. As we discussed above, immune cells are often found in specific niches, maintained by a balance of signaling, both long (e.g., cytokines) and short range (e.g., integrins).

Several computational methods have emerged to predict possible ligand-receptor interactions, independent of spatial information. CellPhoneDB and CellChat use expression levels of known receptor-ligand pairs from scRNA-Seq clusters to predict

possible cell-cell communication pathways [122, 123]. NicheNet approaches this issue from a different perspective, looking instead at the expression of known upregulated genes downstream of a receptor rather than the expression of the receptor itself, essentially the transcriptomic “footprint” of the ligand-receptor interaction [124]. Meanwhile, Tensor-cell2cell models cell-cell communication strengths varying over many contexts at once as a 4D tensor [125]. Decomposition allows the fourth dimension, the effective context profile to be extracted for a given L-R pair between two cell types; this profile could represent varying signaling strengths over time or spatial contexts.

Integrating these methodologies with spatial information would greatly enhance the confidence in the imputed signaling; for instance, a juxtacrine signaling pathway would be far more likely to occur in close spatial proximity between sender and receiver. Several computational methods have explicitly integrated spatial elements into their workflows including Giotto [117], MISTy [126], and SpaOTsc [127].

4.3 *Building a Spatial Compendium of Tumors*

With the wealth of technologies discussed here, we can be confident that the applications described represent just the tip of the iceberg as more and more studies incorporate spatial transcriptomic data. Here we discuss briefly where these technologies may see the most usage and promise.

As mentioned above, major efforts are being made to profile the immune compartment of human tumors, looking for relevant metrics to use for prediction of patient survival and response to ICB. A major step will be the construction of spatial profile compendia to complement the existing databases of single-cell and bulk transcriptomics. Given the throughput necessary to undertake such an endeavor and the preference for banked FFPE samples, commercially available solutions such as Visium may be the go-to approach. Samples paired with scRNA-Seq will be especially powerful in this case, allowing for the computational deconvolution of Visium “spots” as we discussed before [102]. Combined with pathologist annotations of H & E imaging, this spatial data can be placed into context with tissue architecture.

Some considerations must be made in terms of sample acquisition protocol. As many of the approaches described rely on thin (~10 micron) sections, ensuring that sections are representative of the tumor is of great importance. For example, TLS are often found in the stroma surrounding the tumor core [35]; thus, these features will be missed with biopsy sampling of just the tumor mass itself.

With the added dimensions of space, finding the latent, most biologically relevant metrics to describe spatial patterns of immune cell gene expression becomes crucial when trying to find correlation with clinical outcomes. Previous correlative pan-cancer studies used measures such as percentages of populations and TPMs of genes of interest; spatially resolved datasets will require new ways of describing the TME. Metrics such as nearest cell-cell distances, degree of intermixing/

sequestration, and alignment with spatial vectors could represent a good start. No doubt, the field can borrow much from the spatial statistics already developed for analyzing geographical or demographic datasets.

4.4 Spatial Transcriptomics Applied to Organoids

The applications we describe have been performed on naturally developing tissues. For human tissues, this usually means we necessarily get a retrospective view when it comes to perturbations such as infection, inflammation, or tumorigenesis. We also lose the capability to introduce our own perturbations to the system such as pharmacological screening or gene editing.

Organoids have emerged as a promising solution to create *in vitro* models of multicellular tissues that can be derived from primary cells dissociated from patient samples [128]. Organoids generated from banked patient samples can provide more relevant models for disease in many tissue settings (e.g., intestine, brain, tumor) and enable high-throughput assays. For example, tumor organoids can be combined with immune cells to provide a tractable model system for studying tumor-intrinsic mechanisms for influencing the state of infiltrating immune cells. We anticipate a powerful synergy between the development of new organoid models and the use of spatial transcriptomic technologies in the years to come.

5 Conclusion

Future studies employing spatial transcriptomics will need to balance the trade-offs in capture efficiency, spatial resolution, single-cell or multi-cell transcriptomics, infrastructure/equipment needs, and sample requirements, among other myriad considerations. In addition, the data generated will require the use of specialized analytical tools, which can range from existing tools for transcriptomic analysis to pipelines incorporating image analysis, cell segmentation, and novel spatial algorithms. In many instances, this data must also be overlaid with imaging data to provide clues as to how a given cell's local environment is tied to its expression pattern.

We can anticipate the arrival of novel, ever-improving spatial techniques in the ecosystem of transcriptomics tools and the symbiotic analysis tools that accompany them. Simultaneously, the approaches described here will likely see rapid iterative improvements in capabilities (e.g., SLIDESeq to SLIDESeq v2) and application to a wider set of tissue types and questions. We might also anticipate the addition of new -omics modalities such as epigenetic information and the integration of multiple high-dimensional data types using methods such as a recently published “weighted nearest-neighbor” approach by Hao et al. but applied to spatial coordinates [129].

The development of emergent spatial transcriptomic approaches was motivated by the promise that marriage of the transcriptional dimension with the physical would enable a new crop of discoveries in tissue biology. It remains to be seen how the approaches described will deliver on this promise in the field of immunology and indeed the real proof of concept will be what new biology is revealed that was unattainable via microscopy or scRNA-Seq alone. The next half-decade or so will likely see the same maturation of spatial transcriptomics that single-cell sequencing has witnessed (for reference, the first droplet-based scRNA-Seq methods were published only in 2015 [130, 131]). Investigators hoping to tap into this projected growth should consider the unique strengths/weaknesses of approaches, what spatial features and metrics are most appropriate for their question, and the computational applications for fully leveraging these rich datasets. Ultimately, there are now enough choices of spatial transcriptomic approaches with a sufficiently broad range of strengths and weaknesses that research questions should motivate the choice of tool rather than the other way around.

Compliance with Ethical Standards Funding: K.H.H. is funded by the American Cancer Society and the Jean Perkins Foundation through a postdoctoral fellowship [133078-PF-19-222-01-LIB].

Conflict of Interest: K.H.H. has received a speaker honorarium from Illumina.

Ethical Approval: No human or animal research was directly involved in the writing of this chapter.

References

1. Hwang B, Lee JH, Bang D. Single-cell RNA sequencing technologies and bioinformatics pipelines. *Exp Mol Med*. 2018;50:1–14. <https://doi.org/10.1038/s12276-018-0071-8>.
2. Mimitou EP, Lareau CA, Chen KY, Zorzetto-Fernandes AL, Hao Y, Takeshima Y, et al. Scalable, multimodal profiling of chromatin accessibility, gene expression and protein levels in single cells. *Nat Biotechnol*. 2021;39:1246–58. <https://doi.org/10.1038/s41587-021-00927-2>.
3. Moses L, Pachter L. Museum of Spatial Transcriptomics. *bioRxiv*. 2021.; 2021.05.11.443152; <https://doi.org/10.1101/2021.05.11.443152>.
4. Dries R, Chen J, del Rossi N, Khan MM, Sistig A, Yuan G-C. Advances in spatial transcriptomic data analysis. *Genome Res*. 2021;31:1706–18. <https://doi.org/10.1101/gr.275224.121>.
5. Lewis SM, Asselin-Labat M-L, Nguyen Q, Berthelet J, Tan X, Wimmer VC, et al. Spatial omics and multiplexed imaging to explore cancer biology. *Nat Methods*. 2021;18:997–1012. <https://doi.org/10.1038/s41592-021-01203-6>.
6. Fu T, Dai L-J, Wu S-Y, Xiao Y, Ma D, Jiang Y-Z, et al. Spatial architecture of the immune microenvironment orchestrates tumor immunity and therapeutic response. *J Hematol Oncol*. 2021;14:98. <https://doi.org/10.1186/s13045-021-01103-4>.
7. Maniatis S, Petrescu J, Phatnani H. Spatially resolved transcriptomics and its applications in cancer. *Curr Opin Genet Dev*. 2021;66:70–7. <https://doi.org/10.1016/j.gde.2020.12.002>.
8. Francis K, Palsson BO. Effective intercellular communication distances are determined by the relative time constants for cyto/chemokine secretion and diffusion. *Proc Natl Acad Sci*. 1997;94:12258–62. <https://doi.org/10.1073/pnas.94.23.12258>.

9. Zhou X, Franklin RA, Adler M, Mayo A, Alon U, Medzhitov R, et al. Circuit design features of a stable two-cell system circuit design features of a stable two-cell system. *Cell*. 2018;172:744–7.e17. <https://doi.org/10.1016/j.cell.2018.01.015>.
10. Grant SM, Lou M, Yao L, Germain RN, Radtke AJ. The lymph node at a glance—how spatial organization optimizes the immune response. *J Cell Sci*. 2020;133:1–7. <https://doi.org/10.1242/jcs.241828>.
11. Gerner MY, Casey KA, Kastentmuller W, Germain RN. Dendritic cell and antigen dispersal landscapes regulate T cell immunity. *J Exp Med*. 2017;214:3105–22. <https://doi.org/10.1084/jem.20170335>.
12. Kitano M, Yamazaki C, Takumi A, Ikeno T, Hemmi H, Takahashi N, et al. Imaging of the cross-presenting dendritic cell subsets in the skin-draining lymph node. *Proc Natl Acad Sci*. 2016;113:1044–9. <https://doi.org/10.1073/pnas.1513607113>.
13. Eisenbarth SC. Dendritic cell subsets in T cell programming: location dictates function. *Nat Rev Immunol*. 2019;19:89–103. <https://doi.org/10.1038/s41577-018-0088-1>.
14. Baptista AP, Gola A, Huang Y, Shapiro VS, Gerner MY, Germain RN, et al. The chemoattractant receptor Ebi2 drives article the chemoattractant receptor Ebi2 drives intranodal naive CD4 + T cell peripheralization to promote effective adaptive immunity. *Immunity*. 2019;50:1188–201.e6. <https://doi.org/10.1016/j.immuni.2019.04.001>.
15. Yi T, Cyster JG. EBI2-mediated bridging channel positioning supports splenic dendritic cell homeostasis and particulate antigen capture. *elife*. 2013;2013:1–19. <https://doi.org/10.7554/eLife.00757>.
16. Moran I, Grootveld AK, Nguyen A, Phan TG. Subcapsular sinus macrophages: the seat of innate and adaptive memory in murine lymph nodes. *Trends Immunol*. 2019;40:35–48. <https://doi.org/10.1016/j.it.2018.11.004>.
17. Bajénoff M, Breart B, Huang AYC, Qi H, Cazareth J, Braud VM, et al. Natural killer cell behavior in lymph nodes revealed by static and real-time imaging. *J Exp Med*. 2006;203:619–31. <https://doi.org/10.1084/jem.20051474>.
18. Garrod KR, Wei SH, Parker I, Cahalan MD. Natural killer cells actively patrol peripheral lymph nodes forming stable conjugates to eliminate MHC-mismatched targets. *Proc Natl Acad Sci*. 2007;104:12081–6. <https://doi.org/10.1073/pnas.0702867104>.
19. Hampton HR, Chtanova T. Seminars in immunology the lymph node neutrophil. *Semin Immunol*. 2016;28:129–36. <https://doi.org/10.1016/j.smim.2016.03.008>.
20. Rodda LB, Lu E, Bennett ML, Sokol CL, Wang X, Luther SA, et al. Single-cell RNA sequencing of lymph node stromal cells reveals niche-associated heterogeneity. *Immunity*. 2018;48:1014–1028.e6. <https://doi.org/10.1016/j.immuni.2018.04.006>.
21. Bonnardel J, Jonck WT, Gaublomme D, Elewaut D, Saeys Y, Guillemins M, et al. Imprint the Kupffer cell identity on monocytes colonizing the liver macrophage niche article stellate cells , hepatocytes , and endothelial cells imprint the Kupffer cell identity on monocytes colonizing the liver macrophage niche. *Immunity*. 2019;51:638–54.e9. <https://doi.org/10.1016/j.immuni.2019.08.017>.
22. Nguyen-Lefebvre AT, Horuzsko A. Kupffer cell metabolism and function. *J Enzymol Metab*. 2015;1:139–48.
23. Kabashima K, Honda T, Ginhoux F, Egawa G. The immunological anatomy of the skin. *Nat Rev Immunol*. 2019;19:19–30. <https://doi.org/10.1038/s41577-018-0084-5>.
24. Rahmani W, Sinha S, Biernaskie J. Immune modulation of hair follicle regeneration. *npj Regen Med*. 2020;5:9. <https://doi.org/10.1038/s41536-020-0095-2>.
25. Tang A, Amagai M, Granger LG, Stanley JR, Uddy MC. Adhesion of epidermal Langerhans cells to keratinocytes mediated by E-cadherin. *Nature*. 1993;361:82–5. <https://doi.org/10.1038/361082a0>.
26. Stoitzner P, Stössel H, Romani N, Pfaller K. A close-up view of migrating Langerhans cells in the skin. *J Invest Dermatol*. 2002;118:117–25. <https://doi.org/10.1046/j.0022-202x.2001.01631.x>.

27. Binnewies M, Roberts EW, Kersten K, Chan V, Fearon DF, Merad M, et al. Understanding the tumor immune microenvironment (TIME) for effective therapy. *Nat Med.* 2018;24:541–50. <https://doi.org/10.1038/s41591-018-0014-x>.
28. Bonaventura P, Shekarian T, Alcazer V, Valladeau-Guilemond J, Valsesia-Wittmann S, Amigorena S, et al. Cold tumors: a therapeutic challenge for immunotherapy. *Front Immunol.* 2019;10:1–10. <https://doi.org/10.3389/fimmu.2019.00168>.
29. Broz ML, Binnewies M, Boldajipour B, Nelson AE, Pollack JL, Erle DJ, et al. Dissecting the tumor myeloid compartment reveals rare activating antigen-presenting cells critical for T cell immunity. *Cancer Cell.* 2014;26:638–52. <https://doi.org/10.1016/j.ccell.2014.09.007>.
30. Ratajczak MZ, Bujko K, Mack A, Kucia M, Ratajczak J. Cancer from the perspective of stem cells and misappropriated tissue regeneration mechanisms. *Leukemia.* 2018;32:2519–26. <https://doi.org/10.1038/s41375-018-0294-7>.
31. Vitale I, Shema E, Loi S, Galluzzi L. Intratumoral heterogeneity in cancer progression and response to immunotherapy. *Nat Med.* 2021;27:212–24. <https://doi.org/10.1038/s41591-021-01233-9>.
32. Dieu-Nosjean MC, Goc J, Giraldo NA, Sautès-Fridman C, Fridman WH. Tertiary lymphoid structures in cancer and beyond. *Trends Immunol.* 2014;571–80. <https://doi.org/10.1016/j.it.2014.09.006>.
33. Mitra S, Johansson I, Phung B, Harbst K, Vallon-christersson J, Van SA, et al. Tertiary lymphoid structures improve immunotherapy and survival in melanoma. *Nature.* 2020:577. <https://doi.org/10.1038/s41586-019-1914-8>.
34. Munoz-erazo L, Rhodes JL, Marion VC, Kemp RA. Tertiary lymphoid structures in cancer—considerations for patient prognosis. *Cell Mol Immunol.* 2020; <https://doi.org/10.1038/s41423-020-0457-0>.
35. Sautès-Fridman C, Petitprez F, Calderaro J, Fridman WH. Tertiary lymphoid structures in the era of cancer immunotherapy. *Nat Rev Cancer.* 2019;19:307–25. <https://doi.org/10.1038/s41568-019-0144-6>.
36. Di Pilato M, Kfuri-Rubens R, Pruessmann JN, Ozga AJ, Messemaker M, Cadilha BL, et al. CXCR6 positions cytotoxic T cells to receive critical survival signals in the tumor microenvironment. *Cell.* 2021;184:4512–30.e22. <https://doi.org/10.1016/j.cell.2021.07.015>.
37. Stoltzfus CR, Sivakumar R, Kunz L, Olin Pope BE, Menietti E, Speziale D, et al. Multi-parameter quantitative imaging of tumor microenvironments reveals perivascular immune niches associated with anti-tumor immunity. *Front Immunol.* 2021;12:1–18. <https://doi.org/10.3389/fimmu.2021.726492>.
38. Bagaev A, Kotlov N, Nomie K, Svekolkin V, Gafurov A, Isaeva O, et al. Conserved pan-cancer microenvironment subtypes predict response to immunotherapy. *Cancer Cell.* 2021;39:845–65.e7. <https://doi.org/10.1016/j.ccell.2021.04.014>.
39. Cheng S, Li Z, Gao R, Xing B, Gao Y, Yang Y, et al. A pan-cancer single-cell transcriptional atlas of tumor infiltrating myeloid cells. *Cell.* 2021;184:792–809.e23. <https://doi.org/10.1016/j.cell.2021.01.010>.
40. Combes AJ, Samad B, Tsui J, Chew NW, Yan P, Reeder GC, et al. Discovering dominant tumor immune archetypes in a pan-cancer census. *Cell.* 2022;185:184–203.e19. <https://doi.org/10.1016/j.cell.2021.12.004>.
41. Nearchou IP, Gwyther BM, Georgiakakis ECT, Gavriel CG, Lillard K, Kajiwarra Y, et al. Spatial immune profiling of the colorectal tumor microenvironment predicts good outcome in stage II patients. *npj Digit Med.* 2020;3. <https://doi.org/10.1038/s41746-020-0275-x>.
42. Heindl A, Sestak I, Naidoo K, Cuzick J, Dowsett M, Yuan Y. Relevance of spatial heterogeneity of immune infiltration for predicting risk of recurrence after endocrine therapy of ER+ breast cancer. *JNCI J Natl Cancer Inst.* 2018;110:166–75. <https://doi.org/10.1093/jnci/djx137>.
43. Tsujikawa T, Mitsuda J, Ogi H, Miyagawa-Hayashino A, Konishi E, Itoh K, et al. Prognostic significance of spatial immune profiles in human solid cancers. *Cancer Sci.* 2020;111:3426–34. <https://doi.org/10.1111/cas.14591>.

44. Enfield KSS, Martin SD, Marshall EA, Kung SHY, Gallagher P, Milne K, et al. Hyperspectral cell sociology reveals spatial tumor-immune cell interactions associated with lung cancer recurrence. *J Immunother Cancer*. 2019;7:13. <https://doi.org/10.1186/s40425-018-0488-6>.
45. Ali HR, Jackson HW, Zanotelli VRT, Danenberg E, Fischer JR, Bardwell H, et al. Imaging mass cytometry and multiplatform genomics define the phenogenomic landscape of breast cancer. *Nat Cancer*. 2020;1:163–75. <https://doi.org/10.1038/s43018-020-0026-6>.
46. Keren L, Bosse M, Marquez D, West R, Bendall SC, Angelo M, et al. A structured tumor-immune microenvironment in triple negative breast cancer revealed by multiplexed ion beam imaging article a structured tumor-immune microenvironment in triple negative breast cancer revealed by multiplexed ion beam imaging. *Cell*. 2018;174:1373–87.e19. <https://doi.org/10.1016/j.cell.2018.08.039>.
47. Levy-Jurgenson A, Tekpli X, Kristensen VN, Yakhini Z. Spatial transcriptomics inferred from pathology whole-slide images links tumor heterogeneity to survival in breast and lung cancer. *Sci Rep*. 2020;10:18802. <https://doi.org/10.1038/s41598-020-75708-z>.
48. Mandal R, Samstein RM, Lee K-W, Havel JJ, Wang H, Krishna C, et al. Genetic diversity of tumors with mismatch repair deficiency influences anti-PD-1 immunotherapy response. *Science*. 2019;364:485–91. <https://doi.org/10.1126/science.aau0447>.
49. Salmon H, Franciszkiewicz K, Damotte D, Validire P, Trautmann A, Mami-chouaib F, et al. Matrix architecture defines the preferential localization and migration of T cells into the stroma of human lung tumors. *J Clin Invest*. 2012;122:899–910. <https://doi.org/10.1172/JCI45817DS1>.
50. Lanitis E, Dangaj D, Irving M, Coukos G. Mechanisms regulating T-cell infiltration and activity in solid tumors. *New Front Immunother*. 2017;28:xii18–32. <https://doi.org/10.1093/annonc/mdx238>.
51. Beatty GL, Chiorean EG, Fishman MP, Saboury B, Teitelbaum UR, Sun W, et al. CD40 agonists Alter tumor stroma and show efficacy against pancreatic carcinoma in mice and humans. *Science*. 2011;331:1612–6. <https://doi.org/10.1126/science.1198443>.
52. Clark M, Kroger CJ, Tisch RM. Type 1 diabetes: a chronic anti-self-inflammatory response. *Front Immunol*. 2017;8. <https://doi.org/10.3389/fimmu.2017.01898>.
53. Morgan NG, Leete P, Foulis AK, Richardson SJ. Islet inflammation in human type 1 diabetes mellitus. *IUBMB Life*. 2014;66:723–34. <https://doi.org/10.1002/iub.1330>.
54. Wedgwood KCA, Richardson SJ, Morgan NG, Tsaneva-Atanasova K. Spatiotemporal dynamics of insulinitis in human type 1 diabetes. *Front Physiol*. 2016;7:1–22. <https://doi.org/10.3389/fphys.2016.00633>.
55. Gall JG. The origin of in situ hybridization—a personal history Joseph. *Methods*. 2016;98:4–9. <https://doi.org/10.1016/j.ymeth.2015.11.026.The>.
56. Rudkin GT, Stollar BD. High resolution detection of DNA-RNA hybrids in situ by indirect immunofluorescence [29]. *Nature*. 1977;472–3. <https://doi.org/10.1038/265472a0>.
57. Raj A, van den Bogaard P, Rifkin SA, van Oudenaarden A, Tyagi S. Imaging individual mRNA molecules using multiple singly labeled probes. *Nat Methods*. 2008;5:877–9. <https://doi.org/10.1038/nmeth.1253>.
58. Lubeck E, Cai L. Single-cell systems biology by super-resolution imaging and combinatorial labeling. *Nat Methods*. 2012;9:743–8. <https://doi.org/10.1038/nmeth.2069>.
59. Chen KH, Boettiger AN, Moffitt JR, Wang S, Zhuang X. Spatially resolved, highly multiplexed RNA profiling in single cells. *Science*. 2015;348:1360–3. <https://doi.org/10.1126/science.aaa6090>.
60. Xia C, Fan J, Emanuel G, Hao J, Zhuang X. Spatial transcriptome profiling by MERFISH reveals subcellular RNA compartmentalization and cell cycle-dependent gene expression. *Proc Natl Acad Sci*. 2019;116:19490–9. <https://doi.org/10.1073/pnas.1912459116>.
61. Shah S, Lubeck E, Zhou W, Cai L. In situ transcription profiling of single cells reveals spatial organization of cells in the mouse hippocampus. *Neuron*. 2016;92:342–57. <https://doi.org/10.1016/j.neuron.2016.10.001>.

62. Eng C-HL, Lawson M, Zhu Q, Dries R, Koulena N, Takei Y, et al. Transcriptome-scale super-resolved imaging in tissues by RNA seqFISH+. *Nature*. 2019;568:235–9. <https://doi.org/10.1038/s41586-019-1049-y>.
63. Satija R, Farrell JA, Gennert D, Schier AF, Regev A. Spatial reconstruction of single-cell gene expression data. *Nat Biotechnol*. 2015;33:495–502. <https://doi.org/10.1038/nbt.3192>.
64. Wang X, Allen WE, Wright MA, Sylwestrak EL, Samusik N, Vesuna S, et al. Three-dimensional intact-tissue sequencing of single-cell transcriptional states. *Science*. 2018;361. <https://doi.org/10.1126/science.aat5691>.
65. Gradinaru V, Treweek J, Overton K, Deisseroth K. Hydrogel-tissue chemistry: principles and applications. *Annu Rev Biophys*. 2018;47:355–76. <https://doi.org/10.1146/annurev-biophys-070317-032905>.
66. Alon S, Goodwin DR, Sinha A, Wassie AT, Chen F, Daugharthy ER, et al. Expansion sequencing: spatially precise in situ transcriptomics in intact biological systems. *Science*. 2021;371. <https://doi.org/10.1126/science.aax2656>.
67. Wassie AT, Zhao Y, Boyden ES. Biological research. *Nat Methods*. 2019;16:33–41. <https://doi.org/10.1038/s41592-018-0219-4>.
68. Lee JH, Daugharthy ER, Scheiman J, Kalhor R, Ferrante TC, Terry R, et al. Fluorescent in situ sequencing (FISSEQ) of RNA for gene expression profiling in intact cells and tissues. *Nat Protoc*. 2015;10:442–58. <https://doi.org/10.1038/nprot.2014.191>.
69. Ståhl PL, Salmén F, Vickovic S, Lundmark A, Navarro JF, Magnusson J, et al. Visualization and analysis of gene expression in tissue sections by spatial transcriptomics. *Science*. 2016;353:78–82. <https://doi.org/10.1126/science.aaf2403>.
70. Illumina. Resolve the whole transcriptome within tissue architecture [Internet]. 2021. <https://www.illumina.com/content/dam/illumina/gcs/assembled-assets/marketing-literature/10x-visium-tech-note-m-gl-00177/10x-visium-tech-note-m-gl-00177.pdf>.
71. Rodrigues SG, Stickels RR, Goeva A, Martin CA, Murray E, Vanderburg CR, et al. Slide-seq: a scalable technology for measuring genome-wide expression at high spatial resolution. *Science*. 2019;363:1463–7. <https://doi.org/10.1126/science.aaw1219>.
72. Stickels RR, Murray E, Kumar P, Li J, Marshall JL, Di Bella DJ, et al. Highly sensitive spatial transcriptomics at near-cellular resolution with slide-seqV2. *Nat Biotechnol*. 2021;39:313–9. <https://doi.org/10.1038/s41587-020-0739-1>.
73. Vickovic S, Eraslan G, Salmén F, Klughammer J, Stenbeck L, Schapiro D, et al. High-definition spatial transcriptomics for in situ tissue profiling. *Nat Methods*. 2019;16:987–90. <https://doi.org/10.1038/s41592-019-0548-y>.
74. Cho C-S, Xi J, Si Y, Park S-R, Hsu J-E, Kim M, et al. Microscopic examination of spatial transcriptome using Seq-Scope. *Cell*. 2021;184:3559–72.e22. <https://doi.org/10.1016/j.cell.2021.05.010>.
75. Fu X, Sun L, Chen JY, Dong R, Lin Y, Palmiter RD, et al. Continuous polony gels for tissue mapping with high resolution and RNA capture efficiency. *bioRxiv*. 2021; 2021.03.17.435795
76. Liu Y, Yang M, Deng Y, Su G, Enniful A, Guo CC, et al. High-spatial-resolution multi-omics sequencing via deterministic barcoding in tissue. *Cell*. 2020;183:1665–81.e18. <https://doi.org/10.1016/j.cell.2020.10.026>.
77. Emmert-Buck MR, Bonner RF, Smith PD, Chuaqui RF, Zhuang Z, Goldstein SR, et al. Laser capture microdissection. *Science*. 1996;274:998–1001. <https://doi.org/10.1126/science.274.5289.998>.
78. Chen J, Suo S, Tam PP, Han J-DJ, Peng G, Jing N. Spatial transcriptomic analysis of cryosectioned tissue samples with Geo-seq. *Nat Protoc*. 2017;12:566–80. <https://doi.org/10.1038/nprot.2017.003>.
79. Medaglia C, Giladi A, Stoler-Barak L, De Giovanni M, Salame TM, Biram A, et al. Spatial reconstruction of immune niches by combining photoactivatable reporters and scRNA-seq. *Science*. 2017;358:1622–6. <https://doi.org/10.1126/science.aao4277>.

80. Genshaft AS, Ziegler CGK, Tzouanas CN, Mead BE, Jaeger AM, Navia AW, et al. Live cell tagging tracking and isolation for spatial transcriptomics using photoactivatable cell dyes. *Nat Commun.* 2021;12:4995. <https://doi.org/10.1038/s41467-021-25279-y>.
81. van der Leun AM, Hoekstra ME, Reinalda L, Scheele CLGJ, Toebes M, van de Graaff MJ, et al. Single-cell analysis of regions of interest (SCARI) using a photosensitive tag. *Nat Chem Biol.* 2021;17:1139–47. <https://doi.org/10.1038/s41589-021-00839-x>.
82. Hu KH, Eichorst JP, McGinnis CS, Patterson DM, Chow ED, Kersten K, et al. ZipSeq: barcoding for real-time mapping of single cell transcriptomes. *Nat Methods.* 2020;17:833–43. <https://doi.org/10.1038/s41592-020-0880-2>.
83. Beechem JM. High-plex spatially resolved RNA and protein detection using digital spatial profiling: a technology designed for immuno-oncology biomarker discovery and translational research. *Methods Mol Biol.* 2020:563–83. https://doi.org/10.1007/978-1-4939-9773-2_25.
84. Stoeckius M, Hafemeister C, Stephenson W, Houck-Loomis B, Chattopadhyay PK, Swerdlow H, et al. Simultaneous epitope and transcriptome measurement in single cells. *Nat Methods.* 2017;14:865–8. <https://doi.org/10.1038/nmeth.4380>.
85. Dixit A, Parnas O, Li B, Weissman JS, Friedman N, Dixit A, et al. Perturb-Seq : dissecting molecular circuits with scalable single-cell RNA profiling of pooled genetic resource perturb-Seq : dissecting molecular circuits with scalable single-cell RNA profiling of pooled genetic screens. *Cell.* 2016;167:1853–7.e17. <https://doi.org/10.1016/j.cell.2016.11.038>.
86. Lee Y, Bogdanoff D, Wang Y, Hartoularos GC, Woo JM, Mowery CT, et al. XYZeq: spatially resolved single-cell RNA sequencing reveals expression heterogeneity in the tumor microenvironment. *Sci Adv.* 2021;7:1–15. <https://doi.org/10.1126/sciadv.abg4755>.
87. Srivatsan SR, Regier MC, Barkan E, Franks JM, Packer JS, Grosjean P, et al. Embryo-scale, single-cell spatial transcriptomics. *Science.* 2021;373:111–7. <https://doi.org/10.1126/science.abb9536>.
88. Cao J, Packer JS, Ramani V, Cusanovich DA, Huynh C, Daza R, et al. Comprehensive single-cell transcriptional profiling of a multicellular organism. *Science.* 2017;357:661–7. <https://doi.org/10.1126/science.aam8940>.
89. Daley T, Smith AD. Predicting the molecular complexity of sequencing libraries. *Nat Methods.* 2013;10:325–7. <https://doi.org/10.1038/nmeth.2375>.
90. Kharchenko PV, Silberstein L, Scadden DT. Bayesian approach to single-cell differential expression analysis. *Nat Methods.* 2014;11:740–2. <https://doi.org/10.1038/nmeth.2967>.
91. Saliba A-E, Westermann AJ, Gorski SA, Vogel J. Single-cell RNA-seq: advances and future challenges. *Nucleic Acids Res.* 2014;42:8845–60. <https://doi.org/10.1093/nar/gku555>.
92. Lovén J, Orlando DA, Sigova AA, Lin CY, Rahl PB, Burge CB, et al. Revisiting global gene expression analysis. *Cell.* 2012;151:476–82. <https://doi.org/10.1016/j.cell.2012.10.012>.
93. Wang J, Rieder SA, Wu J, Hayes S, Halpin RA, de los Reyes M, et al. Evaluation of ultra-low input RNA sequencing for the study of human T cell transcriptome. *Sci Rep.* 2019;9:8445. <https://doi.org/10.1038/s41598-019-44902-z>.
94. Wang X, He Y, Zhang Q, Ren X, Zhang Z. Direct comparative analyses of 10X genomics chromium and smart-seq2. *Genomics Proteomics Bioinformatics.* 2021;19:253–66. <https://doi.org/10.1016/j.gpb.2020.02.005>.
95. Xing F, Yang L. Robust nucleus/cell detection and segmentation in digital pathology and microscopy images: a comprehensive review. *IEEE Rev Biomed Eng.* 2016;9:234–63. <https://doi.org/10.1109/RBME.2016.2515127>.
96. Kokkat TJ, Patel MS, McGarvey D, LiVolsi VA, Baloch ZW. Archived formalin-fixed paraffin-embedded (FFPE) blocks: a valuable underexploited resource for extraction of DNA, RNA, and protein. *Biopreserv Biobank.* 2013;11:101–6. <https://doi.org/10.1089/bio.2012.0052>.
97. von Ahlfen S, Missel A, Bendrat K, Schlumpberger M. Determinants of RNA quality from FFPE samples. *PLoS One.* 2007;2:e1261. <https://doi.org/10.1371/journal.pone.0001261>.

98. Foster DS, Januszyk M, Yost KE, Chinta MS, Gulati GS, Nguyen AT, et al. Integrated spatial multiomics reveals fibroblast fate during tissue repair. *Proc Natl Acad Sci.* 2021;118:e2110025118. <https://doi.org/10.1073/pnas.2110025118>.
99. Rosenthal R, Cadieux EL, Salgado R, Al BM, Moore DA, Hiley CT, et al. Neoantigen-directed immune escape in lung cancer evolution. *Nature.* 2019;567:479–85. <https://doi.org/10.1038/s41586-019-1032-7>.
100. Hoekstra ME, Bornes L, Dijkgraaf FE, Philips D, Pardieck IN. Long-distance modulation of bystander tumor cells by CD8 + T cell-secreted IFN γ . *Nat Cancer.* 2020;
101. Nieto P, Elosua-Bayes M, Trincado JL, Marchese D, Massoni-Badosa R, Salvany M, et al. A single-cell tumor immune atlas for precision oncology. *Genome Res.* 2021;31:1913–26. <https://doi.org/10.1101/gr.273300.120>.
102. Elosua-Bayes M, Nieto P, Mereu E, Gut I, Heyn H. SPOTlight: seeded NMF regression to deconvolute spatial transcriptomics spots with single-cell transcriptomes. *Nucleic Acids Res.* 2021;49:e50. <https://doi.org/10.1093/nar/gkab043>.
103. Ji AL, Rubin AJ, Thrane K, Jiang S, Reynolds DL, Meyers RM, et al. Multimodal analysis of composition and spatial architecture in human squamous cell carcinoma. *Cell.* 2020;182:497–514.e22. <https://doi.org/10.1016/j.cell.2020.05.039>.
104. Nagasawa S, Kuze Y, Maeda I, Kojima Y, Motoyoshi A, Onishi T, et al. Genomic profiling reveals heterogeneous populations of ductal carcinoma in situ of the breast. *Commun Biol.* 2021;4:438. <https://doi.org/10.1038/s42003-021-01959-9>.
105. Attalla S, Taifour T, Bui T, Muller W. Insights from transgenic mouse models of PyMT-induced breast cancer: recapitulating human breast cancer progression in vivo. *Oncogene.* 2021;40:475–91. <https://doi.org/10.1038/s41388-020-01560-0>.
106. Kersten K, Hu KH, Combes AJ, Samad B, Harwin T, Ray A, et al. Spatiotemporal co-dependency between macrophages and exhausted CD8 + T cells in cancer. *bioRxiv.* 2021:1–37. <https://doi.org/10.1101/2021.09.27.461866>.
107. Vogel C, Marcotte EM. Insights into the regulation of protein abundance from proteomic and transcriptomic analyses. *Nat Rev Genet.* 2012;13:227–32. <https://doi.org/10.1038/nrg3185>.
108. Edfors F, Danielsson F, Hallström BM, Käll L, Lundberg E, Pontén F, et al. Gene-specific correlation of RNA and protein levels in human cells and tissues. *Mol Syst Biol.* 2016;12:883. <https://doi.org/10.15252/msb.20167144>.
109. Hara T, Chanoch-Myers R, Mathewson ND, Myskiw C, Atta L, Bussema L, et al. Interactions between cancer cells and immune cells drive transitions to mesenchymal-like states in glioblastoma. *Cancer Cell.* 2021;39:779–92.e11. <https://doi.org/10.1016/j.ccell.2021.05.002>.
110. Pelka K, Hofree M, Chen JH, Sarkizova S, Pirl JD, Jorgji V, et al. Spatially organized multicellular immune hubs in human colorectal cancer. *Cell.* 2021;184:4734–52.e20. <https://doi.org/10.1016/j.cell.2021.08.003>.
111. De Giovanni M, Cutillo V, Giladi A, Sala E, Maganuco CG, Medaglia C, et al. Spatiotemporal regulation of type I interferon expression determines the antiviral polarization of CD4+ T cells. *Nat Immunol.* 2020;21:321–30. <https://doi.org/10.1038/s41590-020-0596-6>.
112. Xiang M, Grosso RA, Takeda A, Pan J, Bekkhus T, Brulois K, et al. A single-cell transcriptional roadmap of the mouse and human lymph node lymphatic vasculature. *Front Cardiovasc Med.* 2020;7. <https://doi.org/10.3389/fcvm.2020.00052>.
113. Schultze JL, Aschenbrenner AC. COVID-19 and the human innate immune system. *Cell.* 2021;184:1671–92. <https://doi.org/10.1016/j.cell.2021.02.029>.
114. Delorey TM, Ziegler CGK, Heimberg G, Normand R, Yang Y, Segerstolpe Å, et al. COVID-19 tissue atlases reveal SARS-CoV-2 pathology and cellular targets. *Nature.* 2021;595:107–13. <https://doi.org/10.1038/s41586-021-03570-8>.
115. Carlberg K, Korotkova M, Larsson L, Catrina AI, Ståhl PL, Malmström V. Exploring inflammatory signatures in arthritic joint biopsies with spatial transcriptomics. *Sci Rep.* 2019;9:1–10. <https://doi.org/10.1038/s41598-019-55441-y>.

116. Hardt AU, Carlberg K, Klint E, Sahlström P, Van Vollenhoven A, Machado SH, et al. Integrated single cell and spatial transcriptomics reveal autoreactive differentiated B cells in joints of early rheumatoid arthritis. medRxiv. 2021;
117. Dries R, Zhu Q, Dong R, Eng C-HL, Li H, Liu K, et al. Giotto: a toolbox for integrative analysis and visualization of spatial expression data. *Genome Biol.* 2021;22:78. <https://doi.org/10.1186/s13059-021-02286-2>.
118. Sun S, Zhu J, Zhou X. Statistical analysis of spatial expression patterns for spatially resolved transcriptomic studies. *Nat Methods.* 2020;17:193–200. <https://doi.org/10.1038/s41592-019-0701-7>.
119. Avila Cobos F, Alquicira-Hernandez J, Powell JE, Mestdagh P, De Preter K. Benchmarking of cell type deconvolution pipelines for transcriptomics data. *Nat Commun.* 2020;11:5650. <https://doi.org/10.1038/s41467-020-19015-1>.
120. Kleshchevnikov V, Shmatko A, Dann E, Aivazidis A, King HW, Li T, et al. Comprehensive mapping of tissue cell architecture via integrated single cell and spatial transcriptomics. *bioRxiv.* 2020; 2020.11.15.378125
121. Cable DM, Murray E, Zou LS, Goeva A, Macosko EZ, Chen F, et al. Robust decomposition of cell type mixtures in spatial transcriptomics. *Nat Biotechnol.* 2021; <https://doi.org/10.1038/s41587-021-00830-w>.
122. Jin S, Guerrero-Juarez CF, Zhang L, Chang I, Ramos R, Kuan C, et al. Inference and analysis of cell-cell communication using CellChat. *Nat Commun.* 2021;12:1088. <https://doi.org/10.1038/s41467-021-21246-9>.
123. Efremova M, Vento-tormo M, Teichmann SA. CellPhoneDB: inferring cell—cell communication from combined expression of multi-subunit ligand—receptor complexes. *Nat Protoc.* 2020;15. <https://doi.org/10.1038/s41596-020-0292-x>.
124. Browaeys R, Saelens W, Saeys Y. NicheNet: modeling intercellular communication by linking ligands to target genes. *Nat Methods.* 2020;17:159–62. <https://doi.org/10.1038/s41592-019-0667-5>.
125. Armingol E, Baghdassarian HM, Martino C, Perez-Lopez A, Knight R, Lewis NE. Context-aware deconvolution of cell-cell communication with tensor-cell2cell. *bioRxiv.* 2021; 2021.09.20.461129
126. Tanevski J, Ramirez Flores RO, Gabor A, Schapiro D, Saez-Rodriguez J. Explainable multi-view framework for dissecting inter-cellular signaling from highly multiplexed spatial data. *bioRxiv.* 2020; <https://doi.org/10.1101/2020.05.08.084145>.
127. Cang Z, Nie Q. Inferring spatial and signaling relationships between cells from single cell transcriptomic data. *Nat Commun:*1–13. <https://doi.org/10.1038/s41467-020-15968-5>.
128. Kim J, Koo B, Knoblich JA. Human organoids: model systems for human biology and medicine. *Nat Rev Mol Cell Biol.* 2020;21:571–84. <https://doi.org/10.1038/s41580-020-0259-3>.
129. Hao Y, Hao S, Andersen-nissen E, Gottardo R, Smibert P, Hao Y, et al. Integrated analysis of multimodal single-cell data. *Cell.* 2021;184:3573–87. <https://doi.org/10.1016/j.cell.2021.04.048>.
130. Klein AM, Mazutis L, Akartuna I, Tallapragada N, Veres A, Li V, et al. Droplet barcoding for single-cell transcriptomics applied to embryonic stem cells. *Cell.* 2015;161:1187–201. <https://doi.org/10.1016/j.cell.2015.04.044>.
131. Macosko EZ, Basu A, Satija R, Nemes J, Shekhar K, Goldman M, et al. Highly parallel genome-wide expression profiling of individual cells using nanoliter droplets. *Cell.* 2015;161:1202–14. <https://doi.org/10.1016/j.cell.2015.05.002>.